Fatigue Testing and Analysis under Variable Amplitude Loading Conditions

STP 1439

Peter C. McKeighan
Narayanaswami Ranganathan

ASTM
INTERNATIONAL
Standards Worldwide

STP 1439

Fatigue Testing and Analysis Under Variable Amplitude Loading Conditions

Peter C. McKeighan and Narayanaswami Ranganathan, editors

ASTM Stock Number: STP1439

ASTM
100 Barr Harbor Drive
PO Box C700
West Conshohocken, PA 19428-2959

INTERNATIONAL

Printed in the U.S.A.

Library of Congress Cataloging-in-Publication Data

Fatigue testing and analysis under variable amplitude loading conditions/Peter C. McKeighan and Narayanaswami Ranganathan, editors.

p. cm.—(STP; 1439)

"ASTM Stock Number: STP 1439."

Includes bibliographical references and index.

ISBN 0-8031-3479-7 (alk. paper)

1. Materials—Fatigue—Testing—Congresses. I. McKeighan, P. C. (Peter C.) II. Ranganathan, Narayanaswami. III. Series: ASTM special technical publication; 1439.

TA418.38.F378 2005
620.1'126'0287—dc22

2005004747

Peer Review Policy

Each paper published in this volume was evaluated by two peer reviewers and at least one editor. The authors addressed all of the reviewers' comments to the satisfaction of both the technical editor(s) and the ASTM International Committee on Publications.

To make technical information available as quickly as possible, the peer-reviewed papers in this publication were prepared "camera-ready" as submitted by the authors.

The quality of the papers in this publication reflects not only the obvious efforts of the authors and the technical editor(s), but also the work of the peer reviewers. In keeping with long-standing publication practices, ASTM International maintains the anonymity of the peer reviewers. The ASTM International Committee on Publications acknowledges with appreciation their dedication and contribution of time and effort on behalf of ASTM International.

Printed in Mayfield, PA
May 2005

Foreword

The Symposium on Fatigue Testing and Analysis Under Variable Amplitude Loading Conditions was a joint international event conducted by ASTM International Committee E08 on Fatigue and Fracture and the Fatigue Commision of French Metallurgical and Materials society (SF2M).

The symposium was chaired by Dr. Peter C. McKeighan, Southwest Research Institute, San Antonio, Texas, USA and Professor Narayanaswami Ranganathan, Laboratoire de Mécanique et Rhéologie, University François Rabelais de Tours, Tours, France.

The symposium was held from 29–31 May 2002 in the prestigeous town hall of the city of Tours (Hotel de Ville).

The following two pages show the highlights of the three day symposium. The Symposium would not have been as successful as it was without the assistance from the city of Tours, the Ecole Polytechnique (Département Productique), the University of Tours and all of the other kind sponsors.

There are a number of groups that had a significant impact on the organization of the meeting. These groups functioned at a variety of different levels and are described further below.

INTERNATIONAL SCIENTIFIC COMMITEE

A. Bignonnet (France), A. Braun (USA), A. Davy (France), A de Koning (Holland), K. Donald (USA), G. Glinka (Canada), R. L. Hewitt (Canada), G. Marquis (Finland), E. Macha (Poland), J. C. Newman (USA), I. Sinclair (UK), C. M. Sonsino (Germany) and M. Thomsen (USA).

ORGANIZING COMMITEE

Chairmen: P. C. McKeighan (SwRI, USA), N. Ranganathan (LMR, EIT)

Members: C. Amzallag (EDF), C. Bathias (CNAM), G. Baudry (Ascometal Creas), A. Bignonnet (PSA), J. F. Flavenot (CETIM), Y. Franchot (SF2M), A. Galtier (Usinor R&D), G. Henaff (ENSMA), M. Huther (Bureau Veritas), H. P. Lieurade (CETIM), J. Petit (ENSMA), P. Rabbe (CEM), L. Remy (ENSM Paris), J. Renard (ENSM Paris).

LOCAL ORGANIZING COMMITTEE

D. Sigli, L. Vet, N. Ranganathan, D. Ouahabi, A. Tougui, R. Leroy, O. Girard, P. Meichel, F. Lacroix.

FIG. 1—*Attentive audience.*

FIG. 2—*Welcome speech by the Mayor of Tours, M. Jean Germain, M. Ranganathan helps with the translation.*

FIG. 3—*Distinguished audience—listening to the mayor's speech.*

FIG. 4—*Concert by the children's choir.*

FIG. 5—*The students of the Polytechnique school who helped with organizing the meeting.*

FIG. 6—*A view of the ceiling of the Historic Town Hall of Tours.*

FIG. 7—*One of the speakers.*

FIG. 8—*Discussion in the corridor—Dr. Pete McKeighan.*

Contents

Other Applications

Load Interaction

Probabilistic and Multiaxial Effects

Overview

The type of loading that a fatigue critical structure is subjected to depend largely on what the function of the structure is and what controls the loading applied. In some cases, for instance rotating machinery for power generation, the loading can be adequately simplified and represented by a constant load amplitude cycle. In this case, loading is dictated by function on an angular rotation-by-rotation basis. This is contrasted to the case of a fighter airplane where the loading is dictated by external aerodynamic loads combined with highly variable pilot inputs. In many cases, the use and function of a structure can significantly impact the loading. An example of this is the case of a passenger aircraft where taxis, takeoff, cruise at altitude and landing dictate a primary loading cycle. Given that most of the service time is spent at cruise, the magnitude of the repeated load for the fuselage is largely driven by the cabin pressurization.

Whatever the source and magnitude of the cyclic loading, the challenge for the structural engineer is to determine the amplitude of the variable amplitude spectrum loading and simplify it in a manner that can then be combined with analytical fatigue design approaches to adequately size the structure. Design tools and approaches have been available for many years to assist in accomplishing this objective. The term 'fatigue' was originally coined by Wohler in the 1840's when he examined railroad car axle failures. Sixty years later Goodman and Basquin examined the mean stress effect and developed the stress-life approach to design. The second World War spurred a significant amount of activity including development of the concept of linear damage as postulated by Palmgren and Miner. Methods to design and maintain aircraft when cracks are growing in a structure were developed after a series of high profile failures in the 1970's by the USAF. All of these developments have culminated in the design tools now available to treat fatigue crack initiation and propagation under variable amplitude loading.

Applying these fatigue design strategies often requires a significant mechanical testing effort to *tune* the analytical models to predict actual laboratory observation. Hampering this process is the absence of any standardized test method to perform fatigue testing under spectrum loading conditions. While standards have been developed to characterize material responses to fatigue loading, no methods yet exist for the more complicated spectrum loading test and laboratories have consequently developed their own custom approaches. Although little standardization also exists for fatigue analyses, there are some accepted methods and techniques available for treating variable amplitude loading. Nevertheless each organization that performs this type of work tends to have customized the methods to suit their needs and specific approaches. One of the primary goals of this symposium was to provide a forum to communicate amongst technical professionals involved in this type of work. Applications reported on include those focused purely on testing, fatigue design techniques/approaches as well as a combination of both.

The technical papers in this book represent peer reviewed and approved papers of those presented at an international symposium focused on fatigue testing and analysis under variable amplitude spectrum loading conditions. To aid in assimilating this information, the papers are categorized into six sections: Fatigue Testing, Aerospace Applications, Design Approach and Modelling, Other Applications, Load Interaction, and Probabilistic and Multiaxial Approaches.

The first section begins with a historical overview paper by Sonsino, which presents the development of variable amplitude tests starting with the approach of Gassner in the 1930's. This paper lays the groundwork and background for the scientific problems addressed in the remainder of the symposium. The paper by Hopkins et al. presents the efforts made by different non-ASTM standardization organizations to develop a future standard for carrying out variable amplitude fatigue tests. This is followed by another standardization-related paper by McKeighan and McMaster presenting a framework for a standardization approach for fatigue crack growth testing under spectrum loading conditions. Donald and George follow this paper with an examination of a state-of-the-art variable load amplitude test control and monitoring system. The paper by Pöting et al presents a variable amplitude test facility using resonance principles. This is followed by a paper by George et al examining non-visual crack length calibration issues associated with part-through cracked specimens.

The section addressing aerospace applications leads off with three papers addressing full-scale aircraft testing. A paper by Sullentrup discusses one organization's experiences during full-scale testing of the F/A-18. Hewitt et al then discuss Canadian experiences on spectrum editing of a fighter aircraft wing. Loading spectra complications associated with commercial aircraft are then addressed in a paper by Le Divenah and Beaufils associated with spectrum testing Airbus aircraft. This is followed by a paper by Yanishevsky and Everett that examines the spectrum fatigue tests carried out on the CF188 Hornet in Canada. Transient load effects at different temperatures in a titanium alloy are next examined in a paper by Stephens et al. McMaster and McKeighan examine the topic of life improvement of fastener holes under spectrum loading considering the effect of cold working and different fastener geometries. This paper is followed by one by Gérard et al showing that fatigue crack initiation life can be treated as a short crack growth life considering the proper crack configuration. The section concludes with a paper by Tumanov presenting random fatigue tests for aircraft engine fan blades, using an equivalent load amplitude concept.

The paper by Marquis et al opens the section on design approaches and modelling with an examination of a high cycle variable amplitude fatigue test program on a nodular cast iron where a fracture mechanics based closure model is used to correlate the data. Newman and Phillips then explore the life prediction capability of a plasticity induced closure model applied to selected variable amplitude tests in a titanium alloy. This is followed by a paper by Ball examining a fracture mechanics approach to notch tip plasticity effects. McClung et al continue discussions of strip yield models, in this case examining spectrum loading on aluminum alloy materials. Sunder et al assess the broader implications of variable amplitude fatigue loading examining multiple mechanisms. This is followed by a paper by Song et al who show that fatigue life under selected narrow and broadband loading can be modelled using crack closure concepts for short and long cracks. Stress intensity factor calculation is addressed by Wu et al under complex stress conditions. The section concludes with a paper by El-Ratal et al concerning fatigue life modelling and accelerated testing.

The next section opens with a paper by McEvily et al examining reasons why the Palmgren-Miner rule deviates from unity with examinations of three variable amplitude loading conditions. Thomas et al then address some of the issues related to fatigue testing in the automotive world. Continuing in the automotive vane, Morel and Ranganathan then examine high cycle fatigue testing and analysis using a car wheel loading sequence. This is followed by a paper by Petermann et al considering composite materials and examining a two-stress block loading that exhibited load-sequencing effects. Tomita et al who again showed with analysis and experiment clear sequence effects then examine fatigue loading of ship structure with a paper. The section concludes with a paper by Hünecke and Schöne examining short crack behavior as applied to low carbon steel.

The section of the book examining load interaction opens with a paper by Romeiro et al who studied load interaction in carbon steel concluding that interaction effects are closely related to the cyclic plastic zone size and Bauschinger effect. Two papers continue with load interaction examining overload effects including (a) Ranganathan et al who examine plasticity and environmental considerations testing 7075 and 2024 alloy and (b) Tabernig et al who examined primarily the near threshold regime for two different aluminum alloys. Darcis and Recho deal with the reliability analysis of welded specimens using a probabilistic approach to the overload effect. Finally, the paper by Aubin et al deals with the effect of load history examining strain amplitude and loading path on duplex stainless steel.

The final section is devoted to probabilistic and multiaxial approaches starting with a paper by Akpan et al developing a fuzzy probabilistic approach to aircraft components that permits the estimations of the distribution of reliability index and failure probability. Huther et al focuses on the development of a probabilistic approach used in the ship building industry. The paper by Łagoda et al compare a rain flow analysis and that based on power spectral density to fatigue life estimations under uniaxial and multiaxial loadings. A paper by Fischer follows this on multiaxial laboratory tests on complex automotive structures. Finally, the paper by Banvillet et al applies different multiaxial fatigue damage models to the life estimation under random loading for tension and bending conditions.

In conclusion, this book reflects the state-of-the-art in fatigue testing and analysis under variable amplitude loading and can therefore serve as an important reference for engineers and scientists for years to come.

Finally, we regret to report that one of the authors, Michael Sullentrup, recently passed away under tragic circumstances. We offer our heartfelt condolences to his family. Many of us will miss Mike's wisdom, humor and technical contributions to the fatigue testing world.

Peter C. McKeighan
Southwest Research Institute
San Antonio, Texas
Symposium Co-chairman and Editor

Narayanaswami Ranganathan
University François Rabelais de Tours
Tours, France
Symposium Co-chairman and Editor

FATIGUE TESTING AND LABORATORY EXPERIENCE

Journal of ASTM International, Nov./Dec. 2004, Vol. 1, No. 10
Paper ID JAI19018
Available online at www.astm.org

Cetin Morris Sonsino[1]

Principles of Variable Amplitude Fatigue Design and Testing

ABSTRACT: The proper consideration of variable amplitude loading by utilizing service spectra and appropriate Gassner-lines is essential for the design of light-weight components and structures by allowing loads in significant excess of the Woehler-line (S-N curve). This permits higher stresses than under constant amplitude loading and renders reduced component dimensions. Reliable reconstitution and simulation methods for service load-time histories require not only the rainflow matrices, but also information about the order of the cycles described by Markovian matrices, the power spectral density and, for multiaxial applications, the cross-correlations between the particular load directions as well as the phase relations. A major problem in numerical fatigue life assessment is still the fatigue life calculations for spectrum loading, because of the scattering of the real damage sum D over a wide range, which is not entirely understood. These findings demonstrate the need for experimental spectrum tests, which are indispensable for ensuring the safety of parts. With regard to safety and liability requirements, the failure probability resulting from the probability of occurrence of the spectrum, from the scattering of the fatigue strength and from the failure criterion (technical crack or propagation), must be taken into account.

KEYWORDS: variable amplitude fatigue, design and test spectra, damage accumulation, rainflow counting, reconstitution, fatigue life assessment, experimental proof

Nomenclature

A_5	elongation
C	probability of confidence
D	damage sum
F	load
I	irregularity factor
K_t	theoretical stress concentration factor
L	fatigue life
L_s	spectrum size
N, $\bar{N}$	number of cycles, constant and variable amplitude loading
N_k	fatigue life at knee point
P_s, P_f, P_o	probability of survival, failure, occurrence
R_m, $R_{po,2}$	strength, ultimate, yield
R_x, $\bar{R}_x$	load, stress or strain ratio, $R_x = X_{min}/X_{max}$, for constant and variable amplitude loading
T_N, $\bar{T}_N$	fatigue life scatter between P_s = 10 and 90 %, for constant and variable amplitude loading
Z	area reduction

Manuscript received 16 April 2002; accepted for publication 17 July 2003; published November 2004. Presented at ASTM Symposium on Fatigue Testing and Analysis Under Variable Amplitude Loading Conditions on 29 31 May 2002 in Tours, France; P. C. McKeighan and N. Ranganathan, Guest Editors.

[1] Professor, Fraunhofer-Institute for Structural Durability (LBF), Bartningstr. 47, D-64289 Darmstadt, Germany.

ε, $\bar{\varepsilon}$ strain, constant and variable amplitude loading
σ, $\bar{\sigma}$ stress, constant and variable amplitude loading
σ_{ak} knee point of the S-N curve
a amplitude
f frequency, failure
$j_{R,C}$ risk factor
j_N safety factor
k, $\bar{k}$ slope of the fatigue life curve, for constant and variable amplitude loading
l longitudinal
m mean
n number of tests, number of cycles
s_N standard deviation
t time

Introduction

The assessment of the service durability of components and structures has become more important in a variety of technical areas, such as vehicles (automotive, railway), aeronautics, transportation, energy production, heavy machinery, and maritime technology, with regard to the increasing trend toward light-weight constructions and greater demands concerning costs, reduction of time-to-market periods, product safety, and liability. In order to fulfill these demands, numerical and experimental methods must be applied for effective development and proof of products. This survey focuses on variable amplitude fatigue design and testing, which also may be influenced by other aspects of structural durability, such as special loads (overloads, buckling, impact), creep, and wear (Fig. 1).

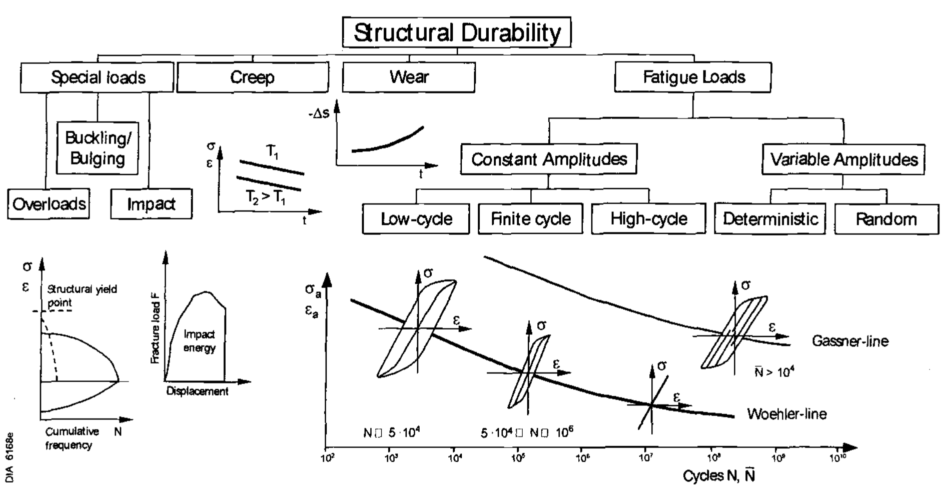

FIG. 1 *Partition of structural durability.*

Historical Background

With regard to variable amplitude loading, the importance of load spectra was recognized by Ernst Gassner, who, in 1939, was the first to formulate a procedure for simulating variable amplitude loading: the historical blocked program sequence (Fig. 2) with a Gaussian-like distribution of loads [1].

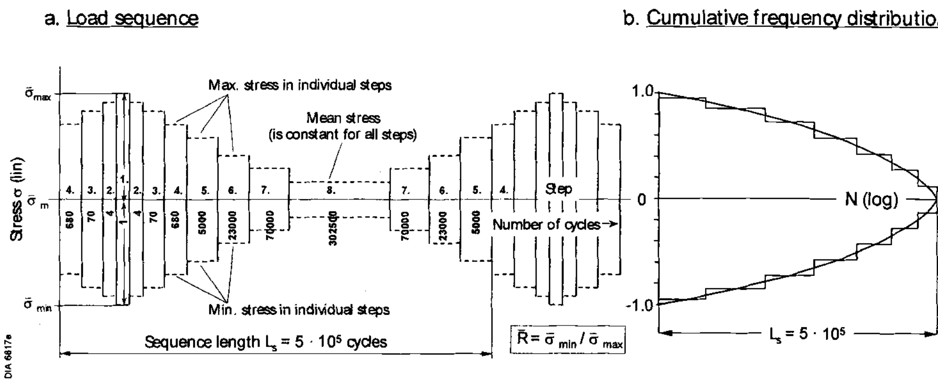

FIG. 2 *Ernst Gassner's historical 8 step-blocked-program-sequence (1939).*

This sequence was used frequently as a standard into the 1970s, until blocked program tests were replaced by random load sequences applied with modern servo-hydraulic actuators. In the meantime, different standardized load spectra for different application areas were developed, mainly for testing and comparisons [2]. Computer controlled multiaxial test facilities for the experimental proof testing of structures and units, the establishment of new counting methods (rain-flow), spectrum generation, and local concepts based on continuum and fracture mechanics accompanied these developments [3].

Spectrum and Structural Dimensions

Variable amplitude loading is often discussed in the context of fatigue life assessment, forgetting the main benefit recognized by Gassner, namely the influence of spectrum loading on fatigue life and especially fatigue strength with regard to structural dimensions. Figure 3 shows the Woehler- and Gassner-curves for a steering rod tested under constant amplitude loading (rectangular spectrum), a Gaussian spectrum, and a straight-line spectrum. The fatigue life curves (Gassner line) correspond to variable amplitude loading, while the S-N curve (Woehler line) relates to constant amplitude loading conditions.

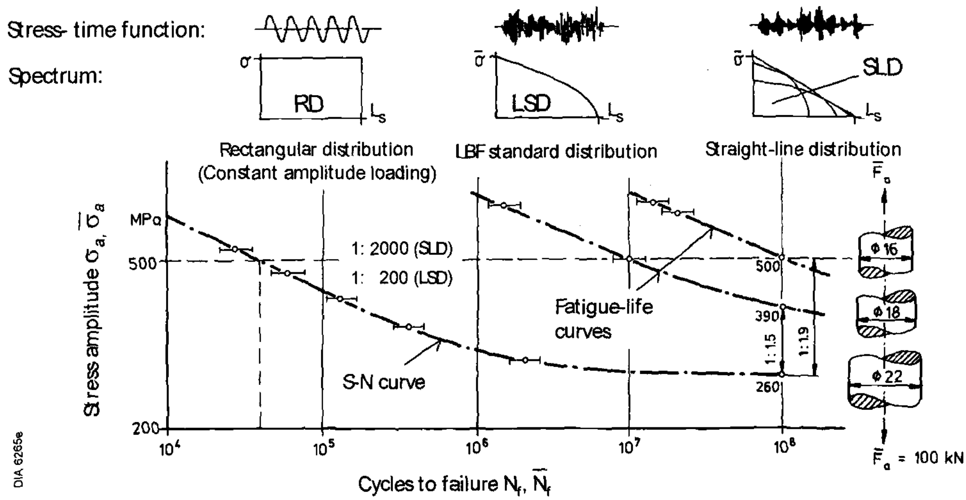

FIG. 3 *Influence of spectrum-shape on fatigue life and component dimensions.*

Fatigue life is seen to increase with decreasing fullness of the spectrum: the higher the amount of small amplitudes, the longer the fatigue life. On the other hand, the increasing fatigue life displayed by the position of the Gassner-curves can be exploited for the reduction of dimensions; for a fatigue life of 10^8 variable amplitude cycles of a steering rod, the maximum endurable stresses are 50 100 % higher than the constant amplitude fatigue limit, depending on the spectrum shape. So significant reductions of cross-sectional size and component weight can be realized; however, it must also be ascertained that an impact load does not lead to a catastrophic (brittle) failure, if a crack should be present. This last example underlines the contribution of spectrum shape to light-weight design.

Testing and Presentation of Results

A further important issue in variable amplitude loading is the method used for testing and the presentation of results. Tests are carried out using a load sequence which is defined by the load-time history; the maximum value of the load; strain or stress amplitude, $\bar{F}_a$, $\bar{\varepsilon}_a$, or $\bar{\sigma}_a$; the ratio between the minimum and maximum values $\bar{R}$; the sequence length L_S; and the spectrum shape (cumulative frequency distributions according to different cycle counting methods). In cases where not single components but systems are tested, the power spectral density distribution is an additional piece of necessary information [4,5]. Tests are carried out at different load levels, repeating the sequence until failure (defined crack depth or length, deformation, or total rupture). The only variable is the load, which affects the level of all amplitudes and mean values, and is linearly amplified or reduced (Fig. 4). It is obvious that the amount of repetition of the sequence is larger on a lower level than on a higher level. A variable amplitude test is valid only when the sequence is repeated more than five to ten times [6].

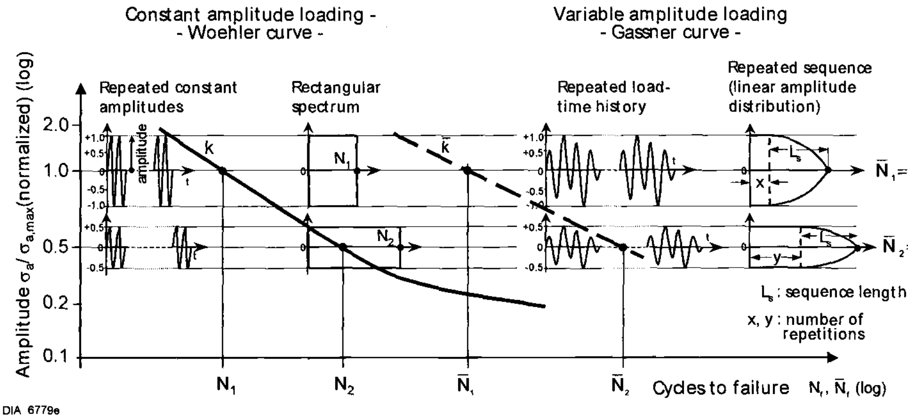

FIG. 4 *Performance of variable amplitude tests and presentation of results.*

According to Gassner, results are presented via the maximum load (strain or stress) amplitude and the number of cycles until failure $\bar{N}_f$. This method of presentation enables the engineer to compare the maximum spectrum load directly to the material's yield stress or component's structural yield point [7] and also to evaluate the degree to which constant amplitude high-cycle fatigue strength is exceeded. There are also other ways to present variable amplitude test results, e.g., by the effective mean value of the spectrum or by weighing the spectrum with the slope of the Woehler curve [8]. Such methods intend to transform the variable amplitude test results into the scatter band of the Woehler curve and to circumvent cumulative damage calculations. However, such methods cannot be recommended, not only because they often fail, but mainly because the information with respect to the distance to the yield stress and the exceeding of the Woehler curve is suppressed.

Gassner's idea of using a defined sequence to be repeated until failure is justified by the fact that in most applications, mission profiles occur periodically, e.g., flights between two destinations, travelling of a train along the same routes, repetition of sea-states (wave heights), or driving routes of a vehicle from one year to another.

In the following sections, selected subjects of variable amplitude loading, such as description of load-time-histories, derivation of design and test spectra, experimental simulation, fatigue lifing, and last, but not least, reliability aspects, will be addressed.

Description Criteria of Load-Time Histories and Determination of Spectra

Variable amplitude loading has multiple causes and origins [4], as compiled in Fig. 5. According to this systematic separation of the different origins, variable amplitude loading can be grouped into discontinuous and partially continuous random processes. Figure 6 displays, for the example of a wheel-bearing-suspension assembly, different local strain/stress-time histories produced under the same external loading [9]. On rotating components, i.e., wheel or hub, the local strain/stress-time histories are more or less amplitude modulations around a mean-load resulting from dead weight. However, on non-rotating parts, such as the stub-axle, a large mean-value fluctuation is observed.

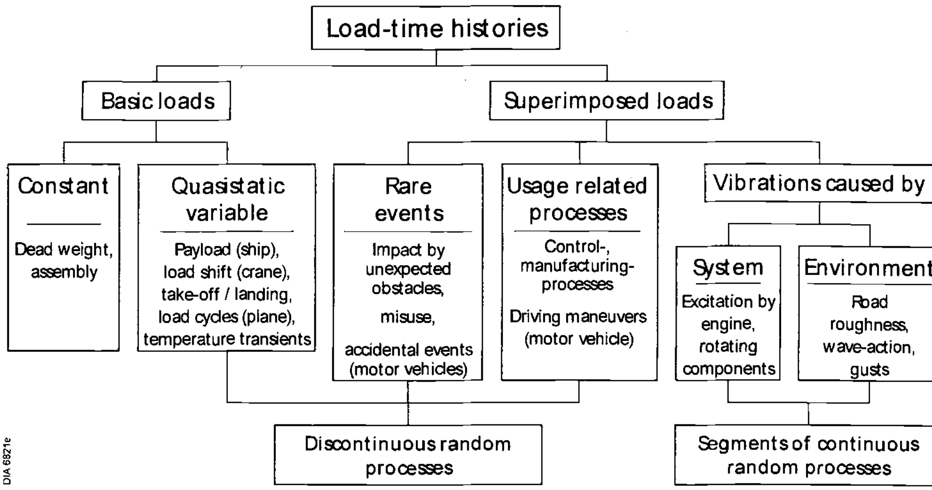

FIG. 5 *Origin of load-time histories.*

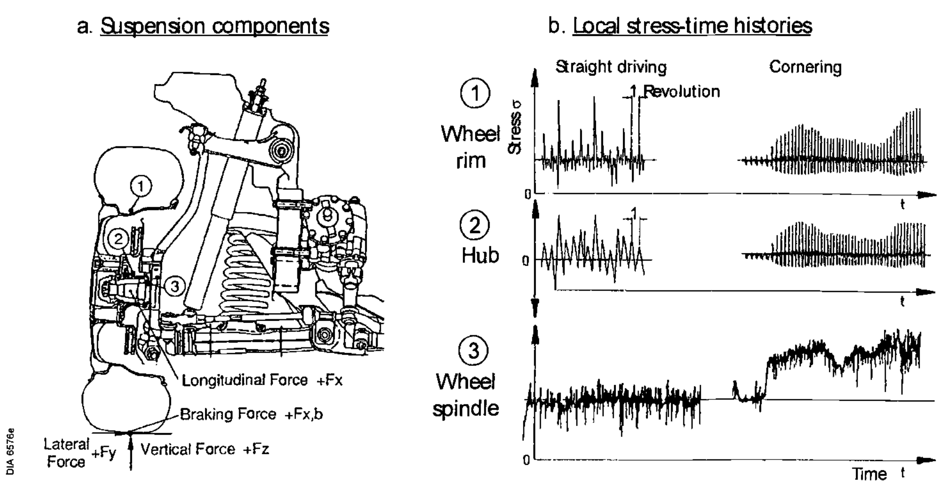

FIG. 6 *Local stress-time histories on different suspension parts.*

The knowledge of these random processes, which can be determined only by service measurements and not by calculations, is essential for the following purposes: the recognition of the causes for concluding consequences for operation, e.g., how to decrease or avoid damaging loads; the determination of the design spectra for fatigue lifing and design; and the experimental simulation and proof testing of components and systems.

Design and Test Spectrum

Design spectra for the required service duration of particular components and structures, e.g., 25 years for offshore rigs or railway buggies, 300 000 km for automotive suspension components (wheels, front, and rear axles), 250 000 km for gearbox transmission axles, 50 000 flights for passenger aircraft, etc., must include all possible loading conditions resulting from usage (operator, maneuvers), environment (sea-states, road roughness), and structure (stiffness, damping) [3]. For these applications the design spectra may have a length of $1 \cdot 10^8$ to $5 \cdot 10^9$ cycles, but in order to allow for testing in a reasonable time, the test spectrum is shortened to a damage equivalent spectrum (Fig. 7). Note that the damage sums of the design spectra obtained by a linear damage accumulation must be identical for equivalent spectra. This is achieved by increasing the amount of higher stress cycles. If mean stresses are present, they also must be considered by an amplitude transformation using a mean-stress-amplitude diagram or a damage parameter. The test spectrum should not be shorter than about $5 \cdot 10^6$ cycles for considering damaging influences by fretting or environmental corrosion. For testing, the test spectrum must be partitioned into sequences, which are then repeated.

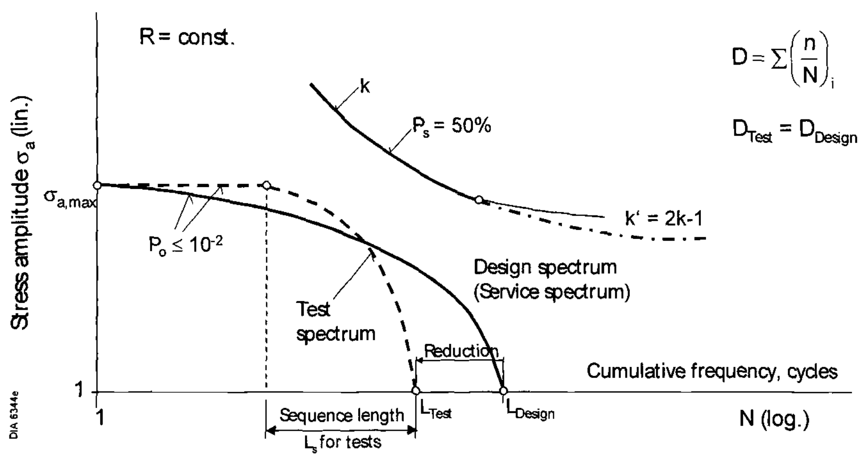

FIG. 7 *Damage equivalent design and test spectra for reduction of testing time.*

There are also other possibilities for the reduction of testing time, like increasing the maximum spectrum load or omission [3]. An increase that exceeds the maximum service load must be avoided because of the possibility of yielding and consequently producing unrealistic fatigue lives; omission without damage equivalent compensation is also not recommended [3].

Methods of Cycle Counting

The derivation of spectra is performed by cycle counting methods [4] (Fig. 8), which is accomplished by additional methods for the reconstitution of the load-time histories for the purpose of cycle by cycle calculation and experimental simulation.

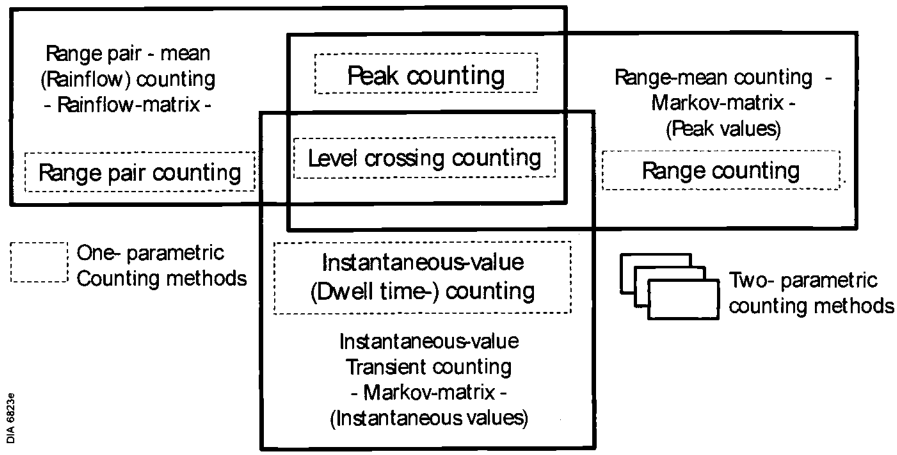

FIG. 8 *Most important one- and two-parameter counting methods.*

The one-parameter level-crossing and range-pair counting methods are historically well established, while the most commonly used two-parametric rainflow method was developed in the 1970s [10,11]. The reason that both counting methods are applied simultaneously is to determine if mean-load (stress) fluctuations are present because they can influence fatigue life significantly, and to compare the maximum values of the level-crossing spectrum directly with the yield stress and the constant amplitude high-cycle fatigue strength. After the introduction of the rainflow method, which contains the counting of level crossings and range pairs, one parameter counting methods unfortunately have been applied rarely because the more elegant rainflow counting allows for an immediate amplitude transformation for fatigue lifing [5,12] with the resulting plotting of related means and amplitudes. However, the illustration of spectra by both older counting methods should not be given up completely for the reasons mentioned already.

Reconstitution

The main disadvantages of the rainflow counting method are that the order of the cycles and their frequency content disappear. Such information is especially significant for the reconstitution of the load-time histories because from one rainflow matrix, different load-time histories can be composed randomly or blockwise (Fig. 9) [13,14].

However, with regard to the ordering of the cycles, the best reconstitution is realized if the instantaneous-value transient counting of the original load-time history, i.e., the Markov-matrix, is available. In Fig. 9, the Markov-matrix of the original sequence is better approached by the random arrangement than by the block arrangement. This has an important influence on the fatigue life (Fig. 10).

While the random arrangement results in the same fatigue life as the original sequence, the block arrangement delivers a higher fatigue life [13], due to coaxing effects. But by appropriate mixing of the blocks, the original fatigue life can be obtained.

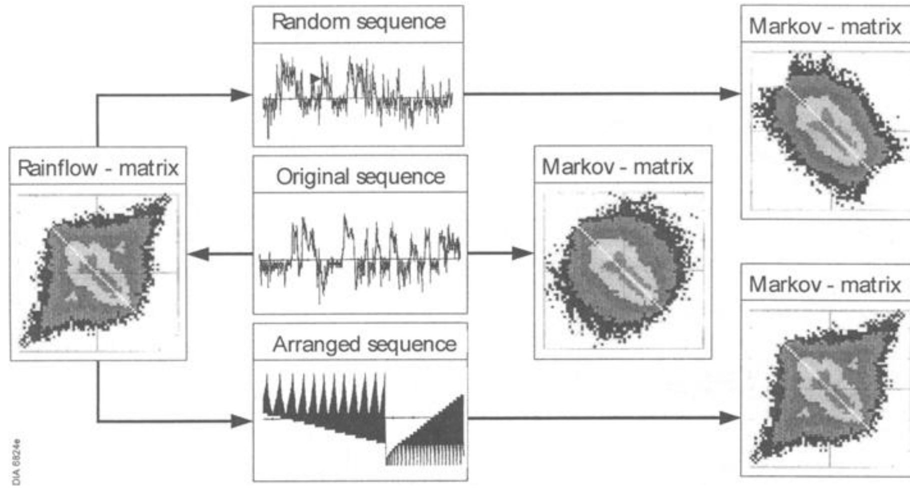

FIG. 9 *Different load sequences with identical rainflow-matrix.*

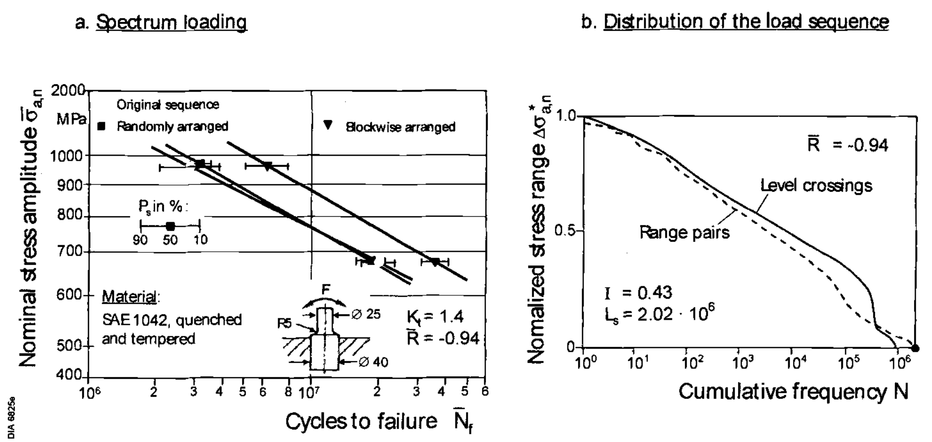

FIG. 10 *Influence of sequence arrangement on fatigue life.*

In [15], a modified Gassner's blocked-program sequence with a length of $L_s = 5.2\ 10^5$ cycles resulted in a fatigue life that was a factor of more than three higher than for a random sequence of same size and almost same Gaussian-like amplitude distribution (Fig. 11). An omission of the sixth step with the lowest stress level did not influence the fatigue life. However, tests carried out with a partitioning of this sequence into five subblocks of size $L_s = 4 \cdot 10^4$ cycles delivered almost the same fatigue life of the random sequence, proving that a random arrangement is not conditionally required to reproduce the original fatigue life.

The frequency content of a load-time-history, described by the power spectral density (Fig. 12), may be neglected for single component testing as long as temperature, cyclic creep, and corrosion effects are not involved. However, when complete systems are tested multiaxially, e.g., suspension units, the reproduction of the original frequency range is required, although interactions between hydraulic actuators and non-linear elements of the system, such as dampers or elastomers, may limit the quality of mechanical simulation. Limitations may result not only from non-linearities, but also from heating of non-metallic materials, such as composites, or friction. For multiaxial testing, the reconstitution of load-time histories also must maintain phase relations between the different axes [16]. This is controlled by cross correlations.

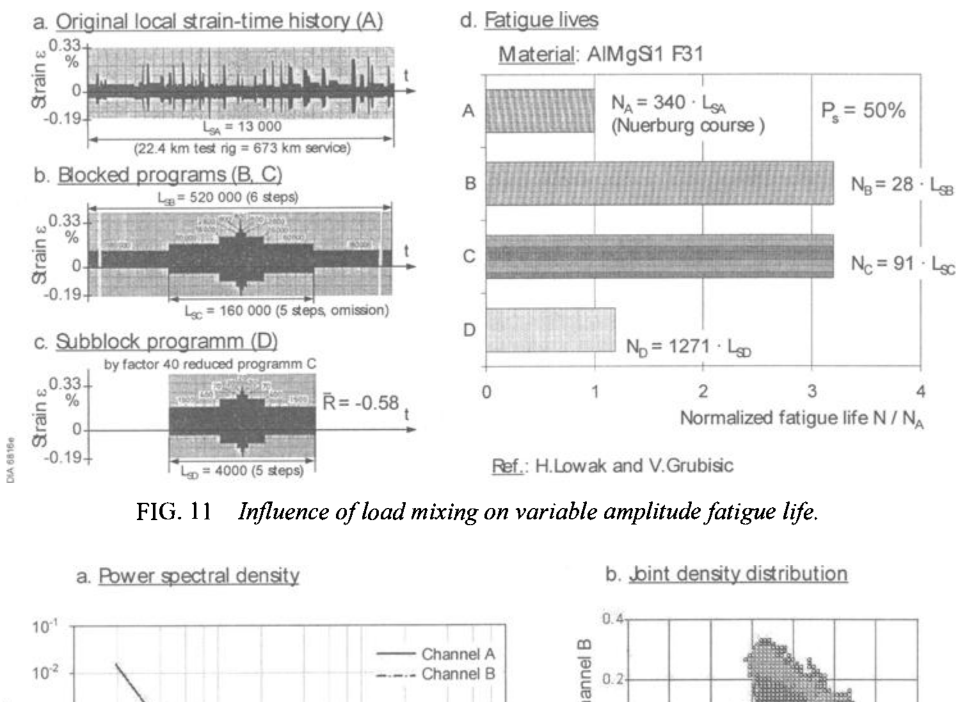

FIG. 11 *Influence of load mixing on variable amplitude fatigue life.*

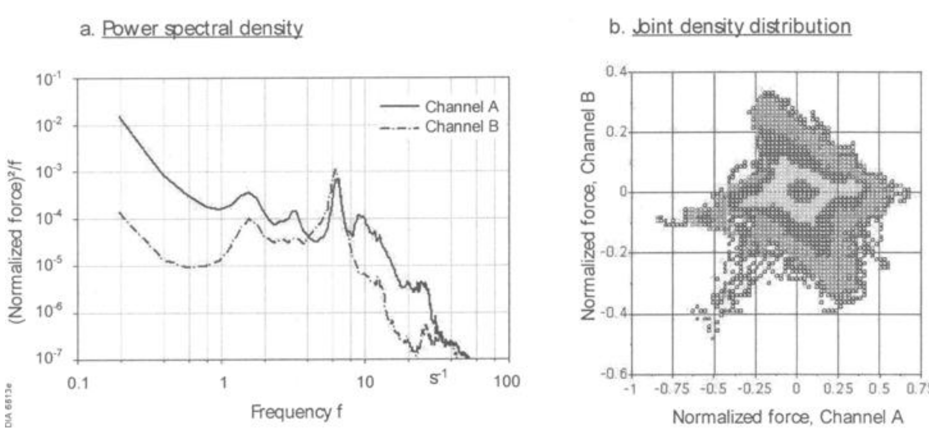

FIG. 12 *Power spectral density and joint density distribution.*

Fatigue Lifing

Cumulative Damage Calculation

Since Palmgren (1924) and Miner (1944), attempts to estimate damage and fatigue life have continued [17 19]. Despite the complexity of this issue, the most commonly used method is still the modification of the Palmgren-Miner Rule, where in the high-cycle fatigue area the inclination k of the S-N curve is maintained (k′ = k) or reduced (k′ = 2k-i), depending on the material [5] (Fig. 13) in order to account for the damaging influence of small load cycles.

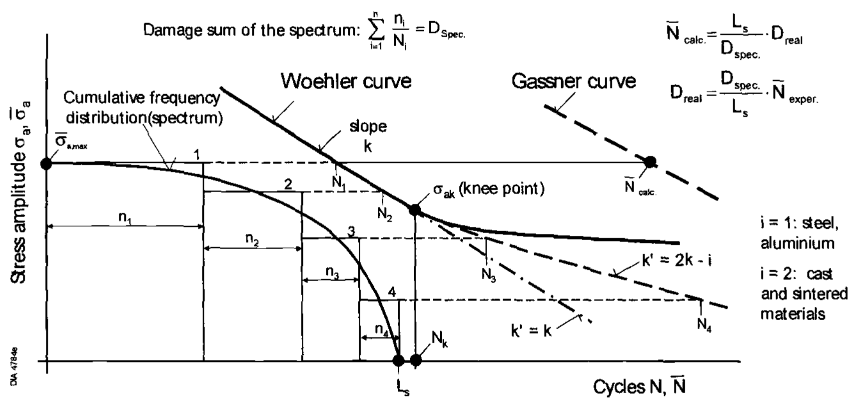

FIG. 13 *Most commonly used cumulative damage calculation methods.*

In addition, these modifications postulate failure when the damage sum $D = \Sigma (n/N)_i = 1.0$ is reached. However, an extensive research project evaluating a vast database [20] revealed a large scatter of the real damage sums ($D_{real} = \bar{N}_{exp} / \bar{N}_{cal}$ (D=1.0)) for different materials, loading modes, stress ratios, and spectra. Figure 14 displays results obtained for wrought steels with the failure criterion of crack initiation, as well as total rupture, using a modification of the Palmgren-Miner Rule with the fictive prolongation of the S-N curve with the slope k′ = 2k − 1. The probability of finding the conventional value of $D \geq 1.0$ is only 5 10 %; this means that only 5 10 % of the fatigue life estimates were on the "safe" side, while the rest were "unsafe."

Some causes for this large scatter can be explained by the previous examples in Figs. 10 and 11 where, despite the same rainflow-matrices, fatigue life differences with a factor of 2 10 were observed due to different load-time histories. Again, this demonstrates that the knowledge of a rainflow matrix is not sufficient for a proper fatigue life calculation. Another reason for the significant failing of fatigue life calculations results from the fact that for load-time histories with mean value fluctuations, the additional damaging effect caused by the mean values is not accounted for properly; the consideration of the mean values by a mean-stress-amplitude diagram or a damage parameter is not enough. This is demonstrated by investigations carried out on forged stub-axles of commercial vehicles [21,22]. The fatigue tests were performed with a truck load sequence ($\bar{R} = -1.4$, I = 0.45, $L_s = 0.95 \cdot 10^5$) derived from service measurements and containing mean value fluctuations caused by cornering, which are superposed on the mean value from the weight and payload (Fig. 15).

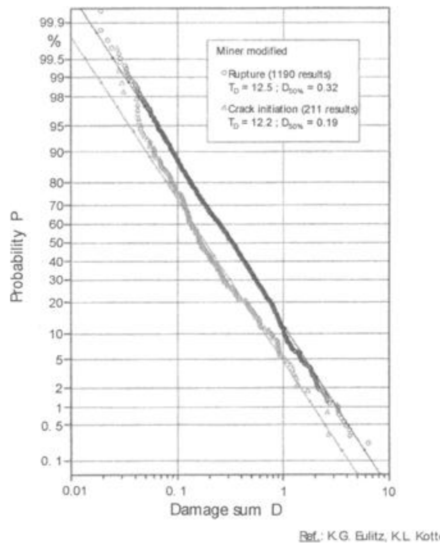

FIG. 14 *Real damage sum distribution for wrought steels.*

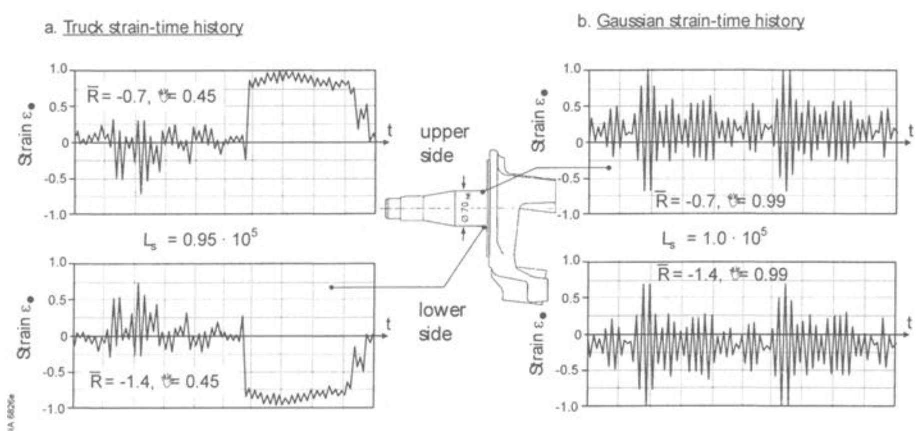

FIG. 15 *Applied local strain-time histories on a stub-axle and failure locations.*

In order to study the effects resulting from mean values, a second test series with a Gaussian load sequence and a constant mean strain ($\overline{R} = -0.7$, I = 0.99, $L_s = 1 \quad 10^5$) was also carried out. For both strain-time histories with comparable sequence lengths, the upper side of the stub-axles was the expected failure location because of the more tensile strains. However, this was only observed to be true for the Gaussian sequence with the constant mean strain level.

In Figs. 16 and 17, applied spectra using different counting methods are presented for the particular failure locations identified in Fig. 15.

The variable amplitude test results obtained with both spectra are plotted in Fig. 18 for the criteria of crack initiation for a defined crack depth of a = 0.5 mm. Figure 18 also contains the calculated Gassner lines. The fatigue lives to crack initiation were assessed on the basis of the rainflow matrices and the cyclic data of the material (cyclic stress-strain, strain-cycle, and damage parameter-cycle curves). For the damage accumulation of small amplitudes in the high-cycle region ($N > 10^6$), the slope of the elastic part of the S-N curve was kept, and failure was assumed for $D = 1.0$.

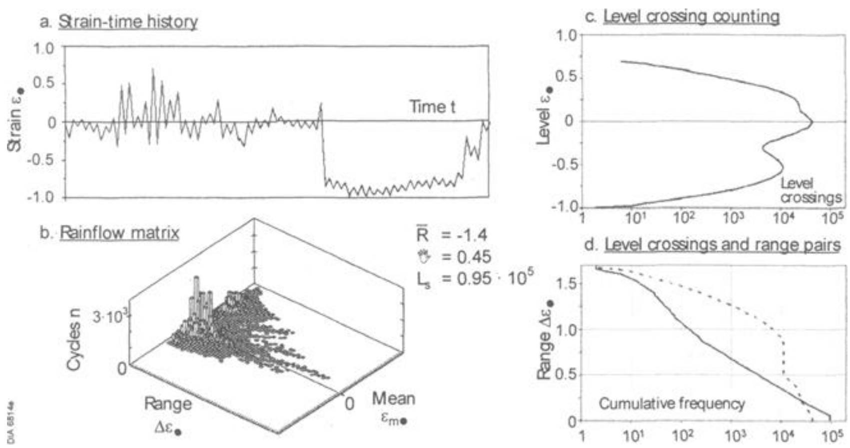

FIG. 16 *Truck load sequence.*

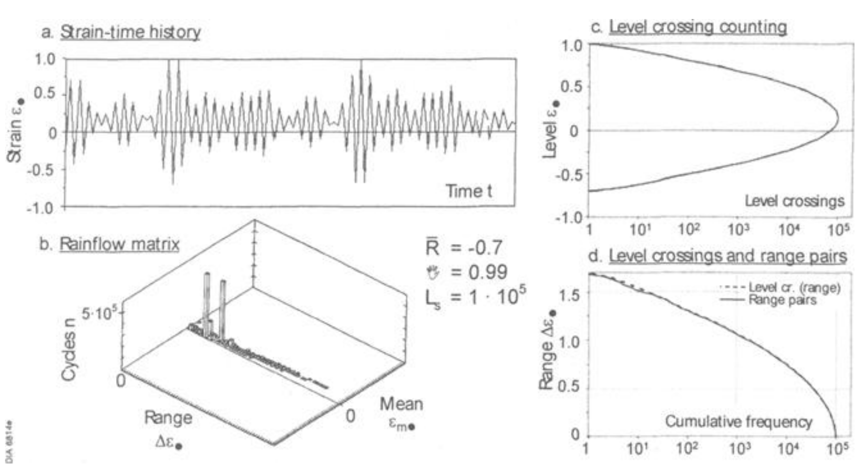

FIG. 17 *Gaussian load sequence.*

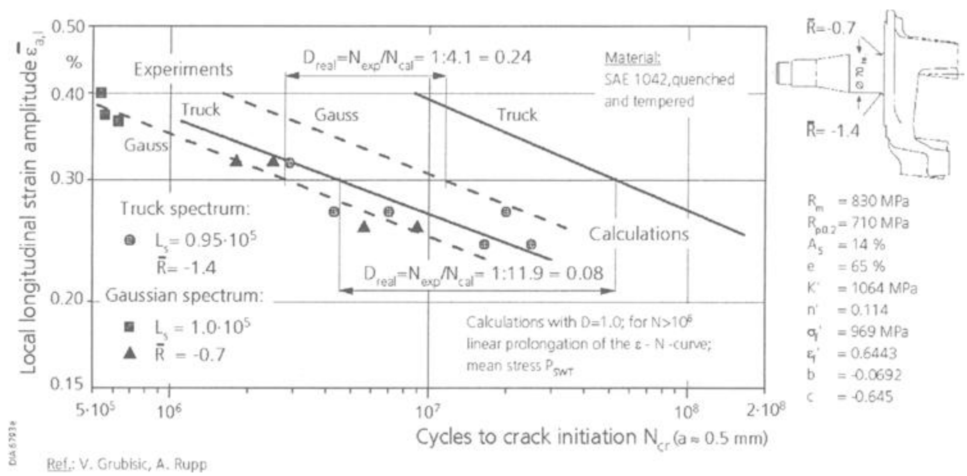

FIG. 18 *Experimental and calculated Gassner-lines.*

For both spectra, the numerical assessment is on the unsafe side: for the Gaussian sequence with the constant mean value by a factor of about four corresponding to a real damage sum, $D_{real} = 0.24$, and for the truck sequence with the high mean value fluctuation by a factor of about 12, meaning $D_{real} = 0.08$.

This example underlines two important messages which justify the performance of variable amplitude testing, especially for complex structures:

- Despite the simple geometry of the stub-axle, the failure location for the truck sequence, the lower side, could not be predicted by the conventional local strain approach.
- Even if the fatigue life assessment uses the strain-time history of the failure location, the fatigue life is significantly overestimated for the sequence with the high mean value fluctuation.

Fatigue life calculations for the stub-axle, also considering short crack propagation [22,23], could not improve the quality of the assessments.

Another inconsistency of fatigue life calculation can be understood from the comparison of Woehler- and Gassner-curves for different cast nodular iron materials (R_m=400, 600, and 1000 MPa) in Fig. 19. The low-strength material (GGG 40) has a ferritic microstructure, the medium strength material (GGG 60) a ferritic-pearlitic microstructure, and the high strength material (GGG 100) an ausferritic microstructure.

The fatigue-life relations between the materials determined under constant amplitude loading change completely under the variable amplitude loading with the Gaussian spectrum ($\bar{R} = -1$, I = 0.99, $L_s = 5{\cdot}10^5$) [24]. A damage accumulation calculation would not only fail in the assessment of the right position of the Gassner-curves, but it would also maintain more or less the same ratios found under constant amplitude loading.

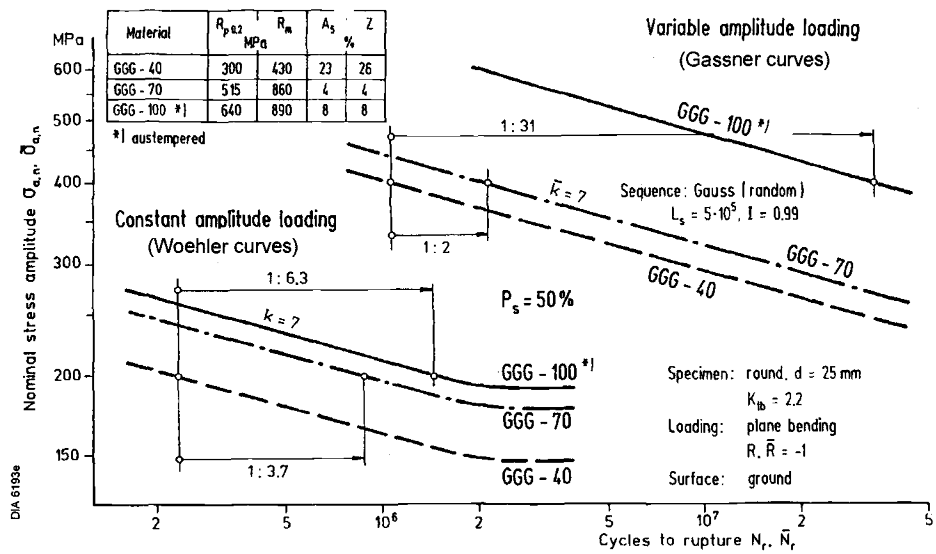

FIG. 19 *Constant and variable amplitude fatigue behavior of different cast nodular irons.*

The reason why the Gassner curves for GGG 40 and GGG 60 are closer to each other than under constant amplitude loading is not understood, but the extreme life increase observed for the GGG 100 can be explained. The local plastic deformations under the variable amplitude loading transform the ausferritic microstructure into a martensitic one, thereby developing a higher strength.

The most probable reason that all present assessment methods fail is that they are based on constant amplitude fatigue data, while the physics of damage under variable amplitude loading is not comparable to the physics of constant amplitude loading. However, despite the inconsistencies demonstrated, fatigue life calculations are still very useful for relative comparisons. In cases where experimental results with similar spectra, materials, and manufacturing are available, experience can be adapted to increase the reliability of the assessment [25].

Test and Design Criteria with Regard to Safety and Liability

The occurrence of variable amplitudes does not necessarily require spectrum testing when amplitudes are below the constant amplitude high-cycle fatigue strength (Fig. 20). This is the case for connecting rods, valves, and crankshafts, where during a fatigue life of about $5 \cdot 10^9$ cycles, the maximum stresses occur more than 10^6 times and therefore allow a strength evaluation and design to be based on constant amplitude fatigue data. Variable amplitude testing and evaluation become necessary when a certain number of stress amplitudes exceeds the Woehler line.

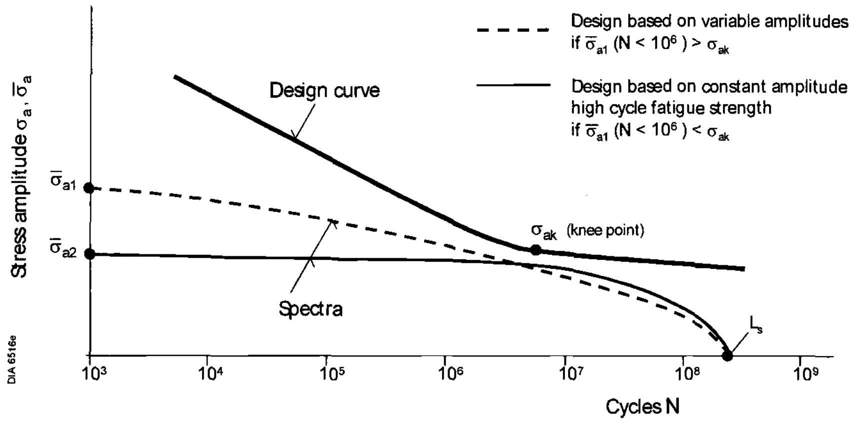

FIG. 20 *Criteria for component design based on constant and variable amplitude loading.*

Another important design criterion is the safety requirement for a component, which can be expressed by a theoretical probability of failure P_f corresponding to a safety factor [26,27]. The design probability of failure P_f is determined based on the importance of the part itself. For a secondary component (e.g., a connecting rod), where failure only affects functionality, the probability of failure is handled in a tolerant way. However, for a safety-critical component (primary component), where failure would cause danger to the user and the environment, numerical and experimental validation (proof-testing) procedures must be carried out according to liability requirements. For this, the following prerequisites (Fig. 21) are necessary [25,26]:

- Design spectra for the expected life cycle containing all loading conditions, from normal usage to accident-like special events.
- The design spectrum must cover the scatter of stresses resulting from service by a defined probability of occurrence, e.g., for safety-critical parts $P_o \leq 1$ %, meaning that 99 % of service is related to the lower stresses.
- The quality of the component must be assumed by design and manufacturing in the way that mean value and scatter of the strength must remain above an allowable level, e.g., a probability of survival, $P_s = 99$ %.
- This results in a probability of failure of the component of $P_f \leq P_o \cdot (1 - P_s) = 10^{-4}$ for one design life.
- The tolerated probability of failure also depends on the failure criterion. If only crack initiation is allowed, a higher P_f value will be assigned to the component than if crack propagation is included.
- As a damage occurrence can never be excluded, safety-critical parts must be designed so that a catastrophic brittle failure is at least avoided.

If the design life is exceeded, the probability of failure increases. For safety-critical components that might be used for more than one design life, a higher degree of safety can be achieved if, by design, the service stresses are decreased or the allowable stresses are increased, e.g., by appropriate surface treatments.

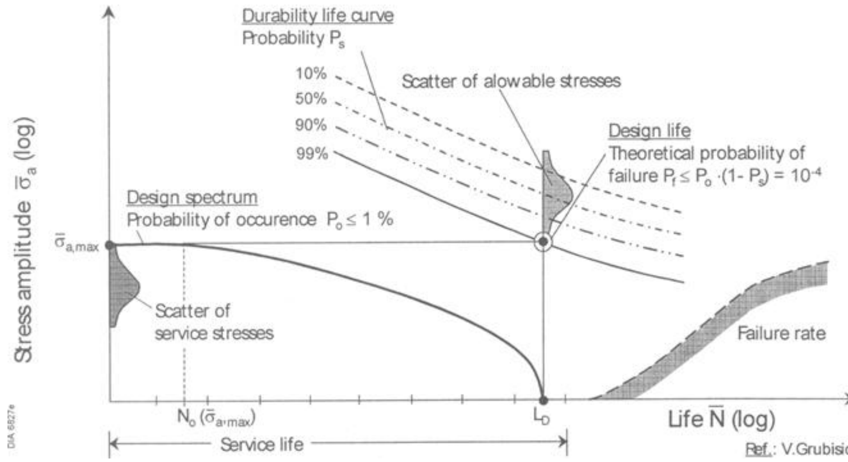

FIG. 21 *Determination of durability life for safety components.*

With regard to experimental testing, the derivation of the test spectrum from the design spectrum already has been discussed (Fig. 7). The design spectrum has the same probability of occurrence of the test spectrum.

The scattering of the component's strength is determined under spectrum loading. In cases where not many components can be tested, statistical methods [3,5,27,28] must be used in order to cover the risks associated with a small number of test specimens and to correct the mean fatigue life L_{n,P_s} = 50 % resulting from few fatigue tests. The risk factor

$$j_{R,C=90\%} = \left(\frac{1}{T_N}\right)^{\left(\frac{1}{\sqrt{4n}}\right)} \tag{1}$$

with which the required design life must be repeated, depends on the confidence level (C = 90 % is considered to be sufficient), the number of tests n, and the expected life scatter

$$T_N = 1 : (\bar{N}_{10\%} / \bar{N}_{90\%}) \tag{2}$$

of a particular component, which is assumed on the basis of experiences with variable amplitude fatigue tests, e.g., $T_N = 1 : 4$. In Gaussian statistics, the scatter T_N is related to the standard deviation by following relation

$$T_N = 10^{-2.56 \cdot s_N} \tag{3}$$

With this value, the fatigue life for a required theoretical probability of failure

$$P_f^* = 1 - P_s \tag{4}$$

of the fatigue life curve is calculated

$$j_N = \left(\frac{1}{T_N}\right)^{\left[\frac{(2.36 x \sqrt{|\lg P_f^*|})-1}{2.56}\right]} \quad (5)$$

The risk-compensated fatigue life for a required theoretical probability of failure P_f* of the fatigue life curve reads

$$L_{P_f^*} = \frac{L_{n,P_s=50\%}}{j_{R,C} \cdot j_N} \quad (6)$$

The total theoretical probability of failure P_f of a component results from the interaction between the probability P_f* and the probability of occurrence P_o of the spectrum

$$P_f \leq P_o \cdot P_f^* \quad (7)$$

Figure 22 displays a fatigue life assessment of the driving shaft of a gearbox [27] under consideration of few durability tests under spectrum loading. The question to be answered was: how many times can the load sequence for one life cycle (250 000 km) be applied without exceeding the theoretical probability of failure $P_f = 10^{-5}$ [27]?

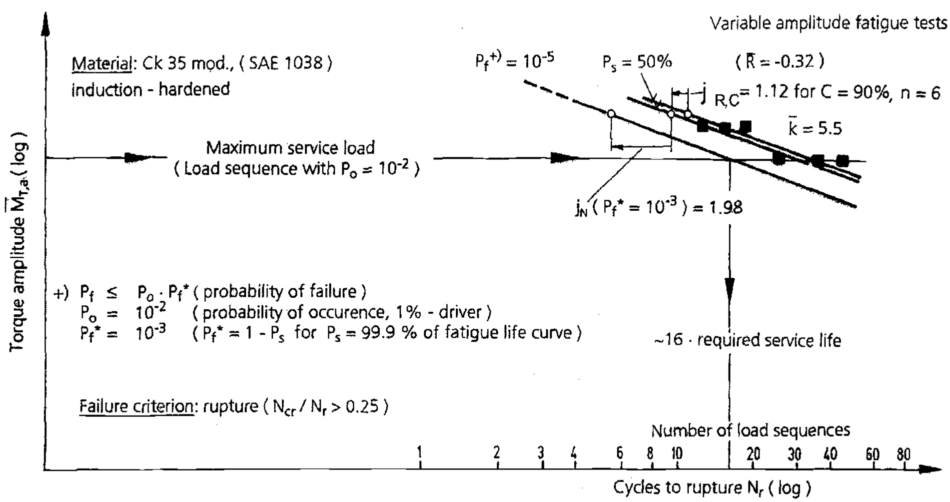

FIG. 22 *Safety analysis of a drive shaft.*

Conclusions and Outlook

The proper design of components subjected to variable amplitude loading requires the design spectrum and the strength properties, i.e., Woehler- and Gassner-curves. While today service load-time histories can be reconstituted and experimentally simulated fairly well, the most critical part of variable amplitude fatigue design remains the fatigue life assessment. Presently used damage accumulation hypotheses, which originate most commonly from the Palmgren-

Miner Rule, reveal a high and unacceptable scatter of the real damage sum and result in unsafe fatigue life estimations. This fact makes experimental validations inevitable, especially for safety critical parts, because of the safety and liability requirements.

The present unsatisfactory state of the fatigue life prediction process requires new and unconventional solutions (e.g., the use of constant amplitude data, which are based on a very different physics of damage) to be given up. On the other hand, it is clear that spectrum intensity and damage accumulation lead to failure, so means to reduce them and to increase the fatigue life and the reliability of structures should be developed. In the future, for many components and structures, these improvements will be realizable by the development and application of adaptive smart materials [29] with sensor – and actuator - functions (Fig. 23). The main requirement and challenge for these new materials will be longer durability and functionality than the structures on which they are applied.

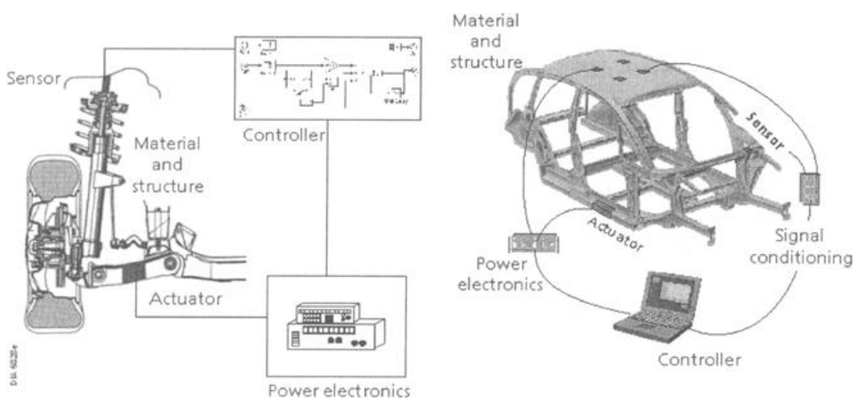

FIG. 23 *Adaptive elements for reduction of spectrum intensity on steering and chassis components.*

References

[1] Gassner, E., "Festigkeitsversuche mit wiederholter Beanspruchung im Flugzeugbau," *Luftwissen*, 1939, No. 6, pp. 61 64.

[2] Heuler, P. and Schütz, W., "Standardized Load-Time Histories – Status and Trends," In: *Proc. Of the 4th Int. Conf. on Low-Cycle Fatigue and Elasto-Plastic Behaviour of Materials*, Garmisch-Partenkirchen, Germany 1998, pp. 729 734.

[3] Berger, C., Eulitz, K.-G., Heuler, P., Kotte, K.-L., Naundorf, H., Schütz, W., et al., "Betriebsfestigkeit in Germany – An Overview," *International Journal of Fatigue*, Vol. 24, No. 6, 2002, pp. 603 625.

[4] Buxbaum, O., "Betriebsfestigkeit – Sichere und wirtschaftliche Bemessung schwingbruchgefährdeter Bauteile," *Verlag Stahleisen*, Düsseldorf, 1992.

[5] Haibach, E., "Betriebsfestigkeit – Verfahren und Daten zur Berechnung," *VDI-Verlag*, Düsseldorf, 1989.

[6] Schijve, J., "Fatigue of Structures and Materials," Kluwer Academic Publishers, AH Dordrecht, 2001.

[7] Grubisic, V. and Sonsino, C. M., "Influence of Local Strain Distribution on Low-Cycle Fatigue Behaviour of Thick Walled Structures," *Low-Cycle Fatigue and Life Prediction, ASTM STP 770*, C. Amzallag, B. N. Leis, and P. Rabbe, Eds., ASTM International, West Conshohocken, PA, 1982, pp. 612 629.

[8] Sonsino, C. M., "Limitations in the Use of RMS-Values and Equivalent Stresses in Variable Amplitude Loading," *Int. Journal of Fatigue*, Vol. 11, No. 3, 1989, pp. 142 152.

[9] Grubisic, V., "Criteria and Methodology for Lightweight Design of Vehicle Components," Fraunhofer-Institute for Structural Durability LBF, Darmstadt, Germany, Report No. TB-176, 1986.

[10] de Jonge, J. B., "Counting Methods for the Analysis of Load Time Histories," *NLR Memorandum*, SB-80-106 U, 1980.

[11] Endo, T., et al., "Damage Evaluation of Metals for Random or Varying Loading. Three Aspects of Rain-Flow Method," In: *Proc. of the 1974 Symp. on Mech. Behavior of Materials*, Soc. of. Mat. Science Japan, 1974, pp. 372 380.

[12] Smith, K. N., Watson, P., Topper, T. H., "A Stress-Strain Function for the Fatigue of Metals," *Journal of Materials*, Vol. 5, No. 4, 1970, pp. 767 778.

[13] Buxbaum, O., Klätschke, H., Oppermann, H., "Effect of Loading Sequence on the Fatigue Life of Notched Specimens Made from Steel and Aluminium Alloys," *Applied Mechanics Reviews*, Vol. 44, No. 1, 1991, pp. 27 35.

[14] Perret, B. H. E., "An Evaluation of a Method of Reconstituting Fatigue Loading from Rainflow Counting," In: *New Materials and Fatigue Resistant Aircraft Design*, Proc. of the 14th ICAF-Symposium, D. L. Simpson, Ed., Engineering Materials Advisory Services (EMAS), Warley, 1987, pp. 355 401.

[15] Lowak, H. and Grubisic, V., "Möglichkeiten zur Lebensdauervorhersage für Bauteile aus Aluminiumlegierungen," *Materialprüfung*, Vol. 27, No. 11, 1985, pp. 337 343.

[16] Schütz, D., Klätschke, H., Steinhilber, H., Heuler, P., and Schütz, W., "Standardized Load Sequences for Car Wheel Suspension Components (Car Loading Standard)," Fraunhofer-Institute for Structural Durability LBF, Darmstadt/Germany, Report No. FB-191 / IABG-Report No. TF-2695, 1990.

[17] Dowling, N. E., "A Review of Fatigue Life Prediction Methods," SAE Paper No. 871966, *SAE Passenger Car Meeting and Exposition*, Dearborn, MI, October 19 22, 1987.

[18] Chaboche, J. L. and Lesne, P. M., "A Non-Linear Continuous Fatigue Damage Model," *Fatigue and Fracture of Engineering Materials and Structures*, Vol. 11, No. 1, 1988, pp. 1 7.

[19] Fatemi, A. and Yang, L., "Cumulative Fatigue Damage and Life Prediction Theories: A Survey of the State of the Art for Homogeneous Materials," *Int. J. Fatigue*, Vol. 20, No. 1, 1998, pp. 9 34.

[20] Eulitz, K.-G. and Kotte, K. L., "Damage Accumulation-Limitations and Perspectives for Fatigue Life Assessment," *Materials Week 2000 – Proceedings*, Werkstoffwoche-Partnerschaft, Ed. and Organizer, Frankfurt, 25 28 September 2000, (www.materialsweek.org/proceedings).

[21] Grubisic, V. and Rupp, A., "Gegenüberstellung der experimentell und rechnerisch bestimmten Lebensdauer von Bauteilen und Probestäben," *In: „Bauteilleben-sdauer: Rechnung und Versuch" 19. Vortragsveranstaltung der DVM-Arbeits-kreises Betriebsfestigkeit*, München, Hrsg. Dt. Verband für Materialforschung und –prüfung, Berlin, 1993, pp. 271 291.

[22] Sonsino, C. M., Kaufmann, H., and Grubisic, V., "Transferability of Material Data for the Example of a Randomly Forged Truck Stub Axle," *SAE Transactions Section 5, Journal of Materials and Manufacturing 106*, 1997, pp. 649 670.

[23] Vormwald, M., "Anrißlebensdauervorhersage auf der Basis der Schwingbruch-mechanik für kurze Risse (Crack Initiation Life Prediction on the Basis of Fracture Mechanics for Short Cracks)," *Veröffentlichung des Instituts für Stahlbau und Werkstoffmechanik der Technischen Hochschule Darmstadt*, Heft 47, 1989.

[24] Sonsino, C. M. and Grubisic, V., "Requirements for Operational Fatigue Strength of High Quality Cast Components," *Materialwissenschaft und Werkstofftechnik*, Vol. 27, No. 8, 1996, pp. 373 390.

[25] Grubisic, V. and Fischer, G., "Methodology for Effective Design Evaluation and Durability Approval of Car Suspension Components," *SAE Paper 970094*, 1997.

[26] Grubisic, V., "Design Procedures and Liability Requirements," In: *Proceedings of XXIX Convegno Nazionale dell'Associazione Italiana per l'Analisi delle Sollecitazioni*, Lucca/Italy, Sept. 7, 2000.

[27] Sonsino, C. M., Kaufmann, H., Foth, J., and Jauch, F., "Fatigue Strength of Driving Shafts of Automatic Transmission Gearboxes Under Operational Torques," *SAE Transactions Section 5, Journal of Materials and Manufacturing 106*, 1997, pp. 635 648.

[28] Sonsino, C. M. and Bacher-Höchst, M., "Methodology for the Safe and Economical Fatigue Design of Components in ABS/ETC Braking Systems under Variable Amplitude Loading," *SAE International Congress and Exhibition*, Detroit, MI, March 1 4, 1999, SAE Paper No. 990366.

[29] Hanselka, H. and Sachau, D., "German Industrial Research Project ADAPTRONIK: Content, Results and Outlook," *Society of Photo-Optical Instrumentation Engineers*, Bellingham, WA, 2001, pp. 29 36.

S. W. Hopkins,[1] *M. R. Mitchell,*[2] *& J. Ménigault*[3]

Role of Variable Amplitude Fatigue Standards in Improving Structural Integrity

REFERENCE: Hopkins, S. W., Mitchell, M. R., and Ménigault, J., "**Role of Variable Amplitude Fatigue Standards in Improving Structural Integrity,**" *Fatigue Testing and Analysis Under Variable Amplitude Loading Conditions, ASTM STP 1439,* P. C. McKeighan and N. Ranganathan, Eds., ASTM International, West Conshohocken, PA, 2005.

ABSTRACT: Fatigue failures of structural components continue to be a serious concern to the well-being and economics of our worldwide society because the majority of all such components fail by this mechanism. If some of these failures could be prevented through better design with our understanding of how materials behave, it would have a major impact on the economics of society.

American Society for Testing and Materials International (ASTM) Committee E08 on Fatigue and Fracture, International Organization for Standardization, Technical Committee 164, Subcommittee 5 (ISO/TC164/SC5) on Fatigue Testing of Metallic Materials and other relevant committees interested in the fatigue phenomena are involved in developing standards for testing and analysis under variable amplitude loading. Currently no variable amplitude fatigue testing standards exist. The organizational structures of some committees are provided along with examples of variable amplitude fatigue failures. There is some interaction between ASTM, European Structural Integrity Society (ESIS), and ISO, and it is hoped that additional interaction will occur so that all of the vast knowledge on fatigue from around the world may be focused to develop standards that will benefit everyone.

To demonstrate the need for such international standards, several examples of variable amplitude-type failures are presented and discussed. As a result of such failures, there is an obvious need to translate the constant amplitude and variable amplitude laboratory test data into the design of real structures.

KEYWORDS: Fatigue, constant amplitude, variable amplitude, endurance limit, standards, AFNOR, ASTM, ANSI, ECISS, ESIS, ISO, structure integrity

Introduction

The economic benefits of improving the structural integrity of the equipment and components being built today can be immense! In the early 1980s, the National Bureau of Standards issued Special Publication 647 that assessed the costs to the United States for material fractures for a single year (1978) [1]. The estimated total cost was $119 billion dollars per year (1982 dollars) or 4% of the Gross National Product. The publication authors believe that almost 1/3 ($35 billion per year) could be saved through the use of currently available technology and almost another 1/4 ($28 billion per year)

[1] Exponent Failure Analysis Associates, 149 Commonwealth Drive, Menlo Park, CA 94025 USA.
[2] W. L. Gore & Associates, 3450 West Kiltie Lane, Flagstaff, AZ, 86002 USA.
[3] BNS, Iron & Steel Standards Office, 11-13 Cours Valmy, F.92 070, La Défense, France.

could be saved through fracture-related research. It was concluded that these savings could be realized by reducing the uncertainty related to structural design through better lifetime predictions of structural performance from material properties, better process and quality control, in-service monitoring, and decreased materials variability. The \$119 billion per year cost of fracture includes all sectors of the economy including: automotive, aircraft, building construction, petroleum-refining, etc. Since that report was written (20 years ago), it is hoped that some of these savings have resulted. The authors of this paper are not aware of any follow-up report(s) that documents the current cost of material fractures. It is believed, through education and material testing standards, that some material fractures have been avoided, thereby reducing this \$119 billion dollar/year cost estimate. However, some failures or fractures will still happen simply due to human error and other non-controllable occurrences.

Material testing standards that result in reproducible fatigue data assist our understanding of how materials behave under fatigue loading situations, and provide the basis for improvements in designs. Fatigue loading on most, if not all, structural components is variable amplitude and not constant amplitude. In spite of this, the vast majority of the material testing is conducted at constant amplitude and all of the current testing standards (e.g., Association francaise de normalisation (AFNOR), American Society for Testing and Materials (ASTM), British Standards Institution (BSI), Deutsches Institut fur Normung (DIN), European Committee for Iron and Steel Standardization (ECISS), European Structural Integrity Society (ESIS), and International Organization for Standardization (ISO)) on fatigue methodology deal only with constant amplitude loading.

In order to understand correctly variable amplitude fatigue effects, it is obvious that constant amplitude fatigue behavior must first be understood.

Fatigue Failures

Some fractures are more noteworthy than others are, but all contribute to this economic loss. The Aloha Airline Flight 243 plane that suddenly became a convertible during flight on April 28, 1988, is shown in Figure 1 [2]. Reportedly this fracture was driven by the number of flights (pressurizations) that the plane had experienced, such that small fatigue cracks were growing within the fuselage until, on the critical last flight, the cracks became unstable and grew to failure. Airplane fuselages typically experience a fatigue cycle as a result of every flight due to pressurization of the interior of the fuselage and the depressurization after the flight. In 1954, there were two high altitude catastrophic failures of British airplanes design known as the Comet. The Comet was the first jet powered passenger airplane. One Comet crashed in 1954 into the Mediterranean Sea just four days after an inspection. The team investigating these accidents concluded that small fatigue cracks originated from sharp re-entrant window corners in the fuselages. The fatigue loading cycle was again the pressurization of the airplane [3].

Another example of a fatigue failure that was less dramatic, but still very important and very expensive in terms of lost production, was a drive shaft that failed at a continuous hot rolling stand in 1980 at a French steel plant. This fracture surface is shown in Figure 2. Major cyclic loads were generated when the steel strip entered and exited the roll stand and minor cyclic loads were generated during rolling due to the irregular shape of the strip (e.g., seams at the strip edges). High cyclic loads might be generated by slight changes of the strip shape and therefore produce fatigue stresses in the shaft.

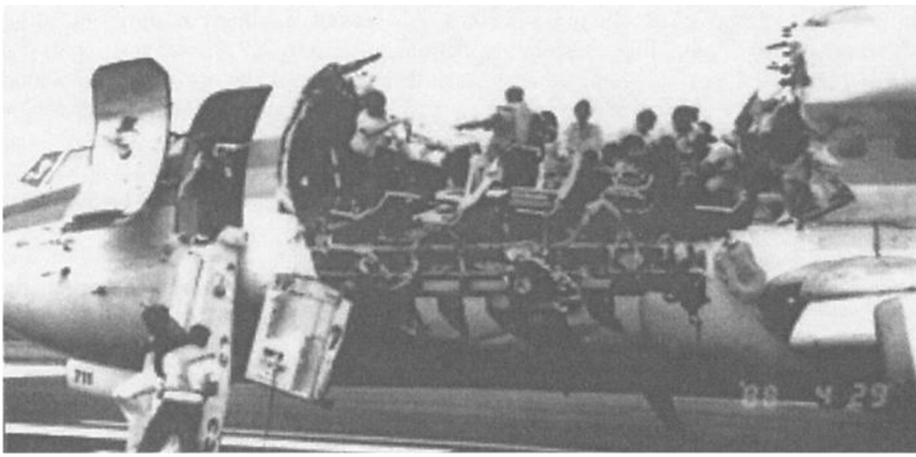

FIG. 1—*Aloha Airlines Flight 243, April 28, 1988.*

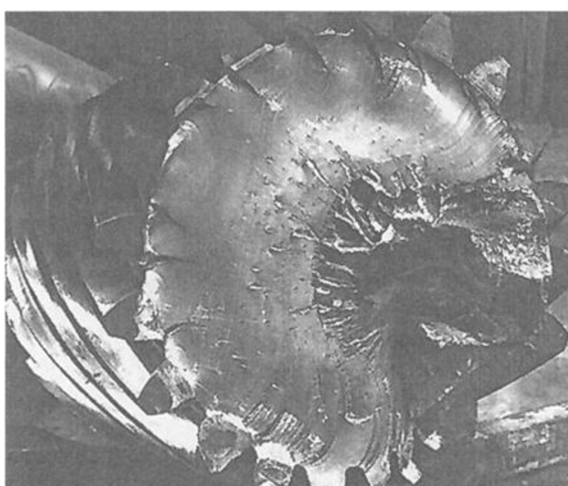

FIG. 2—*Broken shaft in a roll stand, the shaft diameter is 900 mm (courtesy of J. P. Bertrand, IRSID - Steel Processing R&D Center of the ARCELOR Steel Group).*

The shaft, being directly connected to the rolls, was subjected to the cyclic loads without any damping. It was also loaded mainly in rotating bending and torsion. This roll stand had been in service for 20 years without any trouble. Then, after a regular maintenance inspection, the shaft failed 18 months later. During that 18-month period of additional operation the electric power needed for rolling was 20% greater than before the inspection. During the maintenance and inspection, the steel production process also changed: ingot casting was replaced by continuous casting. Since rolling slabs produced by a continuous caster are harder than rolling slabs formerly produced from ingots, the cyclic load amplitudes at the rolling stand had increased substantially. This would explain the fatigue failure after a short time as well as the rise in electric power consumption needed for strip rolling. The sequence of cyclic loads generated by strips entering, leaving, and to a lesser extent, passing through the roll stand is a typical example of a variable amplitude stress history leading to complete fracture of the component.

The cost of this shaft was approximately 1,500,000 French francs (228,600 € or $200,400 US). It should be noted that the cost of an eight-hour production loss and the repair cost of the roll stand should be added to the abovementioned component cost to obtain the global cost of such a failure.

No paper on variable amplitude fatigue would be complete without showing at least one railroad fracture, given the history of the subject. In the late 1970s, a series of train trucks that support the commuter train were experiencing surface cracking in a number of different components attached to these trucks. The railroad axles were not cracking, but most of the other items associated with these trucks were cracking. Figure 3 shows a complete truck after the commuter train had been removed. Fortunately, these cracks were detected and the cracked trucks were removed from service before any serious injuries had occurred. The issue was to identify the cause of the cracking and whether it was a result of unanticipated loading from the rail tracks or due to the trucks being under-designed. Repair and/or replacement of a large fleet of these trucks were very expensive, as much as $72 million US. The conclusion of this investigation was that these trucks were failing due to the unmeasured, variable amplitude loadings. During the design stage of this project the variable amplitude loading was experimentally measured with strain gages placed at "critical locations" on the truck frame. Unfortunately, the data was filtered to eliminate what was believed to be electrical noise from the strain gage signals. By filtering the data, they missed the exceptionally large impact forces and the trucks' response to those forces. Subsequently, the engineers designed the trucks to the reduced measured forces, and the trucks failed by fatigue and crack propagation because of the unmeasured high impact forces. This latest example is included to emphasize the point that proper reduction of experimental field data in a variable amplitude history is extremely important.

Lifetime Predictions

One of the most famous early researches on fatigue was performed by August Wohler in Germany on railway axles in the 1850s. He systematically conducted constant amplitude fatigue tests on railway axles and showed that below a certain cyclic stress amplitude the axle would not fail. This introduced the concept of the "Fatigue Limit" or "Endurance Limit." Thus, Wohler has been called the "Father" of fatigue research [4]. Then Palmgren in 1924 and later Miner in 1945 suggested that a linear cumulative fatigue damage criterion could be used for variable amplitude fatigue lifetime predictions using as input the constant amplitude material property data. This linear fatigue damage criterion is now recognized as the Palmgren-Miner Rule. Although this rule has some shortcomings, it remains an important tool in fatigue life prediction under variable amplitude loading after more than 50 years.

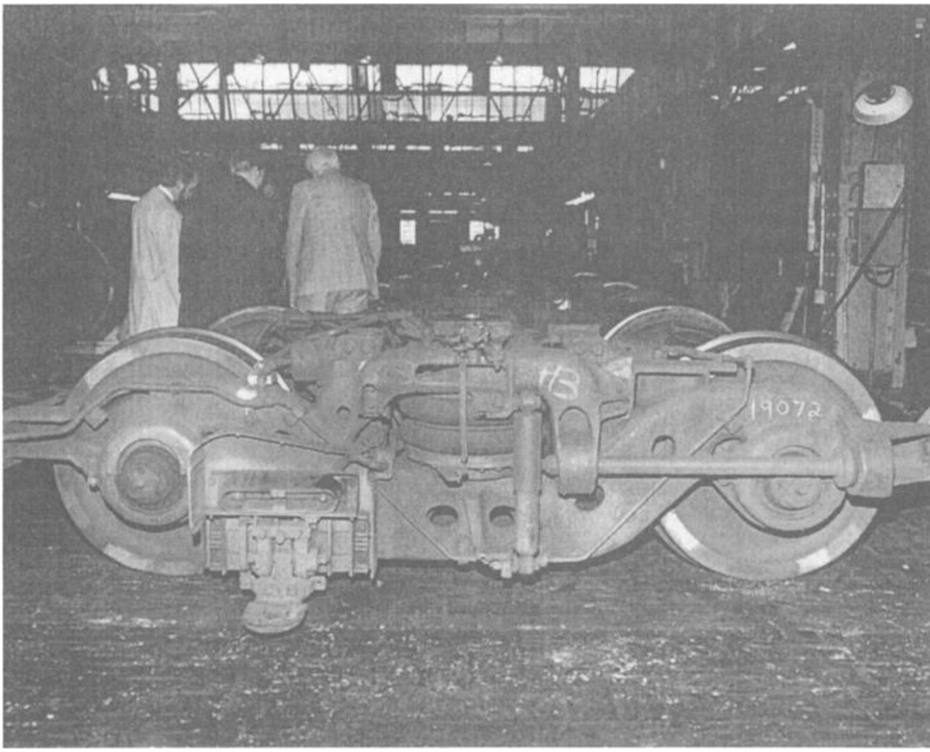

FIG. 3—*Train truck with commuter train removed.*

One of the important issues in design of structures subjected to variable amplitude fatigue is the "Endurance Limit." If all of the cycles in a stress history are below the "Endurance Limit," then it is presumed that the structure is not going to fail by fatigue. However, in the presence of an occasional large stress or strain cycle, Brose, Dowling, and Morrow [5] showed that a stress cycle slightly above the "Endurance Limit" will contribute significantly to the fatigue process and result in a non-conservative estimate of fatigue life. In fact, they showed that the "knee" in the S-N curve is completely eliminated by an occasional overstrain that is quite common in a variable amplitude history.

The most accurate way to do variable amplitude fatigue life prediction is to subject the exact structure to the exact service loads in the laboratory until the structure fails. This approach is extremely expensive and time consuming. A less expensive and more expeditious approach is shown in Figure 4. One starts by directly measuring all of the in-service forces and then analyzes the data using a cycle counting procedure such as "zero crossing up" or "rain flow." From this one can generate a cumulative exceedance diagram and then divide the data into programmed blocks or develop a transition matrix that points are drawn from in a random manner. After this, some engineering judgment can be applied to eliminate most of the "non-damaging" occurrences. This edited information is then used as input to subject a laboratory fatigue specimen to these cyclic loads. These results are then used to closely approximate the projected life of the structure.

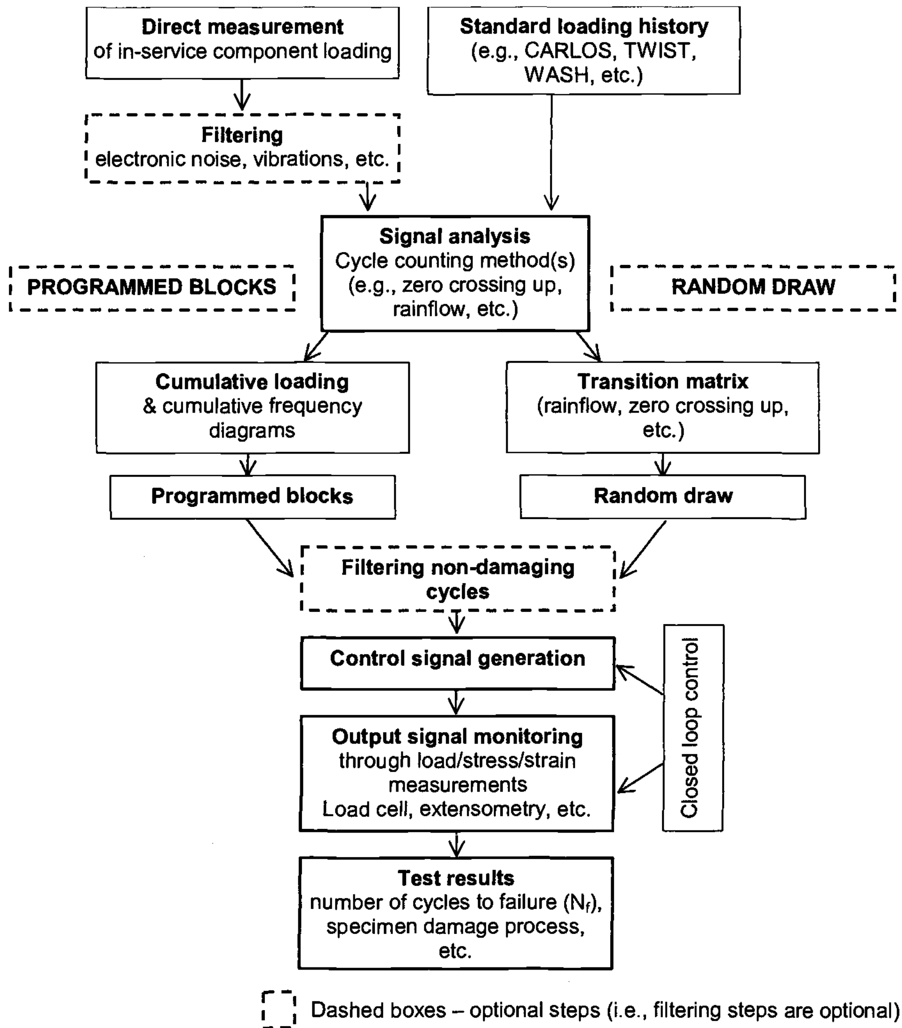

FIG. 4—*Flowchart for collecting variable amplitude loading data and converting it into input data for conducting laboratory variable fatigue tests.*

Even this approach can be costly and very time consuming. Therefore, several "standard" variable amplitude-loading histories have been developed, such as CARLOS, TWIST, and WASH, for the automotive, aircraft and offshore industries respectively. Using these standardized loading histories on different materials, the designer can make use of the information without actually conducting a fatigue test himself. The designer will still have to establish which standardized loading history best represents the service loading for the structure under study and the conversion in lifetime between the actual service loading and the standardized loading history that was selected. Therefore, standardizing how in-service data is converted to programmed blocks or random draw, and standardizing loading histories so the results are valuable to a large group of designers, will help reduce design costs.

Developing a good standard is difficult and quite time consuming. If the test standard is too loose, the resulting data will have additional scatter. If the standard is too tight, the cost of the resulting data will be too great and fewer people will actually conduct the tests. For the fatigue and fracture community, a number of different countries and regions have their own organizations developing standards. For example, there is the Japanese Standards Association (JSA) in Japan, AFNOR in France, American National Standards Institute (ANSI), ASTM, Society of Automotive Engineers (SAE) in the United States, and ISO. Each organization is different and in this paper, the authors will provide only the structure of the French, European Union, ASTM International, and ISO standardization systems. Unfortunately, there are no current standards concerning variable amplitude fatigue testing. This situation most likely reflects the idea that not all of the variables that affect the resulting data are clearly understood. A standard can only be developed after most, if not all, of the variables are understood.

French Standardization System

AFNOR is the official French standardization institute like BSI in England or DIN in Germany, for instance. AFNOR manages the whole French standardization process and acts on behalf of corporate sectors and French governmental institutions (mainly Ministry of Industry, Ministry of Agriculture, Ministry of Health, Ministry of Transportation, etc., as well). The French standardization system is shown in Figure 5.

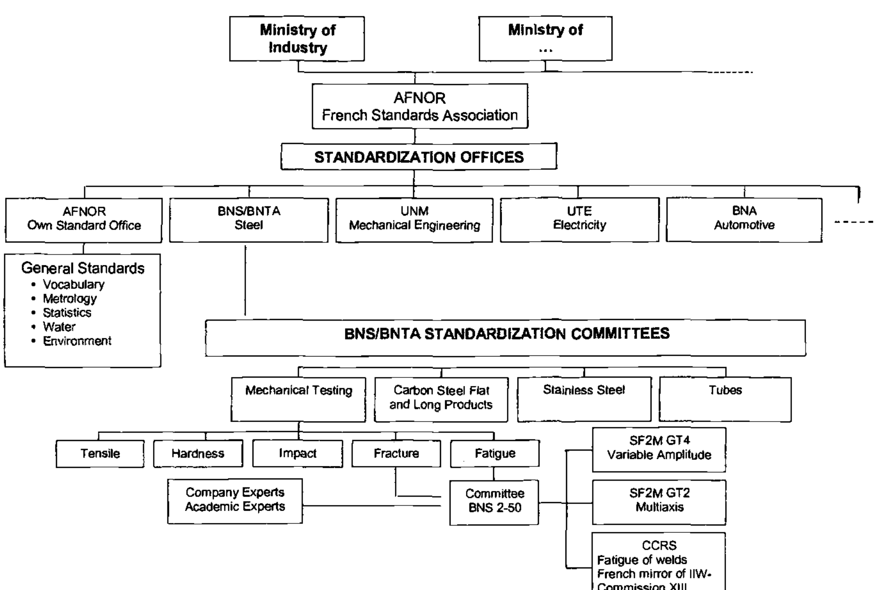

FIG. 5—*French Standardization System.*

Standardization offices specialized in various industrial sectors do the technical work within standardization committees, which gather experts representing companies, state-owned institutes, universities, etc. Each company or institution counts for one vote. Consensus is reached upon a majority rule but negative votes are taken into account and committee chairmen always try to reach agreement through compromise arrangements. Each standardization office is dedicated to an industrial sector, for instance: Union de Normalisation de la Mécanique (UNM) for mechanical engineering, Bureau de Normalisation de l'Automobile (BNA) for automotive, Bureau de Normalisation de l'Aéronautique et de l'Espase (BNAE) for aerospace, Bureau de Normalisation de la Sidérurgie/Bureau de Normalisation des Tubes d'Acier (BNS/BNTA) for steel. AFNOR has its own standardization office responsible for general standards (statistics, metrology, waste management, environment, etc.). Like others, BNS and BNTA (BNS for steel and BNTA for steel tubes and pipes) manage many standardization committees dedicated to steel products (carbon flat and long steel products, stainless steels, tubes, etc.). There is one standardization committee devoted to mechanical testing of metals and concerns all metallic materials, not only steel.

The standardization committee on mechanical testing of metals is the French mirror committee of the European Committee for Iron and Steel Standardization/Technical Committee 1 (ECISS/TC1) and of the International Organization for Standardization/Technical Committee 164 (ISO/TC164). It is divided into working groups, each specializing in one type of mechanical test: tensile, hardness, impact, and one working group on both fatigue and fracture mechanics. The standardization working groups on fatigue and fracture works in cooperation with fatigue working groups of the French materials society SF2M and the CCRS-Fatigue Committee, which is the French mirror committee of IIW-Commission XIII (Fatigue Commission of the International Institute of Welding).

European Union Standardization System

European standards are produced by three institutions: European Standardization Committee (CEN), European Committee for Electricity Standardization (CENELEC), and European Telecommunications Standards Institute (ETSI). The last two deal with electricity and telecommunications respectively while the first deals with everything else. Figure 6 shows the details of the European Union Standardization System.

The three institutions work in close relationship with the European Commission; especially, when the Commission orders the institutions to produce harmonized standards, which are standards, related to European Directives, and therefore become mandatory within the European Union (EU). CEN manages technical committees (CEN/TCs) specialized in technical aspects in a wide variety of sectors, both industrial and non-industrial (e.g., agriculture, banking, environment). However, two Associated Standards Bodies act on behalf of CEN, which are AECMA for aerospace and ECISS for steel. Those Associated Standards Bodies were founded to support the intensive intra-European cooperation in aeronautics and steel making. In the case of steel, ECISS had been initiated by European Community for Steel and Coal (ECSC) and contributes to intra-European free trade of steel products, which had been the main aim of ECSC.

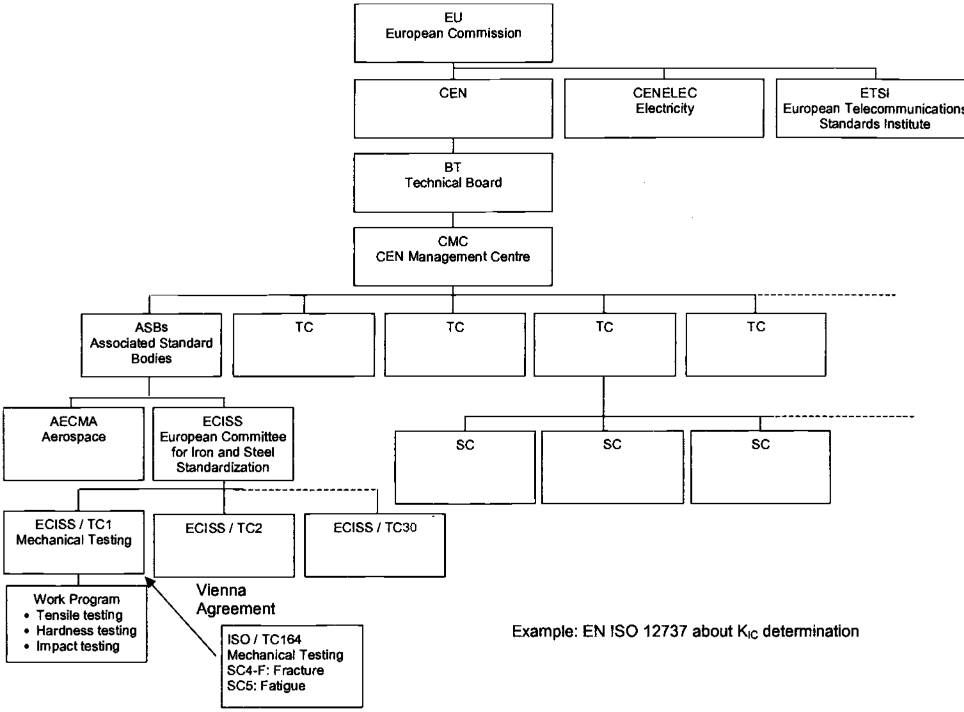

FIG. 6—*European Union Standardization System.*

ECISS manages technical committees (ECISS/TCs) similar to the CEN/TCs. Among the TCs, ECISS/TC1 is responsible for mechanical testing of metals. ECISS/TC1 is in charge of drafting standards about tensile, hardness, impact testing, and other monotonic tests. ECISS/TC1 does not work on fracture and fatigue since work on these items is already done by ISO/TC164/SC4-F and SC5, respectively.

When CEN needs a standard on fatigue or fracture mechanics, the Vienna Agreement between CEN and ISO applies. So far, the Vienna Agreement has been used once to adopt at the European level, international standard ISO 12737 about K_{IC} determination that therefore became EN ISO 12737. European standardization conducted by CEN is of utmost importance because once a European standard is ratified; all EU Member States have to incorporate it into their own national collection of standards replacing the national standards dealing with the same subject. In other words, these national standards are automatically withdrawn and replaced by the European Standard.

ASTM International Standardization System

ASTM started in 1894 by specializing in the testing of materials, especially mechanical tests. It has expanded the areas it covers since then and recently changed its name and logo and is now known as ASTM International with a tag line of "Standards Worldwide." Materials and testing standard development is performed within the ASTM International technical committees and subcommittees in a similar way as in CEN, ECISS, or ISO, with some key differences. Three key differences are: any technical expert can join and participate within ASTM International from any country; technical expert represents himself, not his country or his company; and one negative vote can stop a document from becoming a standard. The ASTM International standardization system is totally voluntary and members do not receive compensation for attending or participating in standards development. There are other standards development organizations (SDOs) in the United States; most are dedicated to main industrial sectors. These SDOs are like the French Standardization Offices but at a much greater scale. There are ASTM, ASME, SAE, API, and IEEE, which work on materials and testing, mechanical engineering, automotive and aerospace, and petroleum and electronics, respectively, among the most famous SDOs. The American National Standards Institution (ANSI) of the United States like AFNOR is for France, DIN is for Germany, and BSI is for England.

The Fatigue and Fracture Committee (E08) has eight subcommittees as shown in Figure 7. Variable amplitude fatigue activities are occurring within E08.04 on "Structural Applications" and E08.05 on "Cyclic Deformation and Crack Formation." Subcommittee E08.05 does have a standard on cycle counting (ASTM E 1049) that is important to this subject, and Subcommittee E08.04 is concerned with how to separate those cyclic loadings that are "damaging" from those that are "non-damaging." The laboratory test can be conducted much faster once all of the non-damaging cycles have been removed.

ISO Standardization System

ISO standards are considered to be international standards and have been prepared to assist free trade across borders. ISO standards are typically a blending of national standards from its members (AFNOR, ANSI, BSI, DIN, etc.). The standards are drafted within ISO Technical Committees and Subcommittees composed of international experts from various countries. Organizationally the countries that join an ISO committee need to decide if they want to be a "P"articipating or an "O"bserving member of that committee. Both "P" & "O" members can send representatives to the meeting but only the "P" member countries have a vote. There is one vote per country. The technical experts that attend the ISO meetings have to be selected by their country to attend and they represent their country. All voting on standards is done electronically through the ISO website and each country either votes affirmative or negative on the standard. A negative vote does not stop the document from becoming a standard provided a sufficient percentage of the "P" member countries vote affirmative. Typically, five "P" member countries are required to vote affirmative for a standard to pass. To avoid duplication of work, ISO has made agreements with other SDOs, such as the "Vienna Agreement" with CEN.

ISO/TC164 is dedicated to mechanical testing of metallic materials. The organizational structure of ISO/TC164 is shown in Figure 8. Subcommittees SC1, SC2, SC3, and SC4 work on monotonic test methods including impact tests and fracture mechanics tests.

The Fatigue and Fatigue Crack Growth Subcommittee (ISO/TC164/SC5) is the one committee on cyclic loading and has 13 working groups (WG) or activities as shown in Figure 9. WG8 is Project 12110 on "Variable Amplitude Method" of fatigue and is at present collecting information before they decide what standard should be developed first.

ASTM E8 Fatigue and Fracture Committee

Year 2002-2003

Chairman	*Michael R. Mitchell*
Vice Chairman (LRP)	*James L. Rudd*
Vice Chairman (Standards)	*Ravinder Chona*
Recording Secretary	*Gerald Petrak*
Membership Secretary	*Mark L. Thomsen*
ASTM Staff Manager	*Jeff Adkins*

Subcommittees

E8.01	E8.02	E8.03	E8.04	E8.05
Research & Education	Standards & Terminology	Advanced Apparatus & Techniques	Structural Applications	Cyclic Deformation & Crack Formation
Steve Daniewicz	*C. Belsick*	*Arthur A. Braun*	*Jeffrey Bunch*	*Sreeramesh Kalluri*

E8.06	E8.07	E8.08
Crack Growth Behavior	Linear-Elastic Fracture	Elastic-Plastic Fracture
John J. Ruschau	*Gary H. Bray*	*John Landes*

Members-At-Large

Norman E. Dowling	*Richard Rice*
James A. Joyce	*Ashok Saxena*
R. Craig McClung	*W. Alan VanDerSluys*
James C. Newman, Jr.	*Dale A. Wilson*

FIG. 7—*Organizational chart of ASTM E08 Committee on Fatigue and Fracture.*

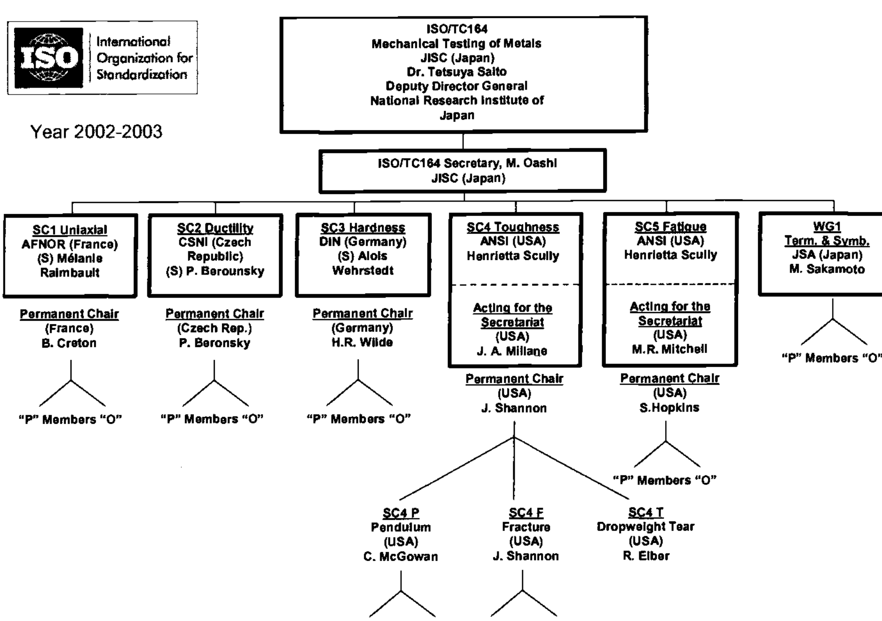

FIG. 8—*ISO/TC164 organizational chart showing the secretariat and chairman of each group.*

International Organization for Standardization

ISO Fatigue Subcommittee

Year 2002-2003

Secretariat, USA (ANSI)
Chairman: S.W. Hopkins (USA)
Secretary: M.R. Mitchell (USA)

Project Groups within ISO/TC164/SC5 Fatigue

WG 1	WG 2	WG 3	WG 4	WG 5
Project 12105 Fatigue Testing General Principles	**FDIS 12106 Axial Strain Control Low-Cycle Method**	**FDIS 12107 Statistical Planning & Analysis for Fatigue Testing**	**FDIS 1099 Axial Force Control Fatigue Method**	**Project 4965 Dynamic Force Calibration**
Brian Powell (UK) / S. Hopkins (USA)	*M.R. Mitchell (USA)*	*Satoshi Nishijima (Japan)*	*Bernd Jaenicke (FRG) / M.R. Mitchell (USA)*	*Mike Sanders (UK)*

WG 6	WG 7	WG 8	WG 9	WG 10
FDIS 12108 Fatigue Crack Growth Method	**Project 12109 Computer Control Testing / Data Acquisition / Data Analysis**	**Project 12110 Variable Amplitude Method**	**Project 12111 Thermal-Mechanical Fatigue Testing**	**Project 12112 Multi-Axis Fatigue Testing**
Russell Cervay (USA)	*Murray Nicolson (UK)*	*Jean Menigault (France)*	*Mike McGaw (USA)*	*Andre Galtier (France)*

WG 11	WG 12	WG 13	WG 14	WG 15
Project 12XXX Axial-Alignment of Fatigue Machines	**Project 1143 Rotating Bar Fatigue**	**Project 1352 Torsional Fatigue**		
Fathy Kandil (UK)	*Yifei Gao / Boqun Wu (China)*	*Yong-Hak Huh (Korea)*		

FIG. 9—*ISO/TC164/SC5 organizational chart showing the 13 working groups and their conveners.*

Conclusions

Standardized test methodologies are very important and we hope through such standardization of variable amplitude fatigue test methods that laboratory data will be generated and used by people around the world. Only through such standardization, can meaningful intra- and inter-laboratory results be cross-correlated and readily references with some semblance of continuity and meaning.

References

[1] Reed, R. P., Smith, J. H., and Christ, B. W., "The Economic Effects of Fracture in the United States," US Department of Commerce, National Bureau of Standards, Gaithersburg, MD, Special Publication 647, March 1983.

[2] Job, M., "Aloha 243-You Still Up?," Air Disaster, Vol. 2, Aerospace Publication, March 1996.

[3] Fuchs, H. O. and Stephens, R. I., *Metal Fatigue in Engineering*, John Wiley & Sons, 1980.

[4] Mann, J. Y., "The Historical Development of Research on the Fatigue of Materials and Structures," The Journal of the Australian Institute of Metals, Vol. 3, No.3, November 1958.

[5] Brose, W., Dowling, N. E., and Morrow, J-D., "Effect of Periodic Large Strain Cycles on the Fatigue Behavior of Steels," Paper No. 740221, SAE, Detroit, MI, Automotive Engineers Congress, February 25 – March 1, 1974.

Journal of ASTM International, Nov./Dec. 2004, Vol. 1, No. 10
Paper ID JAI19037
Available online at www.astm.org

Peter C. McKeighan[1] *and Fraser J. McMaster*[1]

A Framework for a Standardization Effort for Fatigue Crack Growth Testing Under Variable Amplitude Spectrum Loading

ABSTRACT: Fatigue crack growth testing under variable amplitude loading conditions is currently not standardized. Without standardization, the methods and techniques applied by different laboratories vary, and as such, lab-based bias can occur readily. The goal of this paper is to discuss in detail the experience developed and lessons learned during years of spectrum crack growth testing. Issues concerned with specimen geometry, crack geometry, precracking methodology, crack length measurement, spectrum content, load magnitude control, and interpretation of results are addressed herein. Although the ASTM Standard Test Method for Measurement of Fatigue Crack Growth Rates, E 647, provides guidance that is useful to this test, the specialized nature of spectrum testing does provide its own unique set of issues different from da/dN versus ΔK testing.

KEYWORDS: fatigue testing, crack growth testing, variable amplitude loading, spectrum loading, standardization

Introduction

Of the major types of fatigue testing currently performed by laboratories all over the world, fatigue crack growth testing under variable amplitude, spectrum loading conditions remains one test without any unified standardization. The advent of state-of-the-art digital servohydraulic controllers in the laboratory has provided further tools making this type of test possible for a wider range of laboratories. However, there are some specialized concerns during spectrum crack growth (SCG) testing that make the results obtained for this test critically dependent upon the conditions applied.

Without standardization, the methods and techniques applied by different laboratories vary, which inevitably introduces lab-based bias in the crack propagation results obtained from these types of tests. Some of the most relevant issues that require some industry standard guidance include: specimen geometry, precracking load levels, load control methodologies, crack length measurement method(s), crack geometry, character of the load spectrum, and load spectrum editing. Consequently, standardization can assist by ensuring that (a) the test community is at least aware of the issues, and (b) lessons learned during past testing are applied so as to minimize the possibility of laboratory-based bias.

If we assume that spectrum crack growth testing should be standardized, the next question is what form should this standardization take? ASTM standardization documents include the following: standard specification (usually materials and the like), standard terminology (terms, definitions, or abbreviations), standard classification (materials, products, systems, or services),

Manuscript received 28 May 2002; accepted for publication 21 November 2002; published November 2004.
Presented at ASTM Symposium on Fatigue Testing and Analysis Under Variable Amplitude Loading Conditions on 29 31 May 2002 in Tours, France; P. C. McKeighan and N. Ranganathan, Guest Editors.

[1] Manager and Research Engineer, respectively, Southwest Research Institute, Materials Engineering Department, 6220 Culebra Rd., San Antonio, TX 78238-5166.

standard test method, standard practice, and standard guide. Spectrum crack growth testing would nominally fall under one of the last three; however, the standard test method and practice are both specifically "definitive procedures." Since the SCG test is driven by the specific details of the application and as such must be broad and loose in definition, it is believed that the standard guide is the best approach. A standard guide is defined as a series of options or instructions that does not recommend a specific course of action.

In this paper, the issues related to standardization are explored, and, where possible, candidate recommendations for standardized guidelines are provided. These recommendations are based upon suitable fracture mechanics and fatigue calculations as well as empirical lessons derived from standard testing practice over many years of performing these types of tests in the Southwest Research Institute (SwRI™) Solid and Fracture Mechanics Laboratory. The content of this paper is intended as an initial draft or starting point for an ASTM standard guide for spectrum fatigue crack growth testing.

Motivation for Performing SCG Testing

The usual reason for performing spectrum fatigue crack growth tests is to evaluate whether a given component can maintain its structural integrity under service-loading conditions. In the context of this discussion, "component" refers to a simulation of the actual hardware or, if the geometry is sufficiently simple to be gripped in a uniaxial frame and loaded as desired, the hardware itself. Inevitably, the results from a spectrum crack growth test are used in a damage tolerance analysis (DTA). Damage tolerance is the ability of a structure to sustain defects or cracks safely until such a time that action can be taken to eliminate the cracks [1]. In other words, it is the capability of a structure to resist failure and operate safely with damage (e.g., fatigue cracks) in the primary structure. Primarily as a consequence of cracking issues with the F-111, the United States Air Force adopted the damage tolerance methodology for airframe design in the early 1970s [2].

During a durability and damage tolerance assessment, the goal is to (a) determine the effect of a crack on the strength of the structure, (b) calculate the amount of crack growth as a function of time under variable amplitude loading, and (c) determine the inspection threshold and intervals required to operate the structure safely. Due to the complex and multi-faceted nature of a DTA, it is essential to perform some type of validation of the process. In this context, validation refers to the process of demonstrating that predictive models produce results that agree with observations from relevant experiments (e.g., coupon or full-scale tests) and real-world experience (structural teardowns)[2] [3]. Often, part of a validation exercise includes some type of calibration whereby empirical parameters in the model are adjusted depending upon the results obtained.

Validation and calibration of the DTA process is essential due to the complexity of the process and the large number of different models included in the process, for instance:

- loads model (spectrum)
- stress analysis model (finite element models)

[2] This is in contrast to verification, which is the process of demonstrating that predictive models work as intended by comparing to relevant analytical solutions or limiting cases where answers are known. Verification demonstrates that a model is solved correctly; validation demonstrates that the model correctly predicts the results of experiments or service experience.

- fracture mechanics model (stress intensity factor solutions for different crack geometries)
- crack growth model (method to characterize the da/dN versus ΔK data)
- integration model (crack growth software)

Each of these different models possesses its own inherent fidelity, and increasing the accuracy of the overall DTA process depends upon optimizing the performance of each independent model. Practically, this is often achieved by calibrating DTA results to experimentally measured data.

Perhaps the clearest need for calibration during the DTA process occurs when the load spectrum causes crack growth retardation. The earliest DTAs (for instance, that used for the F-111) employed a Wheeler model [4] to predict retardation following an overload. An integral part of this model is an empirical constant determined by comparing life predictions with results from spectrum load tests. Critical inputs into the DTA include the relationship used to describe the crack growth properties. In fact, using normalized damage models for calculating crack growth rate on a flight-per-flight basis, including sequence effects, allows separation of material, geometry, and stress parameters during the DTA [5,6].

Following the initial development of the DTA design process, there was a flurry of activity concerning fatigue crack growth behavior under spectrum loading conditions [7 10]. Nevertheless, this issue has been of less interest for the past 20 years as DTA has evolved past the aerospace sector and into Transportation as well as Oil and Gas Industries. During this period, laboratories have been quietly performing DTA validations and calibrations using unproven methods and techniques with few common forums available to share lessons learned.

Features of SCG Testing

In the absence of any other guideline, the basic requirements of the ASTM fatigue crack growth standard, Standard Test Method for Measurement of Fatigue Crack Growth Rates (E647-00), should be maintained. However, spectrum crack growth testing typically encompasses a broader range of topical issues as compared to standard fatigue crack growth testing where da/dN and ΔK are measured and controlled.

Specimen Configuration and Preparation

The goal of the geometry used during SCG testing is to capture the salient features of the overall geometry of the structure or hardware under evaluation (shown in Fig. 1) without creating a situation that cannot be modeled adequately using damage tolerance philosophies. A structure is typically examined and fatigue critical locations defined as shown in Fig. 1. It is critical that the test specimen geometry be relatively simple to ensure that the DTA model can be calibrated appropriately using the experimental test results. As such, the level of complexity of the test specimen (also called coupon) is often limited by what can be accommodated in the crack growth design software.

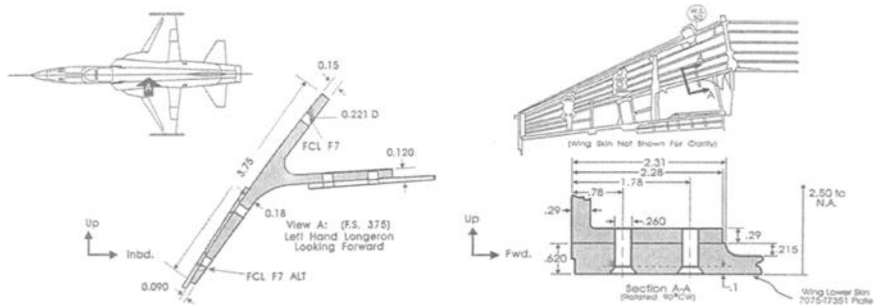

FIG. 1 *Schematic of actual aircraft geometry simulated during SCG testing.*

Some geometries used in the past are shown in Fig. 2. A common feature of these geometries is the stress concentration (hole or geometry change) where cracks nucleate. In the case of Fig. 2*a* and *b*, cracks initiate and grow from features that model an aspect of the actual component geometry. The most common case of a crack growing through the short ligament of a fastener hole is shown in Fig. 2*c*. In addition to capturing the salient geometric features, the test geometry also must capture relevant detail for how the crack will grow in the structure. In the case of Fig. 2*a* and *b*, the type of crack is quite different; it grows as an edge crack in Fig. 2*a* as opposed to a surface crack in Fig. 2*b*.

A more complex 1-1/2 dogbone joint geometry is indicated in Fig. 2*d*. Testing built-up joints is a challenge in the laboratory. It is essential that a sufficient number of strain gages be placed on the joint geometry to ensure that the load path and secondary bending are characterized fully. Results from these strain gages often can be correlated to finite element analyses or theoretical load transfer calculations to ensure that the modeled behavior is consistent with that observed in experiments. Load train stiffness, specimen length (for joint specimens, especially), hydraulic actuator concentric tolerances, and inherent grip features can all contribute to large differences in the applied moment, which has a large effect on secondary bending and to some extent load transfer. Despite these challenges, the complexity of a typical built-up structure necessitates joint testing capability. An excellent AGARD reference [11] is available for candidate joint geometries, detailing their overall mechanical response and providing results from an extensive round-robin test program with eight laboratories.

Unfortunately, there is no universally applicable specimen geometry for a given fatigue critical location. The optimum geometry is a judicious selection balancing realistic modeling of the actual structure with practical laboratory considerations. However, it is always good policy to ensure that the specimen is loaded as expected. This is ensured by strain gaging an uncracked sample and measuring strain levels while loading to 80 100 % of the peak load. As a minimum, this provides sufficient confidence that the boundary conditions applied to the specimen are consistent with expectation.

In addition to strain gaging the specimen, it is also common to polish the specimen metallographically in the region where the crack is expected to grow to aid in making visual crack length measurements.

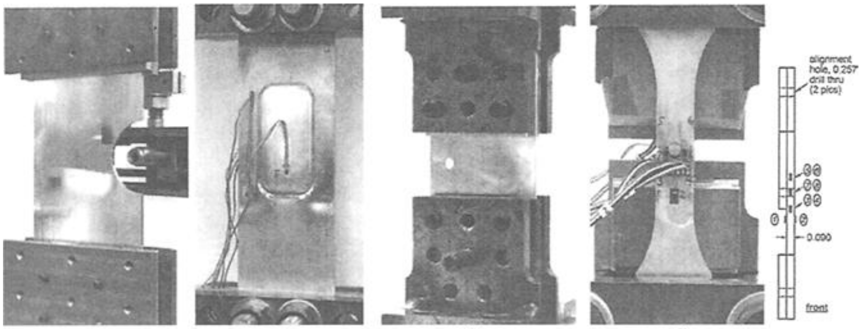

(a) (b) (c) (d)

FIG. 2 *Different specimen geometries including (a) an edge crack at a radius, (b) a surface crack near a scalloped detail, (c) cracking from the edge of a fastener hole, and (d) multiple layer joint simulation with low levels of load transfer.*

Crack Geometries

The vast majority of cracks during SCG testing are initiated from a thin electric discharge machined (via EDM) notch. Nevertheless, in some cases, especially when the desired starting crack length of a test is small, it is desirable to have a freely initiating crack (e.g., one not created at a notch deliberately placed in the coupon). For instance, if the starting crack length from the edge of a hole during a test is on the order of 0.127 mm (0.005 in. or 5 mils), an effective way to do this is to machine an undersize hole, put in a typical EDM crack starter, precrack the specimen, and then use a stepped reamer[3] to carefully drill the hole to the full size. What results is a very small crack; on the order of 0.127 0.254 mm (5 10 mils) is fairly typical.

However, when performing this exercise, care must be taken to ensure that (a) during the reaming process plastic upset is not caused to the crack, (b) the loads are sufficiently low during the initial precracking that the plastic zone at the tip of the small crack is sufficiently small for the new initial loading conditions, and (c) the crack tip environment is not altered by cutting fluids, cleaners, oils, etc. Prior to taking data, it is not uncommon to "freshen the crack" a bit by fatigue cycling at low constant amplitude loads to get the crack growing again.

Four different EDM crack starters are shown in Fig. 3. The most common equilateral corner crack at the edge of a through hole is shown in Fig. 3*a*. Provided the thickness of the specimen is not too large relative to the hole diameter, this type of notch can be created with a wire EDM machine. Sometimes it is not possible to EDM the starter notch, and a jeweler's saw or even a razor blade is used to create an initial notch. Nevertheless, the remaining three notches in Fig. 3*b–d* were created with sinker (e.g., plunge) EDM. In the case of the surface crack, Fig. 3*b*, the starter is a triangular notch pointing through the thickness, whereas in Fig. 3*c* and *d*, the EDM tool left a semi-circular notch. Using a semi-circular notch provides some nominal control over

[3] A stepped reamer has an initial tip diameter equal to the undersize hole diameter gradually flaring to the full diameter of the hole. Hence, the initial portion of the reamer guides through the pilot hole, and material is equally removed around it with the flared portion of the tool. These special order tools are available in any custom desired dimensions.

the aspect ratio (defined by the ratio of the crack surface length to depth) immediately after the crack initiates. Additional detail regarding surface flaw notch creation is contained in the Standard Practice for Fracture Testing with Surface-Crack Tension Specimens, E 740.

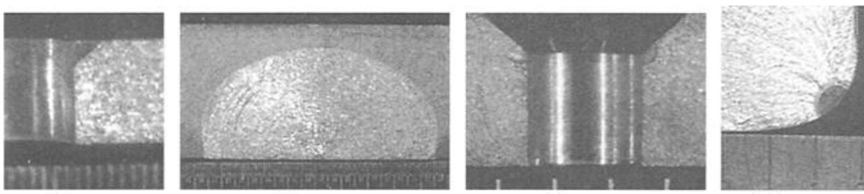

(a) (b) (c) (d)

FIG. 3 *Different types of crack starter notches for part-thru cracks including (*a*) corner at a hole, (*b*) surface, (*c*) corner at a countersink, and (*d*) corner on a radiused lug edge.*

Aspect ratio is relatively difficult to control in SCG coupons. Generally the microstructure or texture of the material, inherent stresses in the part, or the shape of the overall geometry itself controls the aspect ratio of the crack. Sometimes the aspect ratio is stable, whereas other times it changes continually during a test. The aspect ratio of the growing fatigue crack is a critical parameter during this type of testing. It is probably the clearest and most obvious contributor to scatter in spectrum crack growth tests, assuming a significant portion of the life is spent growing a part-through crack. Crack aspect ratio should be measured during or after testing through the use of marker bands, heat tinting, or metallurgical examination after the test.

Precracking Methodologies

The E647 guidelines[4] for precrack length are generally too restrictive for spectrum crack growth testing. For aircraft applications, the spectrum test generally starts at a crack length of 1.27 mm (0.050 in.). The usual approach is to create a fatigue crack extending from the EDM notch that is equal to the width of the notch (on the order of 0.25 mm or 10 mil).

Regardless of whether the crack is naturally initiating or growing from an EDM notch, constant amplitude loading is typically used to precrack the specimen prior to spectrum loading. Although it is not unheard of to precrack the specimen under spectrum loading conditions, this is less common although probably more rigorously accurate from the viewpoint of what the service hardware experiences. The magnitude of the precracking load is typically controlled as a percentage of the peak load in the cycle. An approximate rule of thumb is to start precracking at a constant amplitude low r-ratio with the maximum load 50 % of the peak spectrum load. Higher levels for more benign spectra on the order of 80 %, and on rare occasions 100 % of the peak, have sometimes been necessary due to an absence of crack growth.

The argument for being able to precrack at these high load levels is as follows. After one pass through the spectrum, peak loads higher than the precrack load level will have been applied. Therefore, if anything should be discarded, it should possibly be the first portion of the spectrum pass before the peak load is achieved. Although simple in concept, unfortunately we know that sustained cyclic loading and crack growth at a certain load level will create crack closure

[4] The ASTM E 647guidelines require a precrack length equal to the greater of (a) 10 % of the thickness, (b) the width of the EDM notch, or (c) 1 mm (40 mil).

conditions different than if the crack had grown under variable amplitude loading cycles. Nevertheless, as with many aspects of a spectrum crack growth test, the practicalities of generating data in a finite amount of time trump the theoretical arguments.

Some of the newest analytical modeling tools for crack closure (FASTRAN) could prove beneficial for understanding the role of precrack level on the response of the material under spectrum loading conditions. In the absence of this information, there are some relatively straightforward methods that could be applied to determine the precrack load level. In a subsequent section discussing the spectrum loading, a method is described that can be used to determine the critical cycles that are the most damaging in the full spectrum. Consequently, the most critical cycle magnitude could be used to define the maximum possible constant amplitude level suitable for precracking.

Crack Length Measurement

Variable amplitude fatigue cycling creates some challenges with regard to the conventional methods of non-visual crack length measurement. As a consequence of this, it is critically important to ensure and validate crack length data with periodic visual crack length measurement (using a conventional traveling microscope and vernier scale). Since the primary end result of a spectrum test is the crack length versus cycle count data, it is essential to use care and maximize accuracy when measuring crack length(s).

At SwRI, we perform visual crack length measurement continuously and throughout the spectrum test if possible. Admittedly, this does increase the amount of time that a test takes; however, experience has shown that this is the most effective method of recording crack length. Although it may seem a bit archaic to emphasize visual crack length measurements, there are some specific reasons for why potential drop and compliance (the two most popular forms of non-visual crack length measurement) can be problematic to implement during SCG testing.

Perhaps the most obvious reason is that the cracks created during spectrum tests are rarely thru-thickness cracks. Inevitably, a crack length measurement is desired in two dimensions; for example, on the face of the specimen and along the bore of the hole. Custom mirrors created by polishing drill rod at 45° angles have proven effective in making bore hole measurements of crack length. Even when the crack does transition from part-through to completely through-thickness, it is typical for asymmetry to exist between the front and back face crack length measurements. Typically, this asymmetry continues until specimen failure without the short crack length side ever catching up to the longer side.

The second reason why non-visual crack length methods are difficult to implement is that the specimen geometry is rarely ever sufficiently standard to have either PD or compliance calibrations available. A close examination of the various geometries shown in Fig. 2 clearly illustrates this with unusual geometric cut-outs and thickness changes. The third reason is that the range of crack length measurement typically required during spectrum crack growth tests is quite large. For example, it is not uncommon to desire measurements from 0.64 64 mm (0.025 2.5 in.). Even the most robust non-visual crack length measurement technique would have difficulty coping with two orders of magnitude change in crack length, ensuring that sufficient sensitivity, repeatability, and resolution were available throughout.

Although visual crack length measurements overcome many of the challenges during spectrum fatigue crack growth testing, they are not possible for all specimen geometries. For example, consider the case of the multiple layer joint when the crack grows in a layer obstructed from view by another layer. In this situation, indirect potential drop can be used by adhesively bonding KRAK® gages (Hartrun Corporation, St. Augustine, FL) to the specimen. On the faying surface of the joint that would nominally be in contact with the KRAK gage, a pocket is milled out to ensure that the surface does not rub the face of the KRAK gage. The depth of this pocket is sufficiently small (on the order of 0.5 mm or 20 mils) that it has little or no effect on overall joint stiffness.

Some examples of KRAK gages on joint specimen geometries are shown in Fig. 4. The KRAK gage, Fig. 4*b*, is a pre-calibrated foil gage on a polymeric backing that is affixed to the metallic specimen in a similar manner to a strain gage. The foil gage cracks in parallel with the underlining material, and the associated FRACTOMAT® instrumentation can be used to measure crack length. KRAK gages are available that conform to the edge of a hole and have sufficient sensitivity to measure small cracks. Furthermore, the gages are well tailored to large changes in crack length. In the case of Fig. 4*b*, measurements are made on both the short ligament side of the hole as well as the longer, continuing damage side of the fastener hole. On the short ligament, a scrap piece of aluminum is bonded onto the side of the specimen, with a silicone RTV, to support the KRAK gage and wire terminals.

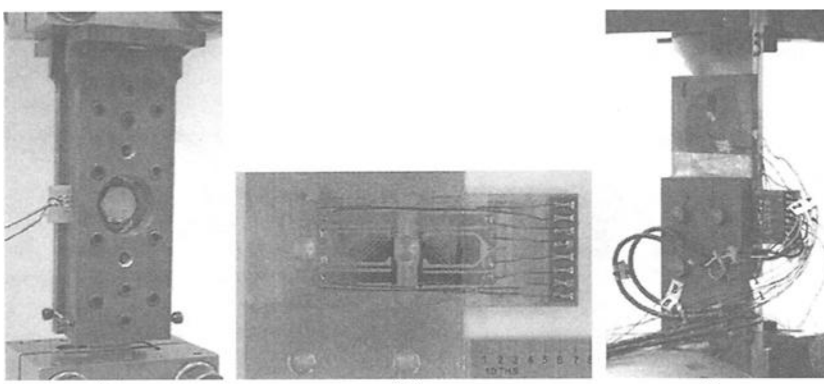

(a) (b) (c)

FIG. 4 *Indirect potential drop used to measure the crack growth on an inner layer of a multiple piece joint (*a,c*). The gage on the specimen in (*c*) is shown close-up in (*b*).*

Although the advantages of KRAK gages for SCG testing are many, users are cautioned to ensure that sufficient physical crack length measurements are available to validate the non-visual measurements that are made. Regardless of which non-visual crack length measurement method is used, it is essential to post-test correct the data to the physical measurements [12]. Some issues have arisen in the past with systematic differences between physical and KRAK gage derived measurements. In [13], a lag on the order of 0.40 0.75 mm (15 30 mil) was observed for low load, crack growth in a 2xxx series aluminum alloy. The greatest challenge in using KRAK gages appears to be with lower yield strength (larger plastic zone size) materials at relatively low stress levels. In these cases, KRAK gages with thinner, more brittle backings (the so-called high temperature series) are recommended to ensure that the gage output tracks the structural response.

Validating KRAK gage output in blind multi-layer joint tests requires using a crack marking scheme whereby a deliberate loading block is applied to create an easily observed artifact on the fracture surface. The simplest form is to use a load fixed at near the maximum load of the spectrum (on the order of 70 90 %) with an r-ratio of approximately 0.85 or higher. Simple cyclic predictions using the Paris relationship can determine how many cycles are required to leave an artifact band 0.05 mm (2 mil) wide. Be aware, however, that it is not uncommon to apply on the order of 50K to 250K cycles of this artifact load to mark the fracture surface. Furthermore, some materials will mark better than others, and it is important to validate the process empirically before relying on it for incremental measurements.

This deliberate form of crack marking is illustrated in Fig. 5*a*. Even to the naked eye, without a moderate to high power light microscope, the dark marker bands are evident. The disadvantage of this type of marking scheme is that it will potentially contribute to different crack tip conditions (possibly change the crack closure state) and therefore impact the growth rate that occurs. This is easily overcome, however, by ensuring that lives are the same both with and without the marking scheme applied. Moreover, it is not uncommon for the spectrum pass itself to mark the fracture surface as shown in Fig. 5*b*. However, these natural marks are difficult to use to discern incremental growth since it is difficult to definitively attribute the marks to any event or know when repeating occurs.

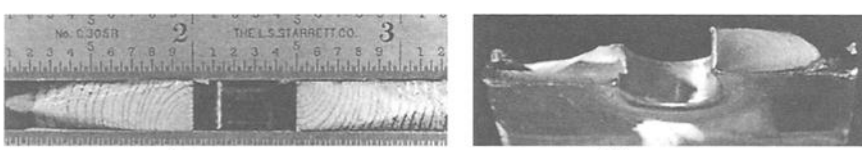

(a) (b)

FIG. 5 *Illustration of fracture surface features or crack marking for (*a*) 12.7 mm (0.5 in.) and (*b*) 6.25 mm (0.25 in.) fastener hole specimens subjected to spectrum loading.*

Previous work examining the influence of different segments of the loading spectrum has utilized a marking scheme that leaves a feature discernable in the scanning electron microscope [14]. One of the most recent methods utilized by Piascik and Willard [15] uses a decreased minimum load segment to leave a series of deliberate sequence of marks, for instance 5-9-3. This allows a complete understanding of the sequence and makes determining incremental growth rate fairly straightforward. Again, however, readers are cautioned to make sure that artificial marking schemes do not influence the overall measured crack growth behavior.

The periodicity required for crack length measurement is a function of how quickly things are changing. Given a conventional concave-up a versus N curve, experience has shown that the salient features of this response can be captured with approximately 20 50 discrete crack length measurements. The measurement interval varies: during the early portion of the test, crack length measurement intervals are on the order of 5× the base resolution of the crack length measurement system. As the crack speeds up, the cycle count between measurements is gradually reduced so that at the end of the test each crack length interval between measurements is on the order of 1.27 2.54 mm (0.05 0.1 in.).

Spectrum Content, Magnitude, and Editing

Multiple treatises could be written addressing the issue of how spectra are measured, processed, and developed. Only some of the major spectrum issues will be addressed briefly herein. There are a number of standardized load sequences available in the literature. NLR in the Netherlands have recently compiled a CD that contains thirteen of the most common standardized load sequences including TWIST, MINTWIST, FALSTAFF, and TURBISTAN [16]. A fuller listing of the different sequences available on this CD, including the application, is shown in Table 1. This excellent resource saves an enormous amount of time by compiling all of the sequences together in one single reference.

TABLE 1 *Listing of the standard spectra available on the NLR CD [16].*

Sequence Name	Application
TWIST, Mini-TWIST	Transport aircraft wing root (lower wing skin)
FALSTAFF, Mini-FALSTAFF	Fighter aircraft wing root (lower wing skin)
ENSTAFF	Tactical aircraft composite wing skin
Cold, Hot TURBISTAN	Cold/hot section disks in fighter aircraft engine
Helix, Helix-32	Hinged helicopter rotors
Felix, Felix-28	Fixed helicopter rotors
WISPER, WISPERX	Horizontal axis wind turbine blades

Whereas generic spectra may be useful in the absence of a specific sequence for ranking materials or making some other type of specialized research assessment, the majority of applied SCG work uses spectra supplied by customers and based upon field measurements. Two example spectra are shown in Fig. 6. The fighter aircraft spectrum, Fig. 6*a*, has a lower effective mean stress when compared to the civil spectrum in Fig. 6*b*. The civil spectrum is also populated by frequent ground-air-ground cycles (the vertical perturbations to slightly compressive loading, e.g., the aircraft sitting on the ground). Taking the time to review a given spectrum in this manner is useful for understanding the essential character of the loading before testing in the laboratory.

The test spectra (also referred to as a "usage" or "sequence" when describing a particular mission mix or series of maneuvers) are often common between a given series of fatigue critical locations. The only modification required is a different scale factor for each. This is determined by a structural engineer calculating the relevant transfer functions to relate loading at the control point where the load is measured and at the fatigue critical locations. Although these transfer functions usually take the form of simple scale factor differences, stress offsets are also sometimes applied to the original supplied sequence. Readers are cautioned that scaling the spectrum is one of the most common errors that can be easily made during this type of testing.

Sometimes an SCG coupon is unable to capture adequately a stress gradient applied to the real structure. For instance, if a certain mix between axial and bending load is evident and the form of the coupon does not simply allow the correct mix between tension and bending, an artificial gradient can be applied by modifying the load as the crack grows. Normally, this takes the form of changing the mean (set point) load incrementally every 2.5 mm (0.1 in.) or so. This adjustment is typically performed manually and not automatically, because an effective automatic crack length measurement method is problematic under spectrum loading.

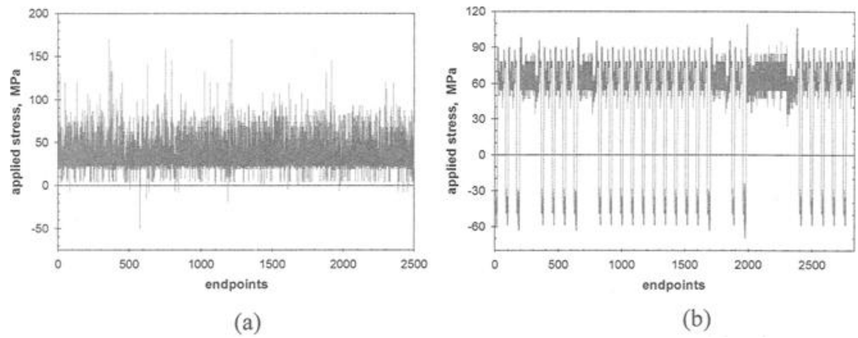

FIG. 6 *Two time history samples of (a) trainer aircraft and (b) civil aircraft loading spectrum.*

A spectrum is typically provided where one pass equals some physical quantity: for instance, flights, miles, hours of operation, etc. There is an enormous number of degrees of freedom in a given spectrum pass. Users are cautioned, however, that if less than ten spectrum passes are made before the test completes, there could be potential sequence effect variables at play where reordering of the spectrum (e.g., changing when certain loads are applied) could make a significant difference in crack growth rate. It is also useful to examine graphically the spectra and analyze some of its features prior to performing testing.

In addition to preparing for the unexpected, some characteristics may necessitate different fixtures in the laboratory. For instance, applying a spectrum with a considerable amount of compression (e.g., compressive load magnitude is in excess of 25 % of the peak tensile load) requires antibuckling fixtures to simulate stiffened, constrained structure. The purpose is to restrain the specimen from buckling/rotating but not overly constrain it so that test data are unrepresentative.

While the nature of the two spectra was characterized by the time history plots in Fig. 6, it is sometimes beneficial to characterize the usage analytically (statistically) prior to testing. Two methods for making this assessment are indicated for a trainer aircraft spectrum in Fig. 7 and a railroad tank car spectrum in Fig. 8. Also shown in Fig. 7 is a damage measure [17] obtained by summing the cubes of the load ranges. This can be an effective measure of damage in the pass from a crack propagation viewpoint (the cube essentially comes from the Paris relationship slope).

Several points are noteworthy from the trainer aircraft spectrum. The most damaging cycles are not the most numerous cycles, nor is the primary damage content confined to a narrow band of loads. The majority of the damage tends to occur for stress ranges in excess of 70 MPa (~10 ksi).

The railroad tank car spectrum shown in Fig. 8 contains an enormous amount of compression, including a large percentage of load cycles that are full compression (e.g., never pass through zero load). Although there are sometimes practical reasons for ordering a sequence to be applied in the sequential manner indicated in Fig. 8 for full-scale structural tests, systematic ordering such as this (minimum load sorted with increasing maximum load) should be avoided for spectrum crack growth testing. Note the smallest loads in the sequence occur immediately after a high load, clearly not a desirable approach from the viewpoint of sequence effects and plasticity induced crack closure.

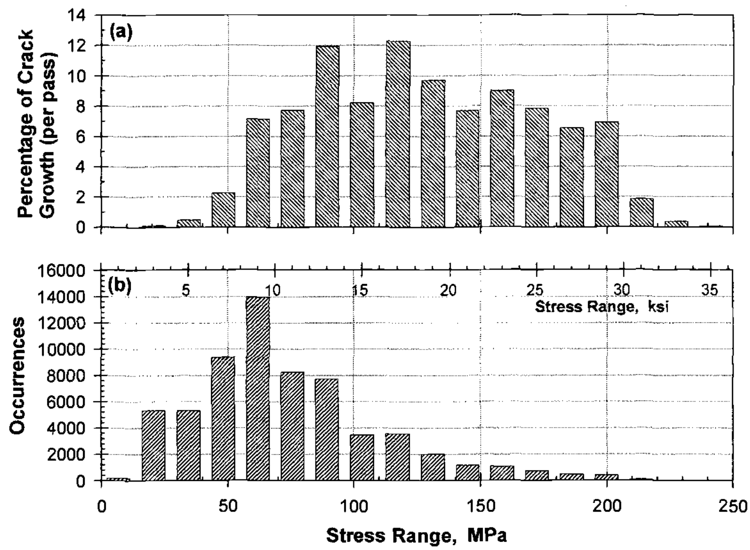

FIG. 7 *Description of a trainer aircraft sequence in terms of (a) fatigue crack growth damage and (b) occurrences as a function of the specific stress ranges applied.*

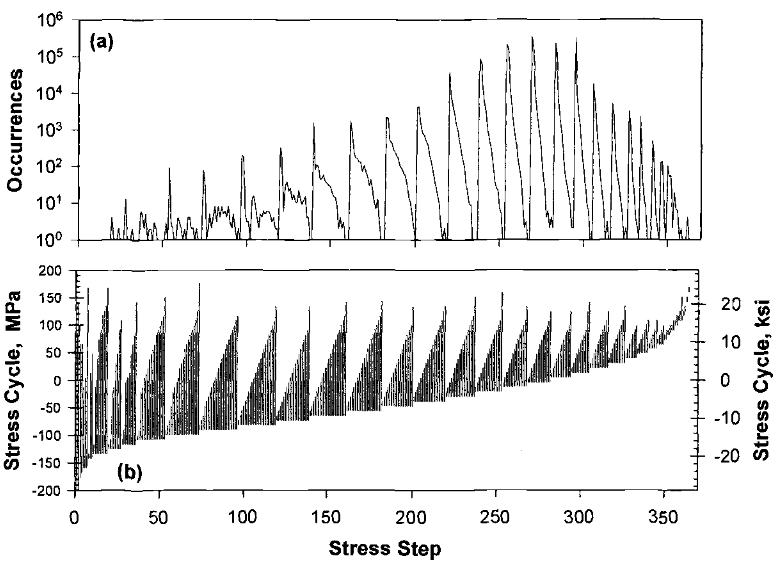

FIG. 8 *Graphical representation of the bending stress spectrum applied to the stub sill of a railroad tank car. Note the high amount of compression present in the spectrum.*

Finally, it is not unheard of to truncate the spectrum by eliminating loads that are not believed to be significant in the overall damage process. This often occurs with low amplitude cycles if the spectrum pass is inordinately long and impractical to use in the test laboratory. Similarly, the largest peak loads in the spectra are sometimes clipped (clipping is the process of limiting the peak load to some specific magnitude). The problem with either of these spectrum modifications is knowing a priori with confidence what the truncation or clipping is doing to the damage content of the sequence. Therefore, before arbitrarily performing some type of spectrum modification, the user is cautioned to perform some analytical modeling to justify the approach and some empirical testing to ensure that the resultant effect has been understood and validated fully.

Load Magnitude Control

Careful load magnitude control is one of the keys to performing a spectrum fatigue crack growth test accurately. This load control issue is one that the ASTM E 08.03 task group on Test Automation and Apparatus is currently addressing. The initial stages of a standardization development process are currently underway in two areas: (a) methods for validating and assessing control algorithms and (b) developing metrics for assessing overall performance. The following paragraphs briefly introduce some of the salient issues involved with controlling the end level magnitudes during spectrum crack growth testing.

A recent publication [17] introduced the concept of a damage parameter for tracking spectrum crack growth test performance. The basic idea is that the traditional method of tracking missed endlevels is insufficient for determining the degree of control (good or bad) in a given test. Clearly, the fewer missed endlevels, the better. But how many missed endlevels is unacceptable? What is the impact? In an effort to address some of these issues, the damage parameter concept in [17] (clearly unproven and as yet not fully developed) was developed and coincidently is the focus of another paper in this symposium [18]. The concept of the damage parameter is that when a test finishes, a metric will be available that includes a real-time range analysis to indicate how much of the theoretical damage (e.g., crack growth) occurred with the imperfect load application. These types of tools have been available to the structural testers for quite some time and are only now being made available to the materials testers.

There are well-established methods for optimizing system performance under variable amplitude loading. Perhaps one of the most effective ways to ensure peak load performance is to develop a to-from correction matrix. This is essentially a two-dimensional matrix that determines the extent required to over- or under-drive an actuator to get from load A to load B. The disadvantage with this approach is that you must have tried to hit the loads once to have anything other than a null value in the matrix. However, experience has shown that the matrix converges fairly quickly, leaving only the first pass through the spectrum problematic. Although this type of control strategy is usually invisible to the typical user, if one is going to perform spectrum crack growth testing it is imperative that one fully understand how the computer control system ensures that the appropriate load is being applied. This is an issue that cannot be stressed enough. Accurate end levels and test computer control are some of the most critical issues for ensuring high quality spectrum test results.

The control strategy also should be sufficiently robust in order to cope with significantly changing specimen compliances. Recall that this is one clear characteristic of a spectrum crack growth test: a range of crack lengths that vary by three orders of magnitude. The coupon designs used during this type of testing tend to be relatively stiff when the test starts, in part because the crack length is typically on the order of 1.25 mm (0.050 in.) at the beginning of the test when the initial spectrum loop control parameters are set. As the crack grows, compliance increases dramatically, thereby putting enormous pressure on the control algorithm to accommodate this significant change in compliance. Inevitably, the loop control parameters will need to be modified. Unsupervised (or open loop) control is simply not good enough for any form of SCG testing.

Finally, one of the most effective methods for running a spectrum test is to perform constant rate loading. This differs from the normal mode of fatigue tests, which is constant load cycle frequency. Effectively, what constant loading rate implies is that the low load magnitude cycles run at a higher frequency than the higher amplitude cycles. For the larger loads, a constant stress rate implies a slower rise time. Although this does introduce another variable into the testing, frequency sensitivity is generally relatively small for the majority of typical structural materials. Yet another similar approach is to set the frequency range desired, say for instance 20 Hz maximum (for the small amplitude cycles) and 5 Hz minimum. Although similar in principle to the constant loading rate approach, this method bounds the meaningful engineering variable (frequency) instead of a less understood loading rate.

Interpretation of Results and Number of Specimen

The fundamental result obtained during spectrum fatigue crack growth tests is the crack length versus cycle count data. A sample plot illustrating typical data is shown in Fig. 9. Although data are sometimes represented on a growth rate basis (slope of the a versus N curve), the difficulty is always determining what parameter to plot for driving force because the concept of a driving force (similar to ΔK) is meaningless for variable amplitude loading. Representing the growth rate data using a logarithmic scale also tends to confuse the differences between data sets clearly evident when plotting on an a versus N basis.

When planning SCG testing, experience has shown it is useful to plan on running 2.5 replicate tests for every given spectrum and specimen geometry combination. The implication of 2.5 replicate tests is that 50 % of the time two tests are run, and 50 % of the time three tests are run. The criteria typically applied to determine whether the test needs to be repeated is based upon the cyclic life for a given crack length interval (usually at least 80 90 % of the full range measured during the test and definitely starting at as small a crack length as possible with the test data). If the cycles required for this crack length interval are within ±10 15 % from each other, the test is deemed successful and not repeated. Obviously, a greater level of scatter implies that the test needs to be repeated. Moreover, if the crack length range is based upon longer crack lengths, the ±10 15 % empirically observed guideline can be lowered significantly.

Although the ±10 15 % factor is purely empirical, in a general sense the Virkler et al. data [19] tend to support it. Virkler et al. carried out 68 replicate crack growth tests on 2024 aluminum. Although the initial notch size in these M(T) samples was longer than a typical SCG test (9 mm or 0.35 in.), the standard deviation $\sigma_{\log N} = 0.03$ for the longest and shortest lives in the Virkler data. Hence, applying $\pm\sigma$ implies a factor of 15 % on cycle count for a given crack growth envelope. It should also be kept in mind that the Virkler et al. data were generated using constant amplitude loading almost 25 years ago.

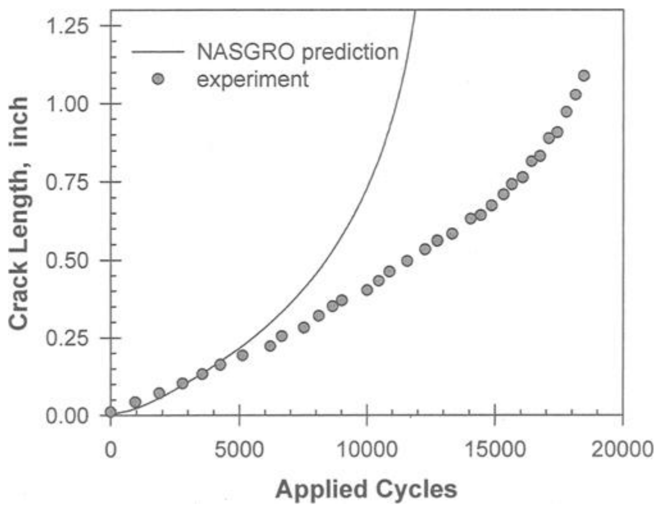

FIG. 9 *Typical primary result from a spectrum crack growth test (crack length versus cycle count or* a *versus* N *plot).*

There are some conditions under which repeatability from specimen-to-specimen appears to be greater. For instance, specimen geometries that tend to be similar to single-edge-notch specimens with fixed clamp grip conditions can be problematic, especially if different test frames are used in the laboratory. Although this has not been validated, it is believed to be a consequence of the fact that different frames have different loading train compliances. Very slight differences in tolerances that an actuator or gripping arrangement has can make a large difference when the geometry is such that a moment is applied to the specimen (inevitable with fixed grip loading of an edge cracked specimen). Although this has not been validated, either modifying the boundary conditions to pin load the specimen or testing on the same frame consistently (sometimes difficult for programs that require a rapid response) would presumably solve this problem. In cases such as this, up to five specimens sometimes have been required to generate the spectrum crack growth response.

Summarizing Remarks

The preceding discussion has highlighted successful methods for conducting spectrum crack growth tests. Are the methods presented the only techniques that could be used? Absolutely not. Furthermore, are they the best methods that are available? This is clearly an arguable point. In engineering laboratories today we tend to do what works and what has proven to be relatively bulletproof in the past. The luxury of striving for the optimum setup and exploring new methods is no longer normally possible given the schedule and financial pressures typically applied. Nevertheless, the techniques described herein have proven effective in at least one laboratory and as such provide a valuable resource for other labs to apply the lessons learned and develop their own empirical base of experience.

The spectrum fatigue crack growth test is not a trivial test to perform. Effective testing requires detailed knowledge of what the designer intends to do with the data. This is always the first issue the test engineer should explore since it can have a significant bearing on what methods are applied in the laboratory. This is also the type of test that requires that the test engineer fully understand how the test control system operates to ensure that it is set appropriately to control the applied loads. During constant amplitude testing, the load magnitude applied can be monitored simply. The danger with variable amplitude testing is that there is no manual method to ensure the loading is accurate, and testing requires complete faith in the test control software. With the complexity of the modern control system software and flexibility that these systems provide, making assumptions regarding test control can be problematic.

It is anticipated that this paper will provide the basis for development of an imminent ASTM standard guide. In addition to providing some guidance for labs that desire to perform this type of testing, development of a standard guide will also spur discussion and debate throughout the technical community. Presumably this discussion and debate would probably not occur without development of some type of formal standardization document.

Acknowledgments

Appreciation is extended to numerous past Southwest Research Institute customers, especially the United States Air Force, which has funded damage tolerance validation testing in our laboratory. The methodology described in this paper, as well as many of the lessons learned, were passed to P. McKeighan by Jack FitzGerald, a veteran test engineer, who demonstrated in his own quiet and dignified manner how little many learned engineers truly knew about testing.

References

[1] Broek, D., *The Practical Use of Fracture Mechanics*, Kluwer Academic Publishers, Dordrecht, The Netherlands, 1989.

[2] Lincoln, J. W., "Damage Tolerance – USAF Experience," *Proceedings of the 13th Symposium of the International Committee on Aeronautical Fatigue*, Pisa, Italy, 1985.

[3] Oberkampf, W. L., "Methodology for Verification and Validation in Engineering Simulations," Presented at the *Symposium for Validation and Verification of Computational Mechanics Codes*, California Institute of Technology, Pasadena, CA, December 1998.

[4] Wheeler, O. E., "Spectrum Loading and Crack Growth," Transactions of the ASME, *Journal of Basic Engineering*, Vol. 94, 1972, pp. 181 186.

[5] Paris, P. C., Tada, H., and Donald, J. K., "Service Load Fatigue Damage – A Historical Perspective," *International Journal of Fatigue*, Vol. 21, 1999, pp. S35 S46.

[6] Goranson, U.G., "Fatigue Issues in Aircraft Maintenance and Repairs," *International Journal of Fatigue*, Vol. 19, Supp. No. 1, 1997, pp. S3 S21.

[7] *Damage Tolerance in Aircraft Structures, ASTM STP 486*, ASTM International, West Conshohocken, PA, 1971.

[8] *Fatigue Crack Growth Under Spectrum Loads, ASTM STP 595*, R. P. Wei, Ed., ASTM International, West Conshohocken, PA, 1976.

[9] *Service Fatigue Loads Monitoring, Simulation and Analysis, ASTM STP 671*, P. R. Abelkis, Ed., ASTM International, West Conshohocken, PA, 1979.

[10] *Effect of Load Spectrum Variables on Fatigue Crack Initiation and Propagation, ASTM STP 714*, D. F. Bryan and J. M. Potter, Eds., ASTM International, West Conshohocken, PA, 1980.

[11] "Fatigue Rated Fastener Systems," AGARD Report No. 721, H. H. VanDerLinden, Ed., North Atlantic Treaty Organization, Advisory Group for Aerospace Research and Development, 1985.

[12] McKeighan, P. C. and Smith, D. J., "Determining the Potential Drop Calibration of a Fatigue Crack Growth Specimen Subject to Limited Experimental Observations," *Journal of Testing and Evaluation*, Vol. 22, No. 4, July 1994, pp. 291 301.

[13] Dwyer, W., "Development of a Supplemental Inspection Document for the Fairchild SA226 and SA227 Aircraft," Part 2, Vol. II, Appendix F-Testing and Analysis for DTA of Fairchild SA226 Main Wing Spar Lower Cap at WS99, DOT/FAA/AR-99/20, P2, Vol. II, October 1999.

[14] Schijve, J., *Fatigue of Structures and Materials*, Kluwer Academic Publishers, 2001.

[15] Piascik, R. S. and Willard, S. A., "The Characteristics of Fatigue Damage in the Fuselage Riveted Lap Splice Joint," NASA/TP-97-206257, NASA Langley Research Center, Hampton, VA, 1997.

[16] "GENESIS 4 Fatigue CD: GENErate StandardIsed Sequences," National Aerospace Laboratory (NLR), Loads and Fatigue Department, Emmeloord, The Netherlands, 2001.

[17] McKeighan, P. C., Fess, F. E. II, Petit, M., and Campbell, F. S., "Quantifying the Magnitude and Effect of Loading Errors During Fatigue Crack Growth Testing Under Constant and Variable Amplitude Loading," *Applications of Automation Technology in Fatigue and Fracture Testing and Analysis: Fourth Volume, ASTM STP 1411*, A. A. Braun, P. C. McKeighan, A. M. Nicolson, and R. D. Lohr, Eds., ASTM International, West Conshohocken, PA, 2002.

[18] Donald, K. J. and George, K., "Variable Amplitude Fatigue Crack Growth Using Digital Signal Processing Technology," *Symposium on Fatigue Testing and Analysis Under Variable Amplitude Loading, ASTM STP 1439*, P. C. McKeighan and N. Ranganathan, Eds., ASTM International, West Conshohocken, PA, 2003.

[19] Virkler, D. A., Hillberry, B. M., and Goel, P. K., "The Statistical Nature of Fatigue Crack Propagation," Transactions of the ASME, *Journal of Engineering Materials and Technology*, Vol. 101, 1979, pp. 148 153.

Journal of ASTM International, October 2004, Vol. 1, No. 9
Paper ID JAI19043
Available online at www.astm.org

J. Keith Donald[1] *and Ken George*[1]

Variable Amplitude Fatigue Crack Growth Using Digital Signal Processing Technology

ABSTRACT: An automated variable amplitude fatigue crack growth system has been developed using digital signal processing (DSP) technology to provide waveform generation, command-feedback verification, and crack growth monitoring. The system is designed to interface with existing analog or digital closed-loop servo-hydraulic mechanical test systems. An important parameter in the control of variable amplitude testing is the effect of loading errors on the fatigue crack growth rate response. A damage parameter (Γ) has been incorporated to quantify the magnitude and effect of loading errors. In this paper, a FALSTAFF, Mini-TWIST, and truncated Mini-TWIST aircraft spectrum were applied to an M(T) crack growth sample to demonstrate the correlation between the damage parameter and fatigue life.

KEYWORDS: fatigue crack growth, variable amplitude, automation, servo-hydraulic closed-loop control, digital signal processing

Introduction

Generating reliable fatigue crack growth data under variable amplitude loading requires sophisticated control and verification to assure that the targeted peak and valley loads have been achieved. A data acquisition and control system will be described that uses digital signal processing (DSP) technology to provide automated fatigue crack growth testing under variable amplitude loading [1]. Quantifying the magnitude and effect of loading errors by incorporating a damage parameter (Γ) represents a significant advance over previously available concepts [2]. Correlating this damage parameter with crack growth rates is an important part of evaluating how well the targeted peak and valley loads have been achieved. The success of this approach was investigated using an M(T) sample of 2524-T3 aluminum alloy and two aircraft spectrums, FALSTAFF and Mini-TWIST [3].

Unique features of the system include:

- A command-feedback optimization method that minimizes the error between the target load and actual load for each endpoint
- Storage of the tuning parameters used to optimize each endpoint, allowing pre-tuning and optimizing prior to generating real test data
- A real-time damage parameter, Γ, that characterizes the degree of command-feedback optimization
- Crack monitoring using compliance, reversing DC potential drop, or foil Krak gages

Manuscript received 29 May 2002; accepted for publication 11 November 2003; published October 2004. Presented at ASTM Symposium on Fatigue Testing and Analysis Under Variable Amplitude Loading Conditions on 29–31 May 2002 in Tours, France; P. C. McKeighan and N. Ranganathan, Guest Editors.

[1] Research Engineers, Fracture Technology Associates, 2001 Stonesthrow Road, Bethlehem, PA 18015.

System Description

The hardware consists of a dedicated DSP processor, local memory, and high-speed 16-bit resolution analog input and output. The process runs independently of the PC operating system using the software language ADBasic for waveform generation, data acquisition, and the data processing required for command-feedback verification, crack length determination, and K-control. Individual modules can be programmed in a high priority mode for time critical functions such as command control and data acquisition. Calculations such as the linear regression analysis for compliance based crack length determination and crack growth rates as a function of the applicable K parameter are performed in a low priority mode. High priority processes can interrupt a low priority process. However, a high priority process cannot be interrupted by another high or low priority process. This guarantees that time critical functions are completed as scheduled. However, the code associated with high priority functions must be sufficiently concise to prevent process delays with other critical events. Either compliance, reversing DC potential drop, or foil Krak gages can be used to monitor crack length. A photograph of the control and data acquisition system is given in Fig. 1.

FIG. 1 *Photograph of data acquisition and control system.*

Microsoft Visual Basic provides the communication link between the DSP process and the user. The software supports a graphical display of the target, command, load, and displacement signals, as well as an online display of crack growth rates. Control and data acquisition are continuous with flexibility to modify test parameters "on the fly" as necessary. In the event of a PC system crash, the DSP system will continue to run, maintaining control and collecting data. The PC can then access the process once it has been rebooted. An example of a graphical display is shown in Fig. 2.

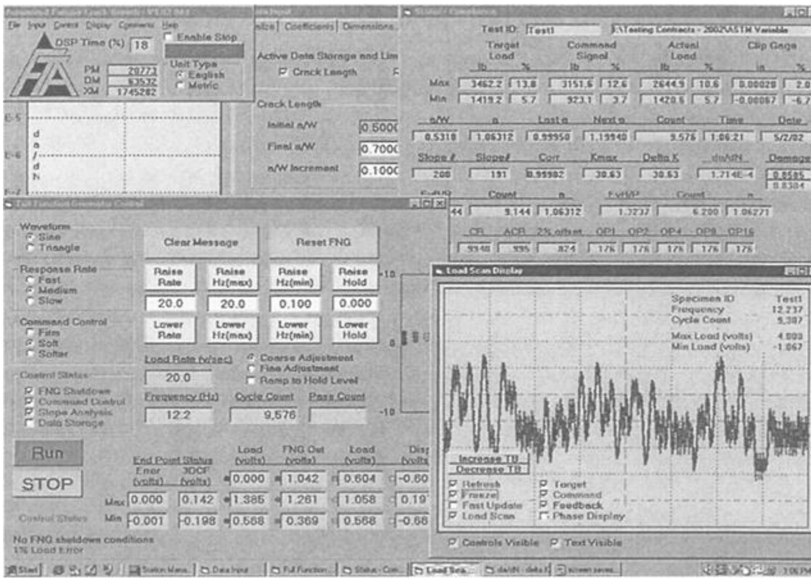

FIG. 2 *An example of the Visual Basic interface. A snapshot of a FALSTAFF spectrum is shown.*

Data Acquisition

The ADBasic module responsible for analog to digital data acquisition is executed at a rate proportional to the loading rate such that a 1 millivolt average change in amplitude can be captured. Up to six channels of data (force, displacement, and four channels of potential drop data) can be acquired at a maximum throughput of 20 kHz. The data are temporarily stored in a 100 000 point circular buffer. This routine includes a three-point rolling average for peak reading [4].

Waveform Generation

The ADBasic module responsible for waveform generation is executed at a rate of 10 kHz. At this rate, the code updates the analog output by scaling a look-up table of either a sine or triangle waveform according to the range of maximum and minimum output desired. Typically the waveform follows a constant peak to peak loading rate. This provides automatic frequency control inversely proportional to the amplitude, thus optimizing the dynamic performance characteristics of a typical servo-hydraulic test machine. In addition, upper and lower frequency limits may be specified. Other modes of control include a block mode that includes hold time capability and allows for changing the block at a specified crack length or after a designated number of cycles. At each peak and valley, the following steps are executed:

- Increment the endpoint count.
- Select the next endpoint.

- Adjust the endpoint for the previously determined target-feedback error.
- Select minimum or maximum level of load-cell feedback for the previous endpoint.

Methodology

Command-Feedback Compensation and Verification

A closed-loop servo-hydraulic system has dynamic performance limitations depending on load capacity, hydraulic flow, servo-valve response, etc. Under dynamic conditions, a significant lag may occur between the command (target load) and the actual load (feedback from the load cell). Figure 3 shows an example of significant lag and under compensation due to poor PID tuning. In this case, the target and the command are identical since command-feedback compensation has not been enabled. This mismatch can usually be minimized through proper tuning of the control loop. However, under variable amplitude loading, it can be very difficult to use simple PID tuning parameters to handle all combinations of endpoints. This is especially true as the cyclic frequency is increased.

Modification of the command signal based on historical performance results in greater load precision than possible with simple PID tuning. In most cases, the target-feedback errors can be reduced to less than 0.1 % of range even if the phase lag between command and feedback is quite large (45 90°). The successful implementation of this approach requires that the historical performance of the command-feedback relationship be based on the level of the previous, current, and next endpoint. Such an approach provides a signature unique to each endpoint. The command-feedback algorithm scans an array to determine if this unique combination of endpoints has occurred in the past. If so, then correction is applied to the next occurrence of this endpoint signature such that the magnitude of this correction is equal to one-half the target-feedback error. The correction of one-half the error may require several passes of a given sequence to reduce the error to less than 0.1 % of range. However, a more aggressive correction scheme could lead to oscillations and instability under certain tuning conditions. Figure 4 illustrates the use of this command-feedback compensation routine. Note that the target and the feedback are out of phase but at the same amplitude. However, the level of command signal for the same target level differs as a function of the previous and next endpoint.

Once the command-feedback compensation has been optimized, the correction array required for the spectrum may be stored in a file for future use. This provision allows reserving an extra sample for tuning the system. Once tuned with command-feedback compensation enabled, the real test sample may be mounted in the test frame with the knowledge that the targeted endpoints will be achieved starting with the first cycle. Since the tuning parameters may change as the test progresses due to compliance change with crack length, it is important to start a test with tuning parameters based on the initial crack length. For tuning purposes, it is not necessary to run the complete spectrum as long as a simplified spectrum has the same unique combination of endpoints. This can greatly simplify the tuning process for large spectrums.

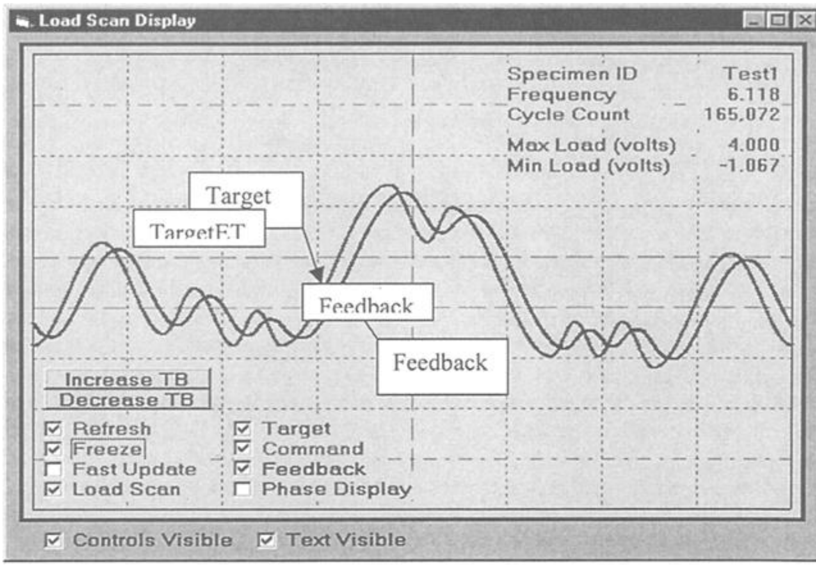

FIG. 3 *Target-feedback response with no command-feedback compensation. The controller was de-tuned to accentuate the desired effect.*

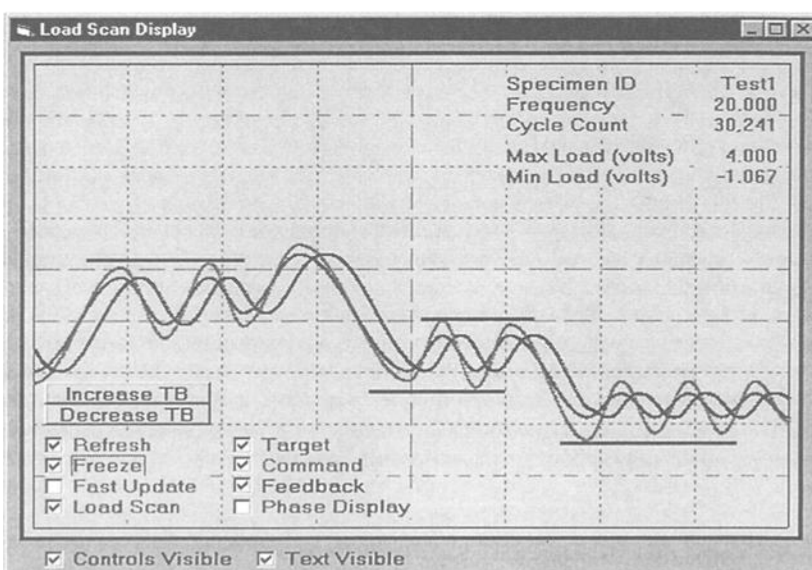

FIG. 4 *Target-command-feedback response with command-feedback compensation enabled. Note that the command level differs for the same target level.*

Damage Parameter

The effect of loading errors on crack growth rates should take into account the Paris relationship [5] between the stress intensity range ΔK and the fatigue crack growth rate da/dN as follows:

$$\frac{da}{dN} = C\Delta K^m \tag{1}$$

where
da = crack length increment,
dN = cycle count increment,
C = intercept,
ΔK = cyclic stress intensity, and
m =power law exponent.

Values of m are generally between 3 and 3.5. Since for a given crack size, ΔK is proportional to ΔP, we can rationalize that the effect of loading errors on fatigue crack growth rates is also proportional to the ratio of the target and actual ΔP raised to the power of m. The accumulated effect is given as follows [2]:

$$\Gamma = \frac{\sum(\Delta P_{Actual})^m}{\sum(\Delta P_{Target})^m} \tag{2}$$

where
Γ = damage parameter,
ΔP_{ACTUAL} = actual cyclic load, and
ΔP_{TARGET} = target cyclic load.

This damage parameter estimates the success in attaining load peaks in a spectrum fatigue test. Figure 5 illustrates the calculation of the damage parameter. A damage parameter of 1.0000 would indicate perfect agreement. Since the magnitude of the exponent, m, may not be precisely known, an integer power of three was selected for real-time calculation of the damage parameter. An integer power greatly speeds up the processing time and guarantees that this calculation can be performed along with other functions during the less than 0.1 millisecond duration of the ADBasic function generation routine. Since this may only approximate the slope of a da/dN-ΔK relationship, an adjusted damage parameter may be estimated given knowledge of the more precise exponent as follows and as illustrated in Fig. 6:

$$\Gamma_{ADJ} = \Gamma^{m/3} \tag{3}$$

where
Γ_{ADJ} = adjusted damage parameter.

An accumulated damage parameter is calculated for every crack growth rate data point. In theory, the damage parameter is now a direct measure of the relative damage accumulated due to errors in loading. For example, for a given increment of applied cycles, a damage parameter of 0.75 would indicate that 75 % of the fatigue damage occurred compared to test where the applied loads were exact (Γ = 1.000). Therefore, the number of cycles applied can be adjusted as follows:

$$\Delta N_{COMP} = \Delta N_{ACT} \cdot \Gamma_{ADJ} \tag{4}$$

where
ΔN_{COMP} = cycle count increment adjusted for damage parameter, and
ΔN_{ACT} = actual cycle count increment for each crack growth data point.

$$\Gamma = \frac{\sum (\Delta P_{Actual})^m}{\sum (\Delta P_{Target})^m} \qquad \frac{da}{dN} = C \cdot \Delta K^m$$

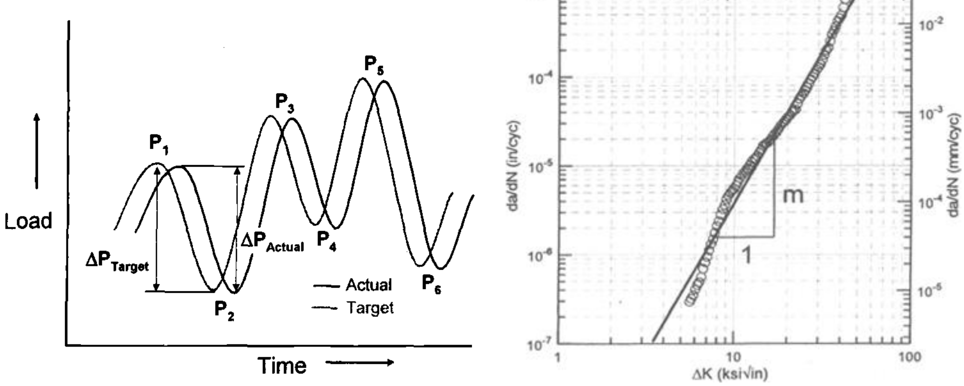

FIG. 5—*Illustration of damage parameter concept.*

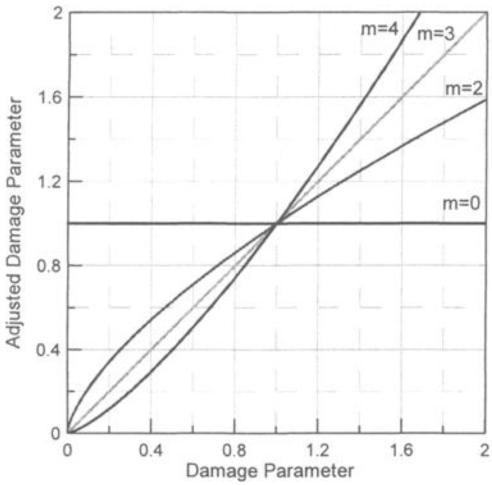

An exponent of 3 was used to calculate a real-time damage parameter.

An adjusted damage parameter to account for a different exponent is estimated by the following:

$$\Gamma_{ADJ} = \Gamma^{m/3}$$

FIG. 6 *Method to calculate adjusted damage parameter.*

Experimental Approach

Objectives

The first objective of the experimental approach was to evaluate fatigue crack growth rate variability [6] in spectrum tests with a well-tuned, command-feedback compensated system (Γ= 1.000). Both material variability and test frame/controller variability were investigated. Triplicate tests were run on two spectrums for this purpose.

The second objective was to evaluate the correlation of the damage parameter with crack growth rates using a poorly tuned system without command-feedback compensation compared to the test data generated using good control as in the first objective. The poorly tuned system was achieved by reducing the controller gain by a factor of two, attenuating the command signal by 5%, and disabling the command-feedback compensation so that no adjustment was made to the command signal. The same de-tuning parameters were made to all three spectrums, resulting in a damage parameter of ~0.75 to ~0.80.

Outline

The experimental approach is outlined with a summary of key test conditions in Table 1. Photographs of the test set-up are shown in Fig. 7. Anti-buckling guides were not used because calculations indicated that the peak compressive loads were about half the allowable limit for fixed grips. Peak tensile forces were also less than the allowable size requirement limit according to ASTM E 647. For compliance measurements, the output of two clip gages was used. This method increased sensitivity and provided a more precise through-the-thickness average compliance. The linear range of the compliance measurements was determined to assure that the measurements were taken with the crack in the fully open state. All samples were pre-cracked under the same constant amplitude loading conditions to the same starting crack length. Visual inspection of the crack length revealed that all crack straightness guidelines were satisfied.

TABLE 1 *Summary of test conditions.*

Material	2524-T3 Alclad aluminum alloy
Mechanical Properties	σ_{ys} = 310 MPa (45 ksi), σ_{ult} = 427 MPa (62 ksi)
Specimen Type	M(T) (B = 4.6mm (0.182 in), W = 101.6mm (4.000 in)
Environment	lab air (23°C, 75°F, relative humidity = 40 50 %)
Crack Size	6.3mm (0.25 in) to 25.4mm (1.00 in)
Constant Loading Rate	945 MPa (137 ksi) /second (typically 5 30 Hz)
Spectrums	FALSTAFF, Mini-TWIST Mini-TWIST truncated above 1.995× the mean stress (level 5)
Special Features	dual clip gages used for compliance measurements

Test Series	Damage Parameter	Spectrum	Comments
A	1.000	FALSTAFF 137.9 MPa (20 ksi) max	Triplicate tests to investigate material variability
B	1.000	Mini-TWIST truncated 68.9 MPa (10 ksi) max	Triplicate tests to investigate material/test frame variability
C	1.000	Mini-TWIST 68.9 MPa (10 ksi) max	Single test to investigate retardation effects
D	~0.75	FALSTAFF	Test with poor control to investigate damage parameter
E	~0.79	Mini-TWIST truncated	Test with poor control to investigate damage parameter
F	~0.80	Mini-TWIST	Test with poor control to investigate damage parameter

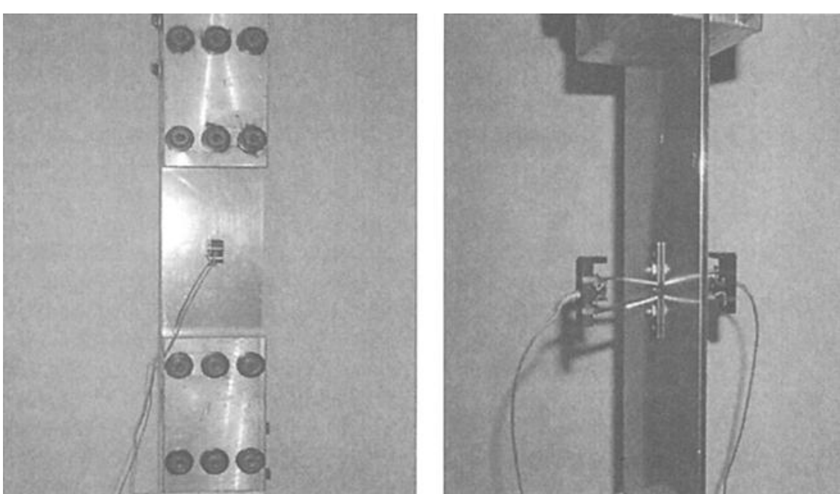

FIG. 7 *Photographs of specimen configuration.*

Results and Discussion

Figure 8 (Test Series A and B) shows excellent agreement between triplicate tests conducted using a FALSTAFF spectrum and a truncated Mini-TWIST spectrum. The variability is well within guidelines of 5 10 % anticipated for these types of tests. The truncated Mini-TWIST was conducted on two frames (one with a digital controller and the other with an analog controller), again showing that neither the material, the test frame, nor the controller are significant sources of variability. In all cases, the indicated damage parameter was 1.0000 ±0.0002. Due to this high degree of repeatability, all damage parameter comparisons and the full Mini-TWIST spectrum were conducted with single tests.

Figure 9 shows the effect of a test conducted with a damage parameter of 1.000 (One test from series A compared to series D) compared to a test with poor control and a typical damage parameter of ~0.75. For computing the cycle count compensated for the damage parameter (Eqs 3 and 4), steady-state FCGR data were used at a stress ratio of 0.1. It is clear that the damage parameter compensated data are shifted to the left more than the baseline data would suggest. However, if the actual spectrum data are used for determining the exponent (see Fig. 10), the agreement between the baseline and damage parameter compensated data is much better. Although the damage parameter accounts for the power law relationship between da/dN and ΔK, there is no provision for retardation in this model. Note also in Fig. 10 the evidence of crack growth retardation as shown by the early downward trend of the da/dN versus K_{max} data. It is probable that the exponent associated with the spectrum provides a more appropriate adjustment to the damage parameter. To see if this works on a different spectrum, the same procedure was applied to a truncated Mini-TWIST spectrum as shown in Fig. 11. Here again the agreement is quite good, although not as good as with the FALSTAFF spectrum.

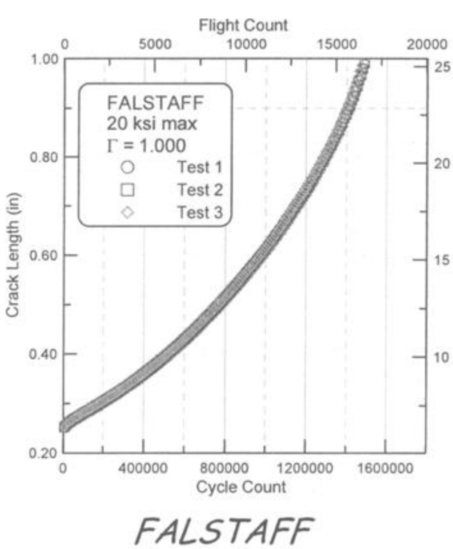

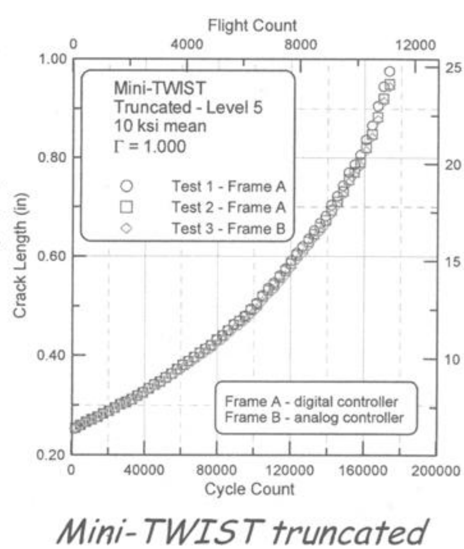

FIG. 8 *Triplicate tests show excellent repeatability (Γ = 1.000).*

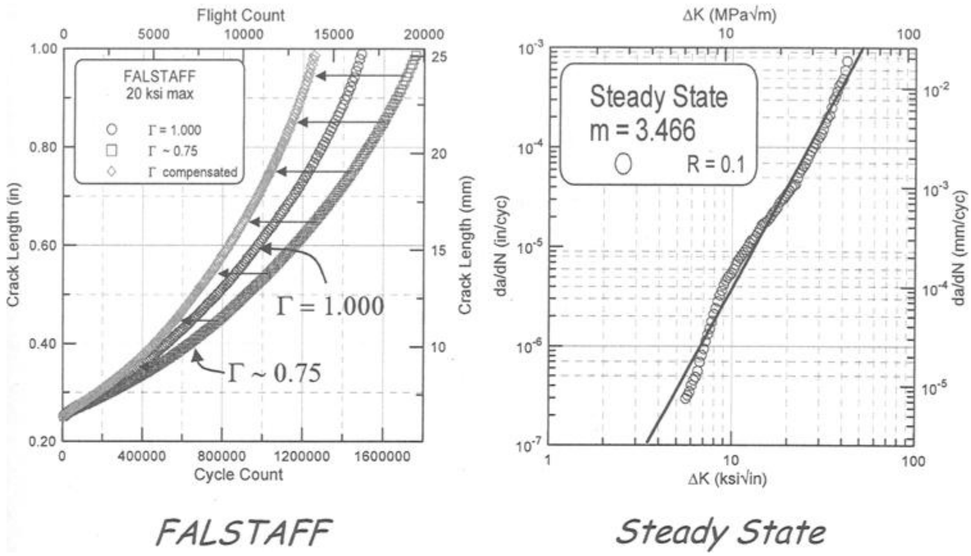

FIG. 9 *Damage parameter compensation based on steady-state FCGR (m = 3.466).*

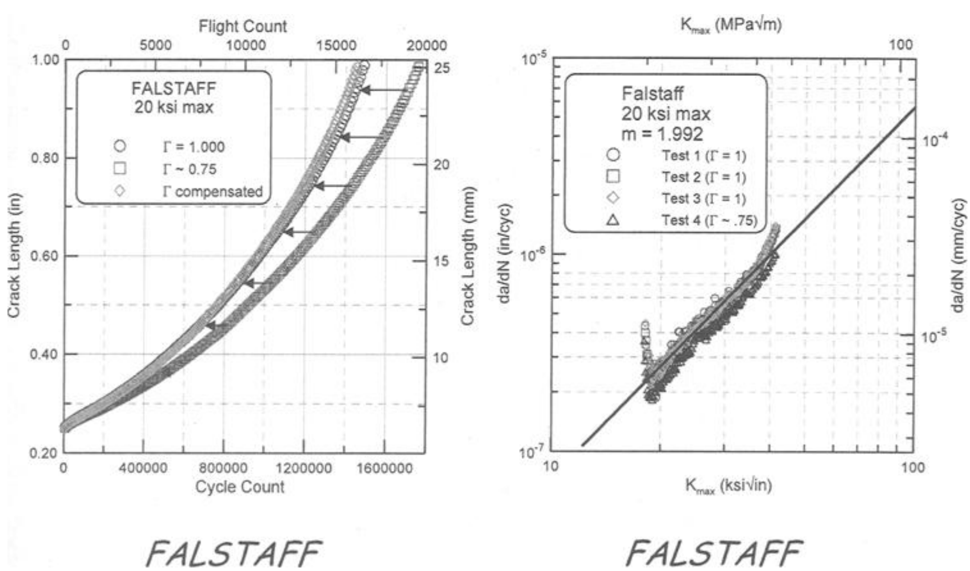

FIG. 10 *Damage parameter compensation based on FALSTAFF spectrum (m = 1.992).*

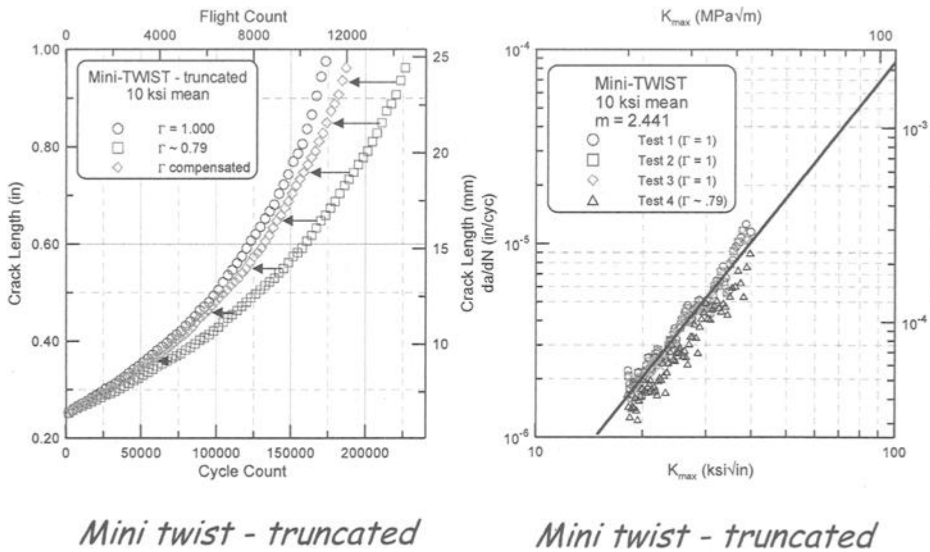

FIG. 11 *Damage parameter compensation based on truncated Mini-TWIST spectrum (m = 2.441).*

In the previous example, a truncated Mini-TWIST spectrum was shown. This spectrum has the same number of cycles per pass as the full spectrum (62 442), but 14 of these cycles were originally above the truncated stress level of 1.995 times the mean stress, the highest being 2.600 times the mean stress level. This truncated spectrum was used to reduce the test time for triplicate tests and to simplify the determination of the exponent, m, for this spectrum. Figure 12 shows the dramatic amount of crack growth retardation associated with the full Mini-TWIST spectrum. The truncated and the full spectrum are identical for the first four data points. This is prior to the occurrence of the first load level of the full spectrum exceeding the truncated level. The retardation is an accumulative effect over several passes, as shown by the almost constant average slope in the crack versus cycle count plot for the first half of the test. This is so, despite the increase in crack size and corresponding increase in K_{ave} or K_{max}. This is almost certainly a crack closure effect and may be more pronounced under plane-stress conditions. Although the sample size was sufficient for validity according to ASTM E 647, the thickness of the sample was not sufficient to remain plane-strain.

Figure 13 shows the damage parameter compensation concept applied to the full Mini-TWIST spectrum. Compensating for loading errors is much less certain for two reasons. First, if only the highest levels were missed, the average damage parameter would remain close to 1.000, yet the effect of these missed levels would be dramatic. Second, determination of an exponent, m, for this spectrum is complicated by the variability in growth rates associated with different segments of the spectrum. As shown by the data on the right in Fig. 13, this slope can vary from a negative value to a very steep value depending on the range of crack length, the size of the Δa increment, and the selection of the independent variable. For this slope determination, a large Δa was selected, and da/dN was the independent variable as per ASTM E 647 threshold fit recommendations.

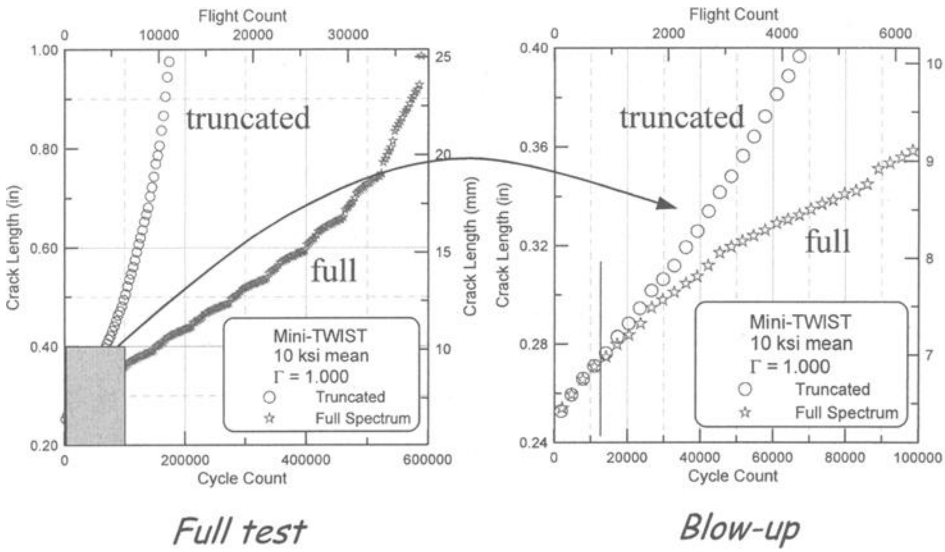

FIG. 12 *Full Mini-TWIST spectrum shows significant retardation.*

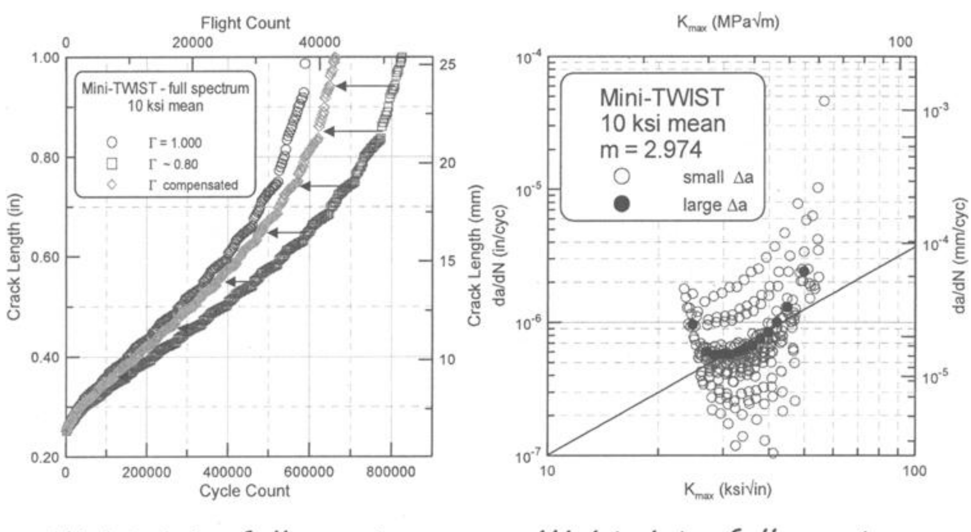

FIG. 13 *Damage parameter compensation based on Mini-TWIST spectrum (m = 2.974).*

Summary and Conclusions

The excellent agreement among the triplicate tests shows that good control with command-feedback compensation leads to more consistent fatigue crack growth rate data from variable amplitude tests.

A real-time damage parameter may be a good indicator of control and, therefore, confidence in the data. However, the damage parameter only accounts for ΔP errors, not mean stress level errors. Because of retardation effects, a damage parameter concept should be combined with a log of "missed endpoints" to guarantee accuracy within a specified tolerance.

Damage parameter adjustment and cycle count compensation should not be used in place of good control and verification of that control.

Acknowledgments

The authors would like to thank Rich Brazill of the Alcoa Technical Center for technical assistance and for providing machined samples of 2524-T3 Alclad aluminum alloy.

References

[1] Donald, J. K., "Automated Variable Amplitude Fatigue Crack Growth Technology," *Applications of Automation Technology to Fatigue and Fracture Testing, ASTM STP 1092*, A. A. Braun, N. E. Ashbaugh, and F. M. Smith, Eds., ASTM International, West Conshohocken, PA, 1990, pp. 167 177.

[2] McKeighan, P. C., Fess II, F. E., Petit, M., and Campbell, F. S., "Quantifying the Magnitude and Effect of Loading Errors During Fatigue Crack Growth Testing Under Constant and Variable Amplitude Loading," *Applications of Automation Technology in Fatigue and Fracture Testing and Analysis: Fourth Volume, ASTM STP 1411*, A. A. Braun, P. C. McKeighan, A. M. Nicolson, and R. D. Lohr, Eds., ASTM International, West Conshohocken, PA, 2000.

[3] Schutz, W., "Standardized Stress-Time Histories – An Overview," *Development of Fatigue Loading Spectra, ASTM STP 1006*, J. M. Potter and R. T. Watanabe, Eds., ASTM International, West Conshohocken, PA, 1989, pp. 3 16.

[4] Donald, J. K., "Sampling Rate Effects in Automated Fatigue Crack Growth Rate Testing," *Automation in Fatigue and Fracture: Testing and Analysis, ASTM STP 1231*, C. Amzallag, Ed., ASTM International, West Conshohocken, PA, 1994, pp. 124 145.

[5] Paris, P. C. and Erdogan, F., "A Critical Analysis of Crack Propagation Laws," ASME, *Journal of Basic Engineering*, Transactions of the ASME, Vol. D85, 1963, pp. 528 534.

[6] Clark, Jr., W. G. and Hudak, Jr., S. J., "Variability in Fatigue Crack Growth Rate Testing," *Journal of Testing and Evaluation*, Vol. 3, No. 6, 1975, pp. 454 476.

Journal of ASTM International, Nov./Dec. 2004, Vol. 1, No. 10
Paper ID JAI19038
Available online at www.astm.org

Stefan Pöting,[1] *Markus Traupe,*[1] *Joachim Hug,*[2] *and Harald Zenner*[1]

Variable Amplitude Loading on a Resonance Test Facility

ABSTRACT: The uncertainty in fatigue lifetime calculations brings up the necessity of experimental verification. Several efforts have been undertaken in the past to improve and introduce new test methods. An alternative method for variable amplitude loading using resonance test facilities is introduced and discussed. A comparison of test results on a resonance test facility with a new control system and a servo hydraulic test facility shows no significant difference in the test results. The compatibility of the test results to those results of accepted fatigue life tests is proven for three test series of different specimens. The introduced resonance test control offers a new way for fatigue life tests, reducing the cost and time, as well as increasing the safety of products because it permits testing to much longer lives in a relatively short time.

KEYWORDS: "beat like" load, random load, resonance test facility, resonance control, fatigue, spectrum load, load time history, electromagnetic test facility, variable amplitude fatigue

Nomenclature

$\overline{D}$	damage sum
h	cycle frequency of a stress level
H_0	block sequence size
H	cumulative frequency of a stress level
k	slope of the S-N curve
v	form parameter of the load spectrum
N	number of cycles to failure (constant amplitude)
$\hat{N}$	number of cycles to failure (variable amplitude)
N_D	point of deflection of the S-N curve
S_a	stress amplitude
$\hat{S}_a$	maximum value of the load spectrum
S_{aD}	fatigue limit
T_D	scatter range of the damage sum D
t	time

Manuscript received 25 April 2002; accepted for publication 8 September 2003; published November 2004. Presented at ASTM Symposium on Fatigue Testing and Analysis Under Variable Amplitude Loading Conditions on 29–31 May 2002 in Tours, France; P. C. McKeighan and N. Ranganathan, Guest Editors.

[1] Research Scientists and Professor, respectively, Institute for Plant Engineering and Fatigue Analysis, Clausthal University of Technology, Leibnizstrasse 32, D-38678 Clausthal-Zellerfeld, Germany.
[2] Manager, SincoTec Bauteilprueftechnik GmbH, Freiberger Strasse 13, D-38678 Clausthal-Zellerfeld, Germany.

Indices

calc	calculation
exp	experiment
i	constant amplitude level i
j	variable amplitude maximum stress level j

Introduction

The experimental safeguarding of safety relevant components has an increasing significance because more and more components are designed using lightweight design philosophies. Even though experiences show good correlations between calculation and experiment, in some cases they do not match that philosophy. Therefore experiments are still essential to verify the safety of components.

Today most fatigue tests under variable amplitude load are performed on servo hydraulic test facilities. In some cases these tests have long test times and high costs because the machines have a high demand on energy and investment costs.

Resonance test facilities for constant amplitude tests are well known. These tests are performed with higher test frequencies and therefore with shorter test times at substantially less cost, (Figs. 1 and 2). Therefore, the question arises whether such facilities can be used for variable amplitude fatigue tests.

Status of the Current Technology

Fatigue Life Test

Fatigue life tests can be divided into random tests and service load duplication tests. The random test applies a stress time history that is generated from a load spectrum. Even though the applied load spectrum is the same, the applied stress-time history can differ from the service load, whereas in service duplication tests the stress-time history is exactly the same. The load spectrum of a stress-time history can be determined by measurements using counting methods such as rainflow counting.

Fatigue life tests on a resonance test facility can be performed only in the sense of random test. The applied load signal comes close to a "beat" signal.

Block Program Loading

In the past, several efforts have been made to use resonance test facilities for variable amplitude loading. The first development was made by the Schenck Company on an out of balance driven resonance test stand. The principle of this test facility is that of a simple mechanical two or three mass swing system with spring, masses, and exciter. The idea of variable amplitude tests on a resonance test facility came from Gaßner. He suggested eight step block program tests. The applied load spectrum is divided into blocks of equal amplitude height. The number of cycles of each amplitude block is divided into smaller blocks of equal length. All blocks of equal length are applied in a defined sequence that sums up to the load spectrum. The machines manufactured by Schenck additionally used hydraulic power for the application of upper four steps of the loading.

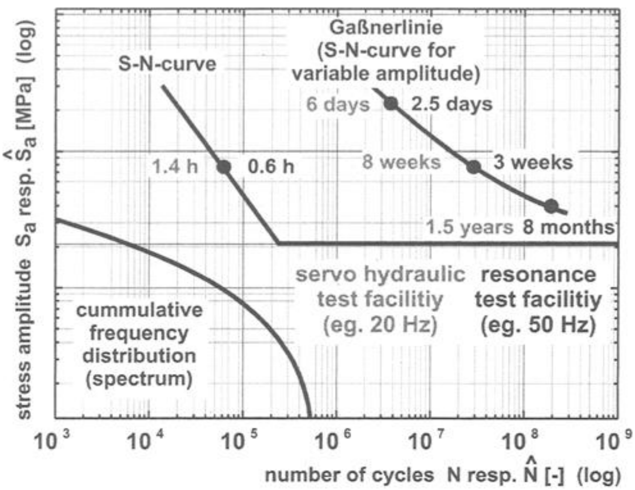

FIG. 1 *Time reduction for spectrum load tests.*

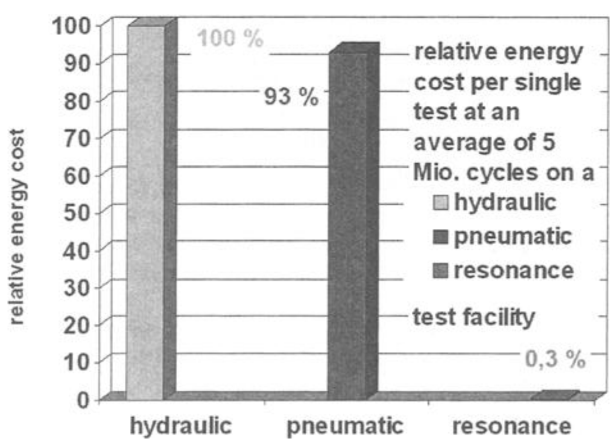

FIG. 2 *Cost reduction for spectrum load tests.*

These test stands were superseded by servo hydraulic test facilities when they became available with peak value control. The experimentally achieved fatigue life on those test facilities match in-service loading [1].

The block program tests show a difference in fatigue life compared to the service duplication tests. A survey referred to in [2] shows the influence of the applied load-time history on the fatigue life derived from experiments. The comparison of test results from random and block program load shows a longer fatigue life for block program loading (Fig. 3). The results are given in "as-normalized" value where the experimental fatigue life is normalized by the calculated fatigue life:

$$\overline{D} = \frac{\hat{N}_{\exp}}{\hat{N}_{calc}} \tag{1}$$

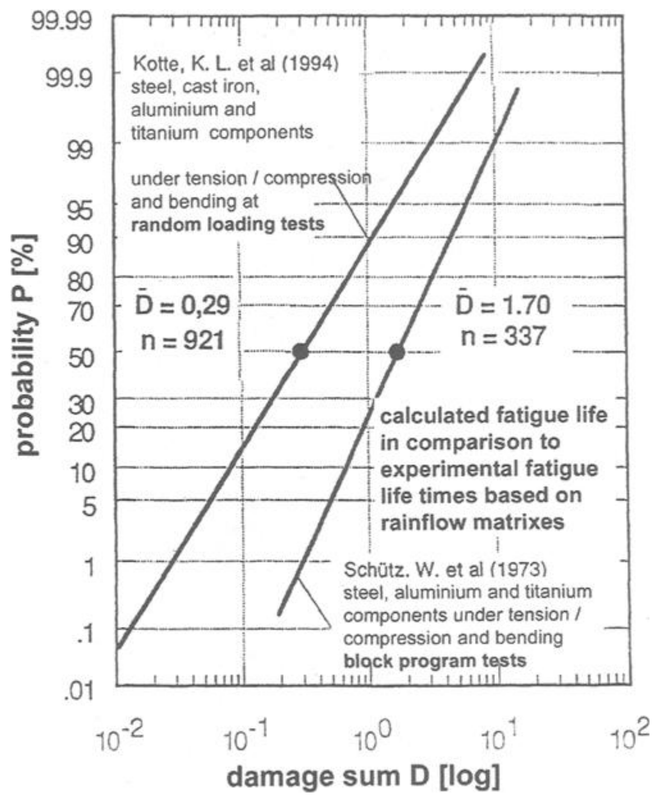

FIG. 3 *Influence of the load time history on the experimental fatigue life.*

Further experiments show that the influence of the block length where the mixture of the block in the sequence has a significant influence on the fatigue life. When the blocks become shorter, and therefore the mixture of the blocks rises, the fatigue life of such block program tests come closer to the one of random tests[3,4].

Noise Generator Control

According to Schütz [5], the first application of a noise generator for a control of a resonance test facility was reported from Edwards and Kirby [6] at the Royal Aircraft Establishment and later by White und Lewszuk [7]. A simple noise generator has the disadvantage of a low Crest-Factor (peak value referring to the RMS-value). Therefore, only a limited use for variable amplitude tests was possible.

Process Computer Control for a Noise Generator

A control using a process computer and a noise generator was developed at the IABG [8] to improve the noise generator control for resonance test facilities [8]. They used a process computer to generate repeatable load-time history with any kind of spectrum form [5,9]. The tests of equal specimen on a resonance and a servo hydraulic facility showed no significant difference in the fatigue life [5]. The system was not brought to industrial application due to the high complexity and cost, but it proved that, in general, variable amplitude tests could be performed on resonance test facilities.

Ultrasound Test Facilities

Another type of resonance test system is the ultrasound system. Small test specimens can be subjected to constant and variable amplitude loading in the test frequency range of 2 20 kHz [10]. Characteristic of these systems is that local strains are applied to the critical section plane that is to be tested. One of the biggest advantages of these systems is the high test frequency, even though only small and defined geometries can be examined. The variable amplitude loading is also available [10,11]. Increasing and decreasing load pulses are being applied sequentially. The achieved spectrums are measured and used for calculation and control.

Variable Amplitude Control for a Resonance Test Facility

The resonance control for variable amplitude consists of two regular personal computers rather than a process computer [12]. The increase in computing speed makes it possible to use one of the PCs to control the time critical resonance system and to use the second to provide the user interface and the non-time critical parameters. The time critical system regulates the power electronics driving the electromagnetic resonance test stand and computes the system signal online (Fig. 4). The user interface control PC is used for the initial data generation and communication with the user (Fig. 5).

The separation of the tasks is necessary to ensure a safe operation of the time critical circuit. The control PC drives the power electronics for the magnet and the mean load motor in this circuit. The machines are presented in Figs. 6 and 7.

Load Spectrum and Load Signal Generation

The applied load spectrum is generated from a continuous load spectrum, which is defined by the maximum stress amplitude, the spectrum shape, and the block sequence size (Fig. 7). The continuous spectrum is transformed into a discrete spectrum. Therefore a continuous spectrum is divided into steps (Fig. 7). All steps have an equally increasing distance of their amplitudes in between the minimum and maximum value of the spectrum. The steps are divided into blocks of equal lengths of 60 cycles. This block length has been tested on a wide range of preliminary test and was verified for the tested specimens. This block length has been evaluated to be the minimum block length, which has no influence on the test results independent of the specimen, material, spectrum, and machinery. The blocks off all steps are then brought into a random sequence using the Markov Algorithm for reconstruction of random load sequences from a rainflow matrix [13].

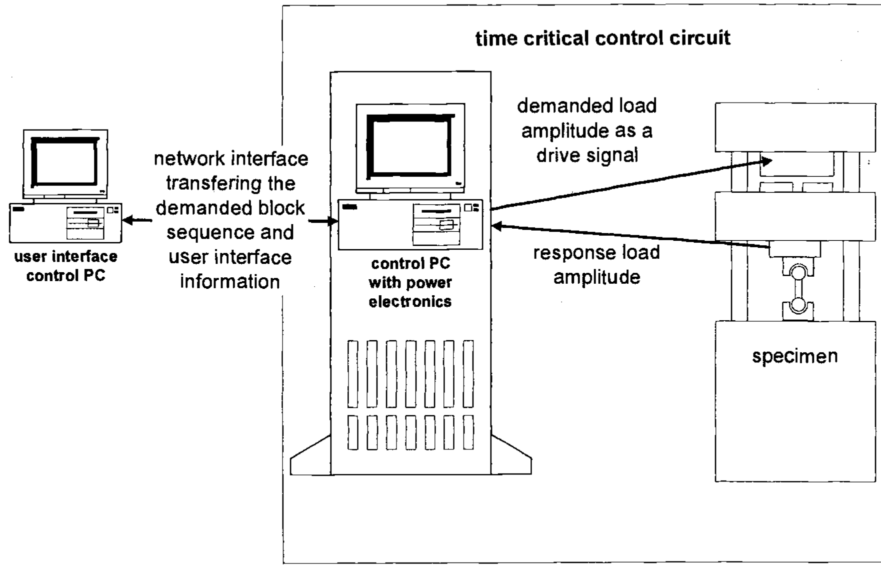

FIG. 4 *Scheme of the resonance test facility for constant and spectrum amplitude load.*

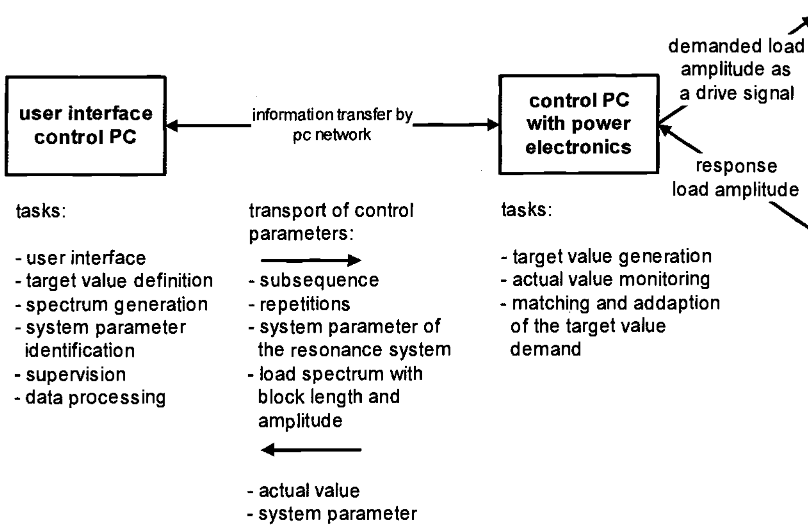

FIG. 5 *Scheme of the tasks of the resonance control PCs.*

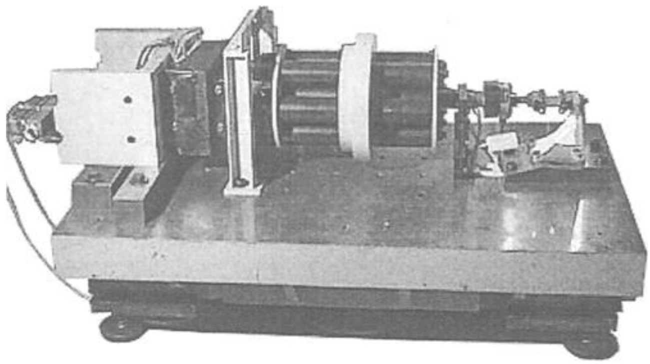

FIG. 6 *Two mass resonance test facility, load: 20 kN amplitude, stress ration $R = -1$, die cast aluminium component in the resonance test facility.*

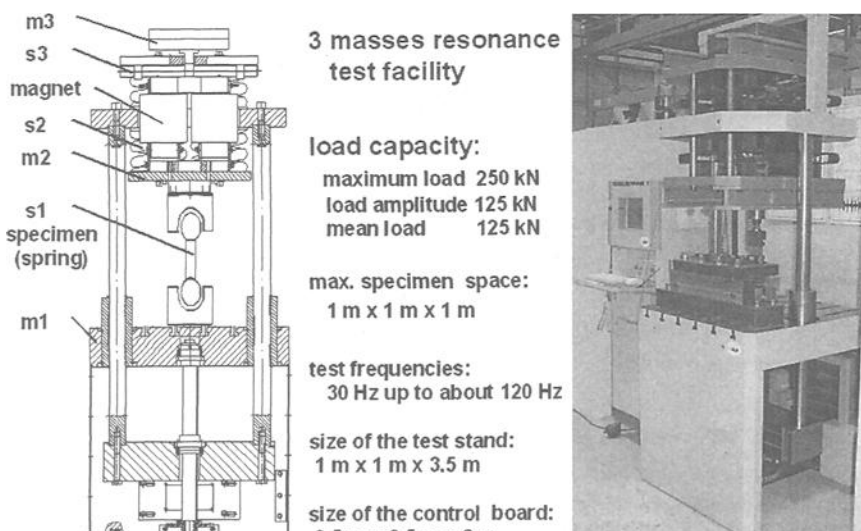

FIG. 7 *Three mass resonance test facility.*

For the resonance test facility the target load spectrum is divided into 20 steps of equal height at amplitudes above a negligible level. The number of steps for the load spectrum has been evaluated with the same preliminary tests as the number of cycles.

This spectrum describes the subsequence of a random sequence of load amplitudes that will be applied at the test facility. The subsequence is reproduced on the test stands until the component fails. The applied load spectrum can be derived from the online rainflow counting and meets the mathematical extrapolation of the subsequence.

Amplitudes inducing stress less than 50 % of the fatigue limit are neglected for random load [14]. This is necessary for the generation and control of the test stand but does not interfere with the test results.

Tests of three different test specimens and materials showed comparable failure behavior for each test series. When the test results were plotted as if the neglected amplitudes had been counted, the results of each series showed comparable numbers to failure for tests with and without neglected amplitudes. Therefore test results of such components can be plotted as if those neglected amplitudes have been included (Fig. 8).

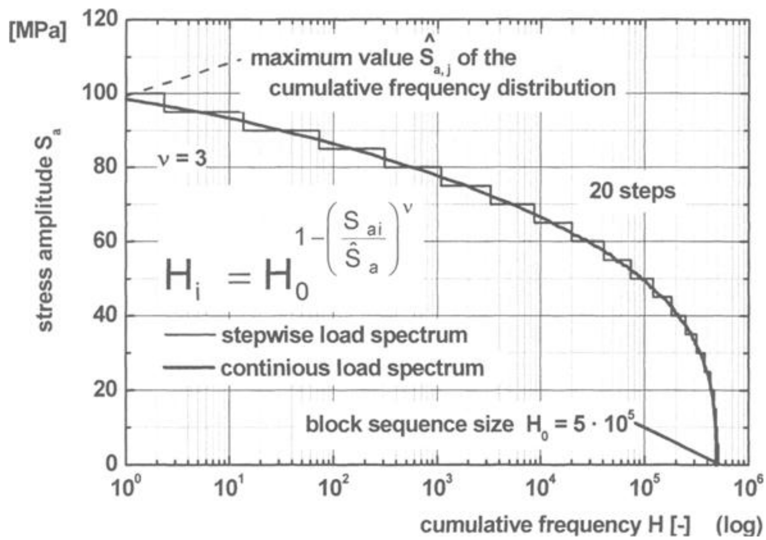

FIG. 8 *Cumulative frequency distribution of a load spectrum.*

Further neglecting of amplitudes for these kinds of tests and components is acceptable for tests in the range up to 10^8 cycles to failure, because in 149 analyzed series of constant and variable amplitude, tests of component failures from the inside as described for smaller specimens and high strength steels [15,16] could not be observed [17,18].

Adaptive Control

The load spectrum is verified by a comparison of the demanded and achieved spectrum derived from an actual measurement. The load amplitude is analyzed using an online rainflow counting. The results of the rainflow counting are transformed into a load spectrum and compared to the demanded spectrum. For a better comparison, the target spectrum is mathematically extrapolated with the number of replications of the spectrum. The comparison of the spectrums shows a good consistency due to the adaptive control (Fig. 9).

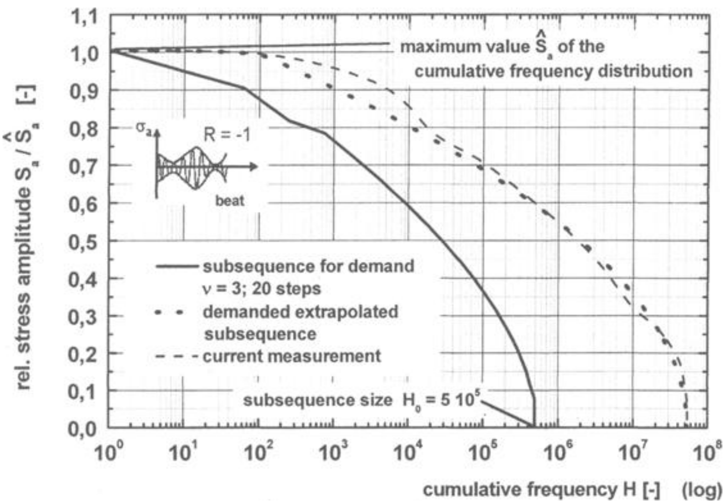

FIG. 9—*Comparison of mathematical extrapolated and achieved spectrum load for a resonance test facility.*

Load Time History of the Resonance Test Facility

The generated load-time history of the resonance test stand differs (Fig. 10) from the random load-time history of a servo hydraulic test stand (Fig. 11). The load-time history of the resonance test stand is similar to a "beat" signal, even though they were generated from the same spectrum. Still, the load-time history of the resonance test facility comes close to service loading of technical systems. Most technical systems have damper and spring behavior, which do not allow sudden changes of the load amplitude between two consecutive cycles. The load cycles in between two relative amplitude maximums have gently increasing and decreasing amplitudes (beat signal). The resonance test facility has smooth changes from high to low or low to high, just as it appears to be in technical systems.

Both time-history plots in Figs. 10 and 11 were recorded from real force signals at test stand. The demanded load spectra were the same; the achieved load spectra were comparable. The power spectrum density of the signals differs, but as it is shown, observed lifetimes are not influenced.

The generated load sequence of a "beat like" signal could have an effect on the experimentally derived fatigue life because the signal can be classified in between a block program load signal and a random load signal. The load-time history has an important influence on the experimental fatigue lifetime [2,15,16]. The significance of the load-time history can be seen from Fig. 3 as the fatigue life of block sequence load is longer by factor of 5.9 for the mean value [1,17–19]. Therefore, the achieved test results with the resonance test facility were verified.

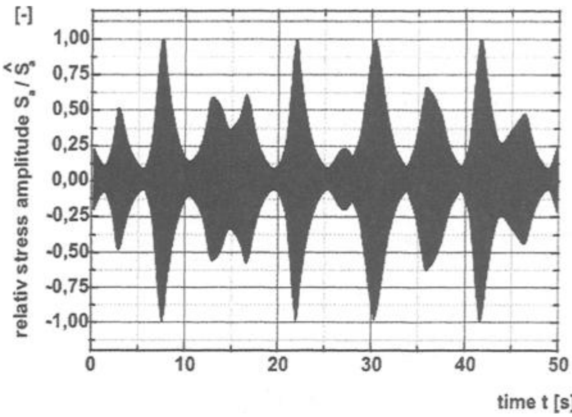

FIG. 10 *Normalized time plot of a "beat like" load sequence.*

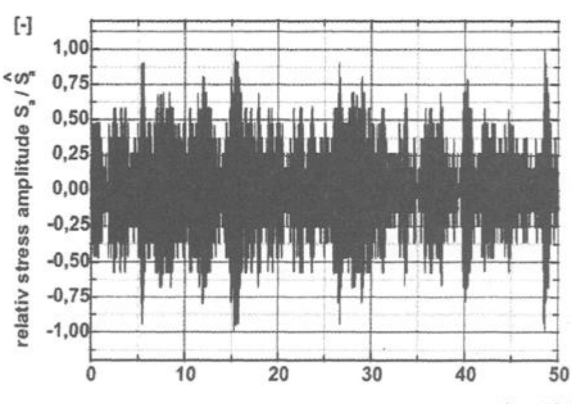

FIG. 11 *Normalized time plot of a random load sequence.*

Verification of the Applicability

A comparison of achieved test results on a "beat like" (resonance test stand) and a random (servo hydraulic test facility) load-time history have been performed for three specimens. They show no significant influence on the fatigue life. The results of the load-time histories can be plotted in a single diagram and scatter band as shown in Figs. 12 14.

The test results for both types of load-time histories applied to a die cast aluminium component, an aluminium and a steel welding in different test series, are shown in Figs. 12 14. These test results were obtained in two research projects on high cycle fatigue. The test facilities are shown in Figs. 6 and 7. The results of the research are published in [20,21]. For each test series it is observed that the results of the "beat like" load and the random load achieved with the test systems fit into the same scatter band. This leads to the expectation that the "beat like" load-time history of a resonance test facility and the random load-time history of a servo hydraulic test stand are damage equivalent.

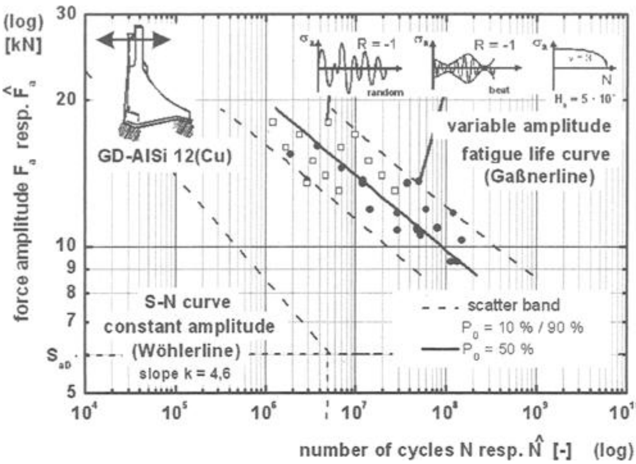

FIG. 12 *Test results for a die cast aluminium motor holder (200 × 130 × 250 mm) at spectrum load for a random and a "beat like" load sequence.*

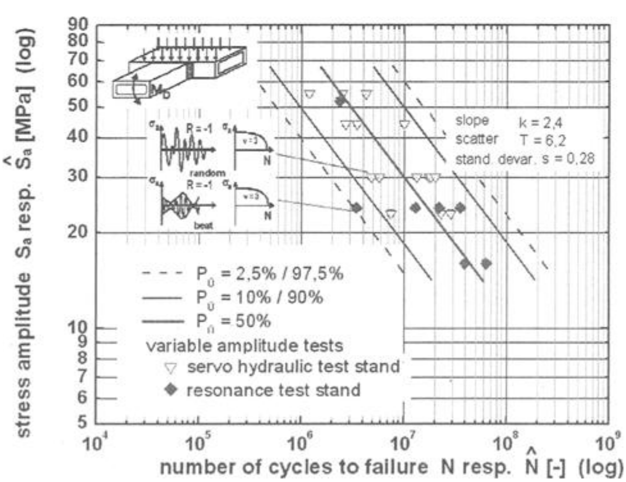

FIG. 13 *Test results for a welded aluminium hollow t-section, AW-6005A, T welding of hollow sections (160 × 80 × 8 mm), lengths 250 mm and 450 mm, at spectrum load for a random and a "beat like" load sequence.*

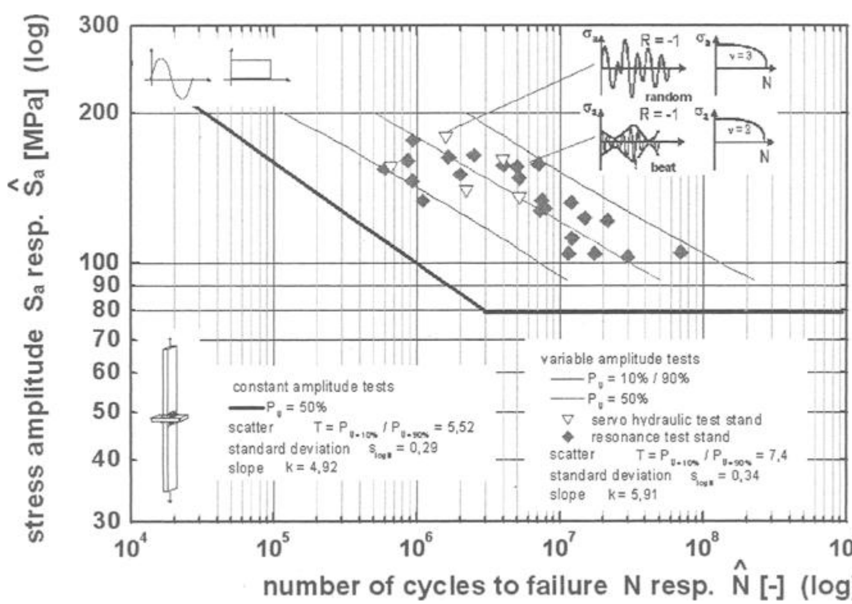

FIG. 14 *Test results for a welded steel cross-section at spectrum load for a random and a "beat like" load sequence, S 235 JRG2, cross section welding, K seam, 220 × 45 × 8 mm.*

Field of Application

Most components in service are subjected to variable amplitude loads. If a safe and economic dimensioning for a definite utilization time is required and no fatigue lifetime information is available about the component, in many cases a fatigue test may be necessary. In case the utilization can be defined by a representative load spectrum and the expected lifetime exceeds more than 10 times the block length of the spectrum, the resonance test control can be used to perform fatigue lifetime tests. The effects of rapidly changing mean values of the load amplitude have not yet been examined with this control system. So far the system is restricted to constant quasi-constant mean stress tests.

Conclusions

A resonance test facility for variable amplitude loading has been validated for testing of components. The system generates and controls online the amplitude loading of a defined load spectrum. The load spectrum is met and repeated continuously. The system has been tested on full scale components. The results of these tests can be compared to the once-commonly used servo hydraulic test. Even though the applied load-time-history differs for the tests, the results in failure and lifetime are equal. For three series of aluminium and steel components, a sequence effect due to the applied load-time-history could not be observed, even though an effect of other load-time-histories has been observed in other publications. The resonance control system allows to reduce test time and cost significantly for full scale component tests.

References

[1] Gaßner, E. and Lipp, W., "Long Life Random Fatigue Behavior of Notched Specimens in Service, in Service Duplication Tests, and in Program Tests," *Service Fatigue Loads Monitoring, Simulation and Analysis, ASTM STP 671*, P. R. Abelkis and J. M. Potter, Eds., ASTM International, West Conshohocken, PA, 1979, pp. 222 239.

[2] Berger, C., Eulitz, K. G., Heuler, P., Kotte, K. L., Naundorf, H., Schütz, W., et al., "Betriebsfestigkeit in Germany - An Overview," *International Journal of Fatigue*, accepted for publication, 2002.

[3] Gaßner, E. and Kreutz, P., "Bedeutung der Programmbelastungs-Versuche als einfachste Form der Simulation zufallsartiger Beanspruchungen," Forschungsbericht 80, VDI-Z Reihe 5, Nr. 80, VDI-Verlag, Düsseldorf, Germany, 1984.

[4] Gaßner, E. and Lowak, H., "Bedeutung der Unregelmäßigkeit Gauß'scher Zufallsfolgen für die Betriebsfestigkeit," *Werkstofftechnik*, Vol. 9, No. 7, Verlag Chemie GmbH, Weinheim, Germany, 1984.

[5] Schütz, W., "Steuerung von Hochfrequenzpulsern durch Prozessrechner," *Tagungsband des Arbeitskreises Betriebsfestigkeit*, Deutscher Verband für Materialprüfung e.V., Berlin, Germany, 1984.

[6] Kirkby, W. and Edwards, P., "Constant Amplitude or Variable Amplitude Tests as a Basis for Design, Studies, Fatigue Design" *Proceedings of the 4 ICAF-Symposium*, Munich, Germany, 1965.

[7] White, D. J. and Lewszuk, J., "Narrow Band Random Fatigue Testing with Amsler Vibrophore Machines," *Journal Mechanical Engineering Science*, Vol. 11, No. 6, 1969.

[8] Mertens, D., Hück, M., and Schütz, W., "Erweiterung eines HF-Pulsers (Bauart Amsler) auf Randomversuche," Bericht B-TF-V-001, IABG, Ottobrunn, Germany, 1975.

[9] Karl, J. and Schütz, W., "Nachbildung von extern vorgegebenen Zufallsprozessen auf elektromagnetischen Resonanzpulsern," Bericht TF-V-126, IABG, Ottobrunn, Germany, 1981.

[10] Stanzl-Tschegg, S. E., Hollanek, W., and Tschegg, E. K., "Fatigue and Fracture under Variable-Amplitude Loading at Ultrasonic Frequency," *Advances in Fracture Research*, S. R. Valuri, D. M. R. Taplin, T. Rama Rao, F. J. Knott, R. Dubey, Eds., ASTM International, West Conshohocken, PA, 1984.

[11] Mayer, H., "Fatigue Crack Growth and Threshold Measurements at Very High Frequencies," *International Materials Review*, Vol. 44, No. 1, 1999.

[12] Hug, J. and Zenner, H., "Pseudo-Random-Versuche auf Resonanzprüfmaschinen," *Tagungsband des Arbeitskreises Betriebsfestigkeit*, Deutscher Verband für Materialforschung und –prüfung e.V., Berlin, Germany, 1997.

[13] Krüger, L., Scheutzow, M., Beste, A., and Petersen, J., "Markov- und Rainflow-Rekonstruktionen stochastischer Beanspruchungs-Zeitfunktionen," *VDI-Zeitschrift*, Vol. 18, No. 22, VDI-Verlag, Düsseldorf, Germany, 1985.

[14] Heuler, P. and Seeger, T., "A Criterion for Omission of Variable Loading Histories," *International Journal of Fatigue*, Vol. 8, No. 4, 1986, pp. 225 230.

[15] Miller, K. J., Bathias, C., and Stanzl-Tschegg, S., "Gigacycle Fatigue," *Fatigue & Fracture of Engineering Materials & Structures*, Vol. 22, 1999.

[16] Stanzl-Tschegg, S. and Meyer, H., "Variable Amplitude Loading in the Very High Cycle Regime," *Proceedings of the Inernational Conference on Fatigue in the Very High Cycle Regime*, S. Stanzl-Tschegg, H. Meyer, Eds., BOKU, Wien, 2001, pp. 371 378.
[17] Kleemann, U., Traupe, M., Pöting, S., and Zenner, H., "Parameter C Lifetime Calculation for the High Cycle Regime," *Proceedings of the Eighth International Fatigue Congress*, EMAS, Stockholm, Schweden, 2002.
[18] Pöting, S., "Lebensdauerabschätzung im High Cycle Fatigue Bereich," Dissertation, TU Clausthal, 2003.
[19] Gaßner, E., "Festigkeitsversuche mit wiederholter Beanspruchung im Flugzeugbau," *Ausgabe Luftwissen,* Bd. 6, Deutsche Luftwacht, Germany, 1939, S. 61 64.
[20] Gaßner, E., "Auswirkung betriebsähnlicher Belastungsfolgen auf die Festigkeit von Flugzeugbauteilen," *Jahrbuch der deutschen Luft und Raumfahrtforschung*, 1941, S. I 472 I 483.
[21] Ertelt, H.-J., "Einfluss der Parameter Lastfolge, Sequenzklassierung, Teilfolgenumfang und Prozessirregularität einer Betriebsbelastung (Gaußprozess) auf die Lebensdauer eines Bauelementes aus 3.1354 T3 und 3.4377 T761," University of Stuttgart, Stuttgart, Germany, 1988.
[22] Buxbaum, O., Klätschke, H., and Oppermann, H., "Zum Einfluss auf die Lebensdauer von Kerbstäben aus Stahl und Aluminium," Bericht Nr. FB-186, LBF, Darmstadt, Germany, 1989.
[23] Zenner, H., "Lebensdauerkonzepte, Beschreibung - Kritik - Entwicklungen," DVM-Bericht 800, Deutscher Verband für Materialprüfung e.V., Berlin, Germany, 1997, S. 9 35.
[24] Pöting, S. and Zenner, H., "Lebensdauer von Schweißverbindungen im Bereich hoher Lastspielzahlen (HCF)," Abschlußbericht, IMAB - TU Clausthal, Clausthal-Zellerfeld, Germany, 2002.
[25] Pöting, S. and Zenner, H., "High Cycle Fatigue (HCF) von Bauteilen," Abschlußbericht, FVA, Frankfurt, Germany, 2002.

Journal of ASTM International, October 2004, Vol. 1, No. 9
Paper ID JAI19044
Available online at www.astm.org

Kenneth George,[1] *Harold S. Reemsnyder,*[2] *J. Keith Donald,*[1] *and Robert J. Bucci*[3]

Development of a DCPD Calibration for Evaluation of Crack Growth in Corner-Notched, Open-Hole Specimens

ABSTRACT: A direct current potential drop (DCPD) calibration was developed for an open-hole specimen to characterize fatigue crack growth (FCG) behavior of cracks initiating from a small corner flaw and transitioning to a through-thickness crack. A single Mode I stress intensity (K_I) solution was derived covering the entire range of crack growth. The purpose of using this specimen geometry was to: 1) capture short crack behavior for specific crack length intervals of damage tolerance criteria and 2) use the data to evaluate predictive FCG methodology. Driven by these objectives, a non-standard specimen was chosen that better simulated the geometry and stress state of the component of interest: an aircraft wing design detail. Thin panels of selected 7XXX and 2XXX aluminum alloys were prepared with a centrally located open-hole with a corner notch of 0.13 mm (~0.005 in.) to serve as a crack initiation site. Testing was conducted in high-humidity air under constant and variable amplitude loading. Short crack results agreed well with existing, closure-corrected, long crack data. Duplicate tests of the 7XXX alloys confirmed repeatability. The 2XXX alloys exhibited greater variability than the 7XXX alloys in the short crack regime. Evaluation of the predictive methods is beyond the scope of this paper and will be published separately.

KEYWORDS: variable amplitude, fatigue crack growth, short crack, aluminum alloys, direct current potential drop

Introduction

Mechanical testing coupled with computer modeling of FCG behavior has become an integral part of managing the life of damage tolerant structures. Applying modeling technology to material trade studies may afford the opportunity to optimize and improve material selection efficiency by enabling crack growth prediction for various applications, crack configurations, and loading profiles from a single database comprised of standard fracture mechanics tests. Described herein is the use of a single specimen to obtain FCG data over a large range of damage tolerance parameters starting from short crack behavior close to a small notch transitioning to a through crack. This was done to determine the feasibility of producing such data in a timely, cost-effective manner and to employ said data with FCGR modeling for design/material trade study end-use. The modeling and trade study results are ongoing and beyond the scope of this paper.

The selected test parameters were based on durability and damage tolerance allowables of a specific structural application: the tension-loaded upper skin of a transport aircraft horizontal stabilizer. The open-hole specimen geometry was chosen because it was the closest match to the application, and it provided flexibility in starter notch geometry and location. An approximate

Manuscript received 10 July 2002; accepted for publication 17 July 2003; published October 2004. Presented at ASTM Symposium on Fatigue Testing and Analysis Under Variable Amplitude Loading Conditions on 29 31 May 2002 in Tours, France; P. C. McKeighan and N. Ranganathan, Guest Editors.

[1] Research Engineer, Fracture Technology Associates, 2001 Stones Throw Rd, Bethlehem, PA 18015.
[2] Consulting Engineer, 2005 Johnston Drive, Bethlehem, PA 18017.
[3] Technical Consultant, Alcoa Technical Center, 100 Technical Dr., Alcoa Center, PA 15069.

0.100 mm (~0.004 in.) notch was cut on one edge of the open hole to represent a worst-case machining imperfection in a fastener hole. The number of cycles to grow a crack from 0.127 to 0.762 mm (0.005 to 0.030 in.) was of particular interest. The 0.762 mm crack length approximates a maximum allowable rework limit enabling complete flaw removal by resizing the hole, thereby returning the hole to its virgin fatigue life state. Also addressed were the number of cycles from a 1.27 mm (0.05 in.) corner crack to a 15 mm (0.60 in.) through crack to simulate a typical aircraft threshold inspection (first interval) requirement for a skin/stiffener joint detail.

Experimental Procedure

Aluminum alloy (AA) panels were machined (Fig. 1) from rolled sheet materials listed in Table 1. A notch was introduced in the open-hole by drawing a serrated razor across one edge at a 45° angle to the specimen face, resulting in triangular cross-sectional geometry. The target size was 0.100 mm for each leg of the triangle. This procedure was delicate and had to be performed under an optical microscope. Notch positioning within 0.5 mm of the hole's centerline was achieved by carefully scribing the specimen. The final notch size and aspect ratio were verified at 30× magnification.

A study was conducted [1] to compare drilling and reaming to end milling to determine the best (least distortion) hole machining practice using phase shift microscopy. Deformation measurements in directions axial (edge height) and radial (width) to the bore (Fig. 2) are summarized in Table 2. End milling was found to produce a minimal deformation of 22.5 μm in the width dimension — less than 25 % of the flaw depth. Therefore, all specimens were machined using the end mill practice. This translated to better repeatability of cycles to crack initiation.

A direct current potential difference (DCPD) calibration was formulated using a marker band technique [2 4] with an AA 7075-T651 specimen. Active and reference leads (0.127 mm diameter platinum wire) were resistance-welded to opposite specimen faces with respective gage lengths of 3.18 mm and 63.5 mm measured from the hole's center (Fig. 1). A reversing direct current of 20-A was applied through threaded fasteners at each end.

The crack's classification differed as the crack front configuration changed to describe it mathematically as an ever-increasing crack. Three classifications were assigned: corner crack, transition, and through crack. With this in mind, the marker band crack lengths were tabulated along with corresponding DCPD values. Applying a splined curve fit to the data leads to the calibration curve of average crack length ($\bar{c}$) versus DCPD. Figure 3 summarizes the marker band specimen topography and crack length definitions. Also shown is the resulting calibration curve with normalized DCPD voltage defined by

$$V_{normalized} = (V_a/V_{a0})/(V_{ref}/V_{ref0}) \tag{1}$$

where

V_a = instantaneous active lead voltage,

$V_{a,0}$ = initial active lead voltage,

V_{ref} = instantaneous reference lead voltage, and

$V_{ref,0}$ = initial reference lead.

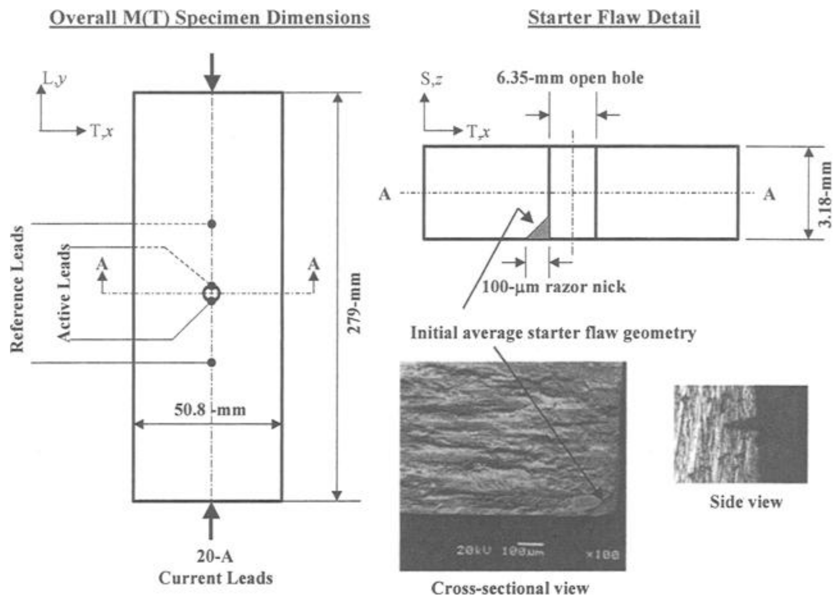

FIG. 1 *Schematic of M(T) open hole specimen with initial starter flaw geometry.*

TABLE 1 *Alloys and selected materials properties.*

Alloy	Lot	Sheet Thickness (mm)	Longitudinal Tensile Properties		
			Yield Strength (MPa)	Tensile Strength (MPa)	Elongation (%)
7075-T651	548-232	7.94	530	570	14.1
7075-T651	783-815	12.70	564	607	12.5
7475-T7351	688-212	12.70	431	495	16.0
7055-T7751	113-402	19.05	627	648	11.1
7150-T7751	113-586	12.70	561	595	13.0
2324-T39	113-401	19.05	452	482	15.7
C433-T39	662-563	19.05	435	469	14.3
C47A-T8	768-941	19.05	437	470	11.8

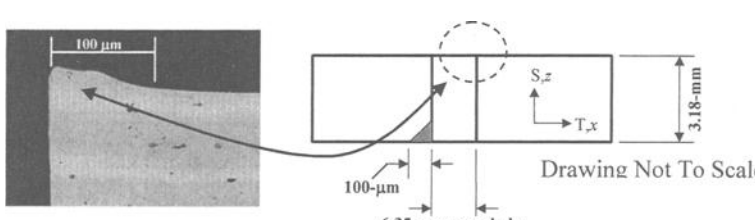

FIG. 2 *Micrograph and schematic showing typical distortion of material at tool exit for drill/ream procedure.*

TABLE 2 *Quantification of distortion due to open hole machining procedure.*

Machining Practice	Position O'clock	Tool Entry Side Edge Height (μm)	Tool Entry Side Width (μm)	Tool Exit Side Edge Height (μm)	Tool Exit Side Width (μm)
End Milled[1]	3	6.3	16.3	2.5	20.4
	9	6.6	17.1	2.7	22.5
Drill/ream[2]	3	0.9	89.6	11.5	89.2
	9	0.9	78.4	10.0	80.5
Drill/ream[3]	3	3.0	117.5	11.2	126.8
	9	4.1	91.4	13.2	100.0

[1] End mill: 0.8 mm/s, 2500 rpm.
[2] Drill: 1.7 mm/s, 800 rpm; Ream: 1.7 mm/s, 250 rpm.
[3] Drill: 4.2 mm/s, 800 rpm; Ream: 1.7mm/s, 250 rpm.

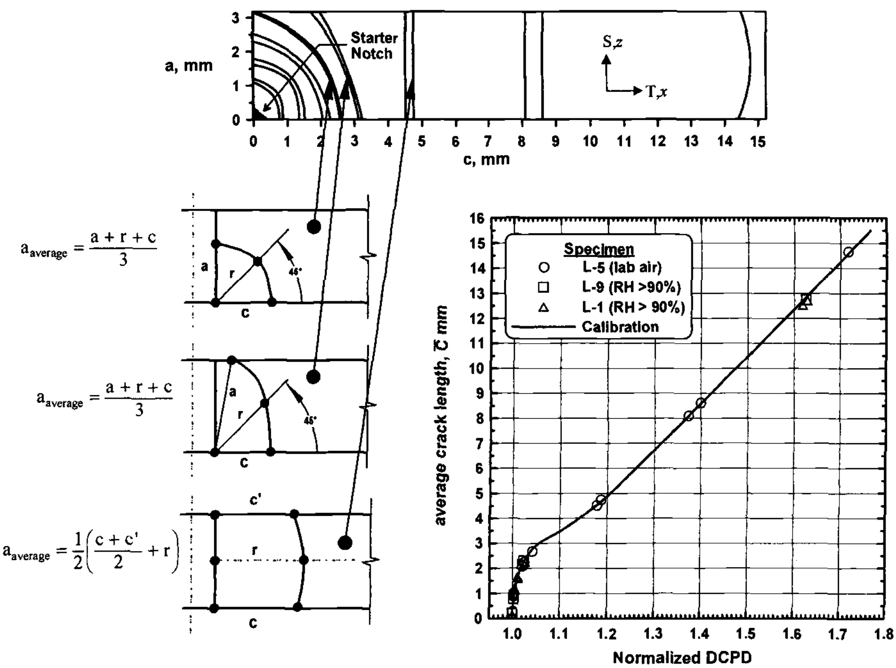

FIG. 3 *Crack length formulation for each crack front configuration and resulting DCPD calibration. Specimen L-5 was the calibration subject, while L-1 and L-9 show corroboration.*

To obtain crack growth information as a function of the applied stress intensity factor (K), Reemsnyder [5] derived a numerical K solution for the specific geometry using AFGROW [6]. The K solution took the form of

$$K_{\bar{c}} = \beta_{\bar{c}} \cdot \sigma\sqrt{\pi \bar{c}} \tag{2}$$

where β factors are computed as a function of crack length $\bar{c}$. Details of the solutions are given in the Appendix.

All testing was performed in a servo-hydraulic test frame under closed-loop computer control. In addition to careful system tuning, the command signal was compensated continuously based on system response to achieve desired end levels. The damage parameter concept [7] was incorporated as a metric for cumulative end level accuracy throughout the spectrum tests. The damage parameter value varied between 0.9995 and 1.0000, where unity is perfect agreement of target and response. Prior to testing, the specimens were subjected to a 12.9-kN compressive load while constrained in an anti-buckling device to promote crack initiation. The device was removed, and the specimens were encased in a Plexiglas humidity chamber to allow in situ crack growth measurements in high-humidity air (HHA) with RH > 90 %.

It is well known that the electrical conductivity of aluminum alloys is acutely sensitive to temperature [3,4]. To ensure sufficient stability, the DCPD signal was observed over time while cycling at low load prior to starting each test. Once the specimen and its local environment were in thermal equilibrium, the signal deviation was less than +/- 0.002 μV, which was deemed adequate for crack growth detection and measurement. When P_{max} was raised to the test level, a short transient period was observed. The voltage at the starting notch length was determined by averaging the voltage signal at max load (excluding the transient readings) prior to crack growth. Once the crack began to grow, a clear rise in the DCPD signal was evident. The cycles pertaining to a 0.127 mm crack length were determined by linear interpolation. This calibration procedure proved robust in terms of probe placement, and no evidence of cracking at the attachment points was found. However, as a result of the chosen probe locations, crack length calculations less than 1 mm were particularly sensitive to small changes in voltage due to the steepness in the early part of the DCPD calibration curve (Fig. 3). Therefore, equipment with nano-volt resolution was required. A typical measured DCPD response and associated crack lengths are depicted in Fig. 4.

Input data for a DCPD test includes an estimate of initial flaw size. Because the growing cracks quickly formed a nearly semi-circular crack front prior to transitioning to a through crack, an equivalent radius, r_{eq}, was found by equating the area of a quarter circle with the triangular flaw. This was assumed to be a more accurate method of establishing a starter flaw size. The equivalent radius was calculated by

$$r_{eq} = \sqrt{\frac{(2 \times l^2)}{\pi}} \tag{3}$$

where l is the length (assumed equal to the base dimension) of one leg of the triangle measured on the specimen surface.

At least one constant amplitude and one spectrum test were performed on each alloy. Duplicate constant and variable amplitude tests were run using the 7075-T651 alloy, and three duplicate variable amplitude tests were performed on the C433-T39 alloy. Load control with a P_{max} corresponding to a constant 82.7 Mpa gross cross-section stress, σ_{ref}, was applied during all tests. Although the selected reference stress was slightly greater than that of the application, it was the lowest stress capable of initiating a crack from the starter flaw within a reasonable 24-h period.

Constant amplitude tests were conducted at 20-Hz. The largest peaks of the variable amplitude spectrum were assumed the most damaging cycles. To form a comparison between constant and variable amplitude tests, the largest amplitudes were matched in terms of stress level and frequency with the constant amplitude tests. Smaller amplitude cycles were limited to a frequency of 40 Hz to maintain good control. The variable amplitude spectrum profile is shown in Fig. 5.

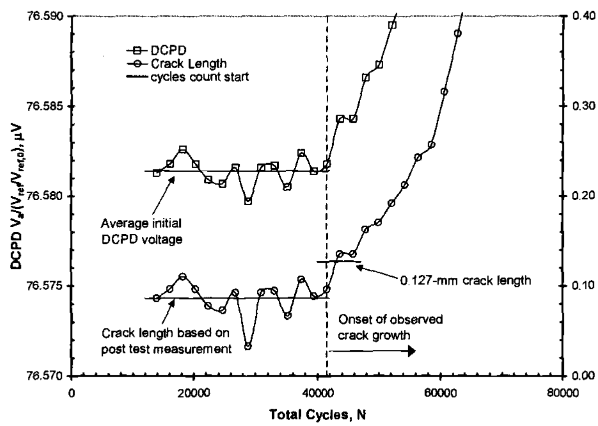

FIG. 4 *Typical DCPD signal versus cycles. Corresponding change in crack length is shown on right.*

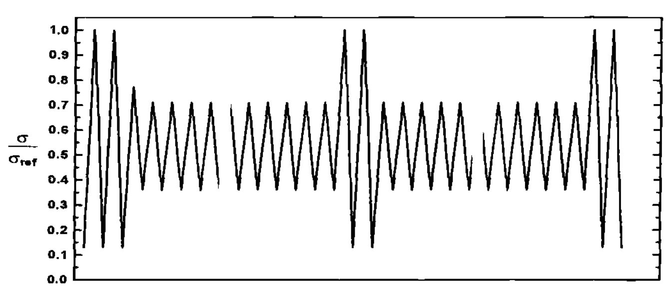

FIG. 5 *Generic civil transport aircraft horizontal stabilizer spectrum. Peak loads correspond to extended flap condition.*

Results and Discussion

Fracture surface measurements were used to refine the analysis [4]. The number of cycles for each test was found by subtracting the cycles incurred prior to a crack length of 0.127 mm. In all cases, the starter notch was less than 0.127 mm, therefore, it was possible to construct curves of crack length versus cycles starting from a consistent sharp crack length of 0.127 mm pertaining to zero cycles.

The results of all constant amplitude and variable amplitude tests in terms of crack length versus number of cycles (or blocks) are shown in Figs. 6 and 7. Approximately 90 % of tests were successful in that a single crack initiated and grew as anticipated. In the remaining 10 %, either a secondary crack was found on the opposite side of the hole, or the specimen failed from cracking at the loading hole (one case). These data were excluded.

It was found that the alloy ranking was preserved between the constant amplitude and variable amplitude testing. Further, the ranking matched existing long crack data [1] obtained using 102 mm wide by 6.4 mm thick M(T) panels at 20 Hz in HAA. Comparison of Figs. 6 and 7 shows close agreement between duplicate testing of AA 7075-T651 in the small crack and long crack regimes, demonstrating repeatability. In Fig. 7, however, duplicate tests of AA C47-T6 and triplicate tests of AA C433-T39 (both 2XXX series alloys) exhibited marked variance with the predominant divergence arising in the small crack regime. Recall that starting the cycle count once the crack length reached 0.127 mm was based on an allowable specific to this work. If, for example, the same data were re-evaluated, and the count zeroed once it became a stable through crack of length 3.8 mm, the scatter associated with small crack behavior would be reduced significantly (Fig. 8).

Figure 9 depicts constant amplitude FCG data for AA 7075-T651 and AA 2324-T39. Here, corner crack data from this study are compared with long cracks [1]. The corner crack data are shown versus $\Delta K_{applied}$ and are assumed closure-free for small crack lengths; the through-crack data have been collected using the compliance method of crack measurement and corrected for closure using the adjusted compliance ratio technique (ACR) [8]. It should be noted that the ACR method works well for accounting for closure in the near threshold regime but yields ΔK_{eff} values approaching $\Delta K_{applied}$ for crack growth rates above 1×10^{-4} mm/cycle for aluminum alloys. Therefore, it was reasonable to expect good agreement between the corner crack data for small crack lengths and existing long-crack ACR closure-corrected data in the near-threshold regime. Also, it was expected that as the cracks became through-thickness cracks, growth rate versus $\Delta K_{applied}$ behavior should again agree with existing increasing K from the M(T) panels. This was proven correct as shown in Fig. 9, lending credence to the specimen design and K-solution.

The fractographs below each da/dN plot in Fig. 9 depict typical fracture surface features of the 7XXX and 2XXX alloys near the starter notch. Note that the relatively flat surface appearance of AA 7075-T651 relates to a smooth da/dN curve, while the rough fracture surface and tortuous crack path of the 2324-T39 corresponds to a jagged da/dN curve. The fracture morphology would be similar in long crack tests as well, but the effect on the da/dN plot is not as apparent (Alcoa M(T)-ACR tests) because: 1) the data have been analyzed by a seven-point polynomial method as opposed to the secant method used for the corner crack data; 2) crack length of an M(T) panel is based on the average of two through-thickness cracks; and 3) the M(T) panels were twice as thick as the corner crack specimens, thereby allowing the crack front to cover a larger number of grains. Combined, these factors have a significant smoothing effect on the data.

A final point of interest is the kink that arises in the da/dN curves as the crack transitions from a corner crack to a through crack (Fig. 10), where FCGR suddenly drops and then accelerates. The behavior is also evident in the a-N curves of Figs. 6 and 7 as a decrease in the slope at a crack length of approximately 3 mm.

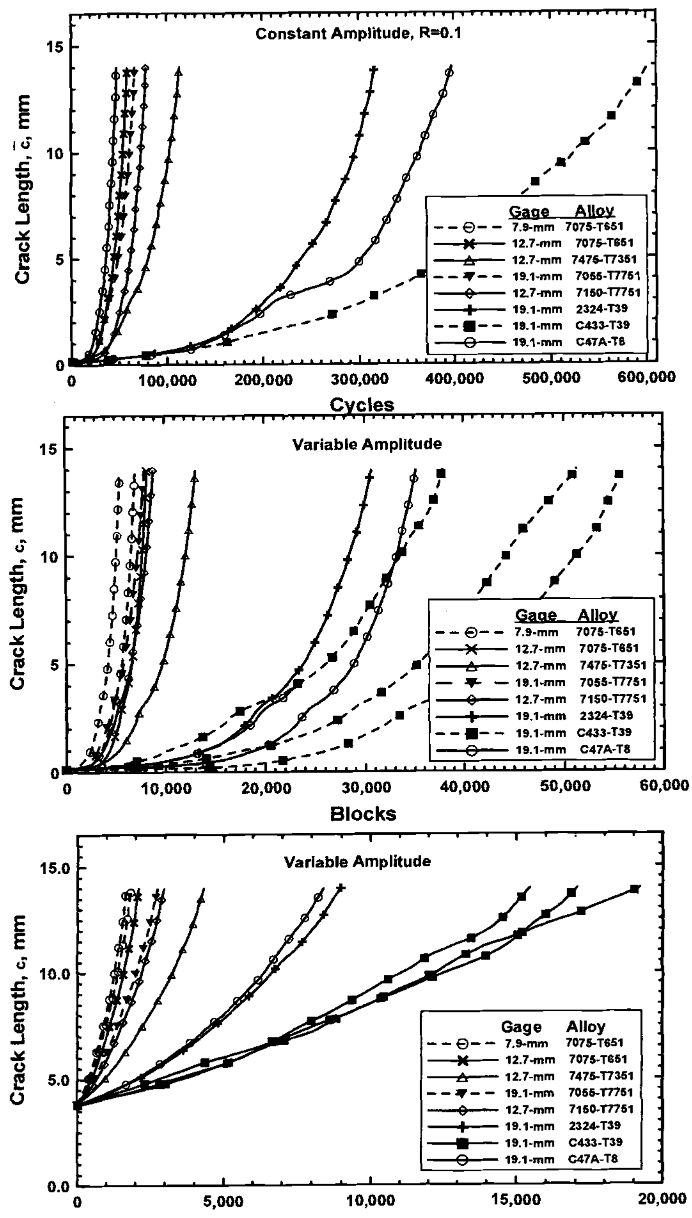

FIGS. 6, 7, and 8—*Crack length versus cycles and crack length versus blocks.*

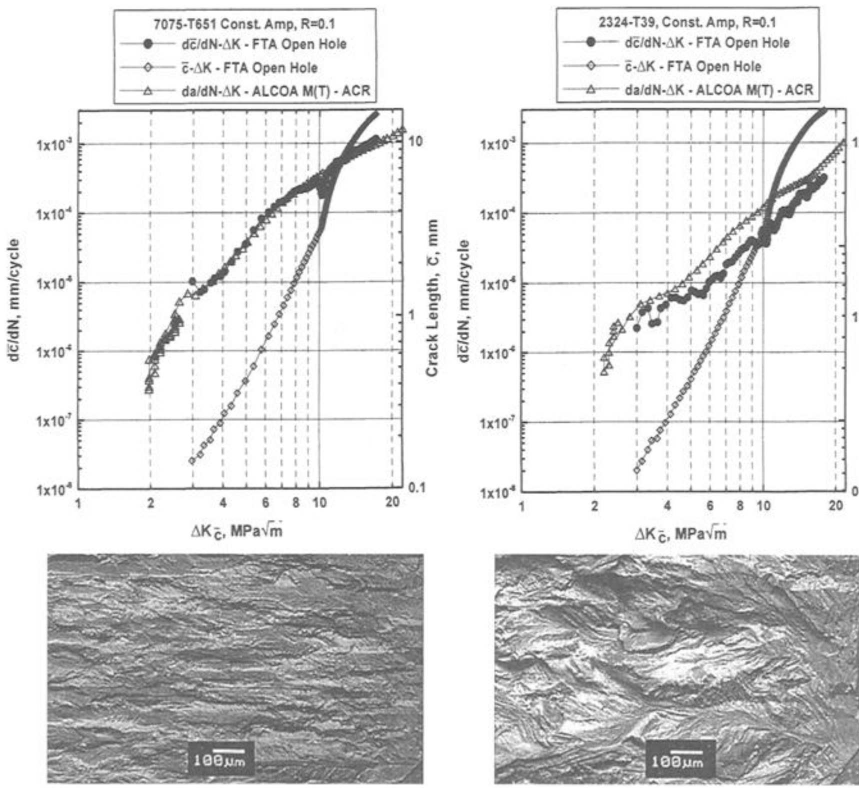

FIG. 9—*Comparison of short crack and closure-corrected long crack da/dN data. Short crack data are assumed essentially closure-free ($\Delta K_{app} = \Delta K_{eff}$). Corresponding crack length of open hole data is shown on secondary Y-axis.*

At first, the kink seen in the da/dN curves was thought to be an artifact of the crack length calculation or K-solution. By plotting the change in area/cycle versus area (dA/dN) versus crack area (A_c), as shown on the right side of Fig. 10, all mathematical physical phenomena of this crack geometry can be seen. One could possibly speculate that as the crack approaches transition, the ligament in the z-direction becomes fully plastic, ultimately failing locally due to overload. This may be the initial rise in growth rate (Fig. 10) at a crack area A_c of 5 mm^2. Following that event, the growth rate slows as the crack front straightens. When an area of 10 mm^2 is attained, the crack is growing along the same curve as the long crack data again. Although this is a curious feature of the geometry requiring further investigation, it should be noted that the number of cycles elapsed during the transition is relatively small compared to the total cycles in the overall a-N curve. Therefore, whether a modeling code simulates this or not will not adversely affect the predicted results in terms of total life.

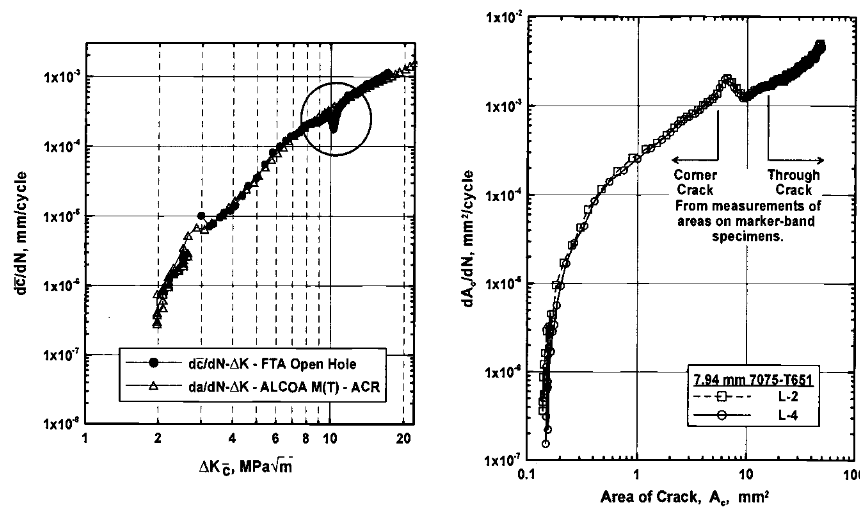

FIG. 10—*Graph on left shows this phenomenon is associated only with the open hole tests. On right, change in crack area/cycles versus area is plotted to remove crack length and K solution assumptions.*

Conclusions

A DCPD calibration and K solution was used successfully to characterize FCG from a small notch through transition to a through-thickness crack. A starter notch size of 0.1 mm was attained routinely. The minimum stress required to induce cracking was approximately 82.7 MPa, corresponding to an approximate K value between 2–3 MPa√m.

Repeatability was demonstrated using duplicate AA 7075-T651 coupons. Use of a sharp end mill reduced hole distortion and increased repeatability by reducing residual stress effects. Precise notch implementation was required.

DCPD equipment with nano-volt resolution was required. Tight control of temperature (+/- 1°C) and the use of a reference probe are recommended.

Within the short crack regime, FCGR is sensitive to local microstructure. This was noticed particularly in the larger-grained 2XXX alloys. Therefore, in certain cases, consideration should be given to selecting the notch depth, test specimen geometry, and crack configuration to represent the physics of the application. Long crack data may not be sufficient as a sole means of material characterization for all cases.

For this specimen geometry, a kink in the da/dN curve occurs when the crack transitions from a corner crack to a through crack. Although not completely understood, the overall cycles associated with the occurrence are small relative to overall life.

References

[1] Bucci, R. J., *Aluminum Empennage Improvement Study*, Alcoa Technical Center, Alcoa Center, PA, September 2001.

[2] Ritchie, R. O. and Bathe, K. J., "On the Calibration of the Electrical Potential Technique for Monitoring Crack Growth Using Finite Element Methods," *International Journal of Fracture*, Vol. 15, No. 1, pp. 47 55.

[3] Gangloff, R. P., Slavid, D. C., Piascik, R. S., and Van Stone, R. H., "Direct Current Electrical Potential Measurement of the Growth of Small Cracks," *Small-Crack Test Methods, ASTM STP 1149*, J. M. Larsen and J. E. Allison, Eds., ASTM International, West Conshohocken, PA, 1992, pp. 116 168.

[4] Donald, J. K. and Ruschau, J., "Direct Current Potential Difference Fatigue Crack Measurement Techniques," In *Fatigue Crack Measurement: Techniques and Applications*, K. J. Marsh, R. A. Smith, and R. O. Ritchie, Eds., Engineering Materials Advisory Service Ltd., Warley, UK, 1991, pp. 11 37.

[5] Reemsnyder, H. S., *Internal Report on K-Calibration of Open Hole Specimen Compatible with DCPD Measurements*, Fracture Technology Associates, Bethlehem, PA, February 2001.

[6] Harter, A., "AFGROW Version 4.0002.12.8," *Air Vehicles Directorate*, Air Force Research Laboratory, Wright-Patterson Air Force Base, OH, May 2000.

[7] McKeighan, P. C., Fess II, F. E., Petit, M., and Campbell, F. S., "Quantifying the Magnitude and Effect of Loading Errors During Fatigue Crack Growth Testing Under Constant and Variable Amplitude Loading," *Applications of Automation Technology in Fatigue and Fracture Testing and Analysis: Fourth Volume, ASTM STP 1411*, A. A. Braun, P. C. McKeighan, A. M. Nicolson, and R. D. Lohr, Eds., ASTM International, West Conshohocken, PA, 2000, pp. 146 164.

[8] Donald, J. K., Bray, G. H., and Bush, R. W., "An Evaluation of the Adjusted Compliance Ratio Technique for Determining the Effective Stress Intensity Factor," *29th National Symposium on Fatigue and Fracture Mechanics, ASTM STP 1332*, T. L. Panontin and S. D. Sheppard, Eds., ASTM International, West Conshohocken, PA, 1997, pp. 674 695.

[9] Newman, J. C. and Raju, I. S., "Stress Intensity Factor Equations for Cracks in Three-Dimensional Bodies Subjected to Tension and Bending Loads," Chapter 9, *Computational Methods in the Mechanics of Fracture*, Elsevier Science Publishers B.V., 1986.

Appendix

Corner Crack – An Ellipse or Not?

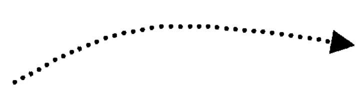

The following verifies that a corner crack growing in the open-hole specimen geometry can be assumed elliptical. The equation of an ellipse is

$$\frac{x^2}{c^2} + \frac{y^2}{a^2} = 1 \quad \text{and at } \phi = 45^\circ,\ x = y. \tag{A1}$$

The corresponding ray length, r, at $\phi = 45°$ is

$$r = c \cdot \sqrt{\frac{2}{1 + \rho^2}} \text{ where the aspect ratio } \rho = \frac{c}{a}. \tag{A2}$$

The corner-crack ray lengths of a calibration specimen as well as several corroboration specimens were measured and compared to the computed ray length of Eq A2 (ϕ = 45° for both cases). In view of the small differences, the assumption of an elliptical crack was reasonable. Measurement results of the calibration specimen 232L5 with comparisons to computed values are shown in Table A1.

TABLE A1—*Comparison of measured versus computed values of elliptical ray length.*

Specimen ID	Measured			Computed		% Diff.[1]
	c, mm	a, mm	r, mm	$\rho = c/a$	r, mm Eq A2	
232L5 (lab air)	0.762	1.092	0.889	0.698	0.889	0.6
	0.864	1.194	1.041	0.723	0.991	5.0
	1.346	1.600	1.549	0.841	1.448	6.0
	1.524	1.778	1.676	0.857	1.626	2.4
	2.057	2.286	2.083	0.900	2.159	–3.8
	2.286	2.515	2.235	0.909	2.388	–7.0
	2.565	3.124	2.667	0.821	2.794	–5.1
	2.616	3.175	2.743	0.824	2.845	–3.7

[1] Percent Difference = $((r_{measured}-r_{computed})/r_{measured})*100$.

For the corner cracks, the potential drop was calibrated versus the average of crack lengths measured at ϕ = 0°, 45°, and 90°, i.e., the equivalent quarter-circle crack shape $\bar{c}$. Generally, the shape of a corner crack is assumed to be that of an ellipse. Equating the area of a quarter-circle to that of a quarter ellipse yields

$$\frac{\pi \bar{c}^2}{4} = \frac{\pi ac}{4} \tag{A3}$$

and thus the equivalent quarter-circle crack length is

$$\bar{c} = \frac{c}{\sqrt{c/a}} \text{ or } c = \bar{c}\sqrt{c/a} \tag{A4}$$

where c/a is the aspect ratio.

K_I Solution

The K_I-solutions of *AFGROW Ver. 4.0002.12.8* fracture mechanics software were used for both the corner-crack and the through crack. The solutions take the form of

$$\beta = \frac{K_I}{\sigma\sqrt{\pi c}} \tag{A5}$$

where σ is the remote axial stress on the gross section area, and c is the general crack length. AFGROW software was used to determine the β factors as a function of crack length corresponding to the specific specimen geometry and two cases of crack front configuration (corner crack and through crack). Details for calculations are included in the AFGROW manual [6] with the corner crack analysis based on the Newman-Raju corner crack stress intensity solutions [9,10]. The tabular output of β factors from AFGROW were fit to polynomial expressions encompassing the corner crack and through crack.

K_I Solution, Corner Crack

In the following, the average K_I, i.e., $K_{average}$ is defined as

$$K_{average} = \frac{K_a + K_c}{2} \tag{A6}$$

where

$$K_a = \beta_a \cdot \sigma\sqrt{\pi a},\ K_c = \beta_c \cdot \sigma\sqrt{\pi c},\ \text{and}\ K_{\bar{c}} = \beta_{\bar{c}} \cdot \sigma\sqrt{\pi \bar{c}}. \tag{A7, 8, 9}$$

Substituting Eqs A7and A8 into A6 yields

$$K_{average} = \frac{\beta_a \cdot \sigma\sqrt{\pi a} + \beta_c \cdot \sigma\sqrt{\pi c}}{2} \tag{A10}$$

or

$$K_{average} = \left(\frac{\beta_a}{\sqrt{c/a}} + \beta_c\right) \cdot \frac{\sigma\sqrt{\pi c}}{2}. \tag{A11}$$

Substituting Eq A4 into Eq A11 yields

$$K_{average} = \sqrt[4]{c/a} \cdot \left(\frac{\beta_a}{\sqrt{c/a}} + \beta_c\right) \cdot \frac{\sigma\sqrt{\pi \bar{c}}}{2} \tag{A12}$$

or

$$K_{\bar{c}} = \beta_{\bar{c}} \cdot \sigma\sqrt{\pi \bar{c}} \tag{A13}$$

where

$$K_{\bar{c}} = K_{average}\ \text{and}\ \beta_{\bar{c}} = \frac{\sqrt[4]{c/a}}{2} \cdot \left(\frac{\beta_a}{\sqrt{c/a}} + \beta_c\right). \tag{A14, 15}$$

K_I Solution, Through Crack

For the through crack, the stress intensity factor is simply expressed by

$$K_c = \beta_c \cdot \sigma\sqrt{\pi c} \tag{A16}$$

where c is the length of the through crack measured from the circumference of the circular hole.

Combined Solution

Using AFGROW, tabular data of βa and βc for aspect ratios of 0.7, 0.8, 0.9, and 1.0 were generated. These data are shown in Fig. A1 with the corner crack region emphasized. Using an expression in the form

$$\beta_c = D_0 + D_1 \cdot c + D_2 \cdot c^2 + D_3 \cdot c^3 + D_4 \cdot c^4 \tag{A17}$$

data pairs of corner crack and through crack β factors of aspect ratios 0.7, 0.8, and 0.9 versus crack length were curve fit to provide continuous K expressions for either case.

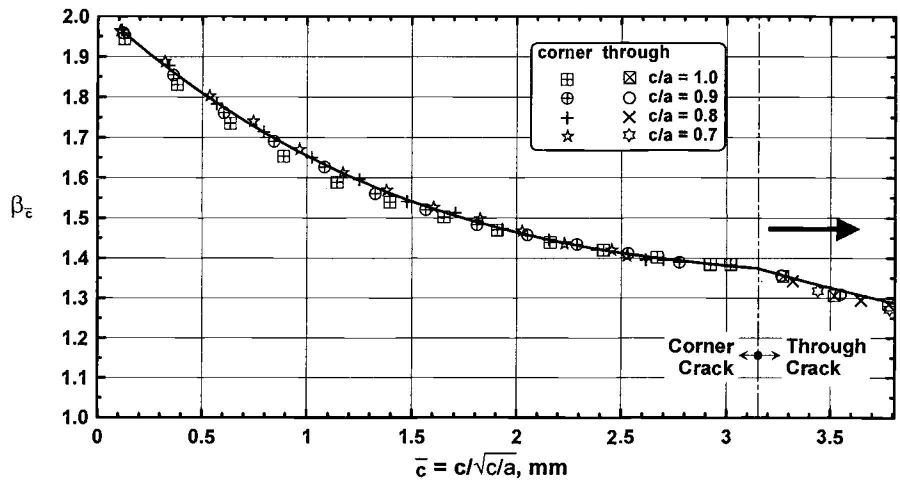

FIG. A1 *β Factors for a range of crack front aspect ratios and resulting 4th order polynomial curve fit for corner cracks and through cracks.*

For the corner-crack, the regression coefficients (based on an average of the aspect ratio of 0.7, 0.8, and 1.0) and statistics are given in Table A2.

TABLE A2—*Regression coefficients and statistics, corner crack.*

Coefficient	c/a = 1.0	c/a = 0.7, 0.8, 0.9
D_0	2.008390774	2.015478053
D_1	−13.40370452	−11.8449015
D_2	106.551886	74.69436031
D_3	−321.7117387	−168.3084932
Parameter	c/a = 1.0	c/a = 0.7, .08, .09
n	13	16
$s_{y\|x}$	0.0025159	0.0032038
R	0.99991	0.99986
$\bar{c}_{int}$ [2]	0.125	0.124

[2] Intersection of the corner crack $K_{average} / K_{\bar{c}} - \bar{c}$ curve with that of the through crack.

For the through crack, the regression coefficients and statistics are given in Table A3.

TABLE A3—*Regression coefficients and statistics, through crack.*

Coefficient	Value
D_0	2.165631381
D_1	–9.651274024
D_2	32.02464844
D_3	–49.30998855
D_4	29.85015335
Parameter	**Value**
n	48
$s_{y\|x}$	0.0041825
R	0.99926
$\overline{c}_{int}$ [3]	0.124

[3] Intersection of the corner crack curve with that of the through crack.

AEROSPACE APPLICATIONS

Michael G. Sullentrup[1]

The F/A-18E/F Full-Scale Static and Fatigue Test Programs – An Overview

REFERENCE: Sullentrup, M. G., **"The F/A-18E/F Full-Scale Static and Fatigue Test Programs – An Overview,"** *Fatigue Testing and Analysis Under Variable Amplitude Loading Conditions, ASTM STP 1439*, P. C. McKeighan and N. Ranganathan Eds., ASTM International, West Conshohocken, PA, 2005.

ABSTRACT: The structural certification of F/A-18E/F airframe included full-scale fatigue and static test programs. This paper outlines the test programs, discusses test objectives, discusses test results, highlights some significant advancements in the state-of-the-art developed to support this test program, and offers recommendations for future full-scale certification test programs.

The method used to correlate static test measured strains to finite element model predictions is discussed. The method used to certify redesigned structural components without the benefit of a full-duration fatigue test is discussed. Innovations involving real-time data monitoring, rapid post-test analysis of results, characterization of measured endpoint strains during fatigue cycling, and comparison of block-to-block measured strain response are discussed.

There were many lessons learned during these test programs. These are summarized and discussed. Recommendations for future full-scale certification test programs are also discussed.

KEYWORDS: full-scale fatigue test, full-scale static test, structural certification, strain measurement

Introduction

The final step in the building-block approach to airframe structural certification is the full-scale ground test program [1]. The F/A-18E/F ground test program encompassed two major testing activities, namely the static and fatigue test programs. Table 1 presents a brief introduction to these test programs. Figure 1 presents the structural configuration of the full-scale static and fatigue test articles.

The static design and test requirement for the airframe was 150% of design limit load. The fatigue design criteria were primarily driven by durability. The airframe was designed to 2.67 lifetimes (16 000 flight hours) and was tested to two lifetimes (12 000 hours).

[1] Associate Technical Fellow, The Boeing Company, P.O. Box 516, MC S106-6420, St. Louis, MO, 63166.

Table 1 — *F/A-18E/F Full-Scale Static and Fatigue Test Programs.*

Test Article Designation	Baseline Test Plan	Stretch Test Plan
ST50 Full-Scale Static Test	Static Test of Critical Design Conditions	Static Test of Flight Loads Outside the Design Envelope, Failure Tests
FT50 Full-Scale Fatigue Test	Fatigue Test of Two Lifetimes of Simulated Design Fleet Usage	Fatigue Test of Third Lifetime of Simulated Design Fleet Usage

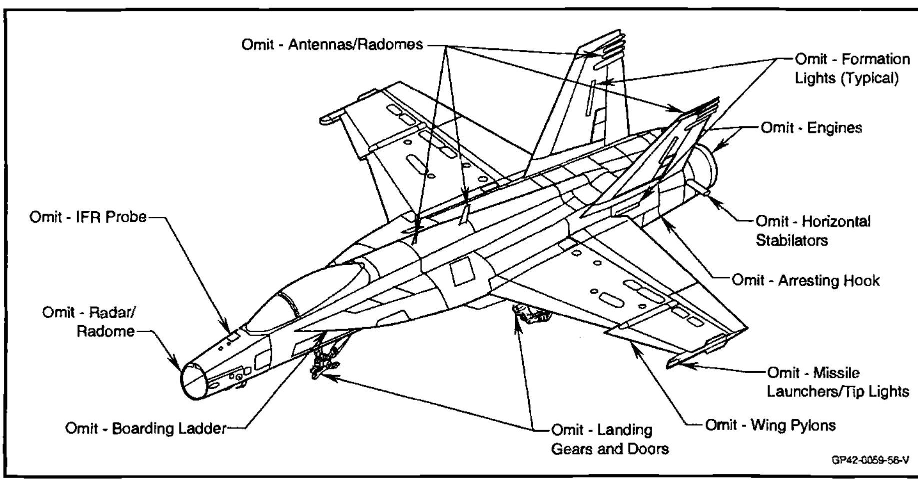

FIG. 1 — *F/A-18E/F Full-Scale Static and Fatigue Test Article Structural Configuration.*

Common Test Setup

The design of the test setup was common to the static and fatigue test articles. Loads were introduced via hydraulic servocylinders that were synchronized through a single load-control computer. Pressure loads were transmitted through neoprene pads bonded to the airframe surface. The pads were connected to the hydraulic cylinders through tension and tension/compression whiffletree systems. Additional loads were transmitted through simulated aircraft components such as store pylons, engines, and horizontal tails. The weight of the test article, simulated aircraft components, and test load application hardware were counterbalanced by compensatory tare loads in the hydraulic loading cylinders, and by weight baskets connected by cable via levers and pulleys.

Full-Scale Static Test Program

Objectives and Success Criteria – The objectives of the full-scale static test program were to demonstrate the static strength capabilities of the various airframe components. The success criteria were that there be no evidence of gross section yielding at 115% of the test limit load (TLL) and no failures at ultimate load (150% TLL).

Test Matrix – A test matrix including some 142 loading conditions was devised to apply critical loading conditions to all parts of the aircraft structure. Table 2 presents a summary of these loading conditions. The static test program was conducted over a seven-year period, with most of the first year dedicated to the major wing and fuselage loading conditions to support rapid expansion of the flight envelope. The extended period also included structural modifications and periods where component fatigue test programs were conducted.

Table 2 — *Static Test Program Loading Conditions.*

Structure	Ultimate Load Conditions Tested	Stretch Conditions Tested	Failure Conditions
Wing, Fuselage, & Vertical Tail	112	3	3
Canopy	2	0	0
Arresting Hook	3	0	0
Stabilator	2	0	1
Main Landing Gear	7	0	0
Nose Landing Gear	9	0	0
Total	135	3	4

Failure conditions are planned for 2003 timeframe.

Static Test Program Results – There were no major failures during the static test program to 150% TLL. However, there were occurrences of fastener failures, bushing migration, composite delamination, a few local buckling instabilities around door edges and minor yielding of the metal structure at 115% of limit load. All the anomalies found during testing were addressed by redesign of the affected structure.

Full-Scale Fatigue Test Program

Objectives and Success Criteria – The objective of the full-scale fatigue test program was to demonstrate that the test article met the fatigue durability design requirements of the design specification [2]. The success criterion was to complete two lifetimes of simulated design loading environment without failure. For metallic structures, the primary failure mode is crack initiation, defined as 0.01 inch (0.254 mm) crack depth.

Fatigue Test Spectrum – The full-scale fatigue test spectrum was based on the requirements of the design specification [2]. For the sake of convenience and efficiency, the events were compiled into a repeatable block of events simulating 1000 flight hours. There were 448 490 loading events required to simulate the flight maneuvering, landing, catapult, and dynamic buffet events in each 1000 simulated flight hours. Figure 2 presents a summary of the multivariate parametric loading events simulated in the fatigue test spectrum.

Service Life (6000 Flight Hours) Requirements

Ground-Air-Ground Cycles 15 750
Field Taxi Runs 8 750
Catapult Launches 2 250

Landings
Arrested 2 250
Touch and Go 450
Field Carrier Landing Practice (FCLP)........... 6 450
Field Mirrored Landing Practice (FMLP).......... 6 600

38% Sea-Based Missions
62% Land-Based Missions

- Various combinations of Mach, altitude, Nz, and stick throw.
- Symmetric and asymmetric flight maneuvers.
- G-jump events due to store release.
- Dynamic buffet events derived from flight-measured data.
- Differential cockpit pressure based on altitude.
- Various store carriage configurations as required for mission type.
- Distributions of aircraft gross weight and off-center angle in the catapult events.
- Distributions of forward landing speed, sink speed, pitch angle, roll angle, roll rate, crosswind velocity, and landing surface condition for the various landing types.
- Distribution of Nz excursion for the taxi events.

FIG. 2 — *F/A-18E/F Full-Scale Fatigue Test Spectrum Synopsis.*

Fatigue Test Setup and Instrumentation – At the time the test program began, the full-scale fatigue test of the F/A-18E/F was one of the most complex ever attempted in terms of its load introduction system and data recording requirements. Figure 3 presents a summary of the instrumentation, applied loads, reactions, and cycling rate performance. Figure 4 presents a photograph of the F/A-18E/F full-scale fatigue test article in the test fixture.

F/A-18E/F Full-Scale Test Program

- Strain Gage Channels at Start of Test.................................... 1 643
- Deflection Potentiometers at Start of Test................................ 89
- Applied Load Actuators 176
- Reactions... 6
- Fatigue Spectrum Lines per 1000 Simulated Flight Hours 448 490
- Pretest Strain Surveys 27
- Channels of Data Recorded for Each Endpoint....................... 1 560
- Maximum Cycling Rate (Lines Per Minute)............................... 14.1

FIG. 3 – *Full-Scale Fatigue Test Summary.*

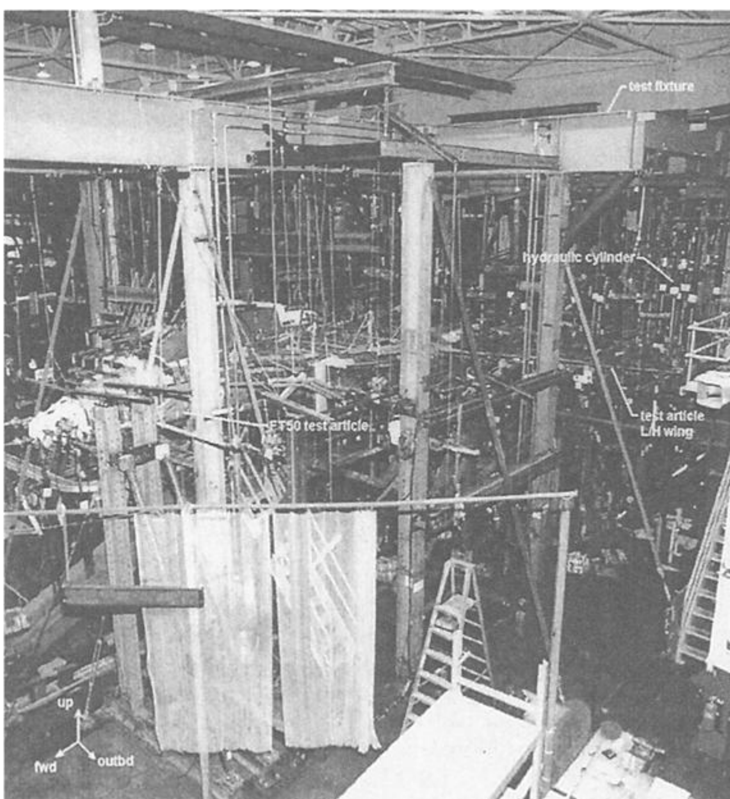

FIG. 4 — *F/A-18E/F Full-Scale Fatigue Test Article in the Test Fixture.*

Fatigue Test Program Results – As with any full-scale fatigue test, a number of structural anomalies with the test article were discovered during the periodic inspections [3]. Each anomaly was documented, as well as the corrective action. There were 487 anomalies documented during the first two lifetimes of fatigue testing. Each was categorized as either significant or insignificant. Insignificant findings included anomalies such as worn or rotating fastener heads, broken fasteners, migrated bushings, hole wear in composite doors, minor composite door delaminations, and the like. All other findings, mostly cracked structural members, were considered significant. Figure 5 presents a summary of the findings.

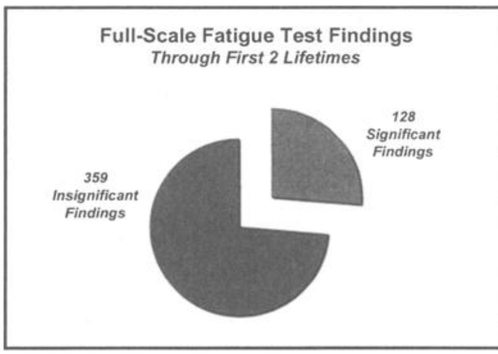

FIG. 5 — *Summary of Full-Scale Fatigue Test Findings.*

The full-scale fatigue test program was executed with great skill and efficiency considering the high degree of complexity in the loading system, data collection requirements, and the large size of the fatigue spectrum. The many improvements to the various processes that were implemented along the way aided in minimizing downtime and completion of this test program. Examples of these improvements include the establishment of an integrated test team led by the Test Authority, the establishment of a requirements change review / approval process, and the establishment of a rapid response team. The Navy customer gave the test program consistently high marks for cost, schedule, and quality performance.

Finite Element Model Correlation

One of the objectives of full-scale static testing was the correlation of measured strains to finite element model predictions. The results of this correlation not only validated the analysis performed to design and build the airframe, but also validated the analytical tools and analysis methods used for fleet modification and repair support activities. It is often difficult to achieve close correlation on a gage-by-gage basis, even in rather simple structures. This issue was addressed by prioritizing the importance of each recorded measurand for each condition. Table 3 presents a summary of the measurand classifications used.

Table 3 – *Full-Scale Static Test Measurand Classifications.*

Designation	Description	Percentage of Active Measurands
EI	Engineering Information Measurands recorded for information only.	~60
LP	Load Path Measurands of secondary interest for a given loading condition.	~33
LPB	Load Path Basic Measurands of primary interest for a given loading condition – most highly loaded / critical areas.	~5
SC	Structural Certification Special classification of LPB measurands located on composite structure. Used to address the fact that critical areas are not tested under in-flight environmental conditions.	~2

By focusing the correlation efforts on the measurands designated Load Path Basic and Structural Certification, a more meaningful and achievable correlation was made possible. In general, measured strains within 15% of the predicted values were considered acceptably close. When acceptably close correlation with FEM-based strain predictions was not possible, an investigation was conducted to understand better the discrepancy and to resolve it.

Root Cause Investigation

Fatigue cracking during full-scale fatigue testing is inevitable. When this happened, a root cause analysis was performed to gain an understanding of the reason for the structural deficiency. The structural analyst had to consider not only how to repair the affected structure in order to resume testing, but also how to certify the redesigned structure. The method used to certify redesigned structural components without the benefit of a full-duration fatigue test is outlined in Figure 6.

Significant Advancements

Numerous significant advancements in the state-of-the-art were realized during the F/A-18E/F ground test program. Each of these improved the cost, schedule, and/or quality of the final product. Some of the more important advancements are discussed in the sections to follow.

Real-Time Data Monitoring - Monitoring the data collected during full-scale static tests in real time is highly desirable since it not only gives the analyst an instantaneous view of structural performance, but it also minimizes risk of test failures. Previous generations of real-time data displays provided very limited capabilities. It was only

F/A-18E/F FATIGUE TEST CERTIFICATION PLAN

5 Step Process

- Step 1 - Understand The Cause Of Failure
- Step 2 - Categorize Complexity Of Analysis And Type Of Redesign Changes
- Step 3 - Establish Redesign Life Criteria
- Step 4 - Quantify Stress Reductions/Life Enhancements
- Step 5 - Document Redesign Stress/Lives

14

FIG. 6 — *Approach to Certification of Redesigned Structural Components.*

possible to view the digital strain output for a very small number of measurands. The display was difficult to interpret and provided a very limited view of the response of the test article.

A state-of-the-art real-time display system was developed that allowed the structural analyst to view easy-to-interpret graphical displays, and the capability to monitor a large number of measurands (up to 1500 for a load condition) in real time. Modern workstations were used to collect and display loads, deflection, and strain measurements in engineering units.

Two types of displays were utilized. The first was a simple x-y plot of measured load, strain, or deflection versus loading level. The measurand prediction was also displayed for reference. The displays were programmed to rescale themselves automatically during the test, if required. Figure 7 presents an example of the line graph display. The second type was a bar chart that displayed the measured loads, strains, and deflections compared to a previous run. The bars were color coded to aid in visual interpretation. This display allowed the analyst to monitor strains quickly and efficiently. Figure 8 presents an example of the bar chart display.

Rapid Post-Test Analysis of Recorded Data - State of the art data collection capabilities allow for the collection and storage of so much test data that it would require excessive time and effort to be properly analyzed. During the F/A-18E/F static test program, it was imperative that test conditions be executed and the data analyzed quickly and efficiently in order to continue to expand the flight envelope to support the concurrent flight test program.

An algorithm was developed to filter out insignificant data readings so as to concentrate on the significant few. Figure 9 presents the rules contained in the filter. Employing this approach reduced data review time from days to hours.

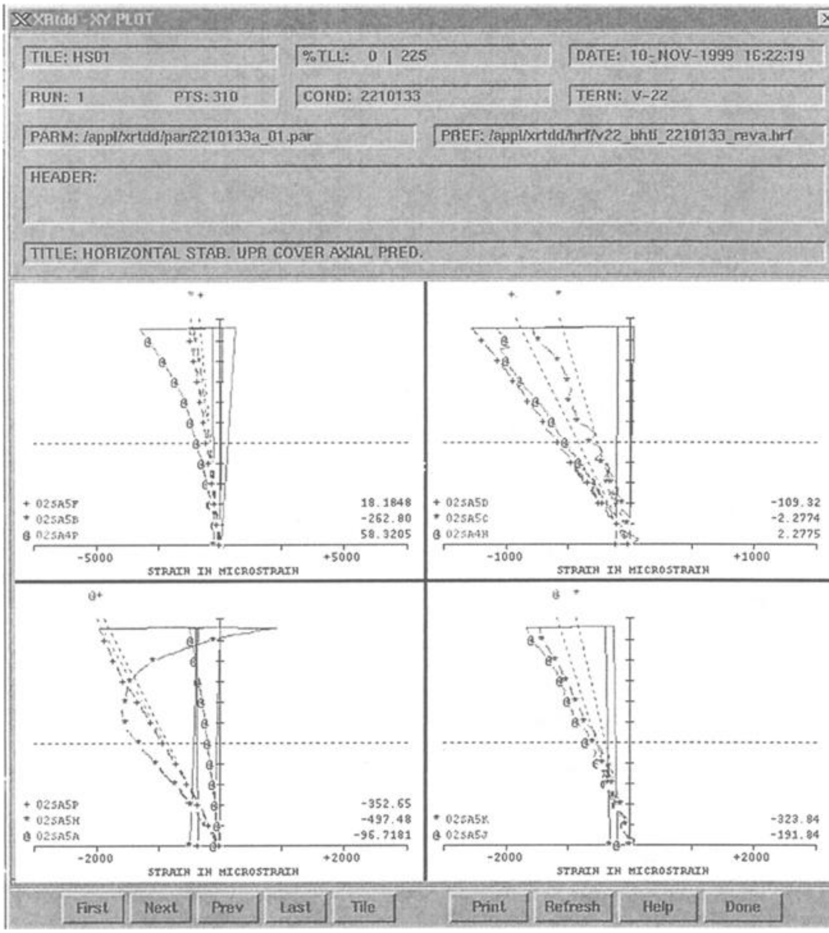

FIG. 7 — *Real-Time Measured Data Display, Line Graph.*

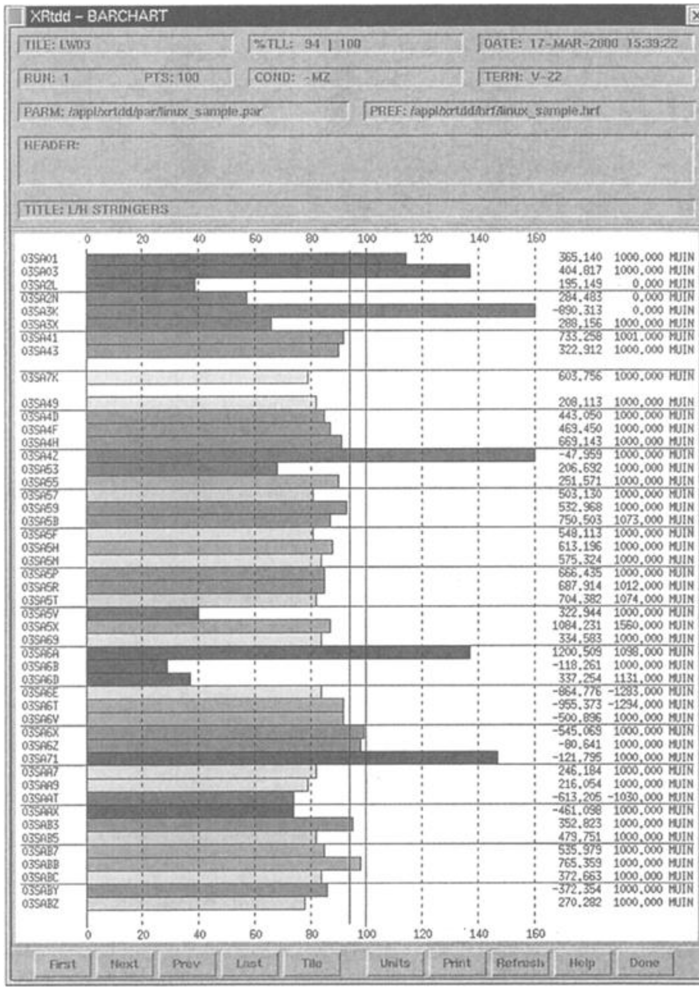

FIG. 8 — *Real-Time Measured Data Display, Bar Chart.*

Measured Filter Criteria

1. Strain magnitude is greater than +/- 20 ksi (137.9 MPa on metal or +/- 2000 microstrain on composite.

2. Deviation from predicted value is greater than +/- 15% and stress greater than +/- 10 ksi (68.95 MPa) on metal or +/- 1000 microstrain on composite.

3. Linearity is such that the computed correlation coefficient is less than +/- 0.95 and stress greater than +/- 10 ksi (68.95 MPa) on metal or +/- 1000 microstrain on composite.

4. The offset measured at 40% TLL is greater than 10% of the measured value at maximum test load and stress greater than +/- 10 ksi (68.95 MPa) on metal or +/- 1000 microstrain on composite.

5. Any other instrumentation channel deemed appropriate for consideration per engineering judgment.

FIG. 9 — *Post-Test Data Analysis Filter.*

Characterization of Measured Endpoint Strains During Fatigue Cycling - During the execution of the full-scale fatigue test of the F/A-18E/F, more than 1500 measurands were sampled and recorded for each line of the fatigue spectrum, resulting in more than eight billion data points to be analyzed. These very large quantities of test data required an innovative approach to efficiently and effectively analyze them.

The methodology to capture and characterize structural response data from any test measurand resulting from the multivariate flight-by-flight spectrum fatigue loading was developed. The technique that worked best was to interrogate the tails of the exceedance curves. The average and number of peaks and valleys that were greater than 75% of the extremes was computed and saved. These parametric characterizations of measurand response at each strain gage location were compared from block-to-block for repeatability.

Using these techniques, a large database of measured strain responses were electronically analyzed and archived. A good block of measured strain response data was captured for more than 90% of the 3000+ strain gages attached to the test article. This information has proven to be quite valuable to address test failures and fleet structural integrity issues.

Intelligent Measured Strain Trend Monitoring - By repeating the characterization process described above for each block of test data collected, it was possible to conduct a parametric comparison of strain response for each measurand for each block of recorded data in a timely manner. Interrogating the large quantity of data collected in this way, potential areas of change in structural integrity were quickly identified, based on changes in the parametric strain response.

There were three notable instances during the completion of the full-scale fatigue test when this approach identified structural cracks in the data. The test was stopped, the local area inspected and repaired, and the test was resumed.

Lessons Learned

There were many lessons learned during the execution of the F/A-18E/F ground test program. These are summarized in Figure 10 below.

Lessons Learned

- ❖ Establish a single Test Authority to coordinate final decisions regarding cost, schedule, quality, and risk
- ❖ Establish a multi-disciplined integrated test team
- ❖ Get the customer fully engaged in the decision-making process from the start
- ❖ Develop a failure notification procedure and have call list available at the test site
- ❖ Establish change request process and change requirement management board
- ❖ Make use of digital photography and e-mail for quick dissemination of test failure information
- ❖ We can record significantly more data than we can analyze with traditional approaches
  - Must develop and rely upon data filters and obtain customer concurrence
  - Real-time data review and rapid post-test data analysis key to keeping the program on track
- ❖ Catalog large volumes of test data throughout testing for future use
- ❖ Actively maintain a good summary of test failures is key to structural certification of redesigned structure
  - 4-panel charts a good way to provide fleet management information
- ❖ Document the redesign certification plans for test failure locations
  - Coordinate and get customer agreement to pave the way for engineering change proposal
- ❖ Form a dedicated Rapid Response Team to address test anomalies and repairs

FIG. 10 — *Lessons Learned.*

Customer involvement was key to the successful execution of this extensive test program. Extensive usage of digital photography and e-mail to disseminate failure information quickly to a large audience was highly effective in keeping the key players informed at all times. A computer system capable of handling the very large quantity of measured test data is imperative to saving these valuable data for future reference. The change request process and requirements change management board were very effective in keeping the test program on track, and implementing appropriate changes to the test plan at appropriate times.

One of the most important requirements was to identify and track significant structural failures discovered during the test. This requirement was expanded also to consider fleet retrofit and redesign implications. Figure 11 presents a typical "four-panel chart" that was used to identify and track such failures. The fleet impacts were efficiently monitored by this means.

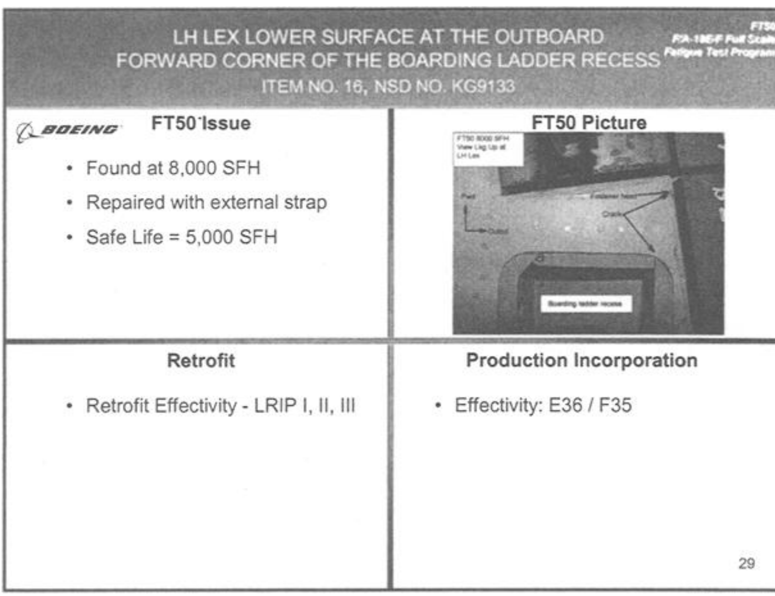

FIG. 11 — *Example of Identification and Tracking of Significant Fatigue Test Failures.*

Recommendations for Future Test Programs

The following are offered as recommended considerations for future full-scale fatigue test programs.

Strategic Allocation and Placement of Strain Gages – A plan to manage strain gage requirements is mandatory. Instrumentation requests can quickly get out of control, resulting in adverse cost and schedule impacts. A disciplined process for the placement of strain gages should also be established. Gages should be located in relatively low strain gradient fields, where significant measured strains are likely, and located coincident with flight test instrumentation.

More Control Points to Ensure Close Design Loads Simulation – It is truly a combination of art and science to create a fatigue loading spectrum that accurately simulates the in-service loading environment. The importance of analytic focus on evaluating the difference between design and test loading conditions at key structural interfaces cannot be overstated. Establishing control points at key fuselage interfaces is very important due to the complexity and redundancy of the internal load paths.

Significant Effort on Load Introduction Evaluation – Special attention must be paid to how the loads from the hydraulic cylinders are introduced into the airframe structure. For instance, it is very difficult to simulate accurately the complex external pressure distributions on flight control surfaces. Detailed evaluation of all load introduction systems is absolutely essential.

Conclusion

The F/A-18E/F full-scale fatigue and static test programs have been an unqualified success. Many significant advances in the state-of-the-art have been realized. Lessons learned from these test programs will be applied to future full-scale test programs.

References

[1] Denney, K.L., "F/A-18E/F Test and Evaluation Program Plan, Master Test Plan," Boeing Internal Report No. MDC 92B0153, Revision K, 16 May 2000, St. Louis, MO.

[2] "Detail Specification For Model F/A-18E/F Aircraft Weapon System," SD565-3, 9 January 1992, Department of the Navy, Naval Air Systems Command, Patuxent River, MD.

[3] Muenks, J.C., "F/A-18E/F Full Scale Airframe First Lifetime (ESF86) and Second Lifetime (ESF87) Fatigue Test – FT50," Boeing Internal Report No. LMV03.04-001, Revision B, 25 April 2001, St. Louis, MO.

Roy L. Hewitt,[1] *Jan P. Weiss,*[1,2] *and Peter K. Nor*[1,3]

Spectrum Editing for a Full-Scale Fatigue Test of a Fighter Aircraft Wing with Buffet Loading

REFERENCE: Hewitt, R. L., Weiss, J. P., and Nor, P. K., "**Spectrum Editing for a Full-Scale Fatigue Test of a Fighter Aircraft Wing with Buffet Loading,**" *Fatigue Testing and Analysis under Variable Amplitude Loading Conditions, ASTM STP 1439,* P. C. McKeighan and N. Ranganathan, Eds., ASTM International, West Conshohocken, PA, 2005.

ABSTRACT: This paper describes the spectrum editing techniques that were used to derive the test spectrum for the full-scale fatigue test of an F/A-18 wing that is currently underway at the Institute for Aerospace Research, National Research Council Canada. The derivation of the baseline spectrum and the truncation methodology are described, together with details of the validation process and the calculated effects of the truncation levels that were accepted.

Even with aggressive truncation, the test spectrum contained nearly 135 000 unique load conditions. Because of control system limitations and the time required to optimize and check the actuator loads for so many load conditions, a binning process was used to reduce the number of unique load conditions to less than 50 000. The process is detailed and the effects on the calculated life are discussed.

KEYWORDS: aircraft, spectrum, fatigue, full-scale testing, truncation, buffet

Introduction

With the advent of on-board data recording devices and digital flight control systems on modern fighter aircraft, it has become possible to derive aircraft manoeuvre loads on an almost continuous basis [1]. It has also been realized that buffet loading can be significant at high angles of attack and must often be included in the loads spectrum. Turbulence effects can also be important, particularly if the aircraft is flown at low altitudes. The raw spectrum then contains many millions of lines, all of which are different. Since it is impractical to apply such a spectrum in a full-scale fatigue test, spectrum editing (typically truncation) is required to reduce the number of load lines.

---

[1] Principal, associate and assistant research officer, respectively, Institute for Aerospace Research, National Research Council Canada, Montreal Road, Ottawa, Ontario, Canada, K1A 0R6.

[2] Currently loads engineer, RUAG Aerospace, TTA, P.O. Box 301, 6032 Emmen, Switzerland.

[3] Currently optical network planner, Nortel Networks, 1285 Baseline Road, Ottawa, Ontario, Canada, K2C 3S3.

Typical truncation levels for a manoeuvre dominated fighter aircraft wing would involve removal of load cycles that were less than about 15% of the maximum for any location. Removal of these cycles would have a negligible effect on fatigue damage. However, for a spectrum that contains buffet or turbulence, there may be sufficient numbers of these small cycles to cause measurable damage and so the truncation level may need to be lower. Alternatively, it may be necessary to accept a non-negligible effect on damage. An added problem with a very large spectrum is the difficulty of experimentally verifying the effects of truncation on the damage using coupon tests because of the very long testing times.

This paper describes the spectrum editing techniques that were used to derive the test spectrum for the full-scale fatigue test of an F/A-18 wing that is currently underway at the Institute for Aerospace Research (IAR), National Research Council Canada, and shown in Figure 1. The derivation of the baseline spectrum is briefly described and the process of truncation of a complete loads spectrum (rather than a single load sequence) is discussed. The methodology used for the wing test is presented, together with details of the validation process and the calculated effects of the truncation levels that were accepted.

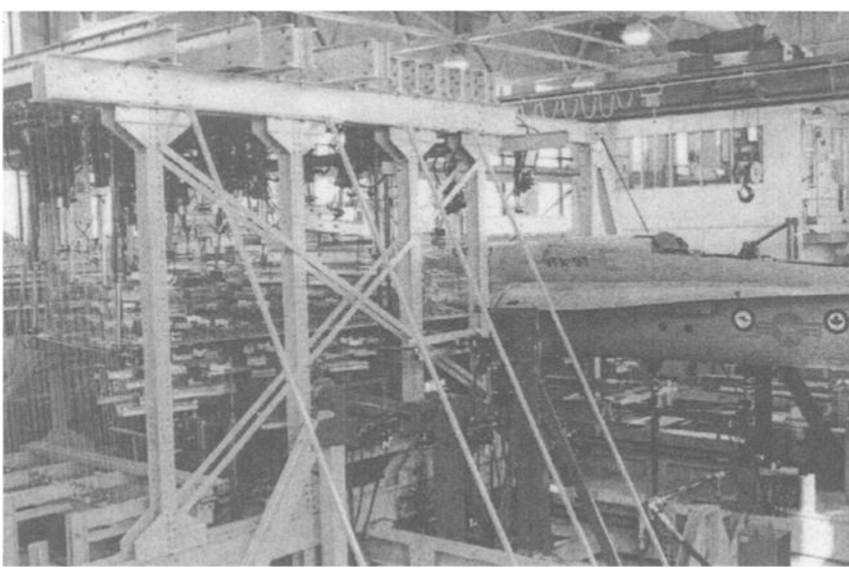

FIG. 1 — *Full-scale fatigue test of F/A-18 wing at IAR.*

Even with aggressive truncation, the test spectrum contained nearly 135 000 unique load conditions. Because of control system limitations and the time required to optimize and check the actuator loads for so many load conditions, a binning process was used to reduce the number of unique load conditions to less than 50 000. This process grouped similar load conditions into bins and then used one of the load conditions in the bin to represent all the loads in that bin. The process is detailed and the effects on the calculated life are discussed.

Derivation of Usage Spectrum

Usage Monitoring

The F/A-18 Maintenance Signal Data Recording System (MSDRS) records flight parameters, engine data, stores data, weapons data and seven channels of strain data automatically at specified frequencies and on specified events. Some data, such as mission type, pilot id and weapons configuration, are also added to the system by the pilot and armorer. These MSDRS data files are available for every flight of every aircraft in the fleet.

Usage Characterization

The usage for the test was defined as the average usage of the most severe squadron. A damage calculation based on the wing root strain obtained from the MSRDS system was used as an initial estimate of individual aircraft usage severity because this was the parameter that the fleet managers were employing. Then two average and two severe usage aircraft were selected from each squadron based on this damage index, and the flying statistics for each squadron were developed from these aircraft. These statistics included mission distribution, stores distributions, g exceedance versus point in the sky (PITS), roll rate exceedance versus PITS and angle of attack (AOA) exceedances versus PITS. The most severe squadron was then selected based on these statistics and an additional six aircraft selected from this squadron for analysis. The average statistics for this squadron were then developed from these ten aircraft.

Usage Spectrum

A time history representative of one year of average flying for this squadron was then developed. This was achieved by assembling a collection of individual flights in such a way as to produce a time history with the same flying statistics as the average of the selected squadron and ordering the flights to give the correct mission distribution with time [2]. This time history of recorded data was the basic usage spectrum.

Loads Derivation

Manoeuvre Loads

An empirical Parametric Loads Formulation (PLF) process was developed at Bombardier Aerospace Defence Services based on a knowledge of the aerodynamic loading actions and an analysis of measured flight loads data. This gave the section loads as a function of flight parameters and control surface deflections. Since the control surface deflections are measured only once every five seconds, intermediate values were derived using the once per second flight parameter data and the flight computer control laws. Calculated loads were verified by comparing against flight measured data for typical missions.

Since the PLF method was able to predict loads at 10 Hz, the manoeuvre loads spectrum contained more than ten million lines before truncation.

Buffet Loads

The wing is also subjected to aerodynamic buffet that adds large numbers of relatively low amplitude cycles to the manoeuvre loads. This was addressed by characterizing the buffet in terms of AOA and dynamic pressure (Q) and collecting time segments of flight test data for relevant wing loads in each of the AOA/Q bins. The flight test buffet data were separated from the manoeuvre data by filtering at 2Hz.

Buffet loads were reconstructed for the test spectrum based on the AOA/Q trace of the spectrum flights by selecting a length of buffet data from the database for the appropriate AOA/Q bin and adding it to the previously developed manoeuvre loads. The dynamic loads were captured at 483 Hz, so the addition of buffet to the spectrum increased the number of lines in the spectrum by an order of magnitude.

Turbulence Loads

Turbulence loads were developed in a similar manner to buffet loads except that they were limited to very low AOAs and low altitude.

Truncation Methodology

Truncation is a process used to remove small cycles that are not considered to be damaging. Two types of truncation are typically used. A range truncation removes cycles that have an amplitude smaller than the chosen range criteria while a deadband truncation removes all cycles within a chosen band (usually around zero).

For a single load or stress sequence, this process is straightforward. For a structural test, however, the concept of a cycle is more complex. A series of four load conditions, for example, may result in two complete cycles for one part of the structure but perhaps only one for another part because two of the load conditions may not be peaks for that part. Thus, for a structural test, it is necessary to derive stress or load sequences for every critical part of the structure, truncate the individual sequences, and then retain every end point that remains in each of the individual sequences.

Although traditionally the individual sequences have been for section loads (wing root bending moment, control surface lug load etc.), truncation on critical stress sequences may be better if the critical areas are known and there are reliable stress transfer functions. This process was used in Reference 3. A similar process was used for the F/A –18 centre fuselage test [1]. However, for the centre fuselage test none of the critical locations for which stress sequences were derived was significantly influenced by wing root torque and yet wing root torque was felt to be important. A wing root torque sequence was therefore also included in the truncation sequences to account for unknown critical locations that might be sensitive to wing root torque.

For the current test, as is usually the case, it was expected that there were unknown critical locations. In addition, there were no reliable load to stress transfer functions for many of the wing critical areas when the truncation process was required. It was therefore decided to use section load sequences for truncation. Basing test spectrum sequences on the critical section loads that drive the critical area stresses ensures that multiple known and unknown critical locations are addressed. These critical section loads were defined as control point loads.

Control Point Loads

The aim of the wing test at IAR is to determine the economic life of the inner and outer wing box under representative loading. The loading actions on the wing were reviewed and it was determined that the twelve section loads listed in Table 1 were the critical section loads that drive the critical area stresses. The loads in this table are listed in approximate order of importance and accuracy of prediction.

Table 1 — *Control Point Loads.*

Control Point Load	Abbreviation	Manoeuvre or Dynamic
wing root bending moment	WRBM	MAN
wing fold bending moment	WFBM	SUM
inboard leading edge flap hinge moment	ILEFHM	MAN
outboard leading edge flap hinge moment	OLEFHM	MAN
trailing edge flap hinge moment	TEFHM	SUM
aileron hinge moment	AILHM	SUM
trailing edge flap outboard vertical lug load	TEFOLZ	SUM
aileron outboard vertical lug load	AILOLZ	SUM
wing tip torsion	WTTOR	SUM
inboard pylon rolling moment	IBPMX	SUM
wing root torsion	WRTOR	MAN
wing fold torsion	WFTOR	MAN

Initially, control points loads were selected based only on manoeuvre (MAN) loads. However, when it was found that dynamic effects on the wing were significant, some additional control points were added. Of the 12 control points, five were manoeuvre (MAN) and seven were for a combination of both manoeuvre and dynamic (SUM) loads.

Methodology for the Assessment of Spectrum Modifications

Whenever changes are made to the spectrum, it is important to be able to assess the effect of the changes on the life of critical components in the structure. Ideally, spectrum modifications should not change the fatigue life of any component by more than a few percent. It is both time-consuming and expensive to assess all changes experimentally because of the large number of specimens required for statistically significant results when trying to assess changes of only a few percent. The situation is even worse for this test because of the very large number of cycles in the basic spectrum. The effects of changes must therefore be assessed using an experimentally verified analytical tool.

A strain life prediction method was previously verified for use with a manoeuvre-dominated spectrum. This used hysteresis loop counting with the spectrum rearranged so that it started with the peak spectrum load. The Smith Watson Topper [4] equivalent strain equation was used together with pre-strained material life data. The method was shown to give good relative predictions of life for spectra with different levels of truncation. However, there was some concern that it may not be able to predict reliably the effect of removal of the many lower amplitude cycles associated with buffet.

An extensive coupon test program was therefore undertaken using representative buffet dominated spectra and the primary materials used in the wing, 7050-T7452 aluminum forging and beta annealed Ti-6Al-4V. Some 7050 T7451 coupons manufactured from a 6-inch plate were also tested. Details of parts of this program are reported in References 5 and 6. The results of this coupon test program showed that the life prediction method used provided good relative life predictions for spectra with and without buffet and at various truncation levels. Some typical results for coupons from a 7050-T7452 6-inch hand forging are shown in Figure 2 for several variations of a preliminary trailing edge flap hinge moment spectrum.

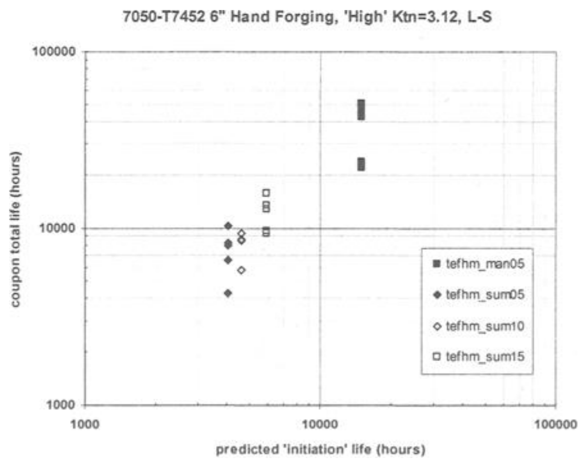

FIG. 2 – *Test versus predicted life for preliminary trailing edge flap hinge moment spectrum.*

The shortest sequence, the manoeuvre only sequence with a 5% range truncation (man05), contained about 17 500 turning points. The longest sequence tested, the combined manoeuvre plus dynamic sequence with a 5% range truncation (sum05), contained about 410 000 turning points. The ratio of predicted lives for these two sequences was 4.6, while the ratio of the log average lives for 5 coupons was 4.7. Sequences with a lower truncation level were not tested as they were too long; the combined sequence with a 1% truncation contained more than 1.2 million turning points.

Baseline Spectrum

The raw spectrum contained the 12 control point loads at 0.1 second intervals for manoeuvre only conditions and every 0.002 seconds where there was dynamic activity. Because there were too many lines even for an analytical life prediction, the baseline spectrum was obtained by performing a 1% range truncation on each of the individual control point load sequences and retaining any line that was retained in any of the individual sequence truncations. The sum of the lines in the individual sequences was about 25 million, which resulted in a full sequence of about 20 million load lines because turning points for some control point loads occurred on the same line.

Fatigue lives were calculated for each of the control point loads using a single load to stress multiplier that was selected to produce a predicted manoeuvre-only life of about twice the original design life. The rationale for this was that no location should fail at less than the original test life, which was performed to two lifetimes under manoeuvre-only loading. Negative multipliers were used for five of the sequences, TEFHM, AILHM, WTTOR, WRTOR and WFTOR, so that they were tension dominated.

Because dynamics were not considered important for some of the control point loads, such as wing root bending moment, dynamic loads were not generated for these loads during the dynamic loads development. Thus, fatigue life calculations were performed using manoeuvre-only loads for these loads, whereas SUM loads were used for the remainder.

Individual Sequence Truncation

Truncation was performed on each control point sequence using a combination of range and deadband truncation. The truncation used for a given spectrum is written as a six-digit code. The first two digits are the upper deadband level, the next two are the lower deadband level (usually negative) and the last two are the range level. The numbers indicate a percentage of the maximum manoeuvre range (MMR) observed during the flight loads survey. For example, the code 101520 indicates a deadband truncation of +10% and −15% and a range truncation of 20% of the MMR. Note that the MMR may be less than the maximum range for control point loads that include a dynamic component, as the MMR was based only on the manoeuvre load component.

The first stage of the truncation sensitivity study was to determine an acceptable range truncation level. Truncations were performed on the raw spectrum for each of the 12 control point loads at 1%, 5%, 10%, 15%, 20% and 25% of MMR. In some cases, further range truncations of 30% and 35% MMR were performed. Results for selected MAN and SUM control point loads are given in Table 2 as a function of load lines remaining and increase in life (decrease in damage) over that for the 1% range truncation.

Table 2 — *Effect of range truncation level on life increase and remaining lines.*

Truncation Level, %	WRBM (MAN)		WTTOR (inverted) (SUM)		TEFOLZ (SUM)	
	remaining lines	% increase in life	remaining lines	% increase in life	remaining lines	% increase in life
1	322124	0.00	2859890	0.0	10405752	0.0
5	48914	0.11	1376670	0.2	2517964	0.1
10	22932	0.42	756326	1.8	1156360	1.7
15	15754	0.96	403944	6.6	618734	5.7
20	11626	2.22	211896	15.4	349846	13.1
25	8700	4.67	112758	28.4	200360	25.6
30			62520	45.6	113122	45.0
35			35180	70.0	63668	74.0

There is clearly a difference in the response to truncation of the MAN and SUM control point loads. The MAN control point load shows the typical relatively small increase in life for low level truncation and then a more rapid increase. This 'knee' in the curve is where the typical manoeuvre truncations are usually set. The SUM control point loads show a similar type of response but the 'knee' occurs at a lower truncation level and a much higher number of remaining lines. This is shown more clearly in Figures 3a and b. The right-hand graph in Figure 3b is an expanded version of the left-hand plot to show more clearly the large number of remaining lines near the 'knee'.

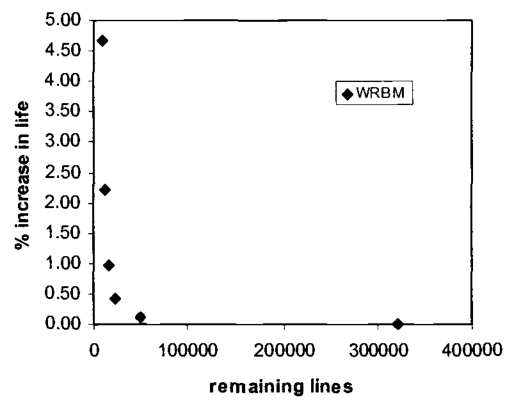

FIG. 3a — *Increase in life versus remaining lines for WRBM.*

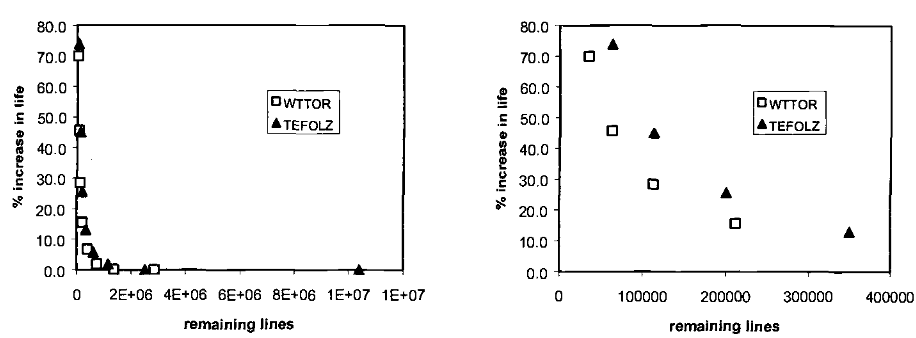

FIG. 3b — *Increase in life versus remaining lines for WTTOR and TEFOLZ.*

Using the 'knee' of the curve for the SUM loads to determine the truncation level would result in a sequence of more than half a million lines for one location with probably more than 5 million lines in the assembled sequence for one year of flying. A test with this number of load lines could not be applied in a reasonable time period. It was therefore necessary to accept relatively large increases in life for the dynamic control point loads.

To assess the effectiveness of a deadband truncation, a range-mean summary was completed for each of the control point loads, and a deadband truncation level was selected for analysis based on the number of cycles that would be removed. Based on the results of these fatigue calculations, the set of truncation parameters shown in Table 3 was finally selected. While the damage increase for many of the control point loads was not negligible, the total number of lines in the spectrum was still more than 150 000. Any number beyond this was considered to be too many to apply in order to get test results while they were still useful for fleet management.

Table 3 — *Effect of Selected Truncation Level on Life.*

Control Point	Type	Truncation Level	% Increase in Life over Baseline
WRBM	MAN	25 25 25	5
WFBM	SUM	25 25 20	14
ILEFHM	MAN	20 20 20	6
OLEFHM	MAN	15 15 20	6
TEFHM	SUM	15 15 15	41
AILHM	SUM	15 15 15	52
TEFOLZ	SUM	35 35 35	74
AILOLZ	SUM	15 15 17	63
WTTOR	SUM	25 25 35	77
IBPMX	SUM	25 25 25	57
WRTOR	MAN	15 15 25	10
WFTOR	MAN	15 15 25	12

However, the damage increases for the loads with dynamic components can be put into perspective by comparing the damage for the manoeuvre only component of the load. While the increases in life for WTTOR and TEFOLZ, for example, are 77 and 74%, respectively, as compared to the 1% truncated sequence, using manoeuvre only loads results in life increases of about 60 and 44 times the baseline life. Thus, the results from this test should be more than an order of magnitude more representative in terms of lives for locations associated with the dynamic control point loads than the original test, which only used manoeuvre loads.

Sequence Re-assembly

The sum of the lines in the 12 individual truncated control point loads sequences was about 200 000 lines. However, some lines are in more than one sequence. When the load lines were put into a single set and the repeats eliminated, the total number of lines was reduced to about 182 000. However, it was observed that the IBPMX dynamic response was independent of the other loads and was therefore not essential to the wing box dynamic distribution. The IBPMX peaks from these lines were therefore moved to the closest adjacent residual time step from the other 11 control points. This reduced the number of lines to about 175 000.

The re-assembly effectively adds a number of small cycles to each individual sequence, thereby reducing the difference from the baseline fatigue lives. For example, the individual truncated sequence for WRBM contained about 9 000 lines compared to the 175 000 lines for the total re-assembled sequence. The damage increase compared to the 1% truncation baseline was reduced to 2% for the re-assembled sequence compared to the 5% for the individual sequence. The effect on life for all the control point loads is shown in Table 4. All show an improved comparison to the baseline lives.

Table 4 — *Effect of Sequence Re-assembly on Life.*

Control Point	Type	% Increase in Life over Baseline
WRBM	MAN	2
WFBM	SUM	9
ILEFHM	MAN	5
OLEFHM	MAN	4
TEFHM	SUM	28
AILHM	SUM	45
TEFOLZ	SUM	72
AILOLZ	SUM	57
WTTOR	SUM	72
IBPMX	SUM	53
WRTOR	MAN	5
WFTOR	MAN	7

Distributed Loads

In order to apply representative loads to the wing, it is necessary to have load distributions over the wing, in addition to the section loads. Of the approximately 175 000 load lines in the total truncated sequence, about 135 000 were independent because there were some repeated flights within the spectrum. Distributed loads for these 135 000 load conditions were developed by Bombardier Aerospace Defence Services based on the aircraft weight distribution for the inertia loads, wind tunnel distributions for the aerodynamic loads and optimized force distributions for the dynamic loads. The latter were optimized to give the correct dynamic control point loads and were checked against a number of measured strains and accelerations from the flight test data.

The aerodynamic distribution process used an optimization process to find the best set of distributed panel loads that matched the wind tunnel distributions and, when integrated, matched the 12 target interface loads (control point loads). Since these target interface loads were predicted from flight parameters and had an associated level of uncertainty, they were allowed to vary within their level of uncertainty during the optimization process to ensure that realistic distributions were obtained. The final control point loads for the distributed loads set were therefore slightly different from the original control point loads. Fatigue calculations were therefore performed for the distributed loads sequence to quantify the effects of these changes. While some of the manoeuvre control point loads now include a dynamic component, e.g., the WRBM increases due to the integration of the additional panel loads resulting from the dynamic loads distribution on the control surfaces and outer wing, only the manoeuvre portion of the load was used in the fatigue calculation to keep it consistent with the baseline.

The results are shown in Table 5. The change from the baseline is given as before, together with the incremental change from the previous life calculations, which were for the truncated and re-assembled loads in this case. Generally, the changes were small, particularly for the most important interface loads. However, there were significant changes for the wing fold and wing root torque load sequences.

Table 5 — *Effect of Distributed Loads Process on Life.*

Control Point	Type	% Increase in Life over Baseline	% Incremental Increase in Life from Previous Sequence
WRBM	MAN	2	0
WFBM	SUM	8	-1
ILEFHM	MAN	5	0
OLEFHM	MAN	4	0
TEFHM	SUM	34	5
AILHM	SUM	56	8
TEFOLZ	SUM	69	-2
AILOLZ	SUM	50	-5
WTTOR	SUM	83	7
IBPMX	SUM	55	1
WRTOR	MAN	693	654
WFTOR	MAN	914	849

When the wing fold and wing root torques were constrained, the optimization produced unrealistic panel loads on the inner wing box. The major drivers for these torques are the control surface hinge moments, and these were considered to be more reliable than the torques (wing torque is notoriously difficult to measure in a flight test). The decision was therefore made not to constrain the torques during the optimization process. This decision was subsequently proved correct, when comparisons to flight test strains were made during the initial strain survey.

Binning

At the time the control system was purchased for this test, the maximum number of independent load conditions that could be accommodated without large economic penalties was 50 000. Thus the number of independent load conditions had to be reduced, or the sequence split into three and continually reloaded throughout the test. The latter solution is prone to making errors. Furthermore, a large number of load conditions significantly increases data handling problems associated with developing actuator loads for application of the load conditions to the test article and their subsequent verification [7]. It was therefore advantageous to reduce the number of independent load conditions.

Since the control point loads can only be predicted to within a certain confidence range, there is some scatter on the loads. It is therefore possible to have two, or more, load cases that exist at different times in the spectrum that, considering the accuracy of their prediction, are essentially the same. The assumption is therefore made that if all of the 12 control point loads for a number of load cases are within a given range, then the resulting load distributions are not distinguishable. This 12-dimensional definition of a load case is referred to as a bin.

The bin size for each load was initially set based on the accuracy of the calculated load and then all bins were equally scaled until the number of occupied bins was less than 50 000. Generally, the bins at low loads (around 1g) were heavily populated while bins at the extremes of the envelope contained only one load case. One load case from each bin was selected for application to the test, generally with near mid bin values. Because the bins at the extremes of the envelope contained only one load case, this was the load case selected and the binning therefore did not alter the extremes of the spectrum. Fatigue life calculations after the binning process are shown in Table 6. Many of the sequences show a small decrease in life; this was done deliberately to recover some of the damage lost in previous processes and was achieved by choosing the representative load case from a bin slightly off mid bin values.

Table 6 — *Effect of Binning Process on Life.*

Control Point	Type	% Increase in Life over Baseline	% Incremental Increase in Life from Previous Sequence
WRBM	MAN	-1%	-3%
WFBM	SUM	8%	-1%
ILEFHM	MAN	1%	-4%
OLEFHM	MAN	1%	-3%
TEFHM	SUM	28%	-5%
AILHM	SUM	60%	2%
TEFOLZ	SUM	72%	2%
AILOLZ	SUM	53%	2%
WTTOR	SUM	82%	-1%
IBPMX	SUM	38%	-12%
WRTOR	MAN	604%	-13%
WFTOR	MAN	974%	6%

When the original load lines are replaced by their representative bin load condition, it is possible to have consecutive lines that are identical. Removal of these consecutive repeat load cases clearly makes no difference to the spectrum.

It is also possible to have consecutive load lines from adjacent bins, where adjacent means that only one of the 12 control point loads is different. If this control point load is not a turning point for either load case, then removal of one of these lines will make no difference to the fatigue life. Similarly, if more than one of the control point loads are different but are not turning points for either load line, they can be removed without changing the fatigue life. Using this logic, all of the turning points for all of the 12 control point spectra were preserved in the final test sequence, but the total number of lines in the spectrum was reduced from about 175 000 to 155 000.

Conclusions

The spectrum editing techniques used to derive the test spectrum for a full-scale fatigue test of an F/A-18 wing with buffet loading have been described. The methodology for assessing the effects of the editing, using an experimentally verified strain-based fatigue life calculation, has also been detailed.

Truncation was based on ranges and deadbands of individual sequences of section loads derived from the full loads sequence for a representative year of flying. Because the buffet added a very large number of end points to the sequences, aggressive truncation was found to be necessary in order to be able to apply the test spectrum in a reasonable time period. Truncation reduced the number of lines in the spectrum from about 20 million for the initial sequence with a 1% range truncation to about 175 000.

Even after this aggressive truncation, it was found that there were about 135 000 independent load cases. This number was reduced to less than 50 000 by a binning process so that the sequence could be accommodated by the test controller.

Overall, the lives based on manoeuvre dominated loads (e.g., wing root bending moment) were not changed by more than a few percent by all the spectrum editing processes. Lives based on buffet dominated loads (e.g. trailing edge flap lug load) increased by up to about 80%. Almost all of the increase was due to the aggressive truncation used for these loads. However, this was still a significant improvement over previous tests, which did not include buffet.

The binning process made a negligible difference to calculated fatigue lives and appears to be a useful tool for reducing the number of independent load cases. This has benefits both in terms of calculating and verifying actuator loads for the test and reducing the size of the file for the test controller.

Acknowledgments

This work has been performed under the Statement of Agreement between the Institute for Aerospace Research and the Department of National Defense regarding the CF-18 Full Scale Wing Test and IAR Fatigue and Damage Tolerance of Structures Program. The program is partially funded by the Department of National Defense Financial Encumbrance A8465-3-NPAB.

References

[1] Hewitt, R. L., Hiscocks, R. J. and Bernard, G., "Loading Spectrum Determination for an Aircraft with a Digital Flight Control System - CF-18 Centre Fuselage Example," *Canadian Aeronautics and Space Journal*, Vol. 42, No. 1, 1996, pp. 5-9.

[2] Simpson, D. L., Zavitz, D., and Hiscocks, R. J., "A Parametric Approach to Spectrum Development," *AGARD Specialists' Meeting on Fatigue Management*, Bath, England, 1991.

[3] Hewitt, R. L. and Rutledge, R. S., "Computer Applications in Full-Scale Aircraft Fatigue Tests," in *Automation in Fatigue and Fracture: Testing and Analysis*, ASTM STP 1231, C. Amzallag, Ed., American Society for Testing and Materials, Philadelphia, 1994, pp. 51-69.

[4] Smith, K. N., Watson, P., and Topper, T. H., "A Stress-Strain Function for the Fatigue of Metals," *Journal of Materials*, Vol. 5, No. 4, 1970, pp.767-778.

[5] Straznicky, P. V., Weiss, J. P., and Hewitt, R. L., "Effects of Low Amplitude Cycles in Spectrum Loading on a Fighter Aircraft," in *Proceedings of 19th Symposium of the International Committee on Aeronautical Fatigue*, R. Cook and P. Poole, Eds., Emas Publishing, UK, 1997, pp.461-479.

[6] Visvanatha, S. K., Straznicky, P. V., and Hewitt, R. L., "Influence of Strain Estimation Methods on Life Predictions using the Local Strain Approach," *International Journal of Fatigue*, Vol. 28, No. 6, 2000, pp. 675-681.

[7] Hiscocks, R. J., Rutledge, R. S., and Hewitt, R. L., "Calculation of Actuator Loads for Full-Scale Aircraft Fatigue Testing," in *Proceedings of 21st Symposium of the International Committee on Aeronautical Fatigue*, J. Rouchon, Ed., Emas Publishing, UK, 2001, pp. 699-712.

Journal of ASTM International, Nov./Dec. 2004, Vol. 1, No. 10
Paper ID JAI19050
Available online at www.astm.org

Laurence Le Divenah[1] *and Jean-Yves Beaufils*[1]

Large Commercial Aircraft Loading Spectra: Overview and State of the Art

ABSTRACT: The purpose of this paper is to present an overview of an Airbus' approach regarding fatigue spectra for large commercial aircraft. An accurate load representation is essential to the modern aircraft fatigue optimization process. The effort to develop spectra must be consistent with the efforts made to optimize materials and geometries. The main characteristics of large commercial aircraft spectra, both for prediction and testing, are presented. Recent advances are specifically highlighted.

KEYWORDS: aircraft, load spectrum, structural analysis, fatigue, damage tolerance

Introduction

An important part of the structural analysis of an aircraft comes from the loads applied to each component. An accurate load representation, through the use of complex spectra, is essential to designing modern large commercial aircraft. This paper presents the Airbus state of the art on this subject. After reviewing briefly the way to manage a fatigue calculation, the method to build a fatigue loading spectrum for prediction will be described. Then the load specificities of large commercial aircraft will be highlighted. The following section will be dedicated to the modification of the spectrum necessary to provide a fatigue test spectrum. The last paragraph will present how to review loading spectra during the aircraft's life, if necessary, to always have an accurate representation throughout that life.

General Overview of Fatigue Calculation

Airworthiness authorities require a fatigue and damage tolerance justification before delivering an airworthiness certificate. Fatigue and damage tolerance analysis consists of both a review of structural parts whose failure may impact airworthiness and the justification that these parts will not have any damage or that any damage will be detected before jeopardizing the integrity of the structure. These calculations lead to a structural maintenance program, consisting of several dates representing the first inspection threshold and inspection intervals. The justification includes crack initiation analysis, crack propagation analysis, and residual strength analysis.

A linear cumulative law (Miner's rule [1]) is used to perform crack initiation analysis.

Manuscript received 29 April 2002; accepted for publication 22 September 2003; published November 2004. Presented at ASTM Symposium on Fatigue Testing and Analysis Under Variable Amplitude Loading Conditions on 29 31 May 2002 in Tours, France; P. C. McKeighan and N. Ranganathan, Guest Editors.

[1] Damage Tolerance Engineers, ESAD, Structure Analysis - Damage Tolerance, Airbus, 316 route de Bayonne 31060 Toulouse Cedex 03, France.

$$D = \frac{n1}{N1} + \frac{n2}{N2} + \ldots \frac{nk}{Nk}; \text{ D = 1 being the failed condition} \tag{1}$$

where

ni = number of stress loading cycles, and
Ni = number of cycles to failure.

Then, thanks to test data, from coupon to full-scale and their analytical representation, the fatigue life is deduced. For example, we can use a representation named IQF law:

$$10^5 \left(\frac{IQF}{\sigma_{max}.f(R)} \right)^p = N \tag{2}$$

where

IQF = index of quality in fatigue (depending on material, geometry, treatments, etc.),
R = stress ratio,
p = material parameter,
σ_{max} = maximum stress value of the cycle, and
N = number of cycles to failure.

The crack propagation, on the other hand, is not based on a linear cumulative damage law. One approach used in Airbus is based on the Elber's [2] opening concept and on a propagation model named PREFFAS, which takes into account the effects of overloads and underloads present in the spectrum.

$$\frac{da}{dN} = C_{eff} \left[\Delta S.f(a).(A + BR) \right]^m \tag{3}$$

where

da/dN = crack growth rate,
C_{eff}, A, B & m = material parameters,
R = stress ratio, and
f(a) = geometrical function.

The non-linearity of the model is of importance because it means that the order of stress cycles influences the propagation of damage. Consequently, the load spectrum has to be described through an individual stress cycle sequence. We cannot achieve a good level of accuracy in fatigue and damage tolerance analysis by studying only cumulative stress cycles.

Building of Fatigue Load Spectrum for Prediction

General

At the beginning of an aircraft design, missions are built in cooperation with potential customers, in order to describe what should be the usage of this new aircraft. Describing a mission consists of splitting a flight into several segments and attributing a duration, an altitude, an aircraft mass, disturbances, etc. to each of these segments. Thanks to this information, external loads are computed, and stresses are then calculated for each part of the aircraft finite element model.

Mission Building

The mission is a series of equilibrium stresses (named n = 1) which represents an equilibrium state of the structure, representing loads having a low evolution along time, such as weight or pressure. Stresses from disturbances are superimposed on the equilibrium stresses. These stresses, called incremental stresses, are due to a quick evolution of loads such as gusts or bumps.

To build a fatigue mission, we must associate disturbances on each segment and decide how to combine them. It is obvious that the description depends on the kind of structure analyzed. For example, the fuselage is sensitive to pressure and to the ground phases (taxi out, take-off roll, roll-out, etc.), whereas the ailerons are not.

Disturbances

To represent the disturbances, Airbus uses cumulative distribution functions (Fig. 1), which represent the number of times that a stress surpasses a given level.

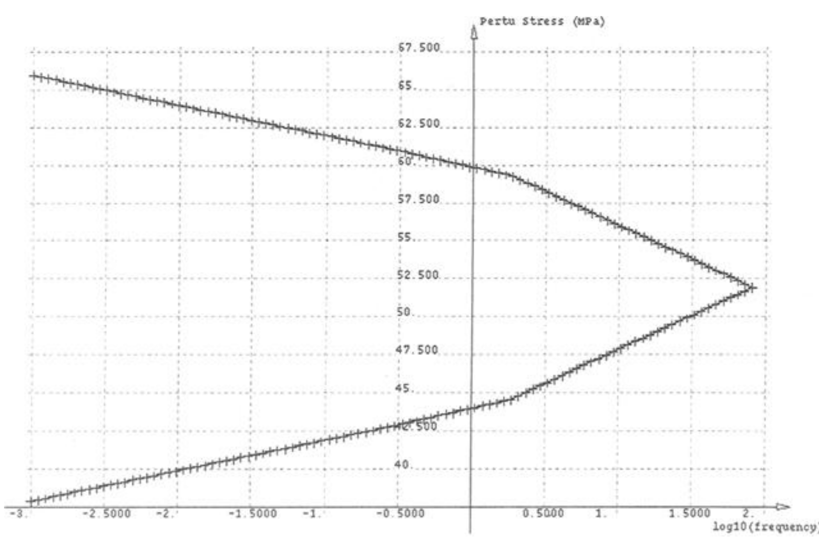

FIG. 1 *Cumulative distribution function.*

In this example, the stress level 50 MPa is surpassed 31 times per flight.

Let us have a closer look at the different kinds of disturbances we have to consider and how to treat them. We can separate disturbances into two great families: continuous and discrete. Continuous disturbances are described with analytical functions. A frequency is associated with any value of the disturbing phenomenon.

For example, for taxiing, the cumulative distribution is

$$f = 10^{Anz+B} \tag{4}$$

where

f = cumulative frequency of the phenomenon,
nz = local acceleration, and
A,B = constants.

This kind of disturbance is represented with a smooth function (Fig. 2).

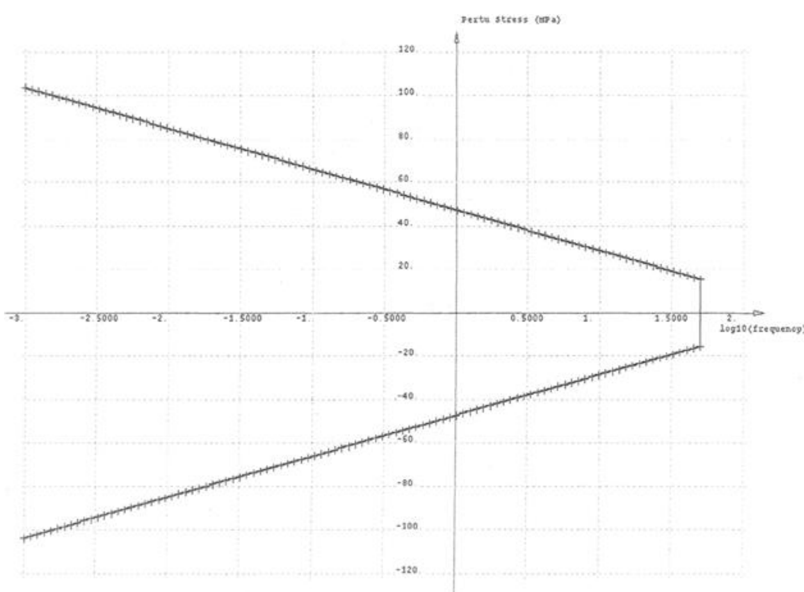

FIG. 2 *Taxi cumulative frequency distribution.*

The other family of disturbances is discrete disturbances, which has only a finite number of values (maneuver angles for ailerons). It also includes disturbances such as dynamic landing, which are not linear with frequencies. Those disturbances are represented with a discontinuous function (Figs. 3 and 4).

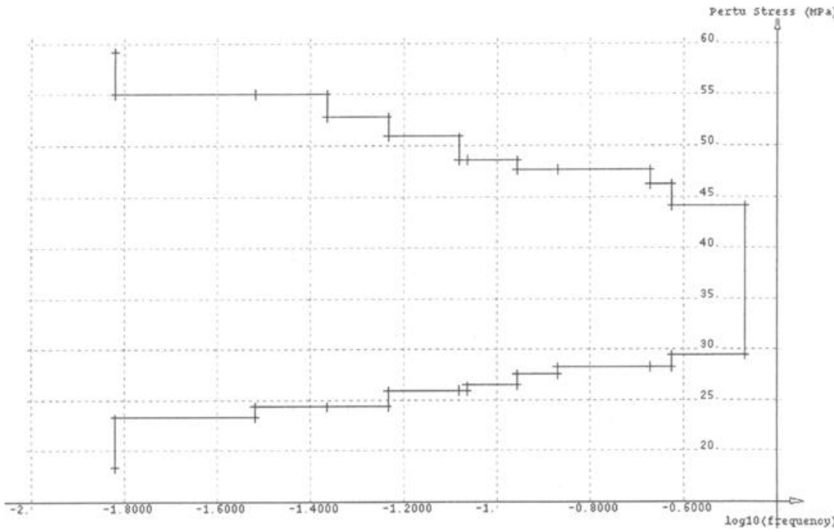

FIG. 3 *Dynamic landing cumulative frequency distribution.*

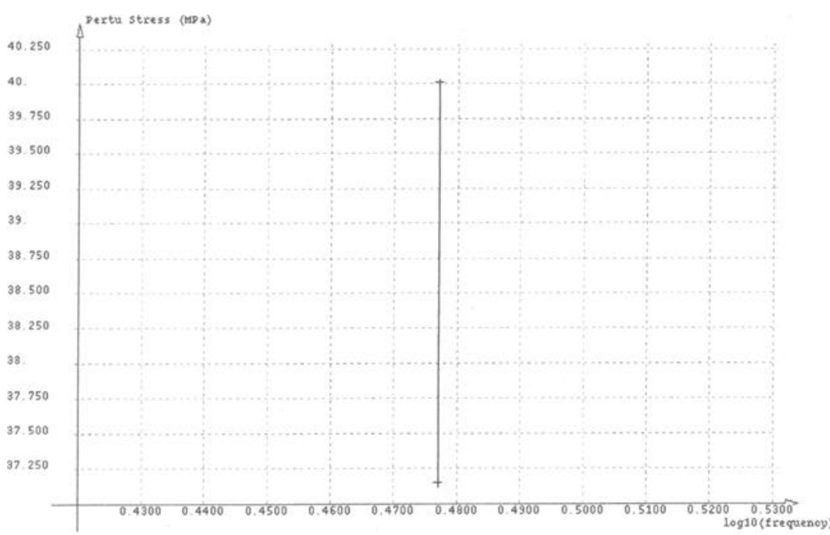

FIG. 4 *Isolated event.*

An important aspect in the statistical description of the mission is to decide how different disturbances have to be treated. At this stage, the disturbances are split again into two new categories: the flight disturbances and the ground disturbances. The hypothesis made here is that flight disturbances may be dependent. For example, if the aircraft is in stormy weather, it will meet very severe disturbances due to vertical gusts, but also to lateral gusts. On the other hand, on the ground, there is no reason if the runway is rough to have very hard braking at the same time, for example. Except in very particular cases, we will consider that disturbances on the ground are independent.

The last point to take into account before generating individual stresses is to decide if stresses are juxtaposed or superimposed. Let us have two examples to illustrate this point. Since gusts are continuous functions, it is not probable that a lateral gust will come exactly at the same time as a vertical gust. That is why we will state that lateral and vertical gusts have to be juxtaposed. On the contrary, it is possible to have a turn on the runway and to meet bumps during this turn. In this case, we will say that the disturbances may be superimposed; the stresses due to the two phenomena may be added (but are not always added; it depends on a statistical approach we will discuss later).

Statistical Description

Since we now have the different segments, the n = 1 stress and the various disturbances associated, the statistical description of the mission may be represented as follows (Fig. 5). This description provides the stress levels reached for each segment of the mission, with their associated cumulative frequencies.

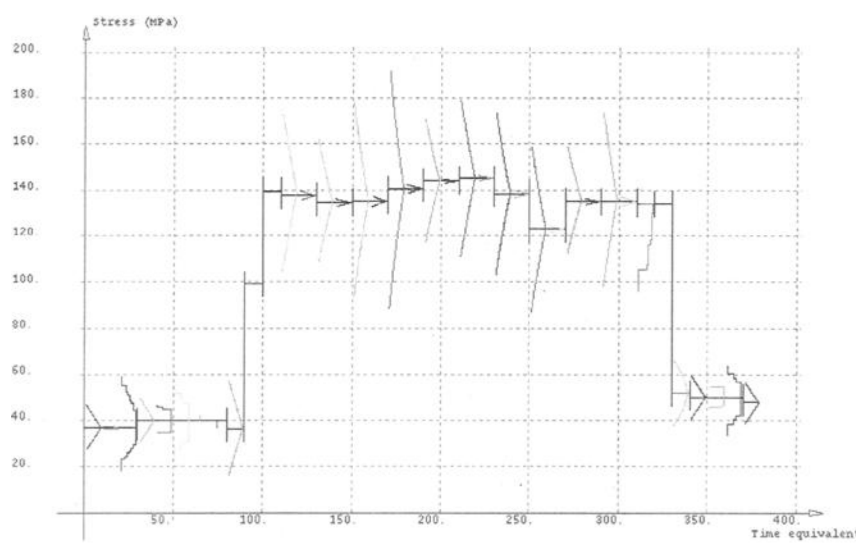

FIG. 5 *Statistical description of the mission.*

Flight by Flight Description

We now have built our fatigue mission, with every disturbance on every segment, and the way to treat them (dependence, juxtaposition). We must now generate individual stresses from the cumulative frequency distributions for a number N of flights. One method used in Airbus is a random drawing of stresses from the cumulative frequency distributions.

Let us have a closer look at this method for a single disturbance, and then we will generalize it. Let us assume that we have the following description of the disturbance (Table 1):

TABLE 1—*Numerical description of the disturbance before drawing.*

Stress Level (in MPa)	Cumulative Frequency
100	1
80	10
50	100
20	1000

Table 1 shows that a stress of 100 MPa is reached exactly once, 80 MPa is reached exactly nine times, and so on, in N flights. To generate the series of stresses, we will draw a random number between 1 and 1000. Let us say 81 for example; 81 is between 10 and 100, and that means that we choose 50 MPa as the first stress of our spectrum. The cumulative description becomes (Table 2):

TABLE 2—*Numerical description of the disturbance after the 1st drawing.*

Stress Level (in MPa)	Cumulative Frequency
100	1
80	10
50	99
20	999

Then, we will draw a random number between 1 and 999. Let us use 253. 253 is between 99 and 999, then we choose 20 MPa as the second stress of our spectrum.

And we continue this random drawing (between 1 and 998) until there is no stress remaining in the table. This way, we have randomly mixed the stresses, and we are sure that all stresses have been included in the spectrum.

This series of stresses is now split into the number N of flights chosen to generate the spectrum. Depending on the kind of disturbance, the partitioning will be done in N equivalent number of stresses, or the number of stresses (due to this disturbance) in each flight will be proportional to the highest stress value of the disturbance in the considered flight. It is the case, for example, for the gusts. If the flight conditions are bad (storm, etc.), the stress values will be high, and the stresses will be numerous.

The same approach is used when there are many disturbances on a segment. If the disturbances are dependent, the stresses of each disturbance will be sorted, and then these stresses will be included within the same flight, disturbance by disturbance. The last step will consist of mixing them. If disturbances are independent, the stresses do not have to be sorted; they are only joined and then mixed flight by flight.

Concerning superposition of disturbances, the aim of the treatment is to enable stresses to be added. Depending on the probability of having two stresses at the same moment, the stresses of the different disturbances will either be juxtaposed or superimposed. For example, if Stress 1 from Disturbance 1 has a probability of 0.1, and if Stress 2 from Disturbance 2 has a probability of 0.05, then the probability that Stress 1 and Stress 2 will occur at the same moment is 0.005. If the number of flights to generate is higher than 200 (1/0.005), then Stress 1 and Stress 2 will be added, or else they will remain separated.

With regard to the methods described earlier, we obtain a description of the load spectrum flight by flight, stress by stress (Fig. 6).

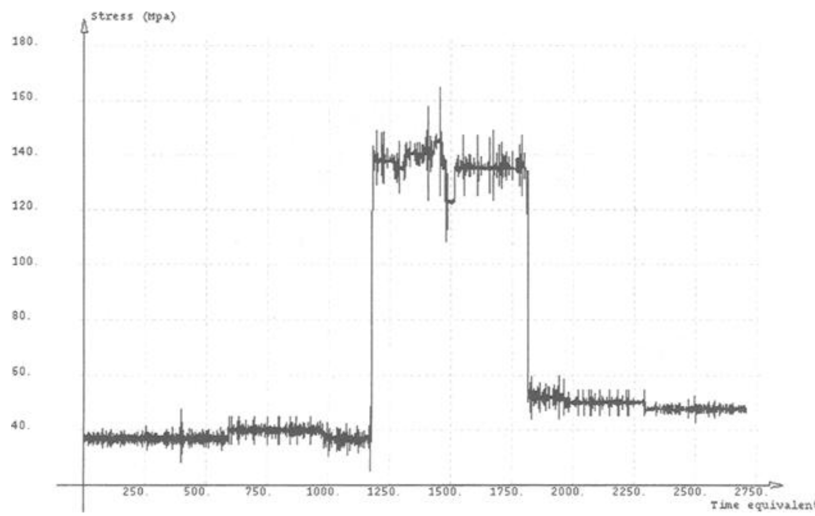

FIG. 6 *Fatigue spectrum flight #128.*

Large Commercial Aircraft Specificities

In this section, two main specificities of large and modern aircraft will be highlighted.

Load Alleviation Function

The first specificity concerns load alleviation and its impact on structural weight. To save weight, we may add some systems enabling the decrease of loads due to some disturbances, because the thickness of a component is directly correlated with the applied loads.

The Load Alleviation Function (LAF) is this kind of system. It enables loads due to vertical gusts to be decreased if they exceed a determined velocity (Fig. 7).

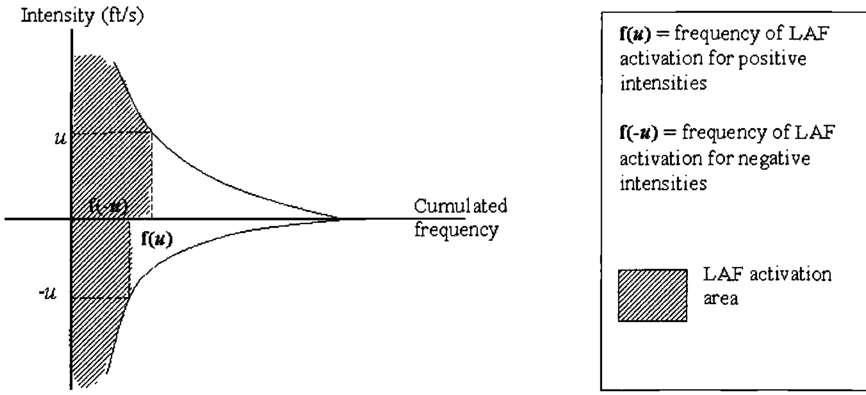

FIG. 7 *LAF activation area on a vertical gust spectrum.*

This kind of system has to be taken into account when modeling a fatigue spectrum since it modifies the statistics associated with vertical gust disturbance.

LAF is expected to have the following two main effects on a mission spectrum when gust velocity exceeds a given level:

- to decrease the equilibrium stress value $\sigma_{n=1}$ of x %
- to alleviate the increment (i.e., the magnitude of a vertical turbulence or maneuver) by y %

The method to consider LAF includes the following:

- generating the series of stresses due to vertical gust for each flight,
- testing each stress level, and
- if the stress value is greater than the LAF activation level, then the stress is modified as follows:

$$\sigma_{dist} = (1 - y)^* \sigma_{dist} - x^* \sigma_{n=1} \tag{5}$$

where

σ_{dist} = incremental stress,
$\sigma_{n=1}$ = steady stress,
x = decrease of equilibrium stress, and
y = decrease of incremental stress.

The LAF provides significant gains in fatigue life.

Mission Mix

Another specificity of modern aircraft is to take into account a mix of mission from design phase. Today, airlines want to operate their aircraft on various missions. Design is made for different missions and also for a mixing of these missions. Indeed, some mixes of missions are more penalizing for fatigue life than any of the missions considered separately. The fatigue spectrum analysis also may be able to mix these missions.

As said in the first paragraph, in the general overview of fatigue calculation, the order of stress cycles is of importance because it influences the propagation of the damage. So the mission mix may not only be a juxtaposition of various missions but also a real mixing subordinate to specific rules.

Once the most severe mix of missions is determined, the approach applied consists of generating the flights for each mission involved in the mix. Then, the flights are sorted depending on their severity. Once sorted, a regular selection (depending on the occurrence in the mix) of the flights is performed. The last step is a mix of these various flights in order to be as close as possible to the real series of missions viewed by the aircraft.

Load Spectrum for Test

A full-scale fatigue test is conducted as part of the type certification program because analysis must be supported by tests. The simplest solution to conduct the test should be to use the complex spectrum used for analysis. The drawback is that testing complexity is the enemy of cost. A pragmatic trade-off between complexity and accuracy is then necessary.

To reach this goal, spectrum reduction (truncation and omission) is an important way of improvement (Fig. 8), but always keep in mind that a test spectrum has to be representative of the real spectrum.

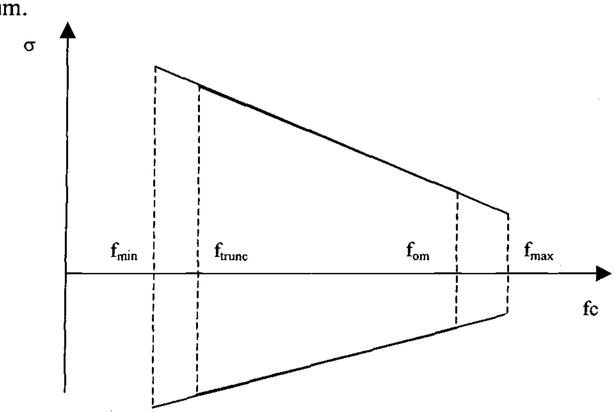

FIG. 8 *Truncation and omission frequencies.*

The truncation frequency (f_{trunc}) depends on the length of the test sequence and the frequency of each kind of flight to be represented. The length of the sequence is usually between 1500 and 2000 flights.

The aim of omission (f_{om}) is to decrease the number of stresses by suppressing the low stresses because they are the most frequent ones and are individually the least damaging.

The next step is to replace a continuous distribution (between truncation frequency and omission frequency) with a discrete one. To do that, we divide the frequency range in equal intervals (in a logarithmic scale). An equivalent stress level is then calculated on each interval by integrating elementary damage. Depending on the area considered, a fatigue or a damage tolerance approach is used. With a fatigue approach, and considering the IQF law described in the first paragraph, we obtain

$$\Delta E_i = \Delta f_i \left[f(R_i)\overline{\sigma_i} \right]^p k \tag{6}$$

where

$\Delta f_i = fc_{i+1} - fc_i$,

$\overline{\sigma_i} = \dfrac{\sigma_i + \sigma_{i+1}}{2}$,

$f(R) = \left(\dfrac{1-R}{0.9} \right)^{0.6}$,

$k = \dfrac{1}{10^5 . IQF^p}$, and

p = material coefficient.

In each interval, the damage corresponding to the range of frequency fc_inf to fc_sup is then

$$E(fc\_\inf ; fc\_\sup) = \sum_{fc\_\inf}^{fc\_\sup} \Delta E_i \tag{7}$$

Concerning the case where $f_{om} < f_{max}$, the damage due to the omitted cycles is taken into account (Fig. 9) using an equivalent approach as described previously.

We determine an equivalent stress σ_{equi}, such as

$$E(fc\_\inf ; fc\_\sup) = (fc\_om - fc\_\inf)\left[f(R_{equi})\sigma_{equi} \right]^p . k \tag{8}$$

This method is iterative: we suppress stresses, and we check by a numerical approach that the damage with omission is always close to the result with no omission. If it is not the case, a new calculation is performed with a higher omission frequency.

In parallel, other methods used to derive the test spectrum from theoretical spectra can be listed, such as filtering process to suppress non-damaging cycles, reduction of the number of segments to be taken into account, regrouping of some disturbances, etc.

Once the test spectrum is generated, stresses may be automatically adapted to reference levels in order to be applied by test equipment.

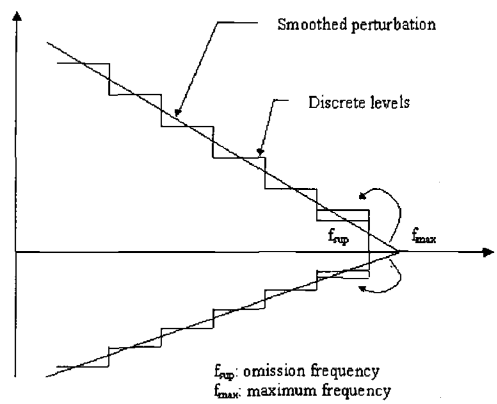

FIG. 9 *Omission method.*

Updated Spectra

During the aircraft life, the fatigue loads spectra are sometimes updated depending on the information coming from the fleet. This review of the usage of the fleet is done not only for safety reasons, but also to improve the maintenance program. Fleet surveys provide information on the missions operated by the airlines (mainly range and weight information). Spectra are updated if airlines do not operate their fleet within the boundaries previously defined for the design phase or from the previous fleet survey. It must be noted that, whatever the result is, even if the spectra are not updated, maintenance programs are reviewed. Indeed, certain areas of the airframe are sensitive to the aircraft flight duration. In these cases, the fatigue damage increases as a function of the flight time. Parametric studies of Airbus aircraft have indicated that several parameters have an effect on fatigue behavior. In general, a representative value for each parameter is chosen for use in fatigue and damage tolerance calculation. However, the range parameter varies so widely in service that to select only one value (long range) severely penalizes short and mid range operators. Consequently, the range parameter is treated independently of the other mission parameters and has been accounted for by a method named flight cycle/flight hour limit. This method enables a maintenance program in flight hours and in flight cycles to be given to each structurally significant item. This way, the degree of conservatism of the maintenance program is reduced but always keeps a whole coverage of the range of utilization of the aircraft.

Spectra also may be updated thanks to recording information on loads. The spectra have to be updated regarding new material or new runways. For example, the tractors to tow aircraft from boarding door to runway have changed in time. Some airports have very fast tractors, impacting phases such as towing phase or push-back phase.

Conclusion

This paper provides an overview of the Airbus way to build a complex fatigue spectrum for the design of large commercial aircraft but also for tests. Thanks to our knowledge of the usage of our fleet and to modern methods, Airbus is able to build an accurate representation of fatigue loads to support its fleet. This accurate representation is essential to process optimization, saving weight, and increasing safety.

References

[1] Miner, "Cumulative Damage in Fatigue," *ASTM Transnational Journal of Applied Mechanics*, Vol. 67, 1945.

[2] Elber, "Fatigue Crack Propagation: Some Effects of Crack Closure on the Mechanisms of Fatigue Crack Propagation and Cyclic Tension Bending," Ph.D. Thesis, University of South Wales, Australia, 1968.

Journal of ASTM International, October 2004, Vol. 1, No. 9
Paper ID JAI19032
Available online at www.astm.org

Marko Yanishevsky[1] *and Richard A. Everett, Jr.*[2]

Spectrum Fatigue Testing and Small-Crack Life Prediction Analysis on a Coupon Similar to a Critical Design Detail of a CF188 Hornet Component

ABSTRACT: Numerous studies have shown that small-crack methodology can be used to predict the total fatigue life of laboratory type (K_T = 1 and 3) specimens under variable amplitude loading. Prior to investigating how well this fatigue life prediction capability could be extended to "real" aircraft structures, an intermediary step was taken where total fatigue life was predicted for a laboratory type specimen similar to a critical design detail in a fighter aircraft fuselage bulkhead. Using the small-crack analysis in the computer code called FASTRAN and assuming an initial crack size of 20 microns, the time to catastrophic failure of the test coupons was predicted to within 10 % of the average test times.

KEYWORDS: aircraft, small-crack life prediction, spectrum fatigue

Introduction

The Canadian Forces (CF) and the Royal Australian Air Force (RAAF) have been involved in a joint International Follow-On Spectrum Test Program (IFOSTP) Full Scale Test of their F/A-18 (CF188) Hornet fighter aircraft since the early 1990s [1]. The goal of the program was to establish appropriate inspections, maintenance actions, and repairs that would allow continued safe and economical operation of the aircraft fleets to reach their full 6000 flight hours potential over a 30-year period. Monitoring of manufacturer installed strain gauges in the wing and fuselage structures showed that the CF and RAAF land-based usage of the aircraft is significantly more severe than the US Navy service fatigue spectrum, to which it was originally designed and tested. During the original ST16 Full Scale Test by McDonnell Douglas, the Original Equipment Manufacturer (OEM), a highly stressed area at location X19 on the Y470.5 wing carry through bulkhead failed catastrophically after 12 205 Simulated Flight Hours (SFH), as shown in Figs. 1 and 2 [2].

To establish the potential fatigue life enhancement benefit offered by shot peening the area, the CF undertook a test program at the Quality Engineering Test Establishment (QETE) [3] to establish the crack nucleation and crack propagation lives of pristine coupons and those with shot peen repair. The test results from pristine coupons were analyzed and predicted in a TTCP (The Technical Cooperation Program) Short Crack Effects program [4] to determine the effectiveness and limitations of small-crack life prediction methodology prior to conducting predictions in real aircraft structure.

Manuscript received 28 May 2002; accepted for publication 17 July 2003; published October 2004. Presented at ASTM Symposium on Fatigue Testing and Analysis Under Variable Amplitude Loading Conditions on 29 31 May 2002 in Tours, France; P. C. McKeighan and N. Ranganathan, Guest Editors.

[1] Senior Research Officer, Institute for Aerospace Research, National Research Council Canada, 1200 Montreal Road, Building M-14, Ottawa, ON, Canada, K1A 0R6.
[2] Senior Aerospace Engineer, U.S. Army Vehicle Technology Directorate, ARL, Mechanics and Durability Branch, 2 West Reid St, MS 188E, NASA Langley Research Center, Hampton, VA 23681-2199.

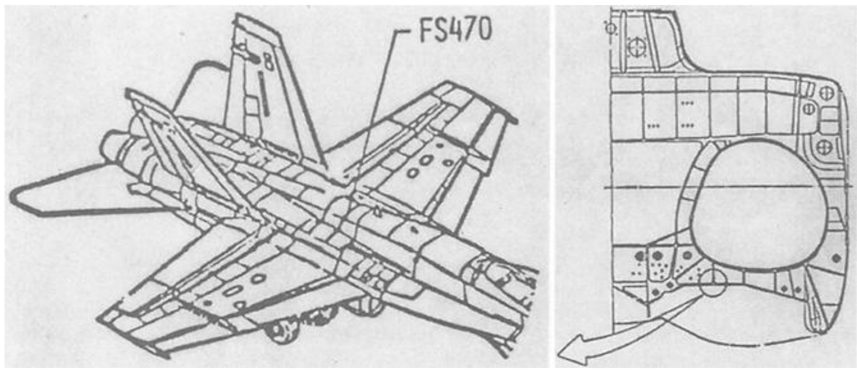

FIG. 1 *CF188 fuselage and the left side of the Y470.5 bulkhead (looking aft).*

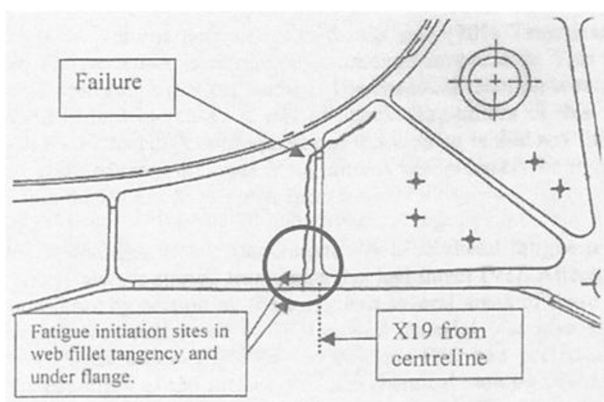

FIG. 2 *Close-up of the location X19 flange/web stiffener where failure occurred during the U.S. Navy ST16 Full Scale Test after 12 205 SFH of usage [2].*

Description of the X19 Coupon and Stress Concentration Analyses

The X19 test coupon was designed by Bombardier Military Division, the CF188 repair and maintenance contractor, with a general geometry and stress concentration similar to the fatigue prone flange/web pocket of the X19 area. The test coupons, shown in Fig. 3, were manufactured from a 102-mm thick 7050-T7451 aluminium (Al) alloy plate, replicating the local X19 24 degree grain orientation with respect to the rolling direction of the plate.

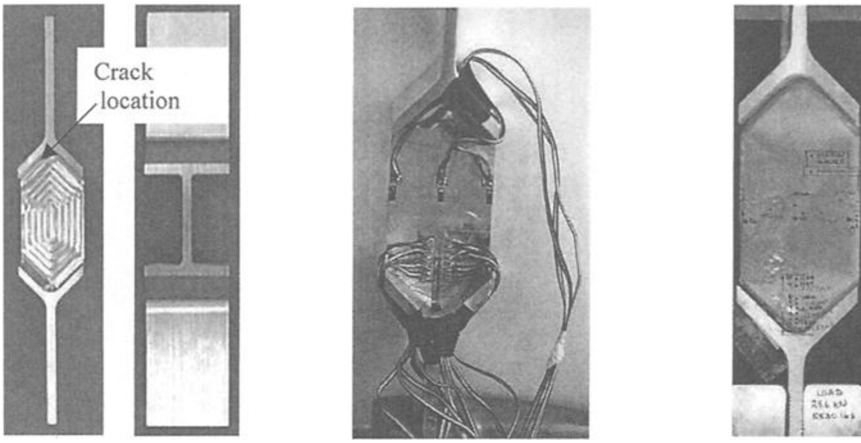

FIG. 3 *The X19 coupon simulating the flange/web transition (circled in Fig. 2): as manufactured (left); instrumented with strain gauges on one side (center); and with photoelastic coating on the opposite side (right).*

The first test coupon produced was instrumented with strain gauges and photoelastic coatings to establish the strain gradient through the flange/web pocket transition. Finite Element Modeling (FEM) of the area was also conducted [5], with the close-up of the flange/web transition, where cracks first originated, shown in Fig. 4. Analysis of the experimental photoelastic coating and strain gauge measurements indicated that the stress concentration in the area of interest was 1.68 [3]. The FEM analysis determined that the stress concentration in the transition area was 2.15 [5].

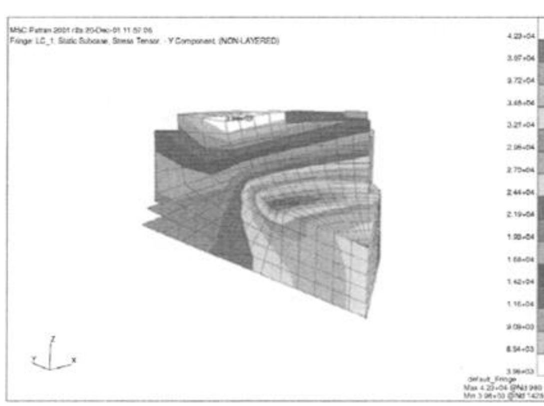

FIG. 4 *Close-up of the FEM analysis of the X19 flange/web pocket [5].*

Loading Spectrum

The IARP03a loading spectrum (Fig. 5) for the IFOSTP program was developed from CF188 fleet data at the National Research Council Canada [6],[7]. The strain spectrum used to test the X19 coupons was measured on the FT55 Full Scale Fuselage Test. The load magnitude was scaled to the cross-sectional area of the X19 coupon geometry, producing a peak remote stress of 258 MPa. The spectrum contained 15 893 end levels representing a typical year of flight of 325 SFH. At a test frequency of 5 Hz, it took 1.25 h to reproduce in the load frame.

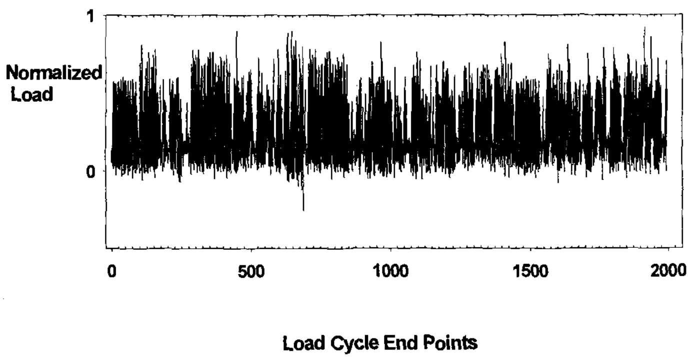

FIG. 5—*Portion of the IARP03a IFOSTP F/A-18 fatigue spectrum.*

Spectrum Fatigue Testing and Crack Inspection Techniques

The symmetric X19 coupon presented four identical crack nucleation/inspection sites, and these were identified as Location 1 (upper front), Location 2 (lower front), Location 3 (upper back) and Location 4 (lower back), evident in Fig. 6*a*.

The coupon was fatigue-tested in a 100 kN computer automated servo hydraulic test system. During fatigue testing, a video microscope system was used to monitor and record crack development and progression; a typical image is shown in Fig. 6*b*.

Surface crack length measurements were conducted using an Enhanced Liquid Penetrant procedure described in [8], whereby a thin layer of penetrant was applied to the area of interest, and the coupon was loaded to 50 % of the maximum test load while the image was recorded on video with the aid of an ultraviolet light. The cracks appeared dark while the rest of the surface was bright, a bright background being necessary for video capture.

The Enhanced Liquid Penetrant Inspection (LPI) technique was found to be significantly more sensitive than Eddy Current (EC) in detecting developing cracks for the X19 geometry. Once cracks were detected by Enhanced LPI, the fatigue prone areas were inspected using the EC method as well. The latter method is used presently on the CF188 aircraft fleet.

As evident in Fig. 6, multiple cracks would develop on different planes and at different points along the flange/web transition. Though there were a few cases of only one to three cracks developing in the radii, in many cases there were in excess of six identifiable cracks measuring less than 1 mm in length (~0.5 mm depth). When one or more of the cracks would become dominant or linking of neighboring cracks occurred, smaller secondary cracks often became dormant.

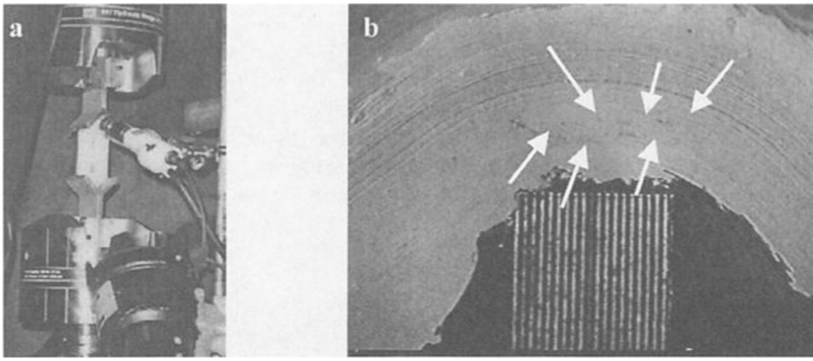

FIG. 6 *Experimental setup showing the test coupon mounted in the load frame, video microscope, and ultra violet illumination (*a*). Close-up of an Enhanced Liquid Penetrant Inspection image of the multiple cracking situation on coupon PL50 Location 3 at the point where EC inspection reliably detected the presence of fatigue cracks (*b*). The reference grid below the fluorescent dye has 0.25 mm spacing.*

Two coupons were sacrificed to measure crack sizes upon detection by EC. The crack sizes were measured after sectioning the coupons and exposing the crack surfaces by breaking them open. The measured crack sizes are shown in Table 1. EC crack detection was on the order of 0.2 1 mm (0.6 mm typically) in depth due to the radius and the local material thickness change at the flange/web transition.

The relationships between EC response to a 7075-T651 Al alloy calibration block with Electron Discharge Machining (EDM) slots and to fatigue cracks in the X19 coupons are provided in Table 2. The spectrum fatigue test results from this program are provided in Table 3.

TABLE 1 *Crack dimensions at first detection by EC on baseline coupons.*

Coupon / Site#	(EC Reading)	Surface Length (2a)	Depth (c)	2a/c Ratio
PL3 #1	(EC = 1/4 div)	0.45 mm	0.21 mm	2.14
PL3 #4	(EC = 1 div)	0.90 mm	0.58 mm	1.55
PL20 #4	(EC = 1/4 div)	0.56 mm	0.30 mm	1.87

TABLE 2 *Comparison of EC response to EDM slots and to fatigue cracks in the X19 flange/web transition on pristine coupons. A 0.5 mm deep fatigue crack provided half a division of EC response; a comparable EDM slot provided a 4 division response.*

	7075-T651 Al Alloy	7050-T7451 Al Alloy Plate	
Eddy Current Response (Divisions)	Flat Plate Calibration Block ~Depth (mm)	X19 coupon flange/web transition 4.0 mm radius ~Depth Range (mm)	Average Depth (mm)
0.5		0.2 1.0	0.6
1	0.2	0.6 1.0	0.8
2		0.4 1.3	1.0
3		1.75	1.75
4	0.5		
Off Screen	1.0		

TABLE 3 *Crack nucleation (to EC ~0.5 div), crack propagation, and total life results.*

Specimen	Location	Total Life (Blocks)	Final Crack Length (mm)	Largest Single Surface Crack (mm)	Crack Nucleation (EC~0.5 div) (Blocks)	Crack Propagation (Blocks)
PL9	1	28.5	20.3			
	2			0.6	18.8	
	3	28.5	20.3			
	4					
PL50	1	27.6	20.3	1	18	9.6
	2					
	3	27.6	20.3	0.8	14	13.6
	4			1	20	

Metallography

An example of the 7050-T7451 Al alloy plate microstructure on the Longitudinal Transverse plane in the vicinity of the failure surfaces with the rolling direction oriented vertically is shown in Fig. 7. The surface was polished and etched with Keller's reagent. Several examples of stringers containing intermetallic particles were found measuring 20 30 μm wide by up to 300 μm long.

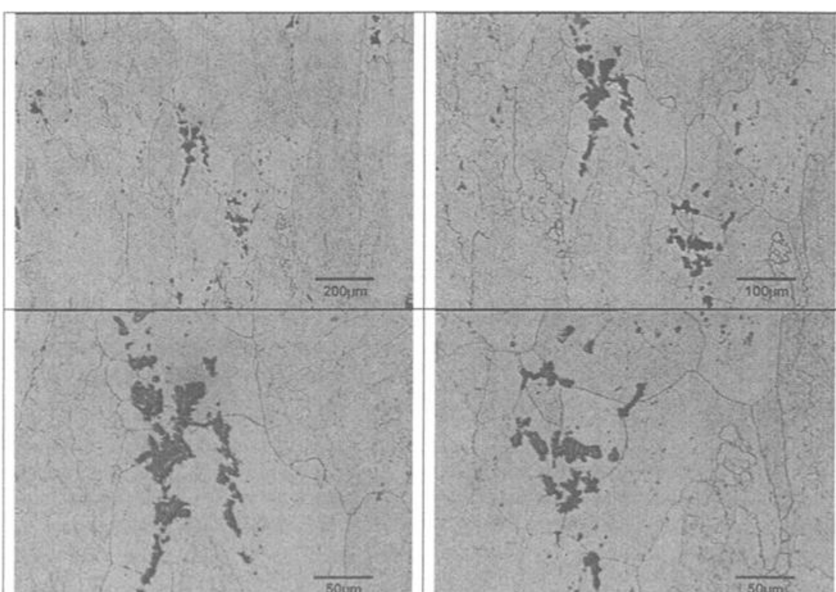

FIG. 7 *The 7050-T7451 Al alloy microstructure near the flange/web transition of the X19 coupons. Lower photos are close-ups of the stringers of particles in the upper photos.*

Fractography

Scanning electron microscope (SEM) examination of the coupon failure surfaces performed at QETE indicated that crack nucleation had occurred at multiple sites, consisting primarily of intermetallics, pores, clusters of pores, and clusters of intermetallics, as well as long shallow machining marks, as shown in Figs. 8 12.

Fatigue Life Analysis

Damage tolerance methods used in the design of conventional aircraft have been used routinely for many years. These methods have used the long crack thresholds for crack growth in successfully defining inspection intervals for maintaining flight safety. Experience has shown that there could be crack growth at stress intensity values significantly below the long crack threshold. In some cases, these cracks have been found to grow rapidly in the early stages. This growth below the long crack threshold, ΔKth, is illustrated in Fig. 13 and is often referred to as the small-crack effect. As stated previously, the TTCP member countries have conducted studies in the small-crack effect for some time [4]. The X19 coupon problem presented an opportunity to conduct such an analysis, predicting fatigue life with small-crack considerations, on a well-characterized coupon loaded to a service representative fatigue spectrum with many similarities to a critical structural detail.

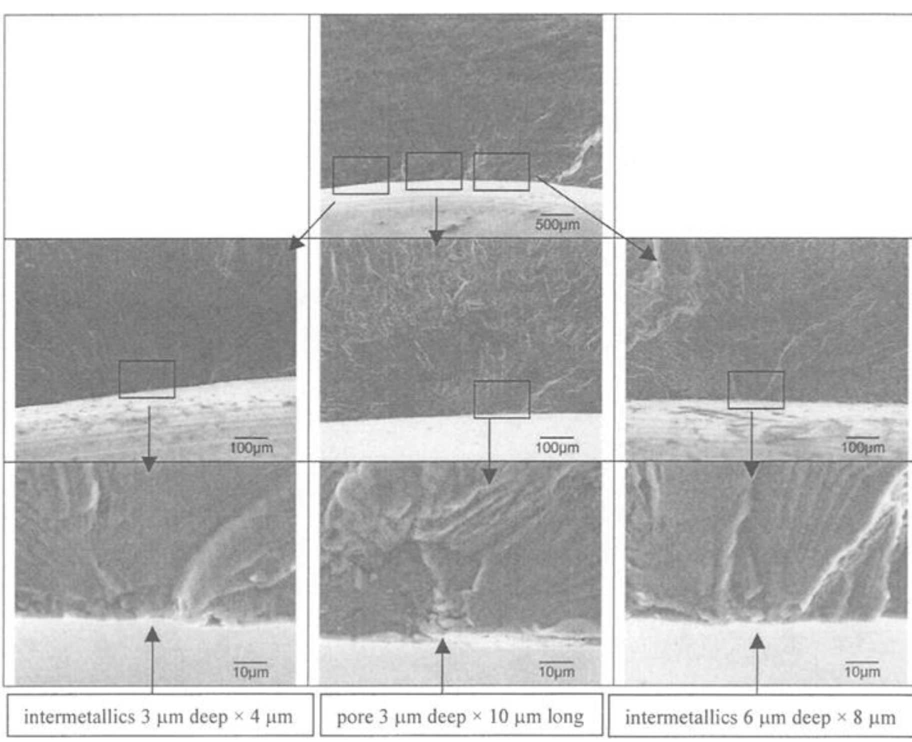

FIG. 8 *SEM photos of coupon PL50 Location 1 with multiple crack nucleation sites.*

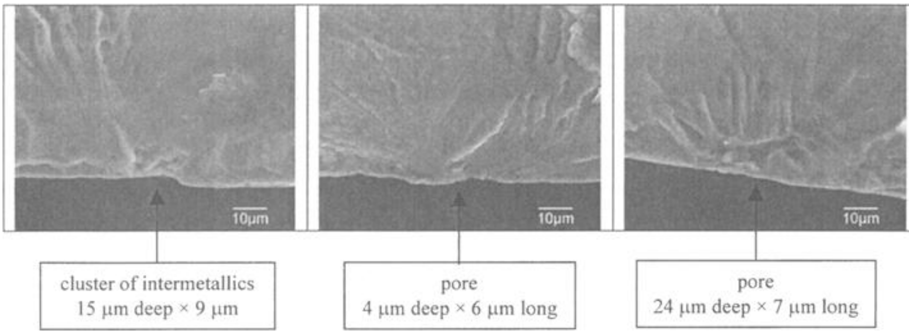

FIG. 9 *SEM photos of coupon PL30 Location 3 with multiple crack nucleation sites.*

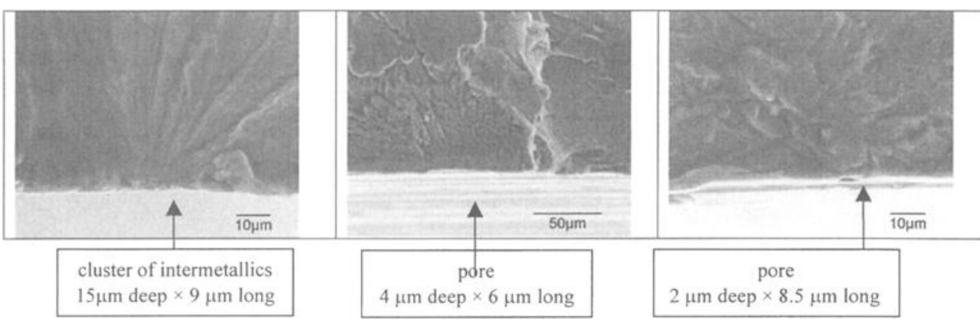

FIG. 10 *SEM photos of crack nucleation sites on: coupon PL9 Location 4 (left), coupon PL9 Location 3 (center), and coupon PL9 Location 2 (right).*

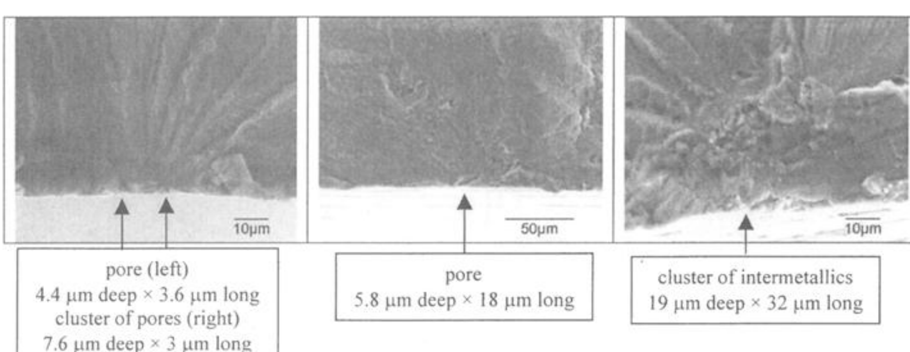

FIG. 11 *SEM photos of coupon PL9 Location 4 (left), PL9 Location 3 (center), and PL50 Location 3 (right) crack nucleation sites.*

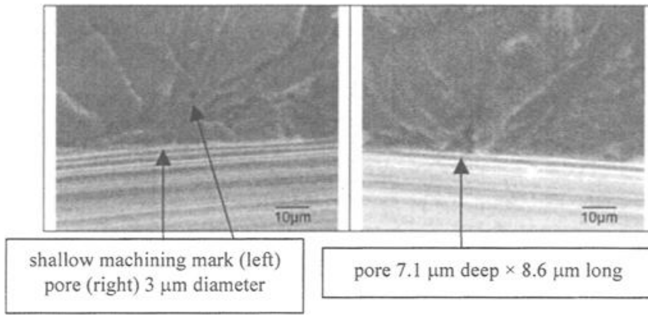

FIG. 12 *SEM photos of coupon PL30 Location 4 with multiple crack nucleation sites.*

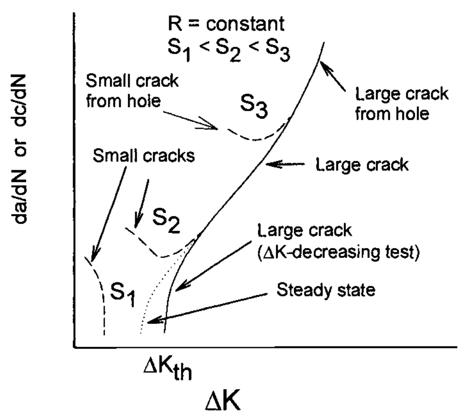

FIG. 13 *Illustration of the small-crack effect. S1, S2, and S3 correspond to remote stress levels.*

Small Crack Data

In order to predict the fatigue life of a material that exhibits a small-crack effect using only crack growth data, the crack-growth rate curve must take into account the small-crack effect as shown by the dashed line in Fig. 14. One source of small-crack data is a small-crack database, which has been under development in the United States ever since the AGARD cooperative test program on small-cracks was started. This work was summarized in December 1988 [9]. Follow-up work to the initial study for the materials 4340 steel and 2090 aluminum-lithium was completed in August 1990 [10]. (It is interesting to note that some materials, such as 4340 steel shown in Fig. 15 [10], do not exhibit a significant small-crack effect.)

In this small-crack database, no data existed for the material used in the X19 test coupon, which was 7050-T7451. However, data did exist for 7075-T6, which is a 7000 series aluminum alloy, as is 7070-T7451. Hence, it was decided to use the 7075-T6 small-crack crack growth data as an estimate of the crack growth behavior of 7050-T7451.

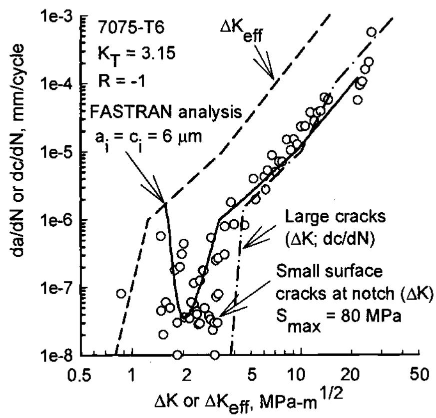

FIG. 14 *Measured and predicted small surface crack growth at a notch in 7075-T6 [9].*

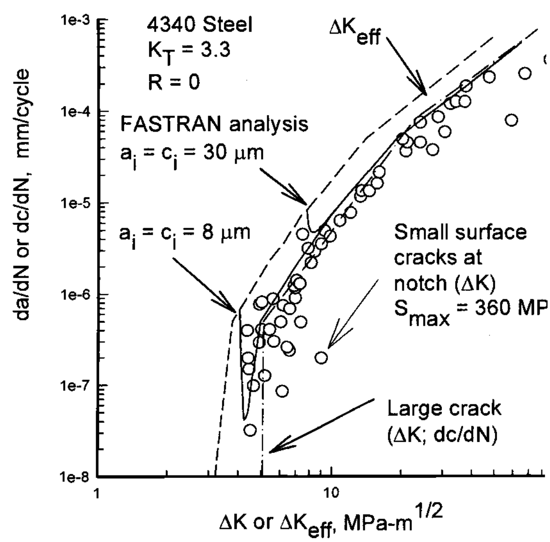

FIG. 15—*Measured and predicted small corner crack growth at a notch in 4340 steel [10].*

Analysis of the Location X19 Coupon

To calculate the total fatigue life using only crack growth data, an equation such as the Paris equation shown in Eq 1 is integrated to solve for the quantity N, which is the number of cycles to failure.

$$da/dN = C(\Delta K)^m \tag{1}$$

In Eq 1, da/dN is the crack growth rate, and ΔK is the stress intensity factor range, with C and m being curve fit parameters. As stated previously, the da/dN data must include the small-crack effect as defined by the dashed line in Fig. 14.

A total fatigue life computer algorithm was developed by J. C. Newman, Jr., based on crack-closure concepts in fracture mechanics and small-crack considerations. The total life of the X19 coupon was predicted using only a crack-growth analysis that employs small-crack methodology. The total fatigue life was calculated by numerically integrating Eq 1 from the initial crack length to failure as:

$$N = \sum_{a_i}^{a_f} \frac{\Delta a}{C\left[\left(S_{\max} - S_O\right)\left(\pi a\right)^{1/2} F\right]^m} \tag{2}$$

where ai is the initial crack length determined from a small-crack study, af is the crack length at failure, Smax is the maximum stress, So is the crack opening stress, and F is the boundary-correction factor. Cycles are summed as the crack grows under the applied loading until Kmax = Kc , where Kc is the fracture toughness of the material. When Kmax = Kc , the summation of the load cycles, N, is the total fatigue life. This computer program was developed almost two decades ago and was originally conceived as a crack growth analysis tool based on fatigue crack-closure concepts in fracture mechanics and was shown to help explain load interaction effects (crack growth retardation and acceleration) in fatigue crack growth. This computer program was originally called FAST (Fatigue Crack Growth Analysis of Structures) [11]. Later the use of "small-crack" concepts was incorporated into FASTRAN, and this analysis was shown to be very effective in calculating total fatigue life based solely on crack growth data [12].

Initial Crack Size and Life Prediction

To calculate the total fatigue life using the computer algorithm developed by Newman [12], the initial crack size, ai, used in the analysis is often determined from a cumulative distribution function of small-crack measurements obtained from a small-crack study based on metallographic examination of etched pristine material and fractographic examination of failed specimens. Scanning electron microscope (SEM) examination of the coupon failure surfaces [3] performed at the Quality Engineering Test Establishment (QETE) indicated that crack nucleation had occurred at multiple sites, consisting primarily of intermetallics, pores, clusters of pores, and clusters of intermetallics, as well as long shallow machining marks, as shown in Figs. 8 12. The range of the crack nucleation sizes in these figures varied from 3 μm deep × 4 μm long to 19 μm deep × 32 μm long.

Another way to determine the appropriate initial crack size is to use engineering judgment based on previous work with the material of interest. Previous tests on the aluminum alloy 7075-T6 determined the initial crack length for constant amplitude predictions at $K_T = 1$ and 3 to be 20 μm and 6 μm, respectively [14.] Since crack nucleation lengths up to 32 μm were seen in the 7050-T7451 used in the test coupon, and the fatigue life predictions described in [14] for 7075-T6 alloy used a 20 μm crack length, it was decided to use a semi-circular crack geometry where $a_i = c_i = 20$ μm as a first try for the life predictions. A second solution was also tried using a crack geometry of 19 μm deep × 32 μm long, which was the largest crack geometry shown in the fractographic study of the crack nucleation sites, as shown in Fig. 11.

A 3-D finite element analysis [5] of the test coupon showed a bivariant stress distribution exists at the flange/web pocket transition where the fatigue cracks occurred (see Fig. 3). The elastic stress concentration, KT, where the fatigue cracks occurred was 2.15 as calculated from the finite element analysis, FEA. The FEA also showed that the stress distribution through the thickness at the flange/web pocket transition is nonlinear. At present, FASTRAN only has a stress intensity, K, solution for a linear variation of stress through the thickness. Consequently, in this analysis the fatigue life was predicted by bounding the fatigue life with a solution for pure tension and pure bending with a linear variation of stress through the thickness. Assuming this approach, the fatigue life from the tests would be bounded by these two solutions. The two tests in the CF188 IFOSTP program failed at 219 337 and 226 490 cycles.

Using a KT of 2.15 from the FEA and the applied stress in the two tests of 207 MPa, the local stress in the vicinity of the crack would be 445 MPa. The results of these two analyses from FASTRAN compared to the test results are shown in Fig. 16. One can see that the pure tension and pure bending solutions using a semi-circular crack geometry bounded the test data very well. The solutions using a crack geometry of 19 μm deep × 32 μm long were slightly unconservative.

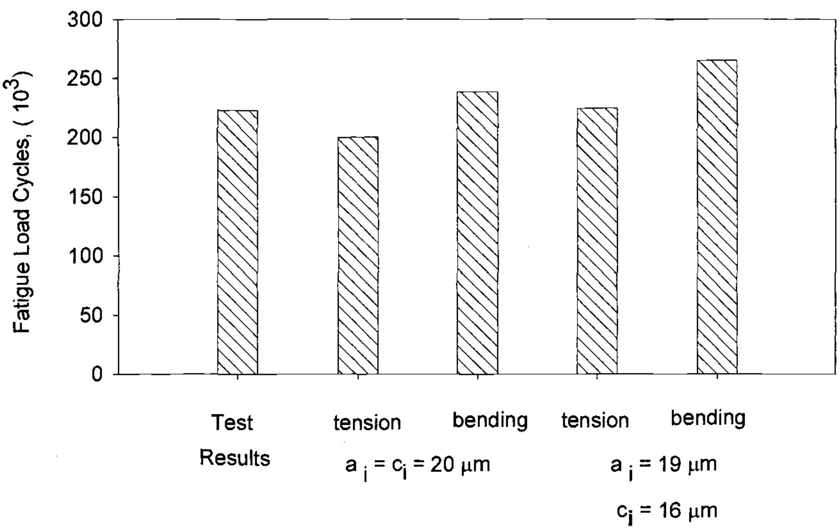

FIG. 16 *Comparison between test results and analytical life predictions of total life.*

Conclusions

Small-crack data on several metallic materials have been assembled and included in a small-crack database. The work presented here has shown that small-crack methodology can be used to predict the total fatigue life of metallic materials. This has been demonstrated in this study on a coupon similar in geometry and stress concentration to a fatigue critical aircraft structural detail on the CF188 Hornet aircraft. The coupon level experimental fatigue test data agreed very well with small-crack analysis using the computer code FASTRAN for 7050-T7451 aluminum alloy.

Acknowledgments

The authors would like to thank Dr. Martin Roth from QETE for the fractography and documentation of the crack origins in the X19 coupons and Dr. Ali Merati from NRC/IAR for the X19 coupon metallography. We would also like to thank QETE NDT Specialists, Mr. Larry Boone, Mr. Michel Montambeault, and Mr. Orville Francescone, for providing the EC and conventional LPI inspections. Their professionalism, dedicated efforts, time, and frustrations providing ideal quality LPI inspection sites inspired the development of the Enhanced LPI technique as an alternative to conventional LPI for laboratory experiments. The authors would like to recognize Mr. Sylvain Forgues and his colleagues at Bombardier Military Aircraft Division for designing the test coupon and Mr. Bruce Waid and Mr. Steve DeGoyer of QETE for the CAD/CAM manufacturing of the X19 coupons. Finally, we would like to acknowledge Professor James C. Newman, Jr. at Mississippi State University and Dr. Mark A. James at the National Institute of Aerospace for their consultation with the fatigue life analysis.

References

[1] Canadian Forces/Royal Australian Air Force, F/A-18 Hornet International Follow-On Structural Test Program (IFOSTP), International Management Plan, Ottawa, ON, 22 May 1992.

[2] Barter, S., Molent, L., Sharp, K., and Clark, G., "Repair and Life Assessment of Critical Fatigue Damaged Aluminium Alloy Structure Using a Peening Rework Method," *USAF ASIP Conference*, December 2000.

[3] Quality Engineering Test Establishment, "CF188 Y470.5 Bulkhead Location X19 Shot Peening Fatigue Enhancement Evaluation," *QETE Project A017496*, Ottawa, ON, in progress.

[4] Everett, R. A., Jr. and Yanishevsky, M., "Summary of Short Crack Efforts in Member Countries," *TTCP Collaborative Program CP 8A-3*, Milestone Report, in progress.

[5] Shi, C. G., Xiong, Y., and Raizenne, D., "Three-Dimensional FE Analysis of X19 Specimens with Bonded Patch Repair," NRC *LTR-ST-2201*, Ottawa, ON, March 1999.

[6] Hewitt, R. L., Hiscocks, R. J., Simpson, D. L., and Weiss, J. P., "Analytical Truncation of IARPO3a," NRC, *LTR-ST-1975*, Ottawa, ON, July 1994.

[7] Zavitz, D., Sullivan, A. B., Hiscocks, R. J., and Simpson, D. L., "CF/RAAF Post-Lex Period Mission Block (IARPO3) Definition and Analysis," NRC, *LTR-ST-1928*, Ottawa, ON, April 1993.

[8] Yanishevsky, M., "An Enhanced Fluorescent Liquid Penetrant Inspection Technique for Measurement of Surface Cracks," *First Pan American Conference for Non Destructive Testing*, Toronto, Canada, Sept. 1998 (http://www.ndt.net/article/pacndt98/44/44.htm).

[9] Newman, J. C., Jr. and Edwards, P. R., "Short-Crack Growth Behavior in an Aluminum Alloy - An AGARD Cooperative Test Programme," *AGARD R-732*, 1988.

[10] Swain, M. H., Everett, R. A., Jr., Newman, J. C., Jr., and Phillips, E. P., "The Growth of Short Cracks in 4340 Steel and Al-Li 2090," Paper No. 7, *AGARD R-767*, 1989.

[11] Everett, R. A., Jr., "A Comparison of Fatigue Life Prediction Methodologies for Rotorcraft," *Journal of the American Helicopter Society*, Vol. 37, No. 2, April 1992.

[12] Newman, J. C., Jr., "Fracture Mechanics Parameters for Small Fatigue Cracks," *Small Crack Test Methods, ASTM STP 1149*, J. Allison and J. Larsen, Eds., ASTM International, West Conshohocken, PA, 1992, pp. 6 28.

[13] Newman, J. C., Jr., "A Crack-Closure Model for Predicting Fatigue Crack Growth Under Aircraft Spectrum Loading," *Methods and Models For Predicting Fatigue Crack Growth Under Random Loading, ASTM STP 748*, J. B. Chang and C. M. Hudson, Eds., ASTM International, West Conshohocken, PA, 1981, pp. 53 84.
[14] Newman, J. C., Jr., Phillips, E. P., and Swain, M. H., "Fatigue Life Prediction Methodology Using Small-Crack Theory," *International Journal of Fatigue*, Vol. 21, 1999, pp. 109 119.

Journal of ASTM International, September 2004, Vol. 1, No. 8
Paper ID JAI19023
Available online at www.astm.org

Robert R. Stephens,[1] *Ralph I. Stephens,*[2] *Shannon C. Berge,*[3] *David E. Lemm,*[3] *and Christopher D. Glancey*[4]

Effect of Transient Loads on Fatigue Crack Growth in Solution Treated and Aged Ti-62222 at –54, 25, and 175°C

ABSTRACT: Transient loads consisting of single tensile overloads and single tensile overloads followed by single compressive underloads were applied to Ti-62222 solution treated and aged titanium alloy at –54, 25, and 175°C. Tensile overload ratios were 2.0 and 2.5, and the compressive underload ratio was –0.5. Four reference steady state ΔK_{ss} values, using constant ΔK testing at $R = 0.1$, were investigated at each temperature. Cycles of delay, fatigue crack growth during delay, and minimum fatigue crack growth rate during a transient load were obtained for all tests. Cycles of delay ranged from zero to crack arrest. Higher tensile overloads caused greater delay cycles, and underloads were often detrimental. Low and high temperatures were primarily beneficial to delay cycles relative to those at room temperature. Crack growth delay distance was always greater than the pertinent reversed plastic zone size. Fatigue crack growth life predictions were made using FASTRAN III and AFGROW computer programs and produced both conservative and non-conservative results with more than half the predictions being within ± 2 of the experimental results. Macro- and microfractography revealed surface crack closure, Mode II displacements, crack tip blunting, branching, and tunneling contributed to the transient fatigue crack growth behavior.

KEYWORDS: titanium alloy, fatigue crack growth, tensile overloads, compressive underloads, temperature, life predictions, fractography

Introduction

Damage-tolerant aspects of fatigue crack growth (FCG) in aircraft require the consideration of load interaction and sequence effects since they affect FCG rates and subsequent fatigue life. Aircraft subjected to subsonic and supersonic speeds are subjected to both spectrum loading and temperature changes. Wing skin temperatures reach –54°C at subsonic flight and 175°C at supersonic flight. These low and high temperatures affect FCG load interaction and sequence effects. Transient loads aimed at FCG in aircraft, consisting of both single tensile overloads and single tensile overloads followed by compressive underloads, have been studied since the 1970s [1]. Despite the fact these transient loads occur at the above three temperatures, most transient load research has been done at room temperature [1 5], and results have been assumed to be conservative or similar at the above low and high temperatures. In titanium or aluminum alloys, transient load FCG life from single tensile overloads and overloads/underloads at 175°C was

Manuscript received 7 June 2002; accepted for publication 8 September 2003; published September 2004.
Presented at ASTM Symposium on Fatigue Testing and Analysis Under Variable Amplitude Loading Conditions on 29 31 May 2002 in Tours, France; P. C. McKeighan and N. Ranganathan, Guest Editors.

[1] Associate Professor, Mechanical Engineering Department, The University of Idaho, Moscow, ID 83843.
[2] Professor, Mechanical and Industrial Engineering Department, The University of Iowa, Iowa City, IA 52242.
[3] Former Graduate Research Assistant, Mechanical and Industrial Engineering Department, The University of Iowa, Iowa City, IA 52242.
[4] Graduate Research Assistant, Mechanical Engineering Department, The University of Idaho, Moscow, ID 83843.

primarily enhanced compared to that at 25°C [6,7], and at –54°C FCG life was found to be both reduced [8] and enhanced [7,9]. The objective of this research is to provide FCG response and life predictions and to evaluate micro/macro mechanisms of solution treated and aged Ti-62222 titanium alloy sheet specimens subjected to single tensile overloads and single tensile overloads followed by single compressive underloads. The overload/underload ratios (OLR/ULR) were 2.0/0, 2.0/ 0.5, 2.5/0, and 2.5/ 0.5. These transient values are consistent with values occurring in aircraft ground-air-ground flight spectra. This research complements previous variable amplitude FCG research with Ti-62222 solution treated and aged material [7,10].

Material

The titanium alloy used in this research was a 1.61 mm thick sheet of alpha-beta Ti-62222 (Ti-6Al-2Sn-2Zr-2Mo-2Cr) that was solution treated at 732°C for ½ h and aged at 510°C for 10 h followed by air cooling. This resulted in an alpha phase dispersed evenly throughout an alpha-plus-beta matrix. The resulting composition is given in Table 1, and the microstructure is shown in Fig. 1 with an estimated grain size less than 10 μm. All test specimens were loaded in the L-T orientation. Monotonic tensile properties, along with ΔK_{th} and $\Delta K_{th,eff}$ values for R = 0.1, obtained from eccentrically-loaded single edge crack tension, ESE(T), specimens are given in Table 2 for all three temperatures. Figure 2 shows constant-amplitude R = 0.1 FCG rate behavior at the three temperatures. From Table 2 and Fig. 2, it is evident that temperature influenced both monotonic tensile and constant amplitude FCG properties. Relative to room temperature, monotonic strength properties, S_y and S_u, increased at –54°C and decreased at 175°C, while constant amplitude nominal FCG resistance primarily increased for both –54°C and 175°C. Fatigue crack growth temperature effects are most notable in Region I, where at near threshold conditions low and high temperatures exhibit lower crack growth rates for a given ΔK than at room temperature. ΔK_{eff} behavior however, as presented in [7], showed a significant shift to the left of the FCG curve at 175°C with a moderate shift at –54°C and 25°C. These curve shifts resulted in lower $\Delta K_{th,eff}$ as given in Table 2. Surface roughness, oxidation, and plasticity-induced closure are attributed to the lateral shifts in the effective da/dN-ΔK curves at the three temperatures.

TABLE 1 *Nominal composition.*

Element	Ti	Al	Sn	Zr	Mo	Cr	Si	O	Fe	C	N
Weight %	85.7	5.74	1.96	2.04	2.10	2.05	.17	.11	.11	.01	.004

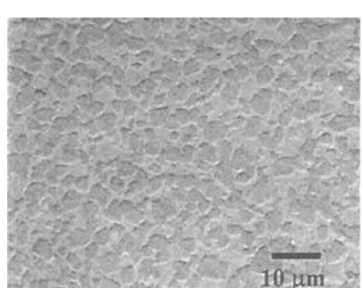

FIG. 1 *SEM micrograph of Ti-62222 STA microstructure.*

TABLE 2 *Mechanical properties.*

Temperature (°C)	S_y (MPa)	S_u (MPa)	Elongation (%)	$\Delta K_{th\,(R=0.1)}$ (MPa√m)	$\Delta K_{th,eff}$ (MPa√m)
−54	1397	1459	7.8	4.1	2.6
25	1223	1341	9.5	3.1	1.9
175	1015	1237	9.4	4.6	1.5

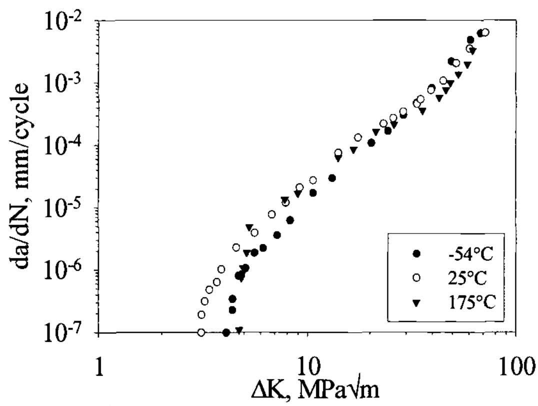

FIG. 2—*da/dN versus ΔK for −54, 25, and 175 °C.*

Test Procedures

All transient tests were performed with a 100 kN servohydraulic test system in computer control using constant ΔK procedures. M(T) test specimens were 1.61 mm thick, 50.8 mm wide, and 178 mm long and were tested in the L-T orientation with clamped ends using hydraulic grips. Starter notches were formed using EDM, followed by pre-cracking at the test temperature. Multiple transient loads were applied to each specimen using 2a/w between 0.25–0.66 with pre-cracking involving load shedding between each transient load. Specimens were polished in the crack growth region for supplementary crack measurements, however, principal crack measurements were made using the compliance method with a centered clip gage spanning the crack according to ASTM Test Method for Measurement of Fatigue Crack Growth Rates (E 647). Specimens were also chemically etched in the crack growth region for pre- and post-test scanning electron microscopy surface observations.

Transient loads consisted of both single tensile overloads and single tensile overloads followed by single compressive underloads. The overload/underload ratios, OLR/ULR, were 2.0/0, 2.0/–0.5, 2.5/0, and 2.5/–0.5. Steady state ΔK_{ss} values of 4.4, 8.8, 13.2, and 17.6 MPa√m with R = 0.1 where used with the transient loads. These steady state values corresponded to Regions I and II constant amplitude fatigue crack growth rates. Steady-state FCG rates were approximately 10^{-9}, 10^{-8}, 5×10^{-8}, and 10^{-7} m/cycle, respectively, for the four different ΔK_{ss} values. Triplicate tests were performed for each transient test condition. Sinusoidal steady-state fatigue cycling was performed at 20 Hz, while transient loads were applied at 0.02 Hz. Compliance crack growth data were taken every 0.04 mm, and between 9 and 15 data points were taken in the pre- and post-steady-state regions for each transient loading. Crack arrest was defined as 500 000 cycles of delay following a transient load without measurable crack extension. All room temperature tests (25°C) were performed in laboratory air, while –54°C tests were performed by enclosing the test specimen in a temperature chamber cooled with liquid nitrogen. A resistance thermal gage was attached to the specimen to provide low temperature measurement and feedback to the coolant controller. All 175°C tests were performed in laboratory air with strip heaters placed above and below the crack plane.

Figure 3 shows the schematic transient response and parameter definitions. TL stands for transient load, and b_1 and b_2 are the pre- and post-steady state FCG rates, which were usually similar for a given test condition. Cycles of delay, N_d, and fatigue crack growth during delay, a_d, were obtained for all tests during a transient load. a_s was the crack extension that sometimes occurred during the transient loading. a_d was compared to appropriate reversed plastic zone sizes, $2r_y'$. Both macro and micro scanning electron microscopic analysis of crack profiles and fracture surfaces were performed with representative transient conditions at all temperatures.

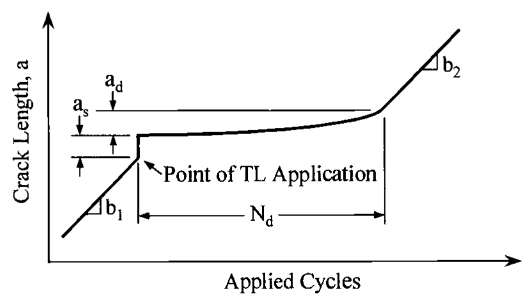

FIG. 3 *a versus N schematic illustrating transient load parameter definitions.*

Results and Discussion

FCG Delay

The average of triplicate tests for all transient test results are given in Table 3. This includes N_d and a_d for each of the three temperatures for given ΔK_{ss} and OLR/ULR conditions. Scatter in triplicate tests for both a_d and N_d was within a factor of two or three for the vast majority of test conditions. Exceptions occurred if a specimen would arrest while a replicate specimen would not. The total scatter was considered to be reasonable. No data are included for ΔK_{ss} = 4.4 MPa$\sqrt{m}$ at 175°C due to an inability to pre-crack the specimen to ΔK_{ss} = 4.4 MPa$\sqrt{m}$, since this is essentially less than ΔK_{th} at this temperature.

It is seen in Table 3 that a_d varied from 0 0.30 mm, and for a given temperature and overload condition, a_d tended to increase as ΔK_{ss} increased. For a given transient condition, a_d decreased at –54°C for most conditions, while at 175°C a_d decreased or was similar to that at 25°C. From Table 3, N_d varied from zero to crack arrest (500 000 cycles) depending on ΔK_{ss}, the transient event, and the temperature. No consistent correlation or trend between N_d and ΔK_{ss} for a given transient condition could be made. However, 14 of 16 tests at –54°C and 11 of 12 tests at 175°C provided greater or equivalent delay cycles, N_d, than at 25°C.

TABLE 3 *Delay cycles (N_d) and delay distance (a_d), average of three tests.*

ΔK_{ss} (MPa$\sqrt{m}$)	OLR/ULR	Delay Cycles, N_d			Delay Distance, a_d (mm)		
		−54°C	25°C	175°C	−54°C	25°C	175°C
	2.0/ 0.5	0	0	No test	0	0	No test
4.4	2.0/0.0	0	110 000	No test	0	0.09	No test
	2.5/ 0.5	Arrest	Arrest	No test			No test
	2.5/0.0	Arrest	Arrest	No test			No test
	2.0/ 0.5	3 500	3 700	> 230 000*	0.02	0.06	0.06
8.8	2.0/0.0	15 000	3 700	140 000	0.08	0.04	0.05
	2.5/ 0.5	31 000	16 700	Arrest	0.08	0.08	
	2.5/0.0	62 000	43 000	Arrest	0.08	0.12	
	2.0/ 0.5	5 500	2 800	20 000	0.09	0.11	0.16
13.2	2.0/0.0	7 500	3 900	18 000	0.09	0.13	0.16
	2.5/ 0.5	61 000	14 000	145 000	0.12	0.23	0.14
	2.5/0.0	195 000	34 500	> 235 000*	0.11	0.26	0.12
	2.0/ 0.5	8 000	3 200	6 500	0.16	0.21	0.14
17.6	2.0/0.0	9 500	3 500	8 500	0.12	0.15	0.19
	2.5/ 0.5	77 000	38 000	41 000	0.10	0.30	0.23
	2.5/0.0	210 000	> 400 000**	43 000	0.13	0.30	0.22

* One of three tests arrested.
** Two of three tests arrested.

Typical average crack length, a, versus applied cycles, N, for triplicate tests is shown in Fig. 4 for ΔK_{ss} = 13.2 MPa$\sqrt{m}$ at −54°C for all four transient load types. N = 0 represents the transient load application point. The small scatter in the pre- and post- transient a versus N data is evident. The effect of the higher overload ratio of 2.5, as compared to 2.0, is evident in that significant delay cycles, or even crack arrest, occurred for the higher overload. Arrest is indicated in Table 3 for only the 2.5/0 or 2.5/ 0.5 transient conditions. Also evident in Fig. 4 is that the underload following the overload decreased delay cycles for OLR = 2.5 but not significantly for OLR = 2. This was rather common for all conditions as given in Table 3. The discrepancy can be due to the small delay cycles, N_d, that occurred for the 2.0 overloads relative to that for the 2.5 overloads.

Figure 5 shows the average da/dN versus a curves associated with Fig. 4. Scatter is increased in the figure due to the secant method used for reduction of data. da/dN following the transient loads is shown to decrease by up to two orders of magnitude. The largest decrease in da/dN occurred with only the tensile overload and the highest overload ratio (OLR/ULR = 2.5/0). The minimum da/dN for all tests occurred at less than 0.05 mm of crack extension following the transient event. Figure 6 shows a comparison of average da/dN versus a for ΔK_{ss} = 13.2 MPa$\sqrt{m}$ and an OLR/ULR = 2.5/-0.5 for the three test temperatures. The minimum crack growth rate occurred at 175°C, followed by −54°C and then 25°C. The condition associated with minimum crack growth rate after the transient load is coincident with the largest delay cycles, which can be seen in Table 3. This trend was typical for all tests involving the various transient events, ΔK_{ss}, and test temperatures.

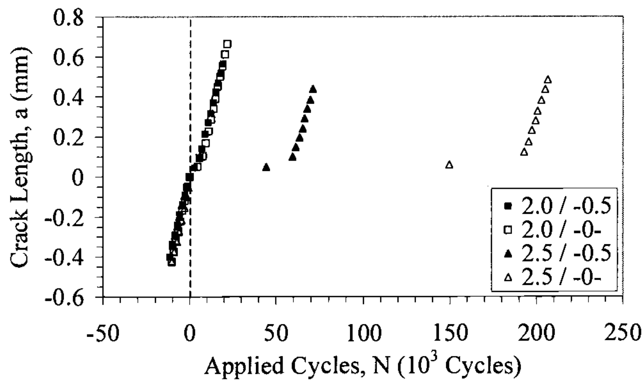

FIG. 4 *Average crack length versus cycles: ΔK_{ss} = 13.2 MPa$\sqrt{m}$, T = –54 °C. Zero reference: point of transient load application.*

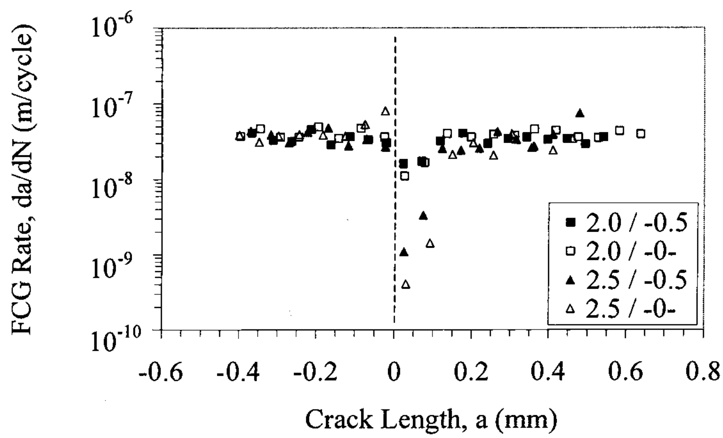

FIG. 5—*Average FCG rate versus crack length: ΔK_{ss} = 13.2 MPa$\sqrt{m}$, T = –54 °C. Zero reference: point of transient load application.*

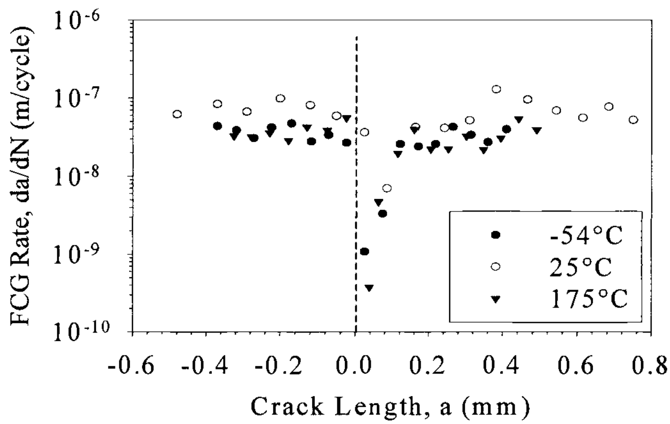

FIG. 6—*Average FCG rate vs. crack length: ΔK_{ss} = 13.2 MPa$\sqrt{m}$, OLR/ULR = 2.5/-0.5, T = –54, 25 and 175°C. Zero reference: point of transient load application.*

Plastic Zone Size Correlation With a_d

Plastic zone sizes corresponding to steady state and transient load levels were calculated using LEFM. However, before such calculations could be made, the stress state related to each of the load levels and specimen geometry had to be determined. Specimen and loading combinations were assumed to be either plane stress or plane strain. No mixed-state assumptions were made. Equation 1 from ASTM Standard E 647 was used to determine plane strain conditions. If a given set of test conditions violated this criterion, the test was assumed to be associated with plane stress.

$$B,\ a,\ (w/2-a),\ h \geq 2.5(K/S_y)^2 \tag{1}$$

In Eq 1, B is the specimen thickness, a is the fatigue crack length, (w/2–a) is the uncracked ligament, h is the half-height of the ungripped portion of the specimen, K is the stress intensity factor associated with the applied load, and S_y is the material yield strength for a given temperature. K_{max} values associated with steady state and transient load levels were used for K in the plane strain criterion calculations. If the plane strain criterion was satisfied, LEFM plastic zone size restrictions were automatically satisfied. Plane strain occurred for all steady state loading conditions. When the plane strain criterion was not satisfied during transient loadings, Eq 2 was used to ensure that LEFM assumptions were valid. All loadings satisfied this LEFM criterion.

$$a,\ (w/2-a),\ h \geq (4/\pi)(K/S_y)^2 \tag{2}$$

Monotonic plastic zone size, $2r_y$, and reversed plastic zone size, $2r'_y$, were calculated using Eqs 3 or 4 [11].

$$\text{plane stress: } 2r_y = (1/\pi)(K/S_y)^2 \qquad 2r'_y = (1/\pi)(\Delta K/2S_y)^2 \tag{3}$$

$$\text{plane strain: } 2r_y = (1/3\pi)(K/S_y)^2 \qquad 2r'_y = (1/3\pi)(\Delta K/2S_y)^2 \tag{4}$$

$K_{max,ss}$ and K_{OL}, were used to calculate $2r_y$, while $\Delta K_{TL} = K_{max,ss} - K_{min,ss}$ for no underload and $\Delta K_{TL} = K_{max,ss} - 0$ with underload was used to calculate $2r'_{y,TL}$. Steady state monotonic plastic zone sizes were all under plane strain. Transient reversed plastic zone sizes were under plane strain or plane stress conditions depending on the ΔK_{ss} and OLR, where higher ΔK_{ss} levels tended to promote plane stress.

Table 4 gives ratios that compare average delay distances to the corresponding calculated transient load reversed plastic zone for tests that resulted in post-transient load FCG. These ratios are denoted $a_d/2r'_{y,TL}$ and are often assumed to be one in fatigue crack growth retardation life prediction models. In Table 4, ratios that involve plane strain plastic zone sizes are shown in standard print, and ratios that involve plane stress are shown in bold print. Table 4 shows $a_d/2r'_{y,TL}$ ratios that involved plane strain plastic zones varied from 0 57, but these two extremes are significant outliers that occurred only with ΔK_{ss} = 4.4 MPa$\sqrt{m}$. The remaining ratios involving plane strain varied from 3.8 11.8. That is, the average delay distance for these conditions were 3.8 11.8 times larger than the applicable plane strain reversed plastic zone size. For tests associated with plane stress conditions, the average delay distances were only 1.0 4.0 times larger than the applicable plane stress reversed plastic zone size. These results distinctly show a better correlation (closer to the value of 1) with tests associated with plane stress conditions.

TABLE 4 *Ratio of delay distance/reversed plastic zone size ($a_d/2r'_{y,TL}$).*

Temperature (°C)	OLR/ULR	ΔK_{ss} (MPa$\sqrt{m}$)* 4.4	8.8	13.2	17.6
	2.0/-0.5	0.0	3.8	7.7	**2.6**
−54	2.0/0.0	0.0	17.0	8.5	**2.1**
	2.5/-0.5	Arrest	9.8	**2.2**	**1.0**
	2.5/0.0	Arrest	10.7	**2.2**	**1.4**
	2.0/-0.5	0	8.8	7.4	**2.6**
25	2.0/0.0	57	6.5	9.1	**2.1**
	2.5/-0.5	Arrest	7.9	**3.1**	**2.4**
	2.5/0.0	Arrest	11.8	**4.0**	Arrest
	2.0/-0.5	N/A	6.1	**2.4**	**1.2**
175	2.0/0.0	N/A	5.6	**2.7**	**1.8**
	2.5/-0.5	N/A	Arrest	**1.3**	**1.2**
	2.5/0.0	N/A	Arrest	**1.2**	**1.3**

*Bold-faced values indicate plane stress.

For a given state of stress, plastic zone sizes (Eqs 3 and 4) are proportional to $(1/S_y)^2$. Thus, for a given state of stress, $2r'_{y,TL}$ values at −54°C were about ¾ that at 25°C, while at 175°C they were about 1.5 times larger than at 25°C. These ratios were valid for all transient test conditions except at ΔK_{ss} = 13.2 MPa$\sqrt{m}$ with 2.0/0 and 2.0/ 0.5 transient loads where plane strain existed at 25°C and −54°C and plane stress existed at 175°C. This gives even a smaller value of $2r'_{y,TL}$ at 25°C and −54°C for these tests. Because delay cycles, N_d, at both −54°C and 175°C were generally larger than at 25°C for a given test condition, this implies that reversed plastic zone size, $2r'_{y,TL}$, was not a consistent indication of delay in these tests.

FCG Life Predictions

FASTRAN III and AFGROW computational fatigue crack growth life software were used to predict the fatigue crack growth delay cycles for each temperature, OLR/ULR, and ΔK_{ss} condition. Details of the FASTRAN III and AFGROW programs can be found in the users' handbooks [12,13]. However, general comments regarding use of each program will be provided. FASTRAN III is a structural analysis program that was developed at NASA by Newman [12] and is based on the plasticity-induced crack closure concept. It utilizes a plasticity-induced closure model that resembles the Dugdale strip-yield model and takes into account load interaction effects. AFGROW is a crack growth life prediction program developed by Harter [13] at Wright-Patterson Air Force Base that has three different load interaction models to choose from. These include models such as the Elber, Willenborg, and Walker.

Like most life prediction/calculation computer codes, FASTRAN III and AFGROW rely heavily on constant amplitude FCG data for input parameters. The constant amplitude fatigue crack growth data itself, as presented in Fig. 2, is not directly used in FASTRAN III but instead is modified in a program called DKEFF. The purpose of DKEFF is to take the da/dN - ΔK data from a constant amplitude test and convert it to a da/dN - ΔK_{eff} relationship. The FASTRAN III code was developed to utilize the effective stress intensity factor and not the nominal stress intensity factor. AFGROW, on the other hand, does not require da/dN - ΔK_{eff} but uses nominal da/dN - ΔK data. Experimental da/dN - ΔK data are curve fit in AFGROW and used as the FCG data input. Both codes include use of adjustable material constants to allow better fit of calculated to experimental results. Default values suggested for various materials within each code also can be chosen.

The purpose of the life predictions in this study was to generate unbiased fatigue crack growth life predictions for the various temperature and loading conditions and to compare the predicted and experimental results. Modifications to various input parameters that allow better fit to calculated values were not done, while suggested or calculated input parameters within each code were used. An important element to the FASTRAN III model is the variable constraint regime between fully-flat (plane strain) and fully-slant (plane stress) crack growth. The constraint loss value, α, was chosen as 2.0 for plane strain and 1.2 for plane stress. In FASTRAN III, α varies from 2 1.2 as the crack grows from a state of plane strain (flat fracture) to one of plane stress (slant fracture). In AFGROW, α remains constant at 2 for all crack growth rates. FASTRAN III also utilizes two FCG rate values (rate1 and rate2) as primary input, where these FCG rates are associated with the transition region from plane strain to plane stress where the constraint varies linearly. The transition point is defined by [12]:

$$\Delta K_{eff,T} = \mu\, \sigma_o \sqrt{B} \tag{5}$$

where $\Delta K_{eff,T}$ is the effective stress intensity factor range at transition, μ is the proportionality coefficient, σ_o is the flow stress (the average of S_y and S_u), and B is the specimen thickness. A value of 0.5 was used for μ as suggested for a wide range of materials and thickness [12]. The extent of the transition region is not well understood, but it is estimated conservatively at 1.5 decades of FCG rate. Based on the calculated $\Delta K_{eff,T}$ at each temperature, the corresponding rates were then determined.

The closure model selected for AFGROW works by determining a value for the crack opening load ratio (P_{op}/P_{max}) for R = 0 called Cf, the closure factor. The closure model is based on a material parameter Cf_o, defined by the following relationship:

$$Cf_o = [(Cf - 1)/(1 + 0.6R)(1 - R)] + 1 \tag{6}$$

where R is the stress ratio. The initial crack opening load level to determine Cf can either be determined from the first cycle of an input spectrum or input by the user if the load history is known. A generic default value of $Cf_o = 0.3$ is suggested in the operation manual. However, a Cf_o value of 0.33 was used, as determined by K_{op}/K_{max} at $\Delta K = 5$ MPa$\sqrt{m}$, for the constant amplitude FCG data associated with Fig. 2 and Table 1. Variations of Cf_o and their effects on the life predictions will be discussed later.

Figure 7 shows a typical da/dN versus a output using FASTRAN III for $\Delta K_{ss} = 13.2$ MPa$\sqrt{m}$ at −54°C for all four transient load types. These crack growth prediction curves are for the same ΔK_{ss} as the experimental data shown in Fig. 5. The minimum crack growth rate for the four OLR/ULR conditions shown is lower for the FASTRAN III predictions than the experimental results. This leads to longer delay lives for the FASTRAN III predictions as discussed later. It should be noted that the FASTRAN III life predictions using the Dugdale yield strip model predicted an initial acceleration following the transient event, then an abrupt deceleration. Fatigue crack growth predictions using FASTRAN III for other temperature and ΔK_{ss} levels produced similar trends.

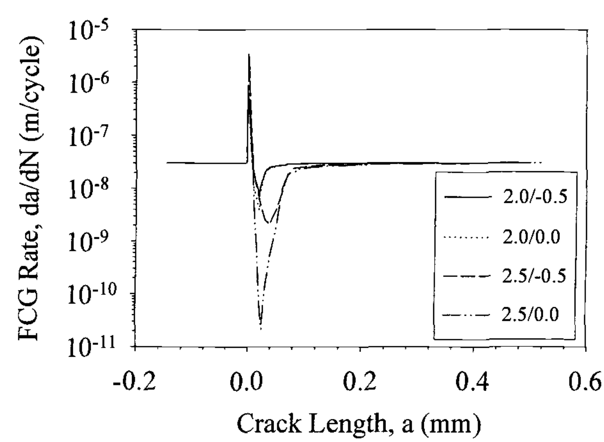

FIG. 7 *FASTRAN III predicted FCG rate versus crack length: $\Delta K_{ss} = 13.2$ MPa $\sqrt{m}$, T = −54°C.*

Table 5 shows the ratio of predicted ($N_{d,pre}$) and experimental ($N_{d,exp}$) fatigue crack growth delay cycles, $N_{d,pre}/N_{d,exp}$, for the FASTRAN III and AFGROW results. Ratios less than one mean conservative life predictions, while ratios greater than one mean non-conservative life predictions. In general, room temperature life predictions compared more favorably to experimental lives than the low and high temperature results, with the high temperature results being least favorable. At 175°C, half of the predictions were overly conservative ($N_{d,pre}/N_{d,exp}$ <

0.5), with AFGROW being more conservative than FASTRAN III. Life predictions were conservative in more cases than non-conservative at each temperature, with each code having a similar number of conservative or non-conservative results. Of the 88 comparable results, 48 were within ± 2 ($0.5 \leq N_{d,pre}/N_{d,exp} \leq 2$) of the experimental results, 19 were overly non-conservative ($N_{d,pre}/N_{d,exp} > 2$), and 21 were overly conservative. Most of the overly conservative life predictions occurred at the two higher ΔK_{ss} conditions (13.2 MPa√m and 17.6 MPa√m), while most of the overly non-conservative life predictions occurred when crack arrest was predicted. FASTRAN III was not able to pre-crack to ΔK_{ss} = 4.4 MPa√m at 175°C, similar to the experimental results, while AFGROW was able to, yet AFGROW calculated arrest with the application of the transient load events. These are designated in Table 5 as "No Test" and "Arrest." In general, FASTRAN III produced slightly better life predictions than AFGROW at room temperature, while the accuracies obtained at –54°C and 175°C were similar for each code. In all transient load events, FCG life predictions at –54°C and 175°C were equal to or greater than FCG life predictions at 25°C for both FASTRAN III and AFGROW. This behavior is consistent with experimental results reported in Table 3.

TABLE 5 *Fatigue life ratio of predicted delay and experimental delay ($N_{d,pre}/N_{d,exp}$).*

		-54°C		25°C		175°C	
ΔK_{ss} (MPa√m)	OLR/ULR	FASTRAN ($N_{d,pre}/N_{d,exp}$)	AFGROW	FASTRAN ($N_{d,pre}/N_{d,exp}$)	AFGROW	FASTRAN ($N_{d,pre}/N_{d,exp}$)	AFGROW
4.4	2.0/-0.5	∞[1]	∞[1]	∞[1]	∞[1]	No test	Arrest
	2.0/0.0	∞[1]	∞[1]	>4	>4	No test	Arrest
	2.5/-0.5	1[2]	1[2]	1[2]	1[2]	No test	Arrest
	2.5/0.0	1[2]	1[2]	1[2]	1[2]	No test	Arrest
8.8	2.0/-0.5	1.8	1.2	1.1	0.6	<0.02[3]	<0.01[3]
	2.0/0.0	0.6	1.1	1.4	1.5	0.6	0.1
	2.5/-0.5	1.4	>16	0.6	0.9	1[2]	1[2]
	2.5/0.0	>8	>8	4.2	>11	1[2]	1[2]
13.2	2.0/-0.5	0.5	0.5	0.8	0.6	0.2	0.1
	2.0/0.0	0.7	0.9	1.0	1.1	0.3	0.3
	2.5/-0.5	0.3	0.3	0.7	0.7	0.1	0.1
	2.5/0.0	0.6	>2	1.2	2.3	1[3]	1[3]
17.6	2.0/-0.5	0.5	0.3	0.8	0.5	0.7	0.3
	2.0/0.0	0.7	0.6	1.4	1.0	0.9	0.5
	2.5/-0.5	0.3	0.2	0.3	0.3	0.4	0.3
	2.5/0.0	>2	>2	<0.6[3]	<0.1[3]	>11	>11

[1] Indicates zero experimental delay.
[2] Indicates experimental arrest and predicted arrest.
[3] Indicates at least one out of three experimental arrests.

The life predictions made using both FASTRAN III and AFGROW are extremely sensitive to key input values as previously mentioned. The FCG rates (rate1 and rate2) used to define the flat to slant transition in FASTRAN III are most accurately obtained by trial and error methods to match experimental and calculated values [12]. In this study, however, Eq 5 was used to define ΔK_{eff} at transition, which then allowed determination of rate1 and rate2 based on 1.5 decades of crack growth rate. At room temperature, the rates (rate1 and rate2) determined and used in the code appear to be good estimates as most of the life predictions were within a factor of ± 2 of the experimental. However, at –54°C and 175°C, the life predictions did not fair as well. Thus the suggestion that the transition region take place over 1.5 decades of growth appear to be most accurate for room temperature FCG behavior.

Life predictions made using AFGROW used $Cf_o = 0.33$ for all three test temperatures. This value was determined using crack opening data from an earlier study [7] where at near threshold ($\Delta K = 5$ MPa$\sqrt{m}$), $Cf = K_{op}/K_{max} = 0.36$ for both –54°C and 25°C. However, at the same ΔK ($\Delta K = 5$ MPa$\sqrt{m}$) at 175°C, $Cf = 0.72$, resulting in $Cf_o = 0.71$. Life predictions performed using $Cf_o = 0.71$ resulted in complete arrest at all ΔK_{ss} and OLR/ULR test conditions, thus this value of Cf_o was unreasonable. To be consistent, Cf_o was chosen as 0.33 for all three temperatures. A $Cf_o = 0.37$ used to make subsequent calculations at 175°C did produce more favorable results, however, these results were not included, as they were generated in a biased manner. Selecting $Cf_o = 0.3$ as suggested in the manual as a default value resulted in even more conservative life predictions than using $Cf_o = 0.33$.

The better FCG life predictions observed at 25°C in comparison to –54°C and 175°C are attributed to the fact that other closure mechanisms are operating at –54°C and 175°C, such as roughness-induced and oxide-induced in conjunction with plasticity-induced closure [7]. Neither FASTRAN III nor AFGROW account for these other closure mechanisms. Development of computer codes that take into account the various crack closure mechanisms will lead to the ability to make more accurate life predictions for a wide range of load and temperature conditions.

Fractography

Fractographic analysis using scanning electron microscopy was made for many of the transient loadings. Most analysis was performed near the end of a specimen testing to minimize load history effects. Analysis consisted of surface crack profiles and the fracture surfaces. In all micrographs that follow, fatigue crack growth is from left to right.

Figure 8 shows fatigue crack profiles along the specimen surfaces for $\Delta K_{ss} = 8.8$ MPa$\sqrt{m}$ with OLR/ULR = 2.5/0 at –54°C and 175°C. Transient load applications are noted with arrows. Surface crack closure is observed for a distance of approximately 40 μm (0.04 mm) in the post-transient load application region at both temperatures, but is more evident at –54°C, Fig. 8*a*. No crack closure is evident in the pre-transient load fatigue region. In fact, the crack is open approximately 2 3 μm along the surface crack profile prior to the overload and approximately the same amount after the surface crack closure region. Surface Mode II displacement is evident at both temperatures and was also observed at 25°C at this and other ΔK_{ss}. Under all temperature and loading conditions, fatigue crack growth before, during, and after a transient load was transcrystalline. At $\Delta K_{ss} = 4.4$ MPa$\sqrt{m}$ and 8.8 MPa$\sqrt{m}$, no surface crack extension (stretch) during a transient load event was observable using a 30× traveling microscope.

Figure 9 shows typical fractographs involving mid-thickness fracture surface morphology from the transient event shown in Fig. 8. While no stretch was observable on the surface profiles at $\Delta K_{ss} = 8.8$ MPa$\sqrt{m}$, Fig. 8, stretch zones were apparent at both –54°C and 175°C at the mid-section. For a given transient event, stretch zones were largest at –54°C and smallest at 175°C. The stretch zone shown in Fig. 9*a* is relatively flat with limited faceting, while the stretch zone in Fig. 9*b* is small and resembles a beachmark, identifying the transient load application.

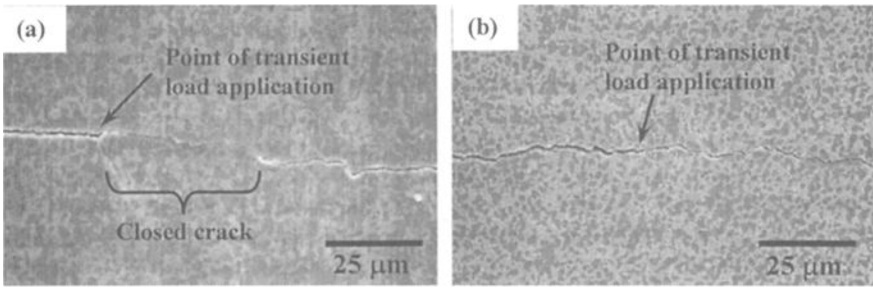

FIG. 8 *Transient load surface profile: ΔK_{ss} = 8.8 MPa$\sqrt{m}$, OLR/ULR = 2.5/0: (a) −54°C, (b) 175°C.*

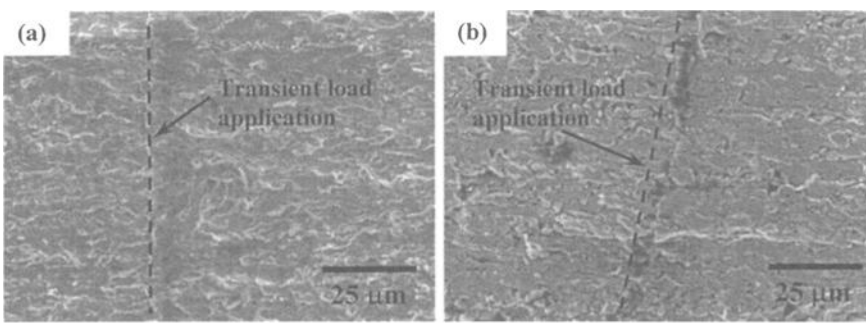

FIG. 9 *Transient load fracture surface: ΔK_{ss} = 8.8 MPa$\sqrt{m}$, OLR/ULR = 2.5/0: (a) −54°C, (b) 175°C.*

Figure 10 shows typical surface crack profiles at ΔK_{ss} = 17.6 MPa$\sqrt{m}$ with an OLR/ULR = 2.5/0 at all three temperatures. Surface deflection behavior as evident in Fig. 10 was common for higher ΔK_{ss} levels where plane stress conditions due to the overload existed, as identified in Table 4. Surface crack deflection typically occurred at about 45°, and with subsequent growth, returned primarily to a Mode I crack extension. At higher ΔK_{ss} levels, stretch during a transient load event was observed on the free surface, unlike that at ΔK_{ss} = 8.8 MPa$\sqrt{m}$. At higher ΔK_{ss} and higher OLR transient load applications, crack branching, crack tip blunting, and secondary cracking were more prevalent than at lower ΔK_{ss} values. Surface crack closure was observed in some cases after the point of transient load application and at the higher ΔK_{ss} levels, crack closure often encompassed the surface stretch zone portion of the crack.

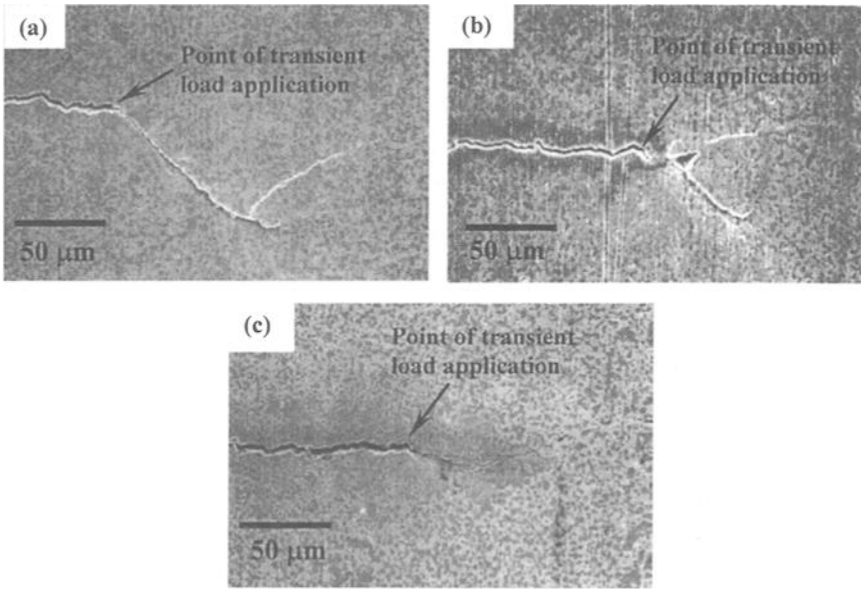

FIG. 10 *Transient load surface profile: ΔK_{ss} = 17.6 MPa$\sqrt{m}$, OLR/ULR = 2.5/0:* (a) *−54°C,* (b) *25°C,* (c) *175°C.*

Macro fracture surfaces showing typical stretch zones during transient loading are shown in Fig. 11 for −54°C and 25°C. Stretch zones observed at higher ΔK_{ss} levels were usually rough or granular in texture and increased in size with higher ΔK_{ss}, higher overload, and lower temperature. Stretch at the mid-section approached 0.5 mm at ΔK = 17.6 MPa$\sqrt{m}$, OLR = 2.5, and −54°C, yet was less than 0.1 mm at 25°C for the same OLR. For a given transient event, the extent of the stretch zone did not necessarily dictate the degree of crack growth delay. Stretch zones were much more prominent at OLR = 2.5 in comparison to OLR = 2. Stretch zone behavior was similar for both overload only and overload followed by an underload, where the underload had little influence on the stretch zone. The top and bottom of Fig. 11 (*a* and *b*) approximately indicate the free surface of the specimens showing very little stretch at the surface with significant stretch or crack tip tunneling, at the mid-section of the specimen. The higher magnification section shown in Fig. 11*a* indicates the different morphology associated with a transient load and a return to steady state. The overload region (K_{max} = 49 MPa$\sqrt{m}$) was characterized by ductile dimples, while elongated facets in the direction of crack growth characterized the transition and steady state region. The transition region following the stretch zone, as seen in Fig. 11*a*, was always less than the delay distance, a_d. In many cases, the transition region was not discernible from the steady state region.

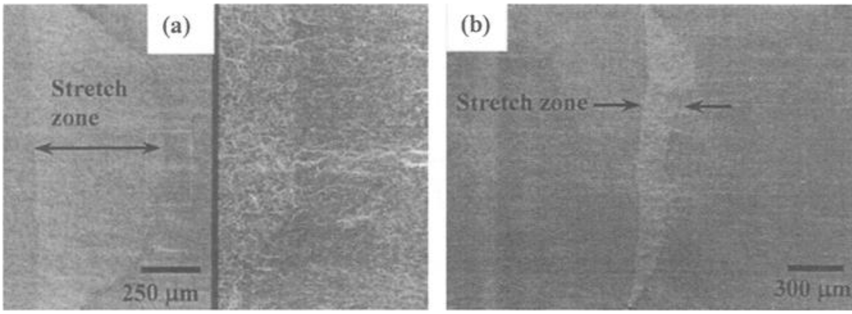

FIG. 11 *Transient load fracture surface: ΔK_{ss} = 17.6 MPa$\sqrt{m}$, OLR/ULR = 2.5/-0.5: (a) –54°C, (b) 25°C.*

Comparison with Ti-62222 Mill Annealed Material

A similar transient load test program was applied previously to Ti-62222 1.61 mm thick M(T) sheet specimens in the mill annealed, MA, condition at the same three temperatures [9]. This condition resulted in about a 15 % decrease in monotonic strength properties relative to the solution treated and aged, STA, condition. The MA FCG was also transcrystalline. For both materials, higher OLR increased delay cycles at all temperatures except when fracture occurred in MA at –54°C with the higher OLR and highest ΔK_{ss}. Underloads were usually detrimental. N_d was consistently larger for MA relative to STA at –54°C and 25°C, with greater similarity at 175°C. The MA material, as with the STA material, had increased or similar delay cycles at –54°C and 175°C relative to 25°C. The ratio a_d /$2r'_{y,TL}$ for the MA material was also not a correlating factor with values ranging from 0 60. Multiple FCG mechanisms from transient loads also were observed with the MA material.

Summary and Conclusions

1. Fatigue crack growth response to a transient load was dependent upon ΔK_{ss}, OLR/ULR, and temperature. Specific trends, however, were sometimes mixed, making it more difficult to draw specific conclusions.
2. Delay cycles, N_d, increased with the overload ratio, while an underload following an overload tended to decrease delay life particularly at the higher OLR of 2.5.
3. Delay cycles, N_d, for a given transient load, were usually greater at –54°C and 175°C than at 25°C, consistent with FASTRAN III and AFGROW predictions.
4. Minimum FCG rates following a transient loading ranged from 1 3 orders of magnitude lower than steady state rates.
5. A 1:1 correlation between measured average delay distance, a_d, and reversed plastic zone size, $2r'_{y,TL}$, was not evident, since delay distances were often much larger than the reversed plastic zone. $2r'_{y,TL}$ by itself was also not a consistent indication of delay cycles. Most of the delay cycles occurred within about 0.05 mm of crack growth following a transient event.

6. More than half of the FCG life predictions using FASTRAN III and AFGROW for the various load/temperature conditions gave results within ± 2 times those of the experimental results.
7. Life predictions were more accurate at 25°C in comparison to –54°C and 175°C. This was attributed to the fact that FASTRAN III and AFGROW are based on plasticity-induced closure models, while at –54°C and 175°C, other closure mechanisms are significant and operate in conjunction with plasticity-induced closure.
8. Stretch zones due to transient loading often experienced significant tunneling and increased with OLR and ΔK_{ss}. Stretch zone size also increased at –54°C but decreased at 175°C.
9. Surface crack profiling revealed transcrystalline FCG only, Mode II displacements, no crack closure before transient loadings, and crack closure, crack tip deflection, blunting, and branching after transient loadings. Fractographic evaluation indicated elongated facets and isolated secondary cracking. Stretch zones contained ductile dimples. These fractographic findings indicate multiple mechanisms are involved with this transient behavior and include crack closure, crack tip tunneling, blunting, and branching.

References

[1] *Fatigue Crack Growth Under Spectrum Loading, ASTM STP 595*, ASTM International, West Conshohocken, PA, 1976.

[2] Wei, R. P. and Shih, T. T., "Delay in Fatigue Crack Growth," *International Journal of Fracture*, Vol. 10, 1974, pp. 77 85.

[3] Vecchio, R. S., Hertzberg, R. W., and Jaccard, R., "Overload Induced Crack Growth Rate Attenuation Behavior in Aluminum Alloys," *Scripta Metallurgica*, Vol. 17, 1983, pp. 343 346.

[4] Ward-Close, C. M. and Ritchie, R. O., "On the Role of Crack Closure Mechanisms in Influencing Fatigue Crack Growth Following Tensile Overloads in a Titanium Alloy: Near Threshold Versus Higher ΔK Behavior," *Mechanics of Fatigue Crack Closure, ASTM STP 982*, J. C. Newman, Jr. and W. Elber, Eds., ASTM International, West Conshohocken, PA, 1988, pp. 93 111.

[5] Wheatley, G., Hu, X. Z., Estrin Y., "Effects of a Single Tensile Overload on Fatigue Crack Growth in a 316L Steel," *Fatigue and Fracture of Engineering Materials and Structures*, Vol. 22, 1999, pp. 1041 1051.

[6] Phillips, E., "Periodic Overload and Transport Spectrum Fatigue Crack Growth Tests in Ti-62222 STA and Al-2024-T3 Sheets," Langley Research Center, Hampton, VA, NASA TM 208995, NASA, 1999.

[7] Stephens, R. R., Stephens, R. I., Lemm, D. E., Berge, S. G., Liknes, H. O., and Cousins, C. J., "Role of Crack Closure Mechanisms on Fatigue Crack Growth of Ti-62222 Under Constant Amplitude and Transient Loading at –54, 25, and 175°C," *Advances in Fatigue Crack Closure Measurements and Analysis, ASTM STP 1343*, R. C. McClung and J. C. Newman, Jr., Eds., ASTM International, West Conshohocken, PA, 1999, pp. 224 245.

[8] Cox, J. M., Pettit, D. E., and Langenbeck, S. L., "Effect of Temperature on the Fatigue Properties of 7475-T761 Aluminum," *Fatigue at Low Temperature, ASTM STP 857*, R. I. Stephens, Ed., ASTM International, West Conshohocken, PA, 1985, pp. 241 256.

[9] Stephens, R. I., Stephens, R. R., and Schoenefeld, D. A., "Effect of Transient Loads on Fatigue Crack Growth in Mill Annealed Ti-62222 at –54, 25, and 175°C," *Fatigue and*

Fracture Mechanics: 33rd Vol., ASTM STP 1417, W. G. Reuter and R. S. Piascik, Eds., ASTM International, West Conshohocken, PA, 2002, pp. 557 572.

[10] Stephens, R. R., Stephens, R. I., Veit, A. L., and Albertson, T. P., "Fatigue Crack Growth of Ti-62222 Titanium Alloy Under Constant Amplitude and miniTWIST Flight Spectra at 25°C and 175°C," *International Journal of Fatigue*, Vol. 19, No.4, 1997, pp.301 308.

[11] Stephens, R. I., Fatemi, A., Stephens, R. R., and Fuchs, H. O., *Metal Fatigue in Engineering*, 2nd Ed., John Wiley & Sons, Inc., New York, 2001.

[12] Newman, J. C. Jr., "FASTRAN II-A Fatigue Crack Growth Structural Analysis Program," NASA TM 104159, NASA, 1992.

[13] Harter, J. A., "AFGROW Users Guide and Technical Manual," AFRL-VA-WP-RP-2000, Wright Patterson Air Force Base, OH, 2000.

Journal of ASTM International, September 2004, Vol. 1, No. 8
Paper ID JAI19036
Available online at www.astm.org

Fraser J. McMaster[1] *and Peter C. McKeighan*[1]

Spectrum Coupon Testing of Fatigue-Resistant Fasteners for an Aging Military Aircraft

ABSTRACT: An experimental program of work was undertaken to assess the life improvement gained through utilizing cold expansion technology to enhance the resistance of cracking at fatigue critical locations (FCLs) in an aging military trainer aircraft. The FCLs considered included a countersunk hole and nutplate on two different wing spars. The overall goal of the experimental work was to provide a comparative assessment of the influence of the major variables examined, which included cold expansion method and process, hole size, countersink size, nutplate geometry, flight spectrum, and joint configurations. The results of this work clearly illustrated the inherent sensitivity of life improvement factors to the myriad of variables involved. Nevertheless, the foregoing experimental work clearly demonstrated the valuable life improvement that is provided by cold expansion for nearly all cases examined.

KEYWORDS: cold expansion, fatigue, life improvement, spectrum testing

Introduction

Historically, the highest incidence of aircraft structural fatigue has been associated with holes in fastened joints and other stress concentrations in the structure. Modern manufacturing technologies and closer attention to detailed design and analysis of fatigue-sensitive joints have substantially reduced the occurrences of severe structural fatigue damage at holes in newer aircraft. However, in many cases the growing need to extend the operational lives of existing aircraft to well beyond their original life expectancies requires the use of all tools available to maximize the fatigue lives at holes and other stress concentrations. Relatively simple and cost-effective techniques have been used for many years to improve the fatigue resistance of fastener holes. An example is the cold expansion process, which generates beneficial residual stresses around the hole by permanently enlarging the hole. The work described in this paper outlines a testing program undertaken to assess the life improvement gained through utilizing cold expansion technology to enhance the resistance of crack initiation and propagation at fatigue-critical wing locations on the United States Air Force (USAF) T-38 trainer aircraft [1].

The introduction of the cold expansion process to the T-38 wing refurbishment program was performed so as to obtain the target service life of the wing; that is, 4000 and 12 000 flight hours for the Lead In Fighter (LIF) and Student Undergraduate Pilot Training (SUPT) usages, respectively. The fatigue critical locations (FCLs) considered in this testing program included a nutplate configuration around the aileron access door (44 % spar) at wing station (WS) 92, and a

Manuscript received 28 May 2002; accepted for publication 8 April 2003; published September 2004. Presented at ASTM Symposium on Fatigue Testing and Analysis Under Variable Amplitude Loading Conditions on 29 31 May 2002 in Tours, France; P. C. McKeighan and N. Ranganathan, Guest Editors.

[1] Senior Research Engineer and Manager, respectively, Mechanical and Materials Engineering Division, Southwest Research Institute®, 6220 Culebra Road, San Antonio, TX, 78238-5166.

countersunk hole along the 15 % spar at WS 64.8. Both of these FCL geometries have a short edge distance. The overall goals of this program included a number of key interrelated efforts:

- determine the benefits of cold working for a countersunk hole
- evaluate the effectiveness of contractor-developed tooling for countersunk holes
- determine the effect of various cold expansion techniques for a nutplate hole geometry
- assess the difference between fastener-filled holes and load-carrying joints
- compare the relative life improvement gained with different hole geometries
- assess the difference between two different cold expansion procedures

In this paper, the key variables and conditions evaluated during the testing program are outlined, with the results of experimental fatigue tests performed on the nominated FCLs provided. Relevant discussion of the key observations and conclusions made during the testing program are presented.

Test Program

Material

The material used in the lower wing structure of the T-38 aircraft is 7075-T7351 aluminum plate. Given the geometric dimensions for each of the FCLs, a 0.250 in. (6.35 mm) thick plate, 48 in. × 144 in. (1.220 m × 3.658 m) section, was selected as the most appropriate to manufacture the relevant specimens. Limited tensile tests, performed in accordance with ASTM Standard Test Methods for Tension Testing of Metallic Materials (E8-00), were undertaken to verify that the 7075-T7351 plate did in fact meet aerospace grade material specifications. The blanks were machined into standard specimens with gage lengths of 2.000 in. (50.8 mm). A summary of the tensile data obtained for the 7075-T7351 aluminum plate is shown in Table 1. All data exceeded the minimums provided for this material as presented in MIL Handbook 5G [2].

TABLE 1 *Average mechanical properties of Al 7075-T7351.*

Orientation	Elastic Modulus, E (GPa)	0.2 % Yield Stress (MPa)	UTS (MPa)	Elongation (%)
Longitudinal	71.6	427.5	497.8	11.9
MIL HNDBK 5G min	71.0	393.0	468.9	7.0

Specimen Geometries and Cold Working Methods

The fatigue testing included in this program evaluated the influence of cold working on total fatigue life, including crack initiation and propagation. Two different types of specimen geometries were considered: a countersunk fastener hole and a nutplate geometry, as shown schematically in Fig. 1.

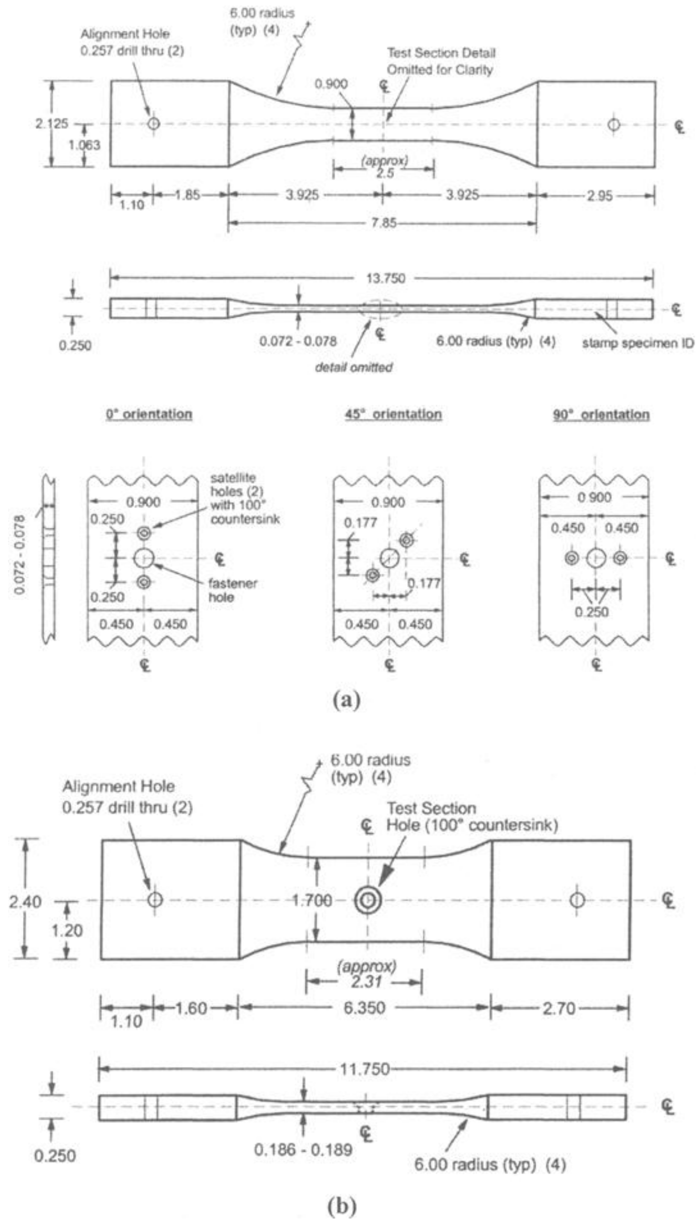

FIG. 1 *Test specimen geometries: (a) the nutplate hole specimen and (b) the countersunk hole specimen. All dimensions in inches.*

The manufacture of the required specimens was a multi-step process involving specimen machining, cold working, and installation of fasteners. Seven different types of countersunk hole specimens and four different types of nutplate specimens were manufactured, as detailed in Tables 2 and 3, respectively.

TABLE 2 *Details of the countersunk hole specimen testing.*

Flight Spectrum	Type of Hole	Specimen Configuration
LIF	CO	conventional C-sunk hole
	OS	1st oversize C-sunk hole
	OE	1st oversize cold-expanded C-sunk hole
	OE′	1st oversize cold-expanded C-sunk hole (undersize C-sink)
	COJ	conventional C-sunk hole joint
	OEJ	1st oversize cold-expanded C-sunk hole joint
	OE′J	1st oversize cold-expanded C-sunk hole (undersize C-sink) joint
SUPT	CO	conventional C-sunk hole
	OS	1st oversize C-sunk hole
	OE	1st oversize cold-expanded C-sunk hole
	OE′	1st oversize cold-expanded C-sunk hole (undersize C-sink)

TABLE 3 *Details of the nutplate specimen testing.*

Flight Spectrum	Configuration	Cold Expansion		Satellite Hole	Hole Description
		Procedure	Done By		
LIF	conventional nutplate	None		0°	filled
				0°	open
				45°	filled
				90°	filled
				90°	open
	nominal ForceTec®	FTI	FTI	0°	filled
				45°	filled
				90°	filled
	nominal ForceMate®	FTI	FTI	0°	filled
				45°	filled
				90°	filled
		FTI	USAF	45°	filled
		USAF	USAF	45°	filled
	2nd oversize ForceMate®	FTI	FTI	0°	filled
				45°	filled
				90°	filled
		USAF	USAF	45°	filled

The two types of cold-expansion methods used on the nutplate specimens were the ForceTec® and ForceMate® methods (Fatigue Technologies, Inc., Seattle, WA). Both cold-expansion arrangements are illustrated in Fig. 2. The rivetless nutplate (or ForceTec®) system, patented by Fatigue Technologies Inc (FTI), uses an interference fit to hold the nutplate in place as opposed to the two satellite hole fasteners for the conventional nutplate and ForceMate® configuration. In order to reflect the T-38 wing hardware, coupons were processed already having a conventional nutplate geometry machined in them. The ForceMate® method radially expands an initially clearance fit, internally lubricated bushing into the hole using a tapered expansion mandrel. When the mandrel is drawn through the bushing, the bushing and surrounding metal are subjected to radial expansion forces. The radial expansion and subsequent unloading impart residual stresses around the hole and simultaneously install the bushing with a high interference fit.

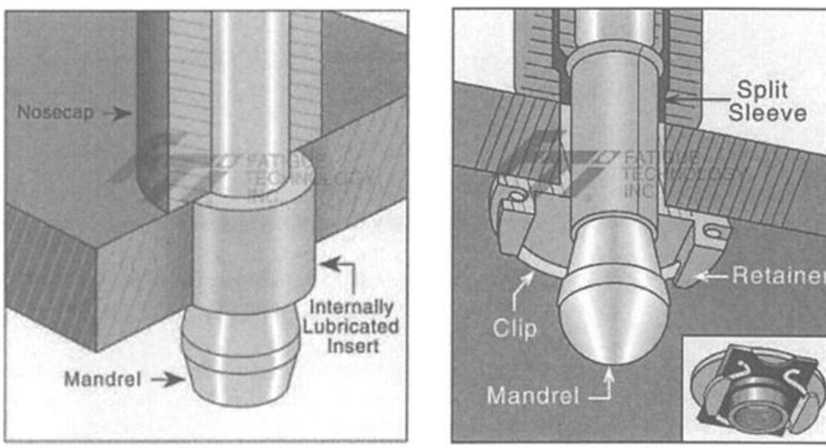

(a) (b)

FIG. 2 *The cold-expansion methods used on the nutplate geometry: (a) ForceMate® and (b) ForceTec® (figures obtained from FTI website: www.fatiguetech.com).*

An extension to the nutplate testing program was added, which centered on the cold expansion process used when applying the ForceMate® method. The two processes involved (i) the FTI recommended approach and (ii) the streamlined USAF technique. Both of these processes are described in detail in Table 4.

The amount of cold expansion for all specimens approximately ranged from 4.5 5.0 %. For the countersunk specimen, an aluminum backup plate was used to provide in-plane stability and to simulate a stiff rib in the T-38 wing for the 15 % spar location. A limited number of load transfer joints was also considered in this work. The coupon design used was a relatively low load transfer, single shear lap joint termed a 1½ dogbone specimen. This configuration has been analyzed and used in other studies involving the fatigue behavior of joints [3 5]. These studies have shown that between 25 35 % of the load is transferred from the half-length specimen to the longer, full-length specimen. However, for this testing the measured load transfer (from strain gaged specimens) was approximately 2 3.5 %. The majority of specimens tested had fasteners installed in the holes and therefore required spacer blocks between the specimen and fastener end to simulate built-up structure. This was a built-up structure simulation only, since no load was transferred through the fastener. Nevertheless, the clamping force as well as the rubbing and fretting associated with built-up structure are simulated with this arrangement.

TABLE 4 *Overview of the ForceMate® cold-expansion procedures.*

Step	Original Cx Procedure (FTI)	Revised Cx Procedure (USAF)
1	Ream screw hole to presize	Ream screw hole to presize
2	Ream rivet holes to presize	
3	Pin rivet holes	
4	ForceMate® bush screw hole	ForceMate® bush screw hole
5	Remove pins from rivet holes	Ream rivet holes to presize
6	Pin bushing in screw hole	
7	Cold work rivet holes	Cold work rivet holes
8	Remove pin from screw hole	

Stress Spectra Development

Stress sequences for this program were based on flight-recorded data from the LIF and SUPT usages. The USAF collected the LIF usage data during the period of April 1987 February 1992. The SUPT usage data was collected by Southwest Research Institute (SwRI®) during the period of November 1993 April 1994. These data were expressed as tables of discrete normal load factor (N_z) occurrences by flight condition as computed by the Spectra and Operational Usage Profiles (SOUP) program [6].

These tables of N_z occurrences were used as input to the modified Aircraft Stress Sequence Program (ACSTRSEQ) [7]. ACSTRSEQ chooses a random sequence of N_z occurrences, determines the aircraft external loads for each occurrence, computes the stress based on established stress-to-load ratios, and outputs the stresses in proper sequence format.

A summary of each of the three spectra, indicating the number of cycles per pass and the minimum and maximum applied stress, is indicated in Table 5. In terms of stress levels, there appears to be little significant difference between the different spectra. Figure 3 examines each sequence in terms of stress range after rainflow counting the stresses for the countersunk hole FCL on the 15 % spar. The overall span of the stress range does not differ by much between spectra, with the percent of cycles (per pass) for the higher stress ranges greater in the LIF spectrum. Although the spectra data presented in Fig. 3 is for the 15 % spar FCL, the general trend and relative level of usage severity is the same for the nutplate FCL.

TABLE 5 *Summary of applied test spectra.*

Specimen Type	Spectra	Cycles per Pass	Stress Levels (MPa)	
			Max.	Min.
countersunk hole	LIF	63 280	238.5	–73.2
countersunk hole	SUPT	34 184	232.2	–64.5
nutplate	LIF	63 171	254.6	–62.9

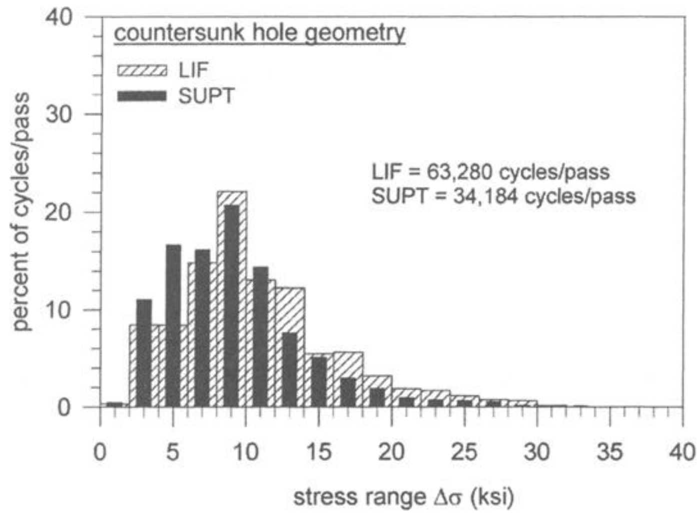

FIG. 3 *Comparison between the two spectra used for the testing.*

Testing Procedures

The test procedures used during the fatigue testing of the countersunk and nutplate specimens were developed from many years of experience performing similar testing. Although the testing was highly non-standard, basic practice loosely conformed to the relevant ASTM crack propagation and initiation standards (e.g., E647 Test Method for Measurement of Fatigue Crack Growth Rates and E606 Practice for Strain-Controlled Fatigue Testing). Prior to applying a spectrum to the test specimen, special procedures were employed to ensure computer file integrity. These procedures included:

- verifying that the minimum and maximum spectrum loads (or stresses) were consistent with previous analysis
- verifying the number of endpoints, or alternatively cycles, was in accordance with analysis

Experience has shown that this is effective for making sure that the load files, typically quite long and difficult to review manually, do not become electronically corrupted in the transfer process.

The spectrum test utilized closed-loop, servohydraulic testing systems specially designed to apply variable amplitude waveforms. The stress spectra were stored electronically in a format compatible with SwRI's computer software/hardware systems. The closed-looped control systems [8] used in the test systems ensure that the peak load levels are applied to the specimen during cycling. One of the key features of the systems used in the lab is a command/feedback certification procedure utilizing modification of the command signal based on the historical feedback performance during the last spectrum pass. This assures the most accurate and consistent loading of the specimen during testing.

The grips and fixtures employed were based upon proven methods for obtaining axial tension-compression data from test coupons under spectrum loading conditions. Clamp-type test clevises provided the primary gripping action, and the alignment was achieved with strain gaged dummy specimens, so as to ensure the loading train was aligned within the minimum specified in E647. The alignment was locked in place with spiral washers after the application of a tensile load that was greater than any occurrence in the test spectrum. Thus, the alignment was fixed, and the backlash associated with the threaded connection to the load cell and hydraulic ram was eliminated.

A fixed constraint, or anti-buckling guide, was attached to the main clevis to provide support for a variety of Teflon-coated movable, or free, constraints. The movable constraints located between the fixed constraint and test section were free to move in a vertical direction only. Horizontal constraint was achieved through set screws that were located in the fixed constraint.

A selection of the countersunk hole joint specimens was strain gaged with a number of gages so that periodic compliance traces could be recorded during the joint fatigue tests. Conventional gage installation methods were used to affix the gages to the specimens adhesively. The periodic compliance trace is obtained by recording a load-strain cycle for a load excursion from 0 80 % of the peak spectrum load. The compliance traces were subsequently least-squares fit to calculate the slope of the linear region for the loading and unloading portion of the cycle.

The compliance traces also provided enough information to calculate the amount of load transfer obtained in the structural joint. The degree of load transfer gives an indication of how much of the load in the full dogbone is transferred through the joint into the ½ dogbone section.

Spectrum Fatigue Testing Results

Countersunk Hole Specimens

The total fatigue life for all tests performed on the countersunk hole specimens is shown in Fig. 4 in terms of spectrum usage and hole configuration. Specimen details are given in Table 2. These fatigue life values include both crack initiation and propagation to failure. The fatigue life is presented in terms of thousand spectrum flight hours (kSFH), which represents one pass through the spectrum. The mean life (± two standard deviations) is presented, with the standard deviation range representing a 95 % confidence interval assuming the distribution of total life is distributed normally. Discussion of the results will be based on the average results unless otherwise stated.

Comparing the non-cold worked specimens (type CO and OS, as shown in Fig. 4), a factor of 1.5 improvement in life in the first oversized specimens (OS) is shown. This is surprising in that the larger OS hole has a much smaller net section due to the larger, deeper countersink and hole diameter and would be expected to show lower fatigue lives. However the OS specimens did show larger scatter in fatigue lives compared to the CO specimens.

A comparison between the LIF and SUPT spectra for similar specimen types is provided in Table 6, with fatigue life given as a ratio of the average LIF and SUPT lives. As shown, the SUPT usage has between a 2 5 increase in fatigue life. This is to be expected as the LIF spectrum has significantly more cycles than the SUPT usage (1.85×). The amount of scatter was by far the greatest in the SUPT spectrum tests, with up to 14 times greater spread in standard deviation (2SD) for the SUPT tests.

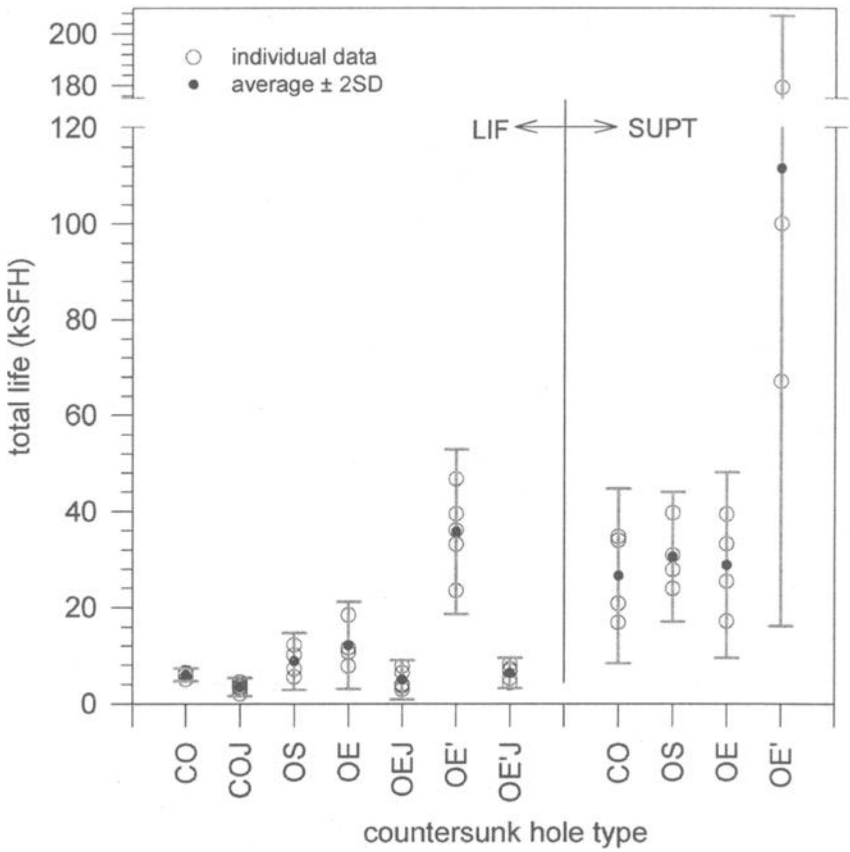

FIG. 4 *Summary of fatigue life results for the countersunk hole geometry.*

TABLE 6 *The effect on fatigue life for the two different flight spectra.*

Type of Hole	Configuration	Fatigue Life Ratio (N_{SUPT}/N_{LIF})
CO	conventional C-sunk hole	4.46
OS	1st oversize C-sunk hole	3.49
OE	1st oversize cold-expanded C-sunk hole	2.38
OE′	1st oversize cold-expanded C-sunk hole (undersize C-sink)	3.12

The improvement in life obtained by cold working will depend on a number of factors, which include the degree of expansion, the type of loading, material, hole geometry, and the load transfer characteristics of the joint. A number of studies [9 11] have indicated that the cold expansion process can increase the fatigue life by factors of 2 5×. A comparison between the cold worked and non-cold worked countersunk hole specimens is provided in Table 7, with the fatigue life given as a ratio of the average cold worked and non-cold worked lives. The mean lives of the cold expanded specimens increased for both the LIF and SUPT spectra, however, the degree of scatter increased for the cold expanded specimens, with the standard deviation bars on Fig. 4 encompassing the non-cold worked specimen results, apart from the OE′ geometry, which had significantly greater fatigue lives. Consequently, little statistically significant difference between a conventional and cold worked countersunk hole is indicated if a conservative approach is applied.

One exception to the above observation is the extremely good performance of the OE′ geometry specimens under both the LIF and SUPT spectra (see Fig. 4). Recall that these were specimens with an oversized hole and an undersized countersink. Two of the specimens tested under the SUPT spectrum were stopped prior to failure due to the number of flight hours reaching the designated runout level (100 kSFH). However, one specimen was allowed to continue past this runout ceiling and reached a total of 179 kSFH before failure. The results obtained in a previous program [2] indicated that the fatigue life for a similar countersunk hole (unfilled) with the OE′ geometry had unusually good performance (compared to the OE and CO geometries). Therefore, a large improvement in fatigue life is attainable by using cold expansion, an undersize countersink, and shear head fastener in the non-joint configuration.

TABLE 7 *The effect on fatigue life for cold worked and non-cold worked specimens.*

Flight Spectrum	Type of Hole	Configuration	Fatigue Life Ratio ($N_{Cx}/N_{non\text{-}Cx}$)
LIF	OE	1st oversize Cx C-sunk hole	1.08
	OE′	1st oversize Cx C-sunk hole (undersize C-sink)	4.20
SUPT	OE	1st oversize Cx C-sunk hole	2.03
	OE′	1st oversize Cx C-sunk hole (undersize C-sink)	6.01

A number of specialized joint tests were also undertaken for the countersunk hole geometry. A comparison of the fatigue lives for these joint specimens is provided in Table 8, with fatigue life given as a ratio of the average joint and non-joint lives. The average fatigue lives for the countersunk hole joint specimens showed a large decrease compared to the non-joint specimens. This could be attributed to the introduction of bending stresses in the test section, caused by the asymmetry of the joint geometry, which would have a detrimental effect on the fatigue lives.

TABLE 8 *The effect on fatigue life for countersunk hole joint specimens.*

Flight Spectrum	Type of Hole	Configuration	Fatigue Life Ratio ($N_{joint}/N_{non\text{-}joint}$)
LIF	CO	conventional C-sunk hole	0.57
	OE	1st oversize Cx C-sunk hole	0.41
	OE′	1st oversize Cx C-sunk hole (undersize C-sink)	0.18

Nutplate Specimens

The types of nutplate specimens tested in this program consisted of conventional nutplates, cold expanded rivetless nutplates (ForceTec®), and cold expanded bushed hole nutplates (ForceMate®). A number of different variables was studied using these three types of nutplates, including nominal versus oversized holes, filled versus open holes, and differences in cold expansion procedures.

The total fatigue life for all nutplate tests performed is shown in Fig. 5 in terms of nutplate configuration and cold expansion method. Specimen details are given in Table 3. Again, the fatigue life is presented in terms of thousand spectrum flight hours (kSFH), with the mean life (± two standard deviations) also presented. Due to the large amount of data presented in Fig. 5, a number of different comparative tables will be presented that more clearly detail the different variables tested using the nutplate geometry.

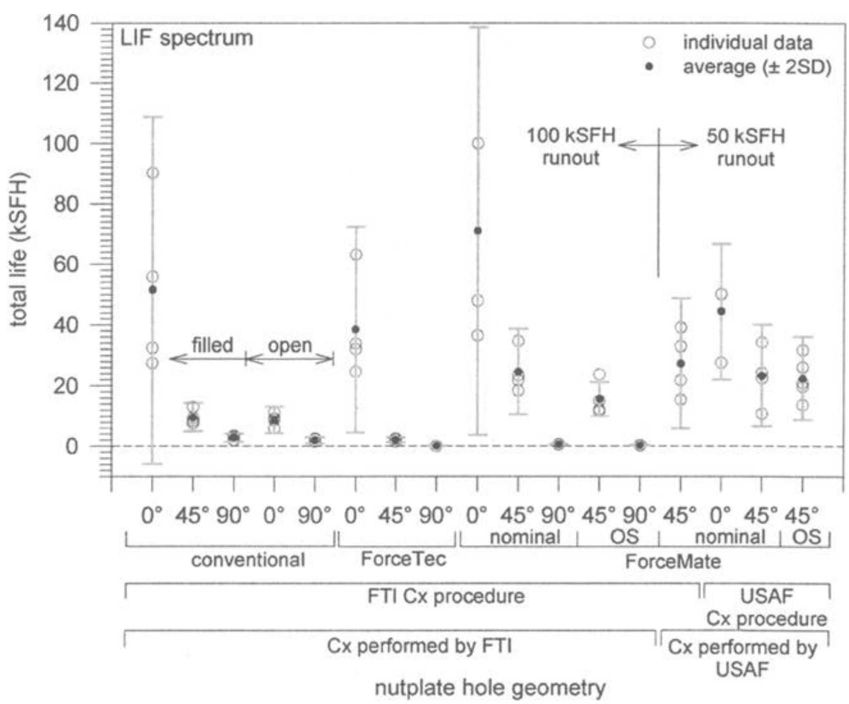

FIG. 5 *Summary of fatigue life results for the nutplate hole geometry.*

A direct comparison between a filled and open hole conventional nutplate (0° and 90° orientation) was performed in this program with the results summarized in Table 9 in terms of a fatigue life ratio of the open and filled hole fatigue lives. The ratio is calculated from the average fatigue lives of the tests. The much longer fatigue lives for the filled fastener hole are to be expected. As a filled specimen is loaded and the hole deforms, the fastener would be squeezed and subsequently impart a compressive stress at the most critical location of the hole, therefore improving the fatigue life of the nutplate specimen. This improvement in average fatigue life for a filled hole compared to an open hole was found to be in excess of 5× for the 0° orientation nutplate. However, for the 90° orientation nutplate, this increase in average fatigue life was only 1.5×, with the scatter of the individual fatigue lives for filled and open holes overlapping considerably, with no conclusive difference to be found from the results. Also the results for all tests performed on the 90° orientation nutplate specimens, both conventional and cold worked, produced very low fatigue lives as will be discussed below.

TABLE 9 *The effect on fatigue life for nutplate specimens with open/filled holes.*

Flight Spectrum	Configuration	Satellite Hole	Fatigue Life Ratio (N_{open}/N_{filled})
LIF	Conventional nutplate	0°	0.17
		90°	0.68

Comparing the fatigue lives for the cold expanded nutplate geometries with the conventional nutplate highlights some interesting differences between the specimens. The results for the cold expanded nutplates (cold expansion performed by FTI) are summarized in Table 10 in terms of a fatigue life ratio of the conventional and cold expanded fatigue lives for each nutplate orientation. A surprising observation from Table 10 is the low fatigue lives obtained for the ForceTec® cold expansion method compared to the conventional (non-cold worked) nutplate. The beneficial effect on fatigue life of the compressive stresses due to the cold expansion process are overwhelmed by the detrimental effect of the fretting between the fastener and hole during testing. Although the ForceTec® cold expansion method does not require rivets (and is thus termed a rivetless nutplate), the cold expansion methods were being considered for use on existing aircraft hardware. Therefore the rivet holes were machined in the ForceTec® specimens, cold worked, and filled with standard rivets.

TABLE 10 *The effect on fatigue life for cold expanded nutplate specimens.*

Flight Spectrum	Satellite Hole	Configuration	Fatigue Life Ratio ($N_{Cx}/N_{non\text{-}Cx}$)
LIF	0°	nominal ForceTec®	0.75
		nominal ForceMate®	1.38
	45°	nominal ForceTec®	0.21
		nominal ForceMate®	2.57
		2nd oversize ForceMate®	1.63
	90°	nominal ForceTec®	0.01
		nominal ForceMate®	0.20
		2nd oversize ForceMate®	0.10

Clearly, the most successful cold expansion method in this case is the ForceMate® or bushed hole process. Although fatigue life improvements occurred for the 0° and 45° orientation, a dramatic decrease in fatigue life is observed for the 90° orientation. However, for all 90° orientation nutplate specimens, the fatigue lives were very low compared to the other nutplate orientations. The low fatigue lives associated with the 90° orientation can be rationalized in terms of the orientation of the satellite holes to the loading direction, with multiple initiation sites in the satellite holes.

After completion of the above testing on the countersunk hole and nutplate geometries, further nutplate testing was proposed to examine the effect of modifying the ForceMate® cold expansion process. The two processes involved the FTI recommended approach and the streamlined USAF technique, with both processes previously described in Table 4. The cold working for this portion of the program was undertaken by the USAF, thus enabling a direct comparison between the variability of cold working for two different vendors. A comparison in the fatigue life for the ForceMate® cold expansion method using the two different processes is given in Table 11 in terms of a fatigue life ratio of the FTI-performed and USAF-performed cold expansion.

The similarity in results for the USAF-processed nutplate specimens indicates that the change in cold expansion process, undertaken to increase the efficiency during cold working the T-38 wings, has little effect on the overall fatigue life of the nutplate geometry. The similarity in the USAF-processed specimens using the FTI method compared to the FTI-processed specimens (see Table 11) also highlights the consistency of the cold expansion process between two independent vendors. The nutplate life decrease shown for the 0° orientation specimens is a consequence of the spectrum flight hour runout level assumed for these two test phases. The runout level for the main testing phase was 100 kSFH, however, for the additional phase testing the cold expansion process, the runout level was reduced to 50 kSFH. Three of the five tests reached the 50 kSFH runout level, with the fourth specimen prematurely initiating a crack at the spacer/specimen interface, and the fifth specimen fracturing due to a test anomaly. In general, changing the ForceMate® cold expansion process showed no detrimental effect.

TABLE 11 *The effect of the cold expansion process on fatigue life for the ForceMate® method.*

Flight Spectrum	Satellite Hole	Configuration	Fatigue Life Ratio (N_{FTI}/N_{USAF})
LIF	0°	nominal ForceMate®	0.63*
	45°	nominal ForceMate®	0.94
		2nd oversize ForceMate®	1.44
		nominal ForceMate® (FTI process/USAF performed)	1.11

* The runout for the USAF-processed tests was 50 kSFH, compared to 100 kSFH for the FTI-processed tests.

Conclusions

The cold expansion methods and processes examined in this program were intended for a life extension program for existing wing structure that has already been cycled under flight conditions through a portion of its fatigue life. Therefore this program could be viewed as representing a non-conservative life improvement assessment, as the test specimens representing the FCLs were not fatigued prior to cold working. It has been suggested [12] that residual fatigue damage prior to cold expansion does not influence the total life, however, this assumption has not been tested in this program.

The test results presented in this paper have considerable value as a comparative assessment of the influence of the major variables examined, which included: cold expansion method and process, hole size, countersink size, nutplate geometry, flight spectrum, and joint configurations. The relative life differences observed between the conditions tested in this program can be used in conjunction with either the full-scale wing test results or a DTA analysis to predict relative life improvement.

The spectrum fatigue testing described in this paper provides an assessment of the life improvement gained through cold working different fatigue critical locations of the T-38 lower wing skin. The fatigue results for both the countersunk hole and nutplate geometry can be summarized briefly with major conclusions indicated below.

1. As expected, the LIF spectrum usage exhibited the lowest total fatigue lives. The average decrease in fatigue lives for the LIF usage was on the order of 2 5× compared to the SUPT usage.
2. Cold expansion of the countersunk hole geometry led to an increase in fatigue life by a factor of between 1.08 6×. The cold expansion process also increased the level of variability between fatigue lives, with the 99 % confidence interval completely overlapping the non-cold worked fatigue life results (apart from the OE′ configuration). A vast improvement in fatigue life was shown to occur in the OE′ configuration (oversized hole and an undersized countersink) with a 4 6× life improvement over the non-cold worked specimens.
3. The countersunk hole joint geometry exhibited a decreased fatigue life of between 1.75 5.5× compared to the non-jointed specimen. Unusual crack initiation in the OE joint specimens occurred around the bore of the specimen without penetrating into the bore.
4. Generally, a life improvement was found in the nutplate geometry for the 0° and 45° orientation, following cold expansion using the ForceMate® method. However, for the ForceTec® method (all orientations) and the ForceMate® method (90° orientation), life decreases on the order of between 1.3 10× were observed (excluding the statically failed 90° orientation ForceTec® specimens).
5. The fatigue life for the two different ForceMate® cold expansion processes (FTI and USAF) was found to be very similar, with no degradation in fatigue life occurring due to the shorter process performed by the USAF.

Acknowledgments

This test program was conducted under USAF contract F41608-96-D-0108. The technical monitor at the San Antonio Air Logistics Center was Paul Piper. The authors would like to thank Dale Haines, Darryl Wagar, Tom Masden, and Forrest Campbell for their help with testing. Also, appreciation is extended to FTI, who performed a large amount of the Cx work.

References

[1] McMaster, F. J. and McKeighan, P. C., "Coupon Testing of Fatigue-Resistant Fasteners for the T-38 Lower Wing Skin," Southwest Research Institute Project No. 18-8330, San Antonio, TX, February 1999.

[2] *Military Handbook: Metallic Materials and Elements for Aerospace Vehicle Structures*, MIL-HNDBK-5G, United States Department of Defense, Wright-Patterson AFB, OH, November 1994.

[3] Lee, E. U., "Effect of Load Transfer on Fatigue of Mechanically Fastened Metallic Joints," *Fatigue in Mechanically Fastened Composite and Metallic Joints, ASTM STP 927*, ASTM International, West Conshohocken, PA, 1986, pp. 95 117.

[4] McKeighan, P. C. and McMaster, F. J., "Fatigue Performance of a Re-Designed 66% Spar for the T-38," Southwest Research Institute Project No. 06-8417, San Antonio, TX, July 1998.

[5] "Fatigue Rated Fastener Systems," AGARD Report No. 721, H. H. VanDerLinden, Ed., November 1985.

[6] "Fighter, Tactical, Trainer Aircraft Spectra and Operational Usage Profiles Development and Analysis, Options, Count, Display Programs," SA-ALC Contract F41608-85-C-C261, multiple volumes, 1988.

[7] Southwest Research Institute, "Aircraft Stress Sequence Development Program User/Program Logic Manual (ACSTRSEQ)," Report A005, SA-ALC Contract F41608-90-D-2060-0017, June 1993.

[8] Donald, J. K., "Automated Variable Amplitude Fatigue Crack Growth Technology," *Applications of Automation Technology to Fatigue and Fracture Testing, ASTM STP 1092*, A. A. Braun, N. E. Ashbaugh, and F. M. Smith, Eds., ASTM International, West Conshohocken, PA, 1990, pp. 167 177.

[9] Finney, J. M. and Evans, R. L., "Extending the Fatigue Life of Multi-Layer Metal Joints," *Fatigue and Fracture of Engineering Materials and Structures*, Vol. 18, No. 11, 1995, pp. 1231 1247.

[10] Ball, D. L., "Elastic-Plastic Stress Analysis of Cold Expanded Fastener Holes," *Fatigue and Fracture of Engineering Materials and Structures*, Vol. 18, No. 1, 1995, pp. 47 63.

[11] Chang, J. B., "Analytical Prediction of Fatigue Crack Growth at Cold-Worked Fastener Holes," AIAA Paper No. 75-805, Presented at the AIAA/ASME/SAE 16th Structures, Structural Dynamics and Materials Conference, Denver, CO, May 1975.

[12] Pell, R. A., Beaver, P. W., Mann, J. Y., and Sparrow, J. G., "Fatigue of Thick-Section Cold-Expanded Holes With and Without Cracks," *Fatigue and Fracture of Engineering Materials and Structures*, Vol. 12, No. 6, 1989, pp. 553 567.

Journal of ASTM International, October 2004, Vol. 1, No. 9
Paper ID JAI19063
Available online at www.astm.org

Nicolas Gérard,[1] *René Leroy,*[2] *Olivier Girard,*[2] *and Narayanaswami Ranganathan*[2]

Crack Initiation at a Notch under Constant and Selected Variable Amplitude Loading Conditions

ABSTRACT: In a previous study, we showed that crack initiation life at a notch tip can be modeled as the micro crack propagation life from an initial microstructural defect up to a crack size of about 500 μm. This model is based upon the assumption that short cracks at a notch propagate without any significant closure effects. In our present experimental study, the results of fatigue tests to verify this hypothesis are presented and discussed.

The fatigue tests were conducted in ambient air on single edge notched specimens with a theoretical stress concentration factor of 3.14 on thin sheets of 1.2 mm thick Aluminum alloy 2024 T351. The test conditions studied are: constant amplitude tests at stress ratios of 0.1, 0.3, and 0.5 and variable amplitude tests using an extract from the TWIST spectrum. The tests were carried out at a nominal frequency of 10 Hz. At selected intervals, micro crack advance (if any) was determined using replicas. The measurements were made at the maximum stress for constant amplitude tests and at a chosen positive stress for variable amplitude tests (avoiding any overload). The smallest crack size detected is about 10 μm.

KEYWORDS: notch, crack initiation, fatigue life, local strain, short crack, prediction, fracture mechanics.

Introduction

The mechanisms involved in the early stages of crack formation at notches still are an open question, and several approaches exist to predict the crack initiation life. Notable examples, based on the local stress levels in the vicinity of a notch, are the Neuber's empirical approach and the Glinka's energy based model [1,2]. More recently, short crack propagation models have been proposed that usually consider that a crack-like defect exists at the notch tip right from the first cycle. Based on such models, the crack initiation life represents, in fact, the propagation life of the initial crack as it grows under the fatigue loading to reach a size detectable by current non-destructive inspection methods [3,4]. In this approach, the main difficulty resides in modeling of the short crack propagation law. Numerous authors have pointed out the differences between short and long crack growth behavior. One of the reasons evoked is that short cracks are not significantly affected by closure effects, as the plastic wake responsible for closure is not strong enough to provoke crack closure [5]. Empirical methods have been developed to evaluate directly the crack initiation phase (i.e., up to a macro-crack size) [6 8], but the use of such methods is limited to the studied materials and geometries.

Manuscript received 25 June 2002; accepted for publication 17 July 2003; published October 2004. Presented at ASTM Symposium on Fatigue Testing and Analysis Under Variable Amplitude Loading Conditions on 29 31 May 2002 in Tours, France; P. C. McKeighan and N. Ranganathan, Guest Editors.

[1] Engineer, Spie Thermatome, 2 rue Eugène Gouin, B.P. 531, 37205 Tours Cedex 3, France.
[2] Associate Professor, Engineer, and Professor, respectively, Laboratoire de Mécanique et Rhéologie, University François Rabelais de Tours, 7 avenue Marcel Dassault, 37200 TOURS, France.

This study presents a comparison between experimental and predicted crack initiation lives, evaluated using a model based on short crack propagation at notches [9]. In this model, short cracks at notches are assumed to propagate at a notch without any significant closure effects. A previous study has shown that experimentally observed crack initiation lives for notched specimens subjected to an aircraft wing loading spectrum can be predicted with sufficient accuracy based on this model [3,9]. In the current study, experiments conducted to verify the underlying hypothesis of this model are presented and discussed.

Experimental Details

The material used was 2024 T351. The nominal composition and material properties can be found in [10].

Notched Specimens

Notched specimens, shown in Fig. 1, were cut using spark-erosion machining in a 1.2 mm thick sheet. Determination of the notch geometry was done using Finite Element calculations, in order to produce a stress concentration factor K_t close to 3 (its value is $K_T = 3.14$). The notch root radius is 3 mm. The grip zone was also designed by Finite Element methods, and the height of the specimen was evaluated in order to eliminate the interaction between the remote stress application zone and the notch root.

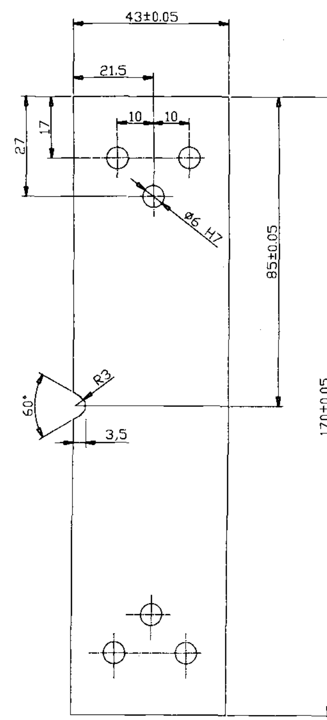

FIG. 1 *Notched specimen geometry, K_T = 3.14 (thickness = 1.2 mm).*

Fatigue Loading

Due to the thickness of specimens, to avoid buckling it was decided not to submit them to compressive stresses.

The notched specimens were submitted to two kinds of fatigue loading, constant amplitude loading (R = 0.1, 0.3, and 0.5) and variable amplitude loading (extract from the TWIST spectrum). The remote stress level history, corresponding to typical flight from the Twist extract, is shown in Fig. 2. The remote stress amplitude was chosen to avoid global yielding of the uncracked ligament. The TWIST extract is composed of 505 cycles, representing 23 flights (take off, cruising regime, and landing phases).

Crack Growth Monitoring—The short crack growth was monitored using optical measurement on the lateral surface of the specimen, and replicas were made at regular intervals on this surface, especially in order to detect cracks as early as possible (the minimal detectable size was close to 10 μm). These replicas were then observed with an optical microscope at a magnification of (1000×).

For constant amplitude loading, the stress level was held at the maximum stress value during the replicating process, whereas for the variable amplitude loading, the stress was held "as is" in order to avoid overloads.

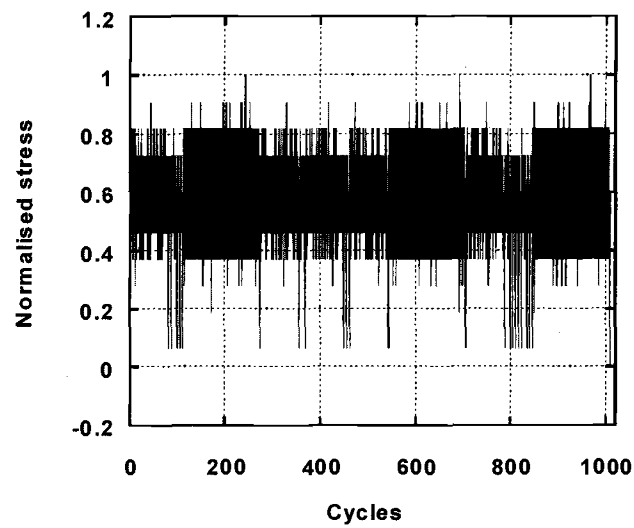

FIG. 2 *A typical flight from TWIST extract (23 flights): normalized stress versus number of cycles.*

Experimental Results and Discussion

Constant Amplitude Loading

Notched specimens were submitted to constant amplitude loading at three stress ratios, R, of 0.1, 0.3, and 0.5. To evaluate the effect of the mean stress, tests were conducted at the same stress amplitude at different R ratios; an example is given in Table 1. The experimentally observed crack initiation lives and the final crack lengths are given in Table 2.

TABLE 1 *Correspondence between loading conditions at stress ratios R=0.1 and R=0.3.*

Stress amplitude $\Delta\sigma$ (MPa)	Maximum stress R = 0.1	Maximum stress R = 0.3
108	120	154.3
126	140	180

TABLE 2 *Experimental crack initiation lives (up to a macro-crack size of 500 μm).*

Specimen Identification No.	R	σ_{max} (MPa)	Stress Amplitude (MPa)	Crack Length (μm)	N_i (cycles)
1	0.1	160	144	189	36 000
2	0.1	160	144	487	32 900
3	0.1	160	144	535	27 000
7	0.1	140	126	Close to 500*	40 000
8	0.1	140	126	480	58 000
9	0.1	120	108	Close to 500*	82 000
10	0.1	120	108	449	189 000
11	0.1	180	162	Close to 500*	29 192
12	0.1	180	162	570	29 000
13	0.3	180	126	Close to 500*	37 000
14	0.3	180	126	573	40 000
15	0.3	154.3	108	515	63 711
16	0.5	216	108	442	49 000
17	0.5	252	126	507	29 000

* In some cases, the crack could not be monitored because:

a. observations were not done on both sides of the specimens, or
b. the crack grew too fast to be followed (regular load holding was programmed), especially in the cases where the crack length on the lateral surface grew suddenly.

The experimental scatter is close to the one generally observed for fatigue lives of mechanical components, i.e., for the same loading conditions life can vary by a factor of 2. The scatter is more pronounced for the smallest stress amplitude studied.

The crack initiation lives, with respect to the remote stress amplitude for these tests, can be seen in Fig. 3, where the stress amplitude applied is drawn as a function of the crack initiation life (number of cycles). The effect of the stress ratio is obvious on such a graph. The crack initiation life can be divided by two, as seen between specimen Numbers 8 and 17, conducted at the same stress amplitude of 126 MPa, while the stress ratio goes from 0.1 0.5.

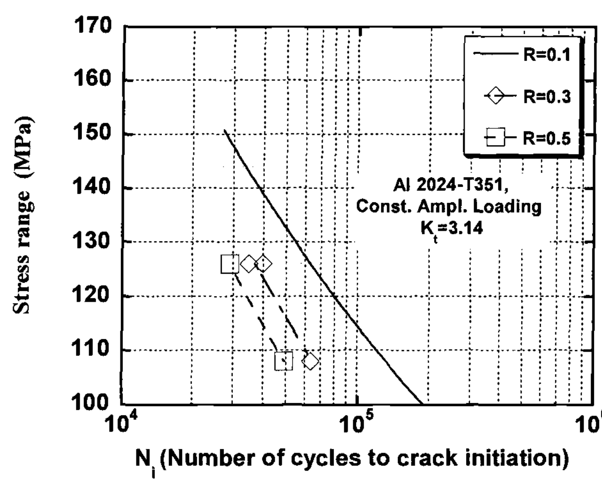

FIG. 3 *Crack initiation lives of notched specimens under constant amplitude loading.*

Critical Evaluation of the Studied Model Based on Crack Growth Kinetics

Short Crack Model

The short crack model is based on the following assumptions:

1) Short cracks propagate without any significant crack closure, and a crack growth law obtained for long cracks, corrected for the closure effect (i.e., $\frac{da}{dN} \sim \Delta K_{eff}$ power law) can describe their crack growth kinetics. The law used in this study is of the form given in Eq 1, and the constants in this equation are given in Table 3.

$$\frac{da}{dN}(mm/cycle) = c\Delta K_{eff}^{\ \ n} \tag{1}$$

TABLE 3 *Value of c and n in Eq 1.*

ΔK_{eff} range (MPa √m)	C	n
1–2	1e-8	7.59
2–5	4.58e-8	1.97
5–10	1.67e-8	4

2) Short cracks initiate at microstructural typical features, such as inclusions, or microstructural flaws and cracks exist from the very first cycle.
3) The stress intensity factor used to evaluate the short crack growth kinetics is evaluated by the FEM method using perfectly elastic conditions. The stress intensity factor is then evaluated at each cycle as a function of the crack length and the "local" stress amplitude ($\Delta\sigma$) applied at the notch root after Glinka's formula [9]. One of the basic questions concerning crack initiation at a notch is the crack geometry that cannot be predicted. Thus, three crack configurations were considered: through-thickness, corner, and semi-elliptical embedded crack. For the latter two crack geometries, the crack shape (i.e., aspect ratio) was assumed to remain constant (at a value of 1) with crack length. The curves obtained (relating the stress intensity factor, in mode I propagation, to the crack length) are shown in Fig. 4.

The minimum crack length considered was 10 μm. The effective crack growth threshold for long cracks for the material studied is on the order of 0.8 MPa √m [10]. As can be seen in Fig. 4, the minimum K value for the three geometries studied is about 1 MPa.√m. Thus, the assumption concerning the presence of a crack right from the first cycle is justified for a remote stress greater than 100 MPa.

It can also be seen here for a given crack length that the severity, in terms of the stress intensity factor, is in the following order:

$$K_{\text{through-thickness}} > K_{\text{corner crack}} > K_{\text{elliptic embedded crack}}$$

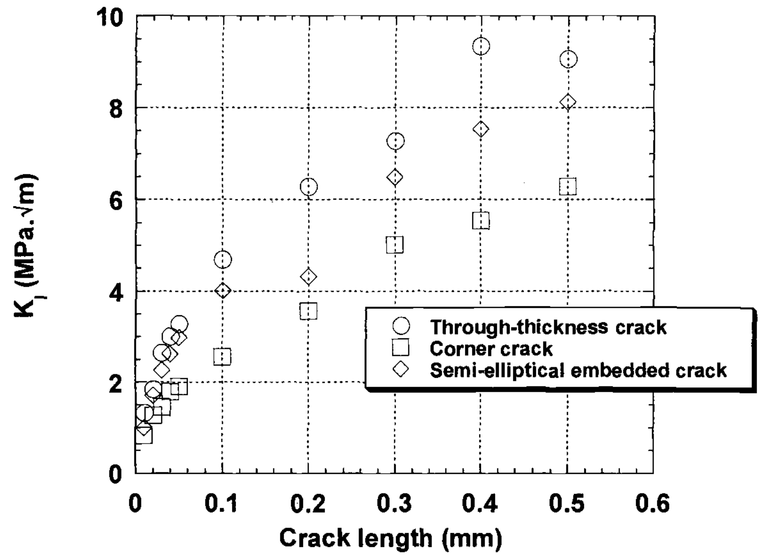

FIG. 4 *Stress intensity factor as a function of crack length for different geometrical crack configurations,* $\sigma_\infty = 100$ *MPa.*

Study of Crack Growth Kinetics under CA Loading

From the above-mentioned results, it can be surmised that crack length evolutions should depend upon the crack geometry. Thus, the crack length measurements for the tests studied here are compared to the predicted crack length evolutions for through-thickness and corner crack configurations. The semi-elliptical crack geometry was not considered, at a first approximation, as it led to over-conservative predictions.

The comparison between measured and evaluated crack growth evolution for specimens 1, 2, and 3 ($\sigma_{max} = 160$ MPa, R = 0.1) can be seen in Fig. 5. It is confirmed here that the experimental crack growth evolutions are almost totally embedded in the "scatter band" composed by the two different crack geometry configurations

The results obtained for the test conducted at the lowest maximum stress are given in Fig. 6. It can be seen that both the two predicted crack configurations lead to highly conservative predictions. Three reasons can explain this result:

1. The crack configuration can be different in this case (probably an elliptic embedded crack in the early stages – not detected here).
2. The existence of crack closure was not taken into account in the model.
3. The existence of a crack initiation phase was not considered in this study.

Such a behavior was, however, exceptional under the test conditions studied.

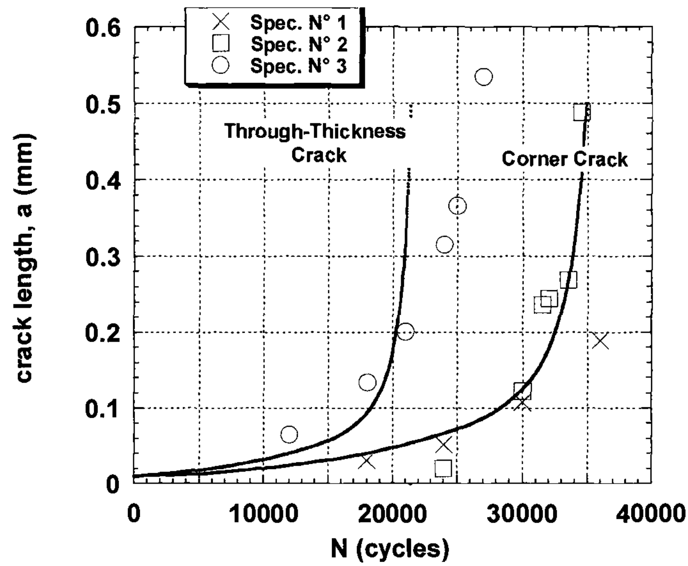

FIG. 5 *Comparison between estimated and measured crack growth evolution (Spec. 1, 2, and 3, σ_{max} = 160 MPa, R = 0.1).*

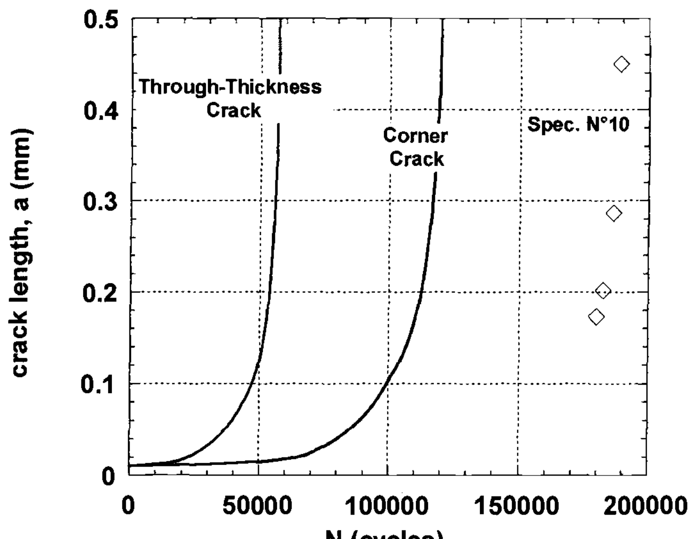

FIG. 6 *Comparison between estimated and measured crack growth evolution (Spec.10, σ_{max} = 120 MPa, R = 0.1).*

A careful examination of all the test results showed that for most of the observed test conditions, the measured crack length evolutions follow the predictions for either of the two crack configurations presented above.

In Fig. 7, predicted lives considering these two crack geometries are compared with the experimental data for tests at R = 0.1 (as most of the data corresponds to this R-ratio). It is seen here that the corner crack configuration leads to very good predictions. For the lowest stress level, the prediction seems to be over-conservative considering the experimental scatter.

These results show that, in most of the cases studied here, the assumptions used in the model are justified.

Considering that closure effects are minimal, the estimated crack initiation lives are given in Table 4, considering corner crack and through thickness crack configurations.

The predictions obtained with the short crack model lead to the conclusion that most cracks grew as corner cracks for constant amplitude loading conditions.

Variable Amplitude Loading

Three specimens were submitted to the variable amplitude loading described in the previous paragraph at different maximum stress levels. The experimental crack initiation lives can be seen in Fig. 8. Under such loading, a usually encountered curve shape is obtained, and the effect of the maximum stress level is similar to that observed under constant amplitude loading.

These specimens were submitted to the previously described spectrum (TWIST-extract, without compressive stress) at three different maximum stress values. Figure 9 shows the crack growth evolution compared with estimations obtained with the short crack model, for a maximum stress of 220 MPa, and Fig. 10 shows the results for stresses of 240 MPa.

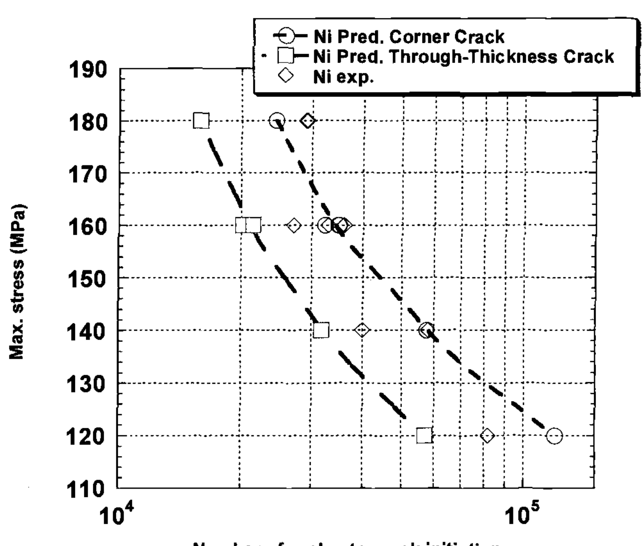

FIG. 7 *Comparison of predicted and observed crack initiation lives at R = 0.1.*

TABLE 4—*Comparison between predicted crack initiation lives (corner and through-thickness crack configurations) and measured ones, constant amplitude loading.*

Max. Remote stress (MPa)	R	Ni (cycles) Theoretical		Ni (cycles) Experimental
		Corner	Through-thickness	
160	0.1	32 230	20 160	36 000
160	0.1	34 810	21 360	32 900
160	0.1	34 960	21 420	27 000
140	0.1			40 000
140	0.1	57 580	31 830	58 000
120	0.1			82 000
120	0.1	119 650	57 110	189 000
180	0.1			29 192
180	0.1	24 400	15 770	29 000
180	0.3			37 000
180	0.3	58 030	32 030	40 000
154.28	0.3	120 370	57 430	63 711
216	0.5	119 560	57 070	49 000
252	0.5	57 730	31 890	29 000

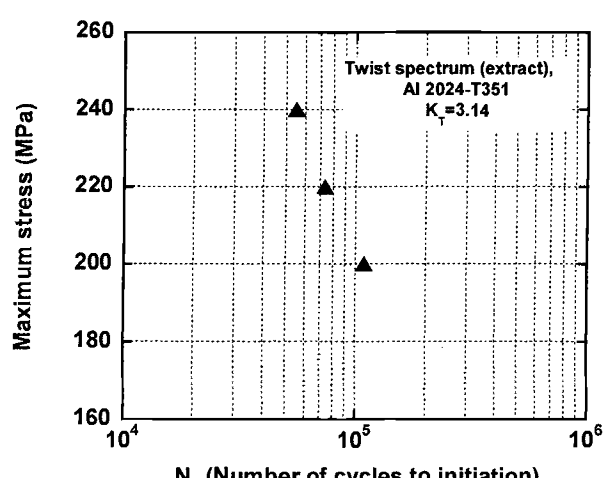

FIG. 8 *Crack initiation lives for notched specimens submitted to variable amplitude loading (TWIST extract).*

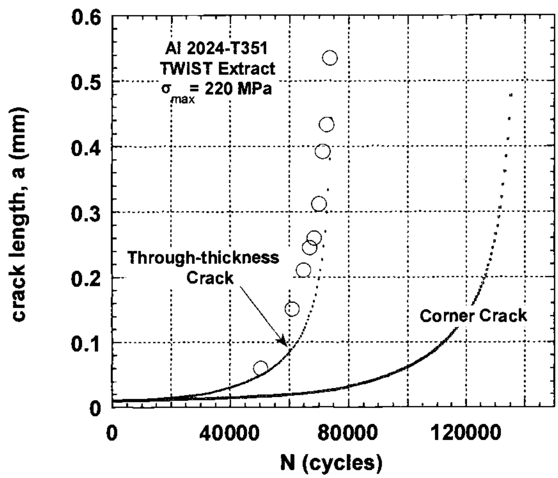

FIG. 9 *Crack growth evolution compared with estimation made with the short crack model for TWIST extract spectrum, σ_{max} = 220 MPa.*

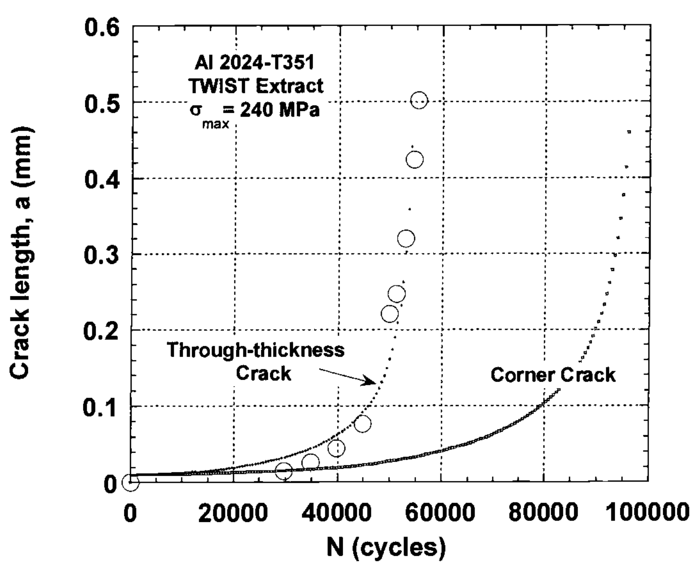

FIG. 10 *Crack growth evolution compared with estimation made with the short crack model for twist extract spectrum, σ_{max} = 240 MPa.*

It must be pointed out that for each case, the short crack model predictions are accurate, and the crack geometry configuration was the through-thickness crack. This is believed to be due to the fact that large cycles of the twist-extract spectrum allow the crack front to reach the same length on both faces. This is quite different from CA conditions, where the most probable configuration is a corner crack.

General Remarks

The present study indicates that crack initiation lives under fatigue can be predicted successfully using the short crack approach, despite some simple assumptions (such as minimal closure effects for short cracks and neglecting a possible crack initiation phase at the notch tip).

This aspect is now discussed based on experimental results under CA conditions where the crack growth analysis is complete. In the experimental measurements, we followed the crack advance on one side using replicas. In certain cases, the crack seems to have propagated from the other side. To overcome this difficulty, crack advances were also measured across the specimen bulk, by measuring the striation spacing. An example of the fracture surface is given in Fig. 11.

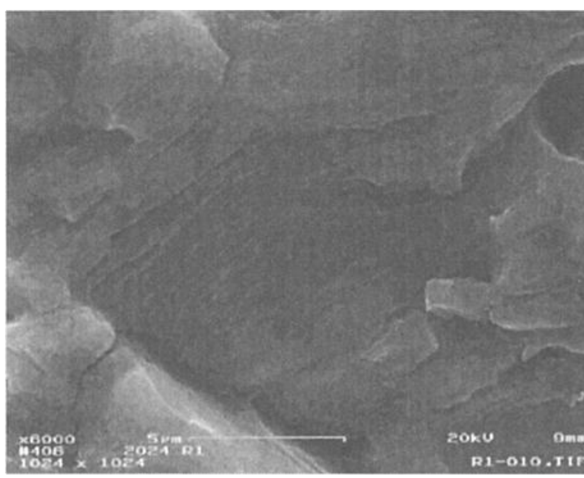

FIG. 11 *Striations on the fracture surface, R = 0.1,* σ_{max} *= 160 MPa.*

In Figure 12, we compare the crack growth rate obtained by the following methods:

a) Optical measurements
b) Striation spacing
c) Model prediction

The crack growth data for short cracks is given in terms of ΔK, and the model prediction is given in terms of ΔK_{eff} (data from [12], for long cracks). From this figure, if we compare optical measurements (for short cracks) and the model predictions, it would appear that the model predictions are conservative. On the other hand, the striation spacing measurements seem to agree very well with the model prediction. This analysis has been done only for one specimen, but this result alone seems to indicate that crack closure effects, if any, are minimal for the experimental conditions studied here. Similar results have been reported in a previous study, on the 7075 -T7351 alloy [13].

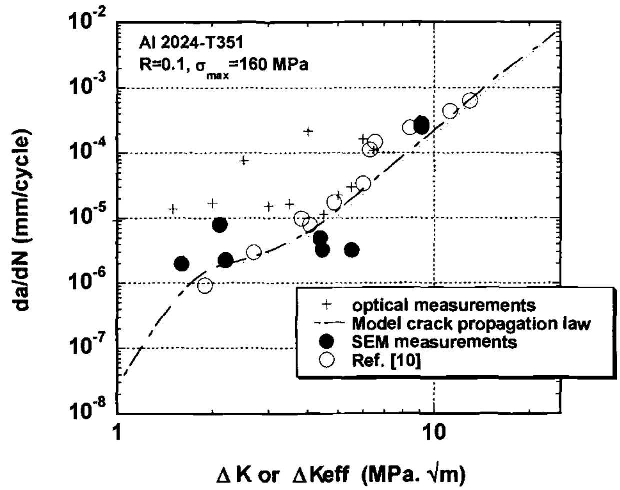

FIG. 12 *Comparison of crack growth behavior of short and long crack.*

Figure 13 shows the results obtained using a similar approach for a more complete loading spectrum, containing 1000 flights and 22 547 cycles [9]. In this case, the local stress intensity factor was determined using the Kujawski approximation [15], which is, in fact, a curve fitting for Newman's more rigorous approach [16,17]. In this figure, results for conventional local crack initiation lives using the SWT [18] and Glinka's method [2] using appropriate mean stress correction are also given for comparison. It can be seen that the predictions using the short crack approach are as good as the conventional models. For the lowest stress level studied here, the experimental scatter was modeled as possible variations of input in the crack growth model (initial defect size and variations in material cyclic properties). It can be seen here that the predicted scatter is comparable with the experimental one, the predictions being slightly conservative. This result is encouraging.

It should be noted that the test spectra studied here contain very little load interaction effects (tension dominated spectra, very few overloads, etc. [19]). The concepts exposed here have to be verified for more discriminating conditions.

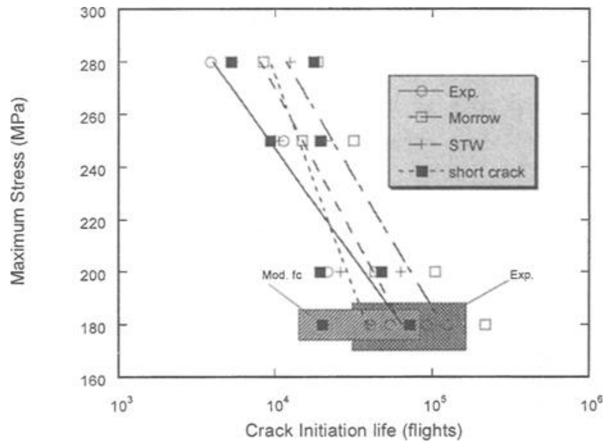

FIG. 13—*Predicted and experimental lives for another flight simulation spectrum.*

Conclusion

In the present experimental study, it has been shown that small crack propagation concepts can be successfully used to predict the life to initiate a crack of a dimension on the order of 500 μm, starting from an initial size of about 10 μm. The basic assumptions of the model used seem to be verified under the experimental conditions studied here.

References

[1] Neuber, H., *Journal of Applied Mechanics*, 1961, Vol. 28, pp. 544–560.

[2] Glinka, G., Ott, W., and Nowack, H. "Elasto-Plastic Plane Strain Analysis of Stresses and Strains at the Notch Root," *Journal of Engineering Materials and Technology*, Vol. 110, No. 3, 1988, pp. 195–204.

[3] Ranganathan, N., Morel, F., and Nadot, Y., *Engineering Against Fatigue*, T. Lindley, R. Smith, P. Tomkins, R. Beynon, and T. Brown, Eds., Balkema Pubs., Holland, 1999, pp. 183–189.

[4] Gerard, N., Leroy, R., Tougui, A., and Ranganathan, N., "Notch Effect In Fatigue: Comparison of Local Strain and Fracture Mechanics Approches," *Euromat 2000* D. Miannay, P. Costa, D. François, and A. Pineau, Eds., 2000, Vol. 2, pp. 1047–1052.

[5] Chong-Myong, P. and Song, J.-H., "Crack Growth and Closure Behaviour of Short Cracks at Notches," *Engineering Fracture Mechanics*, Vol. 47, No. 3, 1994, pp. 327–343.

[6] Zheng, X.-L., "Modelling Fatigue Crack Initiation Life," *International Journal of Fatigue*, Vol. 15, No. 6, 1993, pp. 461–466.

[7] Sato, T. and Shimada, H., "Evaluation of Fatigue Crack Initiation Life from a Notch," *International Journal of Fatigue*, Vol. 10, No. 4, 1988, pp. 243–247.

[8] Shang, D.-G., Yao, W.-X., and Wang, D.-J., "A New Approach to the Determination of Fatigue Crack Initiation Size," *International Journal of Fatigue*, Vol. 20, No. 9, 1998, pp. 683 687.

[9] Gérard, N., Ranganathan, N., Leroy, R., Mazari, M., and Bachir-Bouiadjira, B-A., "Fatigue Crack Initiation Life Estimation at a Notch: A New Software," *Applications of Automation Technology in Fatigue and Fracture Testing and Analysis: Fourth Volume, ASTM STP 1411*, A. A. Braun, P. C. McKeighan, A. M. Nicolson, and R. D. Lohr, Eds., ASTM International, West Conshohocken, PA, 2002, pp. 181 202.

[10] Ranganathan, N., Benguediab, M., Henaff, G., and Adiwijayanto, F., "Quantitative Fracture Surface Analysis of Fatigue Crack Propagation under Variable Amplitude Loading," *Fractography of Modern Engineering Materials: Composites and Metals, Second Volume, ASTM STP 1205*, Kohn E. Masters and Leslie N. Gilbertson, Eds., ASTM International, West Conshohocken, PA, 1993, pp. 71 89.

[11] Petit, J., *Fatigue Crack Threshold Concepts*, D. Davidson and S. Suresh, Eds., TMS AIME Symposium, New York, 1984, pp. 3 25.

[12] Ranganathan, N. and Desforges, J. R., *Fatigue and Fracture of Engineering Materials and Structures*, Vol. 19, No. 8, 1996, pp. 997 1003.

[13] Desforges, J. R., "Propagation en fatigue des Fissures Courtes dans les Alliages d'Aluminium," Ph.D. Thesis, University of Poitiers, France, 1996.

[14] Kujawski, D., "Estimations of Stress Intensity Factors for Small Cracks at Notches," *Fatigue and Fracture Engineering of Materials and Structures*, Vol. 14, No. 10, 1991, pp. 953 965.

[15] Newman, J. C. and Raju, I. S., "Stress-Intensity Factor Equations for Cracks in Three-Dimensional Finite Bodies Subjected to Tension and Bending Loads," *Computational Methods in the Mechanics of Fracture*, Atluri, Ed., Vol. 2, In *Computational Methods in Mechanics*, Elsevier Science Publ. Co., Inc., 1986, pp. 311 334.

[16] Newman, J. C., Jr., Wu, X. R., Venneri, S. L. and Li, C. G., "Small Crack Effects in High Strength Aluminium Alloys, A NASA/ CAE Cooperative Program," *NASA Reference Publication 1309*, May 1994.

[17] Smith, K. N., Watson, P., and Topper, J. H., *Journal of Metals, JMSA*, 1970, Vol. 5, pp. 767 782

[18] Ranganathan, N. "Certain Aspects of Variable Amplitude Fatigue," *Fatigue 2002*, A. F. Blom, Ed., Emas Publications, 2002, Vol. 1, pp. 613 621.

Nikolay V. Tumanov[1]

Fatigue Resistance Evaluation and Crack Kinetics Study for Aero Engine Fan Blades under Random Vibration

REFERENCE: Tumanov, N. V., "**Fatigue Resistance Evaluation and Crack Kinetics Study for Aero Engine Fan Blades under Random Vibration,**" *Fatigue Testing and Analysis Under Variable Amplitude Loading Conditions, ASTM STP 1439*, P. C. McKeighan and N. Ranganathan, Eds., ASTM International, West Conshohocken, PA, 2005.

ABSTRACT: Various types of violent random vibration of aero engine fan blades were investigated. Technique for random fatigue resistance evaluation of the blades has been developed which is based on the relation obtained between amplitude of equivalent sinusoidal stresses, parameters of random stress envelope, and data of conventional constant amplitude tests. Experimental validation of the technique has been carried out on the base of comparison between the calculated and experimental values of equivalent amplitude. For this purpose fatigue tests were performed in the course of which the features of intense service random vibration of the blades were simulated. Some peculiarities of fatigue crack kinetics under random loading were studied.

KEYWORDS: random fatigue, service random vibration, stress envelope, stochastic resonance, equivalent amplitude, fatigue tests under random vibration, reconstitution of fatigue crack kinetics from fractographic observation by scanning electron microscope, self-similar crack propagation mesomechanism by periodic splitting-rupture.

Introduction

Improvement of up-to-date aero engines is accompanied by an increase of the aerodynamic loads on the fan blades. The loads are often of random nature. This paper presents a method for fatigue resistance evaluation of aero engine fan blades subjected to the action of intense random loads. The study comprises the following parts:

1) Investigation of the violent random vibration of the fan blades with the aim to determine probability distribution laws describing the envelope of random vibratory stresses,

2) Definition of the parameter characterizing fatigue under random loading and elaboration of the procedure for estimation of this parameter,

3) Experimental validation of the technique, and

4) Analysis of fatigue crack kinetics peculiarities under random vibration.

[1]Senior researcher, Central Institute of Aviation Motors (CIAM),
2, Aviamotornaya St., Moscow, 111116, Russia, e-mail: tumanov@ciam.ru

Violent Random Vibration of Fan Blades and Probability Distribution Laws for Envelope of the Vibratory Stresses

The sources of fan blades random vibration are random aerodynamic forces caused by turbulent flow in air inlet or gas-air path of aero engine. These forces are added to the deterministic aerodynamic forces due to deterministic circumferential space irregularity of the flow. Peculiarities of random vibratory stresses in fan blades arise both from low damping decrement δ of blades and from availability of the deterministic component. The low decrement value results in narrow band character of violent random vibratory stresses. Under these conditions the dominant frequency f_0 of the vibration is close to a blade natural frequency, and probability distribution of stress amplitude coincides with probability distribution $p(A)$ of stress envelope $A(t)$ (Figures 1 and 2). The highest level of vibratory stresses is achieved in the stochastic resonance condition, that is, when narrow band random vibratory stresses are added to the resonant deterministic ones (Figures 1d-f and 2c,d). In this case the vibratory stresses constitute a non-Gaussian random process.

If random vibration is caused by small-scale turbulence, the vibratory stresses in the non-resonance condition are also sufficiently high (Figure 1). When large-scale turbulence is the source of excitation, the violent random vibration takes place only in the resonance condition. This situation is peculiar to stage-1 fan blades (Figure 2).

Stress envelope probability distribution is described well by gamma-distribution and Rayleigh-Rice-distribution both in the absence of resonant deterministic stresses (then the coefficient of stress envelope variation $v_A \approx 0.5$) and in a stochastic resonance condition ($v_A < 0.5$) [1-3].

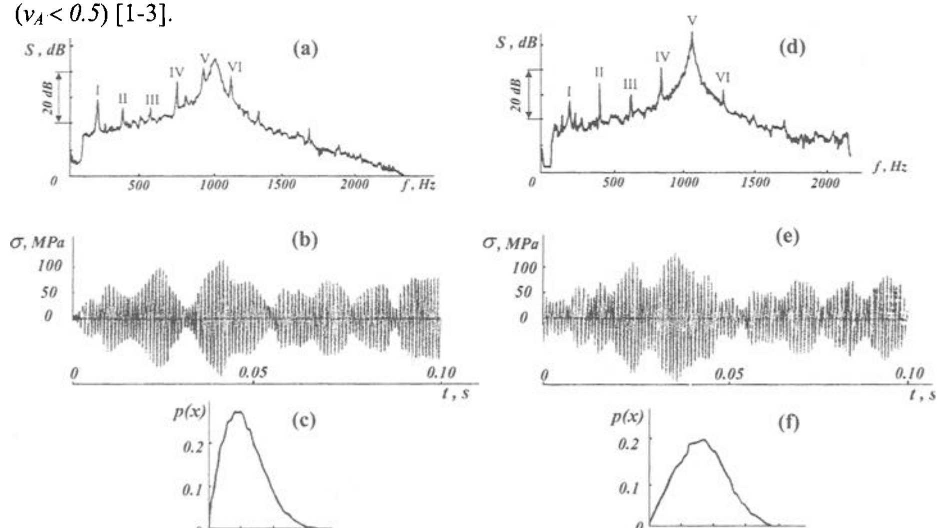

Figure 1 – *Power spectrums S(f) (a,d), oscillograms σ(t) (b,e), and envelope probability distributions p(x) (c,f) of random vibratory stresses in a fan blade in the vicinity (a,b,c) (coefficient of stress envelope variation* $v_A \approx 0.5$*) and in a stochastic resonance condition (d,e,f)* ($v_A \approx 0.4$)*: x is dimensionless value of stress envelope (harmonics of flow circumferential irregularity are numbered by Roman numerals).*

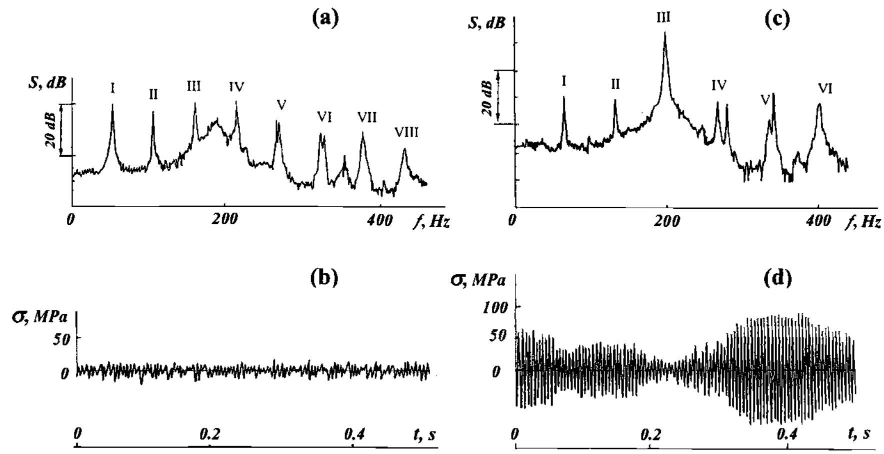

Figure 2 – *Power spectrums S(f) (a,c) and oscillograms σ(t) (b,d) of random vibratory stresses in a stage-1 fan blade in the vicinity (a,b) and in a stochastic resonance condition ($v_A = 0.43$) (c,d).*

Equivalent Amplitude as a Parameter Characterizing Random Fatigue

Fatigue damage cumulation under random loading is caused not only by mean value $\bar{A}$ of stress envelope but it also depends on random overloads. Exponent of power m in fatigue curve

$$N_F A^m = const \tag{1}$$

(here $N_F\ (A)$ is number of cycles to failure with the stress amplitude A) and stress envelope variation coefficient v_A determine the increase of fatigue damage at random overloads. Therefore, a parameter depending on values of $\bar{A}$, v_A, and m would be appropriate for use as a measure of random fatigue. As such a parameter we assume the amplitude of equivalent sinusoidal stresses A_{eq} that provide the damage cumulation velocity

$$V_D(A) = [N_F(A)]^{-1} \tag{2}$$

equal to average damage cumulation velocity $\bar{V}$ at random stresses

$$\bar{V} = \int_0^{A_{max}} V_D(A)\, p(A)\, dA \tag{3}$$

where A_{max} is the maximum value of stress envelope A.

Equating Eqs 2 and 3 with the use of Eq 1 and gamma-distribution as $p(A)$, after transformations we obtain relationship for the equivalence coefficient

$$k = \frac{A_{eq}}{\overline{A}} = \sqrt[m]{J(x_{\max}, \alpha)\prod_{j=1}^{m-1}(1 + jv_A^2)} \tag{4}$$

where $\alpha = m + v_A^{-2}$, $x_{max} = A_{max} / v_A^2\overline{A}$, and J is the incomplete gamma-function (the expression has been derived for whole values of m).

Dependencies 4 and A_{max}/A_{eq} are given in Figure 3 (the A_p quantile of the gamma-distribution corresponding to the probability $p = 0.999$ is used as A_{max}). As can be seen, the A_{eq} value is placed between $\overline{A}$ and A_{max} receding from $\overline{A}$ with increase of v_A and m, and moving closer to A_{max} with decrease of v_A and increase of m. For sinusoidal loading ($v_A = 0$, $\overline{A} = A$) we have $k = 1$, and A_{eq} coincides with the amplitude A of sinusoidal stresses.

In the practically important range $0.25 \leq v_A \leq 0.50$ and $m \leq 25$ dependence (4) can be approximated well by the simple relationship [1,3]

$$k = (4v_A - 0.5)\lg m - 1.6v_A + 1.2 \tag{5}$$

and then

$$A_{eq} = \overline{A}\,[(4v_A - 0.5)\lg m - 1.6v_A + 1.2] \tag{6}$$

Random fatigue resistance evaluation by the use of Eq 6 consists in comparing A_{eq} value with the fatigue limit obtained on the basis of conventional constant amplitude fatigue tests [4]. Thereby the same standardized safety margins may be used both for constant and random amplitude loading.

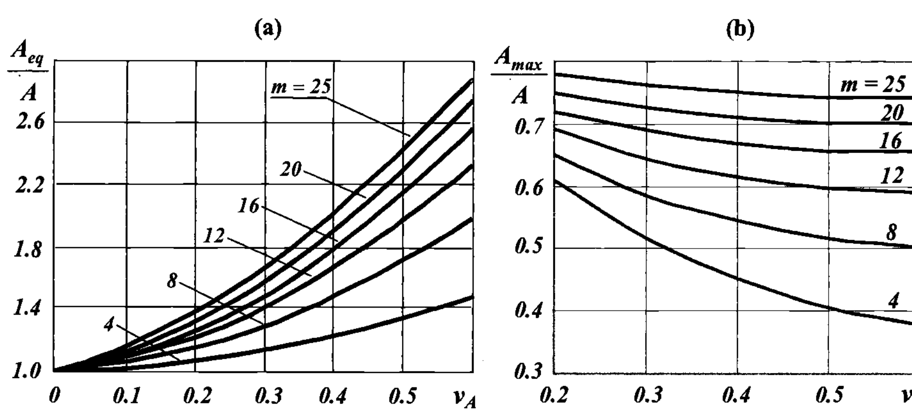

Figure 3 – *Dependencies of* $A_{eq}/\overline{A}$ *(a) and* A_{max}/A_{eq} *(b) on* v_A *and* m.

Determination of Random Vibratory Stress Realization Length Required for A_{eq} Estimation

Working Eq 6 involves parameters $\overline{A}$ and v_A the values of which are estimated on a basis of analysis of stress envelope realization. Consequently, the estimate of A_{eq}, calculated according to Eq 6, has a relative statistical error ε depending on the length T of the realization. If random vibration is caused by small-scale turbulence flow, the realization length, required for A_{eq} estimation with root-mean-square error σ_ε, may be defined as

$$T = \frac{2}{\sigma_\varepsilon^2 \delta f_0} \tag{7}$$

In particular, for $\delta = 0.05$ the number of cycles $N = Tf_0$, ensuring the A_{eq} estimation with error not exceeding $\sigma_\varepsilon = 0.1$, according to Eq 7 is equal to $4\ 000$ cycles.

Equation 7 is deduced in the following way. Required for A_{eq} estimation a length of realization is

$$T = n\ \tau_A \tag{8}$$

where n is the required amount of independent envelope readings and τ_A is stress envelope correlation interval which separates these readings. For wide-band action, which is characteristic of small-scale turbulence, and for Rayleigh-Rice-distributed envelope, the τ_A value is given by

$$\tau_A = 1.5(b + 1)/\delta f_0 \tag{9}$$

where

$b = a^2[I_0(a^2/4)+I_1(a^2/4)]^2/\{a^2[I_0(a^2/4)+I_1(a^2/4)]^2 + I_0^2(a^2/4)+ I_1^2(a^2/4)\}$,
$a = A_S/\sigma$ is «signal /noise» ratio,
A_S = amplitude of sinusoidal stresses,
σ = root-mean-square deviation of random vibratory stresses, and
I_0 and I_1 are modified Bessel functions of the first kind and zero order and of the first kind and first order, respectively.

For gamma-distributed envelope, the upper estimate of n value, providing estimation of A_{eq} with root-mean-square error σ_ε, can be determined as follows [1]

$$n = \frac{1 + 3v_A}{2\sigma_\varepsilon^{\ 2}} \tag{10}$$

Substituting Eqs 9 and 10 into Eq 8 results in

$$T = \frac{0.75(b + 1)(1 + 3v_A^2)}{\sigma_\varepsilon^{\ 2}\delta f_0} \tag{11}$$

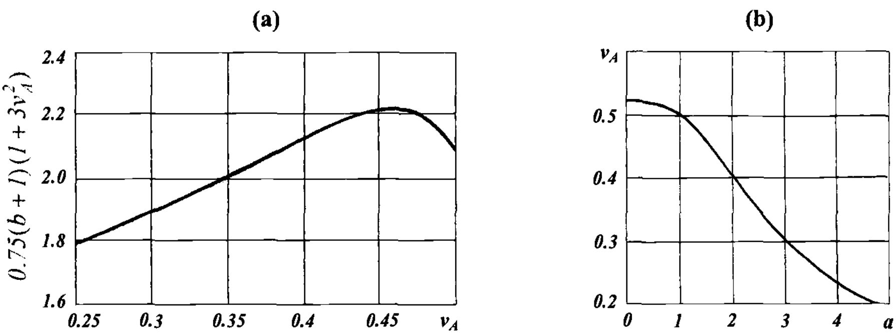

Figure 4 – *For the deduction of equation 7: a – plot of function in numerator of Eq 11 versus v_A, b – dependence v_A on a.*

The function in numerator of Eq 11 is plotted in Figure 4a (the dependence is derived with allowance for the connection between v_A and a for Rayleigh-Rice-distribution given in Figure 4b). As can be seen, in the practically important range $0.25 \leq v_A \leq 0.50$ the function may be replaced by constant value equal to *2* with error not exceeding *10%*. As a result, we come to Eq 7.

Experimental Verification

Validation of the technique was performed by comparison between the values of A_{eq} evaluated according to Eq 6 and on the base of experimental data, obtained from the literature and in the course of the fatigue tests of blades [1]. Thereby the test rig specially developed for random fatigue study was used which makes it possible to simulate service envelope probability distributions of random vibratory stresses in aero engine blades (Figure 5) and to carry out fatigue testing under random loading for various values of v_A (Figure 6).

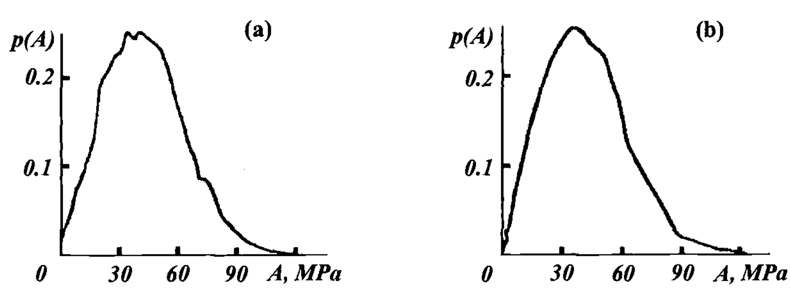

Figure 5 – *Modeling of the stress envelope probability distribution in a fan blade in the stochastic resonance condition for $v_A \approx 0.4$: a – service condition, b – vibrostand.*

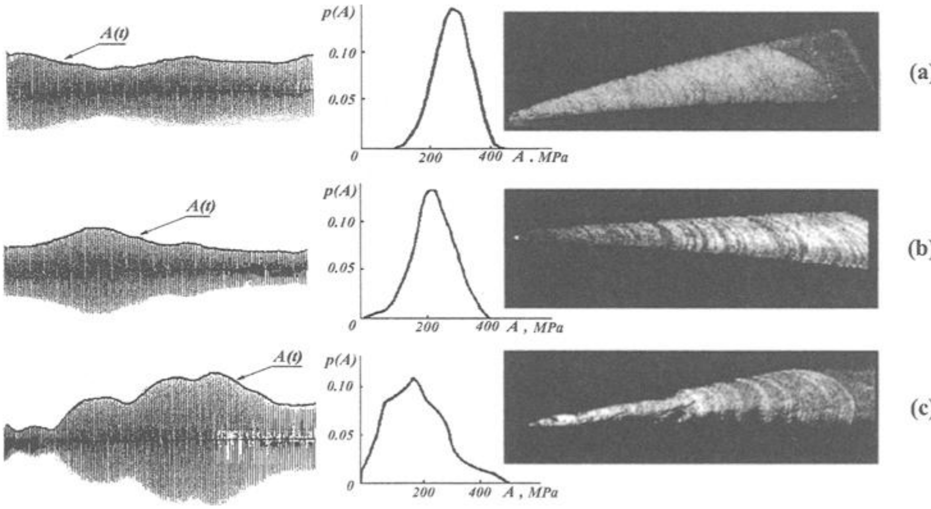

Figure 6 – *Stress oscillograms, envelopes A(t), envelopes probability distributions p(A), and fracture surfaces of aero engine blades under random fatigue tests: (a)* $v_A \approx 0.2$, *(b)* $v_A \approx 0.3$, *(c)* $v_A \approx 0.4$.

As an example, Figure 7 shows the results of fatigue tests of blades under deterministic and stochastic resonance condition (stress amplitude value A and mean value of stress envelope $\bar{A}$ for sinusoidal and random loading, respectively, are plotted along the vertical axis). The fatigue curve under sinusoidal loading determined by least-squares method is also drawn there (exponent of its power $m = 11.4$). Under random loading the variation coefficient v_A was kept constant at 0.4, which is typical for stochastic resonance.

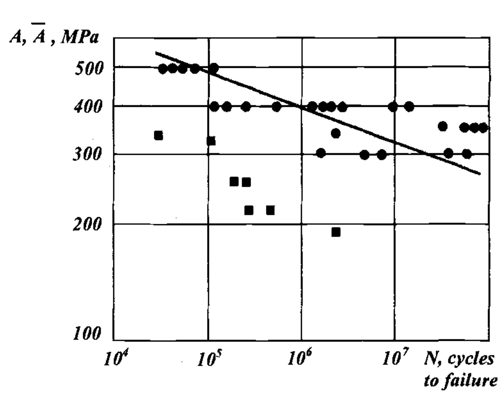

Figure 7 – *The results of blades fatigue tests:*
● *– sinusoidal loading,* ■ *– random loading.*

If we assume that the failure corresponds to the same damage level both under sinusoidal and random loading, the verification procedure issues directly from the above definition of the equivalent amplitude. Really, in this case the equality of damage cumulation velocities under sinusoidal and random loading implies the equality of cycles to failure. Then experimental value of equivalence coefficient $k = A_{eq} / \overline{A}$ may be determined as value inverse to the ratio between ordinate of experimental point in Figure 7, obtained under random loading, and fatigue curve ordinate, corresponding to the same cycles to failure under sinusoidal loading. The mean value of k for experimental points in Figure 7 is equal to *1.78*. Value of k, evaluated according to Eq 5 at $m = 11.4$ and $v_A = 0.4$, is equal to *1.72*.

Peculiarities of Fatigue Crack Kinetics under Random Vibration

Random vibration of the blades causes the stochasticity of fatigue crack kinetics. Two types of this stochasticity have been established on the basis of fractographic study. At Stage II fatigue crack growth the microfluctuations of crack speed take place which result in smooth variation of fatigue striation spacing (Figure 8). Macrofluctuations of crack speed are inherent in the next stage of crack growth. This stage is lacking under constant amplitude loading. The macrofluctuations are caused by transitions between two mechanisms of fatigue crack propagation – mechanism of periodic splitting-rupture (MPSR) [5-8] and mechanism of micropores growth and coalescence (MMGC). On the fracture surface the macrofluctuations of crack speed are manifested in alternating light and dark bands (see Figures 6 and 9a) with striations and dimples, respectively. Time variation of striation spacing (and accordingly of crack speed) occurs alternately in two different scales: a slow change within the fatigue bands and a fast change near the boundaries of the bands (Figure 9b,c) [9].

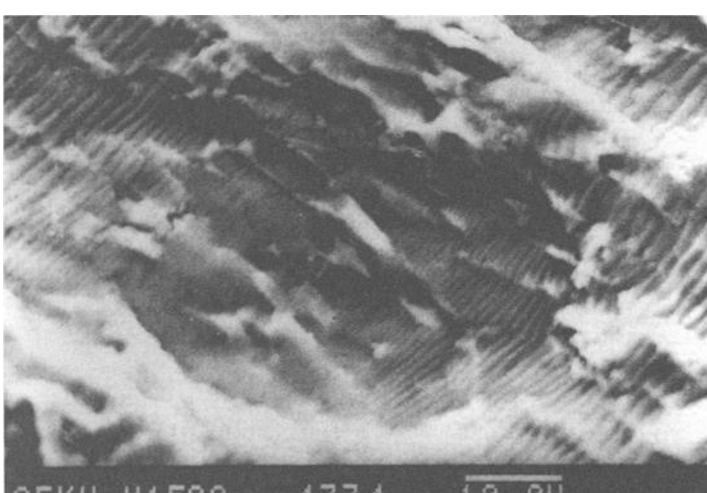

Figure 8 — *Variation of fatigue striation spacing under random vibration at Stage II crack growth (scale in μm is at the right bottom).*

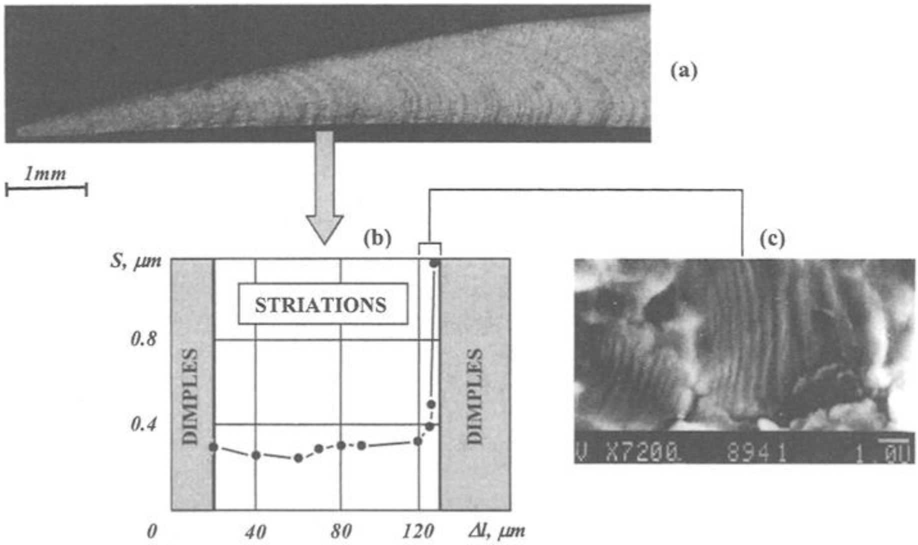

Figure 9 – *Connection between macro-and microrelief of fatigue fracture surface under random vibration: a – fracture surface of a blade under random fatigue tests, b – change of striation spacing S within the fatigue band, c – striation spacing increase at the fatigue band output.*

Such jump-like variation of crack speed is fundamentally different from the smooth variation of stress amplitude (see Figure 6). It is evidence of high nonlinearity of the «crack tip – material at its front» system (CM-system [10]). As a result, the CM-system can intensify stochasticity of loading. This intensification is due to noise-induced transitions [11] between two states of CM-system that are determined by two above-mentioned mechanisms of fatigue crack kinetics. The fall of crack speed at transition from MMGC to MPSR as well as sharp increase of crack speed at reverse transition indicate that the MPSR is sufficiently more energy-consuming fracture mechanism than MMGS.

The underlying mechanism responsible for such high-energy-type crack propagation under high- and low-cycle constant and variable amplitude loading, the nature of which was clarified recently [5-8,12], is caused by highly ordered self-organized deformation mesostructure localized ahead of crack front. This fragmented structure, common to a highly deformed state [13], determines local properties of material, the shape of crack front, and the fracture mechanism. Similarly to the Cook-Gordon mechanism [14], the MPSR is due to transversal splitting ahead of the crack front under the action of tensile stresses parallel to crack plane (Figure 10a). The splitting forms in each loading cycle lengthways to the overstressed boundary of deformation structure that are placed ahead of crack front along the maximum principal deformation direction. As a result, each fatigue striation constitutes the relic of the two-dimensional neck remaining after the rupture of peculiar two-dimensional mesospecimen – the ligament between T-shaped crack front and the above transversal splitting (Figure 10b,c). In the course of deformation and rapture of the neck-ligament the similar processes of the splits and necks formation can take place inside the ligament.

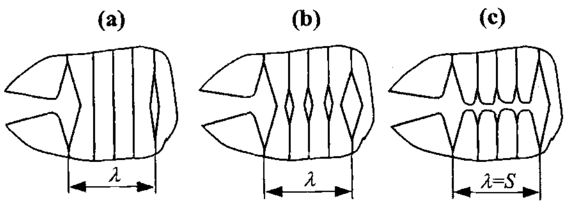

Figure 10 – *The scheme of fatigue striation formation (of periodic splitting-rupture mesomechanism operation).*

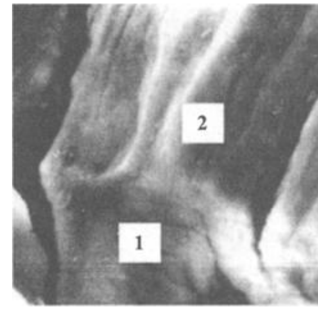

Figure 11 – *Cross section (1) and surface (2) of the fatigue striation.*

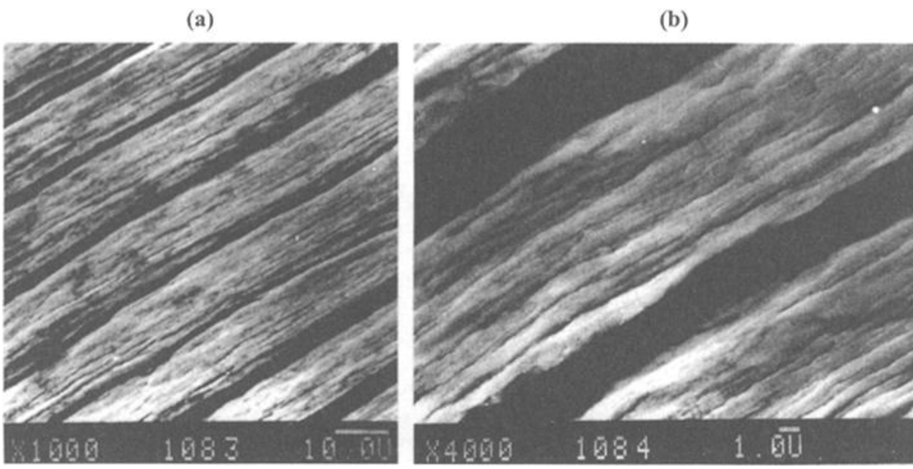

Figure 12 – *Fractal structure of fatigue striation surface revealing itself at variation of magnification in an electron microscope: a – × 1 000, b – × 4 000.*

From the above discussion it follows that: 1) a striation spacing S coincides with a ligament width λ and represents the crack advance in mesoscale within one cycle of loading, 2) a crack path is roughly normal to the maximum principal deformation direction, 3) a striation surface may have fractal (self-similar) character. Morphological diversity of fatigue striations can be caused by an asymmetry of splitting ahead of crack front which results in an asymmetric rupture of the ligament between this splitting and crack front [8].

The splits and highly deformed ruptured ligament between them (that is, fatigue striation) are well seen in Figure 11. Self-similar processes at MPSR operation are manifested by fractal structure of fatigue striation surface (Figure 12): the secondary striations are placed inside the basic striations and the tertiary striations are located inside the secondary ones. Self-similarity of the MPSR are revealed in the macroscale by self-similar power law $S \sim \Delta K^2$ (ΔK is the stress intensity factor range) true over a wide range of S [5-8,12].

Understanding of periodic splitting-rupture mesomechanism and extrapolation of this understanding on micro- and macroscales enables one to connect micro- and macroprocesses of fracture and to deduce macrocrack growth law from fundamental fracture microcriterion – fracture condition of interatomic links ahead of crack front [6,7,12].

Conclusion

1. Stress envelope probability distribution for various types of violent random vibration of aero engine fan blades is described well by gamma-distribution and Rayleigh-Rice-distribution.

2. Amplitude of equivalent sinusoidal stresses A_{eq}, that provide the damage cumulation velocity equal to average damage cumulation velocity at random stresses with gamma-distributed envelope, may be used as a measure of random fatigue. Analytically derived evaluation formula links the A_{eq} value with parameters of random stress envelope and fatigue resistance that can be measured.

   The relation is obtained for calculation of random stress realization length, providing the estimation of A_{eq} with any statistical error.

3. The technique has been verified by comparison between the calculated and experimental values of A_{eq}. The latter data were obtained from fatigue tests under constant and random amplitude loading.

4. The technique is not solely related to aero engine fan blades but can also be applied to various engineering fields where structural parts of high frequency selectivity are subjected to the action of random loads.

5. Random vibration of the blades causes the stochasticity of fatigue crack kinetics. On the fracture surface the stochasticity manifested both by random fluctuations of fatigue striation spacing and by alternating bands with striations and dimples. These bands result from jump-like transitions between two fracture mechanisms operating at the crack front.

   The fall of crack speed corresponding to transitions from dimples to striations as well as sharp increase in crack speed corresponding to inverse transitions are evidences that mesomechanism of periodic splitting-rupture, responsible for fatigue striation formation, is high-energy-type fracture mechanism.

References

[1] Tumanov, N.V., "Vibration Strength Evaluation Technique for Turbojet Blades under Random Oscillation", *Proceedings of the 5th International Conference on Biaxial/Multiaxial Fatigue and Fracture*, Cracow, Poland, E. Macha and Z. Mróz, Eds., Technical University of Opole, Vol. 3 (Supplement), 1997, pp. 91-102.

[2] Lokshtanov, E. A. and Tumanov, N. V., "Applying of Maximal Non-Bias Principle for Random Stress Envelope Description and for Comparative Estimation of Structural Part Fatigue Life", *Problems of Air Science and Engineering*, E. A. Lokshtanov and B. F. Shorr, Eds., Central Institute of Aviation Motors, Moscow, No. 4, 2000, pp. 20-42 (in Russian).

[3] Tumanov, N. V., "Fatigue Strength Evaluation of Gas Turbine Engine Blades under Random Oscillations", *Problems of Air Science and Engineering*, E. A. Lokshtanov and B. F. Shorr, Eds., Central Institute of Aviation Motors, Moscow, No. 4, 2000, pp. 43-56 (in Russian).

[4] Shorr, B. F., Lokshtanov, E. A., Tumanov, N. V., and Halatov, Y. M., "Estimation of Safety Margins for Structural Parts at Random Oscillations", *Science Contribution to Design of Aircraft Engines*, V. A. Skibin and V. I. Solonin, Eds., Mashinostroenie, Moscow, Vol.1, 2000, pp. 513-516 (in Russian).

[5] Tumanov, N. V., "Mechanisms of Fatigue Fracture in Metals", *Proceedings of the 7th International Conference on Fatigue*, Beijing, China, R. X. Wu, Ed., EMAS, Vol. 2, 1999, pp. 765-770.

[6] Tumanov, N. V., "Mechanism of Stable Growth of Fatigue Cracks", *Advances in Mechanical Behaviour, Plasticity and Damage (Proceedings of EUROMAT 2000)*, Tours, France, D. Miannay, P. Costa, D. François, A. Pineau, Eds., Elsevier Science, Vol. 2, 2000, pp. 1065-1070.

[7] Tumanov, N. V., "Physics and Mechanics of Strength: Synthesis within the Framework of Fatigue Crack Stable Growth Mechanism Model. Part 1. Theoretical Background", *Proceedings of the 4th International Symposium of Current Problem of Strenth*, Staraya Russa, Russia, V. I. Malinin, Ed., Novgorod State University, Vol. 1, 2000, pp. 217-222 (in Russian).

[8] Tumanov, N. V. and Cherkasova, S. A., "Physics and Mechanics of Strength: Synthesis within the Framework of Fatigue Crack Stable Growth Mechanism Model. Part 2. Model Verification", *Proceedings of the 4th International Symposium of Current Problem of Strenth*, Staraya Russa, Russia, V. I. Malinin, Ed., Novgorod State University, Vol. 1, 2000, pp. 223-228 (in Russian).

[9] Tumanov, N. V. and Cherkasova, S. A., "Experimental Background for the Fatigue Cracks Kinetics Simulation", *Proceedings of the 11th European Conference on Fracture*, Poitiers-Futuroscope, France, J. Petit, Ed., EMAS, Vol. 2, 1996, pp. 1349-1354.

[10] Tumanov, N. V., "Theoretical Background for the Fatigue Cracks Kinetics Simulation", *Proceedings of the 11th European Conference on Fracture*, Poitiers-Futuroscope, France, J. Petit, Ed., EMAS, Vol. 2, 1996, pp. 1367-1372.

[11] Horsthemke, W., and Lefever, R., "Noise-Induced Transition", Springer-Verlag, Berlin, 1984.

[12] Tumanov, N. V., Cherkasova, S. A., Lavrenteva, M. A., Gestovskiy, V. V., and Vilter, N. P., "Study of Low-Cycle Fatigue Crack Kinetics in Aero Engine Discs", Report 12654, Central Institute of Aviation Motors, Moscow, 2001 (in Russian).

[13] Rybin, V. V., "Large Plastic Deformation and Fracture of Metals", Metallurgia, Moscow, 1986 (in Russian).

[14] Cook, J., and Gordon, J. E., "A Mechanism for the Control of Crack Propagation in All-Brittle Systems", *Proceedings of the Royal Society*, Series A, Vol. 282, No. 1391, 1964, pp. 508-520.

DESIGN APPROACHES AND MODELLING

Journal of ASTM International, September 2004, Vol. 1, No. 8
Paper ID JAI19021
Available online at www.astm.org

Gary B. Marquis,[1] *B. Roger Rabb,*[2] *and Päivi Karjalainen-Roikonen*[3]

High Cycle Variable Amplitude Fatigue of a Nodular Cast Iron

ABSTRACT: This paper provides a brief summary of life prediction methods for variable amplitude fatigue. Special attention is given to cracks propagating from nominally defect free components in the high cycle regime where a significant portion of the fatigue damage can be attributed to cycles with amplitude less than the fatigue limit observed under constant amplitude loading. Constant and variable amplitude fatigue data for a nodular cast iron are presented. An effective stress method for variable amplitude loaded similar to the Topper model is developed. Most model parameters are derived from constant amplitude S-N curves and the Haigh diagram, but two sets of long life variable amplitude tests are needed to derive the variable amplitude interaction parameters.

KEYWORDS: nodular cast iron, variable amplitude fatigue, high cycle fatigue, crack closure

Introduction

Variable Amplitude Life Prediction Methods

Because of its significance in both the aircraft and ground vehicle industries, variable amplitude fatigue has been studied extensively for several decades, and numerous predictive models have been developed. Many overviews of variable amplitude life prediction methods have been published [1 5]. Figure 1 shows the relationships between several classes of models used for predicting fatigue crack propagation under variable amplitude loading. The non-interaction models on the left side of this figure are examples of models that were developed primarily for predicting the effect of R-ratio on the growth of fatigue cracks. These models can be applied to variable amplitude loading, but they predict that crack growth from any cycle is a function only of the magnitude and stress ratio of the cycle itself without regard for previous events. Forman [6] and Walker [7] proposed models of this type for the "Paris law" area of the crack growth rate curve, while Barsom [8] and Lal [9] have proposed relationships for the near threshold region.

Models that consider the interaction between the current fatigue cycle and preceding cycles generally can be classified into closure based models and crack tip stress models. The yield zone models of Wheeler [10] and Willenborg [11] are based on the concept of residual stresses in the plastic zone. Wheeler used the ratio of the current and previous plastic zone sizes to compute crack retardation, while Willenborg computed effective values of ΔK and R as a function of the overload plastic zone size. These models have historic significance in that they were attempts to use fracture mechanics concepts to explain changes in the crack growth rates observed during

Manuscript received 3 May 2002; accepted for publication 19 June 2003; published September 2004. Presented at ASTM Symposium on Fatigue Testing and Analysis Under Variable Amplitude Loading Conditions on 29 31 May 2004 in Tour, France; P. C. McKeighan and N. Ranganathan, Guest Editors.

[1] Professor, Lappeenranta University of Technology, P. O. Box 20, FIN-53851, Lappeenranta, Finland.
[2] Section Manager, Wärtsilä Technology, P. O. Box 244, FIN- 65101, Vaasa, Finland.
[3] Senior Research Scientist, VTT Industrial Systems, P. O. Box 1704, FIN-02044 VTT (Espoo), Finland.

variable amplitude loading. However, following the observations of crack closure by Elber [12,13], these models are rarely used in the scientific literature. Recent observations have led Sadananda et al. [14] to reject the significance of closure and to propose the "Unified Approach" variable amplitude model based the stress state ahead of the crack tip. Sehitoglu and Sun [15] noted especially the significance of residual stresses ahead of the crack tip during plane strain and variable amplitude loading or for crack growth from micro notches.

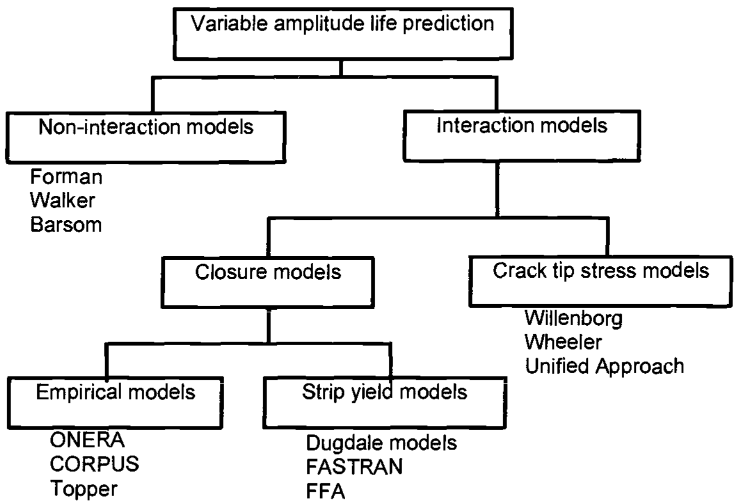

FIG. 1 *Classes of variable amplitude fatigue life prediction models.*

The empirical closure models are intended to account especially for the effect of plasticity induced crack closure on fatigue crack propagation [16 18]. They model the effective stress intensity factor defined by Elber, $\Delta K_{eff} = (S_{max} - S_{op})\ F\ (\pi a)^{0.5}$, where S_{max} is the maximum stress, S_{op} is the stress at which a crack is open, and F is the geometry factor. Most empirical models have been developed with aircraft fatigue problems in mind. The ductile materials, load spectra with large mean stress shifts, and thin sections found in these applications result in relatively large plastic zone sizes and frequently high degrees of closure. The Topper model also has been used for small cracks in ductile aluminum and steels. Various empirical relationships for computing S_{op} have been proposed, and the models show significant improvements in life prediction capability as compared to non-interaction models [1]. The suitability for these models for other materials and other classes of load spectra is not fully confirmed.

Yield strip type models attempt to physically model the growing crack tip area and the plastic wake generated [19 21]. Modifications of the Dugdale-type plastic zone concept [22] are made so as to leave deformed material in the wake of an advancing crack. The crack closure contribution of this deformed plastic wake as a function of crack advance is computed. These models are usually computationally demanding, but they are successful in modeling a variety of transient events, including multiple overloads and delayed retardation.

Small Cycle Damage

Machine components and structures are frequently subjected to variable amplitude loading in which significant portions of the fatigue cycles have amplitudes less than fatigue limit observed under constant amplitude loading. Small amplitude cycles usually are associated with normal operation of rotating equipment, but maintenance operations, thermal events, or other transients may induce some cycles with amplitudes exceeding the conventional fatigue limit. Numerous experimental studies have shown that small amplitude cycles that are part of a load spectrum are more damaging than the same size cycle applied using constant amplitude loading [23 49].

Topper and co-workers have performed numerous series of tests on both smooth and notched specimens of SAE 1045 steel, 2024-T231 aluminum, and 319 cast aluminum alloy [23 31]. Intermittent over- or understraining was applied to specimens followed by blocks of low amplitude cycling. These authors found that cycles below the fatigue limit became damaging, and cycles slightly above the fatigue limit showed increased damage in the presence of either over- or understresses. The increase in damage for the small cycles was at a maximum immediately following the over- or understress and then returned to a steady state value as cycling progressed.

The number of experimental programs directed toward the problem of near-threshold fatigue under variable amplitude loading is limited, so some observations for spectrum load testing of nominally smooth components also are relevant. Conle and Topper [25,26] studied the question of small cycle fatigue damage with the goal of accelerating test times while retaining a sufficient portion of the fatigue damage. Small smooth specimens were tested under axial strain control loading. By successively editing out smaller and smaller fatigue cycles, the actual damage caused by cycles with different strain ranges could be determined. The actual damage produced by cycles with strain ranges below the endurance limit far exceeded what was predicted by constant amplitude test data. Three small cycle omission criteria were tested, but it was consistently observed that the actual damage omitted was greater than what was predicted, i.e., the small cycles were always more damaging in practice than what would be predicted based on constant amplitude tests.

In a similar set of experiments, constant amplitude fatigue life results and the bi-linear damage accumulation line as proposed by Haibach [32] were used to predict the fatigue life of simple notched steel components subject to random fatigue loads. The predicted lives were non-conservative by a factor of six at $N_f = 1 \times 10^6$ and by a factor of 12 at $N_f = 1 \times 10^7$ [33]. In another large set of tests on five different automotive suspension components subject to constant amplitude and service loads, Schütz and Heuler [34] found that fatigue life was consistently over-predicted when life estimations were based on linear damage accumulation rules and constant amplitude testing. Four damage accumulation hypotheses, including the three most common versions of Miner's rule, were used. It was argued that the complex process of crack initiation and propagation is oversimplified by linear damage accumulation rules. In general, the Zenner-Liu rule [35], which attributes an artificially large damage contribution to cycles with $\Delta S > \Delta S_o/2$, best fits the service load data.

Tokaji and Ando [36] conducted two level tests where the secondary stress was below ΔS_0. They found that the smaller stress cycles had little influence on the initiation of surface cracks up to about 80 μm in length. Scatter in these results, however, was very large, with some tests showing a large damage contribution due to the small cycles and with others showing a negative contribution, (i.e., small cycles delayed crack initiation). Small cycles contributed significantly to crack growth in the range of 80 200 μm, but periods of both slow and fast propagation were observed. For cracks longer than 200 μm, even the lower stress cycles produced stress intensity ranges exceeding ΔK_{th}.

Yan et al. [37] have suggested an alternate curve-fitting algorithm for long-life specimen fatigue data. This method essentially recognizes that the constant amplitude fatigue process will have three regimes depending on stress level: 1) the low cycle regime, 2) the high cycle regime, and 3) the endurance regime. When computing the proposed elastic strain amplitude versus reversals to failure regression line, i.e., $\Delta e_{elastic}/2$ vs. $2N_f$, only data in the high cycle regime should be included, and this line should be extrapolated below the endurance regime when estimating the damage contribution of small cycles as part of a spectrum. The proposed $\Delta e_{elastic}/2$ versus $2N_f$ curve has a steeper slope and, therefore, attributes more damage to small amplitude cycles than would be observed during constant amplitude loading. This method was shown to give better life predictions for spectrum loaded specimens as compared to the more conventional approach in which all elastic strain range data are used to compute the $\Delta e_{elastic}/2$ vs. $2N_f$ regression line.

Stanzl-Tschegg et al. [38] investigated the high cycle fatigue behavior of cast aluminum alloys under both constant amplitude and service load conditions with a cumulative frequency distribution considered representative of car wheel loading. The number of cycles to failure ranged from 10^6 to more than 10^9. Experimental lives were found to be 7 23 times shorter than the fatigue life predicted using the original Palmgren-Miner damage accumulation rule.

Crack closure arguments are frequently used to explain the differences between constant and variable amplitude fatigue damage accumulation. Vormvald and Seeger [39] found that larger strain cycles caused an instantaneous change in the crack closure strain of the smaller cycles. The crack closure strain of the large cycle was approximately the same under both constant amplitude and variable amplitude loading. During a small strain cycle, the crack, which was closed for a considerable portion of the cycle under constant amplitude loading, was always open under variable amplitude loading. The effective strain range during which the crack was open was greater during variable amplitude loading, and more crack growth per cycle occurred.

Variable amplitude load where a significant portion of the fatigue cycles are smaller than the fatigue limit brings up significant questions with regard to damage accumulation. It is clear that in such cases the linear damage rule proposed by Palmgren [50] and Miner [51] cannot be used because this simple rule attributes no damage to cycles less than the fatigue limit. This problem has led researchers to a variety of more complex damage accumulation rules. Fatemi and Yang [52] surveyed and categorized many of this many of these rules and report more than 50 modifications of Palmgren-Miner rule. Many of these were developed to account for the effect of cycles below the fatigue limit.

The Model

The life prediction model used in this paper is based on several fundamental assumptions:

1. The fatigue process is governed by the propagation/non-propagation of fatigue cracks in which growth rate per cycle is related to the effective stress intensity factor range by a Paris-type equation.
2. The effective crack driving stress is affected by both maximum and minimum stresses in a history.
3. The material has an intrinsic threshold below which cracks will not propagate if the effective stress range is less than the threshold.

4. High cycle fatigue behavior of this material is controlled by the presence of shrinkage pores that behave as initial cracks.
5. Over- or underload events alter the crack driving force, and if a crack is not arrested, the driving force returns to the steady state value as an exponential function similar to that in the Topper model.

The most difficult aspect in developing the model is determining the intrinsic threshold, i.e., defining the effective driving force at the limit where crack propagation is not observed, $\Delta K_{th,int}$. During the variable amplitude underload tests at high mean stresses, it was observed that cycles with amplitudes equivalent to 60 % of the constant amplitude fatigue limit produced failure at about 100 million cycles in about half of the test specimens. This value is therefore used as a practical engineering value.

If it is assumed that the effective stress is related to the intrinsic threshold at the fatigue limit, a relationship between effective driving force and applied stress can be established. Effective driving force can be defined in terms of S_{max} and S_{min}. This is illustrated in Fig. 2, which indicates that under completely reversed loading only a small portion of the applied stress cycle is effective in propagating a crack.

In the experiments reported here, no attempts were made to specifically measure the crack opening loads of the small cracks during the fatigue process. Such measurements have been reported by DuQuesnay et al. [27], Varvani-Farahani and Topper [28], Vormwald and Seeger [39], and McClung and Sehitoglu [53]. In the current experiments, the difference between applied stress range and effective stress range may be attributable to crack closure, but some researchers have suggested that stresses ahead of the crack tip are more significant than closure stresses [2,14,15]. Stresses ahead of the crack tip become more significant in the case of plane strain or cracks propagating from micro notches, as is the case with nodular cast iron.

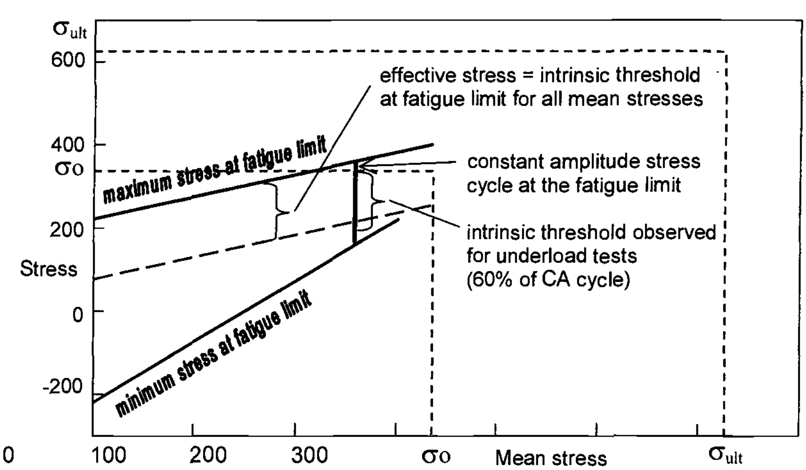

FIG. 2 *Smith diagram: relationship between maximum and effective stress.*

Most types of defects for thick-section castings can be avoided using high quality foundry practices, however, shrinkage pores cannot be avoided completely. The role of micro shrinkage pores on the high cycle fatigue behavior of this nodular cast iron has been well documented [54 58]. SEM investigations have shown that long life fatigue failures in test specimens can normally be attributed to crack initiation and growth from individual defects. The statistical size distribution of shrinkage pores also has been determined. Throughout this paper, a maximum defect size corresponding to 50 % probability of occurrence is used. Using a crack propagation based model it is also possible to compute other probability of failure curves based on the statistical distribution of defects.

After the issues of initial crack size and intrinsic threshold stress intensity are established, the crack growth constants C and m used in a modified Paris-type relationship are relatively easy to establish based on either finite life test data or direct observations of small crack propagation

$$\frac{da}{dN} = C\left[\left(K_{max} - K_{op}\right)^m - \Delta K_{th,int}{}^m\right] \tag{1}$$

The variable amplitude interaction model chosen is based on that used by Topper and colleagues [18,22,23]. This model assumes that the interactive damage for a given cycle decreased as an exponential function of the number of small cycles following an overload or underload. It is assumed that, under constant amplitude loading, a small crack will have a certain driving force based on the maximum stress, stress ratio, and crack size. In the case of underloads, the driving force is assumed to increase immediately after the underload and then gradually decay back toward the original constant amplitude state.

Experiments

Test Material

Nodular cast iron is used extensively in the production of ground vehicle components and large machinery. Casting provides an economical advantage over other production methods by offering significant freedom in geometrical shaping for functionality and material utilization. When compared to gray iron, nodular cast irons have significantly higher fatigue strengths that can be used to advantage in the design of fatigue-loaded components. Interest in this material for fatigue-loaded components is reflected in the large number of recent scientific publications devoted to this material [54 68]. Rigid quality control during the casting operation can eliminate the relatively large defects often associated with complex castings, but small microstructural irregularities can never be eliminated completely for large thick-section castings. These shrinkage pores, inclusions, and other types of naturally occurring defects have a controlling effect on the endurance limit strength. Numerous studies have shown that non-propagating defects are initiated at these defects at stress amplitudes below the conventional fatigue limit, and that the fatigue limit is associated with a crack propagation limit rather than a crack initiation limit [57 58,61].

Test bars were cut from either 100 × 100 × 300 mm ingots or from the cylinder head of a Wärtsilä 64 medium speed diesel engine. The cylinder head is a complex casting with outside dimensions of approximately 750 × 1000 × 1400 mm. Material from both the ingots and cylinder head were nominally identical, GRP 500/ISO 1083 nodular cast iron, but were received from two different foundries.

Material taken from the cylinder head had average yield strength, $R_{p0.2}$ = 307 MPa and ultimate strength, R_m = 517 Mpa, while material taken from the ingots was slightly stronger with $R_{p0.2}$ = 340 Mpa, and R_m = 620 MPa. Both showed approximately the same distribution of nodular graphites and a dual ferritic-pearlitic matrix. Material from the cylinder head was approximately 50 % pearlite, 40 % ferrite and 10 % graphite, while material from the ingots was 77 % pearlite, 10 % ferrite and 13 % graphite.

Fatigue Testing

Fatigue testing was accomplished using a computer-controlled resonant type test machine. Test frequency was nominally 160 Hz. Axial test specimens were ϕ12 mm with a 30 mm gage section and 50 mm transition radius. Specimens were polished with emery paper and diamond paste so that no scratches or machining marks perpendicular to the loading direction were visible under 20× magnification. Axial testing was performed using several stress ratios or mean stress levels. The staircase strategy was used to determine the constant amplitude fatigue limit at several different R ratios. Tests exceeding 1×10^7 cycles were considered run-outs. The staircase strategy and analysis method have been described by Rabb [69]. Material from both foundries was used in the constant amplitude fatigue limit testing. In most cases, 15 specimens were used to determine the fatigue limit at a single mean stress. Several series of constant amplitude fatigue limit torsion tests based on tubular specimens also were performed [54,55].

The variable amplitude history is illustrated generally in Fig. 3 with details of the spectra given in Table 1. In all cases, the variable amplitude spectrum consisted of a large number of small amplitude cycles at a high mean stress followed by a single unloading event to near zero stress. Only the material taken from the ingots was used in the variable amplitude testing. Due to the natural scatter in result found in fatigue of cast iron, most variable amplitude histories were repeated. The number of specimens used for a single load history also is given in Table 1.

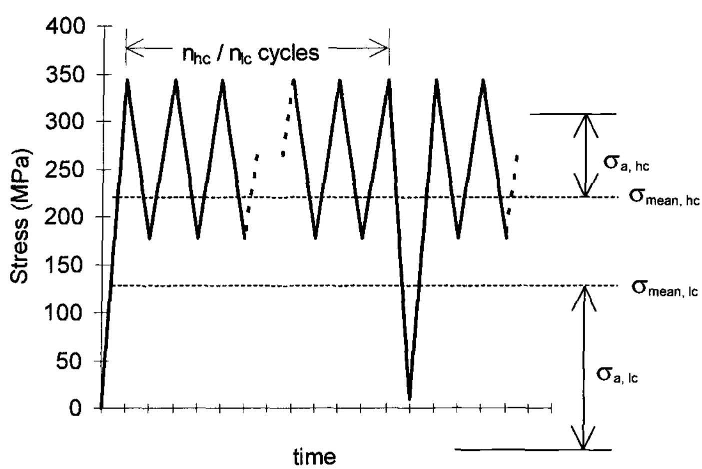

FIG. 3 *Aspects of the variable amplitude spectrum (see also Table 1).*

TABLE 1 *Details of variable amplitude test matrix.*

$\sigma_{mean, lc}$	$\sigma_{a, lc}$	$\sigma_{mean, hc}$	$\sigma_{a, hc}$	Mean Cycles to Failure, N_f	n_{hc}/n_{lc}	# of Specimens
190	180.5	260	111	543 900	3 300	10
177.5	167	260	83,5	4 636 200	20 000	10
167.5	157.5	260	65	> 80 000 000*	300 000	10
180.4	170.4	260	90,7	3 274 000	10 000	3
180.4	170.4	260	90,7	47 800 000	100 000	1
177.5	167	260	83,5	27 026 000	220 000	6
177.5	167	260	83,5	3 986 000	5 000	1

* Six of ten specimens with this history resulted in run-outs, $N_f > 150 \times 10^6$.

Results and Discussion

Constant Amplitude Fatigue

Results from the constant amplitude fatigue limit tests are presented in Fig. 4 in the form of a Haigh diagram. Because the nominally identical material was obtained from two foundries, both the mean stress and amplitude in this figure are normalized by the flow strength where flow strength is defined as the average of the yield strength and ultimate strength of the material. Figure 4 represents a 50 % probability of failure curve and shows a near linear change in allowable stress amplitude with respect to mean stress for a large variety of stress ratios. The form of the curve represents a compromise between the Goodman and Soderberg mean stress corrections and is given by

$$\Delta\sigma = \left(\frac{1}{(1-0.25\lambda)} - \frac{2 \cdot \sigma_m}{R_m + R_{p0.2}} \right) \cdot \Delta\sigma_w \tag{2}$$

where $\Delta\sigma$ is the allowable stress range at mean stress σ_m, and $\Delta\sigma_w$ is the stress range at the fatigue limit for $R = -1$. The use of the biaxial stress ratio, λ, is based on fracture mechanics arguments and is used for correlating axial tension and torsion data [54,55].

Crack Growth Parameters

Since the work of Elber on crack closure, many studies have been devoted to quantifying the effect of closure under a variety of load situations. Several empirical or semi-empirical relationships have been proposed to compute the crack opening stress based on a combination of loading and material parameters. Models by Newman [70], Sehitoglu [71], and DuQuesnay et al. [27] are similar in the respect that opening load is computed to be a function of S_{max}, S_{min} (or R ratio), and material strength, i.e., yield strength, cyclic yield strength, or flow strength.

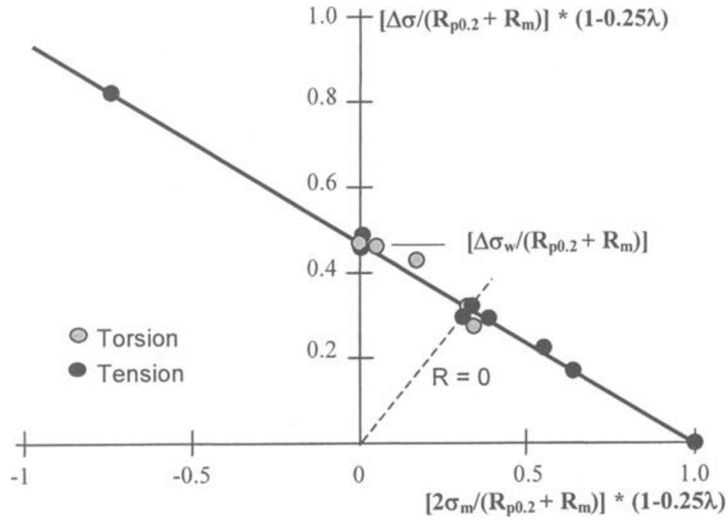

FIG. 4 *Constant amplitude Haigh diagram for nodular iron ($N_f > 10^7$).*

If it is assumed that the small cracks reported here grow in plane strain, the Newman model applied to near threshold crack growth predicts that small cracks are fully open for stress ratios above approximately 0.2. Similarly, the DuQuesnay et al. model for positive stress ratios assumes that there is a minimum stress above which the stress range at the fatigue limit becomes constant. As seen from Fig. 4, the nodular iron reported here shows no such constant stress range, even for stress ratios approaching 0.5.

Based on the Smith diagram of Fig. 2, it is assumed that, at the fatigue limit, the effective crack driving stress is independent of mean stress. This allows the crack opening stress to be formulated as a linear function of either the maximum or minimum stress. The variable amplitude spectra of interest consisted only of underload histories, so it was chosen to use a linear function of minimum stress

$$S_{op} = 170 + 0.36 \cdot S_{min} \tag{3}$$

For other types of load histories it would be necessary to formulate opening stress in terms of S_{max} and S_{min}.

For material taken from ingots, a 50 % probability of occurrence defect size was about 180 μm [57], i.e., half-circular defect with radius 180 μm. Figure 5 shows the extreme value distribution of maximum defect size for a 3400 mm^3 test volume.

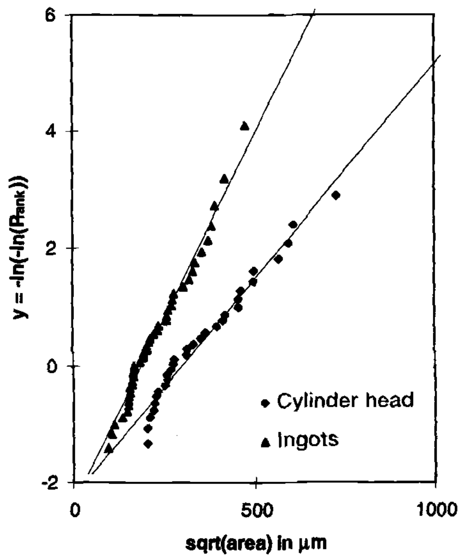

FIG. 5—*Extreme value distributions of shrinkage pore defects.*

As previously presented, the intrinsic threshold stress range was about 60 % of the applied stress range in the longest variable amplitude tests. This correlates to an intrinsic threshold stress intensity factor of 2.2 MPa $m^{1/2}$ for da/dN < 1 × 10^{-9} mm/cy. The crack growth rate da/dN < 1 × 10^{-9} mm/cy is assumed because no macroscopic crack propagation was observed within 1 × 10^{8} cycles for most of the variable amplitude specimens tested at the lowest stress level. It should be remembered that the value of 60 % was found for stress cycles with relatively high R ratios, R ≈ 0.4. For completely reversed strain cycles, Bonnen and Topper [30] found no effect from the small cycles only when the amplitude was one-third the fatigue limit. The current data would be very close to this value for R = −1 cycling. On a microstructural level it has been observed that cycles as small as $\Delta S_0/2$ still cause changes in the materials dislocation structure [72].

Based on the constant amplitude finite life data, crack growth parameters for the Paris equation are found to be m = 4 and C = 4 × 10^{-9} (units: mm/cycle, MPa $m^{1/2}$). Constant amplitude fatigue life from experiment and analysis are show in Fig. 6. At high stress amplitudes for the high mean stress data, the analytical predictions give slightly longer fatigue lives. This is partially explained in that the maximum stress for these cases is approaching the flow strength of the material, so significant plastic deformation is present, and linear elastic assumptions are violated. Scatter in the experiment results is due largely to the significant scatter observed in the initial defect sizes.

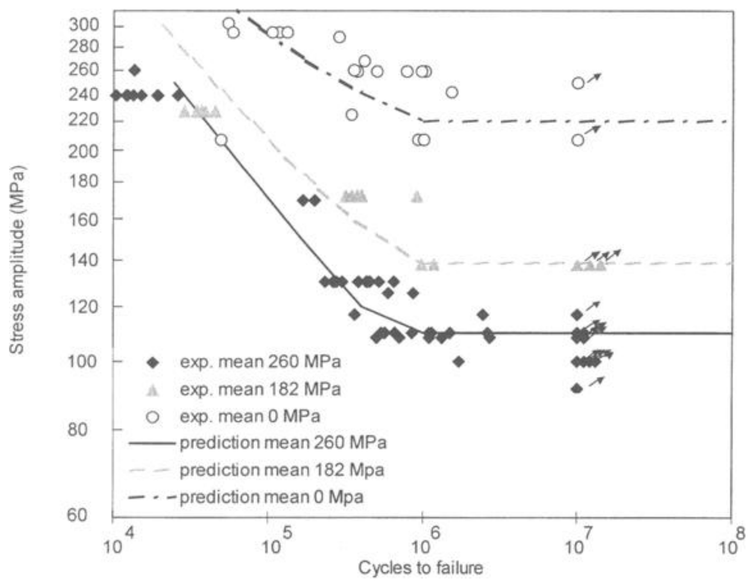

FIG. 6 *Experimental constant amplitude data and crack growth predictions.*

Variable Amplitude Life Predictions

Table 1 gives the number of specimens tested for each of the seven variable amplitude histories and the mean fatigue life. It can be noted from this table that the number of repetitions of the underload stress was always very small. The damage contribution of the larger stress cycles was always less than 1 %. In a typical case the large cycle was repeated 300 times in a variable amplitude test where a cycle of that size in constant amplitude loads would require 2×10^5 repetitions for failure, i.e., large cycle damage contribution = $300 / 2 \times 10^5 = 0.15$ %.

Based on a comparison of variable amplitude tests with similar $\sigma_{a,lc}$, $\sigma_{m,lc}$, $\sigma_{a,hc}$, and $\sigma_{m,hc}$, but with different N_{hc}/N_{lc}, it was possible to compute the rate at which the crack growth rate returned to a steady state value. A best fit was obtained for $\kappa = -0.0008$, where

$$\Delta S_{eff,N_{UL}} = \Delta S_{eff,CA} + \left(\Delta S_{eff,ul} - \Delta S_{eff,CA}\right)e^{\kappa N_{UL}} \tag{4}$$

In this equation, $\Delta S_{eff,N_{UL}}$ is the effective stress range for cycle N_{UL} after the under load, $\Delta S_{eff,CA}$ is the effective crack driving stress range of the small amplitude cycle under constant amplitude loading, and $\Delta S_{eff,ul}$ is the effective driving force of the underload cycle during constant amplitude loading. The value $\kappa = -0.0008$ means that for 6000 load cycles following an underload, the crack driving stress range has returned to within 1 % of the constant amplitude stress value. Linking the change in crack driving stress range to the number of cycles following an underload event is a matter of convenience. Physically it would be more appropriate to link this to the crack advance.

Crack growth for a typical variable amplitude test, $\sigma_{a,lc} = 83.5$, $N_{hc}/N_{lc} = 20\ 000$, is shown in Fig. 7. The prediction in this figure is made based on previous computed values of C, m, $\Delta K_{th,int}$, and κ.

Figure 8 shows the predicted S-N curves in comparison to the experimental data for the long-life variable amplitude tests. These curves tend to follow the mean of the experiment data. Using this type of fracture mechanics approach, however, it is relatively easy to compute curves representing other failure probabilities based on knowledge of the shrinkage pore distributions.

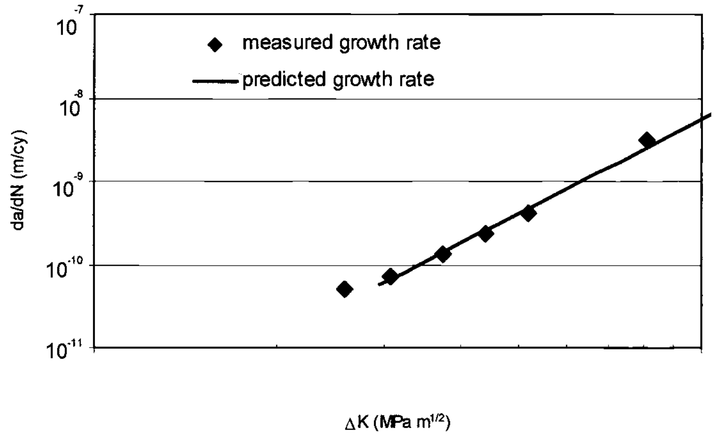

FIG. 7 *Observed and predicted crack growth,* $\sigma_{a,lc} = 83.5$, $N_{hc}/N_{lc} = 20\ 000$.

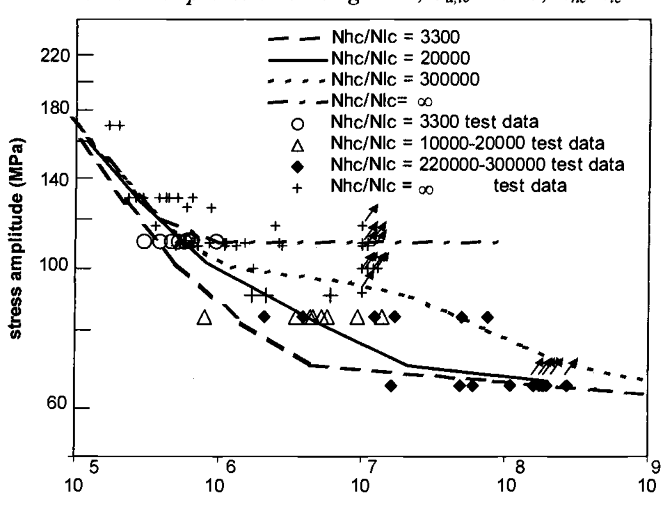

FIG. 8—*Measured fatigue lives and predicted SN curves for several variable amplitude histories.*

Conclusions

This paper has reviewed numerous life prediction methods for variable amplitude fatigue. Special attention was given to cracks propagating from nominally defect free components in the high cycle regime where a significant portion of the fatigue damage can be attributed to cycles with amplitude less than the constant amplitude fatigue limit. An effective stress method for variable amplitude loaded similarly to the Topper model is presented for long-life fatigue of a nodular cast iron. Model parameters are derived from a constant amplitude S-N curve and the Haigh diagram. Two sets of long-life variable amplitude tests were used to derive the underload interaction parameters.

Previously measured shrinkage pore distributions for the iron were used to determine 50 % probability of occurrence initial defect size. This size defect was chosen to illustrate the model, but in design, a much lower probability of occurrence initial defect size would need to be chosen.

Current experiments were limited to constant amplitude loading and variable amplitude loading containing underloads, so the crack driving stress was formulated only in terms of the minimum stress in a cycle of block of cycles. Good agreement is found between the experiments and the model prediction. However, a relationship between the maximum load and the effective crack driving stress would also need to be established for more general loading situations that also include overloads.

References

[1] Schjive, J. *Fatigue of Structures and Materials*, Kluwer Academic Publishers, Dordrecht, 2001.

[2] Sehitoglu, H., Gall, K., and Garcia, A. M., "Recent Advances in Fatigue Crack Growth Modeling," *International Journal of Fracture*, Vol. 80, 1996, pp. 165 192.

[3] Lawson, L., Chen, E. Y., and Meshii, M., "Near-Threshold Fatigue: A Review," *International Journal of Fatigue*, Vol. 21, 1999, pp. 15 34.

[4] Geary, W., "A Review of Some Aspects of Fatigue Crack Growth Under Variable Amplitude Loading," *International Journal of Fatigue*, Vol. 14, 1992, pp. 377 386.

[5] Kumar, R., "A Review on Crack Closure for Single Overload, Programmed and Block Loadings," *Engineering Fracture Mechanics*, Vol. 42, 1992, pp. 151 158.

[6] Forman, R. G., Kearny, V. E., and Engle, R. M., "Numerical Analysis of Crack Propagation in a Cyclic-Loaded Structure," *Transactions of the ASME Journal of Basic Engineering*, Vol. D89, 1967, pp. 458 464.

[7] Walker, K., "The Effect of Stress Ratio During Crack Propagation and Fatigue for 2024-T3 and 7075-T6 Aluminum," In: *Effects of Environment and Complex Load History on Fatigue Life, ASTM STP 462*, ASTM International, West Conshohocken, PA, 1970.

[8] Barsom, J. M. and Rolfe, S. T., *Fracture Control in Structures*, Prentice-Hall, Englewood Cliffs, NJ, 1977.

[9] Lal, D. N., "The Combined Effects of Stress Ratio and Yield Strength on the LEFM Fatigue Threshold Condition," *Fatigue and Fracture of Engineering Materials and Structures*, Vol. 15, 1992, pp. 1199 1212.

[10] Wheeler, O. E., "Spectrum Loading and Crack Growth," *Journal of Basic Engineering*, Vol. 94, 1972, pp. 181 186.

[11] Willenborg, J., Engle, R. M., and Wood, H. A., "A Crack Growth Retardation Model Using an Effective Stress Concept," *AFFDL-TR71-1*, Air Force Flight Dynamic Laboratory, Wright-Patterson Air Force Base, OH, 1971.

[12] Elber, W., "Fatigue Crack Closure Under Cyclic Tension," *Engineering Fracture Mechanics*, Vol. 2, 1970, pp. 37 45.

[13] Elber, W., "The Significance of Fatigue Crack Closure," In: *Damage Tolerant Aircraft Structures, ASTM STP 486*, ASTM International, West Conshohocken, PA, 1971, pp. 230 242.

[14] Sadananda, K, Vasudevan, A. K., Holtz, R. L., and Lee, E. U., "Analysis of Overload Effects and Related Phenomena," *International Journal of Fatigue*, Vol. 21, 1999, pp. S233 S246.

[15] Sehitoglu, H. and Sun, W., "Modeling of Plane Strain Fatigue Crack Closure," *ASME Journal of Engineering Materials and Technology*, Vol. 113, 1990, pp. 31 40.

[16] Baudin, G. and Robert, M., "Crack Growth Life Prediction Under Aeronautical Type Loading," *ECF 5*, Lisbon, 1984, pp. 779 792.

[17] de Koning, A. U., "A Simple Crack Closure Model for Prediction of Fatigue Crack Growth Rates Under Variable-Amplitude Loading," In: *Fracture Mechanics, ASTM STP 743*, R. Roberts, Ed., ASTM International, West Conshohocken, PA, 1981, pp. 63 85.

[18] Topper, T. H. and Yu, M. T., "The Effect of Overloads on Threshold and Crack Closure," *International Journal of Fatigue*, Vol. 7, 1985, pp. 159 164.

[19] Führing, H. and Seeger, T., "Structural Memory of Cracked Components Under Irregular Loading," In: *Fracture Mechanics, ASTM STP 677*, C. W. Smith, Ed., ASTM International, West Conshohocken, PA, 1979, pp. 144 167.

[20] Newman Jr., J. C., "A Crack-Closure Model for Predicting Fatigue Crack Growth Under Aircraft Spectrum Loading," In: *Methods and Models for Predicting Fatigue Crack Growth Under Random Loading, ASTM STP 748*, J. B. Chang and C. M. Hudson, Eds., ASTM International, West Conshohocken, PA, 1981, pp. 53 84.

[21] Wang, G. S. and Blom, A. F., "A Strip Model for Fatigue Crack Growth Prediction Under General Load Conditions," *Engineering Fracture Mechanics*, Vol. 40, 1991, pp. 507 533.

[22] Dugdale, D. S., "Yielding of Steel Sheets Containing Slits," *Journal of Mechanics and Physics of Solids*, Vol. 8, 1960, pp. 100 104.

[23] Pompetzki, M. A., Topper, T. H., and DuQuesnay, D. L., "The Effect of Compressive Underloads and Tensile Overloads on Fatigue Damage Accumulation in SAE 1045 Steel," *International Journal of Fatigue*, Vol. 12, 1990, pp. 207 213.

[24] Jurcevic, R., DuQuesnay, D. L., Topper, T. H., and Pompetzki, M. A., "Fatigue Damage Accumulation in 2024-T351 Aluminium Subjected to Periodic Reversed Overloads," *International Journal of Fatigue*, Vol. 12, 1990, pp. 259 266.

[25] Conle, A. and Topper, T. H., "Evaluation of Small Cycle Omission Criteria for Shortening of Fatigue Service Histories," *International Journal of Fatigue*, Vol. 1, 1979, pp. 23 28.

[26] Conle, A. and Topper, T. H., "Overstrain Effects During Variable Amplitude Service History Testing," *International Journal of Fatigue*, Vol. 2, 1980, pp. 130 136.

[27] DuQuesnay, D. L., Topper, T. H., Yu M. T., and Pompetzki, M. A., "The Effective Stress Range as a Mean Stress Parameter," *International Journal of Fatigue*, Vol. 14, 1992, pp. 45 50.

[28] Varvani-Farahani, A. and Topper, T. H., "Increases in Fatigue Crack Growth Rate and Reductions in Fatigue Strength Due to Periodic Overstrains in Biaxial Fatigue Loading," In: *Fatigue Crack Growth Thresholds, Endurance Limits, and Design, ASTM STP 1372*, J.

C. Newman, Jr. and R. S. Piascik, Eds., ASTM International, West Conshohocken, PA, 2000, pp. 192 206.

[29] MacDougall, C. and Topper, T. H., "The Influence of Variable Amplitude Loading on Crack Closure and Notch Fatigue Behaviour," *International Journal of Fatigue*, Vol. 19, 1997, pp. 389 400.

[30] Bonnen, J. J. F. and Topper, T. H., "The Effect of Bending Overloads on Torsional Fatigue in Normalized 1045 Steel," *International Journal of Fatigue*, Vol. 21, 1999, pp. 23 33.

[31] Lam, T. S., Topper, T. H., and Conle, F. A., "Derivation of Crack Closure and Crack Growth Rate From Effective-Strain Fatigue Life Data for Fracture Mechanics Fatigue Life Predictions," *International Journal of Fatigue*, Vol. 20, 1998, pp. 703 710.

[32] Haibach, E., "The Allowable Stresses Under Variable Amplitude Loading," In: *Proceedings of the Conference on Fatigue of Welded Structures*, Vol. 2. Abington, Cambridge: The Welding Institute. 1971, pp. 328 339.

[33] Gassner, E. and Lipp, W., "Long Life Random Fatigue Behavior of Notched Specimens in Service, in Service Duplication Tests, and in Program Tests," In: *Service Fatigue Loads Monitoring, Simulation and Analysis, ASTM STP 671*, P. R. Abelkis and J. M. Potter, Eds., ASTM International, West Conshohocken, PA, 1979, pp. 222 239.

[34] Schütz, W. and Heuler, P., "Miner's Rule Revisited," 77, AGARD-SMP Meeting, Bordeaux, 27 September–1 October 1993, Ottobrunn: Industrieanlagen-Betriebsgesellshaft GmbH.

[35] Zenner, H. and Liu, J., "Vorschlag zur Verbesserung der Lebensdauerabschätzung nach dem Nennspannung. Konstruction," Vol. 1, 1992, pp. 9 17.

[36] Tokaji, K. and Ando, Z., "Small Fatigue Crack Growth Behaviour Under Two Stress Level Multiple Loading," *Fatigue and Fracture of Engineering Materials and Structures*, Vol. 7, 1984, pp. 109 119.

[37] Yan, X., Cordes, T. S., Vogel, J. H., and Dindinger, P. M., "A Property Fitting Approach for Improved Estimates of Small Cycle Fatigue Damage," *SAE Transactions Journal of Materials and Manufacturing*, Vol. 101, 1992, pp. 544 553.

[38] Stanzl-Tschegg, S. E., Mayer, H. R., Beste, A., and Kroll, S., "Fatigue and Fatigue Crack Propagation in AlSi7Mg Cast Alloys Under In-Service Loading Conditions," *International Journal of Fatigue*, Vol. 17, 1995, pp. 149 155.

[39] Vormwald, M. and Seeger, T., "The Consequences of Short Crack Closure on Fatigue Crack Growth Under Variable Amplitude Loading," *Fatigue and Fracture of Engineering Materials and Structures*, Vol. 14, 1991, pp. 205 225.

[40] Zhou, Z. and Zwerneman, F. J., "Fatigue Damage Due to Sub-Threshold Load Cycles Between Periodic Overloads," In: *Advances in Fatigue Lifetime Predictive Techniques: Second Volume, ASTM STP 1211*, M. R. Mitchell and R. W. Landgraf, Eds., ASTM International, West Conshohocken, Pa, 1993, pp. 45 53.

[41] Hénaff, G., Petit, J., and Journet, B., "Fatigue Crack Propagation Behaviour Under Variable Amplitude Loading in the Near-Threshold Region of a High-Strength Low-Alloy Steel," *Fatigue and Fracture of Engineering Materials and Structures*, Vol. 15, 1992, pp. 1155 1170.

[42] Kikukawa, M., Jono, M., and Kondo, Y., "An Estimation Method of Fatigue Crack Propagation Rate Under Varying Loading Conditions of Low Stress Intensity Level," *Advances in Fracture* Research (Fracture '81), Pergamon Press, Oxford, 1982, pp. 1799 1806.

[43] Koterazawa, R., "Fatigue Crack Propagation Under Periodic Overstressing," *International Journal of Fracture*, Vol. 12, 1976, pp. 169 170.

[44] Koterazawa, R., Mudjijana, Y., Qinsheng, W., Tian-Jian, W., and Nosho, T., "Acceleration of Fatigue Crack Growth Under Intermittent Overstressing with Different Mean Stress Levels," *Fatigue and Fracture of Engineering Materials and Structures*, Vol. 17, 1994, pp. 1033 1041.

[45] Sunder, R., "Contribution of Individual Spectrum Load Cycles to Damage in Notch Root Crack Initiation, Short and Long Crack Growth," In: *Advances in Fatigue Lifetime Predictive Techniques: Second Volume, ASTM STP 1211*, M. R. Mitchell and R. W. Landgraf, Eds., ASTM International, West Conshohocken, PA, 1993, pp. 19 29.

[46] Sunder, R., Prakash, R. V., and Mitchenko, E. I., "Calculation of Spectrum Load Notch Root Crack Growth Rate Under Elastic and Inelastic Conditions," In: *Advances in Fatigue Lifetime Predictive Techniques: Second Volume, ASTM STP 1211*, M. R. Mitchell and R. W. Landgraf, Eds., ASTM International, West Conshohocken, PA, 1993, pp. 30 44.

[47] Sunder, R., "Near-Threshold Fatigue Crack Growth Prediction Under Spectrum Loading," In: *Advances in Fatigue Lifetime Predictive Techniques: Second Volume, ASTM STP 1122*, M. R. Mitchell and R. W. Landgraf, Eds., ASTM International, West Conshohocken, PA, 1992, pp. 161 175.

[48] Marquis, G., *High Cycle Spectrum Fatigue of Welded Components*, VTT Publications 240, Technical Research Centre of Finland, Espoo, Finland, 1995.

[49] Ohta, A., Maeda, Y., Machida, S., and Yoshinari, H., "Near Threshold Fatigue Crack Growth in Welded Joints Under Random Loadings," *Transactions of the Japan Welding Society*, 19, 1988, pp. 69 73.

[50] Palmgren, A, " Die Ledensdauer von Kugellagern," *Verfahrenstechinik*, Berlin, 1924, Vol. 68, 339 341.

[51] Miner, M. A., "Cumulative Damage in Fatigue," *ASME Journal of Applied Mechanics*, Vol. 12, 1945, pp. A159 164.

[52] Fatemi, A. and Yang, L., "Cumulative Fatigue Damage and Life Prediction Theories: A Survey of the State of the Art for Homogeneous Materials," *International Journal of Fatigue*, Vol. 20, 1998, pp. 9 34.

[53] McClung, R. C. and Sehitoglu, H., "Closure Behavior of Small Cracks Under High Strain Fatigue Histories," In: *Mechanics of Fatigue Crack Closure, ASTM STP 982*, ASTM International, West Conshohocken, PA, 1988, pp. 279 299.

[54] Marquis, G. and Karjalainen-Roikonen, P., "Long-Life Multiaxial Fatigue of SG Cast Iron," *Proceedings of the Sixth International Conference on Biaxial/Multiaxial Fatigue and Fracture*, M. M. de Freitas, Ed., 2001, pp. 151 159.

[55] Marquis, G., "Mean Stress in Long-Life Torsion Fatigue," In: *Proceeding of ECF 13*, San Sebastian, Spain, Paper 3m.314, 2000.

[56] Marquis, G. and Solin, J., *Long-Life Fatigue Design of GRP 500 Nodular Cast Iron Components*, VTT Research Notes 2043, Technical Research Centre of Finland, Espoo, 2000, p. 70.

[57] Marquis, G. and Murakami, Y., "Scatter in the Fatigue Limit of Nodular Iron," *Materials Science Research International, Special Technical Publication*, T. Hoshide, Ed., Kyoto, 2001, pp. 92 96.

[58] Marquis, G., Rabb, R., and Siivonen, L., "Endurance Limit Design of Spheroidal Graphite Cast Iron Components Based on Natural Defects," *Fatigue Crack Growth Thresholds, Endurance Limits, and Design, ASTM STP 1372*, J. C. Newman and R. S. Piascik, Eds., ASTM International, West Conshohocken, PA, 1999, pp. 411 426.

[59] Clement, P., Angeli, J. P., and Pineau, A., "Short Crack Behaviour in Nodular Cast Iron," *Fatigue and Fracture of Engineering Materials and Structures*, Vol. 7, 1984, pp. 251 265.
[60] Tokaji, K., Ogawa, T., and Shamoto, K., "Fatigue Crack Propagation in Sheroidal-Graphite Cast Irons with Different Microstructures," *International Journal of Fatigue*, Vol. 16, 1994, pp. 344 350.
[61] Yaacoub Agha, H., Béranger, A.-S., Billardon, R., and Hild, F., "High-Cycle Fatigue Behaviour of Spheroidal Graphite Cast Iron," *Fatigue and Fracture of Engineering Materials and Structures*, Vol. 21, 1998, pp. 287 296.
[62] Nadot, Y., Ranganathan, N., Mendez, J., and Béranger, A.-S., "A Study of Natural Cracks Initiated on Casting Defects by Crack Front Marking," *Scripta Materialica*, Vol. 37, 1997, pp. 549 553.
[63] Palin-Luc, T., Lasserre, S., Froustey, C. and Bérard, J. Y., "Experimental Approach of Damage Accumulation in High Cycle Fatigue with Random Loadings in Blocks," In: *Mechanisms and Mechanics of Damage and Failure: ECF11,* J. Petit, Ed., EMAS, UK, 1996, pp. 1337 1342.
[64] Nadot, Y., Ranganathan, N., Mendez, J., and Béranger, A.-S., "Fatigue Damage in Spheroidal Graphite Cast Iron (SGI)," In: *Mechanisms and Mechanics of Damage and Failure: ECF11,* J. Petit, Ed., EMAS, UK, 1996, pp. 1155 1160.
[65] Schleicher, M., Bomas, H., and Mayr, P., "Fatigue Surface Cracks in Cast Iron with Nodular Graphite," In: *Fracture from Defects: ECF 12*, M.W. Brown, E. R. de los Rios, and K. J. Miller, Eds., EMAS, UK, 1998, pp. 91 96.
[66] Nadot, Y., Ranganathan, N., Mendez, J., and Béranger, A.-S., "Fatigue Limit of Nodular Cast Iron Containing Casting Defects," In: *Fracture from Defects: ECF 12*, M. W. Brown, E. R. de los Rios, and K. J. Miller, Eds., EMAS, UK, 1998, pp. 85 90.
[67] Greno, G. L., Otegui, J. L., and Boeri, R. E., "Mechanisms of Fatigue Crack Growth in Austempered Ductile Iron," *International Journal of Fatigue*, Vol. 21, 1999, pp. 35 43.
[68] Lin, C.-K. and Lee, W.-J., "Effects of Highly Stressed Volume on Fatigue Strength of Austempered Ductile Irons," *International Journal of Fatigue*, Vol. 20, 1998, pp. 301 307.
[69] Rabb, B. R., *Fatigue Testing and Its Statistical Evaluation into Design Rules*, Ph.D. thesis, Tampere University of Technology, Publication 253, Tampere, 1999.
[70] Newman, J. C., Jr. "A Crack Opening Stress Equation for Fatigue Crack Growth," *International Journal of Fracture*, Vol. 24, 1984, R131 R135.
[71] Sehitoglu, H., "Crack Opening and Closure in Fatigue," *Engineering Fracture Mechanics*, Vol. 21, 1985, pp. 329 339.
[72] Fukuoka, C. and Nakagawa, Y. G., "Microstructural Evaluation of Cumulative Fatigue Damage Below the Fatigue Limit," *Scripta Materialica*, Vol. 34, 1996, pp. 1497 1502.

Journal of ASTM International, September 2004, Vol. 1, No. 8
Paper ID JAI19027
Available online at www.astm.org

J. C. Newman, Jr.[1] *and E. P. Phillips*[2]

Prediction of Crack Growth Under Variable-Amplitude and Spectrum Loading in a Titanium Alloy

ABSTRACT: The present paper is concerned with the application of a plasticity-induced crack-closure model, FASTRAN, to predict fatigue-crack growth under various load histories in a thin-sheet Ti-62222 STA titanium alloy. This alloy was a leading candidate for a metallic High-Speed-Civil-Transport (HSCT) aircraft in the United States. The crack-growth model was based on the Dugdale strip-yield model but modified to leave plastically deformed material in the wake of the advancing crack. The model includes the influence of "constraint" on the development of plasticity and closure during constant- and variable-amplitude load histories. The model was used to correlate crack-growth-rate data under constant-amplitude loading over a wide range in crack-growth rates and stress ratios at two service temperatures (room temperature and 175°C). Tests on repeated spike overloads were used to help establish the constraint variations in the model. The model was then used to predict crack growth under two simulated aircraft spectrum load histories at the two temperatures. The spectra were a commercial HSCT wing spectrum and the Mini-TWIST (transport wing spectrum). This paper will demonstrate how constraint plays a leading role in the retardation and acceleration effects that occur under variable-amplitude and spectrum loading. The model was able to calculate the effects of repeated spike overloads on crack growth at the two temperatures, generally within about ± 30 %. Also, the predicted crack-growth behavior under the HSCT spectrum agreed well with test data (within 30 %). However, the model under-predicted the fatigue-crack-growth behavior under the Mini-TWIST spectrum by about a factor-of-two. Some of the differences may be due to fretting-product-debris-induced closure or three-dimensional effects, such as free-surface closure, not included in the model. Further study is needed on life predictions under the Mini-TWIST flight spectrum.

KEYWORDS: cracks, fatigue, fatigue crack growth, fracture mechanics, stress-intensity factor, crack closure, plasticity, constraint

Nomenclature

B	Specimen thickness, mm
C_i	Crack-growth coefficient for segment i
c	Crack length, mm
F	Boundary-correction factor
K_F	Elastic-plastic fracture toughness in TPFC, MPa$\sqrt{m}$
m	Fracture toughness parameter in TPFC
N	Number of cycles
N_f	Number of cycles to failure
n_i	Crack-growth power for segment i
R	Stress ratio (S_{min}/S_{max})

Manuscript received 25 July 2002; accepted for publication 17 July 2003; published September 2004. Presented at ASTM Symposium on Fatigue Testing and Analysis Under Variable Amplitude Loading Conditions on 29 31 May 2002 in Tours, France; P. C. McKeighan and N. Ranganathan, Guest Editors.

[1] Professor, Department of Aerospace Engineering, Mississippi State University, Mississippi State, MS, 39762.
[2] Retired, Mechanics and Durability Branch, NASA Langley Research Center, Hampton, VA, 23681.

S	Applied stress, MPa
S_{CA}	Maximum stress under constant-amplitude loading, MPa
S_o	Crack-opening stress, MPa
S_{max}	Maximum applied stress or maximum stress in HSCT spectrum, MPa
S_{mf}	Mean flight stress level in Mini-TWIST spectrum, MPa
S_{min}	Minimum applied stress, MPa
S_{OL}	Overload stress, MPa
S_{UL}	Under-load stress, MPa
w	Width for ESE(T) and one-half width for M(T) specimen, mm
α	Constraint factor
ΔK	Stress-intensity factor range, MPa$\sqrt{m}$
ΔK_{eff}	Effective stress-intensity factor range, MPa$\sqrt{m}$
$(\Delta K_{eff})_T$	Effective stress-intensity factor range at flat-to-slant crack growth, MPa$\sqrt{m}$
σ_o	Flow stress (average of σ_{ys} and σ_u), MPa
σ_{ys}	Yield stress (0.2 % offset), MPa
σ_u	Ultimate tensile strength, MPa
ESE(T)	Eccentrically-loaded-single-edge crack tension specimen
HSCT	High-Speed Civil Transport
M(T)	Middle-crack tension specimen
TPFC	Two-Parameter Fracture Criterion

Introduction

In 1968, Elber observed that fatigue-crack surfaces contact under cyclic tensile loading. This simple observation and the crack-closure concept [1,2] began to explain many crack-growth characteristics. Since the discovery of "plasticity-induced" crack closure, other closure mechanisms have been identified, such as roughness-, fretting-product-, and oxide-induced closure. These developments have greatly improved our understanding of the complex interactions that occur during fatigue-crack growth under variable-amplitude loading (see Schijve [3]). During the past 20 years, several numerical models of plasticity-induced crack closure have been developed to calculate crack-opening stresses under aircraft spectrum loading, such as the NASA/FASTRAN model by Newman [4,5] or the ESA/NLR STRIPY model by de Koning et al. [6]. The STRIPY model is currently implemented in the NASGRO life-prediction software [7].

The objective of this paper is to use the FASTRAN crack-closure model to correlate constant-amplitude crack-growth-rate data on a thin-sheet Ti-62222 STA titanium alloy [8] and to predict crack growth under variable-amplitude loading and under two different wing spectrum loading (a High-Speed Civil Transport wing spectrum [8] and the Mini-TWIST [9] load sequence). The model includes the influence of "constraint" on the development of crack-tip plasticity and on crack-surface closure. This paper will demonstrate how constraint plays a leading role in crack growth under variable-amplitude loading. Comparisons are made between measured and calculated fatigue-crack-growth lives from an initial crack length to failure for repeated spike overload tests. Comparisons are also made between measured and predicted crack-length-against-cycles for tests subjected to two different aircraft wing spectrum-loading histories at two service temperatures.

Material and Specimen Configurations

The fatigue-crack-growth and fracture test results on the thin-sheet Ti-62222 STA titanium alloy (B = 1.6 1.75 mm) were obtained from several sources. Phillips [8] conducted fatigue-crack growth and fracture tests on middle-crack tension, M(T), specimens (2w = 51 and 76 mm wide). Smith and Piascik [10] and Liknes and Stephens [11] conducted fatigue-crack growth tests on eccentrically-loaded-singe-edge-crack tension, ESE(T), specimens (w = 76 mm wide). Worden (Boeing Airplane Co.) conducted fatigue-crack growth and fracture tests on M(T) specimens (2w = 254 mm wide). The chemical compositions, heat treatments, and tensile properties for these materials are given in Table 1.

TABLE 1 *Ti-62222 STA chemical compositions, heat treatments, and tensile properties.*

Chemical composition (average weight percent):											
Al	Sn	Zr	Mo	Cr	Si	O	Fe	C	N	Y	Ti
5.74	1.96	2.04	2.10	2.05	0.17	0.11	0.11	0.01	0.004	< 50ppm	Balance

Heat treatment:
Solution treated at 900°C for 30 min, air cooled, age at 510°C for 10 h, air cooled.

Tensile properties for longitudinal direction:	Room Temperature	175°C
Ultimate tensile strength:	1310 MPa	1160 MPa
0.2 %-offset yield stress:	1190 MPa	970 MPa
Elongation to failure:	8 %	8 %

Plasticity-Induced Crack-Closure Model

The plasticity-induced crack-closure model was developed for a central through crack and two symmetric through cracks emanating from a circular hole, in a finite-width plate subjected to uniform remote applied stress. The model was based on the Dugdale strip-yield model [12] but modified to leave plastically deformed material in the wake of the crack. The details of the model are given elsewhere and will not be presented here (see Newman [4,5]). One of the most important features of the model, however, is the ability to model three-dimensional constraint effects. A constraint factor α is used to elevate the flow stress (σ_o) at the crack tip to account for the influence of stress state ($\alpha\sigma_o$) on plastic-zone sizes and crack-surface displacements. (The flow stress σ_o is taken as the average between the yield stress σ_{ys} and ultimate tensile strength σ_u of the material.) For plane-stress conditions, α is equal to unity (original Dugdale model); and for simulated plane-strain conditions, α is equal to three. Although the strip-yield model does not model the correct yield-zone pattern for plane-strain conditions, the model with a high constraint factor is able to produce crack-surface displacements and crack-opening stresses quite similar to those calculated from three-dimensional, elastic-plastic, finite-element analyses of crack growth and closure for finite-thickness plates [13,14].

The calculations performed herein were made with FASTRAN Version 3.8. The modifications made to FASTRAN-II (Version 2.0), described in [5], were made to improve the crack-opening stress calculations under variable-amplitude loading, to improve the element "lumping" procedure to maintain the residual plastic deformation history, and to improve computational efficiency.

Effective Stress-Intensity Factor Range

For most damage-tolerance and durability analyses, linear-elastic fatigue-crack growth analyses have been found to be quite adequate. The linear-elastic effective stress-intensity factor range developed by Elber [1,2] is given by

$$\Delta K_{eff} = (S_{max} - S_o) \sqrt{(\pi c)}\ F \tag{1}$$

where S_{max} is the maximum stress, S_o is the crack-opening stress, and F is the boundary-correction factor. In general, for any crack configuration, the effective stress-intensity factor range is given by

$$\Delta K_{eff} = U\,\Delta K = [(1 - S_o/S_{max})/(1 - R)]\,\Delta K \tag{2}$$

Constant-Amplitude Loading

Newman [15] developed steady-state crack-opening stress equations from the plasticity-induced crack-closure model for an M(T) specimen subjected to constant-amplitude loading at various stress levels, stress ratios (R), and constraint factors (α). Crack-closure transients, before the crack-opening stresses stabilize under constant-amplitude loading, are not included in the equations. The FASTRAN model has to be exercised to determine these transient behaviors. Later, the FASTRAN model and the equations were modified (see Newman [5,16]) to account for extreme crack-growth rates, such as those under high loads or proof testing. Equations were then fit to the results from the model, which gave crack-opening stress (S_o) as a function of stress ratio (R), maximum stress level (S_{max}/σ_o), and the constraint factor (α). K-analogy [5] is used to calculate the crack-opening stresses for other specimen types, such as the compact C(T) and ESE(T) specimens. Here it is assumed that the same K_{max} and ΔK will result in the same stabilized crack-opening load. These equations are then used to correlate fatigue-crack-growth-rate data in terms of ΔK_{eff} on M(T) and ESE(T) specimens.

Constraint Effects

In general, the plastic-zone size at a crack front increases as a crack grows in a metallic material under cyclic loading (constant applied stresses). At low stress-intensity factor levels, plane-strain conditions should prevail, but as the plastic-zone size becomes large compared to thickness, a loss of constraint is expected (see Newman et al. [14]). This constraint loss has been associated with the transition from flat-to-slant crack growth. Schijve [17] has shown that the transition occurs at nearly the same crack-growth rate (or ΔK_{eff}) over a wide range in stress ratios for an aluminum alloy. This observation has been used to help select the constraint-loss regime. Newman [16] developed an expression to predict the transition from flat-to-slant crack growth, and the ΔK_{eff} at transition is given by

$$(\Delta K_{eff})_T = 0.5\,\sigma_o \sqrt{B} \tag{3}$$

where σ_o is the flow stress and B is the sheet thickness. The range of the constraint-loss regime, in terms of rate or ΔK_{eff}, is a function of sheet thickness, but this relation has yet to be developed. Trial-and-error methods are currently used to establish the range in crack-growth rates where the constraint-loss regime will occur for a given material and thickness.

In the application of FASTRAN, the constraint-loss regime is controlled by crack-growth rates. For rates lower than a certain (input) value, the constraint factor is high (like plane strain), but if the rate is higher than another (input) rate, then the constraint factor is low (like plane stress). For intermediate rates, a linear relation on log of rates is used to estimate the constraint factor between the upper and lower constraint values. The constraint factor only changes the forward plastic-zone size and crack-surface displacements under the current loading. The crack-growth model does not physically model the shear-lip or slant crack-growth process under either constant- or variable-amplitude loading. Obviously, the crack-growth process under variable-amplitude loading is quite complex, and the FASTRAN model is a simple engineering approach.

Crack-Growth Rate Relation

The crack-growth relation used in FASTRAN was

$$dc/dN = C_i\,(\Delta K_{eff})^{n_i} / [1 - (K_{max}/K_{Ie})^q] \tag{4}$$

where C_i and n_i are the coefficient and power for each linear segment, as shown in Fig. 1, K_{max} is the maximum stress-intensity factor, K_{Ie} is the elastic fracture toughness (which is a function of crack length, specimen width, and specimen type), and q was set to 2.

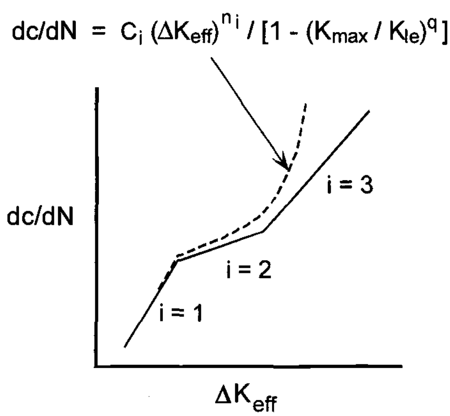

FIG. 1 *Multi-linear fatigue-crack-growth rate relation.*

Fracture

Newman [18] proposed the Two-Parameter Fracture Criterion (TPFC) to correlate fracture data and to predict failure loads on metallic materials. The TPFC equation is

$$K_F = K_{Ie} / (1 - m\, S_n/S_u) \text{ for } S_n < \sigma_{ys} \tag{5}$$

where K_F and m are the two fracture parameters; K_{Ie} is the elastic stress-intensity factor at failure; S_n is the net-section stress; and S_u is the plastic-hinge stress based on the ultimate tensile strength. For example, for an M(T) specimen, S_u is equal to σ_u, the ultimate tensile strength, and for a pure bend specimen, $S_u = 1.5\,\sigma_u$. A similar equation was derived for $S_n > \sigma_{ys}$ [18].

The m-value is both a material and configuration parameter. It is a function of material, thickness, and specimen type (tension, bending, etc.). For brittle materials, m = 0, and the fracture toughness K_F is equal to the elastic stress-intensity at failure (like K_{Ic}, the plane-strain fracture toughness). However, for very ductile materials, m = 1, the fracture toughness K_F is the elastic-plastic fracture toughness, and K_F is the limiting value for very large panels and at very low failure stresses. For m = 1 and a very large K_F value, Eq 5 reduced to a net-section-stress-equal-ultimate-tensile-strength failure criterion. Once K_F and m are known for a material, thickness, and specimen configuration, then the K_{Ie} values can be predicted as

$$K_{Ie} = K_F / \{1 - m\, K_F / [S_u \sqrt{(\pi c)}\, F_n]\} \tag{6}$$

for a given crack length and specimen width. Note that F_n is the usual boundary-correction factor (F) on stress-intensity factor with a net-to-gross section conversion [18], because the net-section stress is used in Eq 5.

Fracture tests were conducted on ESE(T) specimens (w = 38 mm) at the two service temperatures in both the LT- and TL-orientations. The elastic stress-intensity factor at failure, K_{Ie}, using the initial crack length and the failure load, is shown in Fig. 2 as a function of the crack-length-to-width (c/w) ratio. The open symbols show the room temperature results, and the solid symbols show the elevated temperature results. The solid and dashed curves show the calculated results from the TPFC using the appropriate K_F and m values at the respective temperatures. Normally, different specimen widths are required to determine an appropriate m value, but here the m value was selected as unity based on a trial-and-error procedure to fit the limited data. These results show that the elastic K value at failure drops sharply as the crack length approaches the specimen width and that specimens subjected to the elevated temperature have higher fracture toughness values than at room temperature.

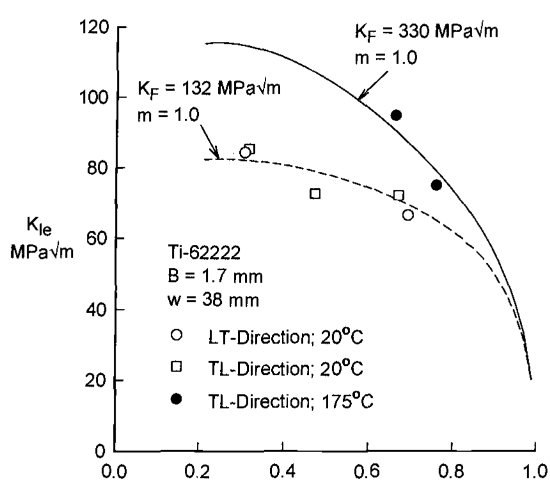

FIG. 2 *Elastic stress-intensity factors at failure for ESE(T) specimens.*

Similar results of K_{Ie} for M(T) specimens are shown in Fig. 3 as a function of crack-length-to-width (c/w) ratio. Tests were conducted in either the LT- or TL-orientation. The open circular symbols show fracture test results on 2w = 51 mm wide specimens; one test (as indicated) was cycled to failure at constant-amplitude fatigue loading. The K_{Ie} at failure on this specimen was calculated using the maximum fatigue stress and the final crack length measured from the fatigue surfaces. Only one test was conducted at the elevated temperature. Again, the m value was selected by trial-and-error to fit the limited data at room temperature, and the same m value was used for the elevated temperature results.

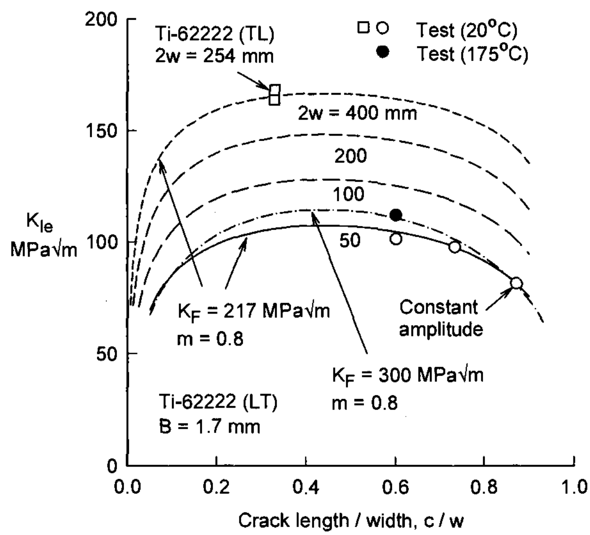

FIG. 3 *Elastic stress-intensity factors at failure for M(T) specimens.*

The solid and dash-dot curves are the calculated results from the TPFC using the appropriate values of K_F and m at the respective temperatures. The various dashed curves show the predicted results for various width specimens tested at room temperature. The upper square symbols show results on large M(T) specimens but tested in the TL-orientation. The predicted K_{Ie} value at failure for the large M(T) specimen was about 8 % too low. (Normally, it is more accurate to fit to the large width specimens and to predict the failure of the smaller width specimens.) These results show that the maximum K_{Ie} value occurs at a c/w ratio of about 0.4, and that the elastic fracture toughness values rapidly drop as the crack length approaches either zero or the specimen width.

Constant-Amplitude Loading

To make crack-growth predictions, ΔK_{eff} as a function of crack-growth rate must be obtained over the widest possible range in rates (from threshold to fracture), especially if spectrum load predictions are required. Under constant-amplitude loading, the only unknown in the analysis is the constraint factor, α. The constraint factor was determined by finding (by trial-and-error) a value (or values) that will correlate the constant-amplitude crack-growth-rate data over a wide range in stresses ratios, as shown by Newman [15]. In the following, the ΔK_{eff}-rate relations for the titanium alloy tested at room or elevated (175°C) temperature were developed.

The thin-sheet titanium alloy Ti-62222 STA (B = 1.6 1.75 mm) was supplied to various participants in the HSCT program. Constant-amplitude fatigue-crack-growth rate tests were conducted on two specimen types: 1) an eccentrically-single-edge crack tension, ESE(T), specimen and 2) a middle-crack tension, M(T), specimen. Smith and Piascik [10] and Liknes and Stephens [11] conducted the ESE(T) tests; and Phillips [8] and Worden (Boeing Airplane Co.) conducted the M(T) tests. Tests were conducted over a wide range in stress ratios (R = minimum to maximum load ratio) and at two temperatures (room and 175°C). Some tests were also conducted using the K_{max}-constant test procedure [10].

The fatigue-crack growth results at room temperature are shown in Fig. 4. This figure shows Elber's effective-stress-intensity-factor, ΔK_{eff}, against crack-growth rate. The crack-opening stress equation [15] from the crack-closure model, FASTRAN, was used to correlate these data. The symbols show the test results from the various laboratories.

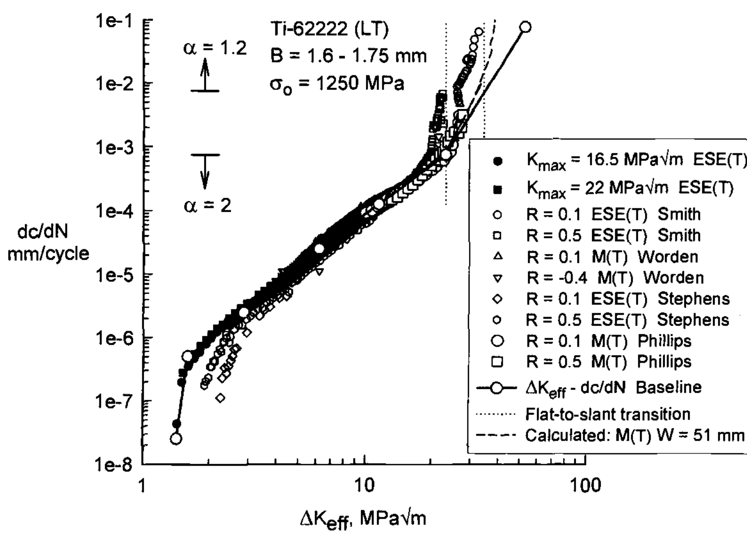

FIG. 4 *Effective stress-intensity factor against rate relation at room temperature.*

For crack-growth rates less than about 8e-4 mm/cycle, a constraint factor, α, of 2 (like plane strain) was used, and above a rate of about 8e-3 mm/cycle, a constraint factor, α, of 1.2 (like plane stress) was used. This constraint-loss regime has been associated with the transition from flat-to-slant (45°) crack growth. The dotted vertical lines show the measured flat-to-slant transition from one of the M(T) specimens. This range also corresponds to the rapid change in rates measured on all specimens. (Equation 3 predicts that the transition should occur at a $(\Delta K_{eff})_T$ value of about 25 MPa√m.) The crack-closure model correlated the fatigue-crack-growth rate data in a tight band over about four orders of magnitude in rates. More scatter was observed in the constraint-loss regime, as the ESE(T) specimens grew to failure and in the near threshold regime. In the threshold regime, the results from Liknes and Stephens [11] at R = 0.1 and 0.5 were determined by using a load-reduction procedure. It has been shown that the load-reduction procedure induces higher crack-closure behavior from tests [19,20] and from analyses [21,22] due to remote closure.

In Fig. 4, the large open circles with the solid lines show the ΔK_{eff}-rate baseline relation chosen to fit these data and used as table-lookup input, Eq 4, in the FASTRAN code. The dashed curve shows a calculation of ΔK_{eff}-against-rate for one of the M(T) specimens to show how the calculated results go to failure similar to the M(T) and ESE(T) specimens.

Similar results were also developed for the elevated temperature (175°C) tests, as shown in Fig. 5. Because crack-growth rate data were not available in the threshold regime, the room temperature results were used to estimate the elevated temperature results. Again, the dotted vertical lines show the measured flat-to-slant transition from one of the M(T) specimens. (At the elevated temperature, Eq 3 predicts that the transition should occur at a $(\Delta K_{eff})_T$ value of about 22 MPa$\sqrt{m}$, which was somewhat low compared to that indicated from the test results.) Again, the large open circles with the solid lines show the ΔK_{eff}-rate baseline relation chosen to fit these data and used in the FASTRAN code. The dashed curve, again, shows a calculation of ΔK_{eff}-against-rate for an ESE(T) specimen to show how the calculated results would go to failure at K_{Ie}.

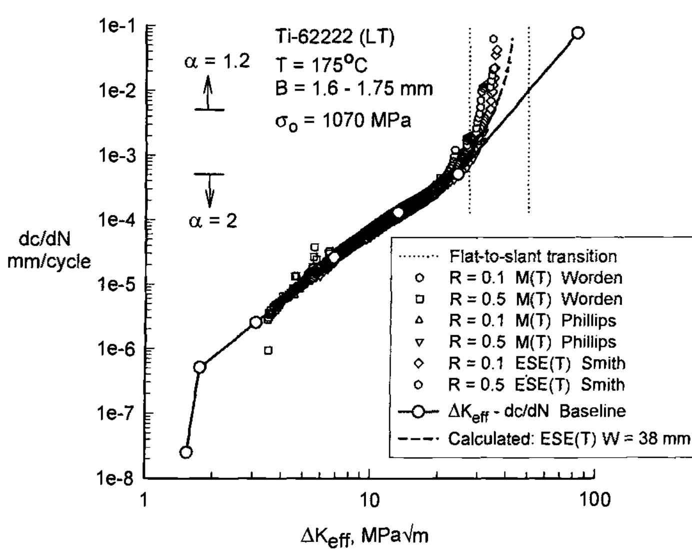

FIG. 5 *Effective stress-intensity factor against rate relation at elevated temperature.*

Variable-Amplitude Loading

A series of M(T) specimens was fatigue pre-cracked at 140 MPa at R = 0.1 from an initial electrical-discharged-notch (2.5 mm) to a crack length (c_i) of 3.8 mm and then subjected to repeated spike overloads and under-loads every 2500 cycles to failure [8]. The specimens were 51 mm wide, and tests were conducted at both room temperature and 175°C. The overload-to-constant-amplitude-stress (S_{OL}/S_{CA}) ratio ranged from 1.5 to 3.5. For an overload ratio of 2.5, the under-load stress (S_{UL}/S_{CA}) ratio ranged from –1 to –3.

FASTRAN was used to calculate the crack-opening stress history during the repeated spike overload tests. The model was used to simulate the pre-cracking stage for an initial notch length of 2.5 mm to a crack of 3.8 mm (the notch surfaces were prevented from contacting in the model). Some typical results are shown in Fig. 6 for a repeated overload (S_{OL}/S_{CA}) ratio of 2. The upper dashed lines show the constant-amplitude maximum applied stress (S_{CA}) and the repeated spike overloads; and the lower dashed line shows the minimum applied stress. The solid curve shows the calculated crack-opening stress levels. The initial portion (up to 2500 cycles) was constant-amplitude loading, and then the first overload was applied. The overload was then applied every 2500 cycles until the specimen failed. The total number of cycles from a crack length of 3.8 mm to failure was recorded. The application of an overload causes an immediate drop in crack-opening stress, but the opening levels rapidly rise as the crack grows into the overload plastic zone, until the next overload was applied, and the process was repeated. As the crack grows, the overall level of crack-opening stresses rise, and the ΔS_{eff} (= $S_{max} - S_o$) becomes smaller, as shown. Thus, one repeated overload test might cover the mid-rate range at the beginning of a test, near the threshold regime later and at threshold near the end of a test.

Some typical results are shown in Fig. 7 for the repeated spike overload tests. Symbols show the test results and the curves show the calculated results from FASTRAN, using the baseline relations from Figures 4 and 5 for the respective temperatures. The trends in the test results and the predicted lives agreed quite well. Generally, the elevated temperature tests and analyses produced longer fatigue-crack-growth lives than those at room temperature at the same overload ratio. At an overload ratio of 2.5 or higher, the crack-opening stresses from FASTRAN were high enough to cause the threshold conditions to be activated under the constant-amplitude loading and, thus, the constant-amplitude cycles did not affect the fatigue lives. These results ($S_{OL}/S_{CA} > 2.5$) are basically constant-amplitude calculations at the overload value.

Aircraft Spectrum Loading

Spectrum load tests were conducted on 76 mm-wide M(T) specimens (B = 1.65 mm) using two different spectra and at two test temperatures (room and 175°C). The first spectrum was an HSCT wing spectrum developed by a major aircraft manufacturer, and the second spectrum was the standard Mini-TWIST wing spectrum. Specimens were pre-cracked under constant-amplitude loading to grow a crack from an initial notch (c_n = 2.54 mm) to a crack length (c_i) of 3.8 mm. The pre-cracking load was at a stress ratio of 0.1 and at a maximum stress of 0.5 of the spectrum maximum stress for the HSCT spectrum, or at a maximum stress of 0.3 of the maximum spectrum stress for the Mini-TWIST spectrum. After pre-cracking, the specimens were subjected to the spectrum loading until failure. Cycles to failure and, in most tests, crack-length-against-cycles data, were recorded in the tests. Tests were conducted at several stress levels for each spectrum. The different stress levels were achieved by multiplying all stresses in the initial stress sequence by a constant factor. The stress levels were picked to interrogate the capability of the crack-growth prediction codes for both short and long crack-growth lives.

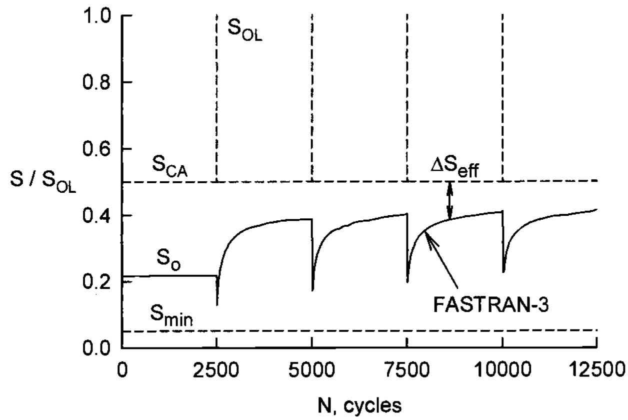

FIG. 6 *Calculated crack-opening stresses for repeated spike overloads.*

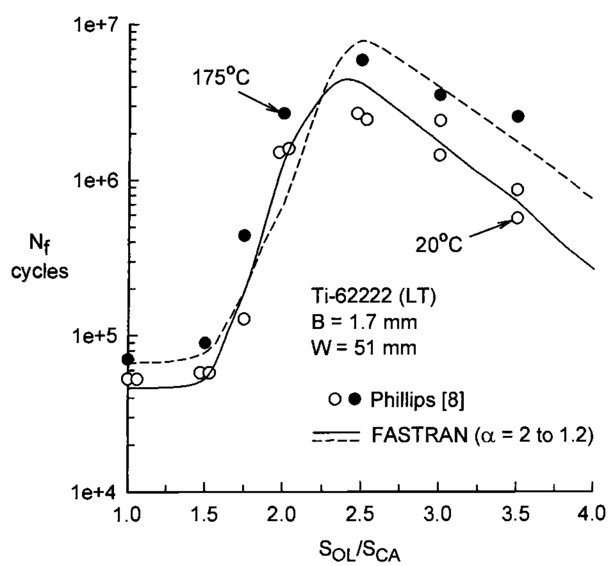

FIG. 7 *Measured and calculated fatigue lives for repeated spike overloads.*

High-Speed Civil Transport (HSCT) Spectrum

Information on the cyclic stress spectrum for a representative location on the HSCT main wing box lower surface was received from a major aircraft manufacturer and was transformed into a test load sequence [8]. In the spectrum description, each flight was divided into seven flight segments (taxi out, climb, supersonic cruise, descent, subsonic cruise, approach, and taxi in), and the frequency of occurrence of cyclic stresses in each of 20 stress ranges was given for each segment. For testing purposes, it was decided to apply the spectrum as a repeated sequence of 1600 flights (about 0.1 of a lifetime). Stresses that occurred less frequently than once per 1600 flights were not included in the tests. Stresses that occurred less frequently than once per flight were added to flights in which the accumulated fractions of an occurrence per flight exceeded a whole number. For example, a single cycle of a stress that had a frequency of 0.3 occurrences per flight would be added in flight number 4, 7, 10, 14, etc. Thus, the big, rare cyclic stresses occurred near the end of the 1600 flight sequence. For testing purposes, once the cyclic content of all flights was defined, the location of each of the 1600 flights within the 1600 flight sequence was randomized. The sequence of occurrence of individual stress cycles within each flight segment also was randomized.

The complete 1600 flight sequence defined by Lockheed-Martin contained 2 304 057 stress cycles (or 4 608 114 stress end points). This was considered too long for economical testing, so a shorter test sequence was generated. For the test stress sequence, the cycles having the two smallest amplitudes in each flight segment were deleted. In addition to deleting the small stress cycles in each segment, the entire taxi segments were replaced by a single excursion to the minimum stress that occurred in the original segment. These deletions resulted in a sequence that contained 105 445 stress cycles. The cyclic content of the test sequence is given in [8]. A portion of the HSCT spectrum sequence covering five flights is shown in Fig. 8.

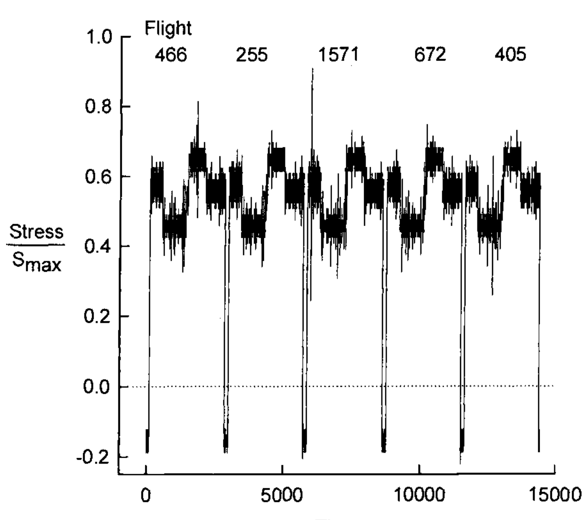

FIG. 8 *Typical high-speed civil transport (HSCT) flight sequence.*

For the HSCT spectrum, tests were conducted at three different maximum stress levels (207, 276, and 345 MPa). The test results are shown in Fig. 9 at room temperature. Generally, only one test was conducted at each stress level, but two tests were conducted at the mid-stress level. The solid curves are the predicted results from FASTRAN using the baseline relation shown in Fig. 4. The predicted results fell slightly short in cycles but agreed very well with the test data.

A comparison of measured and predicted results at elevated temperature are shown in Fig. 10 for the three maximum spectrum stress levels. The predicted results were not as good as those for room temperature, but the predicted cycles to failure were within about 30 % of the test data.

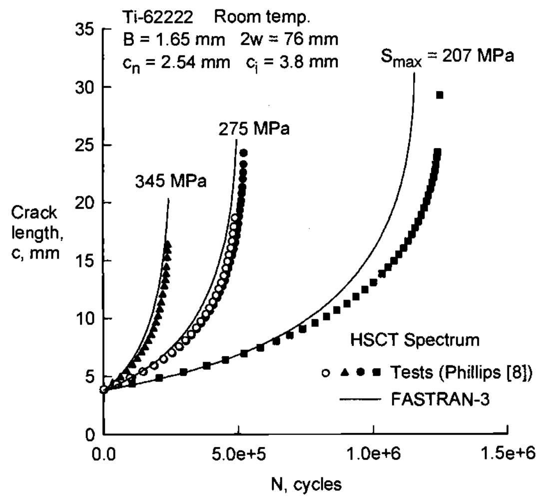

FIG. 9 *Measured and predicted crack-length-against-cycles for HSCT loading at room temperature.*

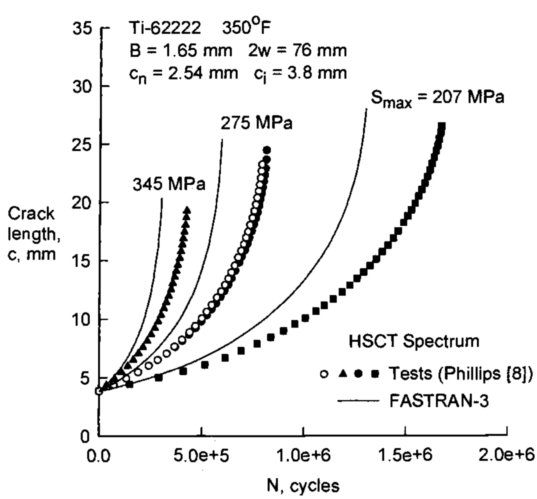

FIG. 10 *Measured and predicted crack-length-against-cycles for HSCT loading at elevated temperature.*

Transport Wing (Mini-TWIST) Spectrum

The Mini-TWIST spectrum [9] is also for a transport lower wing location, but it was derived for aircraft flying at lower altitudes than the HSCT, so it is more severe in terms of flight cyclic stress exceedances per flight hour. Details on the Mini-TWIST test sequence, developed by a European consortium, are given in [9]. A portion of the Mini-TWIST sequence is shown in Fig. 11. Several differences between the Mini-TWIST and HSCT test sequences are evident. Namely, the Mini-TWIST sequence: (a) has a constant flight mean stress, whereas the HSCT sequence has different mean stresses for each flight segment, (b) has a lower flight mean stress and higher cyclic stress excursions from the mean, and (c) has widely differing number of cycles in individual flights, whereas the HSCT sequence does not. Other differences are that the Mini-TWIST sequence repeats after 4000 flights instead of 1600, has 62 442 cycles in the sequence instead of 105 445 and has the flight stress excursions randomized as "half cycles" rather than as whole cycles (positive excursion from the mean is always followed by a negative excursion of equal magnitude).

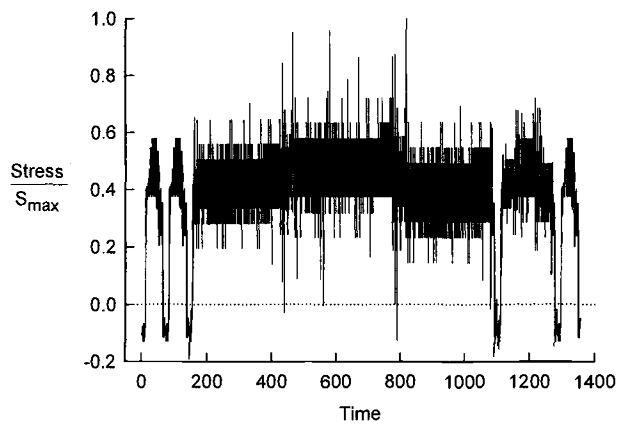

FIG. 11 *Typical transport wing flight sequence.*

Test specimens were subject to the Mini-TWIST wing spectrum at three or four mean flight stress levels (83, 103, 138, and 207 MPa) and at the two test temperatures. The test results at room temperature are shown in Fig. 12 as symbols. Only a single test was conducted at each mean flight stress level. For these tests, the FASTRAN predictions fell considerably short of the test data but were within a factor of two. The predicted results agreed better with the tests conducted at the higher mean flight stress levels. Some of the differences may be due to fretting-product-debris-induced closure or three-dimensional effects, such as free-surface closure (under plane-stress conditions), not included in the model. Also, further study of crack growth in the near threshold regime and whether the K_{max} tests were affected by K_{max}-effects must be investigated.

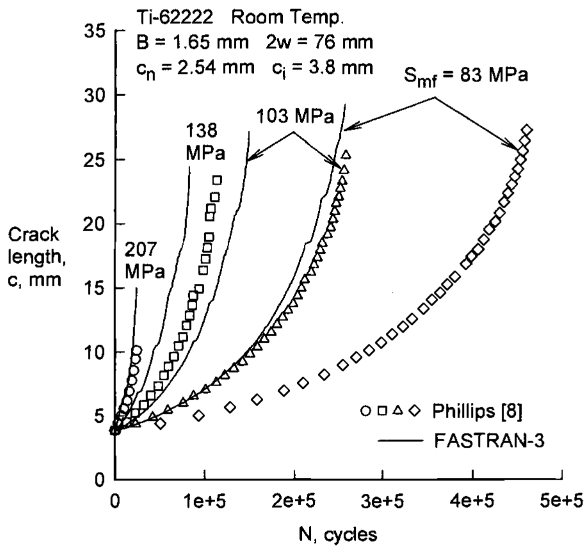

FIG. 12 *Measured and predicted crack-length-against-cycles for full Mini-TWIST loading at room temperature.*

A couple of tests also were conducted in which the three highest stress peaks in the sequence (one Level 1 peak and two Level 2 peaks) were reduced (clipped) to the level of the third highest stress level (Level 3), while all other stress peaks remained the same. This was done to see whether the crack-growth codes could correctly predict the effect of the rare, big stress peaks in the spectrum on crack growth. These results are shown in Fig. 13. The test results indicated that the Level 1 and 2 peak stresses did not significantly affect the crack-growth behavior. Although the FASTRAN analyses were, again, a factor-of-two lower than the test results, the analyses correctly predicted a small effect of clipping the Level 1 and 2 peak stresses.

A comparison of the measured and predicted crack-length-against-cycles for Mini-TWIST tests conducted under the elevated temperature conditions is shown in Fig. 14. Again, the FASTRAN analyses under-predicted the lives by about a factor of two, similar to the room temperature results.

Discussion of Results

The "constraint-loss" regime (plane-strain to plane-stress behavior) is extremely important in the plasticity-induced crack-closure model for predicting crack growth under variable-amplitude and spectrum loading [17]. This region has been associated with the flat-to-slant crack-growth behavior. For the titanium alloy tested in the High-Speed Research Program, the small ESE(T) and M(T) specimens (50 76 mm wide) were developing the flat-to-slant crack-growth regime at about the same K-levels that would cause the specimens to fracture. Thus, the determination of the constraint-loss regime and the effective stress-intensity factor relation was made difficult. Larger width specimens would have a higher elastic stress-intensity factor at failure, and the flat-to-slant transition would have occurred naturally, in a more controlled manner, before fracture conditions were met.

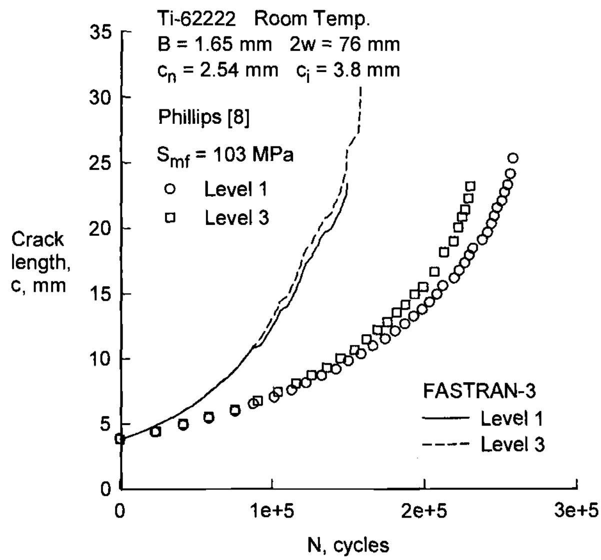

FIG. 13 *Measured and predicted crack-length-against-cycles for full and truncated Mini-TWIST loading at room temperature.*

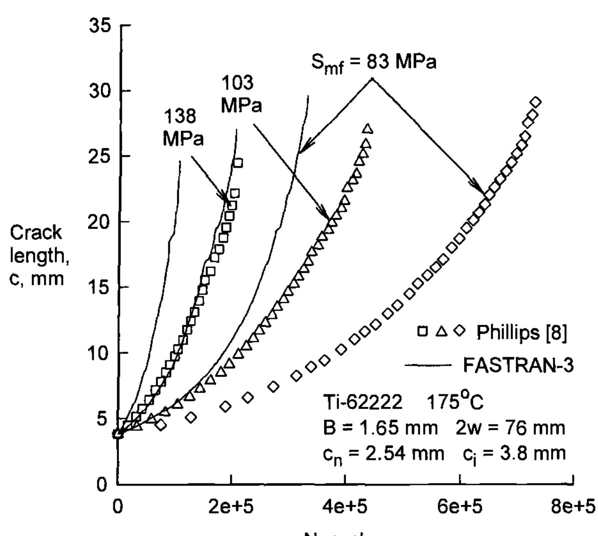

FIG. 14 *Measured and predicted crack-length-against-cycles for full Mini-TWIST loading at elevated temperature.*

The Two-Parameter Fracture Criterion was needed to predict the higher crack-growth rates associated with the small tension and bend specimens fracturing, especially at the higher stress ratios (such as those that occur in the HSCT and Mini-TWIST spectra). Likewise, the determination of the effective stress-intensity factor against crack-growth rate relation in the near threshold regime was made more difficult due to suspected load-history effects on long-crack threshold development using the load-reduction procedure. Further study is needed in the threshold regime to understand fully the relationship between thresholds and K_{max} effects.

In summary, a comparison of the measured and calculated fatigue lives under the repeated spike overloads, and those under the two transport wing spectra, is shown in Fig. 15. The open and solid symbols show the room and elevated temperature results, respectively. Most of the calculated or predicted lives fell within a factor-of-two of the test data. Generally, a factor-of-two is considered satisfactory for spectrum load predictions. The calculated and predicted lives agreed better under room temperature than at elevated temperature. However, the author feels that something is missing in the model (such as fretting-oxide debris-induced closure or some three-dimensional effects at the plane-stress free surface) or in the test data, especially in the near threshold regime. Further study is needed to improve the life-prediction methodology.

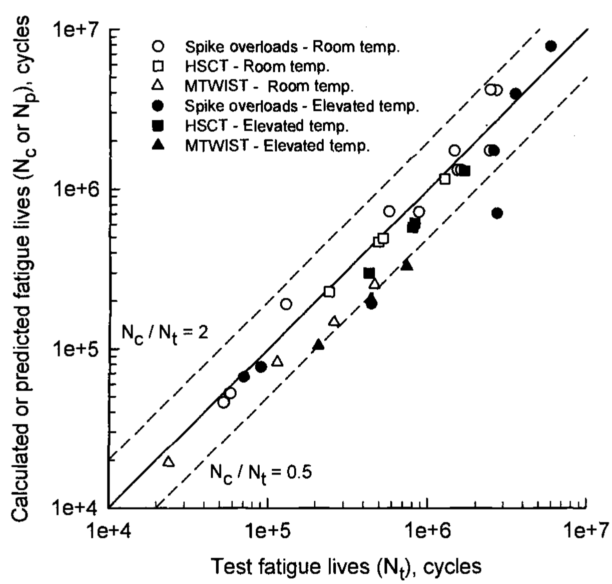

FIG. 15 *Comparison of measured and calculated (or predicted) fatigue lives for repeated spike overloads, HSCT and Mini-TWIST spectra.*

Conclusion

A "plasticity-induced" crack-closure model was used to correlate crack-growth rate data on thin-sheet titanium alloy (Ti-62222 STA; B = 1.6 1.75 mm) under constant-amplitude loading over a wide range of stress ratios (R = –0.4 to 0.5) and crack-growth rates from near threshold to fracture. A constraint factor, which accounts for three-dimensional state-of-stress effects in the crack-front region, was used to determine the effective stress-intensity factor range against crack-growth rate relations. A constraint-loss regime was selected to correspond to the flat-to-slant crack growth region. Comparisons made between measured and calculated fatigue lives under repeated spike overloads agreed quite well (within ± 30 %). Predicted crack-length-against-cycles for the High-Speed Civil Transport wing spectrum generally fell short of the test data, but agreed within about 30 %. However, similar comparisons of measured and predicted lives under the Mini-TWIST spectrum were generally a factor of 2 less than the test results. Further study is needed to resolve the significant differences observed under the Mini-TWIST spectrum.

References

[1] Elber, W., "Fatigue Crack Closure under Cyclic Tension," *Engineering Fracture Mechanics*, Vol. 2, 1970, pp. 37 45.

[2] Elber, W., "The Significance of Fatigue Crack Closure," *Damage Tolerance in Aircraft Structures, ASTM STP 486*, ASTM International, West Conshohocken, PA, 1971, pp. 230 242.

[3] Schijve, J., "Fatigue Crack Closure Observations and Technical Significance," *Mechanics of Fatigue Crack Closure, ASTM STP 982*, J. C. Newman, Jr. and W. Elber, Eds., ASTM International, West Conshohocken, PA, 1988, pp. 5 34.

[4] Newman, J. C., Jr., "A Crack-Closure Model for Predicting Fatigue Crack Growth under Aircraft Spectrum Loading," *Methods and Models for Predicting Fatigue Crack Growth under Random Loading, ASTM STP 748*, J. B. Chang and C. M. Hudson, Eds., ASTM International, West Conshohocken, PA, 1981, pp. 53 84.

[5] Newman, J. C., Jr., "FASTRAN II - A Fatigue Crack Growth Structural Analysis Program," NASA TM 104159, 1992.

[6] de Koning, A. U., ten Hoeve, H. J., and Henriksen, T. K., "Description of Crack Growth Using the Strip-Yield Model for Computation of Crack Opening Loads, Crack Tip Stretch, and Strain Rates," *Advances in Fatigue Crack Closure Measurements and Analysis, Second Volume, ASTM STP 1343*, R. C. McClung and J. C. Newman, Jr., Eds., ASTM International, West Conshohocken, PA, 1999, pp. 459 474.

[7] Forman, R. G., Shivakumar, V., Mettu, S. R., and Newman, J. C., Jr., "Fatigue Crack Growth Computer Program NASGRO – Version 3.0," Technical Report JSC-22267A, NASA Johnson Space Center, 1998.

[8] Phillips, E. P., "Periodic Overload and Transport Spectrum Fatigue Crack Growth Tests of Ti-62222STA and Al2024T3 Sheet," NASA TM-1999-208995, January 1999.

[9] Lowak, H., DeJonge, J. C., Franz, J., and Schütz, D., "MINITWIST: A Shortened Version of TWIST," LBF-TB-146, Laboratorium fur Betriebsfestigkeit, or National Lucht-en Ruimtevaartlaborium (NLR), NLR MP-79018U, 1979.

[10] Smith, S. W. and Piascik, R. S., "An Indirect Technique for Determining Closure-Free Fatigue Crack Growth Behavior," *Fatigue Crack Growth Thresholds, Endurance Limits and Design, ASTM STP 1372*, J. C. Newman, Jr. and R. S. Piascik, Eds., ASTM International, West Conshohocken, PA, 2000, pp. 109 122.

[11] Liknes, H. O. and Stephens, R. R., "Effect of Geometry and Load History on Fatigue Crack Growth in Ti-62222," *Fatigue Crack Growth Thresholds, Endurance Limits and*

Design, ASTM STP 1372, J. C. Newman, Jr. and R. S. Piascik, Eds., ASTM International, West Conshohocken, PA, 2000, pp. 175 191.

[12] Dugdale, D. S., "Yielding of Steel Sheets Containing Slits," *Journal of Mechanics and Physics of Solids*, Vol. 8, 1960, pp. 100 104.

[13] Blom, A. R., Wang, G. S., and Chermahini, R. G., "Comparison of Crack Closure Results Obtained by 3D Elastic-Plastic FEM and Modified Dugdale Model," Localized Damage: Computer-Aided Assessment and Control, M. H. Aliabadi et al., Eds., *Computational Mechanics Publications*, Springer-Verlag, Berlin, 1990, pp. 57 68.

[14] Newman, J. C., Jr., Bigelow, C. A., and Shivakumar, K. N., "Three-Dimensional Elastic-Plastic Finite-Element Analyses of Constraint Variations in Cracked Bodies," *Engineering Fracture Mechanics Journal*, Vol. 46, 1993, pp. 1 13.

[15] Newman, J. C., Jr., "A Crack-Opening Stress Equation for Fatigue Crack Growth," *International Journal of Fracture*, Vol. 24, 1984, R131 R135.

[16] Newman, J. C., Jr., "Effects of Constraint on Crack Growth under Aircraft Spectrum Loading," *Fatigue of Aircraft Materials*, A. Beukers et al., Eds., Delft University Press, 1992, pp. 83 109.

[17] Schijve, J., "Significance of Fatigue Cracks in Micro-Range and Macro-Range," *Fatigue Crack Propagation, ASTM STP 415*, ASTM International, West Conshohocken, PA, 1967, pp. 415 459.

[18] Newman, J. C., Jr., "Fracture Analysis of Various Cracked Configurations in Sheet and Plate Materials," *Properties Related to Fracture Toughness, ASTM STP 605*, ASTM International, West Conshohocken, PA, 1976, pp. 104 123.

[19] Ohta, A., Kosuge, M., Sasake, E., "Fatigue Crack Closure Over the Range of Stress Ratios from –1 to 0.8 Down to Stress Intensity Factor Threshold Level in HT80 Steel and SUS 304 Stainless Steel," *International Journal of Fracture*, Vol. 14, No. 3, 1978, pp. 251 264.

[20] Minakawa, K. and McEvily, A. J., "On Crack Closure in the Near Threshold Region," *Scripta Metallurgica*, Vol. 15, 1981, pp. 633 636.

[21] Newman, J. C., Jr., "A Nonlinear Fracture Mechanics Approach to the Growth of Small Cracks," Behaviour of Short Cracks in Airframe Materials, AGARD CP-328, 1983, pp. 6.1 6.26.

[22] Newman, J. C., Jr., "Analyses of Fatigue Crack Growth and Closure Near Threshold Conditions for Large-Crack Behavior," *Fatigue Crack Growth Thresholds, Endurance Limits, and Design, ASTM STP 1372*, J. C. Newman, Jr. and R. S. Piascik, Eds., ASTM International, West Conshohocken, PA, 2000, pp. 227 251.

Journal of ASTM International, October 2004, Vol. 1, No. 9
Paper ID JAI19045
Available online at www.astm.org

Dale L. Ball[1]

A Model for the Inclusion of Notch Plasticity Effects in Fatigue Crack Growth Analysis

ABSTRACT: Notches or other stress concentrations are by far the most common sites for the initiation and growth of fatigue cracks in aircraft structures. The growth of these cracks is directly influenced by the material stress-strain response in the vicinity of the notch. Specifically, when the applied (remote) stress is sufficient to cause local plastic deformation at the notch, the response (local) stresses can no longer be found using elastic stress concentration factors, and they become dependent on the prior loading history. This is to say that the response stresses can no longer be treated as state variables. The occurrence of fatigue crack growth at notches which experience local yielding one or more times during their design lifetime is, in fact, quite common in many cyclically loaded structures. Some of the assumptions inherent in "traditional" Linear Elastic Fracture Mechanics (LEFM) based fatigue crack growth analysis may be inappropriate for such problems. In particular, the assumption that the stress distribution on a critical plane remains proportional to the elastic distribution throughout the loading history becomes incorrect when one or more of the applied loads causes plastic deformation and introduces or alters a residual stress field in this region. This paper first describes an elastic-plastic stress-strain response algorithm which may be used to estimate response stress distributions on a critical plane on a cycle-by-cycle basis. This is followed by a discussion of the manner by which stress intensity factors may be calculated based on these response stress distributions using Green's functions. Finally, the use of these stress intensity factors for the calculation of crack growth rate and, ultimately, crack growth life, is demonstrated.

KEYWORDS: notch plasticity, Green's functions, fatigue crack growth analysis

Nomenclature

a	crack dimension in the z-coordinate direction
c	crack dimension in the x-coordinate direction
C_F	Forman fatigue crack growth rate equation coefficient
C_{ec}	elastic constraint index
E	modulus of elasticity
E_s	secant modulus
F_{GS}	SIF stress distribution correction factor
F_W, F_2, F_T	SIF boundary correction factors for SIF
G	Green's function (stress intensity factor coefficient)
K_F	Forman crack growth rate equation coefficient
K_I	Mode I stress intensity factor
MSS	maximum spectrum stress
n	strain hardening exponent

Manuscript received 21 May 2002; accepted for publication 12 November 2003; published October 2004.
Presented at ASTM Symposium on Fatigue Testing and Analysis Under Variable Amplitude Loading Conditions on 29 31 May 2002 in Tours, France; P. C. McKeighan and N. Ranganathan, Guest Editors.

[1] Senior Staff Engineer, Lockheed Martin Aeronautics Co., P.O. Box 748, MZ 8862, Fort Worth, TX 76101.

n_F	Forman fatigue crack growth rate equation exponent
p	load
r	radial coordinate in a right cylindrical coordinate system
r_a	radial distance from coordinate origin to notch surface
R_{SO}	generalized Willenborg retardation model overload shutoff ratio
S	deviatoric stress
SIF	stress intensity factor
t	thickness
W	width
x,y,z	coordinates in Cartesian coordinate system
α_i	back stress
ε_i	strain, contracted (Voigt) notation
ϕ	parametric angle for specifying position on crack front of elliptical or part-elliptical cracks
λ_i	ratio of components of applied stress to applied equivalent stress
ν	Poisson's ratio
ρ	notch radius
σ_e	equivalent stress
σ_i	local (response) stress, contracted (Voigt) notation
σ_o	flow stress

Background

The initiation and early stages of growth of cracks in metallic structures are directly influenced by a number of parameters including surface condition, microstructure, and the local state of stress and strain. When cracks form at notches or other points of stress concentration during fatigue loading, the accurate determination of the local response stresses and strains at the notch on a cyclic basis is vital to the determination of crack driving forces and therefore to the determination of fatigue crack growth behavior.

For structural applications which involve notch plasticity but for which computational efficiency is required (namely fatigue loading) only a handful of solution techniques for local response are widely used. In 1961, Neuber [1] proposed a method for the calculation of local stresses and strains at a notch based on knowledge of the applied (field) stresses, the elastic stress concentration factor, and the material stress strain curve. In what has come to be known as Neuber's rule, the geometric mean of the response stress and strain concentration factors for both elastic and elastic-plastic response is assumed constant. This assumption permits direct calculation of the response (presumably elastic-plastic) stresses and strains. Topper et al. [2] extended this approach to cyclic loading by making three major modifications. First, Neuber's rule was written in terms of stress and strain ranges where the applied (field) stress range was given by the excursion from one turning point to the next in the stress time history for the component being analyzed. Second, the response stress and strain for each load point defined the origin from which the Neuber's rule calculation was made for the next load point. (This introduces the history dependence, which is a critical aspect of cyclic elastic-plastic response.) Finally, the material *cyclic* stress-strain curve, rather than the *monotonic* stress-strain curve was used. Up to this point, Neuber's rule had been applied successfully for both monotonic and cyclic analyses involving a uniaxial applied stress and a uniaxial response. It soon became apparent, however, that for general problems, multiaxial stress states would have to be accommodated, particularly for the response. Hoffman and Seeger [3,4] proposed a generalization of Neuber's rule based on the equivalent stress and strain from the theory of plasticity, which permits application for multi-axial stress states. Another widely used technique for estimating the stresses and strains at a notch is the equivalent strain energy density (EEED) method proposed by Molski and Glinka [5,6]. In this method it is assumed that the strain energy density at the notch tip is the same for elastic material response as it is when localized plastic flow occurs. As with Neuber's rule, this assumption allows direct calculation of response stresses and strains given the applied (field) stresses, the elastic stress concentration factor, and the material stress strain curve. It has generally been found that, while Neuber's rule tends to overestimate the response strains at the notch tip, the EEED method tends to underestimate them [7].

Unfortunately, the effects of notch plasticity are considerably more difficult to characterize for fatigue crack growth than they are for fatigue crack initiation. While the crack initiation problem is carried out at a single point, the crack growth problem requires knowledge of the stress-strain response over an entire plane. The bulk of the work that has been done in this area has been directed toward the growth of cracks in residual stress fields at holes and notches. Typically, the characterization of the residual stress profile (in the uncracked body) is external to the crack growth analysis. Once determined, this initial (static) residual stress is used to calculate a residual stress intensity factor that is then superimposed with the applied (cyclic) stress intensity factors. The methods discussed by Hsu et al. [8], Glinka [9], and Parker [10] are typical. The total or "effective" stress intensity factor is then used to estimate the crack growth rate, which in turn is integrated to find crack growth life. As such, this approach fits neatly into existing LEFM-based damage tolerance analysis methodology. However, it fails to address problems in which one or more of the spectrum loads are of sufficient magnitude to cause repeated yielding (and hence redefinition of residual stress fields), and it fails to address the changes in the residual stress field brought about by crack advance (residual stress release).

A number of models that formally address the cyclic plasticity that occurs both ahead of and in the wake of a crack have been developed over the past several decades, usually by extending the Dugdale [11] plastic strip model. These are the so-called strip yield models. Models developed by Dill and Saff [12] and Newman [13] have been applied primarily to the study of crack closure. In these models the crack plane is represented with a series of bar elements whose elastic-plastic response and deformation are calculated on a cycle-by-cycle basis. Crack advance is simulated via the successive failure of these elements, and crack closure is properly represented as the contact of the plastically deformed elements in the wake of the crack front. Glinka [14] has proposed a similar model for crack growth in which the crack is represented as a notch of small but finite radius, and crack advance is simulated via the successive fracture of material elements ahead of the crack. G. S. Wang and A. F. Blom [15,16] have developed a strip yield model for fatigue crack growth in residual stress fields, which accounts for both fatigue induced relaxation and crack growth induced release of the residual stress field. Like the Newman model, this model includes elastic-plastic crack closure analysis. Finally, C. H. Wang et al. [17] have recently developed a strain-based implementation of the Dugdale model, which permits accurate determination of selected fracture parameters (CTOD and crack tip plastic zone size) even under conditions of large scale yielding.

In the current study, an elastic-plastic stress-strain response algorithm that may be used to estimate response stress distributions on a critical plane on a cycle-by-cycle basis was developed. Methods for the calculation of stress intensity factors based on these response stress distributions were then implemented using the Green's function approach. Finally, the use of these stress intensity factors for the calculation of crack growth rate and ultimately crack growth life was demonstrated.

Stress Analysis

In general, the treatment of cyclic elastic-plastic response in metals must address the dependence of the response on the prior loading history and the so-called memory effect. As a result, the response stress calculations must be made on a point-to-point basis. It is not practical, however, to make such calculations formally in the context of fatigue life prediction where tens and even hundreds of thousands of cycles may be involved. In the current approach, to reduce the problem to one of tractable size, a number of simplifying assumptions is made. First, stresses are explicitly addressed only on a single, two-dimensional cross-section through the part. This cross-section is chosen to be coincident with the anticipated plane of crack growth. Second, it is assumed that this plane is a principal, i.e., shear free plane. Third, all loading and unloading paths in principal stress space are assumed to be proportional (radial). And fourth, the response stress calculations are made for the *uncracked* section, the assumption being that the presence of the crack would only cause a local perturbation in the stress field. These assumptions impose limits on the types of crack growth that may be studied using this technique; specifically, the technique is limited to flat, Mode I cracks that are small with respect to the dimensions of the cross-section.

Estimated Elastic Constraint

When calculating the stress-strain response to applied loads, consideration must be given to potential induced stresses that are the result of elastic constraint. For applications involving thick sections and in which the stress-strain response throughout the component being analyzed is predominantly elastic, the stress states at notches or other geometric discontinuities will become increasingly tri-axial as strains in the transverse directions (due to the Poisson effect) are resisted by the surrounding elastic material [18,19]. With the coordinate system defined such that the applied stresses act in the y-direction, normal constraint stresses may be generated in both the in-plane transverse (x-direction) and the transverse (z-direction) directions. See Fig. 1.

Under conditions of plane stress, the transverse components of stress and strain are

$$\sigma_Z = 0 \tag{1}$$

$$\varepsilon_Z^E = \frac{-\nu}{E}\left(\sigma_X + \sigma_Y\right) \tag{2}$$

where the superscript 'E' indicates the elastic component. Note that contracted (Voigt) notation will be used throughout this discussion. Under plane strain, the transverse strain and stress are

$$\varepsilon_Z^E = 0 \tag{3}$$

$$\sigma_z = \nu(\sigma_x + \sigma_y) \tag{4}$$

It is convenient to define an elastic constraint index, C_{ec}, with limiting values of $C_{ec} = 0$ for plane stress and $C_{ec} = 1$ for plane strain. Given the in-plane normal stresses, σ_x and σ_y, the constraint stresses and strains (in the z-direction, due to the Poisson effect) are

$$\sigma_z = C_{ec}\nu(\sigma_x + \sigma_y) \tag{5}$$

$$\varepsilon_z^E = (C_{ec} - 1)\frac{\nu}{E}(\sigma_x + \sigma_y) \tag{6}$$

It is possible, based on inspection of the local geometry, to assume a value for C_{ec}. In fact, to some extent, this index may be used as a "correlating parameter." That is, the value of C_{ec} may be adjusted in order to improve the correlation between calculated and measured crack growth behavior. However, in the current study, the expression for the constraint factor at a notch of radius ρ in a plate of thickness t given by A. Kotousov and C. H. Wang [20] was used

$$C_{ec} = \frac{1}{(1-\nu^2)\left[1+\frac{2\rho}{t}\sqrt{\frac{6}{1-\nu}}\right]\mathrm{EXP}\left[\frac{2(r-r_a)}{t}\sqrt{\frac{6}{1-\nu}}\right]+\nu^2} \tag{7}$$

where $r\text{-}r_a$ is the distance from the edge of the notch to the point at which the index is being evaluated.

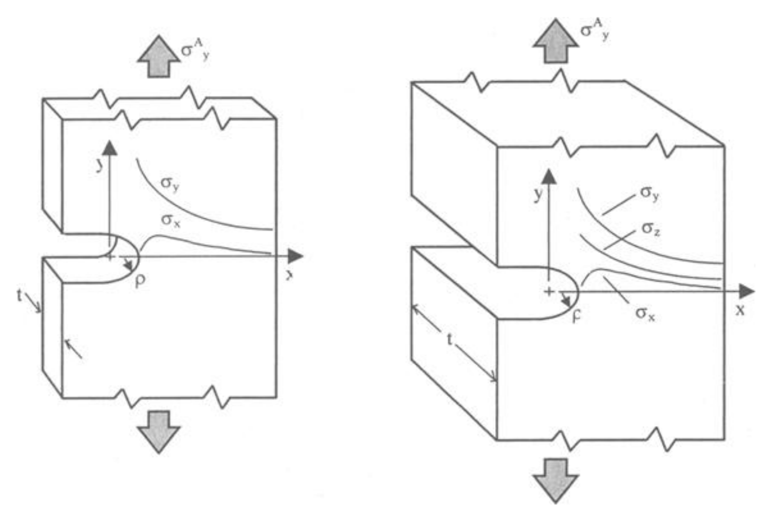

FIG. 1 *Schematic of stress distributions at a notch under plane stress and plane strain conditions.*

Cyclic Stress-Strain Response

In the current method, the fatigue load history is treated as a sequence of half cycles in which the first half cycle is a negative ramp from a prior maximum value to the current minimum value, and the second half cycle is a positive ramp from the current minimum value to the next maximum. For a given applied stress history (i.e., a time sequence of σ^A_i values), the applied (elastic) stress range between successive load points is simply

$$\Delta\sigma_i^A = \left(\sigma_i^A\right)_{k+1} - \left(\sigma_i^A\right)_k \tag{8}$$

Note that here and in the text that follows, k is the load turning point counter, i.e., if a given cycle minimum is turning point k, then the immediately following cycle maximum is turning point k+1. To properly account for the history dependence of the response stresses and strains, they must be calculated on a point to point basis with the response stresses and strains at turning point k serving as the starting point from which the response stresses and strains at turning point k+1 are calculated.

On the shear free plane being considered, the applied stress vector has three non-zero components: $\Delta\sigma^A{}_1$ and $\Delta\sigma^A{}_2$, which are the applied in-plane normal stresses, and $\Delta\sigma^A{}_3$, which is the transverse constraint normal stress (Eq 7). The superscript A is used here to distinguish "applied" values from "response" values. Note that the applied stress values are assumed to include any elastic stress concentration effects.

The distortion energy theorem is used for the definition of the yield criterion. According to this theorem, plastic flow will begin when the "equivalent" stress equals or exceeds the material flow stress. (The initial flow stress is typically the yield strength as measured in a uniaxial tension test). This is stated simply as

$$\sigma_e^A = \sqrt{\frac{3}{2}\left(S_i^A - \alpha_i\right)\left(S_i^A - \alpha_i\right)} \geq \sigma_o \tag{9}$$

where $S^A{}_i$ is the deviatoric stress, and α_i is the so-called back stress. This definition is convenient because, for uniaxial stress states, the equivalent stress reduces to the axial stress. The equality in Eq 9 defines the "yield surface," which for this formulation is a right circular cylinder in principal stress space, whose longitudinal axis lies at equal angles to the three coordinate axes. Points in principal stress space that lie within the cylinder represent elastic states. When the stress state reaches the cylinder, plastic flow begins. The position of any state of stress in stress space may be written in terms of spherical (hydrostatic) and deviatoric components, with the former giving the position along the cylinder axis and the latter giving the radial distance from the cylinder axis. According to Eq 9, it is only the deviatoric components of stress that control the onset of yield; changes in the hydrostatic stress have no effect [21]. (Yield criteria that address possible dependence on hydrostatic stress are considerably more complex than Eq 9 and are not addressed in this study.) The practical result of this is that the maximum principal stress at the notch root may exceed the uniaxial yield strength of the material by a considerable amount before plastic flow begins, if a fully triaxial stress state develops.

In order to define the back stress as well as the components of the response stress, the very important, simplifying assumption is made that all loading and unloading paths in principal stress space are proportional (radial). That is to say, the ratios of the various components to the equivalent stress remain fixed throughout the analysis. These ratios define the proportionality factor, λ

$$\frac{\Delta\sigma_i^A}{\Delta\sigma_e^A} = \lambda_i \tag{10}$$

We require the inclusion of the back stress because we make the assumption that plastic loading causes movement of the yield surface (kinematic hardening) and that the response stress state lies on the displaced yield surface. Since the analysis is isothermal and quasi-static, the yield surface may be translated in stress space, but it retains a fixed size and shape. The coordinates of the origin of the displaced yield surface in principal stress space (typically referred to as the back stress) are given by

$$\alpha_i = \lambda_i(\sigma_e - \sigma_o) \tag{11}$$

where σ_o is the flow stress. It will also be necessary to associate a strain with the back stress, which we will define as

$$\alpha_i^\varepsilon = \lambda_i\left(\varepsilon_e - \frac{\sigma_o}{E}\right) \tag{12}$$

Now, if $\sigma^A{}_e < \sigma_o$, then the stress state at the point k+1 lies within the yield surface, and the material response is elastic. Under these conditions, the response stress increments are equal to the applied stress increments

$$\Delta\sigma_i = \Delta\sigma_i^A \tag{13}$$

and the corresponding strain increments are found using the generalized Hooke's law

$$\Delta\varepsilon_i = M_{ij}\Delta\sigma_j \tag{14}$$

where M_{ij} is the elastic compliance. The stresses and strains are simply

$$(\sigma_i)_{k+1} = \Delta\sigma_i^A + (\sigma_i)_k \tag{15}$$

and

$$(\varepsilon_i)_{k+1} = \Delta\varepsilon_i^A + (\varepsilon_i)_k \tag{16}$$

In this case there is no displacement of the yield surface

$$(\alpha_i)_{k+1} = (\alpha_i)_k \qquad \text{elastic} \tag{17}$$

If $\sigma^A{}_e \geq \sigma_o$, then all or part of the applied stress range causes plastic loading, and both the response stresses and the displacement of the yield surface must be found. The response equivalent stress and strain are found using either a generalized form of Neuber's rule [1]

$$\Delta\sigma_e\Delta\varepsilon_e = \frac{\left(\Delta\sigma_e^A\right)^2}{E} \tag{18}$$

or a generalized form of Glinka's equivalent strain energy density (EEED) method [6]

$$\int_0^{\Delta\varepsilon_e} \Delta\sigma_e d\varepsilon = \frac{\left(\Delta\sigma_e^A\right)^2}{2E} \tag{19}$$

Note that $\Delta\sigma_e$ and $\Delta\varepsilon_e$ are scalar quantities. Either Eq 18 or Eq 19 and the material stress-strain curve provide a system of two equations which may be solved for the two unknowns, σ_e and ε_e. In this case, the material stress-strain curve used is the cyclic stress-strain curve, and the flow stress used in the yield criterion is the cyclic proportional limit. (The cyclic stress-strain curve is a geometric construct that is defined by the locus of reversal points of the series of stable hysteresis loops which are generated by fully reversed (R=–1) strain cycling over a range of strain amplitudes [22]. Like the monotonic stress-strain curve, the cyclic stress-strain curve is assumed to have a linear region, in which the strains are elastic, and a non-linear region, in which the strains are plastic. The upper limit (stress) of this linear region is referred to as the cyclic proportional limit, σ_{cpl}. This value is normally found by inspection of the cyclic stress-strain data. The constant of proportionality in the linear region is always taken to be the modulus of elasticity.)

Since the use of either Neuber's rule or Glinka's EEED method permit the direct calculation of both the final stress and final strain, they in effect define the flow rule

$$\varepsilon_e = f\left(\sigma_e, \sigma_e^A\right) \tag{20}$$

Now, with the assumed proportional loading, the response stress increments are simply

$$\Delta\sigma_i = \lambda_i \Delta\sigma_e \tag{21}$$

and the response stresses are

$$(\sigma_i)_{k+1} = \Delta\sigma_i + (\alpha_i)_k \tag{22}$$

The response strain increments are taken to be the sum of elastic and plastic components

$$\Delta\varepsilon_i^T = \Delta\varepsilon_i^E + \Delta\varepsilon_i^P \tag{23}$$

Using the stress increments given in Eq 21, the elastic strain increments are found using Eq 14, and the plastic increments are given by

$$\Delta\varepsilon_x^P = \left(\frac{1}{E_s} - \frac{1}{E}\right)\left[\Delta\sigma_x - \nu^P\left(\Delta\sigma_y + \Delta\sigma_z\right)\right] \tag{24}$$

$$\Delta\varepsilon_y^P = \left(\frac{1}{E_s} - \frac{1}{E}\right)\left[\Delta\sigma_y - \nu^P\left(\Delta\sigma_z + \Delta\sigma_x\right)\right] \tag{25}$$

$$\Delta\varepsilon_z^P = -\left(\Delta\varepsilon_x^P + \Delta\varepsilon_y^P\right) \tag{26}$$

where E_S is the secant modulus defined at the point ε_e,σ_e on the uniaxial stress-strain curve. Equation 26 results from the assumption that plastic flow is a constant volume process. ν^P is Poisson's ratio for plastic behavior, which is one-half with the assumed incompressibility. Finally, the response strains are

$$(\varepsilon_i)_{k+1} = \Delta\varepsilon_i^E + \Delta\varepsilon_i^P + (\alpha_i^\varepsilon)_k \tag{27}$$

where α^ε_i is the strain corresponding to the back stress α_i. Since the use of Neuber's rule or of the EEED method allows direct calculation of the stress and strain at the completion of a load step, deformation plasticity is implicit.

With the assumption of kinematic hardening, the back stress is altered each time plastic loading occurs, i.e., it is dependent on the prior loading history

$$(\alpha_i)_{k+1} = \lambda_i(\sigma_e - \sigma_o) + (\alpha_i)_k \tag{28}$$

In this model, however, in order to accommodate the so-called memory effect, two additional "memory" back stresses will be defined. Unique values are defined for "negative" and "positive" loading; these are referred to as α_i^- and α_i^+, respectively. As with the instantaneous back stress, the memory back stresses are initially zero. On the first occurrence of plastic loading in the "-" direction, α_i^+ is set equal to α_i. Upon subsequent plastic excursions in the "-" direction, if $|\alpha_i|>|\alpha_i^+|$, then α_i^+ is set equal to α_i. Likewise, on the first occurrence of plastic loading in the "+" direction, α_i^- is set equal to α_i, and upon subsequent loading in the "+" direction, if $|\alpha_i|>|\alpha_i^-|$, then α_i^- is set equal to α_i. In both cases, if the magnitude of the instantaneous back stress is less than that of the memory back stress, then the memory back stress is left unchanged. As shown in Fig. 2, the net effect of these conditions is that the range between the two memory back stresses can only remain constant or increase for a given load sequence; it cannot decrease.

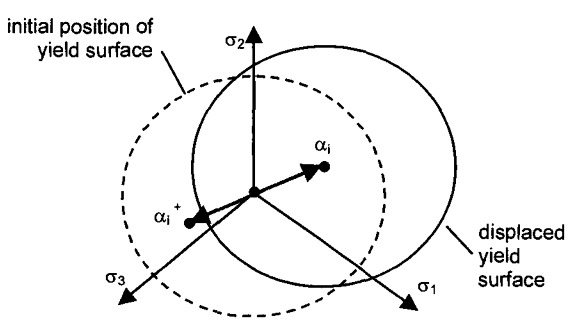

FIG. 2 *Projections of radial load path and yield surface motion onto π-plane in principal stress space.*

For loading in the "-" direction, if the applied stress excursion does not reach the yield surface based on α_i^- (the "memory" surface), then the instantaneous back stress is used to calculate the equivalent stress, and the response is found using Eq 22. If the applied stress does reach the memory surface, then the equivalent stress is found as

$$\sigma_e^A = \sqrt{\frac{3}{2}(S_i^A - \alpha_i^-)(S_i^A - \alpha_i^-)} \tag{29}$$

Likewise, for loading in the "+" direction, if the applied stress excursion does not reach the yield surface based on α_i^+, then the instantaneous back stress is used to calculate the equivalent stress, and the response is again found using Eq 22. If the applied stress does reach the surface, then the equivalent stress is found as

$$\sigma_e^A = \sqrt{\frac{3}{2}\left(S_i^A - \alpha_i^+\right)\left(S_i^A - \alpha_i^+\right)} \tag{30}$$

Again, decomposition of the response strain increments into elastic and plastic components is assumed. The stress ranges used for the calculation of each are given by

$$\Delta\sigma_i = \left(\sigma_i\right)_{k+1} - \left(\alpha_i^x\right)_k \tag{31}$$

where α_i^- is used for "-" direction loading, and α_i^+ is used for "+" direction loading. The response strains are

$$\left(\varepsilon_i\right)_{k+1} = \Delta\varepsilon_i^E + \Delta\varepsilon_i^P + \left(\alpha_i^{\varepsilon x}\right)_k \tag{32}$$

Calculation of response stresses and strains in this manner, i.e., on a point to point basis, will result in the hysteresis loop tracking, which is typical for notch strain analysis [22]. An example set of response calculations for an eight point load sequence was made using Neuber's rule to find the response equivalent stresses (Eq 18) and a three-parameter Ramberg-Osgood equation for the material cyclic stress-strain curve. The results are compared with experimental data from [23] in Fig. 3.

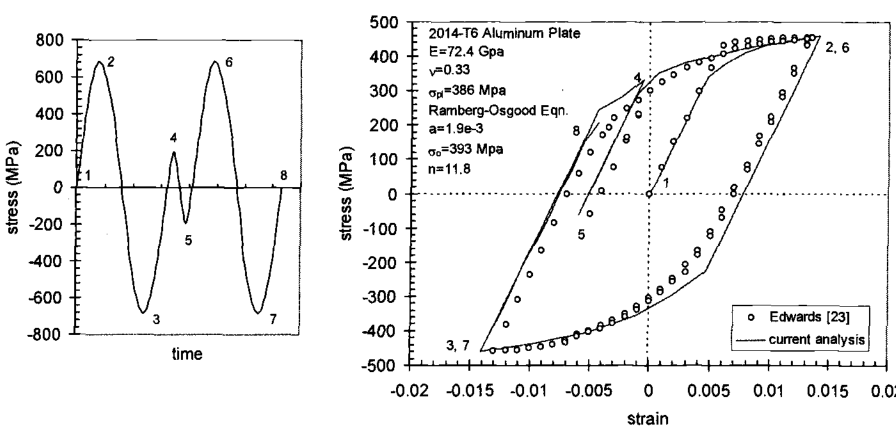

a) 8-point stress versus time history b) predicted versus measured stress-strain response

FIG. 3 *Example of applied stress versus time sequence and corresponding stress-strain response.*

Two-Dimensional Stress Distributions

Up to this point, the development of the response calculation has been limited to a single material element. To permit its usage in a crack growth setting, this technique must be extended to two-dimensional stress distributions. The first step in this process involves the definition of elastic stress distributions on a section that is coincident with the anticipated plane of crack growth. These distributions are assumed to be known from hand analysis, finite element analysis, boundary element analysis, etc. The critical cross-section is discretized into a rectangular array of grid points with "nx" points in the x-direction (c-direction) and "nz" points in the z-direction (a-direction). A typical cross-section grid point array is shown in Fig. 4. The applied stresses are specified at each of these grid points

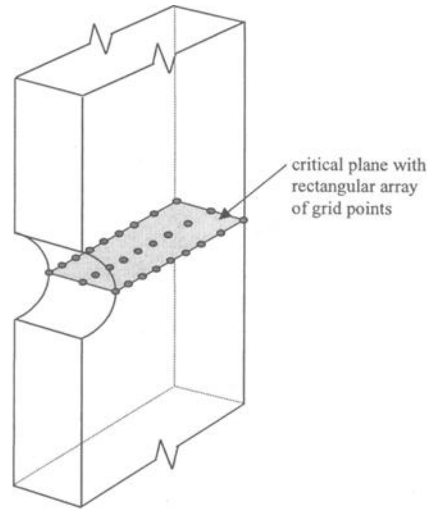

FIG. 4 *Typical cross-section grid point array.*

The array of grid points is then used to define a set of rectangular elements, each of which has a single integration point at its center (i.e., constant stress elements). The stress at the integration point is taken as the average of the four corner grid point stresses. Large stress gradients are accommodated by refining the mesh as required. Note that the crack is not modeled during the response stress analysis; the applied and the response stress distributions are for the notched but uncracked section. Since the analysis requires cycling between minimum and maximum stresses, provision is made for both negative and positive distributions in the event that structure/loading combinations yield distributions of dissimilar shape or magnitude.

Multiple Load Path Solution

If the crack growth model is an integral part of a larger structure, then the decrease in load carried by the model (due to the occurrence of local plastic flow) is presumed to be accompanied by an increase in the load carried by the surrounding structure. While this is not a formal treatment of the load shedding problem, it does eliminate the need for the calculation of load redistribution within the cross-section due to the yielding of one or more of the elements.

Single Load Path Solution

When the assumption of implicit load redistribution is not appropriate, i.e., when the crack growth model represents a single load path component, then the following technique is used to estimate the load redistribution within the cross-section. When the applied (elastic) stress range for a given element exceeds the hysteresis proportional limit, the response stress range will diverge from the elastic value due to plastic flow. The difference between the elastic and the response stress values is an indicator of the reduction in load carrying capability of the element. In the current analysis, response stress gradients are approximated using the assumptions that the cross-section load and moment remain constant during local yielding. So the load "shed" by any one element must be picked up by the remaining elements.

The first constraint we place on the system is that the total load carried by the cross-section remain the same during the yielding process

$$\left[\sum_{j=1}^{m}(p_i)_j\right]_{after} = \left[\sum_{j=1}^{m}(p_i)_j\right]_{before} \tag{33}$$

where m is the total number of elements in the cross-section. When plastic flow occurs in any given element, the load increment in the y-direction (the applied load direction), which is shed due to yielding, is found as

$$\left(\delta p_y\right)_a = \left(\sigma_y - \sigma_y^A\right)_a dA_a \tag{34}$$

where dA is the element area. This load increment is distributed over all of the elements of the cross-section according to

$$\left(\delta p_y\right)_j = \omega_j\left(\delta p_y\right)_a \tag{35}$$

where w_j is a weight coefficient defined such that

$$\sum_{j=1}^{m}\omega_j = 1 \tag{36}$$

In the current model, the load increment from each element that experiences plastic flow is assumed to distribute equally over all of the elements in the cross-section, which is to say that the weight coefficients are assumed uniform and constant

$$\omega_j = \frac{1}{m} \tag{37}$$

In future work, non-uniform coefficient distributions, particularly ones that redistribute the load only in the region of the yielding element and not over the entire cross-section, will be investigated.

Similar calculations are made for the x- and z-directions, with the exception that the load increments in these cases are transmitted only to adjacent elements. So the $(py)_{j,after}$ are found as

$$\left(p_y\right)_{j,after} = \left(\delta p_y\right)_j + \left(p_y\right)_{j,before} \tag{38}$$

To conserve the moment carried by the cross-section, the dp_a subtracted from element "a" is added to an element "b" that is equidistant in both the x and z directions from the cross-section centroid; and the dp_j that are added to each element "j" are subtracted from the elements "k" again, where elements "j" and "k" are equidistant from the cross-section centroid. Once all of the dp_j have been calculated, the new stress distribution may be found as follows

$$\left(\sigma_y\right)_{j,after} = \left(\sigma_y\right)_{j,before} + \frac{\left(\delta p_y\right)_j}{dA_j} \tag{39}$$

This process is repeated for each element in the cross-section until they all have been checked, and the load has been completely redistributed. Once all of the element stresses have been defined, stresses at each grid point are taken as the average of the values of the elements sharing that grid point. And finally, the normal stress at any point with coordinates x,z is found by double linear interpolation between the four surrounding grid points.

The entire procedure is then repeated for each load point (reversal) of the input fatigue load spectrum. As indicated above, these calculations are carried out on a point-to-point basis with the response stress and strain at any given load point in the applied load sequence (k) serving as the effective origin for the response to the next load point (k+1). For example, Fig. 5 shows the estimated response stress distributions on the critical plane for a plate with a semi-circular notch subjected to the eight point loading sequence shown in Fig. 3.

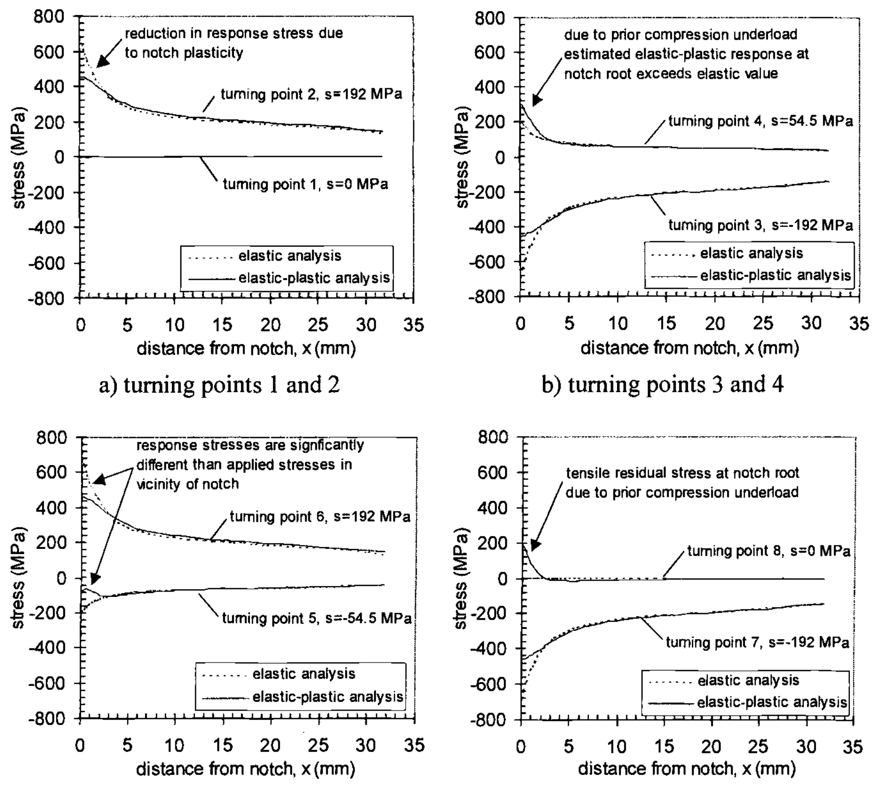

a) turning points 1 and 2

b) turning points 3 and 4

c) turning points 5 and 6

d) turning points 7 and 8

FIG. 5 *Estimated response stress distributions on critical plane.*

Stress Intensity Factor Analysis

Now, given a response stress distribution which includes the effects of notch plasticity, and which therefore may be nothing like the corresponding applied (elastic) distribution, we require a general stress intensity factor (SIF) solution technique that can accommodate *any* stress distribution. The Green's function method was chosen for use here, in part because it meets the requirement of general applicability, but also because Green's functions themselves are readily available for a variety of geometries.

The Green's function approach [24] is closely related to the weight function method of Bueckner [25] and Rice [26], in fact some researchers do not distinguish between the two. From an application point of view, however, the two methods are distinct. The weight function method requires knowledge of the crack opening displacement profile for some reference loading condition. The Green's function method, on the other hand, is based on the SIF solution for a pair of opposing point loads applied to the crack face. Many such point load solutions are available in the literature [27,28].

This technique relies on Bueckner's principle [29], which states that the SIF for a traction-free crack in an externally loaded body is equivalent to that for a pressurized crack in the body with no externally applied loads when the applied pressure distribution is equivalent to the stress field that would exist if the externally loaded body were uncracked. This principle is shown schematically in Fig. 6: the desired solution, case (a), is found by superimposing two known solutions, cases (b) and (c), and since the SIF for case (b) is identically zero, this becomes

$$K_{(a)} = K_{(c)} \tag{40}$$

It is the solution for case (c) that is actually found using the appropriate Green's function.

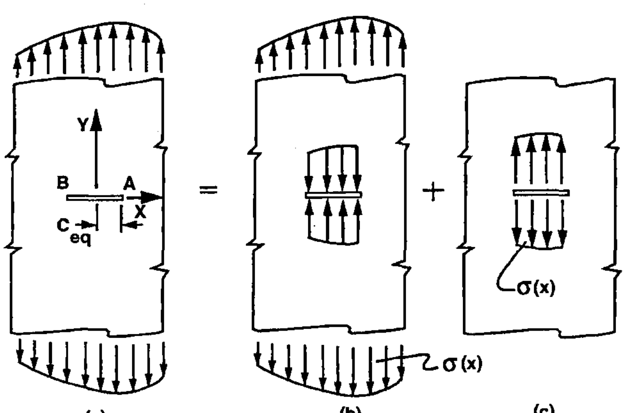

FIG. 6 *Schematic illustration of equivalence between remote body loading and crack pressure loading.*

Semi-Elliptical Edge Crack

When cracks form naturally at notches, they often do so as either surface cracks or corner cracks. In the current study, the surface crack was treated as a semi-elliptical flaw along the short edge of the rectangular cross (net) section. As shown in Fig. 7, it is assumed that the crack lies in the x-z plane. The crack c-dimension is taken to be parallel to the x coordinate axis and the a-dimension parallel to the z-axis.

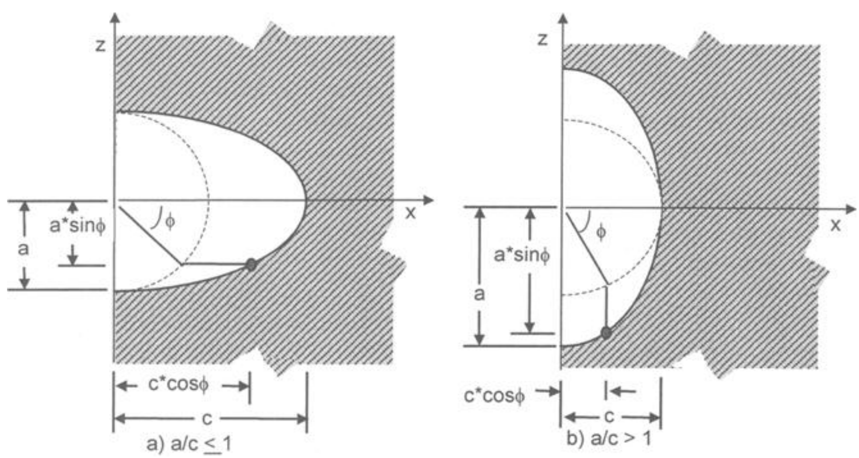

FIG. 7 *Definition of crack dimensions, c and a, and parametric angle, ϕ, for semi-elliptical edge crack.*

We first consider a semi-elliptical crack in a half-space. If we apply a pair of opposing point loads to the crack faces at the point r_i, θ_j, then the SIF may be evaluated at the point on the crack front whose coordinates are $x = c^*\cos(\phi)$, $z = a^*\sin(\phi)$, as follows

$$K_{ij} = p_{ij}G \tag{41}$$

A Green's function for this case was developed in a previous study [30]

$$G = \frac{1}{(\pi R_c)^{3/2}}\left[\frac{a_2\left(1-\xi_i^{a_5}\right)^{a_6}}{1+\xi_i^2-2\xi_i\cos(\Delta\theta_j)}\right] \tag{42}$$

where R_c is radial distance to the crack front at the angle θ, and ξ_i is the normalized radial coordinate, r_i/R_c. For the depth direction ($\phi = 0°$), the a2, a5, and a6 terms were given as

$$a_2 = a_{20} + a_{21}\cos(\theta_L)^{a22} + a_{23}\sin(\theta_L)^{a24} \tag{43}$$

$$a_5 = a_{50} + a_{51}\cos(a_{52}\theta_L)^{a53} + a_{54}\sin(a_{55}\theta_L)^{a56} \tag{44}$$

$$a_6 = a_{60} + a_{61}\cos(a_{62}\theta_L)^{a_{63}} + a_{64}\sin(a_{65}\theta_L)^{a_{66}} \tag{45}$$

where the values of the coefficients a_{20}–a_{24} are given in Table 1, the coefficients a_{50}–a_{56} are given in Table 2, and the coefficients a_{60}–a_{66} are given in Table 3.

TABLE 1 *Coefficient a_{2x} values – depth direction.*

a/c	A_{20}	a_{21}	a_{22}	a_{23}	a_{24}
0.5	0.615	0.39	8	–0.27	1.5
1.0	2.025	0.0		0.0	
1.5	3.5	–1.075	1.8	0.95	3.5
2.0	4.85	–2.265	1.5	2.5	6

TABLE 2 *Coefficient a_{5x} values – depth direction.*

a/c	a_{50}	A_{51}	a_{52}	a_{53}	a_{54}	a_{55}	a_{56}
0.5	0.249	0.753	1.87	18	21.8	0.618	10
1.0	0.433	0.0			8.35	0.437	3.5
1.5	0.55	–0.15	1.0	12	0.77	1.05	5
2.0	0.6	–0.2	1.4	9	0.427	1.32	4

TABLE 3 *Coefficient a_{6x} values – depth direction.*

a/c	a_{60}	A_{61}	a_{62}	a_{63}	a_{64}	a_{65}	a_{66}
0.5	0.259	0.185	1.88	11	1.465	0.684	22
1.0	0.5	0.0			0.0		
1.5	0.648	–0.08	1.25	1	0.03	1.25	6
2.0	0.7	–0.135	0.7	1	0.3	1.35	4

For the surface direction (ϕ = 85°), the a2 and a5 terms are

$$a_2 = a_{20} + a_{21}\cos(\theta_L)^{a_{22}} + a_{23}\sin(\theta_L)^{a_{24}} \tag{46}$$

$$a_5 = a_{50} + a_{51}\theta_L + a_{52}\theta_L^2 + a_{53}\theta_L^3 + a_{54}\theta_L^4 + a_{55}\theta_L^5 + a_{56}\theta_L^6 \tag{47}$$

while the a6 term is

$$a_6 = a_{60} + a_{61}\cos(a_{62}(\theta_L - \theta_E))^{a_{63}} + a_{64}\sin(a_{65}(\theta_L - 0.4))^{a_{66}} \tag{48}$$

for a/c = 0.5, and

$$a_6 = a_{60} + a_{61}\cos(a_{62}(\theta_L - \theta_E))^{a_{63}} + a_{64}\sin(a_{65}(\theta_L - \theta_E))^{a_{66}} \tag{49}$$

for a/c = 1, 1.5, and 2. The coefficients a_{20}–a_{24} are given in Table 4, the coefficients a_{50}–a_{56} are given in Table 5, and the coefficients a_{60}–a_{66} are given in Table 6.

TABLE 4 *Coefficient a_{2x} values – surface direction.*

a/c	a_{20}	a_{21}	a_{22}	a_{23}	a_{24}
0.5	5.7	4	6	–2.2	1.5
1.0	2.95	0		0	
1.5	1.8	–0.54	1.2	0.55	3
2.0	1.25	–0.6	1	0.6	5

TABLE 5 *Coefficient a_{5x} values – surface direction.*

a/c	a_{50}	a_{51}	a_{52}	a_{53}	a_{54}	a_{55}	a_{56}
0.5	0.6209	0.4366	0.8855	–0.2685	–0.5338	–0.0783	0.2544
1.0	0.7162	–0.2365	0.0335	–0.0485	0.1552	0.0817	0.0486
1.5	0.8602	–0.4673	0.1245	0.0055	–0.0146	0.1941	0.0983
2.0	0.8318	–1.1404	0.9864	–0.0007	–1.2245	0.4893	0.5388

TABLE 6 *Coefficient a_{6x} values – surface direction.*

a/c	a_{60}	a_{61}	a_{62}	a_{63}	a_{64}	a_{65}	A_{66}
0.5	1.05	0.33	0.9	48	–.6	0.9	2
1.0	0.5	0.443	0.92	48	0		
1.5	0.35	0.6	0.6	48	0.2	0.5	4
2.0	0.28	0.715	0.5	48	0.35	0.62	10

Now, if we represent the pressure distribution over the crack face using a series of point loads acting normal to the crack

$$p_{ij} = \sigma(r_i, \theta_j) r_i \Delta r \Delta\theta \tag{50}$$

then the total SIF may be found by summing the series

$$K_I = \sum_i \sum_j \left[\frac{\sigma_{ij} r_i \Delta r \Delta\theta}{(\pi R_c)^{3/2}} \left[\frac{a_2 \left(1 - \xi_i^{a_5}\right)^{a_6}}{1 + \xi_i^2 - 2\xi_i \cos(\Delta\theta_j)} \right] \right] \tag{51}$$

In the limit, this summation becomes the integration of the product of the crack face pressure distribution and the Green's function over the crack area

$$K_I = \int_{-\pi/2}^{\pi/2} \int_0^{R_c} \left[\frac{\sigma(r,\theta)}{(\pi R_c)^{3/2}} \frac{a_2 \left(1 - \xi^{a_5}\right)^{a_6}}{\left[1 + \xi^2 - 2\xi \cos(\Delta\theta)\right]} \right] r dr d\theta \tag{52}$$

In order to isolate a modification factor due to the non-uniform stress distribution alone, the stress intensity factor is written in terms of a reference stress

$$K_I = S_{ref}\sqrt{\pi c}\int_{-\pi/2}^{\pi/2}\int_0^{R_c}\left[\frac{\sigma(r,\theta)}{S_{ref}(\pi R_c)^2}\frac{a_2\left(1-\xi^{a_5}\right)^{a_6}}{\left[1+\xi^2-2\xi\cos(\Delta\theta)\right]}\right]rdrd\theta \tag{53}$$

The "stress distribution" correction, F_{GS}, is

$$F_{GS} = \int_{-\pi/2}^{\pi/2}\int_0^{R_c}\left[\frac{\sigma(r,\theta)}{S_{ref}(\pi R_c)^2}\frac{a_2\left(1-\xi^{a_5}\right)^{a_6}}{\left[1+\xi^2-2\xi\cos(\Delta\theta)\right]}\right]rdrd\theta \tag{54}$$

Numerical integration is required for the evaluation of F_{GS}.

Correction for Finite Width and Thickness

Since this result is for a crack in a half-space, in general it will be necessary to compound it with one or more boundary correction factors as required for geometries of practical significance. Compounding is the method by which the SIF for a given applied load is taken as the factorial combination of the fundamental form (in this case the semi-infinite plate solution) and one or more correction terms [31]. For a semi-elliptical edge crack in a finite width and thickness plate, the boundary correction terms given by Newman and Raju [32] are used

$$K = S_{ref}\sqrt{\pi c}F_{GS}F_W F_2 F_T \tag{55}$$

F_W, F_2, and F_T were found by rotating Newman and Raju's surface crack solution by 90 degrees

$$F_W = f_{W0} + f_{W2}\gamma_c^2 + f_{W4}\gamma_c^4 \tag{56}$$

For crack aspect ratios, $a/c \leq 1$, the coefficients of F_W and the F_2 term are

$$f_{W0} = 1 + 0.04\left(\frac{a}{c}\right) \tag{57}$$

$$f_{W2} = 0.2\left(\frac{a}{c}\right)^{7/2} \tag{58}$$

$$f_{W4} = -0.11\left(\frac{a}{c}\right)^{7/2} \tag{59}$$

$$F_2 = 1 + \left[0.1 + 0.35\left(\frac{a}{c}\right)\gamma_c^2\right](1-\cos\phi)^2 \tag{60}$$

while for $a/c > 1$ they are

$$f_{w0} = 1.13 - 0.09\left(\frac{c}{a}\right) \tag{61}$$

$$f_{W2} = -0.54 + \frac{0.89}{0.2 + \left(\frac{c}{a}\right)} \tag{62}$$

$$f_{W4} = 0.5 - \frac{1}{0.65 + \left(\frac{c}{a}\right)} + 14\left(1 - \frac{c}{a}\right)^{24} \tag{63}$$

$$F_2 = 1 + \left[0.1 + 0.35\gamma_c^2\right](1 - \cos\phi)^2 \tag{64}$$

The finite thickness correction, F_T is

$$F_T = \sqrt{\sec\left(\frac{\pi\gamma_a}{2}\sqrt{\gamma_c}\right)} \tag{65}$$

In Eqs 56 65, the normalized crack lengths are, $\gamma_c = c/W$ and $\gamma_a = a/s$, where s is the distance from the crack center-line to the near surface of the plate.

The current expressions were evaluated by calculating SIFs for a configuration for which certain solutions are known. As shown in Fig. 8, the Green's function technique yields accurate results for uniform remote axial loading over the full range of c/W = 0 to c/W = 1, when compared to those generated using the expressions given in [32]. Also shown in Fig. 8 are normalized SIFs calculated using the weight function technique of Shen and Glinka [33] for the depth (c) direction and Shen, Plumtree, and Glinka [34] for the surface (a) direction. In both cases, the current results are in reasonable agreement up to about c/W = 0.7. Note that while bi-variant stress distributions can be treated with the current approach, the cited weight function solutions require uni-variant stress distributions. A similar result is found when comparing the current Green's function and closed form results for in-plane bending (see Fig. 9). Unfortunately, the computational complexity of the current GF makes its use for cycle-by-cycle SIF calculation very burdensome.

Fatigue Crack Growth Analysis

All of the ingredients for cycle-by-cycle fatigue crack growth analysis are now in place. Given an applied stress history and a method for approximating any induced stresses in the vicinity of a notch, the cyclic stress-strain response may be estimated. With the current model, fatigue crack growth analyses may be conducted based on either elastic or estimated elastic-plastic response. In either case, with the stress response known, stress intensity factors are calculated using the techniques described above. The remainder of the analysis is carried out in the manner of traditional, LEFM-based fatigue crack growth analysis [35,36]. The algorithm consists of the following primary steps:

1) Calculate response (elastic or elastic-plastic).
2) Calculate effective stress intensity factors.
3) Check whether calculated SIF exceeds the toughness of the material, and if so, stop.
4) Calculate crack growth rates and crack growth increments and increment crack size.
5) Check for transition, and when transition occurs, redefine the crack geometry accordingly.
6) Check whether maximum crack size has been exceeded, and if so, stop.

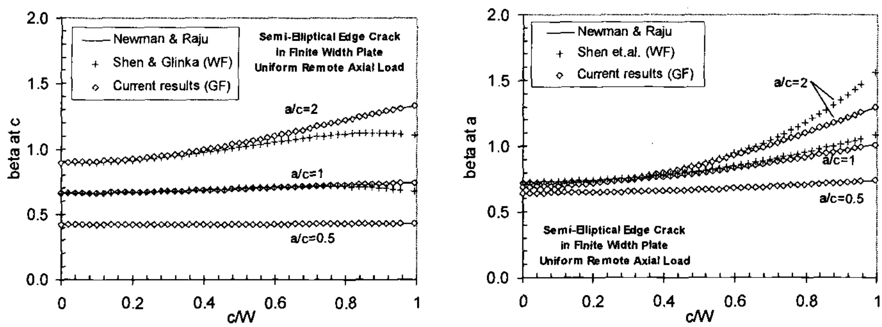

(a) depth direction (phi=0°)

(b) surface direction (phi=85°)

FIG. 8 *Comparison of normalized SIF for a semi-elliptical edge crack in a finite width and thickness plate subjected to uniform remote axial load.*

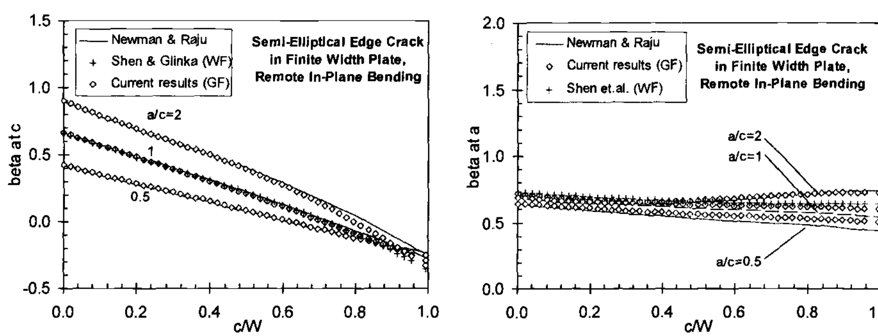

(a) depth direction (phi=0°)

(b) surface direction (phi=85°)

FIG. 9 *Comparison of normalized SIF for a semi-elliptical edge crack in a finite width and thickness plate subjected to remote in-plane bending.*

Effective Stress Intensity Factor

At each load point in the fatigue history, the effective stress intensity factor is determined based on the response stress distribution at that load point using the techniques discussed above. So, for example, if we consider a semi-elliptical crack at a semi-circular notch in a plate subjected to a tensile overload, we would expect to see a reduction in the calculated SIF due to notch plasticity effects. As shown in Fig. 10, this is indeed the case. In order to generate these results, it was first necessary to determine the elastic stress distribution on the uncracked, net section; this was done by finite element analysis using a fine grid model of an SEN test specimen. The elastic SIF results were based on the elastic stress distribution and are shown to be in reasonable agreement with values given by Swain and Newman [37]. The elastic-plastic SIF results are based on the elastic-plastic response stress distribution. As one might expect, since the difference between the elastic and the elastic-plastic response stress distributions is greatest in the immediate vicinity of the notch, the difference between the elastic and the elastic-plastic SIFs is greatest for evaluation points near the surface (i.e., phi = 85°).

The results shown in Fig. 10 are for an applied (field) stress of 192 MPa. This stress results in a peak stress of 680 MPa, the second value of the 8-point load sequence discussed previously. If we calculate the SIFs for a 0.01 × 0.01 in. flaw for each point in the 8-point sequence, we find that there is a significant difference between those calculated based on an assumed elastic response and those calculated based on the estimated elastic-plastic response. As shown in Fig. 11, each time a tensile overload occurs, the response stress is less than the corresponding applied value, and thus the effective SIF is reduced. But of equal importance is the fact that each time a compression overload occurs, the response stress can be higher than the applied stress, and thus the effective SIF can be increased. The implications for fatigue crack growth analysis are very clear: notch plasticity can significantly affect the crack driving force for cracks whose dimensions are of the same magnitude as the notch plastic zone.

It is important to note that since the response stress distributions are estimated for an uncracked cross-section, they do not reflect the influence of the crack. This obviously places a restriction on the range of crack sizes for which this model can be used: the quality of the approximation decreases with increasing crack size. As a general rule, use of the model should be restricted to problems in which the crack length is less than 20 % of the width of the body. This also means that the estimated response distributions contain no information about crack closure. As a result, the minimum effective SIF is not corrected for closure; it is based strictly on the response stress distribution at the cycle minimum. The effective SIF range is found simply as the difference between Keff-max and Keff-min. Comparisons between the effective ΔKs based on notch plasticity and those predicted by a widely used empirical load interaction model [38] are shown in Fig. 12.

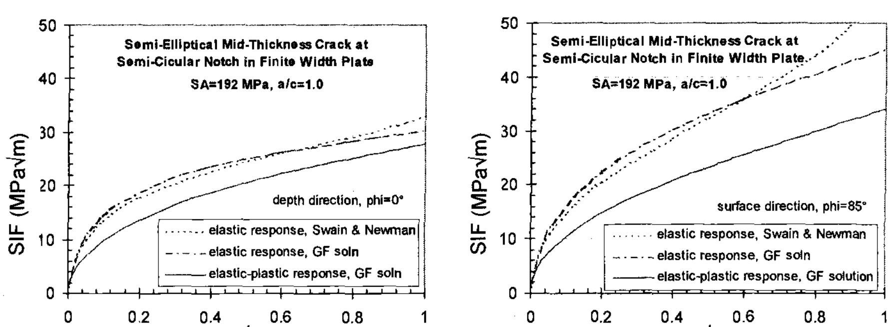

a) depth direction, phi = 0° b) surface direction, phi = 85°

FIG. 10 *Calculated SIFs for a semi-elliptical edge crack at a semi-circular notch in a finite width strip subjected to remote axial load.*

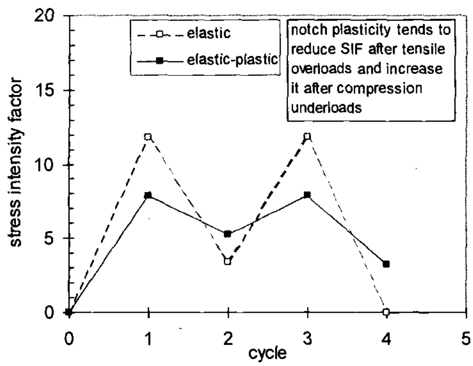

FIG. 11 *Effect of notch plasticity on calculated SIF for semi-elliptical edge crack at semi-circular notch in finite width plate subjected to 8-point stress sequence.*

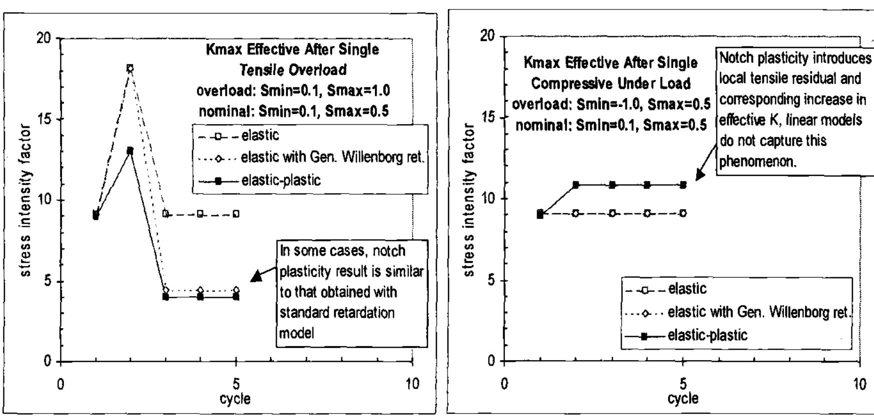

FIG. 12 *Comparison of Effective ΔK for Generalized Willenborg [38] and Notch Plasticity Model.*

Crack Growth Life Prediction

Since the notch plasticity analysis is carried out on a cycle-by-cycle basis, the crack growth analysis is as well. The effective SIF range for a given load cycle is used to determine the crack growth rate for that cycle; this may be done using any one of several empirical crack growth rate equations. For the results shown below, the Forman equation [39] was used.

$$\frac{da}{dN} = \frac{C_f(\Delta K_{eff})^{n_f}}{(1-R)K_f - \Delta K_{eff}} \tag{66}$$

As one might expect, since the notch plasticity model predicts a reduction in effective SIF following a tensile overload, there will be a corresponding reduction in calculated fatigue crack growth rate. Likewise, a compression overload will cause an increase in growth rate. Once a crack growth rate is determined, the corresponding crack growth increments are known. Starting from a prescribed initial size, the crack size is increased by the calculated crack length/depth increment at each cycle. The only datum over and above that normally required for a traditional fatigue crack growth analysis is the cyclic stress-strain curve [40,41] for the material being analyzed.

Example fatigue crack growth calculations were made for a semi-elliptical edge crack at a semi-circular notch in a finite width, 2024-T851 aluminum plate subjected to both tension dominated and compression dominated, variable amplitude spectrum loading [42]. The plate width and thickness were 38.1 mm and 6.35 mm, respectively, while the notch radius was 6.35 mm. The initial crack was semi-elliptical with c = 0.0254 mm and 2a = 0.254 mm, and it was centered at the mid-plane of the plate. Transition to a through thickness crack occurred when the crack-tip growing in the thickness direction reached the plate surface. (Note that the final crack size is below the $c/W < 0.2$ guideline mentioned in the previous section for the validity of the cyclic response/effective SIF model.) The crack growth rate parameters were assumed to be the same in both the crack-length and crack-depth directions (C_F = 2.66E-7, n_F = 2.871, K_F = 40 ksi$\sqrt{\text{in.}}$), and as a result the crack aspect ratio changed as the crack grew. Exceedance curves for the two spectra are shown in Figs. 13 and 14. As shown in Fig. 15, for tension dominated spectrum loading, the occurrence of notch plasticity can cause significant extension in predicted crack growth life. In fact, in this case, the model produced results that are similar to those obtained with "traditional" LEFM techniques. Specifically, the "short life" elastic result shown in Fig. 15 was produced using a linear crack growth analysis with spectrum cycle counting (range pair) but with no retardation, while the "long life" elastic result was generated using both range pair counting and the generalized Willenborg retardation model [38] with Rso = 2.65. However, for compression dominated spectrum loading there can be substantial differences between the two techniques. As shown in Fig. 16, if the spectrum includes compression overloads that are of sufficient magnitude to create tensile residuals, then the current model will predict significant crack growth, whereas the "traditional" LEFM model will not.

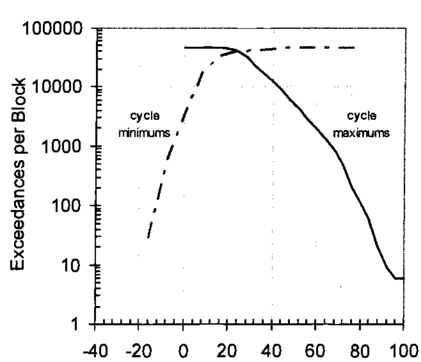

FIG. 13 *Tension dominated spectrum [42].*

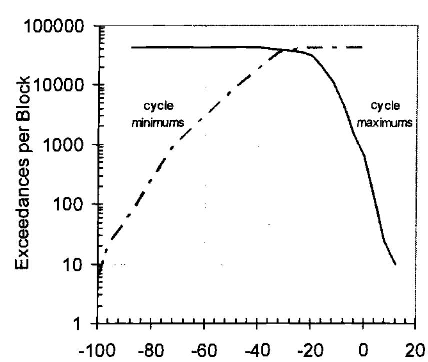

FIG. 14 *Compression dominated spectrum [42].*

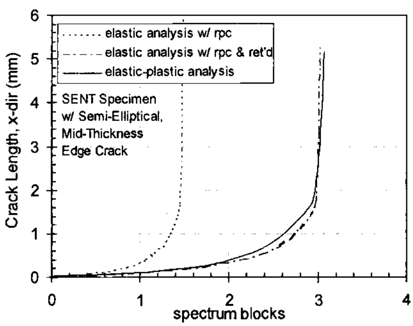

FIG. 15 *Calculated FCG Life, 2024-T851 Aluminum Plate, Tension Dominated Spectrum Loading, MSS=260 Mpa.*

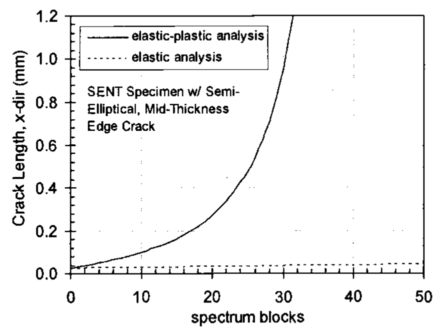

FIG. 16 *Calculated FCG Life, 2024-T851 Aluminum Plate, Compression Dominated Spectrum Loading, MSS=260 Mpa.*

Conclusions and Recommendations

A fatigue crack growth analysis algorithm that accounts for the effects of notch plasticity has been developed. The current capabilities of this algorithm are:

- Prediction of the creation and evolution of both tensile and compressive residual stress fields due to compressive and or tensile overloads, respectively
- Stress intensity factor calculations based on response stress distributions
- Kinematic material hardening

The primary limitations of the approach are:

- Small (with respect to body dimensions) crack size is required for validity of estimated response calculation (no load redistribution due to presence of crack).
- Crack closure is not considered.
- Elastic predominance is still required for validity of LEFM fatigue crack growth approach.
- Current capability is limited to simple geometries.

Recommendations for continued research include the following:

- The use of a fracture parameter, which is more appropriate for elastic-plastic conditions, specifically J and ΔJ, should be investigated.
- Methods for the incorporation of crack closure effects should be investigated.
- Detailed correlations with test data and model revision as required must be performed.

References

[1] Neuber, H., "Theory of Stress Concentration for Shear-Strained Prismatical Bodies with Arbitrary Nonlinear Stress-Strain Law," *Trans. ASME, Journal of Applied Mechanics*, Vol. 8, December 1961, pp. 544 550.

[2] Topper, T. H., Wetzel, R. M., and Morrow, J., "Neuber's Rule Applied to Fatigue of Notched Specimens," *Journal of Materials*, Vol. 4, No. 1, March 1969, pp. 200 209.

[3] Hoffman, M. and Seeger, T., "A Generalized Method for Estimating Multiaxial Elastic-Plastic Notch Stresses and Strains Part 1: Theory," *Trans. ASME, Journal of Engineering Materials and Technology*, Vol. 107, 1985, pp. 250 254.

[4] Hoffman, M. and Seeger, T., "A Generalized Method for Estimating Multiaxial Elastic-Plastic Notch Stresses and Strains Part 2: Application and General Discussion," *Trans. ASME, Journal of Engineering Materials and Technology*, Vol. 107, 1985, pp. 255 260.

[5] Molski, K. and Glinka, G., "A Method of Elastic-Plastic Stress and Strain Calculation at a Notch Root," *Materials Science and Engineering*, Vol. 50, 1981, pp. 93 100.

[6] Glinka, G., "Calculation of Inelastic Notch Tip Strain-Stress Histories Under Cyclic Loading," *Engineering Fracture Mechanics*, Vol. 22, No. 5, 1985, pp. 839 854.

[7] Wang, C. H. and Rose, L. R. F., "Transient and Steady State Deformation at Notch Root Under Cyclic Loading," *Mechanics of Materials*, Vol. 30, 1998, pp. 229 241.

[8] Hsu, T. M., McGee, W. M., and Aberson, J. A., "Extended Study of Flaw Growth at Fastener Holes, Vol. I," AFFDL-TR-77-83, Air Force Flight Dynamics Laboratory, April 1978.

[9] Glinka, G., "Effect of Residual Stresses on Fatigue Crack Growth in Steel Weldments Under Constant and Variable Amplitude Loads," *Fracture Mechanics, ASTM STP 677*, C. W. Smith, Ed., ASTM International, West Conshohocken, PA, 1979, pp. 198 214.

[10] Parker, A. P., "Stress Intensity Factors, Crack Profiles, and Fatigue Crack Growth Rates in Residual Stress Fields," *Residual Stress Effects in Fatigue, ASTM STP 776*, ASTM International, West Conshohocken, PA, 1982, pp. 13 31.

[11] Dugdale, D. S., "Yielding of Steel Sheets Containing Slits," *Journal of the Mechanics and Physics of Solids*, Vol. 8, 1960, pp. 100 108.

[12] Dill, H. D. and Saff, C. R., "Spectrum Crack Growth Prediction Method Based on Crack Surface Displacement and Contact Analyses," *ASTM STP 595*, ASTM International, West Conshohocken, PA, 1976, pp. 306 319.

[13] Newman, J. C., Jr., "A Crack-Closure Model for Predicting Fatigue Crack Growth Under Aircraft Spectrum Loading," *Methods and Models for Predicting Fatigue Crack Growth Under Random Loading, ASTM STP 748*, ASTM International, West Conshohocken, PA, 1981, pp. 53 84.

[14] Glinka, G., "A Notch Stress-Strain Analysis Approach to Fatigue Crack Growth," *Engineering Fracture Mechanics*, Vol. 21, No. 2, 1985, pp. 245 261.

[15] Wang, G. S. and Blom, A. F., "A Strip Model for Fatigue Crack Growth Predictions Under General Load Conditions," *Engineering Fracture Mechanics*, Vol. 40, 1991, pp. 507 533.

[16] Wang, G. S., "A Strip Yield Analysis of Fatigue Crack Growth in the Residual Stress Field," *International Journal of Fracture*, Vol. 96, 1999, pp. 247 277.

[17] Wang, C. H., Rose, L. R. F., and Chen, G. X., "A Strain-Based Dugdale Model for Cracks Under Generally Yielding Conditions," *International Journal of Fracture*, Vol. 113, 2002, pp. 77 104.

[18] Dieter, G. R., "Notch Effects," *Mechanical Metallurgy*, 2nd ed., McGraw-Hill Book Co., New York, 1976, pp. 280 284.

[19] Fuchs, H. O. and Stephens, R. I., "Self Stresses and Notch Strain Analysis," *Metal Fatigue in Engineering*, Wiley, New York, 1980, pp. 125 146.

[20] Kotousov, A. and Wang, C. H., "Three Dimensional Stress Constraint in an Elastic Plate with a Notch," *International Journal of Solids and Structures*, Vol. 39, No. 16, 2002, pp. 4311 4326.

[21] Mendelson, A., "Criteria For Yielding," *Plasticity: Theory and Application*, Krieger Publishing Co., Malabar, FL, 1983, pp. 70 97.

[22] Morrow, J., Martin, J. F., and Dowling, N. E., "Local Stress-Strain Approach to Cumulative Fatigue Damage Analysis," Department of Theoretical and Applied Mechanics, University of Illinois, T. & A. M. Report No. 379, January 1974.

[23] Edwards, P. R., "An Experimental Study of the Stress Histories at Stress Concentrations in Aluminum Alloy Specimens Under Variable Amplitude Loading Sequences," TR-70004, Royal Aircraft Establishment, January 1970.

[24] Cartwright, D. J. and Rooke, D. P., "Green's Functions in Fracture Mechanics," *Fracture Mechanics-Current Status, Future Prospects*, R. A. Smith, Ed., Pergamon, Toronto, 1979, pp. 91 123.

[25] Bueckner, H. F., "A Novel Principle for the Computation of Stress Intensity Factors," *Z. Angew. Math. Mech.*, Vol. 50, No. 9, 1970, pp. 529 546.

[26] Rice, J. R., "Some Remarks on Elastic Crack Tip Stress Fields," *International Journal of Solids and Structures*, Vol. 8, 1972, pp. 751 758.

[27] Tada, H., Paris, P. C., and Irwin, G. R., *The Stress Analysis of Cracks Handbook*, 2nd ed., Del Research Corp., Hellertown, PA, 1985.

[28] Wu, X-R and Carlsson, A. J., *Weight Functions and Stress Intensity Factor Solutions*, Pergamon Press, Oxford, 1991.

[29] Bueckner, H. F., "The Propagation of Cracks and Energy of Elastic Deformation," *Trans. ASME*, Vol. 80, Series E, 1958, pp. 1225 1229.

[30] Ball, D. L., Doerfler, M. T., and Swanton, G. S., "METLIFE Extension Work," FZS-12-38004, Lockheed Martin Aeronautics Co., December 2000.

[31] Rooke, D. P., Baratta, F. I., and Cartwright, D. J., "Simple Methods of Determining Stress Intensity Factors," *Engineering Fracture Mechanics*, Vol. 14, 1981, pp. 397 426.

[32] Newman, J. C., Jr. and Raju, I. S., "Stress Intensity Factor Equations for Cracks in Three-Dimensional Finite Bodies Subjected to Tension and Bending Loads," NASA-TM-85793, April 1984.

[33] Shen, G. and Glinka, G., "Weight Functions for a Surface Semi-Elliptical Crack in a Finite Thickness Plate," *Theoretical and Applied Fracture Mechanics*, Vol. 15, 1991, pp. 247 255.

[34] Shen, G., Plumtree, A., and Glinka, G., "Weight Function for the Surface Point of a Semi-Elliptical Surface Crack in a Finite Thickness Plate," *Engineering Fracture Mechanics*, Vol. 40, No. 1, 1991, pp. 167 176.

[35] Chang, J. B., Hiyama, R. M., and Szamossi, M., "Improved Methods For Predicting Spectrum Loading Effects," AFWAL-TR-81-3092, November 1981.

[36] Chang, J. B., Szamossi, M., and Liu, K-W, "A User's Manual for a Detailed Level Fatigue Crack Growth Analysis Computer Code, Vol. I – The CRKGRO Program," AFWAL-TR- 81-3093, November 1981.

[37] Newman, J. C., Jr. and Edwards, P. R., "Short Crack Growth Behavior in an Aluminum Alloy – An AGARD Cooperative Test Programme," AGARD-R-732, December 1988.

[38] Gallagher, J. P. and Hughes, T. F., "Influence of Yield Strength on Overload Affected Fatigue Crack Growth Behavior in 4340 Steel," AFFDL-TR-74-27, Air Force Flight Dynamics Laboratory, July 1974.

[39] Forman, R. G., Kearney, V. E., and Engle, R. M., "Numerical Analysis of Crack Propagation in Cyclic-Loaded Structures," *Trans. ASME, Journal of Basic Engineering*, Vol. 89, Series D, 1967, pp. 459 464.

[40] Endo, T. and Morrow, J. D., "Cyclic Stress-Strain and Fatigue Behavior of Representative Aircraft Metals," *Journal of Materials, JMLSA*, Vol. 4, No. 1, March 1969, pp. 159 175.

[41] Landgraf, R. W., Morrow, J. D., and Endo, T., "Determination of the Cyclic Stress-Strain Curve," *Journal of Materials, JMLSA*, Vol. 4, No. 1, 1969, pp. 176 188.

[42] Ignjatovic, M., "Fatigue Testing and Analysis of 2024-T851 Edge Notch Specimens Under Conditions of Constant Amplitude and Spectrum Loading, Notch Plasticity and Multi-Site Crack Initiation," ER-F111-57-APM094, Aerostructures Technologies Pty Ltd, 15 May 2001.

Journal of ASTM International, September 2004, Vol. 1, No. 8
Paper ID JAI19041
Available online at www.astm.org

R. Craig McClung,[1] *Fraser J. McMaster,*[1] *and James H. Feiger*[1]

Comparisons of Analytical Crack Closure Models and Experimental Results Under Flight Spectrum Loading

ABSTRACT: Spectrum FCG data were generated with corner cracks at center holes for three contrasting spectrum types and two aluminum alloys, 2124-T851 and 7475-T7351. Existing strip-yield crack closure models for FCG analysis under spectrum loading were evaluated in comparison to conventional FCG models and enhanced as needed. Spectrum editing methods based on closure behavior were developed to reduce both computational and experimental time. FASTRAN was modified to address apparent differences in closure behavior between the surface and bore tips for compression-dominated spectra. Strip yield models successfully predicted FCG lives for contrasting spectra with a common constraint factor, unlike conventional models.

KEYWORDS: fatigue crack growth, aluminum alloys, crack closure, spectrum editing, fracture mechanics, constraint, compression, load interaction

Introduction

Fatigue crack growth (FCG) retardation and acceleration resulting from variable amplitude spectrum loading can dramatically affect FCG life. The load interaction models that simulate these phenomena are a critical part of durability and damage tolerance certification of fighter aircraft. Many FCG load interaction algorithms are based on largely empirical models that require substantial experimental calibration. These models generally only predict retardation, and the calibrated parameters usually cannot be applied to other fatigue critical locations and spectra.

This study focuses on the application of strip-yield crack closure models for FCG. These models are based on physical mechanisms and can predict both retardation and acceleration. The only "free parameter" in the closure model is the constraint factor, α, which describes tendencies toward plane stress or plane strain conditions in the cracked geometry, and hence can be estimated from physical arguments. Furthermore, because the model is based on the mechanics of cycle-by-cycle FCG, it can potentially characterize the damage content—or lack thereof—of each cycle.

The objective of this study was to evaluate and enhance existing strip yield models for FCG analysis of components subjected to spectrum loading. Spectrum FCG data were generated on a representative feature geometry for three contrasting spectrum types (tension-dominated, fully-reversed, and compression-dominated) and two different materials (2124-T851 and 7475-T7351). Strip yield models were used to predict the test results, and the performance of the models was evaluated. Model limitations were identified, and potential solutions were explored.

Manuscript received 29 May 2002; accepted for publication 17 July 2003; published September 2004. Presented at ASTM Symposium on Fatigue Testing and Analysis Under Variable Amplitude Loading Conditions on 29 31 May 2002 in Tours, France; P. C. McKeighan and N. Ranganathan, Guest Editors.

[1] Senior Program Manager, Senior Research Engineer, and Research Engineer, respectively, Southwest Research Institute, P.O. Drawer 28510, San Antonio, TX 78228-0510.

Experimental Procedures

Experiments were conducted on two representative aluminum alloys, 2124-T851 and 7475-T7351. Specimen material was supplied by Lockheed Martin Aeronautics as plate stock of thickness 31.8 mm (1.25 in.) and 21.3 mm (0.84 in.), respectively. The L-T tensile properties (average of four tests) of the two materials are summarized in Table 1.

TABLE 1 *Tensile properties for 2124-T851 and 7475-T7351.*

Material	0.2 % Yield Strength (MPa)	Ultimate Strength (MPa)	Elongation (%)
2124-T851	447	474	10.4
7475-T7351	441	506	13.5

Baseline FCG rate data were collected on standard compact tension specimens (W = 50.8 mm = 2 in.) of thickness 7.94 mm (0.3125 in.) at two stress ratios, R = 0.1 and 0.5. Crack length measurements were based on compliance (front face clip gage) data with periodic visual correction. Tests were performed under K-control at a normalized K-gradient of $C = (1/K)(dK/da) = -0.08$ mm^{-1} (−2 in.$^{-1}$), followed by a K-increasing test segment with $C = +0.12$ mm^{-1} (+ 3 in.$^{-1}$). Testing was performed at room temperature (22 25 C, 72 77°F) and in room air (45 65 %RH). The test frequency was 20 Hz.

Spectrum test specimens had a gage section width of 76.2 mm (3.0 in.) and thickness of 7.94 mm (0.313 in.) and contained a central hole of diameter 9.5 mm (0.375 in.). The total length of the specimen was 444.5 mm (17.5 in.). A sample specimen is shown in Fig. 1. A 0.89 mm (0.035 in.) EDM flaw was placed at one corner of the center hole, and constant amplitude fatigue pre-cracking was used to grow the resulting corner crack to a size of about 1.27 mm (0.050 in.) before the spectrum test began.

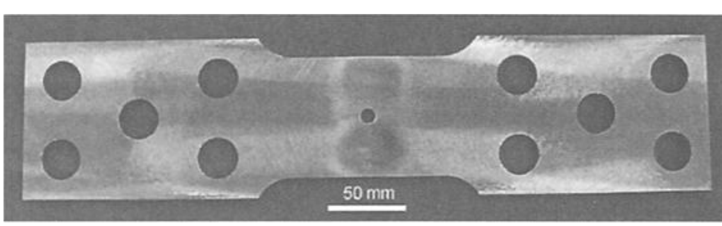

FIG. 1 *Spectrum crack growth specimen.*

The crack lengths on the front specimen surface and in the bore of the hole were independently tracked and measured with traveling microscopes. A 45° mirror was used to measure crack lengths inside the hole. Crack growth on the back specimen surface was tracked and measured once the corner crack had grown through the thickness.

Spectrum specimens were clamped mechanically with preloaded bolt fasteners to minimize backlash during the tension-compression transition. The through holes in the grip area were oversized to avoid any pin loading during testing. Anti-buckling guides with Teflon faying surfaces were used for spectra with large compression loads.

Spectrum loads were applied at frequencies ranging from 10 20 Hz, where the actual applied frequency depended on the dynamic response of the test machine and the magnitude of the load.

Command signals were modified based on the historical feedback performance of previous spectrum passes in order to ensure that all of the peak load magnitudes were actually applied to the coupons.

Three different loading spectra were investigated. All three were derived from actual load histories associated with specific fatigue critical locations on fighter aircraft, but the final spectra were filtered, scaled, or truncated for research purposes. One spectrum was "tension-dominated" (TD) and contained occasional tensile overloads but almost no compression loading. Another spectrum, denoted "fully-reversed" (FR), contained tension and compression peaks of roughly equal magnitude. The third spectrum was "compression-dominated" (CD) and contained significant compression loading but tensile peaks of only about half the compressive magnitude. The maximum stresses (tension or compression) in all three spectra were limited to prevent significant yielding at the notch root. The maximum (absolute value) stress in all three spectra was kept the same for comparison purposes, although a few TD tests were conducted with a 10% smaller scale factor for comparison. The same spectra and scale factors were used for both materials. All three spectra contained 398 flights and between 18 000 20 000 cycles. A limited number of tests was conducted on a modified FR spectrum, from which theoretically non-damaging cycles had been removed, as discussed later.

Analysis Background

So-called "strip yield" methods are analytical representations of fatigue cracks based on the Dugdale model but modified to leave plastically deformed material in the wake of the crack. The plastic-zone size and crack-surface displacements are obtained by superposition of two elastic problems: a crack in a plate subjected to a remote uniform stress, and a crack in a plate subjected to uniform stress acting over a segment of the crack surface. Most current strip yield models are based on a central crack in a finite-width specimen subjected to uniform applied stress.

Two strip yield models have been developed to mature forms and implemented in available software. The FASTRAN code has been under incremental development by Newman for nearly 30 years [1,2]. The current FASTRAN-II [2] includes models for cracks emanating from a circular hole in a finite-width specimen [3]. The STRIPY model of deKoning [4] was incorporated into the NASGRO fracture mechanics analysis software beginning with NASGRO 3.0 [5]. FASTRAN and STRIPY perform similarly, although there are minor differences in their formulation and implementation. Both FASTRAN-II (Version 3.8) and NASGRO (Version 4.0) [6] were used in this study, and the two codes gave similar results in back-to-back comparisons for TD spectra. For convenience, only the FASTRAN results are shown and discussed here.

The first step in preparing for strip-yield analysis is to characterize the baseline FCG data in terms of the effective stress intensity factor, ΔK_{eff}. The closure behavior during the baseline tests was estimated with the Newman closure equations [7], which give the crack opening stress (S_{open}) as a function of stress ratio, applied stress, and constraint state. The constraint state can be estimated by comparing the approximate crack tip plastic zone size to the specimen thickness. Newman [8] has proposed that the transition from full plane-strain behavior toward plane-stress behavior occurs approximately at $(\Delta K_{eff})_T = 0.5\sigma_0\sqrt{B}$, where σ_o is the flow stress (the average of yield and ultimate strengths) and B is the specimen thickness. Because the specimens employed in the SwRI baseline FCG testing were relatively thick, nearly all of the baseline data appear to be in the fully plane-strain regime, and this was confirmed by the flat fracture surfaces on the test specimens. The strip-yield constraint parameter, α, was set equal to 1.73 in all baseline analyses as an appropriate measure of plane strain conditions.

The closure-corrected baseline FCG data are shown in Fig. 2 for 2124-T851 and Fig. 3 for 7475-T7351. Note that the data are shown in terms of ΔK_{eff}, rather than ΔK. Note also how the closure correction collapses the data from different stress ratios. Since the data show some deviation from a simple linear Paris regression, the baseline data were represented for purposes of FASTRAN and NASGRO analysis as a table of *da/dN* versus ΔK_{eff} points. These tabular fits are also shown on the figures.

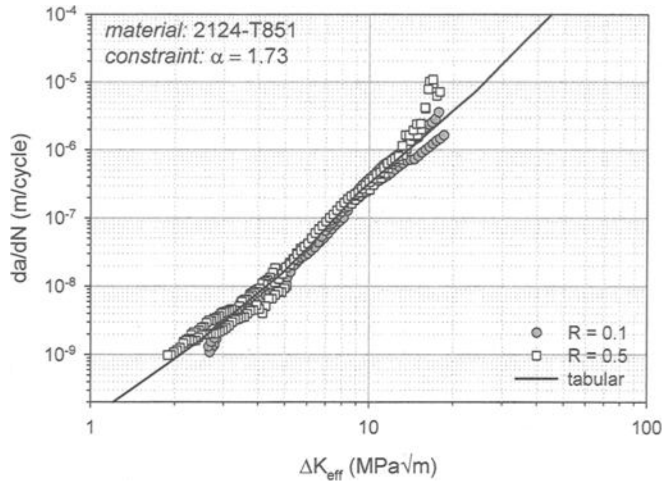

FIG. 2 *Baseline da/dN versus ΔK_{eff} data and tabular fit for 2124-T851.*

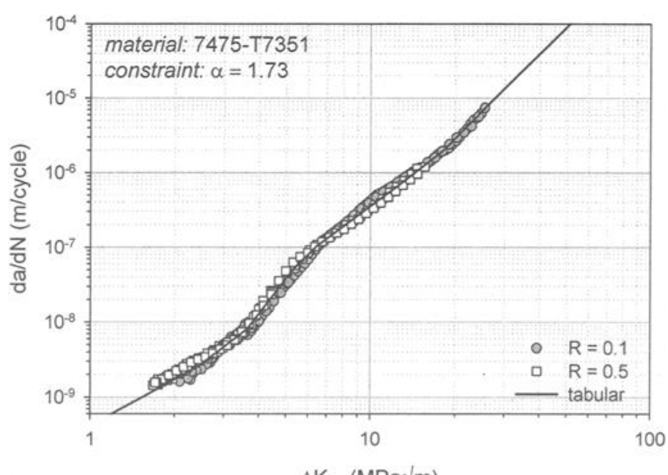

FIG. 3 *Baseline da/dN versus ΔK_{eff} data and tabular fit for 7475-T7351.*

Conventional Fatigue Crack Growth Analyses

Conventional FCG analyses of the spectrum tests were performed for comparative purposes using the NASGRO program. The baseline data were fit to the standard NASGRO equation using the NASMAT module and a constraint parameter of $\alpha = 1.73$. The initial crack length and depth in each analysis corresponded to the measured crack sizes at the beginning of each test, which varied slightly from specimen to specimen. First, a set of "Non-Interaction" (NI) model calculations was performed. This model assumes no load interaction of any kind; crack growth is based on independent cycle-by-cycle (linear damage) calculations. NI results are summarized in Table 2, where all lives are expressed as cycles to failure. Here, "A/P" denotes the ratio of actual to predicted life. The predictions of the TD tests all significantly underestimated the experimental life, because tensile overloads caused substantial crack growth retardation. NI predictions of the FR tests were fairly accurate for 2124, but substantially under-predicted life again for the 7475 tests. NI predictions of the CD tests all substantially over-predicted the test lives, especially for 2124.

TABLE 2 *Summary of non-interaction model predictions.*

Specimen	Material	Spectrum	Max Stress (MPa)	Actual Life	Predicted Life	A/P Ratio
2-3	2124	TD	154.6	729 454	495 225	1.47
2-9	2124	TD	154.6	679 257	444 314	1.53
2-11	2124	TD	154.6	838 470	480 413	1.75
2-7	2124	TD	137.9	938 233	700 986	1.34
average						1.52
2-4	2124	FR	154.6	1 456 898	1 365 947	1.07
2-10	2124	FR	154.6	1 367 814	1 314 352	1.04
average						1.05
2-12	2124	CD	75.8	3 296 415	9 760 832	0.34
2-2	2124	CD	75.8	2 769 960	9 145 536	0.30
average						0.32
7-1	7475	TD	154.6	736 807	361 047	2.04
7-9	7475	TD	154.6	683 289	365 327	1.87
7-2	7475	TD	137.9	980 000	546 649	1.79
7-7	7475	TD	137.9	937 958	511 938	1.83
average						1.88
7-6	7475	FR	154.6	1 813 157	922 492	1.97
7-10	7475	FR	154.6	1 941 968	932 008	2.08
average						2.02
7-4	7475	CD	75.8	3 319 754	5 255 040	0.63
7-5	7475	CD	75.8	3 419 063	4 903 968	0.70
average						0.67

Several semi-empirical load interaction models have been proposed, including Wheeler [9], Willenborg [10], Generalized Willenborg (GW) [11,12], Modified Generalized Willenborg (MGW) [5,6], and Chang-Willenborg (CW) [13]. The Wheeler, Willenborg, and GW models are applicable only to tension-dominated histories and do not compensate for the effects of compression underloads. The MGW and CW models attempt to compensate for these compression effects in an approximate manner. The MGW model was selected for comparative analyses in the current study.

The MGW model extends the GW load interaction model by taking into account the reduction of retardation effects due to underloads. The MGW model, like the GW, utilizes effective stress intensity factors instead of the actual K_{max} and K_{min} within the crack growth equation, thereby retarding the predicted crack growth:

$$\begin{aligned} K_{max}^{eff} &= K_{max} - K_R \\ K_{min}^{eff} &= Max\{(K_{min} - K_R), 0\} \; for \; K_{min} > 0 \\ &= K_{min} \end{aligned} \tag{1}$$

The residual stress intensity factor K_R is given by $K_R = \Phi K_R^W$, where

$$K_R^W = K_{max}^{OL}\left(1 - \frac{\Delta a}{Z_{OL}}\right)^{\frac{1}{2}} - K_{max} \tag{2}$$

K_R^W represents the difference between the stress intensity required to produce a plastic zone equal to $Z_{OL} - \Delta a$ and the current maximum applied stress intensity K_{max}. K_{max}^{OL} is the maximum stress intensity for the overload cycle, and Δa is the crack growth between the overload cycle and the current cycle. The overload plastic zone size is

$$Z_{OL} = \frac{\pi}{8}\left(\frac{K_{max}}{\alpha_g \sigma_{ys}}\right)^2 \tag{3}$$

The constraint factor α_g is taken from a fit developed by Newman for one-dimensional crack models:

$$\alpha_g = 1.15 + 1.4e^{-0.95\left(\frac{K_{max}}{\sigma_{ys}\sqrt{t}}\right)^{1.5}} \tag{4}$$

For two-dimensional cases, limit values of 1.15 or 2.55 are used for α_g ,depending on whether the crack tip is at the free surface (plane stress) or is buried (plane strain).

An underload (i.e., a compressive or tensile load that is lower than the previous minimum load subsequent to the last overload cycle) can reduce such retardation. The stress ratio $R_U = S_{UL}/S_{max}^{OL}$ (the ratio of current underload stress to overload stress) is used to adjust the factor ϕ, which is now given by

$$\phi = 2.523\phi_0 \,/\left(1.0 + 3.5(.25 - R_U)^{.6}\right), \;\; R_U < 0.25 \tag{5}$$

The factor ϕ is set equal to 1 if $R_U \geq 0.25$. The parameter ϕ_0 is the value of ϕ for $R_U = 0$ and is the free parameter in the model.

MGW calculations were conducted to determine the optimum value of ϕ_0 for each test (the value of ϕ_0 for which A/P $\approx$ 1.0). These MGW results for the TD and FR histories are summarized in Table 3. The optimum value of ϕ_0 for the 7475 tests was reasonably consistent, since these test lives were consistently about 2 times longer than NI predictions. In the 2124 tests, however, a substantially different value of ϕ_0 was required to fit the TD and FR tests, and the value of ϕ_0 for the FR tests (0.10) was significantly lower than typical values for this parameter. The MGW approach was completely unsuccessful in predicting the CD test results, giving results scarcely better than NI predictions, even for extreme values of ϕ_0. This failure should not be surprising, because the MGW method was never intended to address such severe compressive loading.

TABLE 3 *Summary of optimized ϕ_0 values for MGW load interaction model.*

Specimen	Material	Spectrum	Max Stress (MPa)	Optimum Φ_0
2-3	2124	TD	154.6	0.28
2-9	2124	TD	154.6	0.30
2-11	2124	TD	154.6	0.37
2-7	2124	TD	137.9	0.24
2-4	2124	FR	154.6	0.11
2-10	2124	FR	154.6	0.10
7-1	7475	TD	154.6	0.42
7-9	7475	TD	154.6	0.38
7-2	7475	TD	137.9	0.36
7-7	7475	TD	137.9	0.36
7-6	7475	FR	154.6	0.35
7-10	7475	FR	154.6	0.38

FASTRAN Efficiency Studies

The added computational effort of calculating S_{open} can substantially increase the computer time required to perform an FCG life analysis, and this may be unacceptable in some engineering environments. Therefore, it is highly desirable to find ways to decrease the total run time without degrading the accuracy of the results. The FASTRAN program itself offers some options toward this goal. In one option, an average S_{open} for the entire spectrum is calculated from a few early passes through the spectrum, and this average S_{open} is then applied to all remaining passes through the spectrum. However, this option was not investigated in the current work, because it sacrifices the fidelity of the closure response to the cycle-by-cycle load spectrum as the crack grows. This study investigated two model parameters—one in the existing model, another created for this study—that directly influence execution time and model accuracy.

Cycle Count for Closure Updating—During crack growth, the crack opening stress in FASTRAN is held constant for a certain amount of crack extension, Δc^*, where Δc^* is set at 20% of the approximate cyclic plastic zone size based on the current maximum and minimum applied stress. However, a new value of S_{open} is calculated and applied when the cycles needed to create Δc^* exceed NMAX. The value of NMAX is fixed at 1000 in the FASTRAN source code. If NMAX is changed to 1, then S_{open} is recalculated on every cycle. This will be the most accurate approach, but at a considerable computational cost.

A series of investigations was conducted to determine the optimum value of NMAX (the largest value—for speed—that still gives acceptable accuracy relative to the NMAX = 1 life) for the TD and FR spectra. Figure 4 shows the predicted life and the percent deviation from the NMAX = 1 prediction for each NMAX value for a specific TD history. Note that NMAX = 1000 can introduce errors of 10 15 % in calculated life. For the TD simulation shown here, NMAX = 30 gave a nearly identical prediction to NMAX = 1, and any NMAX smaller than about 60 gave an answer within ± 5 % of the NMAX = 1 life. For an FR simulation not shown here, NMAX = 60 gave the same result as NMAX = 1, and any NMAX value smaller than 100 gave an answer within 5 % of the NMAX = 1 life. Other studies indicated similar results. As a general rule, NMAX values around 10 to 30 gave accurate predictions for TD histories, and NMAX values on the order of 100 gave accurate predictions for FR histories. The TD simulations in the remainder of this report used NMAX = 25, while the FR simulations used NMAX = 60.

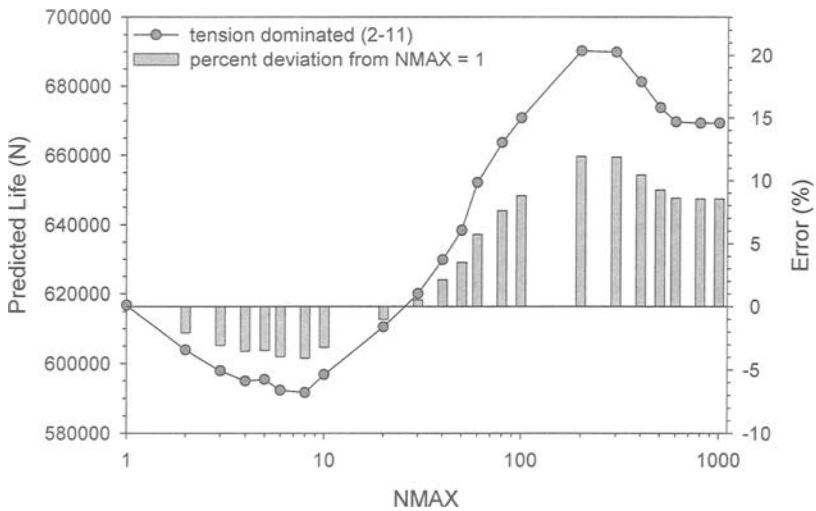

FIG. 4 *Effect of NMAX on calculated life for representative TD history.*

Filtering Parameter—The very nature of the crack closure model for FCG suggests additional opportunities to reduce computational time. The closure model assumes that crack growth is a function of the effective stress intensity factor, ΔK_{eff}. Therefore, any cycle in which the maximum stress is less than the current S_{open} (i.e., $\Delta K_{eff} = 0$) will not cause crack growth. However, cycles in which $\Delta K_{eff} = 0$ may still influence the crack growth behavior, if their minimum load influences the plastic wake. This could be the case, for example, if a cycle contained a large compressive stress. Even though that particular cycle might have a small maximum stress and therefore cause no immediate crack growth, the large compressive stress could substantially decrease the plastic wake and therefore increase the damage caused by subsequent cycles.

This logic implies two simple tests to determine if a given cycle will contribute to crack growth in any way. The first test is whether the maximum stress of the given cycle is greater than the current S_{open}. The second test is whether the minimum stress of the given cycle is lower than the minimum stress of the last cycle that did cause crack growth. If neither test is positive, then the cycle is theoretically non-damaging. If the cycle is non-damaging, then it should be possible to remove the cycle entirely from that particular pass through the spectrum without changing the damage calculation. Removing the cycle from the computation, however, should reduce the computation time.

The FASTRAN source code was modified to implement and test this hypothesis. Cycles were ignored if, and only if: (a) the maximum stress in the cycle was less than a specified fraction of the current S_{open}, and (b) the minimum stress in the cycle was algebraically larger than the minimum stress in the last cycle that was not ignored. The "fraction" in condition (a) was included as a means of preventing errors introduced by minor inaccuracies in the crack opening computation. A parameter "SopFrac" was introduced to characterize this fraction.

The results indicated that SopFrac values as high as 1.0 generally had only a minor effect—one or two percent—on calculated lives. This confirms the fundamental hypothesis, at least analytically. The total execution time for FASTRAN was almost directly proportional to the number of cycles considered, so if 30 % of the cycles were ignored, then the execution time was reduced by approximately 30 %.

While the analytical confirmation of the filtering hypothesis is reassuring, it is also possible—and more important—to confirm the hypothesis experimentally. In order to perform this investigation, FASTRAN was further modified so that a filtered spectrum, based on the analytical conditions outlined above, could be written to a file. This edited spectrum could then be employed to perform a new crack growth experiment, and the results compared with experiments employing the full (unedited) spectrum. Although the total number of cycles to failure would be different, the total number of flights should be the same for both edited and unedited spectra. A special provision in the filtering routines ensured that at least one cycle was retained from each flight, so that the total number of flights in one pass through the spectrum remained the same.

For practical reasons, only a single pass of the spectrum was written to a file. Since crack opening levels can change slightly from pass to pass as the crack grows, it is important to choose a representative pass through the spectrum. A spectrum pass at about one-third of the total FCG life was chosen. Since crack opening stresses generally increase slowly as the crack grows, this was conservative relative to the total life.

The experimental investigation of this spectrum editing concept was limited to the FR spectrum, since FR editing removed a considerably larger fraction of cycles than TD editing, and the CD spectra introduced additional complications (discussed later). For the FR history, the spectrum editing removed about 30 % of the cycles. Note that the spectra as provided to SwRI had already been truncated heavily by Lockheed Martin—eliminating more than 80 % of the smallest cycles—to reduce test time. Therefore, it is even more significant that an additional 30% of the cycles could be removed without substantially changing the damage content of the spectrum.

A single edited-FR test was conducted on each material, and the results were compared with the original test results for the unedited spectrum (two tests had been conducted for each material with the original spectrum). The spectrum scaling remained the same for both edited and unedited spectra. Sample results for 2124 are shown in Fig. 5. For both materials, the FCG behavior for the edited spectrum was very similar to the FCG behavior for the unedited spectrum—exactly as had been predicted.

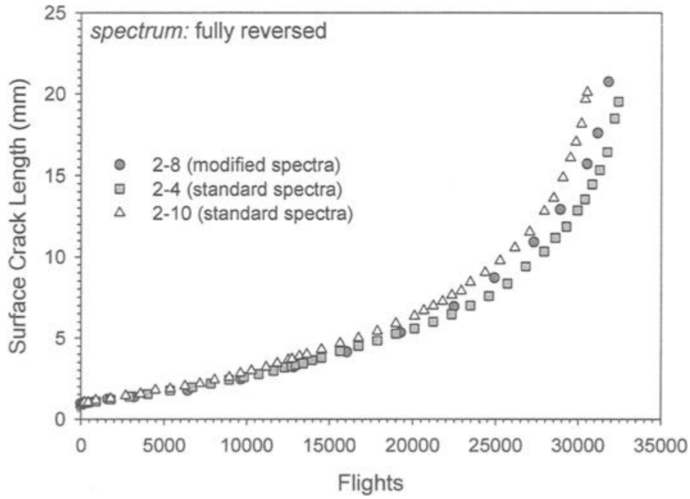

FIG. 5 *Comparison of experimentally determined crack growth in 2124 for edited and unedited FR spectra.*

The crack closure model appears to provide a physically-meaningful method to identify the damage content of each cycle and, in particular, a physically-meaningful method to identify and truncate non-damaging cycles. Of course, the extremely limited experimental study of this issue conducted here is not conclusive evidence that the closure filtering approach is correct. Nevertheless, the concept appears to have considerable promise. Many other spectrum editing techniques are highly empirical in nature and do not consider the physical basis for the damage contribution of each cycle.

FASTRAN Life Prediction Results

Tension-Dominated and Fully-Reversed Spectra—The FASTRAN model was first exercised to determine the optimum α values for each individual test (i.e., that would most closely predict the total number of experimental cycles to failure). Alpha was constrained to remain constant throughout the entire test, which was a reasonable assumption for the thick specimens employed. The filtering parameter SopFrac = 0.8 was held constant for all TD and FR tests.

A summary of the optimum α values thus determined is provided in Table 4. The optimum alpha is reasonably similar for each material, but slightly different from material to material. The average α for 2124 was 2.04, not including test 2-11, which was an experimental outlier (in comparison to the two nominally identical tests 2-3 and 2-9). This α was quite consistent for both TD and FR histories. The average α for 7475 was 1.65, with some minor layering between TD and FR histories.

The real test of a life prediction model is not whether each test can be fit precisely by adjusting a free parameter, but whether a single value of the free parameter gives accurate predictions of the entire data set. Therefore, the average α for each material was used to predict the life of all tests. The results are shown in Table 5, again in terms of cycles to failure. The average $\alpha = 2.04$ predicted all 2124 test lives within 10 %, except for the single outlier test 2-11. The average $\alpha = 1.65$ predicted all 7475 test lives within 22 %, and all tests except one within 15%. In comparison, the normal test-to-test experimental variability among nominally identical tests was on the order of 10 %.

TABLE 4 *Summary of optimized alpha values for FASTRAN load interaction model.*

Specimen	Material	Spectrum	Max Stress (MPa)	Optimum α
2-3	2124	TD	154.6	1.99
2-9	2124	TD	154.6	1.94
2-11	2124	TD	154.6	1.77
2-7	2124	TD	137.9	2.16
2-4	2124	FR	154.6	2.01
2-10	2124	FR	154.6	2.10
2-8	2124	FR-mod	154.6	2.06
7-1	7475	TD	154.6	1.68
7-9	7475	TD	154.6	1.77
7-2	7475	TD	137.9	1.86
7-7	7475	TD	137.9	1.82
7-6	7475	FR	154.6	1.46
7-10	7475	FR	154.6	1.39
7-8	7475	FR-mod	154.6	1.60

TABLE 5 *Summary of FASTRAN TD and FR predictions with average alpha values ($\alpha = 2.04$ for 2024, $\alpha = 1.65$ for 7475).*

Specimen	Material	Spectrum	Max Stress (MPa)	Actual Life	Predicted Life	A/P
2-3	2124	TD	154.6	729454	697336	1.05
2-9	2124	TD	154.6	679257	625625	1.09
2-11	2124	TD	154.6	838470	669751	1.25
2-7	2124	TD	137.9	938233	1032364	0.91
average						1.07
2-4	2124	FR	154.6	1456898	1477005	0.99
2-10	2124	FR	154.6	1367814	1448325	0.94
2-8	2124	FR-mod	154.6	1433715	1474020	0.97
average						0.97
7-1	7475	TD	154.6	736807	746555	0.99
7-9	7475	TD	154.6	683289	751898	0.91
7-2	7475	TD	137.9	980000	1163090	0.84
7-7	7475	TD	137.9	937958	1099491	0.85
average						0.90
7-6	7475	FR	154.6	1813157	1590829	1.14
7-10	7475	FR	154.6	1941968	1597711	1.22
7-8	7475	FR-mod	154.6	1684250	1650321	1.02
average						1.13

Compression-Dominated Spectrum—Initial attempts to predict the life of the CD spectrum tests with FASTRAN were unsuccessful. Even with α set to its highest theoretical value (3.0), the experimental FCG for the 2124 tests was faster than could be predicted by FASTRAN. The 7475 test lives could be predicted successfully, but only with significantly higher values of α than were needed for the TD and FR histories. However, the advantage of the closure-based methods is that the calculations have a meaningful physical basis, and this facilitated more detailed investigations in search of explanations and improvements in the method.

An investigation of the CD tests revealed that the errors appeared to be related to the failure of the FASTRAN model to predict the growth rates (at the *a*-tip) of the crack growing across the bore. Figure 6 shows the experimental crack growth data and the FASTRAN predictions (using an abnormally high α) for both the crack length (the *c*-tip) and crack width (the *a*-tip). In comparison, the FASTRAN model was more successful in predicting the growth rates of the crack growing across the bore for the TD (see Fig. 7) and FR histories, although the FR predictions exhibited some mild inaccuracies in the bore that foreshadowed the more severe problems exhibited by the CD predictions.

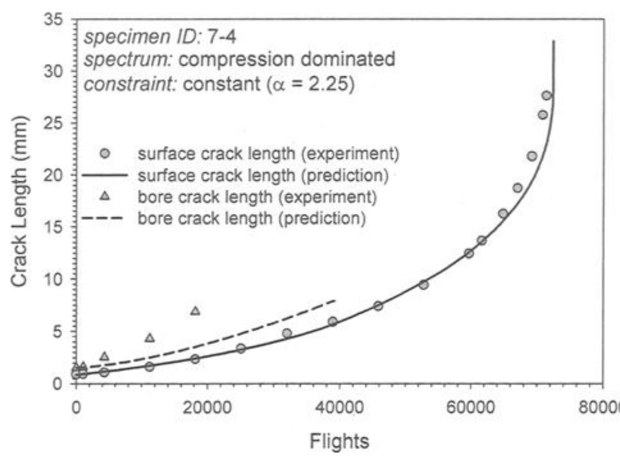

FIG. 6 *Comparison of experimental data and original FASTRAN model for crack length and width under compression-dominated spectrum.*

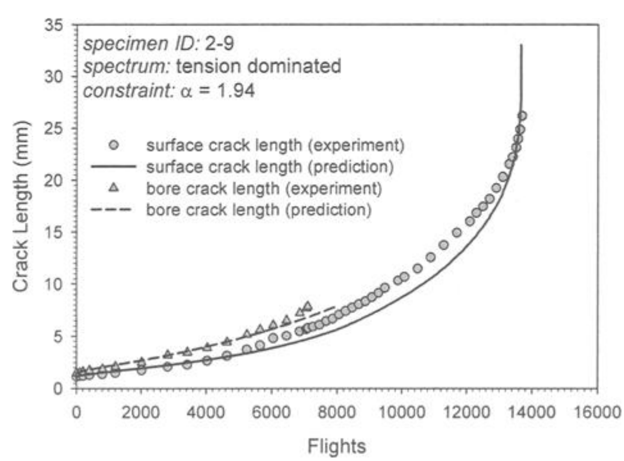

FIG. 7 *Comparison of experimental data and FASTRAN model for crack length and width under tension-dominated spectrum.*

The reasons for this discrepancy may be related to the one-dimensional nature of the FASTRAN model and the effects of stress level and stress ratio on crack closure. The FASTRAN model calculates crack opening behavior for the surface crack tip, which is growing away from the root of the hole, and assumes that opening behavior at the bore crack tip is identical. However, the bore crack tip, growing along the root of the hole, is growing in a local stress field roughly equal to K_tS, where K_t is the stress concentration factor, and S is the far-field stress. The surface crack tip is growing in a steadily declining stress field that eventually approaches the nominal stress S. Therefore, the bore crack tip is growing in a substantially higher local stress field than the surface crack tip.

The nominal applied stresses are known to influence crack opening behavior. Figure 8 summarizes the Newman closure equations [7] for a center-cracked tension specimen under nominal plane strain (α = 1.73) conditions. At higher stress ratios, the effect of the normalized maximum applied stress (S_{max}/σ_0) on normalized crack opening stresses (S_{open}/S_{max}) is mild. However, the effect of maximum stress on opening stress is much more pronounced at lower stress ratios. In comparison, the FASTRAN model did a reasonably good job of describing FCG at both the bore and surface tips for the TD history, where nominal stress ratios are zero to positive; a fair job for the FR history, where the nominal stress ratio of the overall spectrum was $R = -1$, and a poor job for the CD spectrum, where the nominal stress ratio was approximately $R = -2$. This is consistent with Fig. 8: the differences in closure behavior between the bore and surface tips due to maximum stress effects appear to be mild for high R and significant for low R.

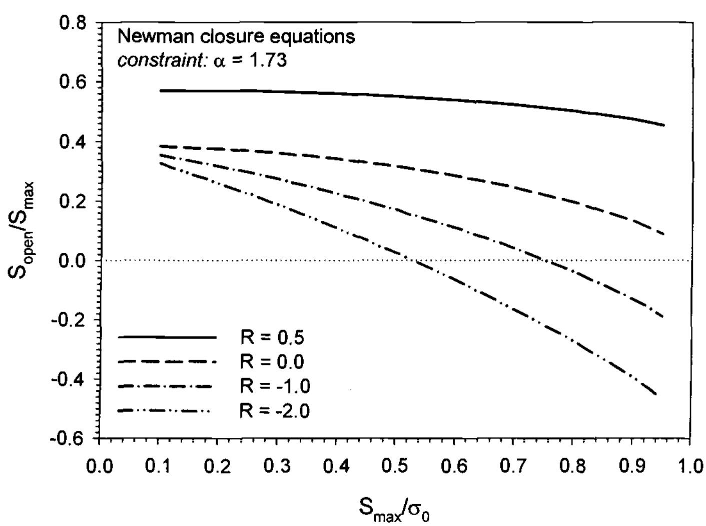

FIG. 8 *Effect of normalized maximum stress on normalized crack opening stress, as predicted by the Newman closure equations [7].*

In order to explore this concept further, additional modifications were made to the FASTRAN code. As a first approximation to addressing the potential differences in closure behavior between bore and surface locations, S_{open} for the bore location was made a user input (denoted SOA). This value was taken as constant throughout the entire history, an obvious simplification, but not unreasonable since the calculated S_{open} at the surface tip was a relatively constant value for the CD history. The SOA value was selected from theoretical considerations: FASTRAN was used to analyze a corner crack in a plate with no hole growing under CD spectrum loading scaled up by a factor of 3 (corresponding to the local $K_t = 3$ in the original hole geometry), and the resulting average S_{open} was calculated. The SopFrac cycle filtering feature was turned off in all CD analyses, because it would no longer be possible to determine which cycles should be ignored based on the calculated surface-tip opening behavior alone. The results of this approach are illustrated in Fig. 9, which demonstrates improvement in the prediction of bore crack growth (here using the average optimum α from the 7475 FR analyses).

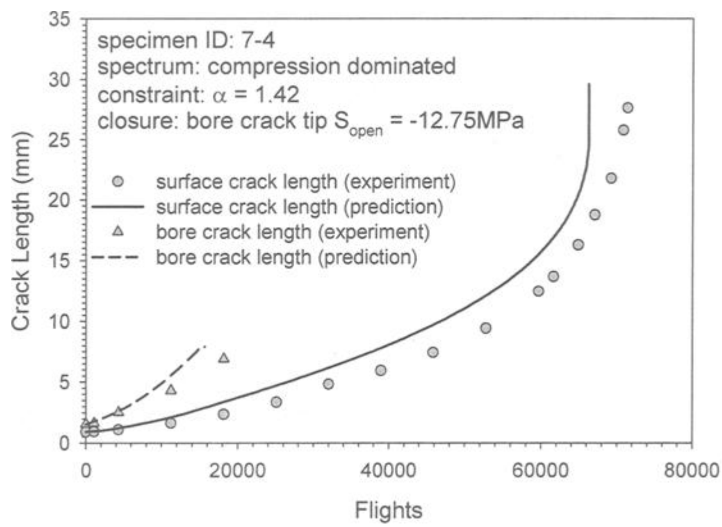

FIG. 9 *Comparison of experimental data and modified FASTRAN model for crack length and width under compression-dominated spectrum.*

In order to assess the suitability of this approach for practical life prediction, another set of genuinely predictive simulations was conducted in which no parameters were allowed to remain free. The α value for each material was chosen as the average optimum α value from the TD and FR tests (2.04 for the 2124 and 1.65 for the 7475). SOA was chosen as −1.85 ksi (−12.75 MPa) based on the FASTRAN analyses cited earlier. The resulting predictions are summarized in Table 6. The quality of the predictions is not quite as good as for the TD and FR tests, but it is still reasonable. All test lives were predicted within 25 %, and three of the four tests were predicted within 18 %.

Questions do remain. The K_tS approach is not entirely satisfying because it neglects the constraining effects of the elastic structure farther away from the hole. Furthermore, although the bore tip and surface tip closure behavior will not be identical, they will likely have some influence on each other and should not be treated as totally independent. Further study is needed to evaluate complex, three-dimensional effects on crack closure near stress concentrations.

Nevertheless, this study appears beneficial because it is focused on the actual physical mechanisms influencing crack growth.

Table 6 *Summary of modified FASTRAN predictions for CD tests.*

Specimen	Material	Spectrum	Alpha	Actual Life	Predicted Life	A/P
2-2	2124	CD	2.04	2769960	3688530	0.75
2-12	2124	CD	2.04	3296415	3830407	0.86
7-4	7475	CD	1.65	3319754	3016738	1.10
7-5	7475	CD	1.65	3419063	2905840	1.18

Of course, no definitive conclusions should be derived from the limited CD data set. The four tests represent only a single spectrum and a single stress level, and the tests exhibit somewhat greater scatter among themselves than the TD and FR tests did. Other factors may also need to be considered, including the effects of cracking at the other side of the hole, the effects of mild compressive yielding at the bore of the hole, and potential inaccuracies in the K solution for corner cracks with high a/c ratios. Nevertheless, these initial results are encouraging and suggest that the modified FASTRAN approach may give acceptable engineering accuracy for a wide range of spectrum types.

Comparisons of Different Crack Growth Models

It is useful to perform a final comparison of all three models considered here (Non-Interaction, Modified Generalized Willenborg, and Strip Yield) on all three spectrum types. In order to perform a fair and meaningful comparison, the average value of ϕ_0 in the MGW model was first determined based on all TD and FR tests, as done earlier for the value of α in the strip yield model. The final predictions for all three spectrum types (TD, FR, and CD) employed the average free parameter value thus obtained. The results highlight the ability (or lack thereof) of each model to address different spectrum types.

Comparisons of the NI, MGW, and Strip Yield models for a representative TD test on each material are shown in Fig. 10. The NI predictions were conservative by 50 80 %. The MGW and FASTRAN strip yield models gave comparable accuracy.

Comparisons for a representative FR test on each material are shown in Fig. 11. The NI model was accurate for the 2124 test but highly conservative for the 7475 test. The MGW model was accurate for the 7475 test but 30 % non-conservative for the 2124 test. The FASTRAN strip-yield model was reasonably accurate for both materials.

Comparisons of the NI, MGW, and enhanced Strip Yield predictions for a representative CD test on each material are shown in Fig. 12. The Non-Interaction and MGW models were highly non-conservative for both materials. The FASTRAN strip yield model, enhanced as described earlier, but employing the same α value as the TD and FR analyses, gave accurate predictions for both materials.

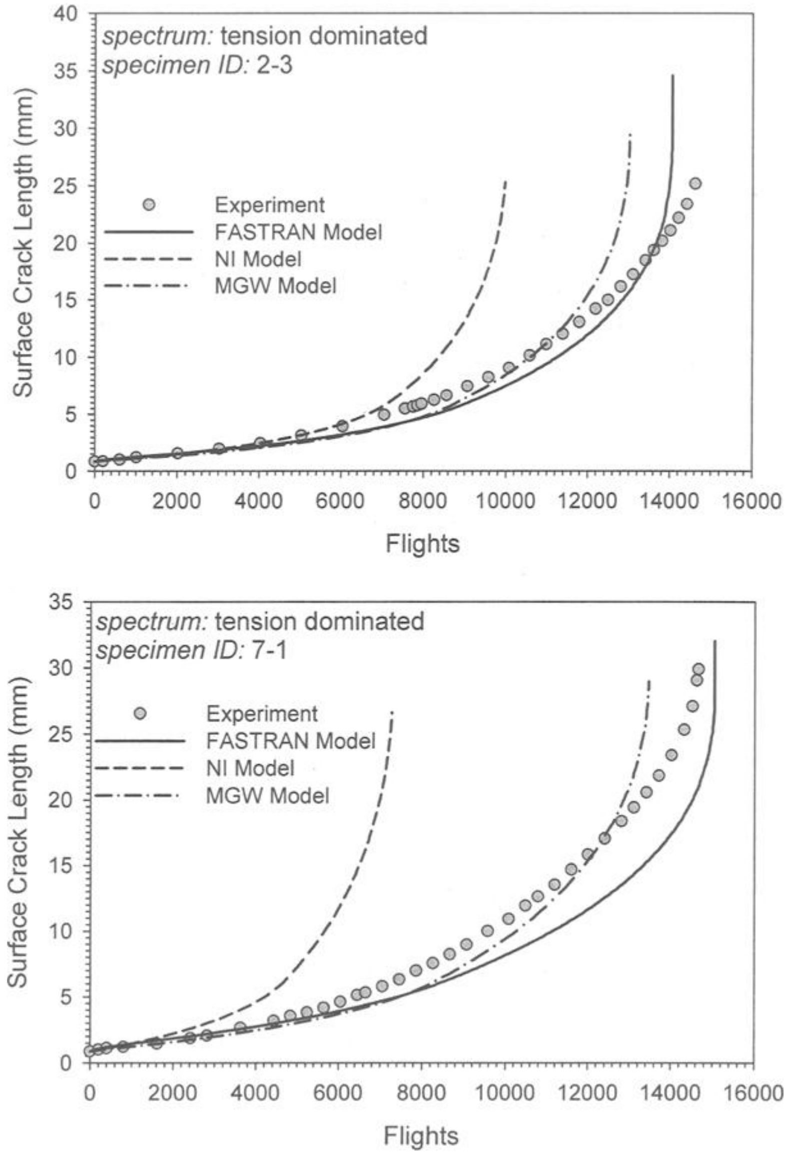

FIG. 10 *Comparison of load interaction models for tension-dominated spectrum: 2124-T851 (top); 7475-T7351 (bottom).*

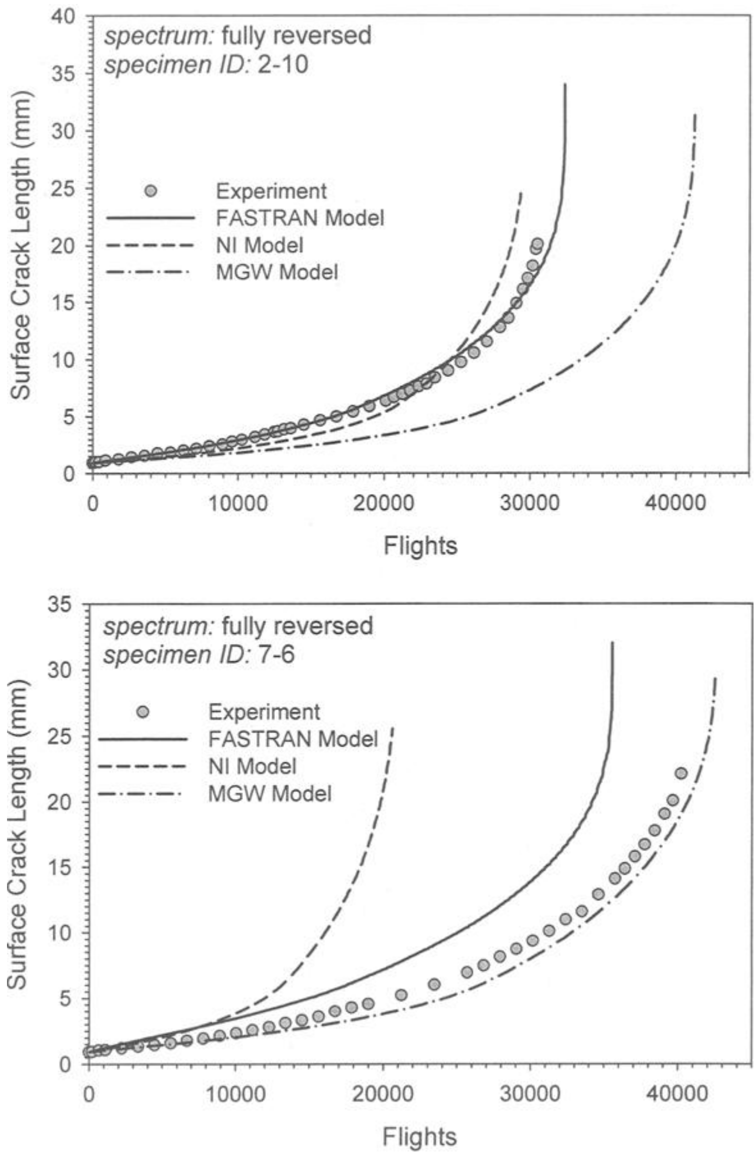

FIG. 11 *Comparison of load interaction models for fully-reversed spectrum: 2124-T851 (top); 7475-T7351 (bottom).*

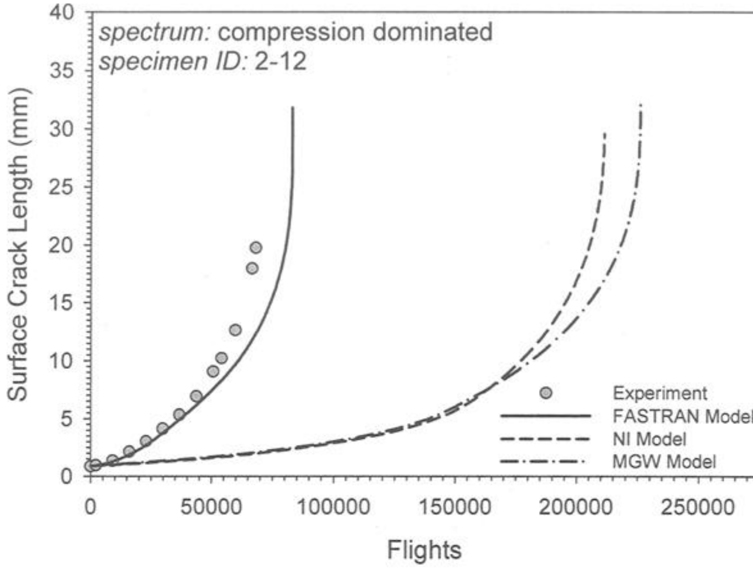

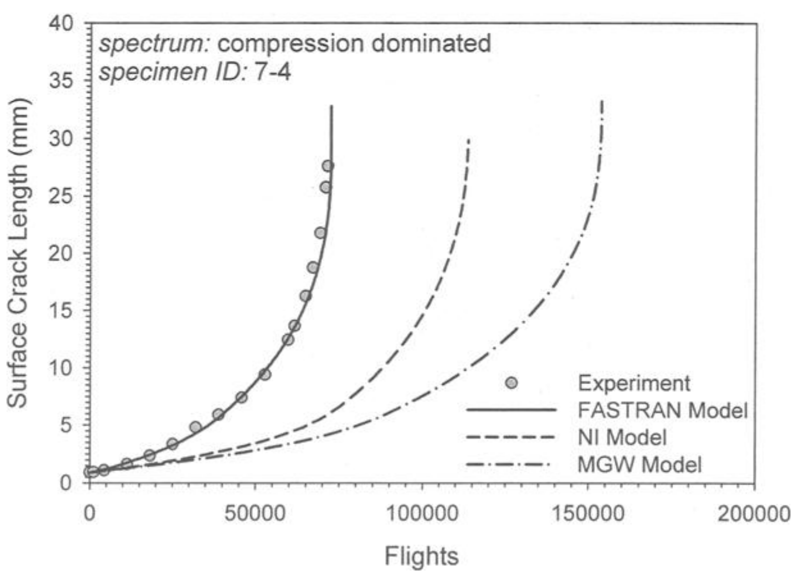

FIG. 12 *Comparison of load interaction models for compression-dominated spectrum: 2124-T851 (top); 7475-T7351 (bottom).*

Discussion

Conventional load interaction models have at least two substantial limitations. First of all, the free parameter in most models has little or no physical meaning, and there is no means to select the optimum value of the parameter prior to performing the analysis of a particular problem. Once the test results are known, it is usually possible to calibrate the empirical model to match the test results reasonably well, especially for TD spectra.

The second major limitation of conventional load interaction models is that they have generally been developed to address TD histories. Although some models have been extended to address occasional compressive excursions, they are generally not able to handle substantial compressive content in the spectrum, as in FR or CD spectra.

The goal of a load interaction model should be to address both limitations: first, it should be possible to select any free parameter *a priori* to give accurate predictions without knowing the results in advance, and second, it should be applicable to a variety of spectrum types, including those with significant compressive loading.

Crack closure models have the potential to solve both of these problems, and the investigations reported here have shown success on both fronts. In particular, the enhanced strip yield models investigated demonstrated their ability to predict TD, FR, and CD spectra to acceptable accuracy with a single, common set of model parameters.

However, it is important to be realistic about the challenges of selecting the free parameter completely *a priori*. As noted earlier, there are many sources of potential error in any FCG analysis. The baseline material properties may not be matched perfectly to the spectrum application, due to slight differences in material condition or inaccuracies in the experiments (baseline or spectrum) themselves. The K solutions may be slightly inaccurate, or the crack geometry idealizations may be slightly inaccurate in comparison to the actual geometry. Complexities of crack growth such as transitioning may not be handled accurately. Other issues, such as residual stresses, may not be addressed adequately by the available models. In reality, all of these factors are likely to introduce some error into the analysis process. And even small errors can multiply quickly—for example, a 4 % error in K alone can easily produce a 15 20 % error in life following the crack growth integration, assuming a typical Paris slope.

When the spectrum crack growth calculation is performed, the free parameter in the load interaction model is typically the only adjustment available to fit the experimental observations. This means that the free parameter must not only address the load interaction effects, but also must compensate for any and all other sources of error in the life prediction system. The load interaction parameter ultimately can become a knob that is turned to make the predicted life longer or shorter, to match the test life.

Even a perfect load interaction model will suffer from some of the same limitations. Ideally, the load interaction model itself will be accurate and robust. And ideally, other sources of error in the life prediction system can be reduced, or at least understood through experience. However, it is unlikely that any load interaction model will permit completely blind, highly accurate life predictions. The challenge is to develop load interaction models that are sufficiently robust and to calibrate those models through select experience, so that they can be applied to new problems with little or no additional calibration and can still give acceptably accurate answers. Based on the limited experience in this study, the strip yield closure models have the potential to meet these specifications.

Summary and Conclusions

1. An exploratory spectrum fatigue crack growth test program was conducted on two materials (2124-T851 and 7475-T7351) and three spectrum types—nominally tension-dominated (TD), fully-reversed (FR), and compression-dominated (CD).
2. Conventional FCG models were unsuccessful at describing observed behavior. Non-interaction models were highly conservative for the TD spectrum, highly non-conservative for the CD spectrum, and accurate or conservative for the FR spectrum. A Modified Generalized Willenborg model made reasonable predictions of the TD tests and some FR tests, but it required extreme values of the free parameter to fit other FR tests and was completely unable to predict the CD tests.
3. The FASTRAN parameter NMAX, which sets the maximum number of cycles before the closure calculation is updated, should be set to a lower number than usually specified in the code in order to preserve the accuracy of the answer.
4. A new method of improving the speed of FASTRAN calculations was developed. Each cycle in the spectrum is evaluated on each pass to determine if it will open the fatigue crack or change the plastic wake behind the crack. If the cycle does neither, then it is removed from the spectrum on that particular pass. The resulting decrease in execution time is roughly proportional to the percentage of cycles thus censored.
5. This computational exercise also suggests a novel method for spectrum editing by identifying non-damaging cycles, based on crack closure theory, and removing them from the spectrum. Two exploratory tests in which 30 % of the cycles were removed from a spectrum that had already been heavily edited gave results consistent with the theory—no significant changes in FCG were observed in comparison to tests with the original spectrum. Further work is required to evaluate the theory more rigorously.
6. The original FASTRAN model was successful in correlating FCG lives from both TD and FR tests in both materials. A single value of the (only) free parameter α, optimized for each material, predicted FCG lives within $\pm$ 15 % for nearly all tests. In comparison, normal test-to-test experimental scatter was on the order of 10 %.
7. The original FASTRAN model did not successfully predict crack growth in the CD tests, because it substantially under-predicted FCG rates across the bore of the hole. FASTRAN was modified so that the crack opening behavior at the bore tip was estimated from a separate FASTRAN analysis, rather than being set equal to the crack opening behavior at the surface tip as in the conventional FASTRAN approach. The modified FASTRAN model was successful at predicting the FCG lives of the CD tests within $\pm$25% for all tests, despite greater-than-usual scatter in the limited experimental data. These predictions employed the optimum α values for each material from the TD and FR analyses, and hence did not contain a free parameter.

Acknowledgments

These investigations were conducted under USAF contract F42620-97-D-0010, Aircraft Structural Integrity Program, ASIP Prime III, and ASIP Prime IV, through subcontracts from Lockheed Martin Aeronautics Company, Fort Worth, Texas. The technical monitor at the Ogden Air Logistics Center was Robert McCowin. Special appreciation is extended to Dr. Dale Ball of Lockheed Martin for his encouragement and assistance. The authors also thank Dr. Peter McKeighan, Dale Haines, and Forrest Campbell for their help with the experiments. Former

SwRI staff member Dr. Peter Laz (now at the University of Denver) provided assistance in the early stages of the research.

References

[1] Newman, J. C., Jr., "A Crack-Closure Model for Predicting Fatigue Crack Growth under Aircraft Spectrum Loading," *Methods and Models for Predicting Fatigue Crack Growth Under Random Loading, ASTM STP 748*, ASTM International, West Conshohocken, PA, 1981, pp. 53 84.

[2] Newman, J. C., Jr., "FASTRAN II - A Fatigue Crack Growth Structural Analysis Program," NASA-TM-104159, NASA Langley Research Center, Hampton, VA, 1992.

[3] Newman, J. C., Jr., "A Nonlinear Fracture Mechanics Approach to the Growth of Small Cracks," *Behaviour of Short Cracks in Airframe Components*, AGARD-CP-328, 1982, pp. 6.1 6.26.

[4] deKoning, A. U. and Liefting, G., "Analysis of Crack Opening Behavior by Application of a Discretized Strip Yield Model," *Mechanics of Fatigue Crack Closure, ASTM STP 982*, ASTM International, West Conshohocken, PA, 1988, pp. 437 458.

[5] Fatigue Crack Growth Computer Program NASGRO Version 3.0, NASA JSC-22267B, Houston, Texas, December 2000.

[6] NASGRO Reference Manual, Version 4.0, NASA Johnson Space Center and Southwest Research Institute, June 2002.

[7] Newman, J. C., Jr., "A Crack Opening Stress Equation for Fatigue Crack Growth," *International Journal of Fracture*, Vol. 24, March 1984, pp. R131 R135.

[8] Newman, J. C., Jr., "Effects of Constraint on Crack Growth Under Aircraft Spectrum Loading," *Fatigue of Aircraft Materials*, A. Beukers, Ed., Delft University Press, 1992, pp. 83 109.

[9] Wheeler, O. E., "Spectrum Loading and Crack Growth," *J. Basic Eng., Trans. ASME*, Vol. D94, No. 1, 1972, pp. 181 186.

[10] Willenborg, J., Engle, R. M., and Wood, H. A., "A Crack Growth Retardation Model Using an Effective Stress Concept," AFFDL TM-71-1-FBR, January 1971.

[11] Gallagher, J. P., "A Generalized Development of Yield Zone Models," AFFDL-TM-74-28-FBR," Wright Patterson Air Force Laboratory, OH, January 1974.

[12] Gallagher, J. P. and Hughes, T. F., "Influence of Yield Strength on Overload Affected Fatigue Crack Growth Behavior in 4340 Steel," AFFDL-TR-74-27-FBR, Wright Patterson Air Force Laboratory, OH, January 1974.

[13] Chang, J. B. and Engle, R. M., "Improved Damage-Tolerance Analysis Methodology," *Journal of Aircraft*, Vol. 21, 1984, pp. 722 730.

Journal of ASTM International, Nov./Dec. 2004, Vol. 1, No. 10
Paper ID JAI19065
Available online at www.astm.org

R. Sunder,[1] *N. E. Ashbaugh,*[2] *W. J. Porter,*[2] *and A. H. Rosenberger*[3]

Multi-Mechanism Synergy in Variable-Amplitude Fatigue

ABSTRACT: Fractographic studies on Al alloys and a nickel-base super-alloy point to the combined action of three major load-interaction mechanisms in controlling crack growth under variable-amplitude loading. These are crack closure, residual stress, and crack front incompatibility. Crack front incompatibility attenuates crack tip response to applied load and can also increase crack closure stress. Notch root residual stress affects crack closure, while crack tip residual stress moderates environment-enhanced fatigue crack extension. The latter effect disappears in vacuum. Experiments designed to isolate the effect of individual mechanisms provide a framework to model their synergistic action, consistent with microscopic observations of crack growth bands in variable amplitude fatigue.

KEYWORDS: crack growth mechanisms, thresholds, residual stress effect, crack closure, crack front incompatibility

Introduction

Several load interaction mechanisms together determine crack growth under variable amplitude loading [1]. Significant among these are fatigue crack closure [2], residual stress in the overload plastic zone [3,4], and crack front incompatibility [5]. Realistic modeling requires analytical, or at least correlative, representation of the quantitative effect of each of these mechanisms. However, none of the predictive models described in the literature addresses the question of multi-mechanism synergy in variable-amplitude fatigue.

Early residual stress based models proposed by Wheeler [3] and Willenborg [4] continue to be used widely. The models assume increased resistance to fatigue through compressive residual stress, as reflected by an empirically determined retardation constant that attenuates growth rate. Both models are correlative by nature: crack growth rate is corrected by a retardation factor given by baseline to overload plastic zone ratio, raised to an empirically determined exponent. An exponent, selected to suit available experimental data on overload effects, may then be used to make predictions. Both of these models fail to explain possible acceleration as well as delayed retardation after overloads.

Unlike the strictly correlative models that precede it, the crack closure mechanism lends itself to analytical modeling [6 10]. Closure models operate on the premise that retardation and acceleration in crack growth are uniquely associated with a change in effective stress intensity determined in turn by crack opening stress. Thus, increased crack opening stress after an overload will cut off a greater part of subsequent baseline loading, leading to retarded crack growth.

Manuscript received 12 July 2002; accepted for publication 12 November 2003; published November 2004.
Presented at ASTM Symposium on Fatigue Testing and Analysis Under Variable Amplitude Loading Conditions on 29 31 May 2002 in Tours, France; P. C. McKeighan and N. Ranganathan, Guest Editors.

[1] BiSS Research, 41A, 1stA Cross, AECS 2nd Stage, Bangalore 560 094, India.
[2] University of Dayton Research Institute, 300 College Park, Dayton, OH 45469.
[3] Air Force Research Laboratory (AFRL/MLLN), Wright-Patterson AFB, OH 45433-7817.

More recently, a parameter called K_{PR} (for K-propagation) was proposed as a load-history sensitive variable that determines a fraction of the applied load cycle, which will grow the crack [11]. K_{PR} is determined empirically by cycling at threshold stress intensity range at progressively increasing mean level in order to pinpoint a stress intensity above which fatigue crack extension occurs. The authors point out significant differences between K_{PR} and closure approach. K_{PR} always exceeds closure stress, explained by the rationale that, at the instant the crack opens, near tip stresses still will be compressive and therefore will not contribute to crack growth. Further, unlike crack closure, K_{PR} is shown to increase instantaneously after a tensile overload, and the authors attribute this to the immediate development of protective compressive residual stresses at the crack-tip.

K_{PR} is associated with both constant amplitude and variable amplitude fatigue, and it may be determined in a reproducible manner using a well-defined process. Further, it explains both acceleration as well as retardation. Transient K_{PR} behavior after single and multiple overloads is modeled through empirical correlation of measured K_{PR} values in such experiments [12].

K_{PR} conceptually relies on the assumption that threshold stress intensity, K_{th}, is an independent material constant. The well-known sensitivity of K_{th} to a number of factors including load history appears to question this premise [13,14].

The inadequacy of available prediction models lies in their inevitable exaggeration of the effect of a single load interaction mechanism for success in accounting for observed crack growth retardation. The motivation for this study stems from the multi-mechanism nature of load interaction effects and the need for their study in isolation as a step toward synergistic modeling.

The next section explains experiments that enabled fractographic study of three major load interaction mechanisms in relative isolation. This is followed by a description of fractographic observations. The paper concludes with a framework for modeling multi-mechanism synergy that may serve future developments in fatigue life prediction.

Experimental Procedure

Mechanism isolation was the primary objective of our fractographic studies. Specially designed programmed load sequences were applied to highlight the action of individual mechanisms. While none of these sequences may be similar to those seen in real-life situations, they provide a unique opportunity for fractographic assessment of how individual mechanisms may induce load interaction.

A load sequence with constant S_{max} and varying S_{min} is not likely to see any closure-induced load interaction effect. If, on the other hand, a sequence is designed to have cycles of equal range but varying maximum stress, it will potentially see at least two load interaction effects, crack closure and residual stress. If the stress ratio of all of these cycles is kept above a certain level, they are all likely to see a fully open crack, thereby eliminating crack closure as a potential load interaction mechanism. The primary cause of crack front incompatibility is mechanism change due to substantial change in crack driving force. Crack extension mechanism is known to change as growth rate moves from one broad bandwidth to another. Therefore, the effect will be seen if the growth rate distribution among cycles is such that they tend to spill onto the next mechanism bandwidth. These considerations formed the basis for our interpretation of fractographic evidence.

The focus of our study was near-threshold fatigue. This region is significant because it controls durability. It also happens to be the most sensitive to load history effects. Unfortunately, near-threshold fatigue is not conducive to conventional electron fractography based on striation measurement. Striations typically form in the growth range of 10^{-4} to 10^{-2} mm/cycle. Even though electron microscopy can resolve much smaller dimensions, other morphological features overshadow the relatively "shallow" growth marks. To overcome this problem, microscopic banding was used, whereby many cycles are embedded between marker cycles. While neither of these may form discernible striations on its own, transition from one to another leads to clearly visible striation-band patterns. This technique permits fractographic observation of growth rates as low as 10^{-8} mm/cycle[4].

While markers enforce discernible crack front marks on the fracture surface, they can also grow the crack, apart from influencing the fatigue process itself. To reduce these effects, marker load cycles were Hi-range, Lo-R to reduce or avoid altogether any overload effect.

Crack Closure Measurements

Crack closure measurements were made using the "Closure" sequence shown in Fig. 1 adapted from the one described in [15]. It is based on the premise that under a repetitive load sequence causing negligible crack extension by comparison to plastic zone size, crack opening stress, S_{op}, will be constant and determined by the extreme loads in the sequence. Then, given S_{op} = Const, and S_{max} = Const, cyclic crack extension will be identical for those cycles with $S_{min} <= S_{op}$. Equally-spaced marker band count in the Closure sequence cannot be attributed to any other known phenomenon[5].

The original method was based on striation spacing from individual cycles as shown in Fig. 1*a*. This was extended to near-threshold fatigue by incorporating multi-cycle blocks with marker loads as shown in Fig. 1*b*. A typical fractograph from a IN-100 C(T) specimen tested at elevated temperature under this load sequence appears in Fig. 1*c*. The five equally spaced striation bands covered by the thick line on the figure point to an S_{op}/S_{max} value of 22.5 % as indicated by the dotted line covering the first five load steps in Fig. 1*b*.

Closure-Free Load Interaction

Closure-free load interaction was studied using the "3-R" sequence described in Fig. 2*a*. It includes three steps of equal amplitude and cycle count with marginally varying stress ratio (0.73, 0.69, and 0.65). Known load interaction mechanisms such as closure cannot explain load interaction effects at Hi-R with such marginal variation of R. The markers effectively preclude closure in the Hi-R steps as confirmed by independent measurements through fractography and laser interferometry [20]. The dotted line indicates expected S_{op} from the marker cycles.

Large cycle steps interspersed with markers enabled the use of fractography to investigate near- and sub-threshold fatigue crack growth, including crack formation. Marker cycle count is controlled to cause sufficient growth to "mark," but at the same contribute less than 10 % of total growth. Marker spacing may thus serve as a measure of crack growth during Hi-R cycles. In order to reduce transients, Hi-R step cycle count is selected to ensure that marker spacing is only a fraction of plastic zone size.

Figure 2*b* shows a typical fractograph from a 2014-T6511 notched coupon tested to failure under repeated application of the load sequence shown in Fig. 2*a*. It shows well defined sets of

[4] The development of appropriate markers involved iterative experiments. Different marker types had to be developed for Al-alloys, Ti-alloy, and nickel-base super-alloy. Details of these sequences appear elsewhere [16 19].
[5] In particular, given the power relationship between ΔK and crack growth rate.

three bands, with the widest one in each set obviously corresponding to the R = 0.73 step. Crack growth in this step is about three times greater than the extension due to the third step at R = 0.64. Note also that highest growth rates seen at bottom right are of the order of 5×10^{-7} mm/cycle. Striations from individual cycles cannot be resolved at this growth rate.

Crack Front Incompatibility

At certain growth rates under 3-R loading, the difference in magnitude between marker and baseline cycles causes visible mechanism change. Fractographs of such regions provide evidence of microscopic crack front incompatibility.

In addition, a variation of the 3-R sequence was used in experiments on Ni-base super-alloy at elevated temperature. A dwell period was included at max load to induce sustained load cracking in air and blunting in vacuum. The goal of these experiments was to examine the effect of transition from trans-granular to inter-granular mode, which constitutes a microstructure-induced CFI mechanism.

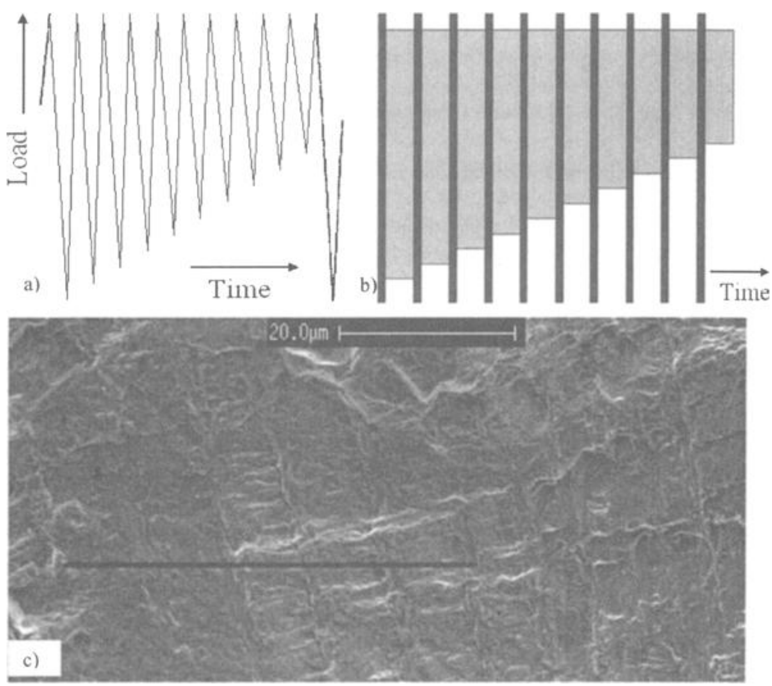

FIG. 1 *(a) Load sequence originally proposed for fractographic measurement of crack closure. When applied repetitively, crack opening stress will be determined by the extreme loads. For cycles with $S_{min} <= S_{op}$, striations will be equally spaced. Their count is a measure of S_{op}. (b) Load sequence in (a) modified for use under conditions where striations from individual cycles may not be visible. (c) Typical fractograph from IN-100 at elevated temperature with load sequence in (b) on C(T) specimen. Five equally-spaced striations shown by bar correspond to S_{op}/S_{max} = 22.5 %. Several experiments on Al-alloys yielded similar results.*

Load

a)

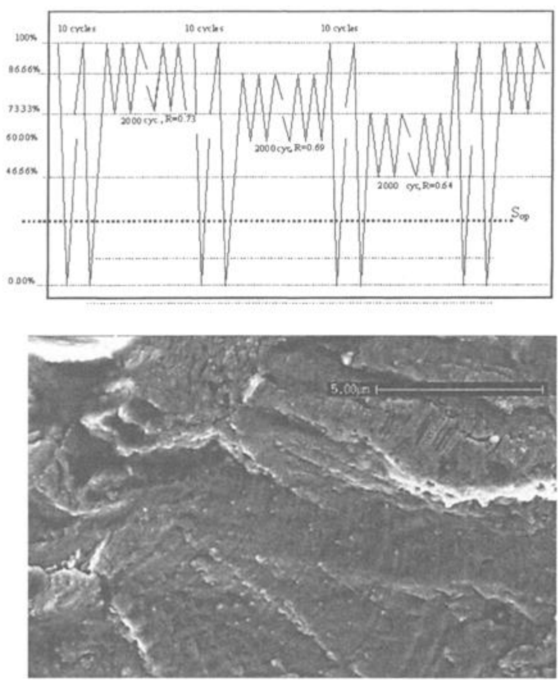

b)

FIG. 2 *(a) Typical 3R load sequence used in near-threshold experiments to isolate closure-unrelated load interaction effects. S_{min} at the lowest R is pegged at 0.466 of highest stress (or at about twice the expected S_{op}) to ensure a fully open crack at all three Rs. Further, the Lo-R markers in between are also expected to "beat down" closure level. (b) Typical marker bands from the 3R sequence about 15 microns away from the crack formation site at top left. Crack growth rate at highest R is about 0.5×10^{-6} mm/cycle, while at the lowest R, it is about 10^{-7} mm/cycle. The approximately 1:5 retardation is remarkable, considering a fully open crack and marginal R-ratio change from 0.73 down to 0.64. A 1:10 retardation was observed over the same R-change on IN-100 nickel-base super-alloy tested at elevated temperature.*

In a few experiments, the Closure and 3-R sequences were combined in order to confirm assumptions regarding the fatigue crack being fully open in the 3-R programs. In all experiments, the sequences were repeated to failure under test frequency ranging from 2 20 Hz depending on cycle magnitude. Fatigue kinetics were measured on the fatigue fracture surface using a high-resolution scanning electron microscope with digital imaging.

The tests were performed on two Al-alloys (2014-T6511 and 2024-T351), Ti-6Al-4V C(T), and IN-100 nickel-base super-alloy [16 19]. The Al-alloy tests included notched coupons to examine natural crack formation and early crack growth. Some tests on Al-alloy and Ni-base super-alloy were repeated in vacuum. Baseline step size and marker cycles required modification in a few experiments. Thus, vacuum test step size was increased from 2000 5000 cycles to accommodate reduced growth rates, and IN-100 experiments used Lo-R high-cycle markers to adapt to material-sensitive fracture morphology. Also, the elevated temperature IN-100 experiments used only two R-steps to simplify fractography.

Fractographic Observations

Long Crack Closure

Under near-zero applied stress ratio, long crack closure level, S_{op}/S_{max}, is between 0.2 and 0.3, where S_{max} is the highest stress in the load program. The same observations were made on 2024 and 2014 Al-alloys as well as in IN-100 nickel-base super-alloy at 482°C. This includes near-threshold conditions with growth rates down to and below 10^{-6} mm/cycle. In the materials studied, our measurements discount the possibility of near-threshold behavior being related to increasing closure levels. Other authors also question exaggerated closure levels at threshold [14].

Analytical modeling assumes S_{op}/S_{max} to be closely related to the so-called constraint factor associated with plane strain conditions [10]. S_{op}/S_{max} is assumed to increase substantially with transition from plane strain to plane stress conditions.

A flat fracture surface is associated with plane strain, and the formation of shear lips is associated with transition to plane stress. Fractographic evidence does indicate increase in S_{op}/S_{max} close to the surface as opposed to the mid-thickness region [15]. However, the increase is only marginal being of the order of about 10 % of S_{max}. Further, we were unable to obtain fractographic evidence suggesting an increase in closure levels with switch from normal to inclined mode of fatigue crack growth. This applies to "stable" conditions as opposed to local mode change that can occur in the event of a single overload.

S_{op}/S_{max} can increase considerably in the event of intense local crack front incompatibility, which essentially imposes local mixed-mode cracking. An example of such a possibility appears in Fig. 3 where striation bands in neighboring grains indicate substantial grain-to-grain variation in S_{op}/S_{max} across the crack front. This fracture was obtained under the 3-R load sequence, where closure is not expected, as supported by the evidence at top left, showing equally spaced bands as was the case all over the fracture surface. The bottom right region shows two equally spaced bands while the third one is substantially narrow. Judging from the load levels indicated in Fig. 2 for the 3-R sequence, S_{op}/S_{max} in this region would be just over 60 %. Grain-to-grain change in S_{op}/S_{max} may be associated with variation in grain or crack plane orientation It is likely that at lowest R, there may have been local orientation-induced obstacles to crack opening in Mode II that were overcome at higher stress ratio. This would be an analog of asperity or roughness induced closure [21,22].

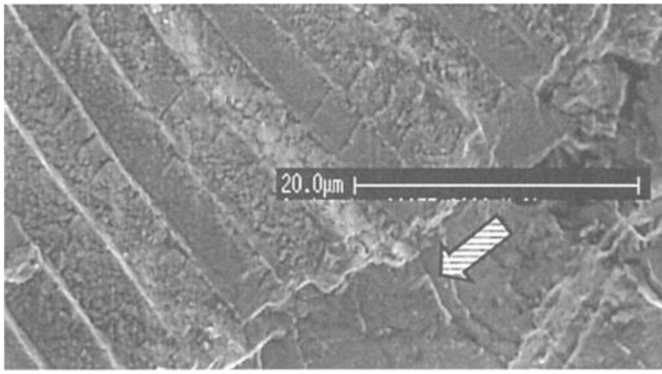

FIG. 3 *Dramatic grain-to-grain variation in S_{op}. All three marker bands are equally spaced under the 3-R sequence at top left, while in the neighboring grain, crack extension at the lowest R is about three times less than in the other two. This appears to indicate grain orientation-sensitivity of closure. Long crack in 5 mm thick 2014-T6511 C(T) specimen. Each band is from 2000 load cycles. Arrow indicates crack growth direction.*

Short Crack Closure

When cracks form at notches, applied stress level and stress concentration factors determine short, part-through crack closure levels. If the notch is blunt and applied stress levels are high, S_{op}/S_{max} can drop to as low as 0.05, with considerable hysteresis in closure behavior [23,24]. Notch root yield in tension leading to local compressive residual stresses upon unloading causes a reduction in local stress ratio. Such behavior is consistent with notch fatigue concepts based on Local Stress-Strain approach [25]. As a consequence, apparent S_{op}/S_{max} can increase to as high as 0.55 [23,26]. This is illustrated by fractographs in Fig. 4 obtained from a test on a notched Al-alloy coupon. The test was performed under a programmed load sequence consisting of a Closure sequence followed by five repetitions of the 3-R sequence. The corresponding striation band patterns appear correspondingly as "C" and "3R" in the figure. Figure 4*a* shows the notch surface at the left, with the first "C" pattern commencing less than 0.05 mm from the notch root. Both the first and second "C" blocks indicate 9 out of 10 striation bands to be equally spaced, suggesting S_{op}/S_{max} = 0.55. Evidence supporting this assessment appears in the form of band spacing during the five 3-R blocks. As indicated in the zoomed-in picture Fig. 4*b*, the third band is less than half of the first one, while the first and second are of similar spacing. Refer now to the 3-R load sequence description in Fig. 2*a* to note that such band spacing would follow from S_{op}/S_{max} between 0.47 and 0.6.

Figure 4*c* is from a region farther away from the notch root. Here, we find that the 3-R bands are equally spaced (crack fully open). This is backed by the "C" bands, of which five or six are equally spaced, suggesting an S_{op}/S_{max} value close to 0.3, typical of long crack behavior. The appearance of striation bands in Fig. 3 (bottom right) and Fig. 4*b* is strikingly similar. Both indicate high S_{op}/S_{max} but were caused by vastly different conditions. The former may have been induced by local mixed-mode conditions, while the second was clearly a consequence of reduced notch root stress ratio due to compressive residual stresses.

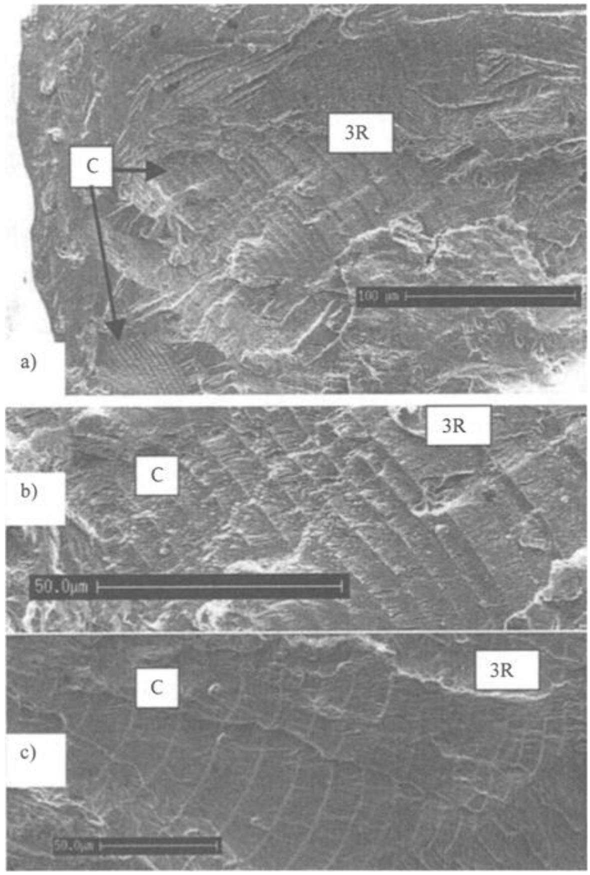

FIG. 4 *Notch root marker bands under combined action of closure block (C) (described in Fig. 1*b*) and five repeats of the 3-R sequence (3R) described in Fig. 2*a. *Material: 2024-T35. C(T) specimen with 2 mm dia key hole notch.* (a) *Notch root area with notch surface at left.* (b) *Zoomed in region from* (a). (c) *Region about 0.35 mm from notch surface. Note that closure stress drops off to long crack level as crack grows out of notch root area of high compressive residual stresses.*

Note that in both cases, middle striation band spacing is identical to the highest-R band. It underscores the "cut-off" role played by closure in multi-mechanism synergy. This is different from an "attenuation" effect, whereby a load cycle is made less severe, rather than having a part of it "cut off" from action.

In summary, fractographic observations confirm the presence and nature of fatigue crack closure as a load interaction mechanism that cannot be ignored if realistic estimates are to be made of fatigue crack growth in variable amplitude fatigue. S_{op}/S_{max} can rise to as high as 0.55 0.6 in small cracks growing within a notch root compressive residual stress field [26]. This is in contrast to short cracks at blunt notches or un-notched surfaces that are known to exhibit closure levels as low as 0.05 [23]. Crack closure can also increase substantially—up to 60 % or even more—in the event of barriers to opening caused by local mixed mode conditions (CFI). However, in the absence of CFI, long cracks do not appear to indicate closure beyond 25 30 % of maximum load. Further, this value does not seem to increase under near threshold conditions.

Residual Stress Effect

The residual stress effect in metal fatigue has been known for more than 150 years. However, its operative mechanisms are not entirely clear. The fractographs in Fig. 4 demonstrate one operative mechanism of residual stress – reduction in local stress ratio leading to an increase in S_{op}/S_{max}. The fractograph in Fig. 2 shows gradual "attenuation" of striation band spacing as opposed to the abrupt "cut off" associated with crack closure, seen in Figs. 3 and 4. The significance of attenuation versus cut-off should be clarified in light of the nature of the 3-R load sequence. The relative load levels in the three Hi-R steps are designed so that if the crack is partially closed only in the lowest step, two equal bands should appear. However, if the crack is partially closed even in the middle step, the lowest R band would be barely visible (because the crack would be barely open), given the power relationship between growth rate and K_{eff}.

There are three potential explanations for gradually attenuated band spacing under the 3-R sequence. One possibility is that S_{op}/S_{max} was not constant. This is discounted by equally spaced bands observed elsewhere and, particularly, at higher growth rates, characterized by greater potential for closure transients due to more rapid increase with crack size in growth rate as opposed to plastic zone size. The second possibility is the natural dependence on stress ratio of growth rate at the three different stress ratios. This also may be discounted by the equally spaced bands at other locations. Besides, the extent of attenuation observed cannot be explained by the relatively minor variation in stress ratio of 0.05 per step. Recent research suggests a third possibility for growth rate attenuation under the 3-R program [17]. Residual compressive stress from higher-R cycles increases resistance of lower-R cycles to environmental fatigue. Moderation of environmental action appears to be a major operative mechanism of the residual stress effect. This was confirmed by experiments in air and vacuum on a notched 2014-T6511 coupon [17] and also in air and vacuum at elevated temperature on an IN-100 C(T) specimen [19] (see Fig. 5). Both materials showed attenuated growth in the lower R cycles in air as did a Ti-alloy C(T) coupon. However, the effect vanishes in vacuum under the same applied loading conditions. In experiments on the Al-alloy coupon, switching the environment between air and vacuum caused an immediate change (both ways) in the ratio of striation band spacing. If this effect were due to any mechanistic phenomenon such as closure or roughness, one would have observed a transient region following the environment switch. This was not the case. Instead, environment switch caused immediate change in growth rate pattern from equally spaced in vacuum to attenuation in air and vice versa. The suggestion that environmental fatigue crack extension may contain two components: environment-sensitive brittle failure and crack-tip blunting/re-sharpening, is not new [27,28]. What is new is the suggestion that the first component may be moderated by history-sensitive residual stress [17,18]. As indicated in a separate paper [29], crack tip hydrostatic stress superposed on history sensitive crack-tip residual stress may be expected to exert a strong influence on crack tip lattice and surface diffusion of environment components. This, in turn, will change crack-tip stress-strain response and induce a load-history sensitive brittle failure mode at the microscopic crack tip surface level. Fractographic evidence indicates this effect is a near-threshold phenomenon that diminishes with increasing growth rate. For modeling purposes, this may be treated as an effect on K_{th}.

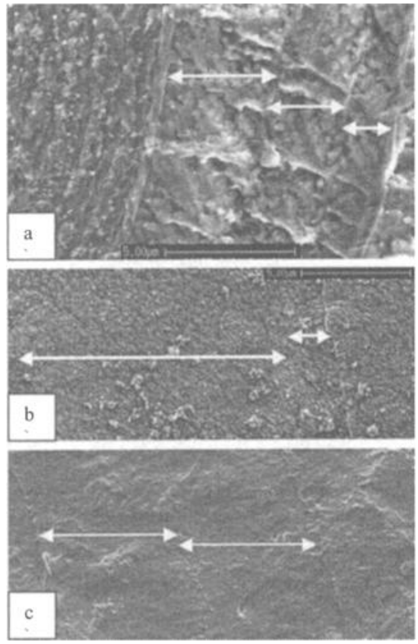

FIG. 5 *(a) Marker bands under 3-R load sequence in vacuum (left) and after switch over to air (right). Crack growth from left to right. 2014-T6511 notched Al-alloy coupon. Long crack marker bands in IN-100 nickel base super-alloy 5 mm thick C(T) coupon at 650°C under 2-R load sequence in air (b) and in vacuum (c). Note the equally spaced bands in vacuum indicating absence of load history or stress ratio effects. Crack closure was absent as indicated by independent measurements. This is also confirmed by bands in (a) that indicate immediate response to change in environment from vacuum to air. If closure were present, there would have been a transient zone required to build up closure.*

Crack Front Incompatibility (CFI) may be broadly defined as any geometric deviation from crack front geometry under constant amplitude loading under the same load. Early work by Schijve et al. highlighted the significance of CFI as a load interaction mechanism [5]. In experiments with engineered CFI through shaping of crack initiators, it was shown that CFI affects stress intensity for a given crack size. Let us consider fractographs showing typical instances of both microscopic as well as macroscopic crack front incompatibility and their likely effect on the fatigue crack growth process.

Figure 6 shows microscopic CFI at the grain level in an Al-alloy subject to programmed loading. Seen in the middle are 20 striations from high amplitude marker cycles. On either side is a step of 500 low amplitude cycles. Growth rates in the two regions are approximately 4×10^{-4} and 4×10^{-6} mm/cycle, respectively. Both growth rates fall into the region where the fatigue fracture is flat. Crack extension in individual grains appears to proceed at different planes associated with preferential orientation. Crack front curvature at higher growth rate indicates retarded growth along grain boundaries that may be due to various reasons, including discrete change in plane, along with potential stress free conditions at grain boundary, particularly if they separated to relieve cyclic tri-axial stress in the cyclic plastic zone. If as suggested earlier, the lower growth rate were largely due to environment-enhanced embrittlement, it would follow that the associated process is insensitive to grain boundary conditions. The twenty striations appear to be spaced equally even though crack front curvature progressively increases. Further, the 500-cycle steps preceding and following the markers also appear unaffected by curvature. The one on the left saw a straight front at commencement, while the one on the right needs to straighten it. One may conclude that such microscopic CFI has a negligible effect on fatigue and may be ignored. From a practical standpoint, a more significant conclusion would be that as long as applied load sequence does not force a change in crack extension plane, there will be no CFI component. Considering growth rate to be a potential criterion that indicates mode, one may conclude that for the material and thickness in question, there will be no CFI component, provided no individual cycle causes a crack extension in excess of 10^{-4} mm/cycle.

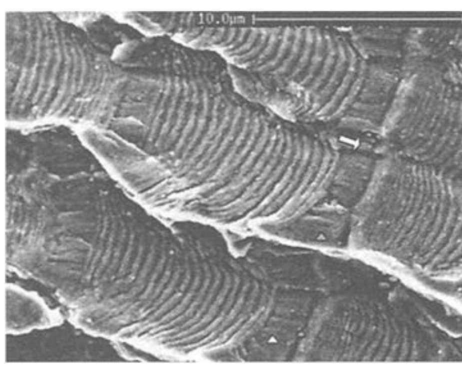

FIG. 6 *Example of microscopic crack front incompatibility (triangles) under mix of small and large cycles with similar* K_{max} *[16]. As large cycles are in the intermediate range (over* 10^{-4} *mm/cycle), their striations tend to curve forward within individual grains. Small cycles correspond to near-threshold growth rate, associated with a straight crack front.*

Higher crack growth rate is associated with a substantial slip component promoting shear mode crack extension. On fatigue failures, this is associated with the formation of shear lips that gradually expand to cover the entire crack front on an inclined plane. If the crack was grown at low growth rate to ensure a flat fracture surface, a sudden increase in crack growth rate can cause branching along slip planes. This can be obvious if more cycles are involved, as shown in Fig. 7. Figures 7*a* and 7*b* were photographically reconstructed from the original picture that appears as Fig. 7*c*. On the left and right, we see the flat mode associated with baseline loading and growth rate under 10^{-5} mm/cycle. Application of 10 marker cycles of higher amplitude creates the illusion of 20 striations. What we actually see are 10 striations each from each of the branched cracks, thanks to the substantial residual opening (0.02 mm) of the non-propagating branched crack. Figures *7a* and *7b* show how the fracture would appear if this breach did not exist. Several CFI aspects, which are likely to affect subsequent fatigue crack growth, show up in this case. If prior cracking were to occur under the same higher load amplitude, perhaps branching may not have taken place, as the crack front may have inclined already. The fact that striation spacing does not show any variation over the 10 cycles (about 0.05 mm of crack growth) indicates the absence of any transient effect associated with the plane transition. However, crack branching or deflection will cause reduced stress intensity [21,22] and associated retardation. Note that in these experiments, increase in cyclic load was achieved by reduced minimum load and not by overloads.

Crack branching also will retard subsequent crack growth under lower amplitude cycling associated with flat fracture. This may occur due to at least two reasons: reduced stress intensity range due to branching/kinking and relaxed iso-static crack tip stresses also due to branching, that will reduce the environment-enhanced component of crack extension. Finally, crack closure may increase substantially due to crack branching and thereby virtually shut out the action of smaller amplitude Lo-R cycles until the crack plane straightens out once again.

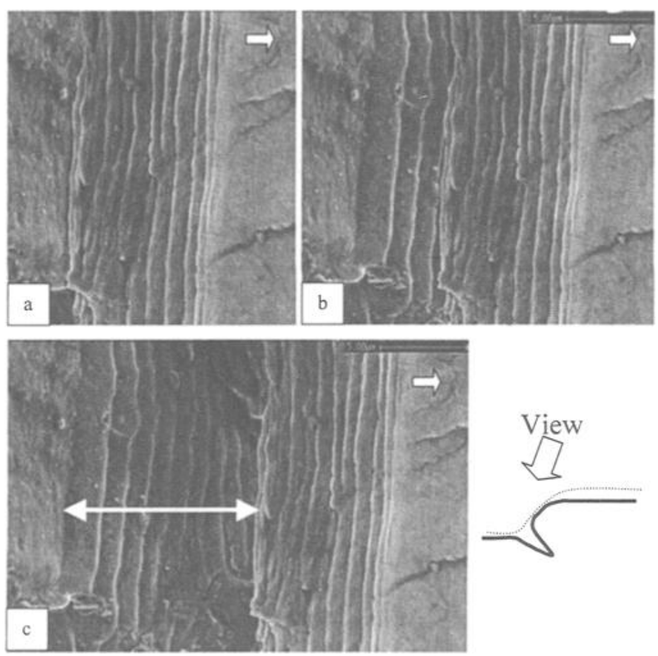

FIG. 7 *Crack branching during 10 large amplitude cycles after a low amplitude near-threshold crack extension segment. As seen in (c), an illusion is created of 20 striations from 10 cycles, while in fact, these are two sets of striations, one from each branched crack. This is confirmed by the photographic reconstruction of the separation as seen in (b) and (a) by moving the image of striations from the top branch to the left, to effectively close the opening caused by the lower branch.*

Figure 8*a* shows the unusual case of crack branching associated with a transition from large to small amplitude loading. Two schematics describe the branched flat mode (reduced growth rate) crack at the right. The top schematic assumes the higher growth rate crack was already in slant mode. On switch to lower amplitude cycling, one branch continues along the same plane, while the dominant crack growth returns to flat mode. The schematic at the bottom appears to be more likely. The crack tip under large cycle amplitude was blunt, as confirmed by the step indicated by the arrow at right. Then, crack branching is due to re-initiation of two parallel cracks at the blunt crack tip from previous loading.

Another example of crack branching appears in Fig. 8*b* from an IN-100 C(T) specimen tested at elevated temperature in vacuum with hold time. Hold time blunts the crack in vacuum, and subsequent cycling causes two cracks to re-initiate as shown by the photographic closure of the breach due to the non-propagating crack. In both cases, the blunt crack tip appears to have a radius of 3 5 microns.

(a)

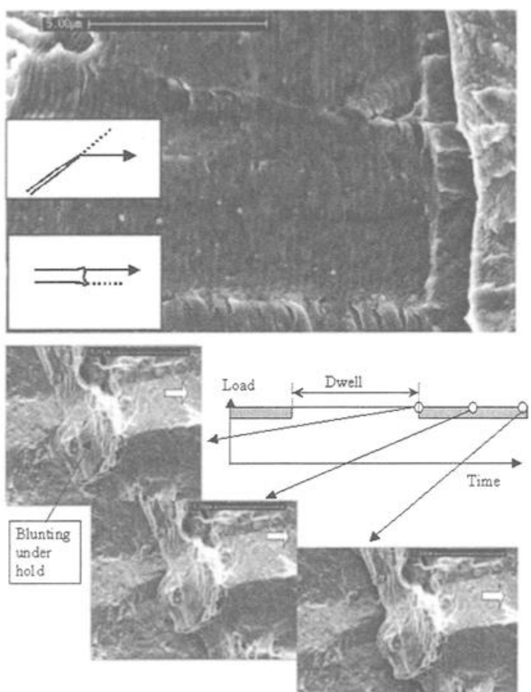

(b)

FIG. 8 *Examples of branched crack growth from a blunted tip in air (a) and in vacuum (b). (a) Crack branching after switch from high to low amplitude in an Al-alloy C(T) specimen. Schematics at left show possible orientation of the two branched cracks seen at right. (b) Evidence of crack branching after blunting due to hold-time in vacuum at 650°C. 5 mm thick C(T) specimen cut from nickel-base super-alloy. Top two pictures reconstructed photographically from the one at bottom right, by closing the breach caused by non-propagating branched crack.*

Figure 9 illustrates an example of CFI due to transition between trans-granular and inter-granular cracking. This fracture was obtained using the same load sequence as the one that caused the fracture shown in Fig. *8b* from an IN-100 C(T) coupon but was tested in air at elevated temperature. Hold time between fatigue cycling causes inter-granular cracking as indicated by the crack front tracing grain boundaries in Fig. *9a*. Sustained load cracking is extremely sensitive to local tensile iso-static stress, which is greatest in the mid-thickness area. This induces tunneling and associated crack front curvature. CFI is induced at both transition points and, in both cases, tends to retard crack growth. At the onset of sustained loading, crack extension is retarded until the trans-granular crack front can find the closest grain boundary. If trans-granular diffusion is inhibited, environmental diffusion will occur along grain boundaries already open in the wake and proceed along them to highly stressed areas immediately ahead of the crack tip. Separation of grains ahead of the crack tip will lead to rupture of un-cracked crack tip ligaments, opening up an entire inter-granular crack front.

On resumption of fatigue cycling, the highly convoluted inter-granular crack front retards fatigue crack extension by attenuating crack driving force due to CFI. Supporting evidence comes by way of retarded growth by comparison to the point just before hold time. Further, as shown in Fig. *9b*, growth rate at lower R is much lower than at higher R. The two bands were identical before hold time. It would appear that after hold time, growth rate dropped to near-threshold levels, where residual stresses further retard growth rate at lower-R as a consequence of increased K_{th}. After sustained load cracking, a transient zone is observed where crack front recovers its original shape. At this point, growth rate in the two steps become even once again. This fractograph appears to confirm that residual compressive stress will enhance K_{th} in environment. If the test were to be continued in vacuum after hold time in air, one also may have observed CFI retarded growth, but with equal bands under the two stress ratios.

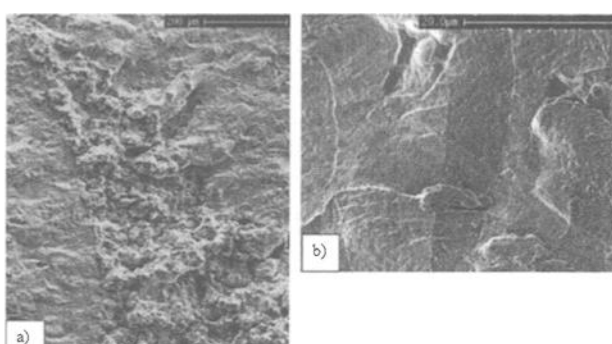

FIG. 9 (a) *Inter-granular cracking during hold time in air at 650°C and* (b) *fatigue cracking immediately after return to cyclic loading was retarded. Note reduced marker band spacing at lower R.*

Some Al-alloys contain a concentration of secondary particulates that represent slip barriers. When crack growth rate is of the same order as their size, which is usually a few microns, the particulates will tend to accumulate sufficient shear strain to cause quasi-static cleavage. The macro in Fig. *10a* shows a typical highly pock-marked region of accelerated crack growth along a shear plane connecting multiple particulates. Figure 10*b* is a zoomed-in view of a typical fatigue void formed by the coalescence of multiple interface cracks forming around a secondary particulate [30].

Figure 10*c* highlights the mix of particulate voids (triangles) along with clusters of coalesced micro-voids associated with local ductile rupture. As shown in the figure, crack extension during large cycles is likely to be accelerated by the quasi-static component, while growth during the subsequent low amplitude cycles will be retarded, if not arrested, due to substantial 3-D crack front disorientation. Rupture along a jagged plane connecting particulates creates the impression of increased void density. As observed elsewhere, this phenomenon will cause momentary crack acceleration during overloads, followed by substantial retardation under smaller cycles [17,31,32].

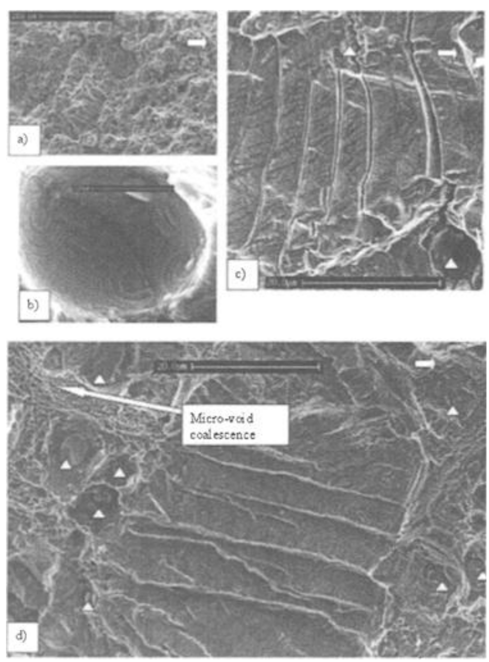

FIG. 10 *(*a*) Tortuous crack burst during marker loads occurring at higher growth rate. Small flat region in the middle is from a Hi-R step of 10 cycles. (*b*) Zoomed-in view of a typical void formed around a particulate [30]. Concentric circles mark the growth of penny-shaped interface cracks that coalesced to separation. This occurs before the major crack sheared the particulate as shown by triangles in (*c*) (local crack branching at single marker striations close to particulate voids). (*d*) Zoomed-in view of (*a*) showing individual fatigue voids indicated by triangles, region of void-free retarded growth during a Hi-R low amplitude step, and a cluster of coalesced micro-voids associated with local quasi-static ductile fracture. Note the difference in size between micro-voids and fatigue-voids. Long crack in Al-alloy.*

Finally, Fig. 11 shows a macroscopic manifestation of CFI under the influence of periodic overloads in a 10 mm thick high strength 7075 Al-alloy C(T) specimen. The crack front is marked by light shaded fatigue bands formed during baseline cycling. Up to a crack size marked by the arrows, the crack front remains straight. Beyond this point, however, due to the overload K_{max} approaches K_{Ic}. Crack extension in the overload cycle thus becomes sensitive to local fracture resistance. While the mid-thickness area is under plane strain, the surface region sees plane stress conditions, where K_c would be the operative fracture toughness. This promotes crack front tunneling (pop-in), with the mid-thickness area tending to static fracture, while crack extension is marginal at the surface. Increased crack front curvature after each overload leads to stress intensity re-distribution across the crack front. The mid-thickness region gets unloaded, while the surface area is overloaded. Finally, at the point marked by the right-most crack front signature, surface stress intensity has risen to a point that static fracture cannot be forestalled anymore. At the point of fracture, crack front tunneling is to an extent of 4 mm, which is almost half the specimen thickness. This sizeable deviation may be modeled as a function of the difference between K_{Ic} and K_c.

The conditions depicted in Fig. 11 are in a sense similar to those in Fig. 10. In both cases, the proximity of a critical parameter (shear deformation in Fig. 10, K_{Ic} in Fig. 11) determined occurrence of CFI. However the latter case may also serve as a unique example of crack acceleration, even premature fracture. It is indeed possible that if the crack had grown all along under large cycles, the crack front may have tilted earlier on, thereby enforcing plane stress conditions and increased resistance to fracture.

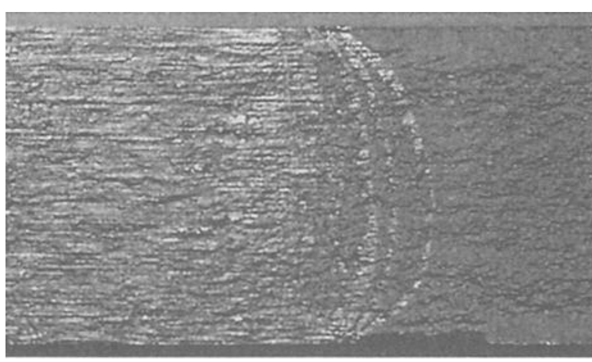

FIG. 11 *Appearance of fatigue fracture surface of 10 mm thick C(T) specimen cut from 7075-T1351. Specimen was subject to 50 % periodic overloads every 2000 cycles of low amplitude baseline loading. Bright area including bands at right are fatigue under baseline loading. Note the sudden quasi-static pop-ins as overload* K_{max} *approaches* K_{Ic} *under load control. Region at right is static fracture at last overload.*

The above list of CFI mechanisms is by no means complete, but it may provide a sampling of the different geometric combinations that need to be addressed to model variable amplitude fatigue in a manner that is microscopically consistent. Other materials systems, particularly engineered materials, may exhibit even more complex forms of crack front incompatibility.

Discussion

Fractographic evidence appears to suggest a certain synergistic model of multi-mechanism load interaction under variable amplitude loading. CFI attenuates crack tip stress field from what may apply to constant amplitude conditions. It can do so through blunting under overload or dwell-time, tunneling, out of plane rotation, branching, and roughness. The exception to this rule (as shown in Fig. 11) is when CFI may actually accelerate fracture due to a "reverse CFI," i.e., slant mode under constant amplitude versus enforced flat mode in variable amplitude fatigue.

CFI also increases S_{op} by stalling crack opening, either through direct obstruction or at least friction between crack faces [22]. Plasticity induced closure levels do not appear to change significantly and remain a fraction of the applied maximum load, typically 20 30 %. Application of overload will therefore directly affect S_{op}, but only to this extent. However, CFI can raise S_{op}/S_{max} to as high as 60 % or more, even in the absence of any tensile overload. The presence of debris on fatigue fractures, particularly associated with CFI, appears to support this possibility.

Notch root residual stress directly affects crack closure, which is determined by local mean stress. Crack tip residual stress moderates environmental action to control the brittle fraction of crack extension in the rising load half-cycle. This component of the residual stress effect will be strong when K_{eff} is near-threshold and will reduce with increasing growth rate. The effect appears to be altogether absent in vacuum.

Figure 12 describes a possible sequence of calculations that may be employed to predict variable amplitude fatigue crack growth. CFI must be assessed first because both crack tip stress response and closure appear to depend on it. This is followed by assessment of residual stress effect on crack closure and on K_{th}. Crack driving force K_{eff} is then computed, to lead to an estimation of fatigue crack extension:

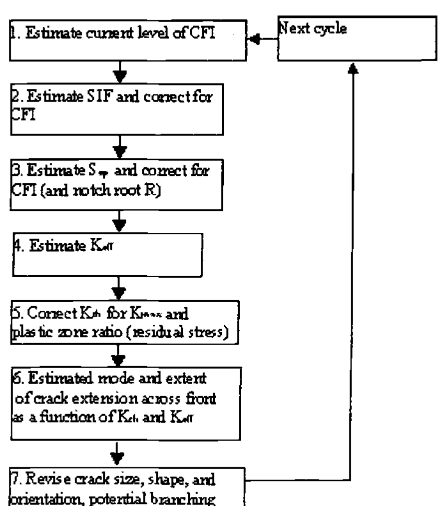

FIG. 12 *Flow-chart describing sequence of modeling synergy in variable amplitude fatigue. Of the three mechanisms, CFI is accounted for first because it can also affect S_{op}, followed by S_{op}. Crack driving force is then estimated and corrected for current level of CFI and S_{op}.*

Finally, history dependent K_{th} is estimated as a function of load history, leading to crack extension over the current counted load cycle.

1. Assessment of CFI needs to provide two indexes, one related to attenuation of crack tip response to applied load, the other related to enhancement of closure. These determine how crack geometry differs from the one associated with constant amplitude conditions of the same magnitude as the current load cycle. Both indexes will be determined by the same parameters, but not necessarily in the same fashion. For example, blunting will attenuate crack tip response to applied stress. However, it also will tend to keep the crack open.
2. Correct SIF for CFI. This step estimates K-distribution across the crack front similar to the requirement for part-through and 3-D crack geometries. Such an approach will assist in modeling tunneling, branching, and out-of-plane rotation, which in turn will affect SIF as well as S_{op}.
3. Estimate S_{op} distribution across the crack front. S_{op} will be sensitive to local residual stress distribution as well as CFI as discussed under item 1. It is known that mid-thickness S_{op} is lower than at surface, and this in turn can affect crack front shape. Also, CFI due to near-surface plane rotation or branching will induce increased S_{op}. Conversely, blunting and underloads will both reduce S_{op}.
4. Estimate crack driving force K_{eff} across the crack front as the difference between local K_{max} and K_{op}.
5. Estimate K_{th} distribution across the crack front as a function of residual stress distribution and local triaxiality. These will determine environmental action and may be ignored for vacuum conditions, where K_{th} may be treated as a material constant.
6. Compute crack extension across the crack front. Suitable da/dN equation may be used, which accounts for K_{eff}, K_{th}, K_{max}, and appropriate value of K_c, which in turn will depend on plane strain/plane stress conditions.
7. Update crack front geometry, CFI, and residual stress indexes for the next iteration. This is the step where the incidence of crack branching will be established, and so also, the point where one may ignore branching and perhaps associated probabilistic aspects. For example, the probability of branching would be remote if all the load cycles thus far caused crack growth in the near-threshold range. This is also the step where transients are tracked. For example, in the event of a crack emanating from a notch, closure levels will be high if tensile overloads caused notch root compressive residual stresses in the unloaded condition. However, as shown earlier, at some distance from the notch surface, the crack tip will no longer see these effects and is likely to behave as a long crack.

Potential flaws in our interpretation of multi-mechanism synergy include the following:

1. All observations are based on fractographic inputs. However, only a small fraction of a fatigue fracture surface carries discernible marker bands that permit quantitative measurements. Inherent in our approach is the assumption that what is depicted by visible marker bands is a fair representation of overall fatigue crack kinetics. Such an assumption would be questionable in the event quasi-static crack extension and other modes not associated with a marking process control fatigue kinetics.

2. Our observations indicate noticeable CFI-related variation in S_{op}. However, we have been unable to obtain quantitative data on how growth rate itself is affected by CFI. This may be a potentially rewarding goal for future work including micro-mechanical modeling as demonstrated in recent work [33]. In the meantime, available expressions for CFI-attenuated crack driving force and increased closure may be assumed to apply [21,22].

Conclusions

1. Fractographic evidence indicates crack closure, residual stress, and crack front incompatibility (CFI) together cause load interaction in variable amplitude fatigue.
2. Near threshold crack closure does not appear to exceed 30 % of maximum applied stress at low stress ratio. However, it can rise to as high as 60 % under two conditions. One is reduced local stress ratio in notch root fatigue due to compressive residual stress, and the other is considerable conflict in local crack plane orientation causing obstruction to opening.
3. Residual stress appears to have two operative mechanisms. One is change of local stress ratio and through it, closure, as pointed out above. The other is moderation of environmental action and associated change in threshold stress intensity. Comparative tests in air and vacuum on two different materials support this conclusion.
4. CFI appears to be a major load interaction mechanism that mainly causes retardation. It is manifest in many ways including crack tip blunting, crack front shape change, enforced mixed mode conditions, crack deflection, crack branching, and increased closure due to one or more of these. It occurs due to mismatch in crack extension plane between successive cycles.
5. A sequential scheme is proposed for modeling multi-mechanism synergy under variable amplitude loading.

Acknowledgments

This work was supported by and performed at Materials & Manufacturing Directorate, Air Force Research Laboratory (AFRL/MLLN), Wright-Patterson AFB, OH 45433-7817, USA.

References

[1] Schijve, J., "Observations on the Prediction of Fatigue Crack Growth Propagation under Variable Amplitude Loading," *ASTM STP 595*, ASTM International, West Conshohocken, PA, 1976, pp. 3 23.
[2] Elber, W., "The Significance of Fatigue Crack Closure," *Damage Tolerance in Aircraft Structures, ASTM STP 486*, ASTM International, West Conshohocken, PA, 1971, pp. 230 242.
[3] Wheeler, O. E., *Journal of Basic Engineering, Trans. ASME*, March 1972, pp. 181 186.
[4] Willenborg, J. D., Engle, R. M., and Wood, H. A., "A Crack Growth Retardation Model Using an Effective Stress Concept," *AFFDL-TM-FBR-71-1*, Air Force Flight Dynamics Laboratory, 1971.
[5] Schijve, J., "Fatigue Damage Accumulation and Incompatible Crack Front Orientation," *Eng. Fract. Mech.*, Vol. 6, 1974, pp. 245 252.

[6] Baudin, G., and Robert, M., "Crack Growth Life Prediction under Aeronautical Type of Loading," *Proc. 5th European Conf. on Fracture*, Lisbon, 1984, pp. 779 792.

[7] de Koning, A. U., "A Simple Crack Closure Model for Prediction of Fatigue Crack Growth Rates under Variable Amplitude Loading," *Fracture Mechanics, ASTM STP 743*, R. Roberts, Ed., 1981, pp. 63 85.

[8] Aliaga, D., Davy, A., and Schaff, H., "A Simple Crack Closure Model for Predicting Fatigue Crack Growth under Flight Simulation Loading," *Durability and Damage Tolerance in Aircraft Design*, A. Salvetti and G. Cavallini, Eds., EMAS, Warley, 1985, pp. 605 630.

[9] Newman, J. C., "A Crack-Closure Model for Predicting Fatigue Crack Growth under Aircraft Spectrum Loading," *Methods and Models for Predicting Fatigue Crack Growth under Random Loading, ASTM STP 748*, J. B. Chang and C. M. Hudson, Eds., ASTM International, West Conshohocken, PA, 1981, pp. 53 84.

[10] Newman, J. C., Jr., Phillips, E. P., and Everett, R. A., "Fatigue Life and Crack Growth Prediction Methodology," *An Assessment of Fatigue Damage and Crack Growth Prediction Techniques, AGARD Report 797*, AGARD, Neuillu sur Seine, 1994, Paper 2.

[11] Lang, M., "A Model for Fatigue Crack Growth, Part I: Phenomenology," *Fatigue Fract. Engg. Mater, Struct.*, Vol. 23, No. 7, 2000, pp. 587 601.

[12] Lang, M. and Marci, G., "The Influence of Single and Multiple Overloads on Fatigue Crack Propagation," *Fatigue Fract. Engg. Mater, Struct.*, Vol. 22, No. 4, 1999, pp. 257 271.

[13] Vasudevan, A. K., Sadananda, K., and Loust, N., "A Review of Crack Closure, Fatigue Crack Threshold and Related Phenomena," *Materials Science and Engineering*, A188, 1994, pp. 1 22.

[14] Hopkins, S. W., Rau, C. A., Leverant, G. R., and Yuen, A., "Effect of Various Programmed Overloads on the Threshold for High-Frequency Fatigue Crack Growth," *Fatigue Crack Growth Under Spectrum Loads, ASTM STP 595*, ASTM International, West Conshohocken, PA, 1976, pp. 125 141.

[15] Sunder, R. and Dash, P. K., "Measurement of Fatigue Crack Closure Through Electron Fractography," *Int. J. Fatigue*, Vol. 4, 1982, pp. 97 105.

[16] Ashbaugh, N. E., Porter, W. J., Prakash. R. V., and Sunder, R., "A Fractographic Study of Load Sequence Induced Mixed-Mode Fatigue Crack Growth in an Al-Cu Alloy," *Mixed-Mode Crack Behavior, ASTM STP 1359*, K. J. Miller and D. L. McDowell, Eds., ASTM International, West Conshohocken, PA, 1999, pp. 258 278.

[17] Sunder, R., Porter, W. J., and Ashbaugh, N. E., "The Role of Air in Fatigue Load Interaction," *Fatigue Fract. Engg Mater Struct*, Vol. 26, 2003, pp. 1 16.

[18] Sunder, R., "An Explanation for the Residual Stress Effect in Metal Fatigue," *Fatigue 2002 – Proc. 8th International Fatigue Congress*, Stockholm, 2002, EMAS, pp. 3339 3350.

[19] Ashbaugh, N. E., Porter, W. J., Rosenberger, A. H., and Sunder, R., "Environment-Related Load History Effects in Elevated Temperature Fatigue of a Nickel-Base Super-Alloy," *Proc., Fatigue 2002*, Stockholm, June 2 7, 2002.

[20] Ashbaugh, N. E., Dattaguru, B., Khobaib, M., Nicholas, T., Prakash, R. V., Ramamurthy, T. S., et al., "Experimental and Analytical Estimates of Fatigue Crack Closure in an Aluminum-Copper Alloy. Part I: Laser Interferometry and Electron Fractography," *Fatigue Fract. Engg. Mater. Struct*, Vol. 20, No. 7, 1997, pp. 951 961.

[21] Ritchie, R. O., "Mechanisms of Fatigue Crack Propagation in Metals, Ceramics and Composites: Role of Shielding," *Materials Science and Engineering*, Vol. A103, 1988, pp. 15 28.
[22] Suresh, S., "Models for Fatigue Crack Deflection," *Fatigue '84*, EMAS, C. J. Beevers, Ed., Vol. 1, 1984, pp. 555 563.
[23] Sunder, R., Prakash, R. V., and Mitchenko, E. I., "Fractographic Study of Notch Fatigue Crack Closure and Growth Rates," *ASTM STP 1203*, J. E. Masters and L. E. Gilbertson, Eds., ASTM International, West Conshohocken, PA, 1993, pp. 113 131.
[24] Sunder, R., "Notch Root Crack Closure under Cyclic Inelasticity," *Fatigue Fract. Engg. Mater. Struct.*, Vol. 16, pp. 677 692.
[25] Morrow, J. D., Wetzel, R. M., and Topper, T. H., "Laboratory Simulation of Structural Fatigue Behavior," *Effects of Environment and Complex Load History on Fatigue Life, ASTM STP 462*, ASTM International, West Conshohocken, PA, 1970, pp. 74 91.
[26] Anandan, K. and Sunder, R., "Closure of Part-Through Cracks at the Notch Root," *Int. J. Fatigue*, Vol. 9, pp. 217 222.
[27] Vogelesang, L. B. and Schijve, J., "Environmental Effects on Fatigue Failure Mode Transition Observed in Aluminium Alloys," *Report LR-289*, Delft University of Technology, Delft, Netherlands, 1979.
[28] Schijve, J. and Arkema, W. J., "Crack Closure and the Environmental Effect on Fatigue Crack Growth," *Report VTH-217*, Delft University of Technology Fac. Aerospace Eng. Delft, Netherlands, 1976.
[29] Sunder, R., "Fatigue Crack Growth as a Consequence of Environment-Enhanced Brittle-Micro Fracture," *Fatigue Fract. Engg. Mater. Struct.*, Accepted for publication, 2003.
[30] Sunder, R., Porter, W. J., and Ashbaugh, N. E., "Fatigue Voids and Their Significance," *Fatigue Fract. Engng Mater Struct.*, Vol. 25, 2002, pp. 1015 1024.
[31] Sanders, T. H., Jr., and Staley, J. T., "Review of Fatigue and Fracture Research on High-Strength Al-Alloys," *Fatigue and Microstructure*, American Society for Metals, Metals Park, OH, 1978, pp. 467 516
[32] Staley, J. T., "How Microstructure Affects Fatigue and Fracture of Aluminum Alloys," Presented at the International Symposium on Fracture Mechanics, George Washington University School of Engineering and Applied Science, Washington, D.C., Sep. 11 13, 1978.
[33] Bennett, V. and McDowell, D. L., "Polycrystal Orientation Effects on Microslip and Mixed-Mode Behavior of Microstructurally Small Cracks," *ASTM STP 1359*, K. J. Miller and D. L. McDowell, Eds., ASTM International, West Conshohocken, PA, 1999, pp. 203 228.

Journal of ASTM International, September 2004, Vol. 1, No. 8
Paper ID JAI19029
Available online at www.astm.org

Ji-Ho Song,[1] *Chung-Youb Kim,*[2] *and Shin-Young Lee*[3]

Crack Growth and Closure Behavior of Short and Long Fatigue Cracks under Random Loading

ABSTRACT: Crack growth and closure behavior of physically short and conventionally long cracks under random loading are extensively investigated, utilizing test results of 2024-T351 aluminum alloy obtained by performing narrow- and wide-band random loading tests for various stress ratios and random loading block lengths. A noise reduction method is developed to determine the crack opening load under random loading more easily, precisely, and economically. Crack growth rates are analyzed mainly in terms of the stress intensity factor range estimated by 2/PI correction proposed by Donald and Paris. The long and short cracks are very different in characteristics of closure behavior under random loading. Crack growth of short and long cracks under random loading can be well described by the crack closure concept. The effects of random spectrum or random block length on crack opening load and crack growth are not significant.

KEYWORDS: fatigue crack growth, crack closure, long cracks, short cracks, random loading

Introduction

A large number of prediction models [1 15] have been proposed to assess fatigue crack growth under random loading. For precise assessment of crack growth under random loading, the effects of at least the three primary factors, i.e., stress intensity factor range ΔK, stress ratio R, and load interaction, must be evaluated accurately. It is most difficult to evaluate the load interaction effects quantitatively. To account for the effects of these three factors, most of the models commonly introduce many parameters to be determined experimentally or assumed appropriately, which makes the models complicated and difficult to apply [3,9 11]. Among the prediction models proposed up to now, the model based on the crack closure concept [2,4,5,8,12 15] has a physical basis as well as appealing features that the model can evaluate the effects of the three factors totally through a single parameter "crack opening load". Accordingly, the model may lead to the simplest, most convenient prediction procedure if crack closure behavior under random loading can be estimated [13,14]. Therefore, it is very important to clarify the crack closure behavior under random loading.

It is worthy to note that the closure model has some disadvantages: experimental measurement of crack closure is, more or less, indispensable, and the crack opening load should be determined accurately. Particularly, it is very difficult to determine the crack opening

Manuscript received 23 April 2002; accepted for publication 20 September 2002; published September 2004.
Presented at ASTM Symposium on Fatigue Testing and Analysis Under Variable Amplitude Loading Conditions on 29 31 May 2004 in Tour, France; P. C. McKeighan and N. Ranganathan, Guest Editors.

[1] Professor, Department of Automation and Design Engineering, Korea Advanced Institute of Science and Technology, 207-43, Cheongryangridong, Dongdamoongu, Seoul, 130-010, Korea.
[2] Assistant Professor, Division of Mechanical and Automotive Engineering, Yosu National University, San 96-1. Doondeok-dong, Yosu, Chonnam, 550-749, Korea.
[3] Principal Engineer, E-CIM Center, Corporate Technology Operations, Samsung Electronics Co., 416, Maetan-3dong, Paldalgu, Suwonsi, Kyunggido, 442-742, Korea.

load accurately and consistently, and the crack opening results obtained are likely to be arbitrary. The crack closure provides information about the circumstances only behind the crack tip, not ahead of the crack tip. This means there are inherent limitations of applicability of the crack closure concept. Despite these disadvantages, no better alternative to the closure model can be found, to our knowledge.

It has been pointed out frequently that the conventional ΔK_{eff} estimation tends to give an underestimate of the substantial effective stress intensity factor range and cannot express fatigue crack growth rates, particularly in the near-threshold regime. Recently, Paris, Tada, and Donald [19] proposed alternative ΔK_{eff} estimation methods called $2/\pi 0$ (2/PI0) and $2/\pi$(2/PI) correction methods based on the partial crack closure model. Their partial crack closure model can be summarized as follows: The crack surface roughness generated by a sliding-off mechanism might mismatch behind the crack tip but not immediately at the tip. Accordingly, the crack closes behind the tip, leaving the tip fully open. This means that an additional driving force for crack propagation exists below the traditional opening load.

The 2/PI0 and 2/PI correction methods estimate ΔK_{eff} approximately by applying the $2/\pi$ factor on the conventionally measured K_{op}. Investigating various methods of estimating ΔK_{eff}, Donald and Paris [20] have reported that the conventional ΔK_{eff} estimation method appears adequate at crack growth rates above 1×10^{-8} m/cycle, while the 2/PI0 or 2/PI methods appear to provide a successful correlation of the crack growth rate data in the near-threshold regime at crack growth rates below 1×10^{-10} m/cycle. Quite recently, one of the authors [21] has reported that, in particular, the 2/PI method provides good results for constant and random loading data.

For past several years, the authors [16 18] have extensively investigated crack growth and closure behavior of conventionally long and physically short cracks under random loading and have obtained much useful information on crack growth characteristics under random loading. However, the effect of stress ratio of the maximum range-pair load cycle (which is hereafter referred to as the largest load cycle) in a random load history on growth and closure behavior of conventionally long cracks has not been clarified.

To elucidate the effect of stress ratio of the largest load cycle, random loading tests are carried out at a negative stress ratio of the largest load cycle for conventionally long cracks in this study.

As it may be expected that the 2/PI correction method provides better results than the conventional ΔK_{eff} estimation, all the data of conventionally long and physically short cracks obtained in previous works [16 18] are reexamined totally, together with the present data, and more direct, systematic comparison of long and short cracks is made.

Particularly in this study, a new technique is developed to determine more easily and precisely the crack opening load under random loading.

Experimental Details

The material used in this study 2024-T351 is aluminum alloy plate. The chemical composition (wt %) is Si 0.14 %, Fe 0.21, Cu 4.58, Mg 1.27, Cr 0.02, Zn 0.03, Mn 0.73, Ti 0.04, and the remainder is Al. The 0.2 % proof stress is 379 MPa, the tensile strength is 480 MPa, elongation is 19.6 %, and the reduction of area is 17.0 %.

Side-grooved, middle tension M(T) specimens were used for conventionally long fatigue crack growth tests [16] and side-grooved, in-plane bending SEB specimens, for short crack growth tests [18]. Two-dimensional, short through-thickness crack is artificially prepared by carefully machining-off the major portion of specimen containing a long through-thickness crack pre-cracked under fatigue loading. The details of the procedure can be found in [18]. The crack plane orientation is L-T. Particularly to obtain reference long crack growth data most relevant to short crack growth data, constant amplitude tests were performed additionally on the side-grooved, in-plane bending specimens.

The M(T) specimens were tested using a servo-hydraulic fatigue testing machine at 7 Hz, and the SEB specimens were tested using a homemade, electro-dynamic, in-plane bending fatigue testing machine of small capacity [22] at 20 Hz.

Two types of random spectra as shown in Figs. 1*a* and *b*, i.e., narrow and wide band random spectra of various history lengths, were generated for random loading tests by computer simulation. Simulation was done by superimposing sinusoidal functions of random phase with uniform distribution [23]. The base line random spectra were used to generate random cycle-by-cycle load histories in terms of peaks and valleys. Random loading tests were performed by repeatedly applying unit random loading block of a specified history length as shown in Fig. 1*c*. The random loading conditions tested are shown in Table 1 where ΔK^{rp}_{max} denotes the maximum range-pair load cycle (which is hereafter referred to as the largest load cycle) in a random loading block, and $R(\Delta K^{rp}_{max})$ represents the stress ratio corresponding to the largest load cycle.

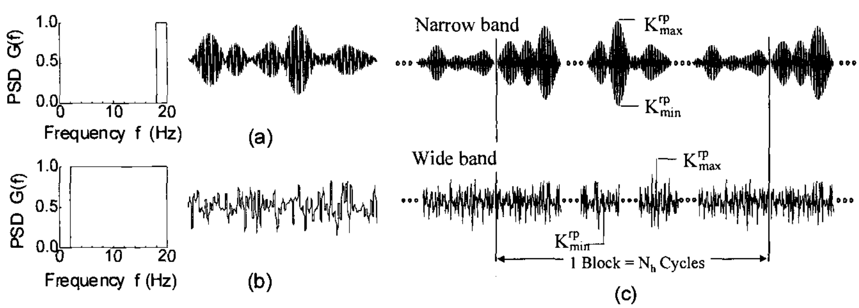

FIG. 1 *Random loading histories.*

TABLE 1—*Test conditions for random loading.*

	Random Loading Spectrum	History Length, N_h (cycles)	$R(\Delta K^{rp}_{max})$
Long Cracks	narrow & wide band	500	−1
	narrow & wide band	500, 1000, 2000, 8000, 16 000	0
Short Cracks	narrow & wide band	500, 1000	−1, −0.5, 0, 0.1, 0.3

Crack length and closure were measured simultaneously and continuously during the test by a refined, computer-aided unloading elastic-compliance technique [24,25] originally developed by Kikukawa et al. [13]. The precision of measurement of crack length is about 17 μm and 27 μm for long and short cracks, respectively, under constant amplitude loading. The displacement for long cracks is measured by the clip-on gage attached in the circular hole at the center of the specimen and the strain for short specimen, by a strain gage bonded on the back face of the specimen. Particularly in this study, a new technique of noise reduction is developed to determine conveniently the crack opening load under random loading.

Experimental Results and Discussion

Crack Growth and Closure Behavior under Constant Amplitude Loading

The growth rates of long cracks of M(T) and SEB specimens are shown as a function of the stress intensity factor range ΔK for various stress ratios in Fig. 2*a*. The effect of stress ratio on the growth rates of long cracks seems to be relatively significant. The growth rates of short cracks are plotted as a function of ΔK for various stress ratios and stress ranges in Fig. 2*b*, where the long crack growth data obtained on SEB specimens are represented as the solid and dashed lines for comparison. The growth rates of short cracks are found to vary, depending on not only stress ratio but also the applied stress range. The well-observed anomalous behavior of short cracks that short cracks grow faster than long cracks at the same ΔK in the low ΔK region can be found clearly for low stress ratios below $R = 0$, but is not clear for higher stress ratios. Figures 2*c* and *d* show the growth rates as a function of the conventional ΔK_{eff} and 2/PI correction effective stress factor range $(\Delta K_{eff})_{2/PI}$, respectively. The effective stress intensity factor ranges are defined as

$$\Delta K_{eff} = K_{max} - K_{op} \tag{1}$$

$$(\Delta K_{eff})_{2/PI} = K_{max} - \frac{2}{\pi} K_{op} - (1 - \frac{2}{\pi}) K_{min} \tag{2}$$

where K_{max} and K_{min} are the maximum and minimum stress intensity factors, respectively, and K_{op} is the conventionally measured, crack opening stress intensity factor. The conventional ΔK_{eff} can express well crack growth rates higher than about 3×10^{-9} m/cycle, irrespective of stress ratio, applied stress range, or crack length. However, for the region of $da/dN < 3 \times 10^{-9}$ m/cycle, short crack growth rates are much lower than long crack growth rates. Employment of $(\Delta K_{eff})_{2/PI}$ reduces remarkably the difference between long and short crack growth rates for low growth rate region, resulting in better results for the whole growth rate region.

The values of K_{op} and crack opening ratio U of long cracks are expressed as a function of K_{max} in Fig. 3, where only the data of $R = 0$ and -1 obtained on the M(T) specimens are shown for clarity of later comparison with the random loading data included. Here the crack opening ratio U is defined as the following conventional one

$$U = \frac{K_{max} - K_{op}}{K_{max} - K_{min}} = \frac{\text{conventional } \Delta K_{eff}}{\Delta K} \tag{3}$$

Under constant amplitude loading, the value of U of long cracks increases initially with K_{max} and then becomes constant. The variation of U of long cracks is somewhat simple.

Examples of the variation of K_{op} and U of short cracks with crack length a and K_{max}, respectively, are shown in Figs. 4*a* and *b*. The variation of K_{op} with crack growth is different depending on the R value. For $R = -1$, values of K_{op} increase from initial $K_{op} \approx 0$ to maximum values and then decrease with the crack growth, while for $R = 0$, values of K_{op} tend to increase continuously. Values of U of short cracks decrease initially with K_{max} to minimum values and then increase, showing the behavior different from long crack one.

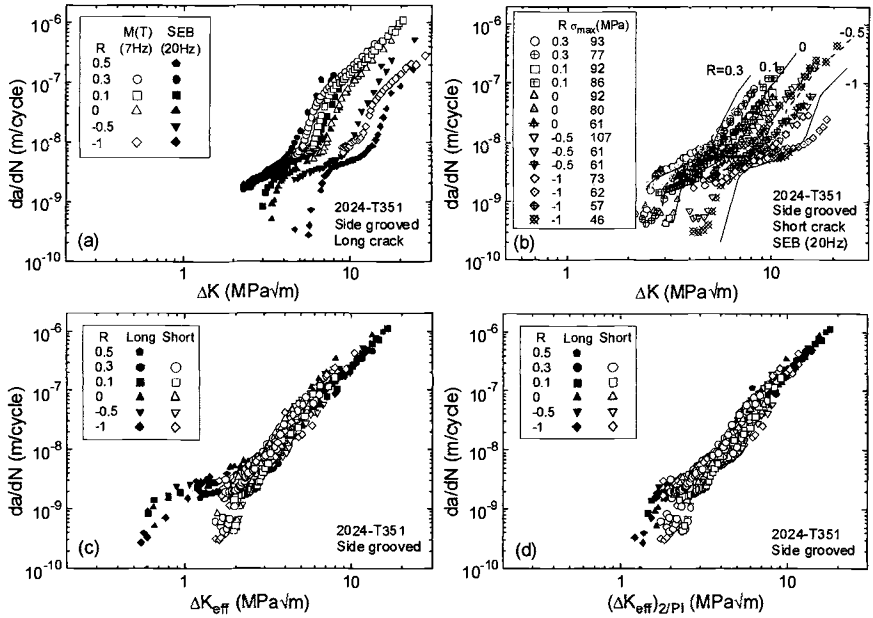

FIG. 2—*Crack growth rates of conventional long cracks and physically short cracks.*

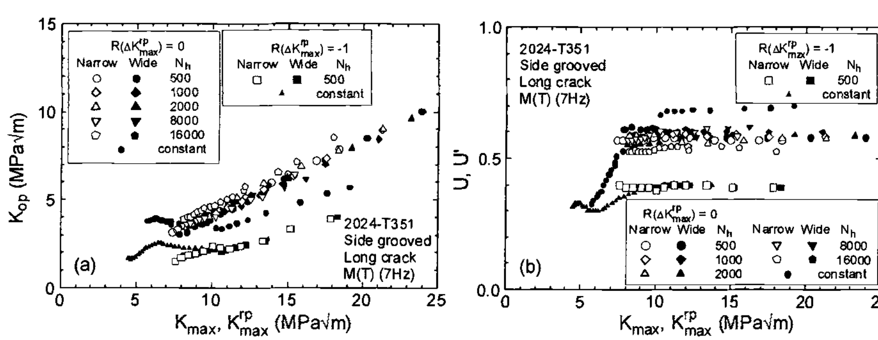

FIG. 3—*Crack opening stress intensity factors and crack opening ratios of long cracks as a function of the maximum stress intensity factor under constant amplitude and random loading.*

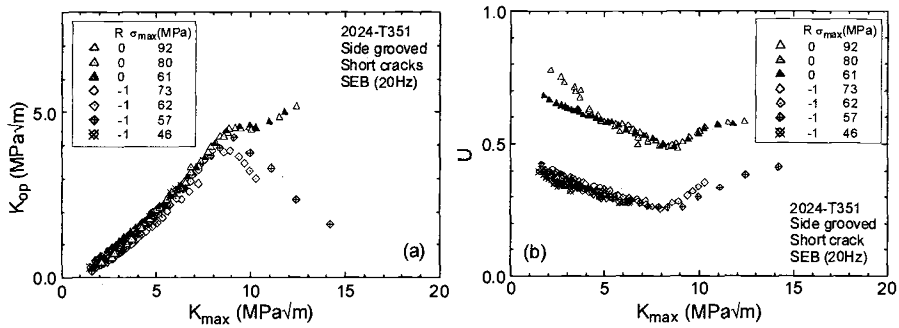

FIG. 4 *Crack opening stress intensity factors and crack opening ratios of short cracks as a function of crack length and K_{max} under constant amplitude loading.*

As has been reported by Jono and Song [24], typical characteristics of U can be expressed successfully as a function of ΔK_{eff}, rather than other parameters such as K_{max} or ΔK. The values of U of short cracks as a function of ΔK_{eff} are shown in Fig. 5 [22], compared with the long crack results. In the figure, the light solid lines represent the long crack results, and the heavy solid lines are the predicted relationship of U versus ΔK_{eff} of short cracks obtained in the previous work [22]. For all the stress ratios, the value of U of a short crack decreases linearly with ΔK_{eff} from an initial high value and merges with the long crack results. The value of U at which the crack opening ratio of a short crack merges with the long crack result corresponds almost to the minimum value for each stress ratio. In the previous work [18], the authors have referred the behavior that the value of U is larger than that of long cracks and also decreases from an initial high value to the minimum value, as to "distinctive characteristic of short crack opening behavior," and further defined the region over which this characteristic of crack opening behavior appears, as "the short crack region." In this short crack region, the value of U decreases almost along the predicted line, which can be said to form an upper bound of experimental data for each R value. It is worthy to note that depending on loading conditions, even a crack as long as several millimeters happens to manifest the opening characteristic of short cracks and may be classified as a kind of short crack according to the above definition. For short crack growth analysis, the above definition of short crack based on the crack opening behavior may be more effective than well-known conventional definitions.

Variation of Crack Opening Load During a Random Loading Block

Typical examples of load versus differential displacement curves observed for long and short cracks during a random loading block are shown in Figs. 6*a* and *b*. In the figures, small numerals represent the sequential number of cycles in a random loading block, and the short horizontal bars on the load versus differential displacement curves represent the measured crack opening points. The crack opening load usually fluctuates through a random loading block, but the range of fluctuation is very small for random block lengths of 500 and 1000, irrespective of random loading spectrum or crack length.

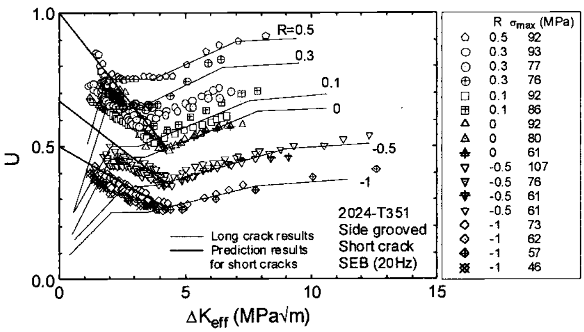

FIG. 5 *Crack opening ratios of short cracks as function of ΔK_{eff} under constant amplitude loading.*

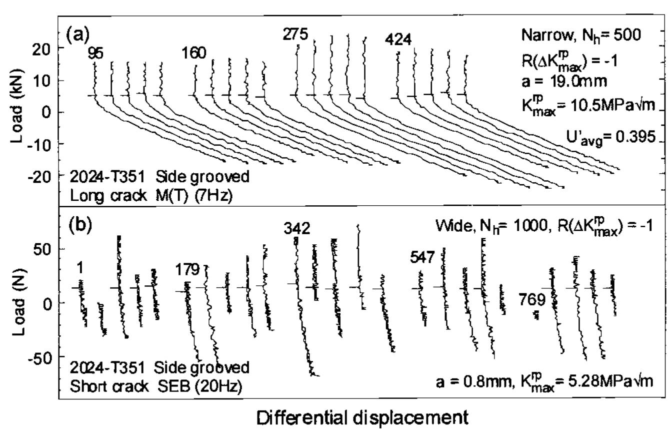

FIG. 6 *Crack opening behavior during a random loading block.*

It has been well reported by Kikukawa, Jono, and their coworkers [13,14,26,27] that the crack opening load of a long crack can be assumed to be nearly constant during a random loading block of relatively long length. Strictly speaking, the behavior of crack opening load during a random loading block should be discussed, considering the crack growth increment during a random loading block, $(\Delta a)_{\text{unit block}}$.

Figure 7 shows examples of the variation of crack opening loads of long cracks during a random loading block when the random loading block length is so long that the growth increment during the random loading block happens to exceed the plastic zone size due to the largest load cycle. In the figure, P_{op} and P_{max} are the crack opening load and the maximum load in a random loading block, respectively, and n is the sequential number of cycles in a random loading block. ω_p^{max} denotes the monotonic plane strain plastic zone size due to the maximum stress intensity factor of the largest load cycle, which is defined as:

$$\omega_p^{max} = \frac{1}{3\pi}\left(\frac{K_{max}^{rp}}{\sigma_y}\right)^2 \tag{4}$$

where K^{rp}_{max} is the maximum stress intensity factor of the largest load cycle in a random loading block, and σ_y is the yield strength of the material. When the crack growth increment $(\Delta a)_{unit\ block}$ is smaller than the plastic zone size ω_p^{max}, the fluctuation of crack opening load is very small as noted above. When $(\Delta a)_{unit\ block}$ is larger than ω_p^{max}, the variation of crack opening load during a random loading block is discernibly enhanced, and the maximum range of fluctuation is about 10 % of the mean value of P_{op}/P_{max}, which is about twice of that for the case of $(\Delta a)_{unit\ block} < \omega_p^{max}$. However, as the range of fluctuation is not so great as to introduce significant error in crack growth analysis, it is more convenient and effective to assume that the crack opening load can be regarded as nearly constant during a random loading block and to represent the crack opening load under random loading by the averaged one over a random loading block, for both long and short cracks. This assumption has been well employed for long cracks by many researchers [13 15,26,27].

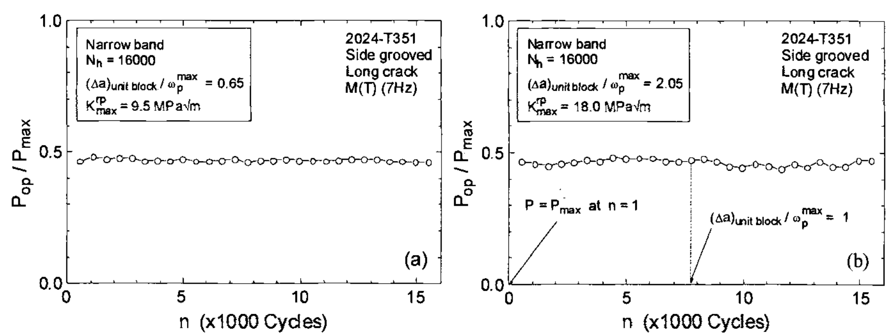

FIG. 7 *Variation of crack opening points during a random loading block when the random loading block length is long.*

Refinement of Determination of Crack Opening Load under Random Loading

In analyzing crack growth under random loading based on the crack closure measurement, what is particularly more difficult compared with constant amplitude loading is determining precisely the crack opening load, because the signal random noise involved in the load versus differential displacement curves cannot be reduced under random loading so easily as under constant amplitude loading. For constant amplitude loading where the magnitudes of loads are constant and there is no sudden change of P_{op} with load cycling, stationary random noise involved in the load versus differential displacement curves can be reduced easily to $1/\sqrt{n}$ by averaging n consecutive cycles synchronously [13,24,25]. This phase-based averaging method normally cannot be applied to random loading where the magnitudes of loads vary.

If the crack opening load under random loading can be assumed to be constant and represented by the averaged one during a random loading block, as described in the preceding section, the signal noise can be reduced by averaging the differential displacement signal data included within sufficiently small load intervals (load-interval-based averaging) as shown in Fig.

8. Figure 8 shows the noise-reduced results of the load versus differential displacement curves shown in Fig. 6*a*. As the number of consecutive cycles to be averaged, N_{avg}, is increased, the straight line portion for the fully open crack becomes more clear and the crack opening load can be determined more easily. The averaged crack opening load is nearly the same, irrespective of the value of N_{avg}. The value of U' averaged fully over a random loading block by the noise reduction method is $U'_{avg} = 0.383$ (for $N_{avg} = 500$ in Fig. 8), slightly lower than the averaged value based on cycle-by-cycle P_{op} determination, $U'_{avg} = 0.395$ (Fig. 6*a*). The difference is not so significant. Here the crack opening ratio under random loading is defined as

$$U' = \frac{K^{rp}_{max} - K_{op}}{K^{rp}_{max} - K^{rp}_{min}} \tag{5}$$

where K^{rp}_{min} is the minimum stress intensity factor of the largest load cycle in a random loading block. The load interval employed is 1 % of the largest load cycle range. Using the noise reduction method proposed, the crack opening load under random loading can be determined more easily, precisely, and economically.

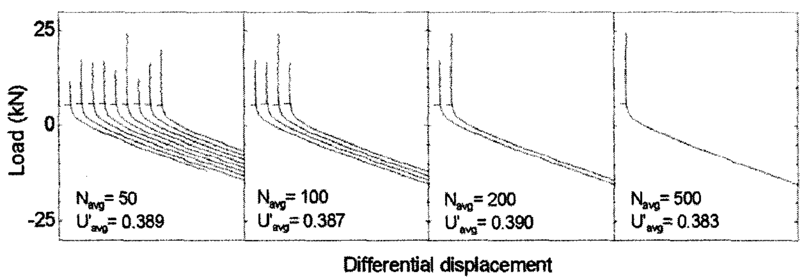

FIG. 8 *Refinement of determination of crack opening load under random loading by noise reduction through load-interval-based averaging.*

Crack Closure Behavior of Conventional Long Cracks under Random Loading

The crack opening stress intensity factor K_{op} and crack opening ratios U' of long cracks under random loading are shown as a function of the maximum stress intensity factor of the largest load cycle in a random loading block K^{rp}_{max} in Fig. 3 already shown. The value of K_{op} is scarcely affected by random load spectrum or random loading block length and is nearly linearly proportional to K^{rp}_{max}.

Compared with the constant amplitude loading data, the value of K_{op} under random loading shows a different trend, depending on the stress ratio of the largest load cycle $R(\Delta K^{rp}_{max})$ for the higher K^{rp}_{max} region; the value of K_{op} at $R(\Delta K^{rp}_{max}) = -1$ agrees well with the constant amplitude loading results, while that at $R(\Delta K^{rp}_{max}) = 0$ is higher than the constant amplitude results. For lower K^{rp}_{max} region, the value of K_{op} is lower under random loading than under constant amplitude loading, irrespective of $R(\Delta K^{rp}_{max})$ value.

The crack opening ratio U' shows characteristic behavior that the value of U' at each $R(\Delta K^{rp}_{max})$ is nearly constant irrespective of K^{rp}_{max}, and consequently, the crack opening ratio under random loading may be represented as a function of $R(\Delta K^{rp}_{max})$ only. This characteristic of U' may be very convenient for estimating crack closure behavior of long cracks under random loading.

Crack Closure Behavior of Physically Short Cracks under Random Loading

A typical example of K_{op} and U' of short cracks under random loading is shown as a function of K^{rp}_{max} in Fig. 9 where the constant amplitude results are also shown by the small symbols. The value of K_{op} seems to be just a little higher under wide-band random loading than under narrow loading, but the difference is nearly negligible. A consistent effect of random block length on K_{op} is not found within this study.

The value of K_{op} is lower under random loading than under constant amplitude loading for the value of K^{rp}_{max}, lower than about 10 MPa$\sqrt{m}$. Correspondingly, for low values of K^{rp}_{max}, the crack opening ratio U' under random loading is considerably higher than the constant amplitude results. This result implies that random loading enhances crack opening, at least for the largest load cycle, in the range of low K^{rp}_{max} values. The crack opening ratio U' under random loading decreases from a relatively high initial value to a minimum value, U'_{min}, around the value at which the random loading data intersect with the constant amplitude results. And thereafter, the value of U' is nearly constant or increases slightly.

For systematic comparison, the crack opening ratio U' of short cracks under random loading are shown as a function of the effective stress intensity factor range of the largest load cycle in a random loading block, $(\Delta K^{rp}_{max})_{eff}$, along with constant amplitude short crack data in Fig. 10 [18]. Since the effects of random spectrum and block length on U' are negligible as noted above, all the data obtained at the same stress ratio are indicated by the same symbol for clarity. The light solid lines in the figure indicate the constant amplitude long crack results.

Compared with the constant amplitude results, the value of U' under random loading decreases more gradually from an initial, higher value to a minimum value U'_{min}, over a broader range of $(\Delta K^{rp}_{max})_{eff}$. If the region where the value of U' is larger than that of long cracks, and if decreases with crack growth may be regarded as the short crack region as already defined in Fig. 8, it can be said from this result that the short crack region is wider under random loading than under constant-amplitude loading. These results indicate that there is significant difference in closure behavior of short cracks between random and constant amplitude loading.

The minimum crack opening ratio U'_{min} corresponds nearly to the value of U at which the random loading data intersect with the constant amplitude results in the region where the short and long crack constant amplitude results are coincident. From this, the data included in the range larger than the value of $(\Delta K^{rp}_{max})_{eff}$ corresponding to U'_{min} can be regarded as long crack random loading data. These (SEB) long crack opening results agree well with the conventionally (M(T)) long crack ones shown in Fig. 3*b*, that for higher K^{rp}_{max} region, the value of U' at $R(\Delta K^{rp}_{max}) = -1$ coincides well with the constant amplitude loading results, while that at $R(\Delta K^{rp}_{max}) = 0$ is lower than the constant amplitude results. For lower K^{rp}_{max} region, the value of U' is higher under random loading than under constant amplitude loading, irrespective of $R(\Delta K^{rp}_{max})$ value. The (SEB) long crack results indicate that also for $R(\Delta K^{rp}_{max}) = -0.5$, 0.1, and 0.3, the value of U' of long cracks at each stress ratio $R(\Delta K^{rp}_{max})$ is nearly constant, irrespective of K^{rp}_{max} and is lower than corresponding constant amplitude results, similarly to the results at $R(\Delta K^{rp}_{max}) = 0$.

The representation of crack opening ratio as a function of the effective stress intensity range can express the characteristics of crack closure behavior of short cracks under random loading as well as constant amplitude loading, as can be seen in Fig. 10.

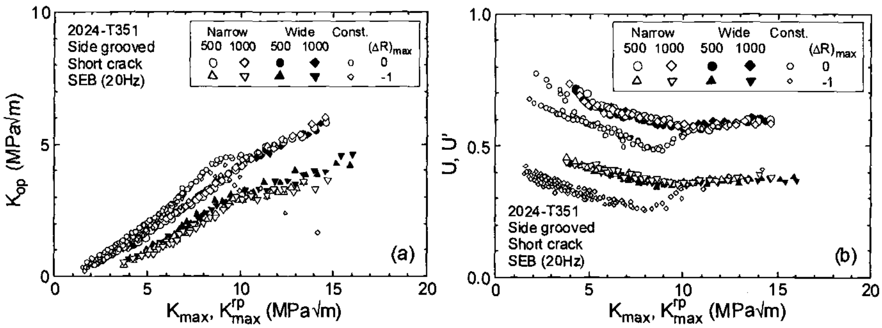

FIG. 9—*Crack opening stress intensity factors and crack opening ratios as a function of the maximum stress intensity factor at $R(\Delta K^{rp}_{max}) = 0$ and -1 under random loading.*

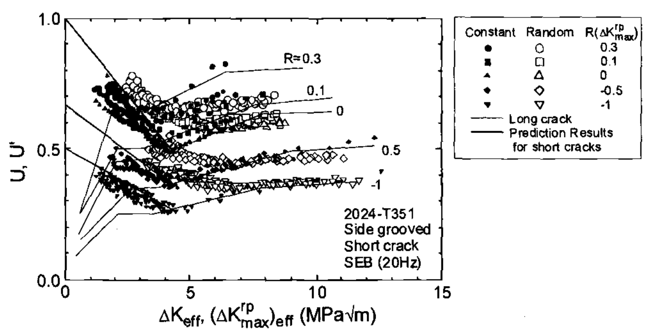

FIG. 10—*Crack opening ratios of short cracks as a function of the effective stress intensity factor range under random loading.*

Predictions of Crack Growth under Random Loading

Fatigue crack growth of long and short cracks under random loading was predicted using the following equation obtained from constant amplitude results

$$\frac{da}{dN} = C\left[(\Delta K_{eff})_{2/PI}\right]^m \tag{6}$$

where C and m are material constants dependent on the growth rate regime. The long crack results shown in Fig. 2*d* were employed as the reference constant amplitude data of da/dN versus $(\Delta K_{eff})_{2/PI}$, which were approximated by four rectilinear segments. The number of cycles needed for a specified crack growth increment (1.5–2.0mm for long cracks and 0.1–0.2mm for short cracks), N_{pred}, is predicted and compared with the experimental one, N_{test}, as shown in Fig. 11, where the prediction ratio N_{pred}/N_{test} is plotted. Among the short crack data of SEB specimens shown in Fig. 11*b*, the solid marks represent the data corresponding to the long crack described in the preceding section. As the consistent effect of the stress ratio $R(\Delta K^{rp}_{max})$ on the prediction results was not found, the data are shown without distinction of stress ratio.

All the predicted data of long cracks and nearly all the data of short cracks are within the factor of 2 scatter band, indicating that crack growth under random loading can be predicted very well by the crack closure concept based on the measured K_{op}, for both long and short cracks. Significant effects of random spectrum or random block length on predicted results are hardly found. These results also show the validity of 2/PI correction for estimating the effective stress intensity factor range.

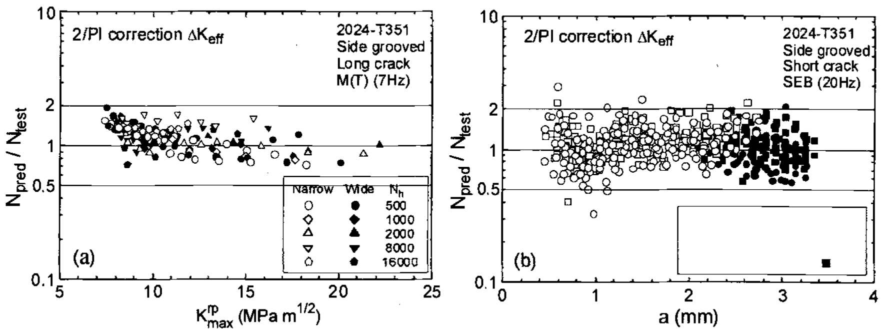

FIG. 11—*Predictions of crack growth under random loading.*

Discussion

As noted in Figs. 6 and 7, it seems reasonable to assume that the crack opening load under random loading is constant during a random loading block, for both long and short cracks, even when the random loading block length is considerable long. This assumption has been well employed [13 18,26,27] and also experimentally verified, although within a limited range, by Kikukawa et al. [13,14]. The characteristic is expected to facilitate the use of closure concept for analysis of crack growth under random loading.

As has been already noted in Figs. 3, 9, and 11, the effects of random loading block length on crack closure and growth are hardly found and consequently need not be considered.

The effect of random spectrum is found on closure behavior of short cracks as shown in Fig. 9 but is not significant. Consistent effect of random spectrum on crack growth is hardly found.

These results indicate that the effects of parameters of random loading are sufficiently small to be neglected, for both long and short cracks.

As can be found in Figs. 3, 9, and 10, the long and short cracks are very different in characteristics of closure behavior under random loading. The crack opening ratio U' of long cracks under random loading is nearly equal to, or in most cases lower than, the constant-amplitude loading results, indicating that random loading may have the effect to retard crack growth, as single overloading. The value of U' of long cracks at a stress ratio of the largest load cycle is nearly constant irrespective of the applied stress intensity factor. This result means that the crack opening ratio of long cracks under random loading may be represented as a function of stress ratio of the largest load cycle only. This characteristic may be very convenient for estimating crack closure behavior of long cracks under random loading. The results of Kikukawa, Jono, and their coworkers [13,14,26,27] or the assumption of Sunder in his CCZT (constant closure zero threshold) [15] that the crack opening load under random loading can be estimated from constant amplitude loading results, appear to correspond to only the stress ratio of $R(\Delta K^{rp}_{max}) = -1$, not to other stress ratios. Performing random loading tests at $R(\Delta K^{rp}_{max}) = 0$ in previous work [16], the authors have obtained the result that the crack opening load under random loading can be estimated from single overloading or periodic single overloading tests. Whether this result can be applied to other stress ratios or not is not clear and remains to be investigated. However, utilizing the characteristic mentioned above, the crack opening load under random loading may be estimated more easily.

On the other hand, the crack opening ratio U' of short cracks for the largest load cycle is much higher under random loading than under constant-amplitude loading, indicating that random loading enhances crack opening of short cracks for the larger load cycles of a random load history. However, as the crack opening load of the largest load cycle is relatively high, a crack is expected to be closed for most smaller load cycles of a random load history, implying that the largest load cycle has an inverse effect to enhance crack closure for the smaller load cycles. Random loading appears to complicate the closure behavior of short cracks. According to the definition of a short crack based on the closure behavior, the region of a short crack is wider under random loading than under constant amplitude loading, as shown in Fig. 10.

Since the closure behavior of short cracks under random loading is significantly different from that under constant amplitude loading, and since it is also more complicated than the closure behavior of long cracks under random loading, it is at present somewhat difficult to estimate the closure behavior of short cracks under random loading.

The prediction results in Fig. 11 indicate that despite the difference in closure behavior between short and long cracks, crack growth of both cracks under random loading can be well described, particularly by using the 2/PI correction method for estimating the effective stress intensity factor range. This indicates that the crack closure is the primary factor governing fatigue crack growth under random loading as well as under constant-amplitude loading.

Accordingly, it is very important to identify or estimate crack opening behavior for evaluating fatigue crack growth under random loading. Generally, the crack opening behavior under random loading cannot be estimated so simply from constant amplitude loading results. It is necessary to investigate methods for estimating crack closure under random loading.

Conclusions

The conclusions obtained are summarized as follows:

1. The crack opening load under random loading is nearly constant during a random loading block, irrespective of random loading spectrum or block length, stress ratio, or crack length. Based on this crack opening behavior, a noise reduction method is proposed to determine the crack opening load under random loading more easily and precisely.
2. The long and short cracks are very different in characteristics of closure behavior under random loading when compared with the closure behavior under constant amplitude loading. The crack opening load of long cracks under random loading is nearly equal to or, in most cases, higher than the constant-amplitude loading results, indicating that random loading may have the effect to retard crack growth, such as single overloading. On the other hand, the crack opening load of short cracks is much lower under random loading than under constant-amplitude loading corresponding to the largest load cycle in a random load history, implying that random loading enhances crack opening of short cracks for the larger load cycles of a random load history.
3. As the crack closure behavior under random loading is usually complicated, it is at present somewhat difficult to estimate precisely the closure behavior under random

loading, particularly for short cracks.

4. Despite the difference in closure behavior between short and long cracks, fatigue crack growth of both cracks under random loading can be well described by the closure concept based on the measured crack opening results. This indicates that the crack closure is the primary factor governing fatigue crack growth under random loading as well as under constant-amplitude loading. The 2/PI correction for estimating the effective stress intensity factor range proposed by Donald and Paris is very promising.

References

[1] Barsom, J. M., "Fatigue-Crack Growth under Variable-Amplitude Loading in ASTM A514-B Steel," *ASTM STP 536*, ASTM International, West Conshohocken, PA, pp. 147 167, 1973.

[2] Elber, W., "Equivalent Constant-Amplitude Concept for Crack Growth under Spectrum Loading," *ASTM STP 595*, ASTM International, West Conshohocken, PA, pp. 236 250, 1976.

[3] Dover, W. D. and Hibberd, R. D., "The Influence of Amplitude Distribution on Random Load Fatigue Crack Growth," *Engineering Fracture Mechanics*, Vol.9, pp. 251 263, 1977.

[4] Schijve, J., "Prediction Methods for Fatigue Crack Growth in Aircraft Materials", *ASTM STP 700*, ASTM International, West Conshohocken, PA, pp. 3 34, 1980.

[5] Socie, D. F. and Artwohl, P. J., "Effect of Spectrum Editing on Fatigue Crack Initiation and Propagation in a Notched Member," *ASTM STP 714*, ASTM International, West Conshohocken, PA, pp. 3 23, 1980.

[6] Chang, J. B., "Round-Robin Crack Growth Predictions on Center-Cracked Tension Specimens under Random Spectrum Loading," *ASTM STP 748*, ASTM International, West Conshohocken, PA, pp. 3 40, 1981.

[7] Hudson, C. M., "A Root-Mean-Square Approach for Predicting Fatigue Crack Growth under Random Loading," *ASTM STP 748*, ASTM International, West Conshohocken, PA, pp. 41 52, 1981.

[8] Newman, J. C., Jr., "A Crack-Closure Model for Predicting Fatigue Crack Growth under Aircraft Spectrum Loading," *ASTM STP 748*, ASTM International, West Conshohocken, PA, pp. 53 84, 1981.

[9] Johnson, W. S., "Multi-Parameter Yield Zone Model for Predicting Spectrum Crack Growth," *ASTM STP 748*, ASTM International, West Conshohocken, PA, pp.85 102, 1981.

[10] Rudd, J. L. and Engle, R. M., Jr., "Crack Growth Behavior of Center-Cracked Panels under Random Spectrum Loading," *ASTM STP 748*, ASTM International, West Conshohocken, PA, pp. 103 114, 1981.

[11] Chang J. B., Szamossi, M., and Liu, K. W., "Random Spectrum Fatigue Crack Life Predictions with or without Considering Load Interactions," *ASTM STP 748*, ASTM International, West Conshohocken, PA, pp. 115 132, 1981.

[12] De Koning, A. U., "A Simple Crack Closure Model for Prediction of Fatigue Crack Growth Rates under Variable Amplitude Loading," *ASTM STP 743*, ASTM International, West Conshohocken, PA, 1981, pp. 63 85.

[13] Kikukawa, M., Jono, M., Kondo, Y., and Mikami, S., "Fatigue Crack Closure and Estimation Method of Crack Propagation Rate under Stationary Varying Loading Conditions Including Random Loading (First Report, Effects of Mean Load and Study on Wave Counting Method)," *Transactions of JSME*, Vol. 48, 1982, pp. 1496 1504 (in

Japanese).
[14] Jono, M., Song, J. H., and Kikukawa, M., "Fatigue Crack Growth and Closure of the Structural Materials under Random Loading," *Proceedings of ICM* 6, 1984, pp. 1735 1742.
[15] Sunder, R., "Near-Threshold Fatigue Crack Growth Prediction under Spectrum Loading," *ASTM STP 1122*, ASTM International, West Conshohocken, PA, 1992, pp. 161 177.
[16] Kim, C. Y. and Song, J. H., "Fatigue Crack Closure and Growth Behavior under Random Loading," *Engineering Fracture Mechanics*, Vol. 49, 1994, pp. 105 120.
[17] Kim, C. Y. and Song, J. H., "Effects of Load Spectrum and History Length on Fatigue Crack Closure and Growth Behavior under Random Loading," *Proceedings of the 6th International Fatigue Congress, Fatigue 96*, Vol. 1, 1996, pp. 529 534.
[18] Lee, S. Y. and Song, J. H., "Crack Closure and Growth Behavior of Physically Short Fatigue Cracks under Random Loading," *Engineering Fracture Mechanics*, Vol. 66, 2000, pp. 321 346.
[19] Paris, P. C., Tada, H., and Donald, J. K., "Service Load Fatigue Damage – A Historical Perspective," *International Journal of Fatigue*, Vol. 21, 1999, pp. S35 S46.
[20] Donald, J. K. and Paris, P. C., "An Evaluation of ΔK_{eff} Estimation Procedure on 6061-T6 and 2024-T351 Aluminum Alloys," *International Journal of Fatigue*, Vol. 21, 1999, pp. S47 S57.
[21] Koo, J. S., Song, J. H., and Kang, J. Y., "A Quantitative Evaluation of K_{op} Determination and ΔK_{eff} Estimation Methods," Submitted to *International Journal of Fatigue*.
[22] Pang, C. M. and Song, J. H., "Crack Growth and Closure Behavior of Short Fatigue Cracks," *Engineering Fracture Mechanics*, Vol. 47, 1995, pp. 327 343.
[23] Kondo, Y., "Study on the Behavior of Fatigue Crack Growth and Closure under Service Loading," Ph.D. Thesis, Osaka University, Osaka, 1980 (in Japanese).
[24] Jono, M. and Song, J. H., "Growth and Closure of Short Fatigue Cracks," *Current Research on Fatigue Cracks, Materials Research Series*, The Society of Materials Science, Vol. 1, 1985, pp. 35 55.
[25] Park, J. H., Song, J. H., Earmme, Y. Y., Kim, C. Y., and Kang, K. J., "Personal Computer Based Fatigue Testing Automation and Improvement in Fatigue Behavior Monitoring," *Transactions of KSME*, Vol. 12, 1988, pp. 123 130 (in Korean).
[26] Jono, M., Song, J. H., and Sugeta, A., "Prediction of Fatigue Crack Growth and Closure under Non-Stationary Random Loading," *Proceedings of ICOSSAR* 4, 1985, pp. 465 474.
[27] Jono, M., Song, J. H., and Sugeta, A., "Fatigue Crack Growth and Closure under Variable Loadings (Effects of Load Variations on Characteristic Form of Crack Growth Rate Curve in Region II)," *Journal of Society for Material Science*, Vol. 34, 1985, pp. 1193 1199 (in Japanese).

Journal of ASTM International, October 2004, Vol. 1, No. 9
Paper ID JAI19055
Available online at www.astm.org

Zhihuan Wu,[1] *Grzegorz Glinka,*[1] *Hieronim Jakubczak,*[2] *and Lena Nilsson*[3]

Calculation of Stress Intensity Factors for Cracks in Structural and Mechanical Components Subjected to Complex Stress Fields

ABSTRACT: One of the difficulties in using fracture mechanics is in determining stress intensity factors of cracked structural and mechanical components. The cracks are often subjected to complex stress fields induced by external loads and residual stresses resulting from the surface treatment. Both stress fields are characterized by non-uniform distributions, and handbook stress intensity factor solutions are seldom available in such cases. The method presented below is based on the generalized weight function technique enabling the stress intensity factors to be calculated for any Mode I loading applied to a planar semi-elliptical surface crack. The stress intensity factor can be determined at any point on the crack tip contour by using the general weight function. The calculation is carried out by integrating the product of the stress field and the weight function over the crack area.

Several examples of point-load weight functions and resulting stress intensity factors are presented in the paper. The method is particularly suitable for modeling fatigue crack growth in the presence of complex stress fields.

KEYWORDS: stress intensity factor, weight function, nonlinear stress field

Nomenclature

a	Depth of an edge crack or the shorter semi-axis of an elliptical crack
c	The longer semi-axis of an elliptical crack
A	Point on the crack contour where the stress intensity factor is to be calculated
FE	Finite element analysis
G_c	Crack contour
G_b	External boundary contour
K_I	Model I stress intensity factor (general)
K_{IA}	Model I stress intensity factor at the point A on the crack front
M	Geometry correction factor, $M = \dfrac{m_A(x,y)}{\sqrt{\pi a}}$
M_i	Coefficients of the 1-D line load weight functions ($i = 1,2,3$)

Manuscript received 10 May 2002; accepted for publication 20 December 2002; published October 2004. Presented at ASTM Symposium on Fatigue Testing and Analysis Under Variable Amplitude Loading Conditions on 29 31 May 2002 in Tours, France; P. C. McKeighan and N. Ranganathan, Guest Editors.

[1] Research Associate and Professor, respectively, Department of Mechanical Engineering, University of Waterloo, 200 University Avenue West, Waterloo, Ontario, N2L 3G1, Canada.
[2] Associate Professor, Warsaw University of Technology, Institute of Heavy Machinery Engineering, Narbutta 84, 02-524 Warsaw, Poland.
[3] Specialist, SAQ KONTROLL AB, Box 49306, 100 29 Stockholm, Sweden.

$m(x,a)$	Weight function (general)
$m(x,y)$	Weight function for point A on the crack contour
Ω	Crack area
F	Point load (force) applied to the crack surface at point $P(x,y)$
$P(x,y)$	Point on the crack surface where the load F is applied
Q	Shape factor, $Q = 1 + 1.464 \cdot \left(\frac{a}{c}\right)^{1.65}$
SIF	Stress intensity factor
s	Shortest distance between the point load and the crack contour
t	Thickness
Γ_c	Inverted crack contour
Γ_b	Inverted free boundary contour
ρ	Distance between the point load and the point on the crack front where the stress intensity factor is to be calculated
r_A	Radius of the inside circle tangent to the ellipse at the point A where the stress intensity factor is to be calculated
R	Radius of the biggest inside circle tangent to the ellipse
σ_m	Membrane (tensile) stress
σ_b	Bending stress
$\sigma(x)$	One-dimensional stress distribution
$\sigma(x,y)$	Two-dimensional stress distribution
Y	Geometry correction factor, $Y = \frac{K}{\sigma_0 \cdot \sqrt{\pi a}}$

Introduction

Most of the existing methods of calculating stress intensity factors require separate analysis of each load and geometry configuration. Fortunately, the weight function method developed by Bueckner [1] and Rice [2] simplifies considerably the determination of stress intensity factors. The important feature of the weight function is that it depends only on the geometry of the cracked body. If the weight function is known for a given cracked body, the stress intensity factor due to any Mode I load system applied to the body can be determined by using the same weight function. If the weight function is known, there is no need to derive ready-made stress intensity factor expressions for each load system and associated internal stress distribution induced in the cracked body. The stress intensity factor for a one-dimensional crack (Fig. 1) can be obtained by multiplying the weight function, $m(x,a)$, and the internal stress distribution, $\sigma(x)$, in the prospective crack plane, and integrating the product over the crack length a:

$$K = \int_0^a \sigma(x) \cdot m(x,a) dx \tag{1}$$

A variety of one-dimensional (line load) weight functions can be found in [3 5]. However, their mathematical forms vary from case to case, making their application inconvenient. Therefore Glinka and Shen [6] have proposed a general weight function (Eq 2), which can be used for a wide variety of one-dimensional Mode I cracks:

$$m(x,a)=\frac{2F}{\sqrt{2\pi(a-x)}}\left[1+M_1\left(1-\frac{x}{a}\right)^{1/2}+M_2\left(1-\frac{x}{a}\right)+M_3\left(1-\frac{x}{a}\right)^{3/2}\right] \tag{2}$$

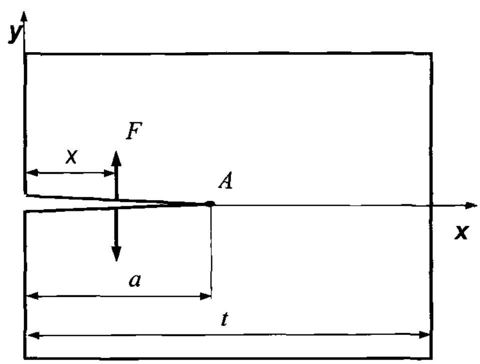

FIG. 1 *The line load (1-D) weight function notation (F = 1).*

The system of coordinates and notation for an edge crack as an example are given in Fig. 1. In order to determine the weight function, $m(x,a)$, for a particular cracked body, it is sufficient to determine the three parameters M_1, M_2, and M_3.

Because the mathematical form of the weight function (Eq 2) is the same for all cracks, the same method can be used for the determination of parameters M_i and calculation of stress intensity factors based on Eq 1. The method of finding M_i parameters was discussed in [7]. A variety of line load weight functions has been derived and published already [6 9].

Point Load Weight Functions for Planar Cracks Subjected to Two-Dimensional Stress Fields

In spite of the high efficiency and usefulness of one-dimensional line load weight functions, they cannot be used if the stress field is two-dimensional in nature, i.e., when the stress field, $\sigma(x,y)$, in the crack plane depends on both x and y coordinates. Therefore, in order to calculate stress intensity factors for planar cracks subjected to a two-dimensional (2-D) stress field, a weight function for a point load (Fig. 2) is needed. There are some solutions for planar cracks available in the literature [10 11]. For example, stress intensity factors for a semi-elliptical surface crack in a flat plate [10] can be calculated using following equation:

$$K_I = (\sigma_m + H\sigma_b)\sqrt{\frac{\pi a}{Q}} f\left(\frac{a}{t}, \frac{a}{c}, \frac{c}{W}, \phi\right) \quad (3)$$

However, the existing solutions for planar cracks can be used only for specific load conditions such as tension and bending. For arbitrary crack configurations and complex two-dimensional stress fields, a 2-D point load weight function is needed.

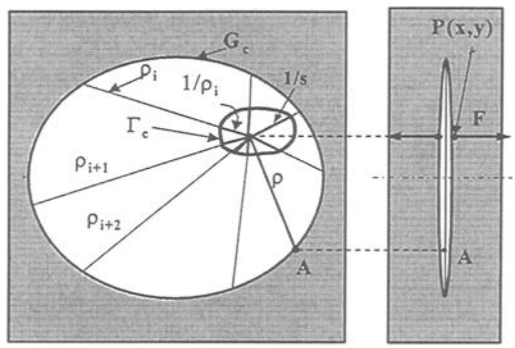

FIG. 2—*The point load (2-D) weight function notation (F = 1).*

The 2-D point-load weight function, $m_A(x,y)$, represents the stress intensity factor at point A (Fig. 2) on the crack front, induced by a pair of unit splitting forces, F, applied to the crack surface at point $P(x,y)$. If such a weight function is known, it is possible to calculate the stress intensity factor at any point on the crack front induced by any Mode I stress fields applied to the crack surface. In order to determine the stress intensity factor induced by a 2-D stress field, $\sigma(x,y)$, at a point A on the crack front, the product of the stress function, $\sigma(x,y)$, and the weight function, $m(x,y)$, need to be integrated over the entire crack surface area, Ω

$$K_A = \iint_{\Omega} \sigma(x,y) m(x,y) dx dy \quad (4)$$

Rice has shown [12] that the 2-D point load weight function for an arbitrary planar crack in an infinite body can be written generally as

$$m_A(x,y) = \frac{\sqrt{2s}}{\pi^{3/2}\rho^2} \cdot w(x,y) \quad (5)$$

Oore and Burns [13] proposed an approximate 2-D point-load weight function (Eq 6), from which the function $w(x,y)$ can be derived for a number of crack configurations.

$$m_A(x,y) = \frac{\sqrt{2}}{\pi\rho^2 \sqrt{\oint_{G_c} \frac{dG_c}{\rho_i^2}}} \quad (6)$$

The notation for the weight function (Eq 5) is given in Fig. 2. Oore and Burns [13] have shown that after deriving closed form expressions for the line integral in (Eq 5), several exact weight functions could be derived for straight and circular cracks in infinite bodies. It also has been found that the line integral represents the arc length, Γ_c, of the crack contour inverted (Fig. 2) with respect to the point, $P(x,y)$. As a consequence, the weight function (Eq 6), can be written in a short form as:

$$K_A = m_A(x,y) = \frac{\sqrt{2}}{\pi\rho^2\sqrt{\Gamma_c}} \tag{7}$$

The inverted contour, Γ_c, can be also viewed (Fig. 2) as the locus of inverted radii $1/\rho_i$. Subsequently, it can also be proven that inverted contours form circles in the case of straight and circular crack contours. In other words, the inverted contour is a circle in the case of cracks with a constant curvature. Therefore, based on Eq 7, it was possible [14] to derive closed form weight functions for a variety of straight and circular crack configurations.

Embedded Cracks in Finite Bodies – The External Boundary Effect

The point load weight function (Eq 7) can be used only for cracks in infinite bodies. However, in the case of finite bodies, both the crack contour and the free boundary contour have to be considered. The existing closed form point load weight function [3] revealed that the following form of the point load weight function (Eq 8) might appropriately account for the free boundary effect

$$m_A(x,y) = \frac{\sqrt{2}}{\pi\rho^2} \times \frac{\sqrt{\Gamma_c + \Gamma_b}}{\Gamma_c} \tag{8}$$

The parameter, Γ_b, is the length of the inverted contour of the free boundary with respect to point A on the crack front (Fig. 3) where the stress intensity factor is to be calculated.

Equation 8 was subsequently used to derive a few specific weight functions for crack configurations available in the literature. The weight function for an infinite straight edge crack approaching a straight free boundary (Fig. 3) is discussed below as an example. The weight function (Eq 9) for configuration shown in Fig. 3 was derived directly from Eq 8

$$m_A(x,y) = \frac{\sqrt{2s}}{\pi^{3/2}\rho^2}\sqrt{1+\frac{s}{d}} \tag{9}$$

The point load weight function (Eq 9) can be further integrated along the line $x = 0$, resulting in the 1-D line load weight function (Eq 10) for an edge crack approaching a free straight boundary.

$$m_A(s) = \oint_{x=0} \frac{\sqrt{2s}}{\pi^{3/2}\rho^2}\sqrt{1+\frac{s}{d}}\,dy = \frac{\sqrt{2}}{\sqrt{\pi s}}\sqrt{1+\frac{s}{d}} \tag{10}$$

However, the weight function (Eq 10) is valid only for configurations where the bending of the uncracked section is negligible.

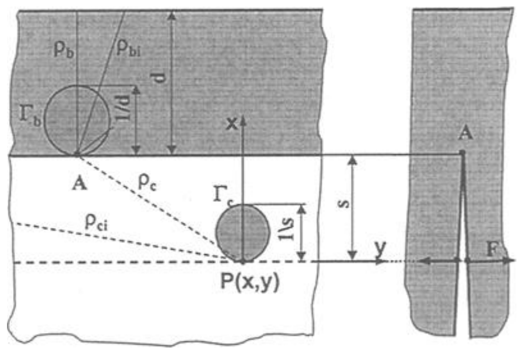

FIG. 3 *An infinite crack approaching* a *free boundary (F = 1).*

The weight function for two edge crack under symmetric loading and separated by a finite thickness ligament (Fig. 4) was analyzed next and resulted in:

$$m_A(s,d)=\left(\frac{\sqrt{2}}{\pi\rho_1^2}+\frac{\sqrt{2}}{\pi\rho_2^2}\right)\times\frac{\sqrt{\Gamma_c+\Gamma_b}}{\Gamma_c}=\frac{\sqrt{2s}}{\pi^{3/2}}\sqrt{\frac{d+s}{d}}\left(\frac{1}{\rho_1^2}+\frac{1}{\rho_2^2}\right) \tag{11}$$

Integration of the point load weight function (Eq 11) for uniformly distributed line load P along the two lines of $x=\pm(d/2+s)$ resulted in the line weight function (Eq 12).

$$m_A(s)=\frac{\sqrt{2}}{\sqrt{\pi s}}\times\frac{d+2s}{\sqrt{d(d+s)}} \tag{12}$$

The weight function (Eq 12) is the same as the exact analytical line weight function derived by Tada [3].

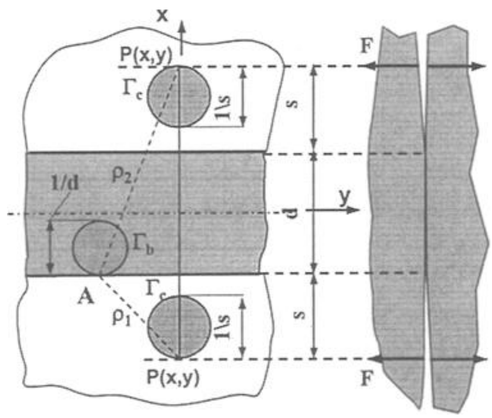

FIG. 4 *Two infinite edge cracks loaded symmetrically and separated by a finite thickness ligament d (F = 1).*

Edge Crack in Infinite Body – Crack Mouth Correction

When a crack has a finite depth (Fig. 5), the effect of the crack mouth boundary has to be taken into account. The general weight function (Eq 8) can be used to derive the point load weight function for such a crack configuration as well.

The point load weight function for the configuration shown in Fig. 5 can be written in the form of Eq 13. The last term in Eq 13 is the correction for the crack mouth effect. The crack mouth correction can be achieved by applying virtual force symmetric with respect to the crack mouth. The distance between the point where the virtual symmetric load is applied and the point where the stress intensity factor is to be calculated is ρ_3

$$m_A(x,y)=\left(\frac{\sqrt{2}}{\pi\rho_1^2}+\frac{\sqrt{2}}{\pi\rho_2^2}\right)\cdot\frac{\sqrt{\Gamma_b+\Gamma_c}}{\Gamma_c}+\frac{1}{\pi\rho_3^2\sqrt{\Gamma_c}} \tag{13}$$

Integration of Eq 13 along line $x=\pm(d+s)$ resulted in the derivation of the line load weight function (Eq 14) for a double edge crack subjected to symmetric loading (Fig. 5)

$$m_A(x)=\frac{2(d+s)}{\sqrt{\pi ds(s+2d)}}+\frac{\sqrt{s}}{\sqrt{\pi}(2a-s)} \tag{14}$$

When the thickness of the ligament tends to infinity, the weight function (Eq 14) takes the form of the weight function for an edge crack in a semi-infinite plate, given in [3]. The comparison of the weight function (Eq 14) based stress intensity factor correction factor, $M=m_A(x,y)/\sqrt{\pi a}$, with Tada's solution [3] is shown in Fig. 6. The good agreement indicates that crack mouth correction in the weight function (Eq 14) can approximately account for the crack mouth boundary effect.

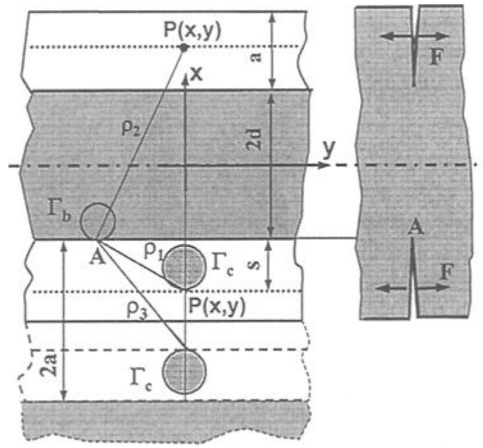

FIG. 5 *Double edge crack in a finite width plate.*

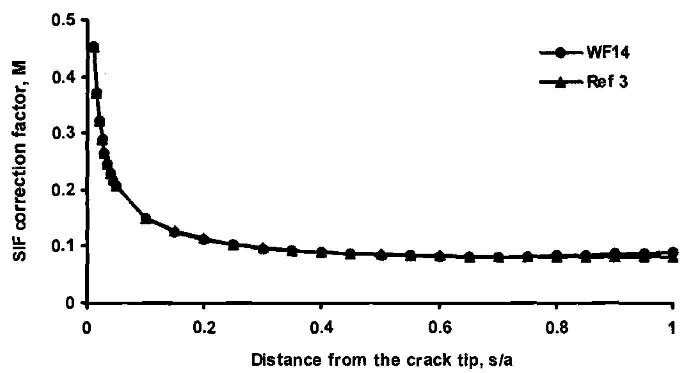

FIG. 6 *Comparison of the geometric correction factor, M, calculated using the weight function (14) with Tada's solution [3] (F = 1).*

Planar Cracks with Variable Crack Front Curvature - The Curvature Effect

It was also found that the accuracy of the weight function (Eq 8) and subsequent accuracy of stress intensity factors for elliptical cracks, having varying curvature of its contour, was decreasing as the ellipses became more slender, i.e., when they departed significantly from the circular constant curvature contour. It was concluded that the inverted crack contour, Γ_c, in Eq 7 is only an average measure of the crack geometry effect. The weight function and the stress intensity factor also depend on the immediate curvature surrounding the point where the stress intensity factor is to be calculated (Fig. 7) and the proximity of the other parts of the crack contour. The correction for the local curvature effect proposed below is empirical in nature and was deducted from the stress intensity data for a wide variety of stress intensity factors for semi-elliptical surface cracks and general properties of the weight function

$$m_A(x,y)=\left(\frac{\sqrt{2}}{\pi\rho_1^2}+\frac{\sqrt{2}}{\pi\rho_2^2}\right)\cdot\frac{\sqrt{\Gamma_b+\Gamma_c\cdot(a/r_A)^{0.5}}}{\Gamma_c\cdot(a/r_A)^{0.5}}+\frac{1}{\pi\rho_3^2\cdot\sqrt{\Gamma_c\cdot(a/r_A)^{0.5}}} \tag{15}$$

Parameter r_A is the radius of an internal circle (Fig. 7) tangent to the ellipse at point A.

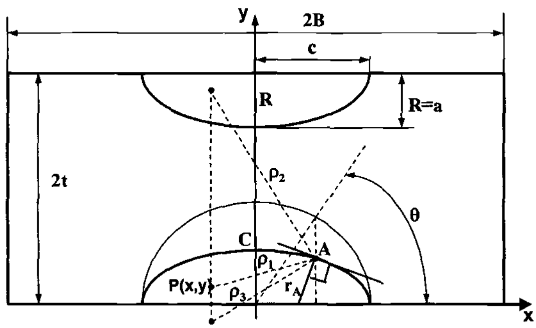

FIG. 7 *A finite thickness plate with a pair of symmetric semi-elliptical surface cracks.*

Stress Intensity Factors for a Pair of Semi-Elliptical Surface Cracks in a Finite Thickness Plate

Using the point load weight function (Eq 15), one can determine the stress intensity factor K for a pair of symmetric semi-elliptical cracks in a finite thickness plate (Fig. 7).

The stress intensity factors at the deepest point C (Fig. 8) were determined for a uniform tensile stress field, $\sigma(x,y)=\sigma_0=1$, using numerical integration of the weight function (Eq 15). The comparison of calculated stress intensity factors in terms of the geometric correction factor, $Y=K/(\sigma_0\cdot\sqrt{\pi a})$, with Isida et al. [15] data for $a/t=0.5$ is presented as an example in Fig. 8. For relative crack depths within the range of $0.2<a/t<0.8$ and the aspect ratio of $0.2\le a/c\le 1$, the maximum difference between analogous two sets of data was 7.9 %.

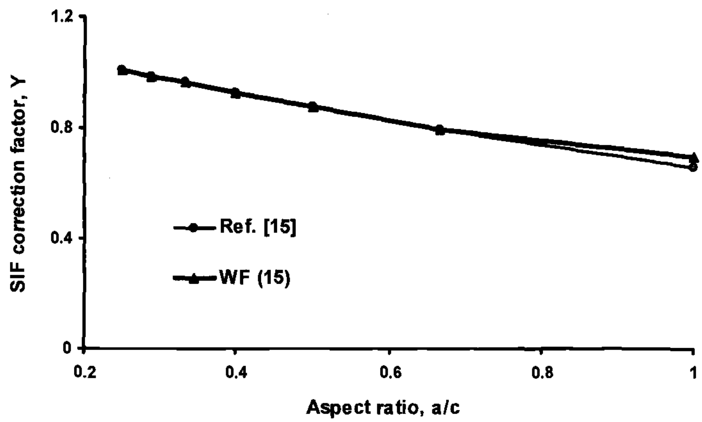

FIG. 8 *Comparison of the weight function based SIFs with Isida, et al. data [15] for various aspect ratios a/c and the relative depth of a/t = 0.5.*

Stress Intensity Factors for a Single Semi-Elliptical Surface Crack in a Finite Thickness Plate

The notation for a semi-elliptical surface crack in a finite thickness plate is shown in Fig. 9. The weight function (Eq 14) was used for the determination of the stress intensity factor for this crack configuration.

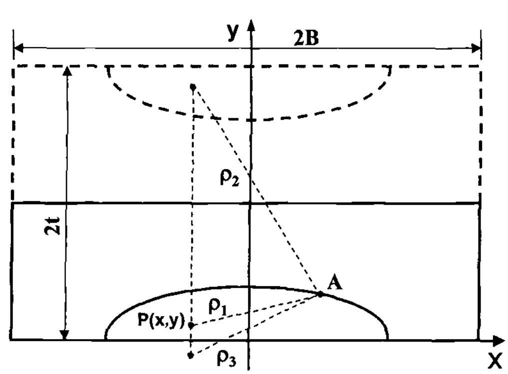

FIG. 9 *Semi-elliptical surface crack in a finite thickness plate.*

Two virtual symmetric loads were used to account for the free boundary and the crack mouth effect. The weight function (Eq 14) gave good stress intensity factor estimations for semi-circular surface crack ($a/c = 1$) with relative crack depths $0 < a/t < 0.8$. The error was less than a few percent for the two non-uniform stress fields used for the analysis, i.e., $\sigma(x,y) = \sigma_0 x/c$ (Fig. 10) and $\sigma(x,y) = \sigma_0 xy/ac$ (Fig. 11).

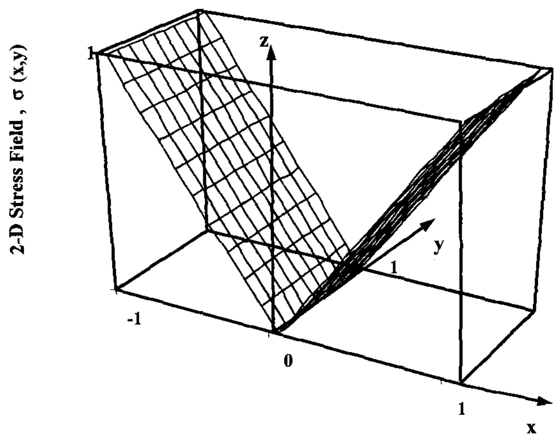

FIG. 10 *2-D stress field, $\sigma(x, y) = \sigma_0 * x / c$ applied to the crack surface.*

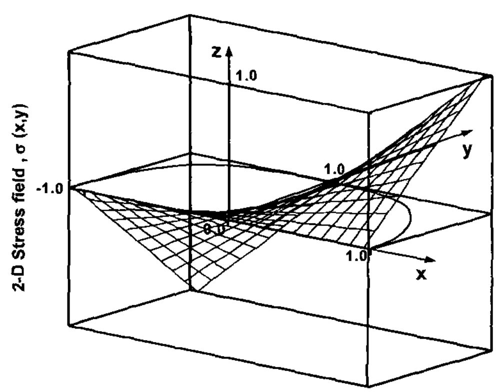

FIG. 11—*2-D stress field, $\sigma(x, y) = \sigma_0 * x\, y/ac$ applied to the crack surface.*

When the crack front approaches the free surface, the weight function based stress intensity factor deviates from the FE data of [11]. One of the reasons is that numerical integration technique was used to deal with singularities for which our integration was not sufficiently accurate. The integration was accurate enough over the region defined by the parametric angle of $5^0 \leq \theta \leq 175^0$. The comparison of the geometric correction factor Y obtained from the weight function (Eq 15) with the FE data of [11] is shown in Figs. 12–14. For a single surface crack in a finite thickness plate, the weight function (Eq 15) yields good results for relatively deep cracks ($0 < a/t < 0.8$) with aspect ratio of $a/c > 0.5$.

Unfortunately the weight function (Eq 15) requires an additional term accounting for the effect of bending occurring in the case of long cracks with aspect ratio of $a/c < 0.3$ and

a/t>0.5. Therefore, further studies are being carried out in order to include the bending effect in edge cracks ($a/c \rightarrow 0$) and semi-elliptical cracks with the aspect ratio of a/c< 0.3. The weight function (Eq 15) yields good results for embedded elliptical and symmetric edge and semi-elliptical cracks.

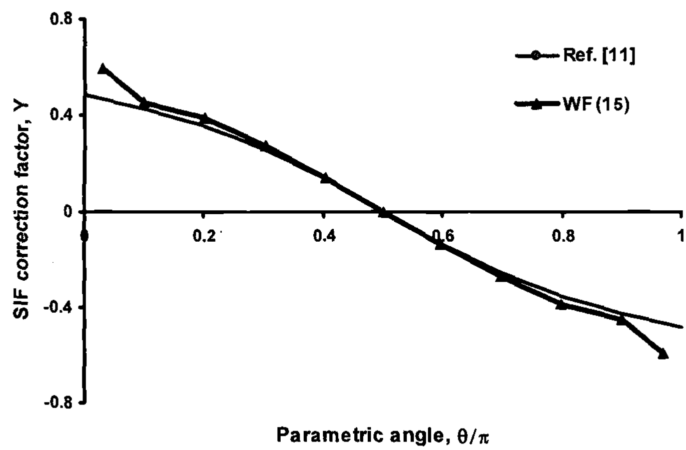

FIG. 12 *Comparison of the weight function based geometric SIF correction factor Y with Nilsson's [11] FE data, [$\sigma(x, y) = \sigma_0 * x/c$, $a/c = 1$, $a/t=0.8$].*

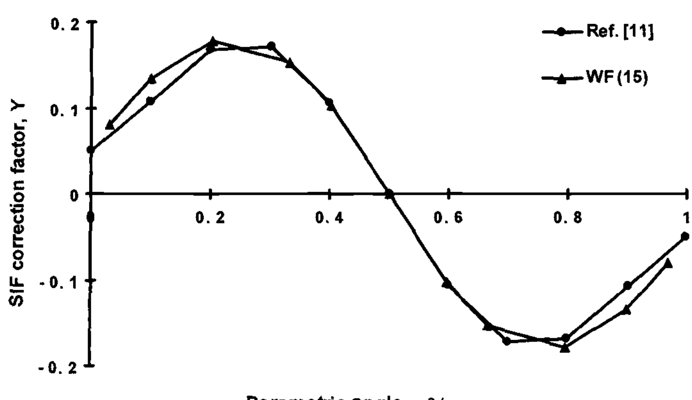

FIG. 13—*Comparison of the weight function based SIFs with Nilsson's [11] FE data, [$\sigma(x,y) = \sigma_0 \cdot xy/ac$, $a/c = 1$, $a/t = 0.8$].*

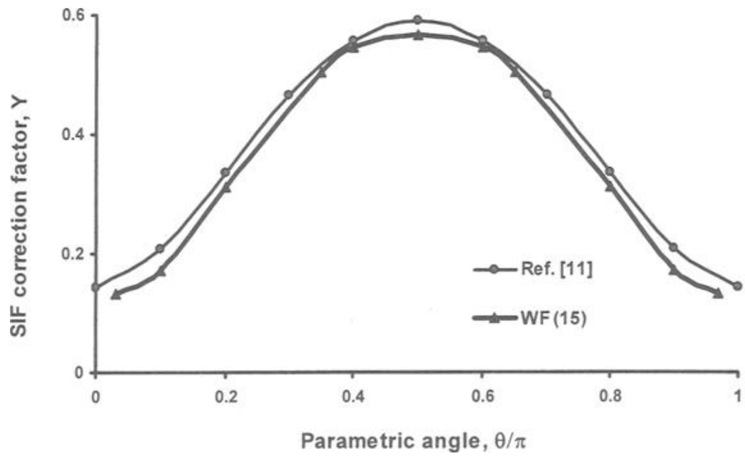

FIG. 14 *Comparison of the weight function based SIFs with Nilsson's [11] FE data,* $[\sigma(x, y) = \sigma_0 * y/a,\ a/c = 0.5,\ a/t = 0.4]$.

Conclusions

The point load weight function (Eq 15) gives good estimation of stress intensity factors of double symmetric edge crack and a semi-elliptical surface crack at the deepest point in a finite thickness plate. The stress intensity factors obtained from weight function (Eq 15) were compared with the results obtained from finite element analyses [11]. The difference between the stress intensity factors obtained from the finite element analysis and the stress intensity factors calculated from weight function (Eq 15) is generally within a few percent for double semi-elliptical surface cracks with the aspect ratio of $a/c >$ 0.25 and relative crack depth of $0 < a/t < 0.8$.

The point load weight function (Eq 15) can be used to calculate stress intensity factors at any point along the crack front for semi-elliptical surface cracks subjected to 2-D stress distribution. The difference between stress intensity factors obtained from the weight function (Eq 15), the Handbook solutions [15], and finite element results [11] are a few percent for semi-elliptical surface cracks depth of $0 < a/t < 0.8$ and aspect ratio of $a/c \geq 0.5$.

The limitation of the point load weight function (Eq 15) is the relative crack depth. When relative crack depth $a/t > 0.4$, the stress intensity factors obtained from the weight function (Eq 15) deviated from the finite element results. Additional research is needed to account for the local bending effect.

References

[1] Bueckner, H. F., "A Novel Principle for the Computation of Stress Intensity Factors," *Zeitschrift fur Angewandte Mathematik Und Mechanik*, Vol. 50, 1970, pp. 529 546.

[2] Rice, J. R, "Some Remarks on Elastic Crack-Tip Stress Field," *International Journal of Solids and Structures*, Vol. 8, 1972, pp. 751 758.

[3] Tada, H., Paris, P., and Irwin, G., *The Stress Analysis of Cracks Handbook*, 2nd ed., Paris Production Inc., 1985, St. Louis, MO.
[4] Wu, X. R. and Carlsson, A. J., *Weight Functions and Stress Intensity Factor Solutions*, 1991, Pergamon Press, Oxford, UK.
[5] Fett, T. and Munz, D., "Stress Intensity Factors and Weight Functions for One-Dimensional Cracks," Report No. KfK 5290, Kernforschungszentrum Karlsruhe, Institut fur Materialforschung, December, 1994, Karlsruhe, Germany.
[6] Glinka, G. and Shen, G., "Universal Features of Weight Functions for Cracks in Model I," *Engineering Fracture Mechanics*, Vol. 40, No. 6, 1991, pp. 1135 1146.
[7] Shen, G. and Glinka G., "Determination of Weight Functions from Reference Stress Intensity Factors," *Theoretical and Applied Fracture Mechanics*, Vol. 15, No. 2, 1991, pp. 237 245.
[8] Shen, G. and Glinka G., "Weight Functions for a Surface Semi-Elliptical Crack in a Finite Thickness Plate," *Theoretical and Applied Fracture Mechanics*, Vol. 15, No. 2, 1991, pp. 247 255.
[9] Zheng, X. J., Glinka, G., and Dubey, R., "Calculation of Stress Intensity Factors for Semi-Elliptical Surface Cracks in a Thick-Wall Cylinder," *International Journal of Pressure Vessels and Piping*, Vol. 62, 1995, pp. 249 258.
[10] Newman, J. C., Raju, I. S., "Stress-Intensity Factor Equations for Cracks in Three-Dimensional Finite Bodies Subjected to Tension and Bending Loads," NASA Technical Memorandum 85793, NASA Langley Research Center, Hampton, VA, 1989.
[11] Lena Nilsson, *SAQ/FoU-Report 98/10, Stress Intensity Factors for Half-Elliptical Surface Cracks in Plates Subjected to a Complex Stress Field*, ISSN 1401-5331.
[12] Rice, J., "Weight Function Theory for Three-Dimensional Elastic Crack Analysis," *Fracture Mechanics Perspectives and Directions (20th Symposium), ASTM STP 1020*, ASTM International, West Conshohocken, PA, 1989, pp. 29 57.
[13] Oore, M. and Burns, D. J., "Estimation of Stress Intensity Factors for Embedded Irregular Cracks Subjected to Arbitrary Normal Stress Fields," *Journal of Pressure Vessel Technology, ASME*, Vol. 102, 1980, pp. 201 211.
[14] Glinka, G. and Reinhardt, W., "Calculation of Stress Intensity Factors for Cracks of Complex Geometry and Subjected to Arbitrary Nonlinear Stress Fields," *Fatigue and Fracture Mechanics, Vol. 31, ASTM STP 1389*, G. R. Halford and J. P. Gallagher, Eds., ASTM International, West Conshohocken, PA, 2000, pp. 348 370
[15] Murakami, Y., *Stress Intensity Factors Handbook*, Vol. 2, 1987, Pergamon Press, Oxford.

W. El-Ratal,[1] M. Bennebach,[2] X. Lin,[2] R. Plaskitt[2]

Fatigue Life Modelling and Accelerated Tests for Components under Variable Amplitude Loads

Reference: El-Ratal, W., Bennebach, M., Lin, X., and Plaskitt, R., **"Fatigue Life Modelling and Accelerated Tests for Components under Variable Amplitude Loads,"** *Fatigue Testing and Analysis Under Variable Amplitude Loading Conditions, ASTM STP 1439*, P. C. McKeighan and N. Ranganathan, Eds., American Society for Testing and Materials, West Conshohocken, PA, 2005.

Abstract: This paper focuses on computer-based techniques used for optimizing and accelerating laboratory fatigue tests. After a short review of the available methodologies, a practical application is presented on a real automotive component undergoing complex loadings. Using a multi-axial non-proportional fatigue damage model to identify damaging sections of loading histories, combined with advanced joining functions of retained time windows, allows accelerating the full test from 34 days to 11 days. Applying the edited signals enables testing 3 suspension modules for the same duration needed to test one system using the original time histories. This reduces costs, time to market and increases design confidence.

Keywords: test acceleration, multiaxial fatigue, suspension modules testing.

Introduction

Manufacturers are under increasing pressure to reduce the time-to-market for their products while assuring high reliability of these products. Durability design and analysis are essential elements in achieving these objectives. Modern software tools are widely used to predict the fatigue life of structures or components at the early stage of a design cycle, and taking into account practical loading histories, it can also help to optimise the design in terms of durability.

Fatigue life predictions can be analytically undertaken by using classical methods like stress-life, strain-life or linear elastic fracture mechanics. The appropriate analysis discipline depends on the proportion of the total fatigue life that is consumed in initiation and growth of a fatigue crack up to final failure. These methods have been widely used in different industries and allow reasonable predictions in simple stress/strain states.

However, real components often have complex shapes and are subjected to combined loads, resulting in multi-axial non-proportional stress states. An appropriate multi-axial model must therefore determine the life of such structures. Research on multi-axial

[1]Fatigue Analysis & Key Life Technical Specialist, Experimental Engineering – ADSE, Visteon, Sterling Heights, Michigan, USA.
[2]nCode International Limited, 230 Woodbourn Road, Sheffield S9 3LQ, UK.

fatigue has made great progress during the past two decades and several well-known models that deal with low or high cycle fatigue are available.

Nevertheless, durability tests are still necessary for design verification or product sign-off, because there are many variables that theoretical fatigue criteria cannot adequately consider, such as manufacturing processes, assembly, material non-homogeneity or residual stresses. This part of the product development cycle is recognised as one of the most critical and time-consuming activities. Based on fatigue damage concepts, some techniques have been developed to make it possible to remove, with confidence, the non-damaging time sequences in a practical test program. A review of these techniques and the data domain in which they operate is presented in this paper, with a practical application to a real automotive component.

Test Acceleration through Fatigue-Based Data Editing

Any data editing method must reduce the testing time in a technically valid, justifiable and repeatable manner. For the laboratory test to represent the in-service behaviour, it must reproduce the loading environment and the fatigue damage content of the original load data. This should ensure the duplication of the same failure modes and locations in the laboratory. Fatigue analysis can be used to mimic the fatigue life of the test before it is undertaken, to check that the edited drive signals still give a comparable fatigue life (in equivalent repeats of sequence) and to estimate the test duration reduction. If the "before" and "after" editing fatigue life does not match closely, then the editing strategy is erroneous.

Editing in the Time Domain

Time series measurement is the only data domain that contains frequency, phase relation, peak-valley and cycle range-mean information. They can be derived by signal processing. Any other data domains contain less information compared with the time domain. In the past, it has been tempting to accelerate a fatigue test by linearly scaling up the inputs and producing a failure at the same location in the component. This is no longer the same test as previously non-damaging events in a random sequence become damaging. Similarly, constant amplitude equivalent loadings have been derived using RMS of ranges. This is also a different test and neither of these methods should be recommended.

Validation of the signal (e.g., spike removal) should be carried out as a matter of course, but other time domain manipulations such as down sampling, linear smoothing or deletion of low amplitude time sections "by eye" have commonly been used prior to testing. These techniques can only be justified if fatigue analysis before and after editing shows the simulated test life to be the same in terms of both repeats of history and damage distribution.

More rational techniques have been developed that can identify and remove time sections, from single or multi-channel rig drives, based on time-correlated damage. Each channel is divided into a number of damage time windows, which are marked for retention (1) or deletion (0) according to the editing criterion (e.g., the material test cut-off life). A logical OR operation across all the channels gives the list of windows to be retained. The corresponding windows from the original time series are then assembled, with joining functions added where necessary to ensure a smooth join from the end of one section of data to the start of the next section. This prevents the generation of artificial spikes or steps on any channel. The joining function must match the dynamics of the signal and the response capability of the test machine. The drive channels have a maximum rate of change, referred to as slew rate, which if exceeded can damage the simulator.

This technique is highly recommended as it produces valid derived significant speed increase factors and maintains phase between multiple target drive channels.

Editing in the Peak-Valley Domain

Peak-valley, or turning point extraction will typically reduce the number of points to reproduce in the test command by a factor of five to ten and is used when frequency is unimportant. It cannot be used in situations where resonance fatigue occurs or for materials sensitive to frequency (e.g., elastomers) but can still be used for multiple target drive channels by a multiple peak-valley extraction process which outputs all corresponding points to any peak or valley and maintains the phase relationship between the multi-channel set. Replaying the reduced signals at a single cyclic frequency optimised to the test rig's capacity can then accelerate component durability tests.

During the peak-valley extraction a range gating can be applied to remove small peak-valley pairs or cycles. Multiple fatigue analysis beforehand can identify the maximum gating threshold that does not change the predicted fatigue life, i.e., without removing damaging cycles. Care should be taken when using this technique in the strain life approach, where the gating must be applied to the local strain history and also when dealing with multi-axial problems, the multi-axial material fatigue behaviour being stress/strain path sensitive.

Editing in the Cycles or Histogram Domains

Rainflow cycle counting can also employ range gating, whether by analysis of time series data or as an on-line data acquisition process. Measuring representative service over a period of weeks or months is impractical in the time domain so on-line rainflow counting is employed. In this way, a time history can be classified with gating and a reduced length peak-valley sequence regenerated from the resulting range-mean histogram. The same comments apply here as for the peak-valley domain and again, the criteria for acceptance is that fatigue analysis before and after editing, shows the simulated test life to be the same in terms of repeats of history.

A histogram can be directly used as input to a fatigue analysis and inspection of cycles and corresponding damage histograms can reveal where to remove non-damaging cycles. Since typically only a small percentage of the cycles do all the damage, regeneration of a peak-valley drive file from an edited histogram can give very substantial speed increase factors to the point where impractical tests become practical.

A major limitation is that these techniques only apply to single channel drive systems.

Editing in the Frequency Domain

It has been common for component test drive signals to be low pass filtered on the basis that high frequency cycles have small amplitudes and are therefore not damaging. Even more common is the practice of low pass filtering at the maximum frequency that the servo hydraulics can achieve. It should be remembered that frequency filtering does not shorten the time series as the number of points is the same and also effects due to attenuation, imperfect filter roll-offs and possible phase shifts can falsify the non-damaging assumption. Fatigue test life prediction by analysis before and after filtering should be used to confirm the validity of the operations. Better still, it is possible to assess the correlation of damage with frequency to determine the optimum filtering strategy.

Long-term data may in fact be captured as frequency spectra and a spectrum may be edited prior to regeneration to a time series of a chosen length with the required frequency content. This technique is not recommended as the time series regenerated from a frequency spectrum does not have the same fatigue life, usually it is considerably longer.

Successful fatigue editing is also possible by combination methods. As an example, frequency correlated damage based filtering can remove cycles whose frequency cannot be achieved and the resulting filtered multi-channel time series set can be further processed in time correlated damage editing to produce reduced time series as the first set of targets for iterative transfer feedback control.

All the fatigue based editing techniques presented are currently available in commercial software tools.

Application to a Vehicle Axle

Problem Description

Combined Structural and Powertrain Road Load Simulator – A full vehicle suspension module durability test is required with both structural and powertrain real time inputs. The test module includes all components rearward of the transmission flange to the rear tires. Items included in the test module are drive shaft, rear axle (beam or independent rear suspension), leaf springs, half-shafts, stay-bar, shocks, upper and lower control arms, etc.

The test machine is a Schenck Pegasus road load simulator with eleven control channels (Figure 1). The channels are fore/aft, lateral, vertical and brake for the left and right, and left wheel speed, differential speed and input driveshaft torque. Four hydraulic actuators are used to simulate the structural durability and three AC dynamometers are incorporated to induce the powertrain durability.

This test scenario presents a challenge, with the interaction of the fast responding hydraulic system (60 Hz) and the slower dynamometer system (5 Hz). This problem is critical, and must be considered by the data editing technique. A machine out-of-control condition referred to as 'ringing' can occur when the dynamometers cannot respond quickly enough to the command signal. Conversely, introducing a delay to enable the dynamometers to respond is unsuitable for the faster responding hydraulic system.

Even though durability testing on a road load simulator is much faster and less expensive than the equivalent test on a proving ground, it is still a time consuming and (relatively) expensive process. To develop each minute of the test rig drive file requires about 30 minutes of developmental runtime on the machine. To insure reliability and statistical confidence a minimum of three samples need to be tested, and they must all pass for design sign-off purposes. If a sample fails prior to the completion of its target durability life, the failed component must be refined and the test repeated. This loses valuable development and testing time.

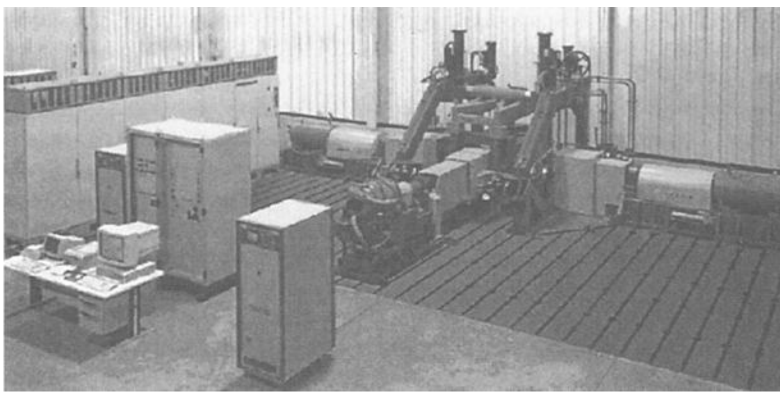

FIG. 1 — *Combined structural and powertrain test rig.*

FIG. 2 — *Instrumented axle.*

To provide a representative durability test, the road load simulator is driven by the real time histories recorded from the proving ground. The drive files are generated after removing the non-damaging or minimally damaging sections of data by using fatigue-editing techniques.

Data Analysis

Road Load Data Description - The data acquisition exercise acquired 24 channels of data, for 30 different sections of the durability test track. The data channels included two wheel force transducers, acquiring forces F_x, F_y, F_z, moments M_x, M_y, M_z, and wheel speed from the rear wheels. Load cells mounted at the axle control arm brackets measured the structural input loads into the axle. Two strain gage rosettes measured strains in critical areas, identified from finite element analysis, on the rear beam axle (Figure 2).

The example time histories are from a 'potholes and bumps' test surface, and were recorded for about 30 minutes. The full time histories for the input torque, left wheel vertical load and left wheel speed are shown in Figure 3a, and a close-up in Figure 3b. The full time history shows a number of periods where the vehicle has stopped, the wheel speed has dropped to zero, and the close-up view focuses on one of these periods. This zoom-in view shows the instantaneous step changes in torque, wheel load and wheel speed.

The corresponding strains for one of the rosette strain gages are shown in Figures 4a and 4b. The full time history shows the periods of high strain values, separated by periods of low strain levels. The close-up view shows that the high wheel vertical loads cause the high strains.

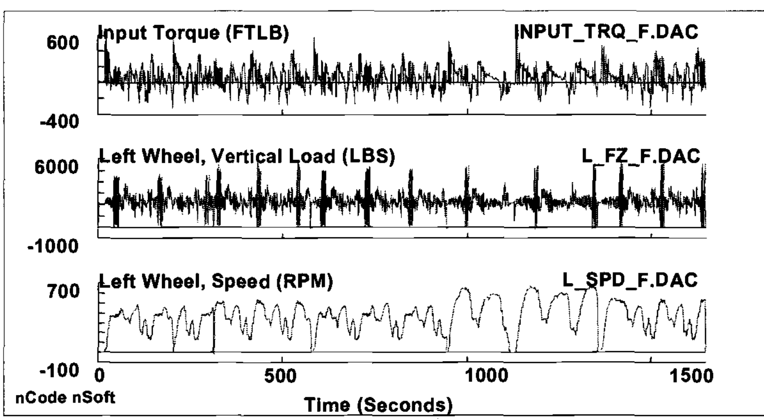

FIG. 3a — *Torque, load and speed.*

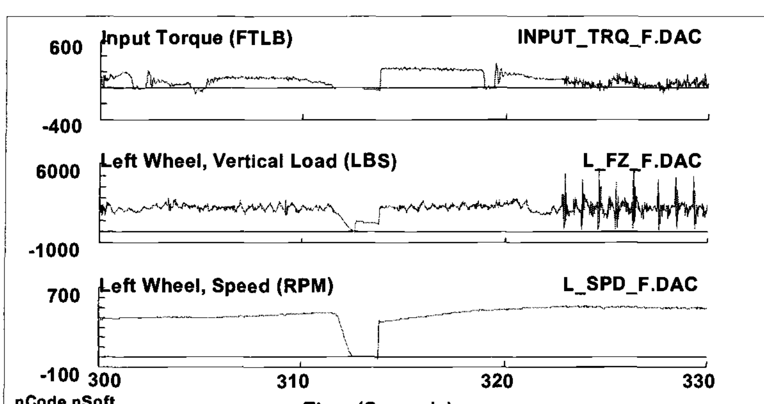

FIG. 3b — *Torque, load and speed (close-up).*

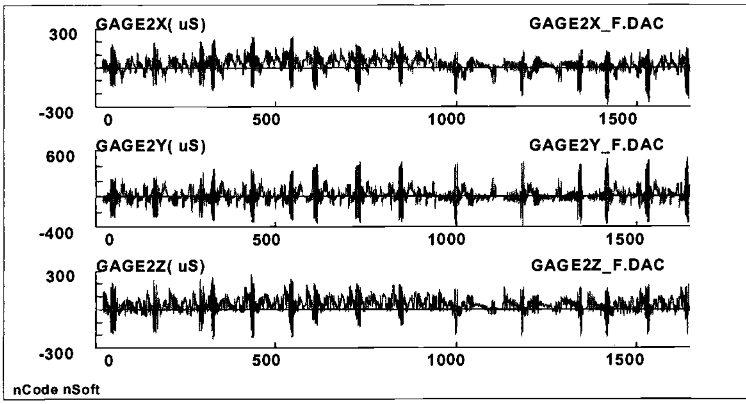

FIG. 4a — *Rosetteg gage 2.*

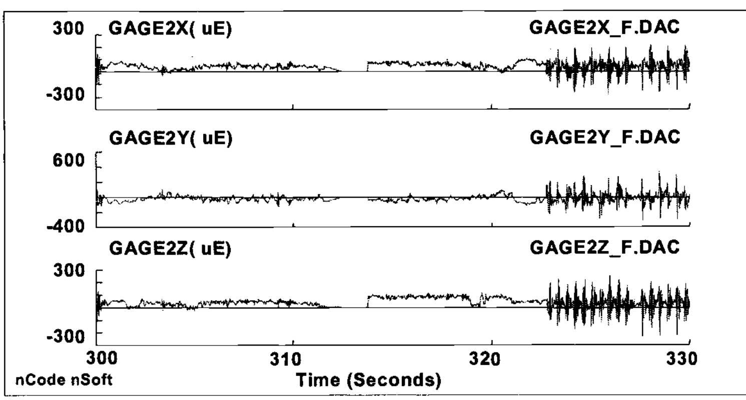

FIG. 4b — *Rosette gage 2 (close-up).*

Complex Loading Assessment - Vehicle suspension / chassis components are subject to multiaxial loads, induced by the vehicle powertrain (engine, gear shift, acceleration, etc), road profile (potholes, corners, etc), and the vehicle inertia. The road load-induced strains are collected using rosette strain gages. A local strain damage model is used to calculate the time-correlated-damage of the rosette strains. To better simulate the material fatigue behavior the component/material fatigue damage model must consider the multiaxiality effect of the loads.

The multiaxial loading case can be divided into two categories, with increasing complexity: proportional and non-proportional cases.

For proportional loading cases, the principal stress directions are constant; thus, equivalent stresses and strain would be calculated from the applied loads (Von Mises, Tresca, Maximum Principal Strain, etc). Many well-documented damage models are available, and could be used to solve such a loading case.

On the other hand, for the non-proportional loading case, both the principal directions and the biaxiality ratio (considering the surface, where fatigue cracks usually initiate) vary in time. All known traditional Uniaxial Strain Hardening models (Neuber, Seeger-Beste, and Mertens-Dittman) fall short of modelling the multiaxiality strain hardening behaviour of the material. The multiaxial strain hardening is modelled using Glinka's algorithm [1] for the implementation of the Mroz-Garud model [2,3].

An analysis of the measured rosette strain gages shows a complex loading environment, which is multiaxial non-proportional. Figures 5a and 5b show this through the wide distribution of biaxiality ratio and the principal angle plots versus the Maximum Principal Strain values.

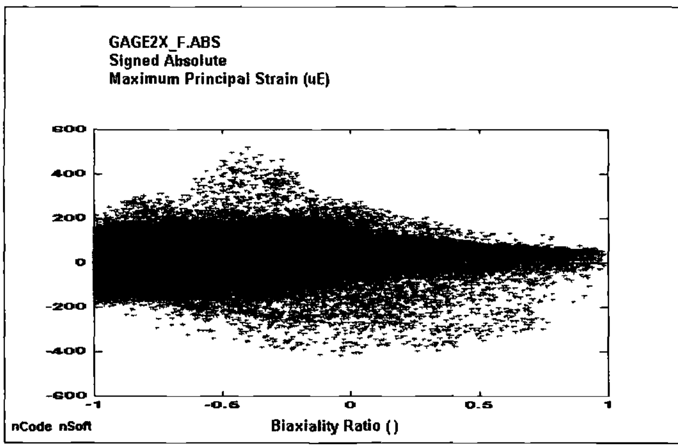

FIG. 5a — *Biaxiality ratio distribution.*

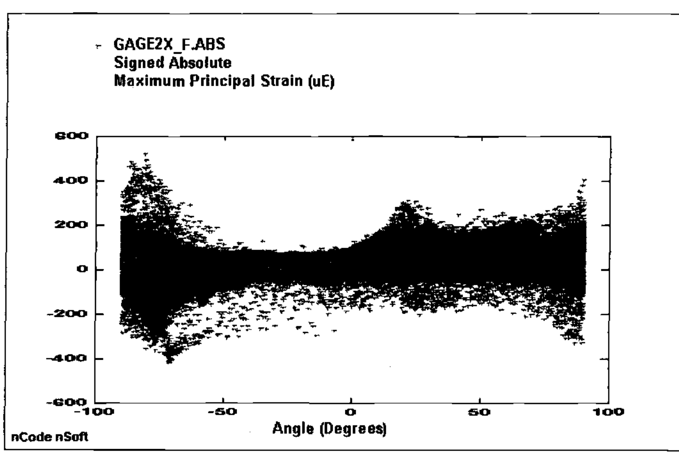

FIG. 5b — *Principal angle distribution.*

Fatigue Analysis

For this complex loading environment, a simple uniaxial fatigue damage model is too non-conservative to analyze these strain gage signals. To calculate fatigue life from a strain gage rosette using a uniaxial damage model requires either the signed absolute maximum principal strain or the signed shear strain (Tresca). Table 1 shows a comparison of predicted life using the Wang Brown multiaxial fatigue damage model [4] versus that of using the local strain uniaxial fatigue damage model.

Table 1 — *Predicted life using multiaxial and uniaxial models.*

Fatigue Damage Model	Predicted Life (repeats)
Multiaxial Fatigue Damage Model (using Wang-Brown)	1.81E8
Local Strain Uniaxial Fatigue Damage Model (using Signed Absolute Maximum Principal Strain)	9.88E8
Local Strain Uniaxial Fatigue Damage Model (using Signed Shear Strain)	6.73E8

Because the multi-axial damage model predicts shorter service life, it may be appropriate to use the Wang-Brown multiaxial fatigue damage model for data editing.

Time Correlated Damage Analysis — The multiaxial material fatigue behavior is strain path sensitive, therefore damage calculations require the rosette strain history files collected at the test track. This calculation procedure includes the loading sequence effect. Computing the fatigue life for small time slices across the whole data file and plotting the results in the time domain, result in the Time-Correlated-Damage file. Because two rosette gages were used during this test, two Time-Correlated-Damage files were generated. Both files showed that there were large sections in the data that produced no or very minimum damage. Common, non-damaging sections of both Time-Correlated-Damage files are filtered out using a cut-off damage window. Breaks in the road load data files are joined using an advanced connection function that considers both the real time test rig capabilities and the road load data frequency content.

Using a similar Y-axis scale, Figure 6a shows the time correlated damage. This highlights the difference in damage magnitude between the multiaxial and the uniaxial analysis. The local strain uniaxial damage model uses Rainflow cycle counting to identify fatigue cycles, and uses the Neuber model to calculate the local stresses and strains. The Wang-Brown multiaxial damage model identifies individual reversals, using a multiaxial Rainflow algorithm to compute the stresses from the measured strain values. This model is strain path sensitive, therefore the sequence of loading cycles is considered.

Figure 6b shows the time-correlated-damage as a percentage of the total. This shows the relative difference in damage magnitude occurring at different times throughout the time history. This difference in damage occurrence in time is due to the loss of damage ranking when using uniaxial damage approaches (Rainflow Counting), whilst the loading sequence is considered when calculating multiaxial damage. If the uniaxial damage model is used in a multiaxial loading environment damaging sections of the time history may not be identified correctly, and may not be retained during fatigue editing.

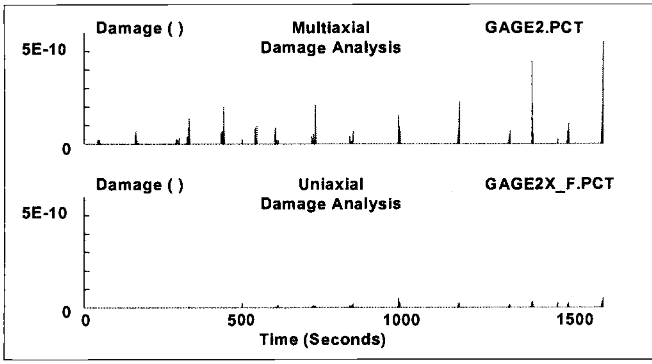

FIG. 6a — *Time correlated damage magnitude difference.*

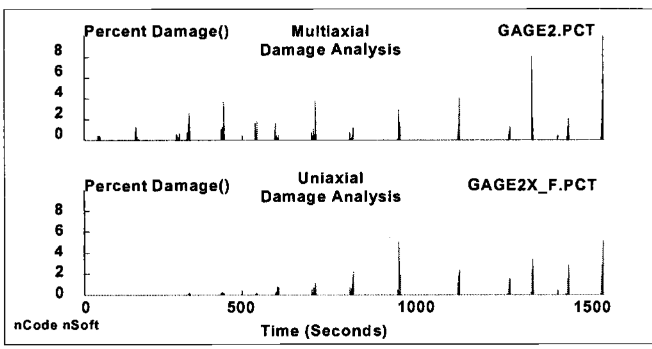

FIG. 6b — *Time correlated damage ranking difference.*

Joining Function for Combined Chassis and Powertrain Testing — The requirement for this application is to use a joining function suitable for the differing dynamics and response characteristics of the drive channels without altering the data frequency content. The hydraulic actuators have a frequency response of 60 Hz. The AC dynamometers are limited to 5 Hz.

A short join window is suitable for the hydraulic actuators, but is unsuitable for the dynamometers. It could exceed the capabilities of the test rig and will result in machine-out-of-control condition that may damage the test rig. A long join window is suitable for the dynamometer, but will introduce a pause into the hydraulic actuators changing the dynamics of the structural test.

The joining function used is based on a sine or linear overlap average of data points. This uses existing non-damaging data immediately succeeding and preceding the time windows to be joined. Two time windows are necessary to define the joining function. The first, the join time window, defines the overall length of the join. It has the same length in time for all data channels to ensure the synchronization of all time histories. The second, the overlap time window, defines a time period, inside the join time window, where the overlap function is applied. This overlap time window could be defined on a channel-by-channel basis. It provides a channel dependent overlap time window, within a fixed join time window. The size of the overlap window reflects the rate of change of the loading channel it is associated with. An overlap time window of the size of the join time window is needed to blend slow response channels, whilst only a section of the join time window is needed to overlap fast response signals.

This is shown graphically for a slow response time history, vehicle speed, in Figures 7a and 7b, and for a fast response time history, wheel load, in Figures 8a and 8b.

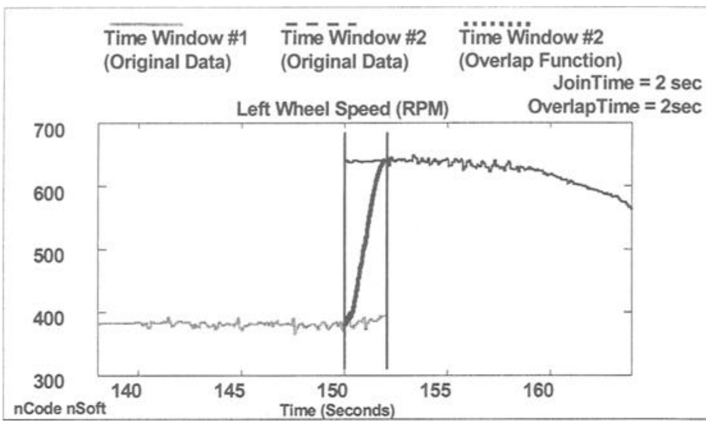

FIG. 7a — *Slow response speed channel first window, join function and second window.*

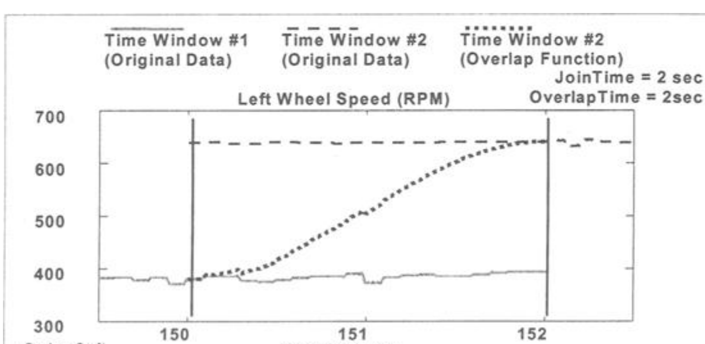

FIG. 7b — *Join function (close-up) join time=2 seconds overlap time=2 seconds.*

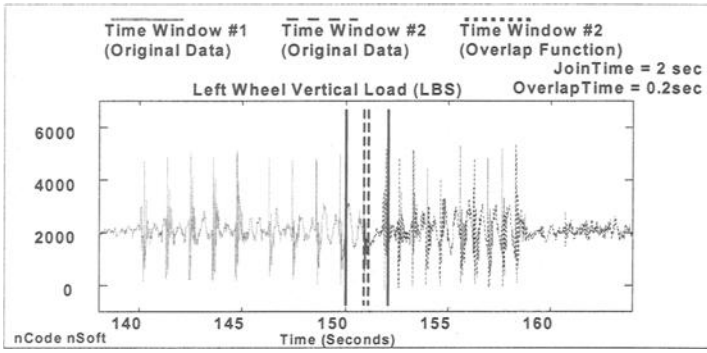

FIG. 8a — *Fast response load channel first window, join function and second window.*

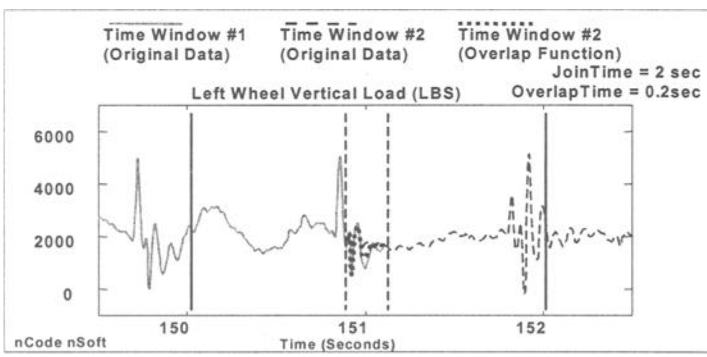

FIG. 8b — *Join function (close-up) join time=2 seconds overlap time=0.2 seconds.*

The benefit of using this technique is the ability to create joining functions that are suitable for data with widely different frequency characteristics without or minimally changing frequency content of the data channels. This process insures that there is no change in the failure modes between the test track and the laboratory durability tests.

Some of its advantages over the traditional join functions are shown in Figures 9, 10, and 11. In Figure 9 the retention of a damaging wheel input load cycle is shown. If a simple linear or half sine join function had been used, this wheel input load cycle would have been omitted. Using the linear or half sine overlap, with Join Time=2 seconds and Overlap Time=2 seconds would retain only 50% of the magnitude of the cycle. The full load cycle was retained by using the overlap function and the inner overlap window, Join Time=2 seconds and Overlap Time=0.2 seconds.

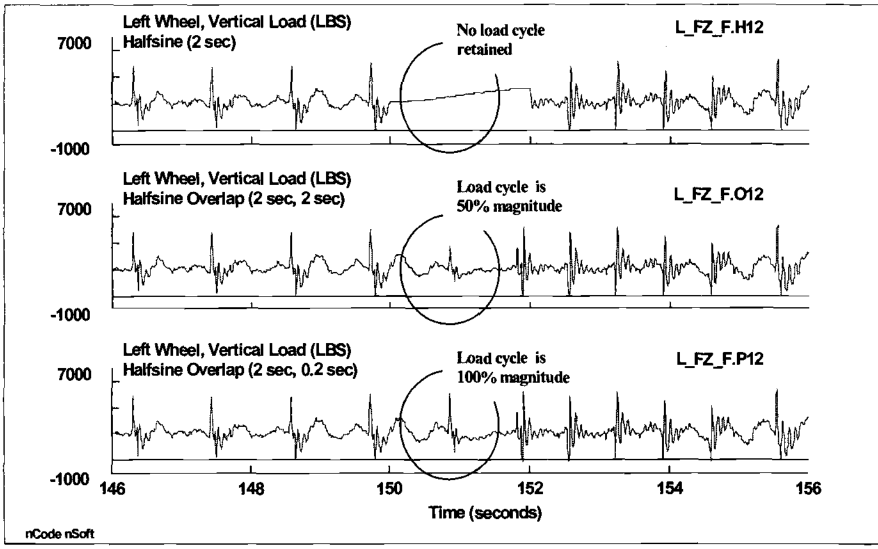

FIG. 9 — *Retaining load cycle.*

Using a simple half sine join function to connect damaging sections of the time history can exceed the maximum slew rate (machine capability) of the test rig. An example of this condition is shown in Figure 10. Therefore, the rig cannot duplicate the durability data files. As a result, both the test rig and the tested components will be subject to high artificial loading spikes that will damage the expensive test rig, and produce unrealistic component failure modes. On the other hand, using the half sine overlap technique, the rig is faithfully capable of reproducing the simulation time history with on line real time iterative feedback. Unrealistic spikes are now minimally induced into the system. This advanced joining function reduces the wear and damage to the test rig, and improves the test track to laboratory test simulation.

Another advantage is to keep real data that would otherwise be discarded. Figure 11 shows a good example of how the smooth half sine join is unrepresentative of the real road load input data. The overlap half sine join gives a better representation of the real road load inputs, and improves the correlation between the test track and the laboratory.

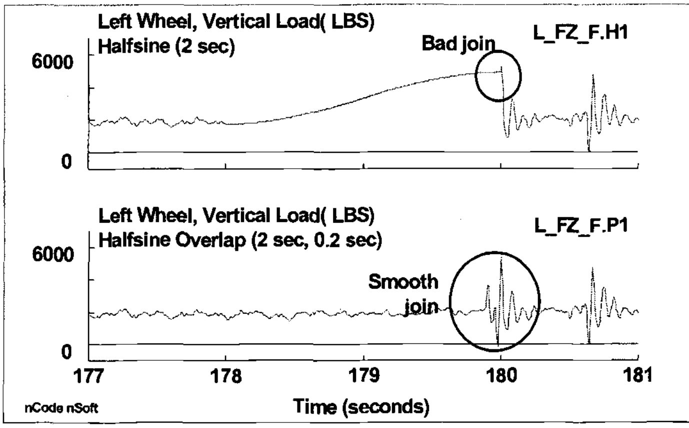

FIG. 10 — *Overlap half sine function eliminates artificial loading spikes.*

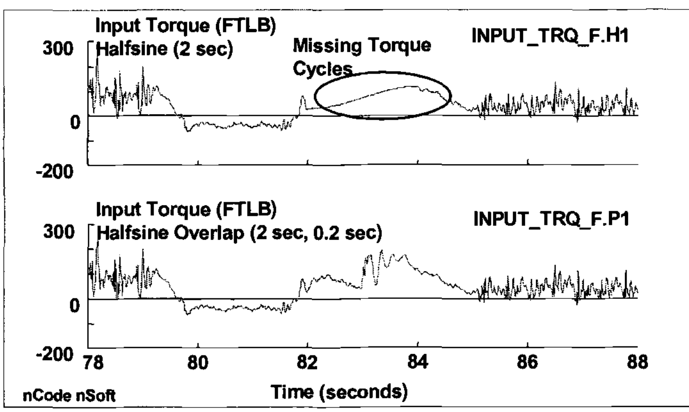

FIG. 11 — *Overlap half sine function retains real load inputs.*

Results

Time Domain Damage Comparison - To have a valid editing technique, the damage content of edited data files should be as close as possible to the damage content of the original data files. Hence, the damage calculations on the edited files must account for any artificial damage induced into the tested components.

Table 2 below shows one section of the durability strain data files and illustrates the damage content before and after data editing. Using a damage time window of 20 seconds, a join time of 0.8 seconds and an overlap time of 0.2 seconds, the original file length, in time, was reduced by a factor of 5. The predicted fatigue life for the original and edited files was calculated using the Wang-Brown multiaxial damage model with mean stress correction. Almost all of the original damage, 99.4% to be precise, was retained in the edited data file.

Table 2 — *Predicted fatigue life before and after editing.*

Data Files	Data Length (seconds)	Predicted Life (repeats)
Original	1650	1.81E8
Edited	330	1.82E8
	Reduction Time Factor = 5	% Damage Simulation = 99.4%

The same editing parameters are used to edit all of the test rig input channels. Figure 12 is a plot of the input axle pinion torque, axle left vertical load, and left wheel speed channels, both in their original length, and after data editing. The edited data files are used as load inputs into the multi-channel test rig for drive file generation, and for durability test acceleration. Using the edited time histories substantially reduces the iterative feedback duration needed for test rig drive file generation.

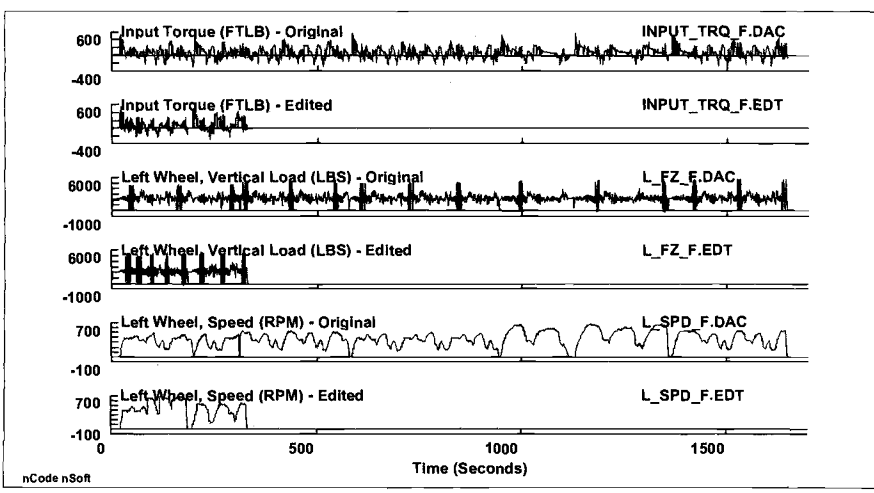

FIG. 12 — *Original and edited time histories.*

Frequency Domain Comparison — Comparing the time-correlated-damage content of edited time histories to that of the original durability files is not enough. For better test track to laboratory simulation purposes, edited data files must include similar frequency content as those of the original time histories. Thus, both edited and original data files are compared in the frequency domain. For correlation study purposes, the Power Spectra are calculated and compared in the overlay plots in Figure 13.

The frequency content of the original and edited files is maintained and the possibility of changing the failure mode is minimized.

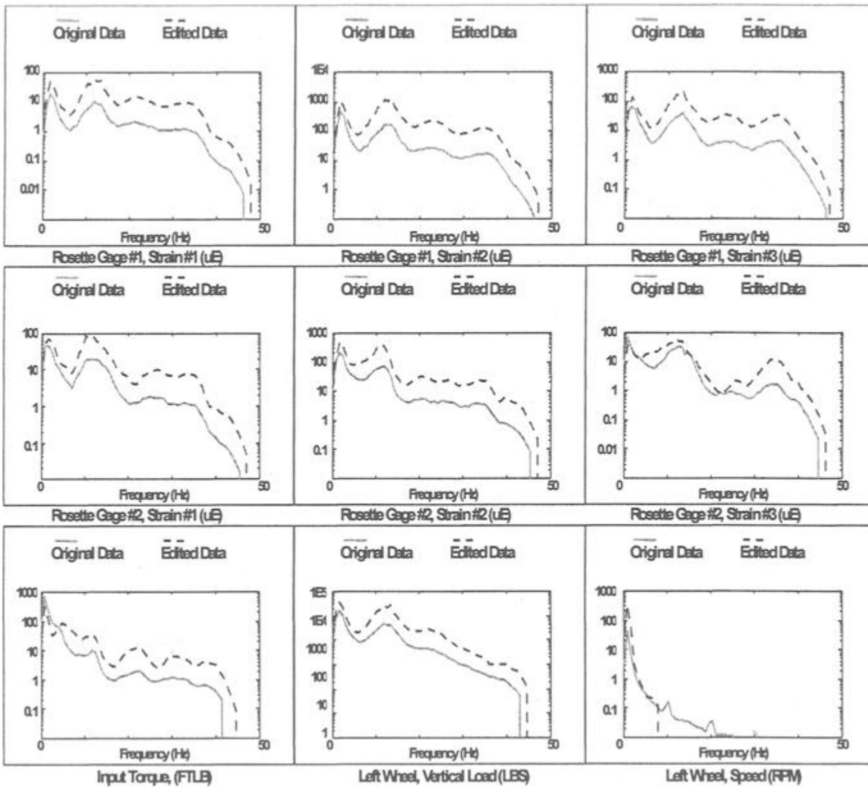

FIG. 13 — *Power spectrum comparison.*

Conclusion

The fatigue-based data editing procedure has proven to be very effective in accelerating the combined structural and powertrain durability test for vehicle components and systems. The use of an appropriate joining function maintains the damaging load cycles from the original road load data and prevents the introduction of artificial loading spikes. The absence of these artificial spikes reduces the wear and damage on the test rig and prevents unrealistic failure modes.

A 'Key Life' test is defined as the simulation of the test track or customer usage in the laboratory. The full durability Key Life test for the rear suspension modules contained a combination of road load data from many different test surfaces. This full test was accelerated from 34 days to 11 days of machine runtime. The 'potholes and bumps' test surface described here contributed a reduction of 11 days to 2 days. In addition, the time required to develop the test rig drive files is substantially reduced.

For reliability and statistical design confidence purposes, a batch of 3 suspension modules was tested on the Road Load Simulator. Before implementing the multiaxial editing technique, such a series of durability tests were prohibitively time consuming and expensive.

In the test, a proving ground crack was reproduced, in both location and failure mode, on the Road Load Simulator, illustrated in Figures 14 and 15.

FIG.14 — *Failure location on rear axle.*

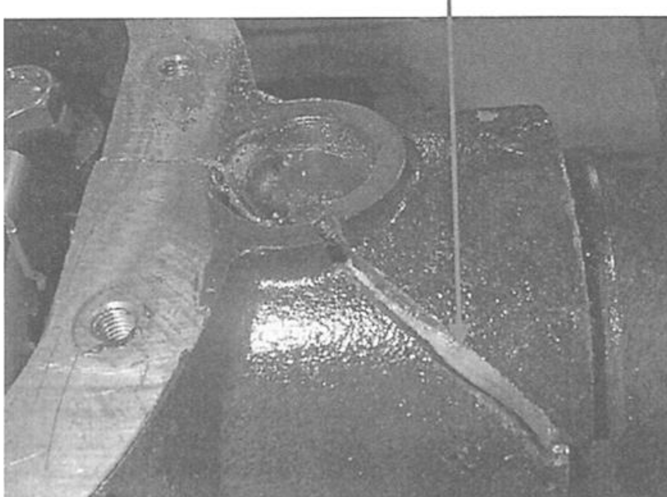

FIG. 15 — *Close-up of failure location.*

Acknowledgements

The authors would like to acknowledge the contribution of Visteon, Chassis Division, ADSE (Axle & Driveline Systems Engineering) Experimental Engineering Department and nCode International.

References

[1] Glinka, G., "Calculation of Inelastic Notch-Tip Strain-Stress Histories under Cyclic Loading," *Engineering Fracture Mechanics*, Vol. 22, No. 5, 1985.

[2] Mroz, Z., "The Description of Anisotropic Work Hardening," *Journal of Mechanics and Physics of Solids*, Vol. 55, No. 3, 1967.

[3] Garud, Y. S., "A New Approach to the Evaluation of Fatigue Under Multiaxial Loading," *Journal of Engineering Materials and Technology*, Vol. 103, 1981.

[4] Wang, C. H., Brown, M. W., "Life Prediction Techniques for Variable Amplitude Multiaxial Fatigue," *Journal of Engineering Materials and Technology*, Vol. 118, 1996.

OTHER APPLICATIONS

Journal of ASTM International, September 2004, Vol. 1, No. 8
Paper ID JAI19025
Available online at www.astm.org

A. J. McEvily,[1] *S. Ishihara,*[2] *and M. Endo*[3]

On the Causes of Deviation from the Palmgren-Miner Rule

ABSTRACT: Based upon considerations of fatigue crack growth, explanations for the observation that the Palmgren-Miner damage summation often deviates from unity can be established. It is assumed that the fatigue lifetime is taken up entirely in fatigue crack propagation, that is the number of cycles spent in crack initiation is a negligibly small fraction of the total lifetime. This assumption permits the fatigue lifetime to be analyzed in terms of a basic constitutive relation for the rate of fatigue crack growth that is given by:

$$\frac{da}{dN} = A(\Delta K_{eff} - \Delta K_{effth})^2$$

where a is the crack length, N is the number of cycles, A is a material-environmental constant, ΔK_{eff} is the effective range of the stress intensity factor, i. e., $K_{max} - K_{op}$, where K_{max} is the maximum value of the stress intensity factor in a loading cycle, K_{op} is the stress intensity factor at the crack opening level, and ΔK_{effth} is the effective value of the stress intensity factor at the threshold level.

Three variable amplitude loading conditions are considered: two-step loading, multiple two-step loading, and overload and underload loading. In each case, the cause for deviation from a Palmgren-Miner damage summation of unity is clarified.

KEYWORDS: fatigue crack growth, damage summation, variable-amplitude loading, two-step loading, multiple two-step loading, overloads, underloads

Introduction

A basic tool for the prediction of fatigue lifetimes under variable amplitude loading is the Palmgren-Miner rule, which is expressed as:

$$\sum_{i=1}^{i=i} \frac{n_i}{N_{fi}} = 1 \tag{1}$$

where n_i is the number of cycles at the i^{th} stress level, and N_{fi} is the number of cycles to failure at that stress level. Experience has shown that this summation, the damage factor, can often deviate significantly from unity, and empirical procedures are used to take this deviation into account for specific loading spectra. In the present paper we examine several causes for this deviation. Three cases will be considered. The first is the classical two-step test in which the damage factor is determined for both high-low (H-L) and low-high (L-H) loading sequences. In this type of test, a specimen is first cycled to a given fraction of its fatigue life at one stress amplitude, and then the stress amplitude is changed, and the specimen is cycled to failure at the second stress amplitude.

Manuscript received 23 April 2002; accepted for publication 19 June 2003; published September 2004. Presented at ASTM Symposium on Fatigue Testing and Analysis Under Variable Amplitude Loading Conditions on 29 31 May 2004 in Tour, France; P. C. McKeighan and N. Ranganathan, Guest Editors.

[1] Professor of Metallurgy, Institute of Materials Science, University of Connecticut, Storrs, CT.
[2] Professor of Mechanical Engineering, Toyama University, Toyama, Japan.
[3] Professor of Mechanical Engineering, Fukuoka University, Fukuoka, Japan.

The second case is that of multiple two-step tests in which the lower stress is below the fatigue strength of the material. The third case involves overloads and underloads. In each of these cases we will be dealing with fatigue crack growth, and the following constitutive relation for fatigue crack growth [1] will provide the basis for the analyses

$$\frac{da}{dN} = A(\Delta K_{eff} - \Delta K_{effth})^2 \tag{2}$$

where a is the crack length, A is a material-environmental constant, ΔK_{eff} is the effective range of the stress intensity factor, i.e., K_{max} -K_{op}, where K_{op} is the stress intensity factor at the crack opening level, and ΔK_{effth} is the range of the stress intensity factor at the threshold level.

Equation 2 has been modified [2] to take into account the following attributes of fatigue crack growth:

- In the very short fatigue crack growth range, the stress for propagation is controlled by the endurance limit of the material rather than by the long crack threshold condition.
- In the short crack regime, small scale yielding conditions are not applicable, and a modification for elastic-plastic conditions is needed.
- Crack closure in the wake of a newly formed crack is zero, but as the crack grows, the crack closure level increases to the level associated with a macroscopic crack in a distance of the order of 1 mm.

With these modifications, Eq 2 is written as

$$\frac{da}{dN} = A[(\sqrt{2\pi r_e F} + Y\sqrt{\pi a F})\Delta\sigma - (1 - e^{-k\lambda})(K_{op\max} - K_{\min}) - \Delta K_{effth}]^2 \tag{3}$$

where r_e is a material constant defined as $[\frac{\Delta K_{effth}}{\sigma_{EL}}]^2[\frac{1}{2\pi F(1 + \sqrt{2}Y + 0.5Y^2)}]$. This constant provides a link between the endurance limit (or the fatigue strength at 10^7 cycles) and the effective threshold level. The value of r_e is of the order of $1 \mu m$. F is given as $\frac{1}{2}(\sec \frac{\pi}{2}\frac{\sigma_{\max}}{\sigma_Y} + 1)$, and accounts for elastic-plastic behavior. Y is a geometrical constant, which, for example, is equal to 0.73 for a semicircular surface flaw. $\Delta\sigma$ is the stress range. The material constant k is an indicator of the rate of development of crack closure, and for steels may have a value of the order of 6000 m^{-1}. The symbol λ represents the distance a new crack has grown. In the case of a smooth specimen, it would correspond to the semi-length of a semi-circular surface flaw. In the case of a notch, it would be the distance measured from the tip of the notch, and in a case that will be treated herein, it is the distance measured from the tip of a fatigue crack that has been heat treated to be closure free. K_{opmax} is the crack closure level associated with a macroscopic crack. K_{min} is the minimum stress intensity associated with a particular loading cycle.

Equation 3 can be written in compact form as

$$\frac{da}{dN} = AM^2 \tag{4}$$

where M is the quantity within brackets in Eq 3. Equations 2–4 will be used in the following analyses.

Analyses

Two-step Tests

Figure 1 is a schematic diagram that is used to illustrate how different crack growth paths on the diagram for a high stress amplitude and for a low stress amplitude can lead to quite different damage summations. For an L-H test, the summation is greater than unity, whereas for an H-L test the reverse is true. Equation 3 predicts this type of crack growth behavior as shown in Fig. 2 [3], which presents the results of fatigue experiments carried out with the aluminum alloy 2017-T4 tested in a salt water environment. It is noted that if the Paris law were used as the constitutive relationship, this type of behavior would not be predicted, since all crack growth paths would then be expected to lie long a single line in Figs. 1 and 2.

Figure 3 [3] is a cumulative damage plot for these tests that compares the predicted behavior with experimental results. There is a reasonable degree of agreement between the predictions and actual behavior. This agreement stems from the inclusion of the ΔK_{effth} term in Eq 1. This term is of greatest influence on the crack growth paths in Figs. 1 and 2 at low stress amplitudes. It is noted that at the higher stress amplitudes there is much less of an effect of this term on the crack path, and Paris law crack growth behavior is approached.

Figure 4 [4] shows results obtained in air with smooth specimens of a 0.45 % carbon steel. In this case it was assumed that the entire fatigue lifetime was spent in fatigue crack growth, an assumption supported by the finding that fatigue cracks of 10 μm length have been observed by the replica method at less than 7 % of the fatigue life in the high cycle regime [4]. It is noted that in the L-H sequence there is an indication that coaxing had occurred, in as much as the life fraction at the second stress level often exceeded unity. This behavior was attributed to a higher rate of closure development, k, in the near threshold region where Stage I growth occurs rather than the usual 6000 m^{-1} [5].

Multiple Two-step Tests

Murakami and Matsuda [6] have carried out multiple two-step tests of a 0.46 % carbon steel specimens. The yield strength was 356 MPa, and the smooth bar endurance limit was 240 MPa. Each specimen was of circular cross-section, and prior to testing an artificial defect measuring 40 μm in diameter and 40 μm in depth was drilled into the surface before carrying out the test program. In one test sequence a fatigue crack was then grown from the defect to a length, $2a$, of 1000 μm, and the specimens were annealed at 873 K in vacuum to remove the prior cyclic history, and an S/N curve for these pre-cracked specimens was determined under R = −1 loading conditions. Figure 5 shows the results of these tests. The experimental value of the fatigue strength for these pre-cracked specimens is approximately 127 MPa.

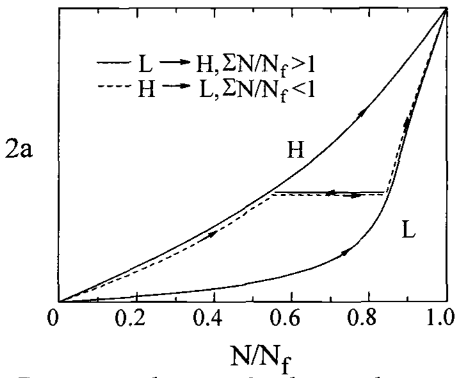

FIG. 1 *A schematic plot showing the expected crack growth behavior at low and high stress levels and* $\sum N_i / N_{fi}$ *values for two-step tests in the absence of a crack initiation period [3].*

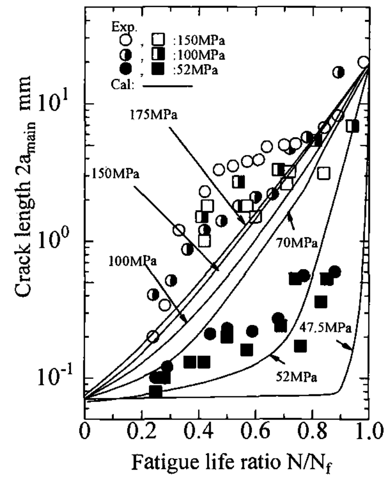

FIG. 2 *Experimental and calculated values of the crack length as a function of the ratio* N/N_f *for the aluminum alloy 2017-T4 at several stress amplitudes. Note that the lowest crack length, 2a, equals 70 μm, and that the grain size is 32 μm [3].*

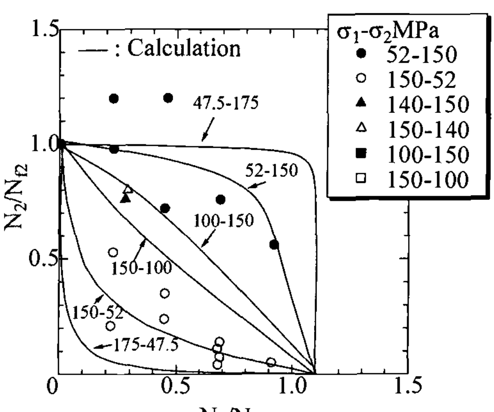

FIG. 3 *A cumulative damage plot showing a comparison between experimental and calculated values of* N_2/N_{f2} *for various combinations of high and low stresses for the aluminum alloy 2017-T4 tested in salt water [3].*

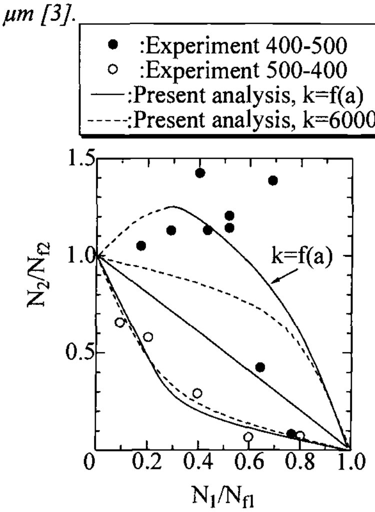

FIG. 4 *Experimental and calculated results for a 400 500 MPa L-H sequence and a 500 400 MPa H-L sequence [4].*

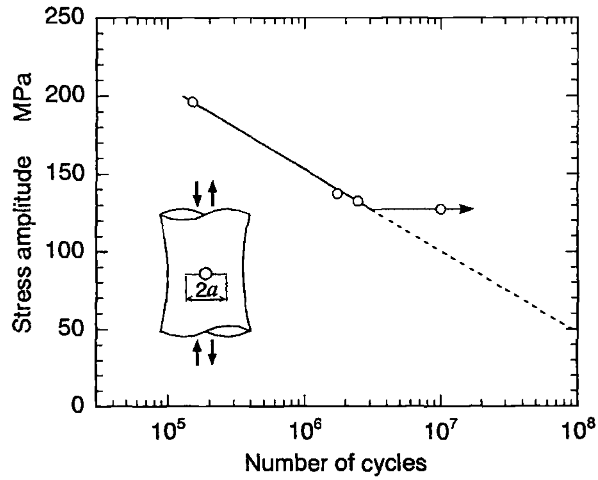

FIG. 5 *S/N curve for a 0.46 % steel containing an initial fatigue crack of length, 2a, equal to 1000 μm tested under axial loading at R = –1 [6].*

One of the two-step sequences used that we will analyze consisted of applying repeated blocks of cycles at R = –1, which were made up of one cycle at 196 MPa followed by 40 cycles at 68.6 MPa. This pattern was repeated until failure occurred. From Fig. 4, the life at 196 MPa is estimated to be 1.5×10^5 cycles. By extrapolation of the upper portion of the S/N curve to stresses below the fatigue strength, as indicated by the dashed line in Fig. 5, it is estimated that the fatigue life at 68.6 MPa is 4×10^7 cycles. This extrapolation procedure traditionally has been used in an attempt to account for the damaging effect of cyclic stress levels that are below the apparent fatigue strength. Figure 6 shows the dependency of the fatigue crack length, 2*a*, on a damage summation based upon the aforementioned lives at the two stress levels, as well as the crack growth curve at just the high stress level for comparison. Here n_H is the number of cycles at the higher stress level, and N_H is the number of cycles to failure at that level under constant amplitude loading conditions, etc. At failure, the value of the damage summation is 0.328, an indication that a stress amplitude well below the fatigue strength can bring about significant damage, for otherwise the summation should have exceeded unity.

In analyzing these results on the basis of Eqs 2 4, it was assumed that the elevated temperature heat treatment prior to the start of the two-step test had completely eliminated the original crack closure. Further, it was assumed that because the fatigue crack length, 2*a*, was 1000 μm in length at the start of the two-step test, the crack faces initially closed at zero stress, and in this case only tensile stresses propagated the crack.

In order to make the calculations, the following values were assigned to the material constants. $\Delta K_{effth} = 2.5\ \text{MPa}\sqrt{m}$, $K_{opmax} = 3.5\ \text{MPa}\sqrt{m}$, $k = 6000\ \text{m}^{-1}$. The value of r_e, based upon an endurance limit (smooth specimen) of 240 MPa and a yield strength of 356 MPa, was determined to be 1.2 μm. The value of the constant A was determined from the plot shown in Fig. 7, which shows the rate of fatigue crack growth obtained from the work of Murakami and Matsuda [6] as a function of the parameter M. A line of slope 2 has been drawn through the data points in accord with Eq 4, and A is related to the rate of fatigue crack growth where M = 1.0, namely $A = 5 \times 10^{-10} (\text{MPa}\sqrt{m})^{-2}$.

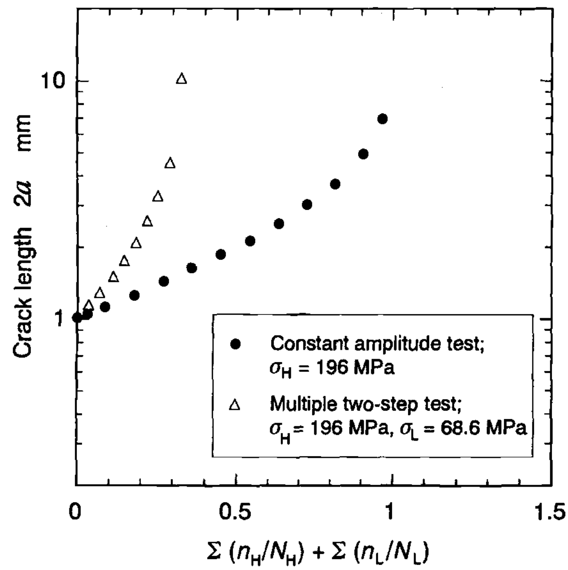

FIG. 6 *The fatigue crack length as a function of the damage summation for an initial crack length, 2a, equal to 1000 μm [6].*

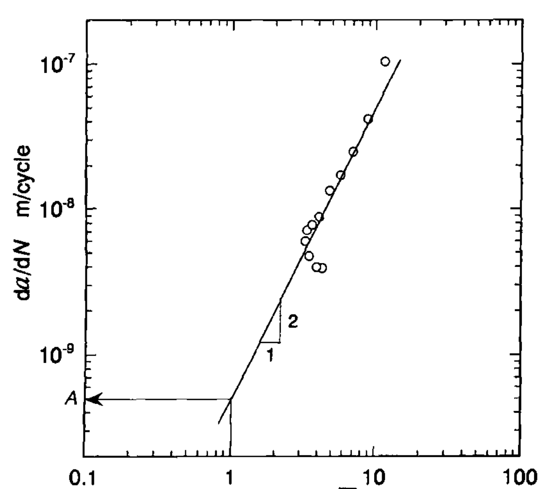

FIG. 7 *The rate of fatigue crack growth for a 0.46 % carbon steel specimen that contained an initial crack of length, 2a, equal to 1000 μm as a function of the parameter M.*

We next consider how the lower stress can act to reduce the damage factor to well below unity. First of all, it is recognized that initially the stress intensity factor, given for a semi-circular surface flaw as

$$K = 0.73\sqrt{\pi a}\ \sigma_a \tag{5}$$

where σ_a is the stress amplitude, equal to 1.98 MPa$\sqrt{m}$ at the 68.6 MPa level. This level is below the ΔK_{effth} value of 2.5 MPa$\sqrt{m}$, so we do not expect any crack propagation at this stress level, at least not until the crack reaches a length *2a* of 1.49 mm. However, prior to reaching that length, the lower stress has already done significant damage as seen in Fig. 6. We propose the damage caused by the lower stress is simply due to the reduction or elimination of crack closure. After each high cycle, the next 40 low cycles at R = –1 serve to erode roughness- induced crack closure. Therefore, the fatigue crack tip is not shielded and the crack can grow at a higher rate.

The results of calculations for constant amplitude loading as well as for two-step loading are shown in Fig. 8. For the constant amplitude test it was assumed that crack closure developed in accordance with Eq 3. For the multiple two-step test, two curves are plotted. One is for crack propagation only at the higher level but with zero crack closure. The other is for crack propagation at both levels, once the critical crack length for propagation had been reached at the lower level. In the latter case, the effects of any crack closure were neglected. It is seen that the experimental trends are followed to within a factor of two or so. Better agreement in the two-step tests could be achieved by introducing some level of crack closure, but for the purpose of understanding the role of the lower stress level, we think the point has been made. It is noted that Ueno et al. [7] found a somewhat similar effect by cycling silicon nitride below the threshold for large numbers of cycles. This led to a subsequent acceleration in fatigue crack growth rate above threshold, an effect that was attributed to a degradation of grain boundary bridging as the result of the large numbers of cycles that had been applied below the threshold level.

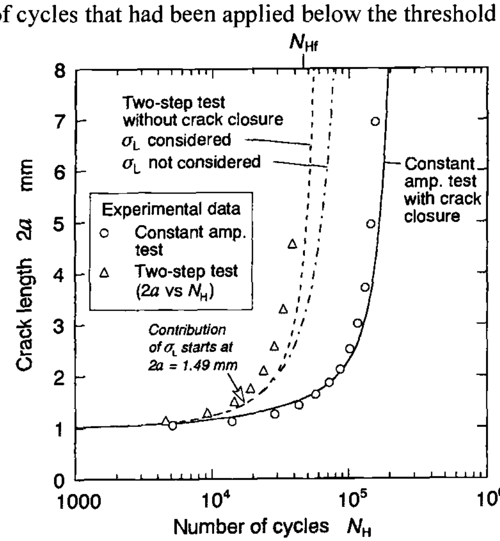

FIG. 8 *A comparison of experimental and calculated fatigue crack growth behavior under constant amplitude and two-step loading. (Each loading block was made up of one high cycle and 40 low cycles).*

The analysis given above indicates that a fatigue lifetime prediction for variable amplitude loading based upon crack propagation considerations will provide a more mechanistically consistent lifetime prediction than the use of currently employed damage summation procedures. Further, it is proposed that a crack growth analysis that neglects the effects of crack closure can provide a conservative estimate of the fatigue lifetime for design purposes under variable amplitude loading conditions.

Overloads and Underloads

For many loading spectra, the range of loading may not be sufficient enough to exert any significant loading history effect. For example, Barsom [8] found that the average fatigue crack growth rate under the moderate variable-amplitude, random-sequence load spectra associated with bridge structures could be expressed as a function of ΔK_{rms}, where ΔK_{rms} is the range of the root mean square stress intensity factor. It has been shown that the rms approach is equivalent to a second power of ΔK law, which in turn can be related to the crack tip opening displacement (CTOD) [9]. In other cases, however, there may be tensile overloads or compressive underloads, which can introduce load history effects that significantly affect the fatigue lifetime. Wu and Schivje [10] have shown that a 100 % overload at R = 0 could lead to a two-fold increase in the crack growth life of an aluminum alloy. However, when the overload was followed by an underload of 80 %, the net gain in the fatigue crack growth lifetime was reduced significantly. In the case of repeated spike overloads applied every 2500 cycles at R = 0 to an aluminum alloy, Dawicke [11] found that the fatigue life could be extended by a factor of 100 for 200 % spike overloads. Interestingly enough, the effect of still higher overloads was not as great. When Dawicke [11] applied spike underloads following each overload, the fatigue lifetimes were reduced relative to those observed for peak overloads alone. In fact, when the ratio of the spike underload stress to the peak constant amplitude stress level was –300 %, the fatigue lifetime was slightly reduced relative to the constant amplitude lifetime. The effect of underloads can largely be attributed to a reduction in the crack closure level, a topic that has been explored in depth by Topper et al. [12]. Further, Newman [13] has shown the Fastran computer program, which employs plasticity-induced crack closure, can be used to predict the observed behavior. Obviously, these sorts of history effects can have a significant effect on the damage summation.

Next we consider the mechanism responsible for the retardation in crack growth rate in sheet material following an overload. Most studies on the effect of a tensile overload on fatigue crack growth behavior have been carried out at baseline R levels greater than zero. Under these circumstances, the overload can lead to an initial acceleration in the rate of fatigue crack growth that is followed by a period of delayed retardation in the crack growth rate. After reaching a minimum value in fatigue crack growth rate, the crack then accelerates and returns to the baseline rate of crack growth as the crack reaches the limit of the overload affected zone. This type of behavior is depicted in Fig. 9 [14]. It is now known that the overload effects in sheet material are primarily associated with the plane stress regions at the specimen surface [14 16]. When the overload is applied, there is a contraction of material in the thickness direction in the plane stress region at the crack tip. This contraction results in additional material being present in a region just below the original surface, and when the load is reduced following the overload, this excess material goes into compression over a distance ahead of the crack equal to the extent of the overload plastic zone size. As a result, these compressive residual stresses exist over a much greater volume of material at the surface than was the case prior to the overload. One consequence is that after the crack has grown into the overload plastic zone, and the specimen is reloaded in tension, there will be two crack opening events as indicated in Fig. 10 [16] for two specimen thicknesses. The first of these corresponds to crack opening everywhere in the wake of the crack front except in the surface overload zone. This opening level is less than that which prevailed prior to the overload due to crack tip blunting caused by the extra material in the region just below the original surface. The second and higher opening event occurs as the crack opens in the overload zone at the surface. Note that this upper opening event will not be observable immediately after the overload. Some growth of the crack is required before it can be detected because initially there is no wake behind the crack tip at the surface following the overload, since the crack has been blunted by the overload. In fact, immediately after the overload, the crack growth rate of the crack at the surface may be higher than the baseline crack growth rate because of the lack of crack tip shielding. However, as the crack advances, plasticity-induced crack closure will be developed in the wake of the crack at the surface due to the relaxation of the overload compressive stresses, and the rate of fatigue crack growth will follow the trend indicated in Fig. 9. The rate of growth following an overload has been analyzed on the basis of Eq 2 at base line R values ranging from 0 0.5, and good correlation has been found [14,16,17]. As might be expected, the overload effect is much more pronounced for thin specimens than thick specimens. Further, the effect of the overload is less pronounced as the R level is increased.

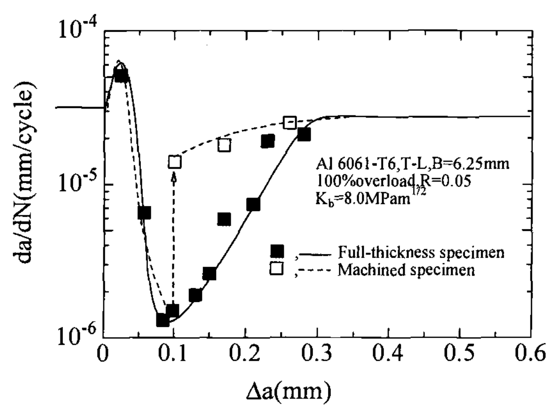

FIG. 9 *Variation in fatigue crack growth rate in the aluminum alloy 6061-T6 following a 100 % overload at $R = 0.05$. The baseline ΔK level was 8 $MPa\sqrt{m}$. Also shown is the effect of machining away the surface layers at the point of minimum crack growth rate on the subsequent crack growth behavior* [14].

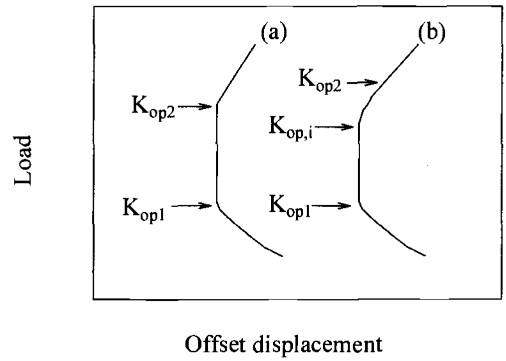

FIG. 10 *A schematic of load-offset displacement plots following an overload after the crack has penetrated into the overload plastic zone:* (a) *for a 6.35 mm thick specimen, and* (b) *for a 0.3 mm thick specimen [16].*

If instead of a tensile overload a compressive overload is applied, the subsequent fatigue crack growth behavior will be quite different. Topper and DuQuesnay [12] have shown that at a baseline cyclic level of R = –1, a sufficiently high compressive underload leads to an immediate reduction in the crack opening level. As a result, the fatigue crack growth rate is increased to a maximum immediately after the compressive underload had been applied before gradually decreasing to the normal rate associated with the baseline level. In these tests, crack closure at the baseline level is through-thickness in nature and is roughness-induced. The compressive overload serves to flatten the asperities on the fracture surface, thereby reducing the crack opening level and increase ΔK_{eff}.

It has been observed recently that a tensile overload followed by cycling at R = –1.5 can lead to an acceleration in the fatigue crack growth rate [18]. At zero load immediately following a tensile overload, the plane-stress overload plastic zone is in a state of compression. As the compressive load is increased in R = –1.5 loading, the compressive stress in the plane-stress plastic zone is increased, and under the influence of a sufficiently high level of compressive loading, the material within this plastic zone can reach the flow stress in compression. When this occurs, material in this zone will flow outward in the lateral direction, i.e., just the opposite of what occurred during the tensile overload. That the material flows in the outward direction is evidenced by an increase in specimen thickness, and the propping-open of the crack due to the stretching in the plane region that had been induced by the overload will be reduced or eliminated. There now will be less material in the region just below the original surface of the specimen, and as the specimen is unloaded from the minimum stress level to the zero stress level, the surface zone will go into a state of residual tension rather than compression. As a result, crack closure will be lost, and the fatigue crack growth rate will accelerate. Therefore the magnitude of the overload as well as the baseline level of cycling can both have a marked effect on the magnitude of the damage summation.

Conclusions

1. In a two-step test, variations of the damage summation from unity occur because of stress-dependent differences in the crack growth path as a function of n_i/N_{fi}.
2. In multiple two-step tests of fatigue-cracked specimens where the lower stress amplitude is below the fatigue strength, a major influence of such a stress level can be to reduce the crack closure level, thereby allowing faster rate of fatigue crack growth at the higher stress level.
3. The retardation effect associated with an overload in sheet material is largely due to the lateral contraction of material in the plane stress overload zone. The acceleration effect associated with an underload is due to a reduction in the crack closure level caused by the flattening of asperities during the underload.
4. The accelerating effect found during cycling at $R = -1.5$ following an overload is associated with the lateral expansion of material in the overload plastic zone.
5. Under many variable amplitude loading conditions, fatigue lifetime predictions based upon fatigue crack growth considerations can provide a more rational and accurate assessment than the Palmgren-Miner rule.

Acknowledgments

The authors express their thanks to Professor Y. Murakami of Kyushu University for helpful discussions during the course of this investigation.

References

[1] Minakawa, K., Levan, G., and McEvily, A. J., "The Influence of Load Ratio on Fatigue Crack Growth in 7090-T6 and IN9021-T4 P/M Aluminum Alloys," *Metallurgical Transactions*, Vol. 17A, 1986, pp. 1787 1795.

[2] McEvily, A. J., Eifler, D., and Macherauch, E. "An Analysis of the Growth of Short Fatigue Cracks," *Engineering Fracture Mechanics*, Vol. 40, 1991, pp. 571 584.

[3] Ishihara, S., McEvily, A. J., and Shiozawa, K., "A Fatigue-Crack Growth Based Analysis of Two-Step Corrosion Fatigue Tests," *Fatigue and Fracture of Engineering Materials and Structures*, Vol. 18, 1995, pp. 1311 1321.

[4] Ishihara, S. and McEvily, A. J., "Analysis of Small Fatigue-Crack Growth under Two-Step Loading Conditions," *Small Fatigue Cracks*, K. S. Ravichandran, R. O. Ritchie, and Y. Murakami, Ed., Elsevier, Oxford, 1999, pp. 389 401.

[5] Ishihara, S. and McEvily, A. J., "A Coaxing Effect in the Small Fatigue Crack Growth Regime," *Scripta Materialia*, Vol. 40, 1999, pp. 617 622.

[6] Murakami, Y. and Matsuda, K., "Cause of Unsuccessful Results of Miner's Rule," *Small Fatigue Cracks*, K. S. Ravichandran, R. O. Ritchie, and Y. Murakami, Ed., Elsevier, Oxford, 1999, pp. 119 130.

[7] Ueno, A., McEvily, A. J., and H. Kishimoto, "The Decrease in the Width of Hysteresis Loops and the Compliance Change Associated with the Grain Bridging Degradation under Cyclic Loading," *Proc. 5th Japan International SAMPE Symposium*, 1997, pp. 593 598.

[8] Barsom, J. M., "Fatigue Crack Growth under Variable Amplitude Loading in Various Bridge Steels," *Fatigue Crack Growth under Spectrum Loads, ASTM STP 595*, ASTM International, West Conshohocken, PA, 1976, pp. 217 235.

[9] McEvily, A. J., Discussion to Ref. 8.

[10] Wu, Y. and Schivje, J., "Fatigue Crack Closure Measurements on 2024-T3 Sheet Specimens," *Fatigue and Fracture of Engineering Materials and Structures*, Vol. 18, 1995, pp. 917 921.

[11] Dawicke, D. S. "Overload and Underload Effects on Fatigue Crack Growth Behavior of Aluminum Alloy 2024-T3," *NASA CR-201668*, 1997.

[12] Topper, T. H. and DuQuesnay, D. L., "The Effect of Overloads in Service Load Histories on Crack Closure and Fatigue Damage," *Fatigue 2001*, P. de Mattos Pimenta, L. C. J. Ricardo, and A. F. Camarao, Eds., SAE Brazil, 2001, pp. 43 54.

[13] Newman, J. C., Jr., "Crack Growth under Variable Amplitude and Spectrum Loading in 2024-T3 Aluminum Alloys," *High Cycle Fatigue in Structural Materials*, W. O. Soboyejo and T. S Srivatsan, Eds., TMS, Warrenville, PA, 1997, pp. 109 121.

[14] McEvily, A. J. and Yang, Z. "The Nature of the Two Opening Levels Following an Overload in Fatigue Crack Growth," *Metallurgical Transactions*, Vol. 21A, 1991, pp. 2717 2727.

[15] McEvily, A. J., Jr., "Current Aspects of Fatigue," *Metal Science*, Vol. 11, (Nos. 8,9), 1977, p. 274.

[16] Bao, H. and McEvily, A. J., "The Effect of an Overload on the Rate of Fatigue Crack Propagation under Plane Stress Conditions," *Metallurgical Transactions*, Vol. 26A, 1995, pp. 1725 33.

[17] McEvily, A. J. and Ishihara, S., "On the Retardation in Fatigue Crack Growth Rate Due to an Overload; A Review," in *Fatigue 2001*, P. de Mattos Pimenta, L. C. J. Ricardo, and A. F. Camarao, Eds., SAE Brazil, 2001, pp.145 150.

[18] Makabe, C., McEvily, A. J., Yamauchi, A., and Purnowidodo, "Effects of Stress Ratio on Fatigue Crack Propagation Behavior After an Overload," *Proc. Conference on Advanced Materials and Performance*, Daegu, Korea, 2002, to be published.

Jean-Jacques Thomas,[1] André Bignonnet,[1] and Georges Perroud[1]

Fatigue Design and Experimentations with Variable Amplitude Loadings in the Automotive Industry

REFERENCE: Thomas, J. J., Bignonnet, A., and Perroud, G., "**Fatigue Design and Experimentations with Variable Amplitude Loadings in the Automotive Industry,**" *Fatigue Testing and Analysis Under Variable Amplitude Loading Conditions, ASTM STP 1439,* P. C. McKeighan and N. Ranganathan, Eds., American Society for Testing and Materials, West Conshohocken, PA, 2005.

ABSTRACT: The paper presented gives an overview of the various problems that should be addressed to take into account the variable amplitude loadings undergone by the car components. One of the most important point is that all the steps of the design procedure (including experiments and computations) should be consistent with each other in terms of damage. For some reasons (efficiency, robustness, capitalization,...), variable amplitude loading may be converted into damage equivalent loadings. Tools such as cycle counting ,damage summation including the mean value effect and rainflow extrapolation are therefore necessary. The paper shows how single component and full scale tests are related with both customer and test track measurements, and how these experimental data are correlated with predictive fatigue computations, including the statistical aspects for reliability purpose. The paper will illustrate that if the consistency mentioned above is guaranteed, then the variable amplitude fatigue computation (such as the ones proposed in commercial codes) is no longer useful. It requires therefore an analysis of the material behavior under variable amplitude loadings in the automotive context. One of the most important advantage of this approach is that under simple assumptions, the computations can be realized before any prototype could be driven on a track. It allows to shorten the developments delays. These assessments will be illustrated by various examples showing how the loadings are analyzed in the measurements stages, and how they are applied in the experimental and computation stages.

KEYWORDS: Stress-strength interference analysis, variable amplitude, fatigue, automotive

Introduction

Various problems should be addressed to take into account the variable amplitude loadings undergone by the car components. One of the most important point is that all the steps of the design procedure (including experiments and computations) should be consistent with each other in terms of damage. For some reasons (efficiency, robustness, capitalization,...), variable amplitude loading may be converted into damage equivalent loadings. Tools such as cycle counting ,damage summation including the mean value

[1] PSA Peugeot Citroën – Applied Mechanics Research Division – Route de Gisy – 78943 Vélizy Villacoublay Cedex – France.

how single component tests and vehicle tests are related with both customer and test track measurements, and how these experimental data are correlated with predictive fatigue computations, including the statistical aspects for reliability purposes. The paper will illustrate that if the consistency mentioned above is guaranteed, then the variable amplitude fatigue computation (such as the ones proposed in various commercial codes) is no longer useful. One of the most important advantages of this approach is that under simple assumptions, the computations representative of the vehicle life can be realized before any prototype could be driven on a track. It allows one to shorten development delays.

Consistency of the Design Procedure

Schematically, the fatigue design procedure of a complete car can be represented by a so called "V cycle" as shown in Figure 1. This figure shows on the top of the descending left branch that the customer usage of the car should be transformed into design specifications at the global level. We are usually provided with loadings at the wheel basis. The car architecture allows, by the mean of multi-body analysis, to transfer loading specifications to each subsystem and component of the car. These extended specifications correspond to the entries on each level of the left branch of the V. The ascending branch is made by the experimental validation corresponding to each level. For each numerical and experimental specification, one must be provided with an acceptance criteria that helps the designer to make a "yes or no" decision.

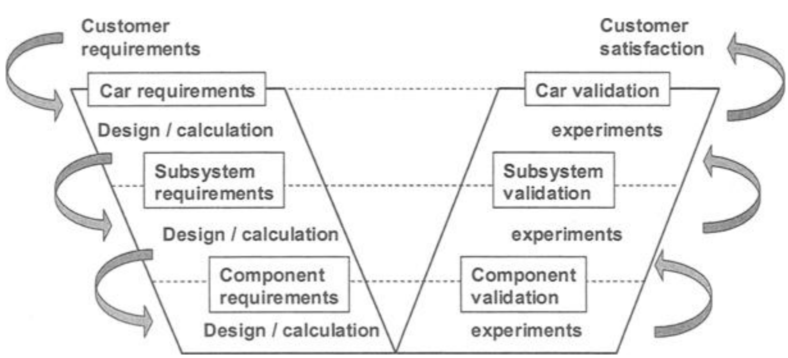

FIG. 1 - *V cycle for fatigue design*

The statements are

- Customer usage may be described as multi-axial/multi-input variable amplitude loadings (including some time information such as frequency and phase).
- Variable amplitude calculations and experiments are expensive and time consuming. They cannot be generalized to each component of the car.
- It is much more significant to perform an equivalent damage loading than a cumulative damage analysis on the stresses issued from a unique random loading.

- The final validation stage (at the car level) should be as representative as possible of the physical situations that a car may encounter.

The key issue to settle an efficient fatigue design procedure is that one must guarantee the consistency of the loading specification and the acceptance criteria from a full scale test to a single component calculation. At PSA Peugeot Citroën, the two main tools used to achieve this are the damage equivalent and the Stress Strength Interference Analysis.

The Stress Strength Interference Analysis

The governing idea of the stress strength interference analysis in the automotive context is that a probabilistic approach is used to guarantee in service reliability and safety.

Statistical Analysis

The first step of the method is to define a maximum failure probability that can be accepted, named R_{max}. In our automotive context, it is clear that this risk is very small. Otherwise it would mean that we would accept failure of some components for a few customers, which is not acceptable. Then, the overall methodology aims at the determination of the two distributions that are customer severity and component strength. Once the two density functions are identified, it is easy to calculate the risk of failure. We can illustrate the calculation of the risk by an academic example where both customer severity and component strength follow a normal law.

The customer distribution has (μ_c , σ_c) for mean value and standard deviation. And the strength distribution is given by (μ_R , σ_R)

The failure probability P_f is given by the risk that a customer would meet a component too weak for him $(S > R)$. The random variable $Z = R - S$ also follows a normal law defined by $\mu_Z = \mu_R - \mu_C$ and $\sigma_Z = \sqrt{\sigma_R^2 + \sigma_C^2}$

$$P_f = \text{Prob}(z < 0) = \text{Prob}\left(u < -\frac{\mu_Z}{\sigma_Z}\right) = \frac{1}{2\pi} \int_{-\infty}^{\frac{\mu_Z}{\sigma_Z}} \exp\left(\frac{x^2}{2}\right) dx \tag{1}$$

It can be easily admitted that the strength distribution follows indeed a normal law (because the strength is a combination of many variables). But the customer severity may take another form (Log-normal or Weibull). The failure probability may then not be derived by analytical equations, but it can be computed through various methods (numerical integration, Monte-Carlo). At this stage, one must emphasize that the key issue is not the way we calculate the failure probability, but how can we provide the car designers with tools that help them to guarantee the reliability of their product. For simplicity of presentation, we will stay in the ideal case of normal law for both customer severity and component strength.

In this probalistic context, the design problem is reduced to this simple question : given a customer severity distribution, where should the strength distribution be to make sure that the failure risk is lower than R_{max} ? The underlying assumption is that a method is available to define the customer severity as a scalar value. This will be discussed in a further paragraph.

Fatigue Context

Before going into details of fatigue analysis, it is necessary to take into account the other aspects of the car design. Actually, the whole life of a car can be separated into two major types of loads : normal usage and exceptional situations. Each situation addresses a different level of load, with a different number of occurrences, and with a different type of associated damage.

The normal usage corresponds to all possible situations as long as the car stays on the road. On the one hand, the parts must withstand these loadings without permanent deformation (the structure remains in its elasticity range) and on the other hand, they must be withstood without apparent fatigue degradation (no crack can be detected). The acceptance criteria are derived from the reliability described in this paper.

The exceptional situations are defined by their low number of occurrences. Such loads are so rare (maximum 10 times in the whole life of the vehicle) that customer surveys are not relevant to identify them. These situations are more likely defined by a few typical situations which cover the possible situations of real life. The acceptance criteria include functionality of the components, eventually reparability, and always the security of the passengers.

Customer Survey

The first type of customer analysis that has been performed at PSA since the 1980s lies on the reliable assumption that the usage of the car by the customer is independent of their behavior. The usage of a customer is defined by the type of road (road, city, mountain, highway) and the weight of the load (empty or more or less loaded). The behavior is linked to the driving style of the customer. The efforts undergone by the components of the car depend on the driving style of the driver.

Two parallel data collections are performed. Paper enquiries are used to identify the numbers of kilometers driven by each interviewed customer in each situation of load (k) and road (l). Table 1 is an example of a customer usage. This table gives the percentages c_k^m of usage for each class of load, and the percentages r_{kl}^m of usage for each type of road. A field measurement gives the knowledge of the loadings undergone by the car for each type of usage (type of road and level of load). Two counting methods are widely used for the signal analysis : the level crossing method, or the rainflow counting method. This last method, which is more widely used now, defines cycles that represent hysteretic stress-strain loops. These cycles can be represented in histograms of alternate loading A_j, associated with mean load values M, versus number of cycles n_{ij} [1]. The result of the usage survey is therefore a set of rainflow matrices $U_{enq}^{klm}\left(M_i, A_j, n_{ij}^{enq}\right)$ where k, l and m refer respectively to the load case, the road type and the customer.

In the customer survey the load histories are recorded on a limited number of kilometers k_{enq} for each type of usage. The measurements must be interpreted for a number of kilometers k_{life}, which is much larger. It is therefore necessary to identify the rainflow matrices $U_{life}\left(M_i, A_j, n_{ij}^{life}\right)$. The extrapolation of the rainflow matrices can be done by a simple linear extension.

$$U_{life} = \frac{k_{life}}{k_{enq}} U_{enq} \text{ or } n_{ij}^{life} = \frac{k_{life}}{k_{enq}} n_{ij}^{enq} \tag{2}$$

TABLE 1 : *Example of Customer Usage*

k	l	*customer* $\rightarrow m$	c_k^m (%)	r_{kl}^m (%)
1		% kilometers without load	27	
	1	Highway		10
	2	Good road		25
	3	Mountain		40
	4	City		25
2		% kilometers with half load	58	
	1	Highway		5
	2	Good road		30
	3	Mountain		30
	4	City		35
3		% kilometers with full load	15	
	1	Highway		15
	2	Good road		25
	3	Mountain		40
	4	City		20

However, the final matrix contains only the cycles really observed during the enquiries, and none of all the missed cycles that may occur during the life of the car. Our goal is more to identify the rainflow matrix which contains the probability of occurrence for each class of cycle, normalized to one kilometer.

To identify this so-called "limiting rainflow matrix" we used the extreme value theory. This work is detailed in [2]. The approach uses the link between the level crossing and the values of the rainflow matrix. This approach is of particular interest because its validity is the highest for the maximum loads, which may have been too rarely measured during the enquiries. Using the limiting rainflow matrix, is possible to write the following expression

$$U_{life}^{klm}\left(M_i, A_j, n_{ij}\right) = k_{life} \cdot U_{\lim}^{klm} \tag{3}$$

where $U_{\lim}^{klm}$ is the limiting rainflow matrix identified from the measured matrix, and normalized for one kilometer.

Using the assumption that usage and behavior are independent variables, those two databases are combined to generate a large number of virtual customers (up to 100 000) that will be interpreted in terms of fatigue severity.

The rainflow matrix of a driver who behaves like driver j, and uses his car like driver i is therefore

$$\left\lfloor U_{\lim}^{ij} \right\rfloor = N \sum_{k,l} c_k^i r_{kl}^i U_{\lim}^{jkl} \tag{4}$$

where N is the number of kilometers for the whole lifetime of the car.

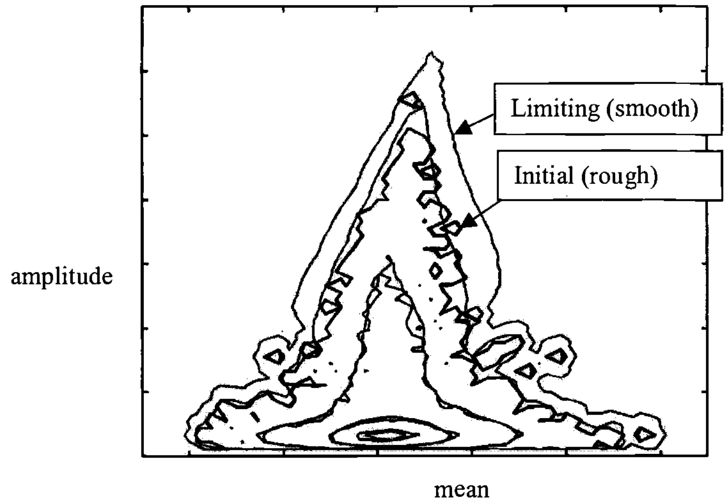

FIG. 2 - *Example of limiting rainflow matrix (smooth / light grey) and comparison with the initial rainflow (rough / dark).*

At this stage, we provide ourselves with a lot of rainflow matrices that are statistically representative of the usage of the car by the population of customers. It is now necessary to analyze these loadings in terms of fatigue damage.

Data Analysis, Handling of Variable Amplitude

To fit into the reliability approach, it is necessary to transform the recorded signal into a single value that measures the severity of the customer. We have seen that the first step is a condensation of the load history into a rainflow matrix that contains all the cycles. One must notice that this requires the assumption that the order of the cycles is not relevant in our fatigue analysis. And this implies the use of the Palmgren - Miner's cumulative damage. In our automotive context, this assumption is consistent for three main reasons :

- the loading history is more closed to a random signal in which it is not possible to say which one of the large amplitude and the small amplitude was the first, and
- the Palmgren – Miner's rule is reputedly correct for high cycle fatigue (no cracks and no plasticity) for random signals.
- the cumulative damage is applied on a complete population of customer. If we assume that the mean damage error is zero, then the effect of damage error is to increase the observed scatter σ_C. In the fatigue design procedure described below, it appears that this is a conservative assumption.

To analyze the loading and to provide the designers with useful information, the fatigue loading recorded on the vehicle is transformed into an equivalent loading (couple : forces of constant amplitude - number of cycles), which produces the same fatigue damage that the vehicle will support in its whole life. The usual procedure can be schematically described as follows.

A global mean value, FATmean, can be defined for the whole loading sequence. It is the mean value of all the M_i value weighted by the associated n_{ij}.

Transformation of each class of cycles with a non zero mean load value (M_j, A_j), to equivalent purely alternate cycles A'_j, using a parametric GERBER parabola normalized to the fatigue limit researched for the component F_{eq}

$$A' = \frac{A}{1-\left(M / K.F_{eq}\right)^2} \tag{5}$$

with K = ratio between the fatigue limit and the ultimate tensile strength of the material considered (typically 2.5 for steels).

The MINER summation is performed with this "objective" histogram and a parametric WHOLER curve normalized to the fatigue limit (i.e., fatigue limit = 1). The desired information is the WOHLER curve defined by the value of F_{eq}, which will give a MINER summation of 1 as shown in Figure 3 (for details see [3] and [4]). Any point of this WOHLER curve (couple : force amplitude - number of cycles) can be taken as an equivalent of the fatigue loading experienced by the objective customer. For suspension systems, the equivalent is usually defined at 10^6 cycles.

With this method, it is possible to define a single value F_{eq} for each customer that represents its severity in terms of fatigue.

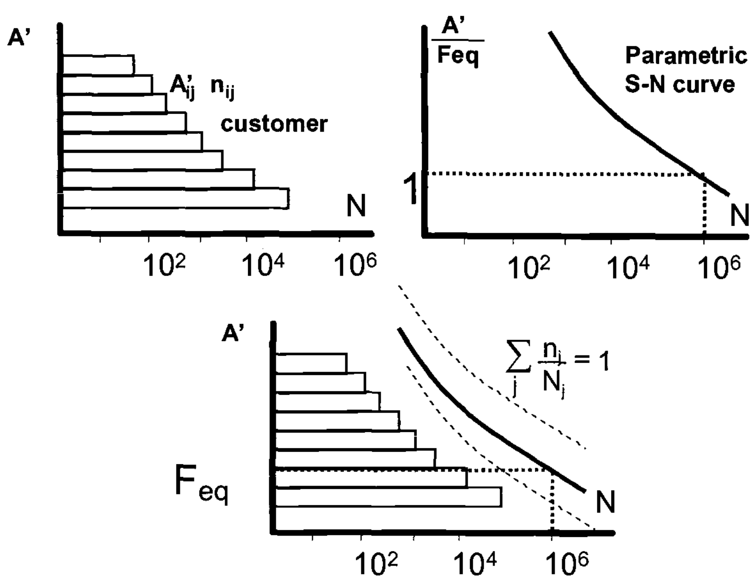

FIG. 3 - *Equivalent fatigue loading*

Production Scatter

As said above, the design problem can be reduced to the identification of the distribution of strength. It means that the designer should identify the parameter of the probability density function of the strength. But the designer who works with virtual design and a few numbers of prototypes has no information on these parameters, which would require a production survey. In order to solve this paradox, we have introduced the assumption that the relative scatter $q = \sigma_R / \mu_R$ is characteristic of a component family and its fabrication process. Then it can be identified on a similar component, with a statistically relevant number of components tested.

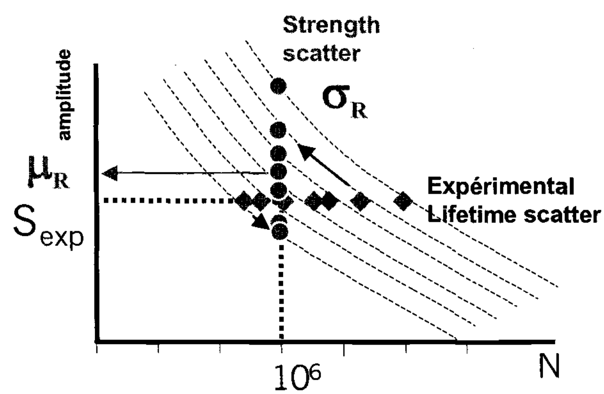

FIG. 4 - *identification of the parameters of the strength scatter.*

To keep consistent with the customer analysis, one must emphasize that the scatter is measured on the strength dimension rather than on the traditional lifetime. Each experimental lifetime is "dragged" along the damage curve which has the same slope as the damage curve of the material (see Figure 4).

The Fatigue Design Procedure

Specification and Validation

At this stage, we provide ourselves with information on the distribution of customer severity, and on the production scatter. The next step is to give designers a simple specification and validation procedure.

Actually Equation 1 shows that the risk is a function of μ_Z / σ_Z, therefore :

$$\frac{\mu_Z}{\sigma_Z} = \frac{\mu_R - \mu_C}{\sqrt{\sigma_R^2 + \sigma_C^2}} \tag{6}$$

"Strength" parameters μ_R and σ_R are estimated with a confidence level γ by two values m_R and s_R obtained from a limited number of components. Therefore, the risk R depends on the chosen confidence level γ and of the number N of tested components.

Usually, the number of tested components ($N \geq 8$) allows a reasonable estimation of the mean value. We can accept the assumption that $\mu_R = m_R$ but on the other hand the standard deviation must be corrected by χ^2

$$\sigma_r = s_r \sqrt{\frac{\nu}{\chi^2_{\gamma(\nu)}}} \tag{7}$$

with $\nu = N-1$ and $\chi^2_{\gamma(\nu)}$ the value for the chosen iso-probability at N-1 d.o.f. If $N = \infty$ then $\sigma_R = s_R$.

The key stone of the method is the introduction of the objective customer F_n at a specific position in the customer distribution. This position is defined by a number α of standard deviations

$$F_n = \mu_C + \alpha\sigma_C \tag{8}$$

Since m_R and s_R are homogeneous to the applied forces they can be normalized by the testing reference

$$m_R^* = \frac{m_R}{F_n} \text{ and } \sigma_R^* = \frac{S_R}{F_n} \tag{9}$$

For an easier analysis of the results a relative scatter parameter is introduced for the customer severity the distributions : $\rho = \sigma_C / \mu_C$ and, ρ is representative of the shape of the "Stress" distribution. Using also the relative scatter q of the strength distribution introduced above, the ratio μ_Z / σ_Z can be written

$$\frac{\mu_Z}{\sigma_Z} = \frac{m_R^* - \dfrac{1}{1+\alpha\rho}}{\sqrt{\left(q m_R^*\right)^2 \dfrac{N-1}{\chi^2_{\gamma(N-1)}} + \left(\dfrac{\rho}{1+\alpha\rho}\right)^2}} \tag{10}$$

The risk R is therefore a function of

$$R = \text{Prob}\left(u < -\frac{\mu_Z}{\sigma_Z}\right) = f\left(\alpha, \rho, m_r^*, q, N, \gamma\right) \tag{11}$$

From the designer point of view, the only variable for the risk is the relative mean value m_R^*. It means that he should assume that the relative scatter of the component he will design is q. And he must design a component having the correct mean strength value.

When performing the experimental validation, the parameters α, ρ, q, N, and γ are known. The validation aims at the checking of the expected ratio between the mean value and the objective customer.

When performing the design calculation, the goal is the same, but it is necessary to introduce β, the number of standard deviation between F_n et m_R : $m_R = F_n + \beta s_R$ from which we can derive : $m_R^* = 1/(1-\beta q)$.

This expression can be introduced in the risk calculation. Then, β becomes the unknown, and one must identify the value that gives the expected risk. In the finite element analysis, the loading is given by F_n, and the acceptance criterion is the material fatigue criterion chosen at the mean value minus β standard deviations. At PSA, the fatigue design is realized with the Dang Van's criterion [5-7]. The material identification is done with a few fatigue limits at various loading ratios. We use the fatigue limits minus β standard deviations under the mean.

The estimation of the component strength scatter (σ_R) is extremely important. An error of 20% on s_R could bring a factor of 10 on the estimation of the Risk R. The lower the number of tested components, the higher the value of σ_R and the greater the risk value. Therefore it is interesting to work with the parameter q which characterizes the component and its fabrication process.

A data base derived from a large number of tests performed on components or specimens can provide a reliable value of the relative scatter parameter q. In this case, only the determination of the mean value of the "Strength" distribution is necessary. This can be carried out with a limited number of components, ten for example. It is no longer necessary to take into account the number of tested components (m_r and q are considered to be representative of the whole components). The calculation of the risk R is more precise and is not penalized by a correction due to the number of tested components.

Simultaneous Engineering

Now we have a global method to guarantee the reliability for customers. This method provides us with specifications and corresponding acceptance criteria for calculation and experimental validation. In the automotive context, there are different levels of specification and validation. The highest level corresponds to the customer requirements for the car (quality, security, fuel consumption,...). These requirements are translated into engineer requirements first at the car level, and then step by step from subsystem level to individual components. At each level of specification there must be an associated experimental validation.

The customer analysis must be seen as the translation of customer requirements into engineer specifications at the car level. Indeed, they are realized with wheel forces that are assumed to be independent of the car architecture. The major interest of this analysis is that the loading specification is given by the objective customer F_n, which can be linked by some relations to global characteristics of the car (weight, length, power, ...). Using these relations, it is possible to determine the objective customer for a new car at the very beginning of the project.

Variable Amplitude & Constant Amplitude - At each level, one must define if variable amplitude or constant amplitude should be used for the fatigue analysis. One also must ensure that the different levels are consistent together in terms of damage.

The strategy used for the fatigue design is the following.

- Use Multi Rigid Body codes to transfer the loadings from the wheel basis to each interface between the components.

- Calculation of each component with the equivalent damage alternate loading F_n. One must guarantee the acceptance criterion defined above.
- Experimental validation of the component with constant amplitude loading. The test is repeated at least ten times. Each component must be broken (if necessary a locati staircase method might be used). One must guarantee that the mean strength is greater than m^*F_n. It means that to ensure that the experimental test remains in the endurance limit region, the loading of the test may be greater than the calculation loading.
- Experimental validation of the suspension system with variable amplitude loadings. This step requires variable amplitude loadings recorded on the test track. It comes later in the project, only when the first prototypes exist. The testing procedure on the track is indeed defined to represent the objective customer $F_n = \mu_C + \alpha\sigma_C$. If necessary, the measurements might be calibrated to make sure that the damage induced is equivalent to the objective customer 10^6 cycles at F_n. We therefore guarantee that the track is representative of customer.
- Experimental validation of the complete car by reproducing the test track loadings.

This strategy is of great interest for three reasons :

- No measurements on a prototype are needed in the early stages of a project, the calculations can be done with specifications that are directly linked to customers.
- Constant amplitude specifications avoid the variable amplitude simulation with multi-body models. The use of such models is restricted to the constant amplitude loadings, and remains therefore very short in delay.
- The constant amplitude experimentation on single components gives good accuracy and allows predict the in-service reliability. The variable amplitude permits the validation of all the assemblies.

Multidimensional Analysis -The car components and structures undergo multidimensional and/or multi input loadings. To handle this statement within the stress strength interference analysis and in the fatigue equivalence analysis, we have proposed the following procedure.

In service loading analysis identifies each of the significant life situation. Figure 5 shows a typical analysis on left and right vertical forces on a front axle.

The customer analysis is done for each life situation. The specification is then a set of loadings corresponding to the objective customer in each situation.

The efficiency of this procedure is based upon the observations that in a real structure, the critical location is close to a geometrical accident (small radius). At this place, the stresses are oriented in a direction that is mainly governed by the structure, rather than by the external loading. The external loading only governs the amplitude of the local stresses. Even though this assumption may appear somewhat hazardous, it has been confirmed by a lot of observations on various type of automotive structures (suspension components, body structure,...). From a theoretical point of view, it is clear that this assumption has an influence on the local damage in the critical locations. This influence depends on the relative weight of the different external loading directions on the local stress, and on the statistical correlation between those directions. The damage increase can be calculated for academic situations that are unfortunately not relevant in the automotive context (purely in phase or purely out of phase loadings).

Usually, one of the life situations is more critical than the other. The damage accumulation can remain separated. If several situations happen to be at the same level of criticality, it is necessary to combine them in the loading specification to guarantee reliability.

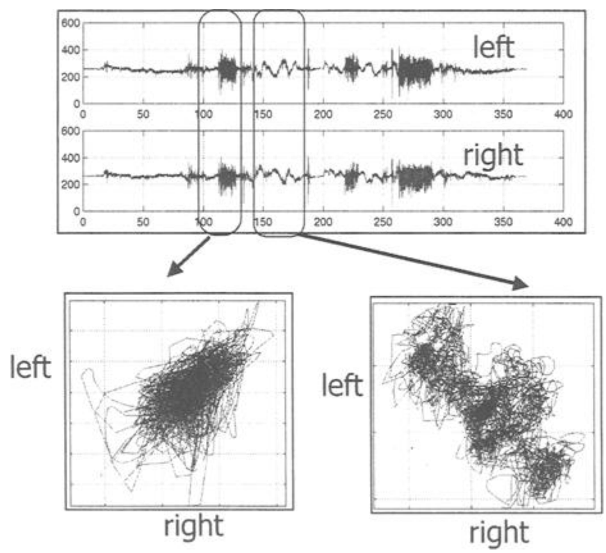

FIG. 5 - *identification of the in phase and opposite phase situation for the left and right vertical loads*

Exemple on a Steering Knuckle

To illustrate the application of the Dang Van's criterion an example of fatigue design for a steering knuckle is shown in figure 6. The component is linked to the suspension arm by a ball joint, and is screwed to the damper. The two life situations identified on this components are steering cycle, and horizontal forces cycles as described in figure 6.

The fatigue criterion requires that the fatigue cycle be described at several discrete times. In the second case of the present example, six values of ωt have been chosen $\omega t = 0, \pi/2, \pi, 3\pi/2$ and two intermediate values, such that DX = DY. The corresponding stress tensors are then calculated by Finite Element Analysis, and stress results are analyzed with Dang Van's fatigue routine. At the design stage, the component is accepted if, under the specified equivalent loading, the load path at the most critical point is below the design line, i.e, mean value minus β standard deviation (β comes from the reliability approach).

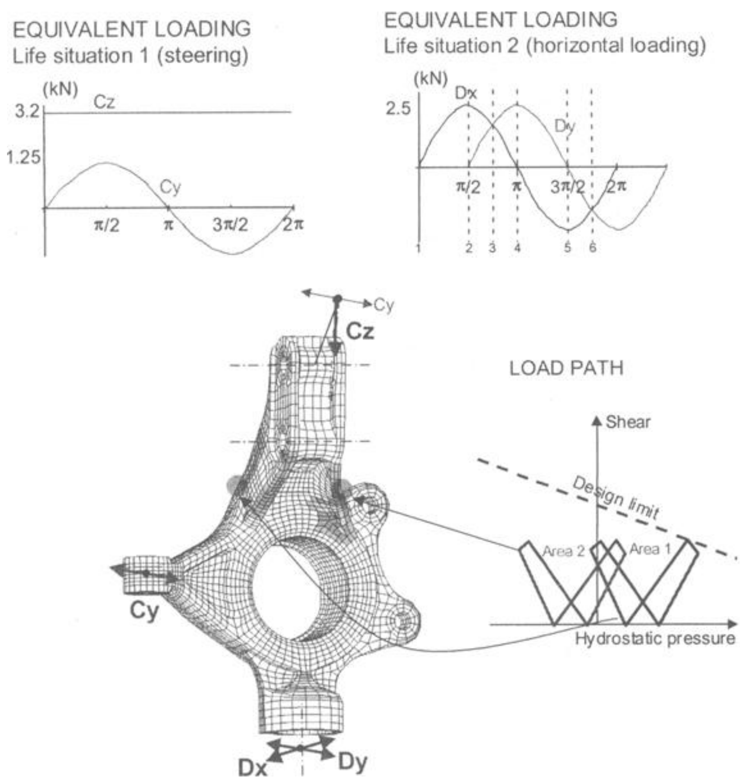

FIG. 6 - *Fatigue assessment of a steering knuckle with the Dang van's criterion.*

Conclusion

This work presents the analysis of the fatigue strength of automotive components in service using the "Stress-Strength" analysis.

The major difficulty is the definition of the service loading, which demands long and costly statistical analysis of car usage and owner behaviour. It is also important to note that the "Stress-Strength" method points out the paramount importance of the relative scatter parameter of fatigue strength.

It is important to point out that mechanical structures usually have complex geometries and that they operate under complex loading. Therefore the description of the behavior of the structure must be as precise as possible and should provide the stress and strain elements necessary for the subsequent fatigue analysis. This fatigue analysis must be appropriate and take into account the structural behavior and specificities of mechanical design (multiaxiality of the stress fields, complex geometries) and is usually computerized with a fatigue routine linked to a finite element code. To that purpose it is not necessarily useful to describe in detail the damage mechanisms of the material, which are anyway very complex. The relative simplicity of the application of the methods proposed here and the limited number of necessary material data allows their use in design offices by engineers and designers who are not fatigue experts.

This reliability approach is possible because variable amplitude analysis is confined within the loading analysis. It is therefore not necessary to perform any finite element fatigue calculation with variable amplitude loadings. The variable amplitude loading analysis and the damage accumulation are performed at the level of the customer loadings, rather than at the more classical but so much heavier level of stresses, which justification is questionable.

References

[1] AFNOR, 1993, Fatigue sous sollicitation d'amplitude variable – Méthode de comptage des cycles, A 03-406

[2] Johannesson P., Thomas J.J., 2000, Extrapolation of rainflow matrices, preprint of Chalmers University, Goteborg.

[3] Morel, F., Mercier, J., Catherin, G., Bignonnet, A. and Petit, J. (1993). Analyse du comportement en fatigue de composants mécaniques par l'approche du chargement équivalent. In proceed. of *Sollicitations en service et comportement en fatigue*, Paris 25-26 mai 1993. Pub. SF2M.

[4] Thomas J.J., Bignonnet A., 1999, Equivalence fatigue - état de l'art, *journée de printemps SF2M*, Paris, Publ. Société Française de Métallurgie et de Matériaux

[5] Dang-Van, K., (1973). Sur la résistance à la fatigue des métaux. *Sciences et Techniques de l'Armement*. 3ème fascicule, pp 647-722

[6] Dang Van, K.,. Introduction to fatigue analysis in mechanical design by the multiscale approach. In CISM courses, n° 392 "*High-Cycle Metal fatigue from Theory to Applications*". Ed. I.V. Papadopoulos, K. Dang Van. Springer-Verlag, 1999.

[7] Ballard, P., Dang-Van, K., Deperrois, A. and Papadopoulos, I.V. (1995). Hich cycle fatigue and finite element analysis. *Fatigue Fract. Engng Mater. Struct.* Vol 18 No. 3, pp. 397-411

Journal of ASTM International, October 2004, Vol. 1, No. 9
Paper ID JAI19047
Available online at www.astm.org

Franck Morel[1] *and Narayanaswami Ranganathan*[2]

High Cycle Fatigue Testing and Analysis Using Car Standard Sequence

ABSTRACT: An original computer software package for controlling a servo-hydraulic machine was used to carry out uniaxial and biaxial variable amplitude loading tests on a high strength steel. Tension-compression and torsion uniaxial tests, as well as combined proportional tension-torsion tests were performed under the car loading sequence CARLOS used for fatigue strength investigations of car wheel suspension components. The number of sequences to crack nucleation was estimated by means of a crack front marking technique using very small amplitude cycles to generate marker bands on the fracture surface. The experimental data obtained from these tests were compared to the predictions of the fatigue life prediction method proposed by Morel and based on a microplasticity analysis. It was shown that all the predictions, though non-conservative, were within an acceptable scatter band.

KEYWORDS: high cycle fatigue, damage accumulation, multiaxial loading, fatigue crack nucleation, variable amplitude loading tests, fatigue life prediction

Introduction

The design of structures and components submitted to variable amplitude loading requires a fatigue life prediction method whose efficiency must be proven by many comparisons to fatigue test results [1]. The testing and analysis under variable amplitude loading is known to be an arduous task and also requires specific test procedures and control. Moreover, in the car industry, it is long known that some safety parts, like the suspension arm, are submitted to very complex multiaxial loading sequences, and it is difficult to reduce the original load sequence to a simple constant amplitude loading. For this reason, a standard sequence called CARLOS (Car Loading Sequence) had been proposed several years ago by two German laboratories (LBF and IABG) to investigate the fatigue strength of car wheel suspension components [2].

This paper aims to present salient details of an original software tool built to perform variable amplitude load controlled tests on cylindrical specimens with special attention paid to the quantification of the errors relative to the desired output and the actual loads in a variable amplitude load sequence.

This control system, coupled with a servo-hydraulic machine, was used to carry out uniaxial and biaxial variable amplitude loading tests under the CARLOS standard sequence on a high strength steel. These experimental data were compared to the predictions of the fatigue life prediction method proposed by Morel [3] and based on a microplasticity analysis.

Manuscript received 19 April 2002; accepted for publication 17 July 2003; published October 2004. Presented at ASTM Symposium on Fatigue Testing and Analysis Under Variable Amplitude Loading Conditions on 29 31 May 2002 in Tours, France; P. C. McKeighan and N. Ranganathan, Guest Editors.

[1] Associate Professor, Laboratoire de Mécanique et de Physique des Matériaux (LMPM), Ecole Nationale de Mécanique et d'Aérotechnique (ENSMA), BP 109, 86960 Futuroscope Cedex, France.
[2] Professor, Laboratoire de Mécanique et de Rhéologie, University François Rabelais de Tours, 7 avenue Marcel Dassault, 37200 Tours, France.

Materials, Specimens, and Test Procedures

Materials and Specimens

The fatigue tests were conducted on a high strength steel 35 NCD 16 (AFNOR Standard) whose chemical composition is given in Table 1. The steel was austenitized at 875°C, followed by air quenching. The tempering temperature was 650°C, resulting in the tensile properties given in Table 2. Cylindrical solid specimens with a 9 mm diameter and 18 mm gage length were used in all tests.

All the specimens were machined from rolled bar in the longitudinal direction and were carefully polished using 6 μm diamond paste.

TABLE 1 *Chemical composition of 35NCD16.*

Element	C	Si	Mn	S	P	Ni	Cr	Mo
Mean %	0.364	0.37	0.39	< 0.003	0.01	3.81	1.7	0.28

TABLE 2 *Room temperature tensile properties of 35NCD16.*

Young Modulus (MPa)	0.2 % Yield Stress (MPa)	Ultimate Tensile Stress (MPa)	Elongation (%)
205 000	930	1070	20.7

Test Procedures

All the variable amplitude tests were conducted in laboratory air at room temperature on servohydraulic fatigue machines, operating in load (and/or torque) control in the frequency range 10 20 Hz.

The fatigue tests were carried out using home built software programmed to drive an A/D converter card that would deliver a calibrated signal to drive the biaxial fatigue testing machine via the external signals input.

The input spectrum (in discrete peaks) in the original data file was transferred to the active memory via a buffer. A sinusoidal signal was generated between two successive peaks, and the system response was continually recorded. If the error between the desired input and output was greater than a chosen value, it was stocked in 3rd order matrix containing the current peak, the previous peak, and the successive peak. The program learned to correct the input signal when the same peak sequence was encountered again.

The full range between the maximum and minimum input signal was divided into several intervals. The RAM memory required increases with the number of desired discrete intervals. For the biaxial variable amplitude tests, 25 intervals were used which gave satisfactory results (the errors recorded on strain gages bonded to the specimens were less than 5 %). Preliminary tests showed that the system response was stable after about two passes of the total load sequence.

The software allowed a choice of data acquisition (up to eight channels) and continuously displayed the values in the error matrix. The test would stop automatically if the error was too large. The test could also be stopped at any point in the loading spectrum and could continue from exactly the same point.

Three uniaxial standard sequences called CARLOS vertical, lateral, and longitudinal were developed several years ago by two German laboratories (LBF and IABG) to investigate the fatigue strength of car wheel suspension components [2], loaded in three perpendicular directions. They are equivalent to a driving distance of 40 000 km on public roads with sporty driving behavior and are recommended for performing tests in the laboratory.

In this study, the variable amplitude loading fatigue tests were conducted by repeatedly applying the uniaxial CARLOS lateral sequence until failure. This sequence originally consisted of 95 180 cycles. Experiments using the original sequence can be very long. To avoid such time-consuming tests, a filtering technique has been applied to the original sequence so as to omit some of the small non-damaging cycles from the sequence. The filtering procedure was built to ensure that the mean value of the small cycles was considered during the extraction (Fig. 1). In the Haigh diagram, the small cycles were omitted when their means and amplitudes belong to the area limited by the two lines determined by the following expressions

$$\frac{\sigma_a}{s_{-1}} + \frac{\sigma_m}{\sigma_u} = \omega \tag{1}$$

and

$$\frac{\sigma_a - \sigma_m}{\sigma_u} = \omega \tag{2}$$

where σ_u is the ultimate strength, s_{-1} is the purely reversed tension fatigue limit, and ω is the filtering parameter. When ω equalled zero, no cycles were omitted. The number of omitted small cycles increased with increasing value of ω.

Two different filtered sequences denoted as CARLOS-f1 and CARLOS-f2 were then deduced from two omission levels, respectively $\omega = 0.4$ and $\omega = 0.6$. CARLOS-f1 had 46656 extrema, and CARLOS-f2 had 13568 extrema (Fig. 2).

To avoid a general yielding of the specimen, it was also verified that the highest level of each sequence, shown in Table 3, was not higher than the material yield stress, shown in Table 2.

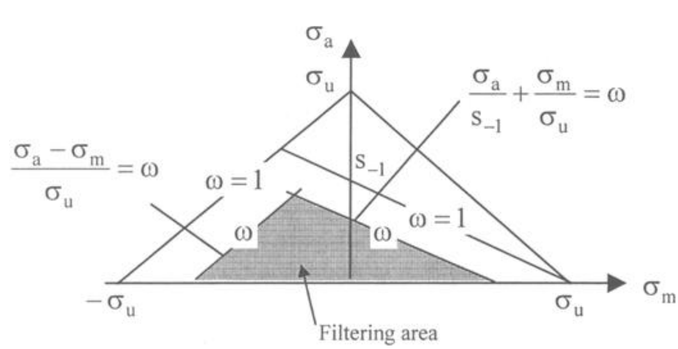

FIG. 1 *Filtering procedure according to the Haigh diagram.*

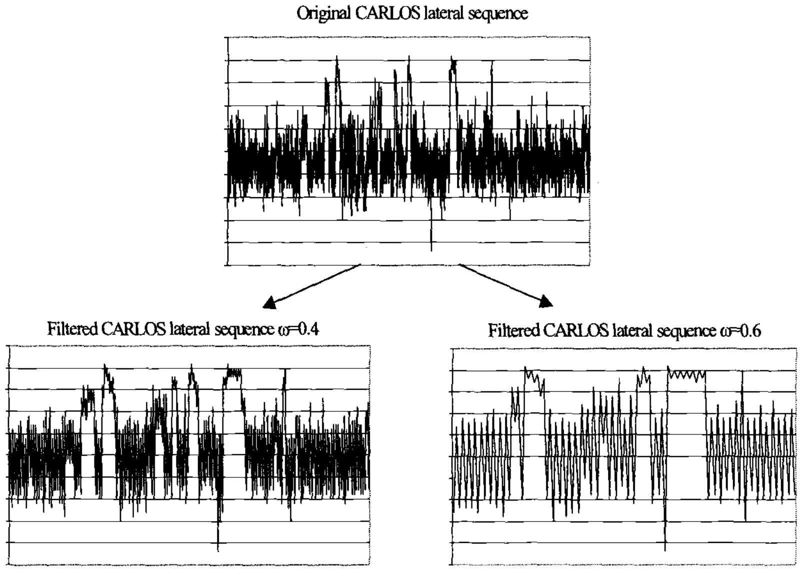

FIG. 2—*CARLOS lateral filtered sequences.*

Results and Observations

The fatigue properties of the high strength steel under constant amplitude loading were estimated from tests carried out on a vibrophore test machine under two loading conditions: purely reversed tension and purely reversed torsion. The stress-life (SN) curves for each loading are shown in Fig. 3. Under tension load conditions and for three stress levels (550 MPa, 480 MPa, and 460 MPa), the specimen surface was observed at different fractions of the lifetime in order to find the number of cycles required to reach a crack size of 100 μm. In the following sections, the crack nucleation is defined as the time to the creation of a 100 μm deep crack. The deduced crack nucleation SN curve was used later in this paper to identify some of the microplasticity model parameters. The identification also required a two level block load test, the results of which are also given in Fig. 3.

The two fatigue limits estimated from these curves are: tension s_{-1} = 450 MPa and torsion t_{-1} = 330 MPa.

Tension-compression and torsion uniaxial tests, as well as combined proportional tension-torsion tests, were also performed under the two filtered car loading sequences, CARLOS-f1 and CARLOS-f2. A crack front marking technique, using marker bands, was used to follow the evolution of the crack growth during the tests. The marker bands were created by 100 very small cycles that are added to the original load sequence each time the highest level was reached. The crack front on the fracture surface is easily distinguished, and the number of sequences to propagation of a crack greater than 100 μm in depth could be deduced from observations of the fractograph (Fig. 4). Preliminary tests showed that the addition of these marker cycles did not affect the total fatigue life of the specimen.

TABLE 3 *Fatigue test results and results of model predictions for tests using the CARLOS lateral sequence.*

Test n°	Loading	Sequence	Σ_{xx} maxi (MPa)	Σ_{xx} mini (MPa)	Σ_{xy} maxi (MPa)	Σ_{xy} mini (MPa)	N_{seqf} failure	N_{seqi} initiation	N_{seqi} / N_{seqf}	N_{seq} initiation (Model)	N_{seq} initiation (Model softening phase)
1	Tension	CARLOS-f1	677	–673	0	0	126	107	0,85	133	28
2	Tension	CARLOS-f1	677	–673	0	0	99	81	0,82	133	28
3	Tension	CARLOS-f1	677	–673	0	0	82	66	0,80	133	28
4	Torsion	CARLOS-f1	0	0	474,5	–500,5	174	151	0,87	193	37
5	Torsion	CARLOS-f1	0	0	474,5	–500,5	125	106	0,85	193	37
6	Torsion	CARLOS-f1	0	0	474,5	–500,5	102	87	0,85	193	37
7	Tension-Torsion	CARLOS-f1	614	–576	307	–288	47	35	0,74	64	16
8	Tension-Torsion	CARLOS-f1	614	–576	307	–288	64	50	0,78	64	16
9	Tension-Torsion	CARLOS-f1	614	–576	307	–288	62	47	0,76	64	16
10	Tension	CARLOS-f2	677	–673	0	0	170	153	0,90	150	30
11	Tension	CARLOS-f2	743	–730	0	0	37	22	0,59	65	16
12	Tension	CARLOS-f2	743	–730	0	0	37	27	0,73	65	16
13	Tension	CARLOS-f2	743	–730	0	0	46	34	0,74	65	16
14	Torsion	CARLOS-f2	0	0	474,5	–500,5	155	132	0,85	193	37
15	Torsion	CARLOS-f2	0	0	511	–539	47	36	0,77	94	21
16	Torsion	CARLOS-f2	0	0	511	–539	64	50	0,78	94	21
17	Torsion	CARLOS-f2	0	0	511	–539	89	70	0,79	94	21
18	Tension-Torsion	CARLOS-f2	614	–576	307	–288	71	55	0,77	68	16
19	Tension-Torsion	CARLOS-f2	614	–576	307	–288	63	47	0,75	68	16
20	Tension-Torsion	CARLOS-f2	614	–576	307	–288	64	45	0,70	68	16

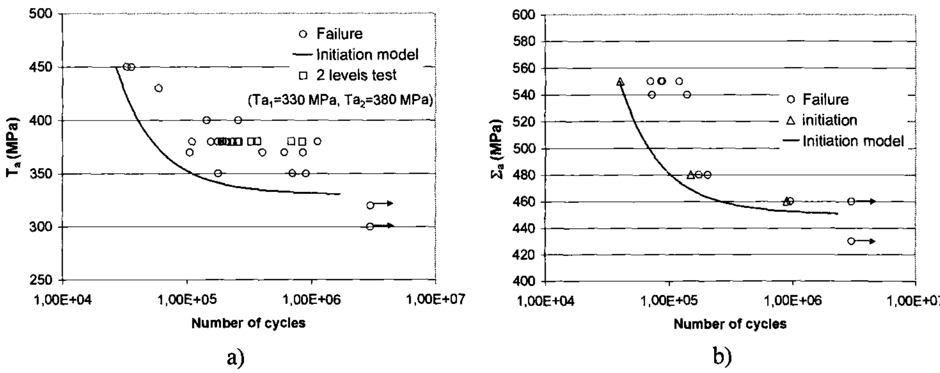

FIG. 3 *(a) Torsion and (b) tension SN curves.*

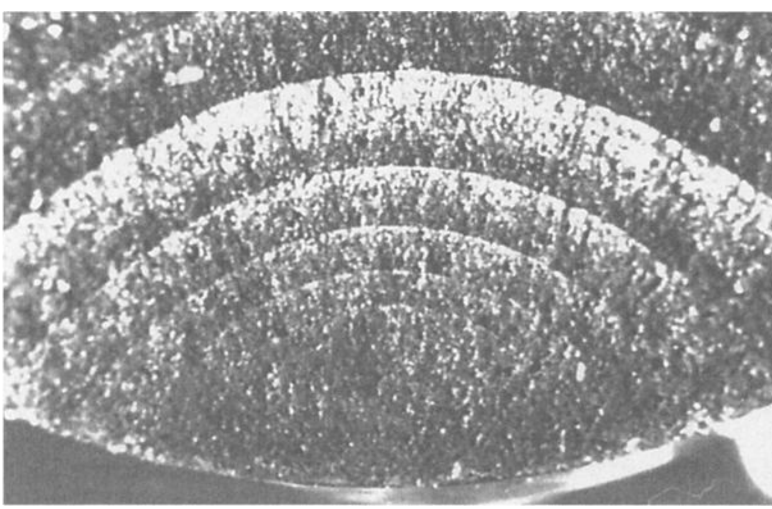

FIG. 4 *Marker bands (due to small cycles added after the maximum level peak) on a fracture surface of a specimen submitted to combined tension and torsion under a CARLOS sequence (test n°7).*

For each kind of loading, it was thus possible to draw the evolution of the crack depth with the number of sequences (Fig. 5) and then deduce the number of sequences to initiation as the difference between the total life and the propagation phase (Table 3).

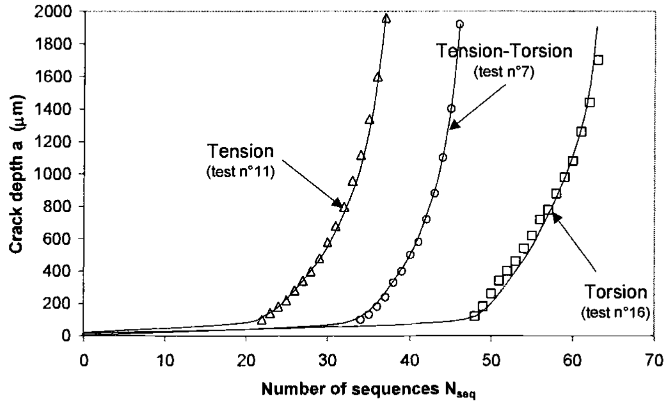

FIG. 5 *Crack depth evolution with the number of sequences according to the crack front marking technique.*

Fatigue Life Prediction Model

Microplasticity Analysis

An original fatigue life to initiation prediction model proposed by Morel [3], based on the previous work of Dang Van [4], Papadopoulos [5], and a microplasticity analysis, was used to analyze the test results relative to the initiation phase.

Because the nucleation of fatigue cracks in metals is known to be a consequence of cyclic plastic strain localization, the cumulative plastic mesostrain has been considered the principal cause of damage accumulation. In the same way as in Papadopoulos' work [5], the crystal is assumed to follow a combined isotropic and kinematical rule when flowing plastically, and the initiation of slip in the crystal is determined by Schmid's law:

$$f(\underline{\tau}, \underline{b}, \tau_y) = (\underline{\tau} - \underline{b}).(\underline{\tau} - \underline{b}) - \tau_y^2 = 0 \tag{3}$$

where $\underline{\tau}$ is the mesoscopic resolved shear stress, τ_y is the mesoscopic yield limit, and $\underline{b}$ is the kinematic hardening parameter.

Three successive linear isotropic hardening rules were adopted to describe the crystal behavior from initial yield to failure, and the crystal was considered to have failed as soon as the yield limit became negligible. The damage variable D equalled the accumulated plastic mesostrain Γ

$$\textit{Hardening} \qquad \dot{\tau}_y = g\dot{\Gamma} \quad \Rightarrow \quad \dot{D} = \dot{\Gamma} = \frac{1}{c + \mu + g}\sqrt{\dot{\underline{T}}.\dot{\underline{T}}} \tag{4}$$

$$\textit{Saturation} \qquad \dot{\tau}_y = 0 \; (\tau_y = \tau_s) \quad \Rightarrow \quad \dot{D} = \dot{\Gamma} = \frac{1}{c + \mu}\sqrt{\dot{\underline{T}}.\dot{\underline{T}}}$$

$$\textit{Softening} \qquad \dot{\tau}_y = -h\dot{\Gamma} \quad \Rightarrow \quad \dot{D} = \dot{\Gamma} = \frac{1}{c + \mu - h}\sqrt{\dot{\underline{T}}.\dot{\underline{T}}}$$

where c is the kinematic hardening parameter, g and h are the isotropic hardening parameters in the hardening and softening phases, μ is Lamé coefficient, and τ_s is the constant yield limit in the saturation phase.

Multiaxial Endurance Criterion

Papadopoulos showed in [5] that the fatigue limit can be linked to some characteristic quantities of an elastic shake-down state reached by plastically deforming crystals of less resistance. It has been demonstrated that the limit to apply on a parameter T_σ, proportional to an upper bound of the plastic mesostrain accumulated in some crystals of V, depends on the maximum value $\Sigma_{H,max}$ that reaches the mesoscopic (equal to the macroscopic) hydrostatic stress during a loading cycle

$$\max_{\theta,\varphi}\left(T_\sigma(\theta,\varphi)\right)+\alpha\Sigma_{H,max} \leq \beta \tag{5}$$

T_σ is a function of the orientation of a material plane Δ through the angles θ and φ, spherical coordinates of the unit normal $\underline{n}$ to the plane Δ

$$\underline{n}=\begin{pmatrix} \sin\theta\cos\varphi \\ \sin\theta\sin\varphi \\ \cos\theta \end{pmatrix} \tag{6}$$

$T_\sigma(\theta,\varphi)$ is estimated by an integration carried out through the whole area of the plane Δ

$$T_\sigma(\theta,\varphi)=\sqrt{\frac{1}{\pi}\int_{\psi=0}^{2\pi} T_a^{\,2}(\theta,\varphi,\psi)d\psi} \tag{7}$$

T_a is the amplitude of the macroscopic resolved shear stress acting on a line of the plane Δ directed by $\underline{m}$. This line is determined by the angle ψ from an arbitrary but fixed axis in Δ.

Hereafter, in order to make relations less cumbersome, the maximum value of T_σ will be denoted as T_Σ

$$T_\Sigma=\max_{\theta,\varphi}\left(T_\sigma(\theta,\varphi)\right) \tag{8}$$

The estimation of the yield limit in the saturation phase τ_s (defining the cyclic behavior of the crystal) was carried out by the definition of a limit loading. A limit multiaxial loading can be readily expressed [3,6] from any multiaxial loading according to the criterion (T_Σ, $\Sigma_{H,max}$). Indeed, this limit loading is such that it keeps the same stress means Σ_{ijm} and phase angles β_{ij} as those of the multiaxial sinusoidal loading under consideration, and a proportional coefficient k applied to the stress components amplitudes $(\Sigma_{ija})_{lim} = k\Sigma_{ija}$ ensures that the endurance criterion equality is verified

$$T_{\Sigma\,lim}+\alpha\Sigma_{H,max\,lim}=\beta \tag{9}$$

and the applied and limit loadings are said to be "similar."

The mechanical parameter $T_{\Sigma lim}$ relative to this limit loading is a function of the ratio $\frac{T_\Sigma}{\Sigma_{H,a}}$ and of the mean hydrostatic pressure $\Sigma_{H,m}$ [3,6]

$$T_{\Sigma lim} = \frac{-\alpha\Sigma_{H,m} + \beta}{\alpha + \frac{T_\Sigma}{\Sigma_{H,a}}} \frac{T_\Sigma}{\Sigma_{H,a}} \tag{10}$$

Let C_A and τ_{lim} be the amplitudes of the macroscopic shear stress acting on the critical plane corresponding to the actual and limit loadings, respectively. τ_{lim} was easily deduced from the relation established in previous papers [3,6] between two "similar" loadings (actual and limit)

$$\frac{T_\Sigma}{C_A} = \frac{T_{\Sigma lim}}{\tau_{lim}} \quad \Rightarrow \quad \tau_{lim} = \frac{T_{\Sigma lim}}{\frac{T_\Sigma}{C_A}} \tag{11}$$

Fatigue Life Prediction

SN Curve to Crack Nucleation—It was assumed that crack nucleation occurs by failure of the most stressed grains along the plane experiencing T_Σ (maximum value of T_σ) and that only one glide system operates on them. Consequently, it seems natural (on this critical plane) to be interested in plastically less resistant grains whose easy glide directions coincided with the direction leading to the maximum value of the macroscopic resolved shear stress C_A. Once the accumulated plastic mesostrain Γ along this particular gliding system reached a critical value Γ_R, these grains were said to be broken, and an analytical expression of the number of cycles to initiation N_i (S-N curve) was achieved [3,6]

$$\Gamma = \Gamma_R \Rightarrow N_i = p\ln\left(\frac{C_A}{C_A - \tau_{lim}}\right) + q\frac{\tau_{lim}}{C_A - \tau_{lim}} \tag{12}$$

where p and q are functions of the hardening parameters of the three phases defined above. To derive this expression, the initial yield limit of the crystal is assumed to be negligible.

The identification of the model parameters requires two endurance limits (parameters α and β of the endurance criterion) and a single S-N curve (parameters p and q).

Variable Amplitude Loading—When dealing with variable amplitude loading, damage accumulation calculation is still carried out by adopting the three successive linear isotropic hardening rules of crystal behavior. Consequently, the mechanical parameters used for damage accumulation are the macroscopic resolved shear stress on a given gliding system and the hydrostatic stress.

Figure 6 shows, for a complex loading, the evolution of the macroscopic resolved shear stress $T(t)$ on a given gliding system and the yield limit $\tau_y^{(i)}$ reached at the ith extremum. It can be derived from the hardening rules (see Eq 4) that the segment length denoted as $\Omega_{i\to i+1}$ is proportional to the plastic mesostrain $\Gamma_{i\to i+1}$ accumulated during the transition from i to i+1

$$\Gamma_{i\to i+1} \propto \Omega_{i\to i+1} \tag{13}$$

and

$$\Omega_{i \rightarrow i+1} = \left| \mathrm{T}_{i+1} - \mathrm{T}_i \right| - 2\tau_y^{(i)} \tag{14}$$

where T_i and T_{i+1} are values of the extrema i and i+1.

If this sequence is applied successively until failure, the yield limit will first increase in the hardening phase, remain constant during saturation, and finally decrease in the softening phase.

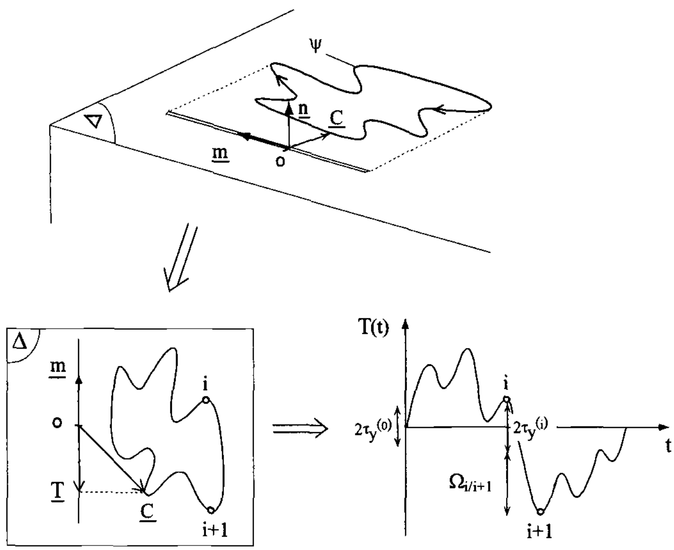

FIG. 6 *Evolutions of the shear stress* $\underline{C}$ *on a material plane, the resolved shear stress* $\underline{T}$ *on a gliding system, and the mesoscopic yield limit* τ_y *for variable amplitude loading.*

Analysis

Parameter Identification

As previously explained, the required material fatigue characteristics are two endurance limits, a SN curve, and a particular two step test. The α and β coefficients of the endurance criterion were deduced from the two fatigue limits: tension s_{-1} = 450 Mpa, and torsion t_{-1} = 330 MPa. More exactly, from (Eq 5) one can deduce

$$\alpha = \frac{t_{-1} - \frac{s_{-1}}{2}}{\frac{s_{-1}}{3}} \qquad \beta = t_{-1} \tag{15}$$

and consequently

$$\begin{aligned} \alpha &= 0.7 \\ \beta &= 330\ MPa \end{aligned} \tag{16}$$

The crack nucleation SN curve in tension was used to find the coefficients p and q of the predicted Wöhler curve (12)

$$\begin{aligned} p &= 10^4 \\ q &= 5\ 10^3 \end{aligned}$$

Finally, a two step block load was carried out by first applying a large number of cycles (i.e., 10^6 or 10^7) at about the fatigue limit level and then by cycling the same specimen at a higher level until failure. The number of cycles at the second level was used to identify one of the hardening parameters that has not been estimated with the single S-N curve.

This work was done for the torsion load condition on nine specimens. The first level 330 MPa (torsion fatigue limit) was applied for three 10^6 cycles, and a second stress of 380 MPa was submitted until failure. The number of cycles to failure is given on the SN curve in Fig. 3. It clearly appears that the application of the first load level (close to the fatigue limit) does not significantly influence the subsequent number of cycles to failure for the higher load level. One can conclude from this experimental observation that the first of the three assumed hardening phases could be neglected. In other words, the evolution of the mesoscopic yield limit could be adequately modelled by means of a saturation phase and a softening phase (Fig. 7).

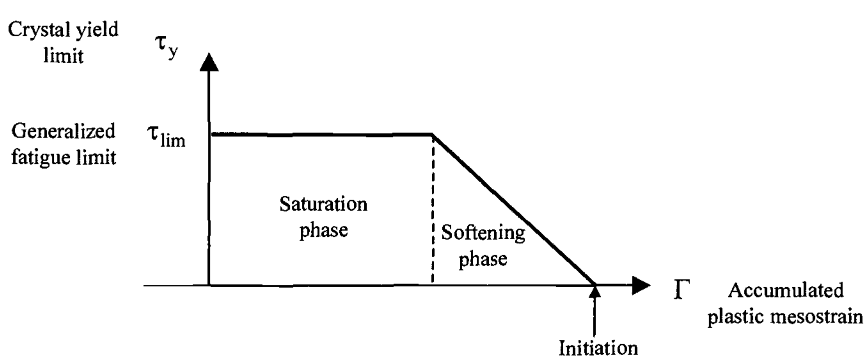

FIG. 7 *Crystal yield limit evolution for 35NCD16: saturation and softening phases.*

Predictions

The model was applied for the three load conditions (tension, torsion, and tension-torsion) and for the two filtered load sequences. The first step of the fatigue life prediction procedure was to locate the critical material plane, which, for these proportional loadings, coincides to the plane experiencing the maximum shear stress. The generalized fatigue limit τ_{lim} (also the yield limit in the saturation phase τ_s) was deduced from the endurance criterion, and the damage accumulation was carried out from the evolution of the macroscopic resolved shear stress $T(t)$ in a direction of the critical plane. The number of sequences to crack nucleation was deduced from the direction leading to the highest accumulated plastic mesostrain.

Table 3 gathers all the predicted numbers of sequences to crack nucleation. During the nucleation of a crack, it was assumed that the plastically deforming grains would show two successive hardening behaviors denoted as saturation and softening. The number of sequences to crack nucleation was composed of a saturation part and a softening part. The numbers of sequences in the softening phase are given in Table 3, and they represent about 20 % of the total fatigue life.

The comparison of the predictions and the experimental data (number of sequences to initiation) is represented in Fig. 8. It is shown that the predictions of the model, though non-conservative, were acceptable because all the predicted number of sequences to initiation were in an error band of ×2 with respect to the experimental measurements.

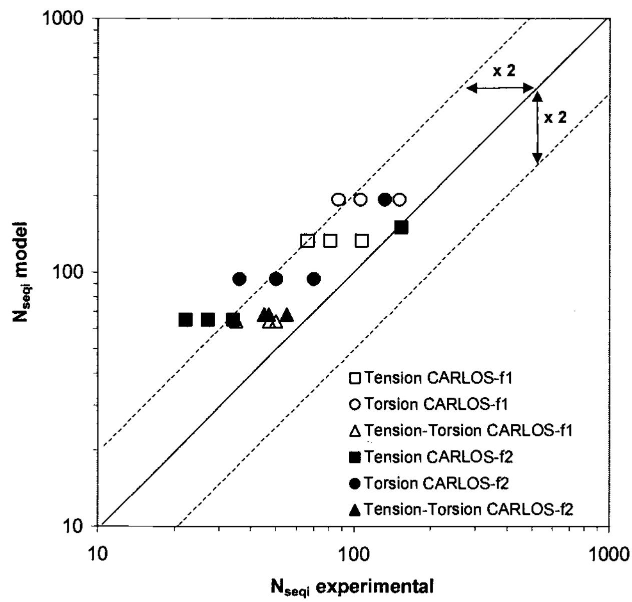

FIG. 8 *Comparison between experimental and calculated number of sequences to crack nucleation.*

The following conclusions were drawn from this comparison:

1. It seems that the model accounted for the three load conditions with the same accuracy. There was no systematic deviation from the general trend of prediction for tension, torsion, or combined tension and torsion. This means that the model was able to account adequately for different states of stress without introducing new errors.
2. The omission level did not significantly affect the predictions. Both sequences led to predictions on the non-conservative side of the graph. Though the proportional tension-torsion load conditions were applied for the two filtered sequences CARLOS-f1 and CARLOS-f2 with the same stress levels, the use of these two different sequences did not induce an important difference between the numbers of sequences to crack nucleation.

3. The model parameter that played the most important role in the prediction accuracy was the coefficient β of the endurance criterion (Eq 5), deduced from the torsion fatigue limit. The sensitivity of this model with regard to this coefficient was important since a 6 % decrease of the fatigue limit (and then of β) would lead to very good predictions (all the points then lie around the diagonal). Obviously, the fatigue limits must be precisely known to ensure predictions of good quality.

Conclusion

This paper describes the results of experiments conducted on a high strength steel under the CARLOS standard sequence by means of a relevant software tool developed for performing load controlled variable amplitude tests. The number of sequences to crack nucleation for tension, torsion, and combined tension and torsion were derived from a crack front marking technique and compared to the predictions of a fatigue life prediction model based on a microplasticity analysis. It was shown that all the predictions, though non-conservative, are within an acceptable scatter band. It was also shown that the omission level and the loading type did not affect the prediction accuracy.

The choice of accumulated plastic mesostrain as damage variable and the use of appropriate hardening rules were shown to be an efficient way to understand and describe the physical mechanisms of crack nucleation under variable amplitude loading.

Acknowledgments

We are grateful for the financial and technical support of PSA Peugeot Citroën.

References

[1] Schütz, W., "The Prediction of Fatigue Life in the Crack Initiation and Propagation Stages – A State of the Art Survey," *Engineering Fracture Mechanics,* Vol. 11, 1979, pp. 405 421.
[2] Schütz, D., Klätschke, H., Steinhilber, H., Heuler, P., and Schütz W., "Standardized Load Sequences for Car Wheel Suspension Components, Fraunhofer-Institut für Betriebsfestigkeit (LBF)," Darmstadt, Report N° FB-191, 1990.
[3] Morel, F., "A Critical Plane Approach for Life Prediction of High Cycle Fatigue under Multiaxial Variable Amplitude Loading," *International Journal of Fatigue,* Vol. 22, 2000, pp. 101 119.
[4] Dang Van, K., "Macro-Micro Approach in High-Cycle Multiaxial Fatigue," *ASTM STP 1191 Advances in Multiaxial Fatigue*, D. L. McDowell and R. Ellis, Eds., ASTM International, West Conshohocken, PA, 1993, pp. 120 130.
[5] Papadopoulos, I. V., "Fatigue Limit of Metals under Multiaxial Stress Conditions: The Mesoscopic Approach," Technical Note No. I.93.101, Commission of the European Communities, Joint Research Centre, ISEI/IE 2495/93, 1993, 46 pp.
[6] Morel, F., "A Critical Plane Fatigue Model Applied to Out-of-Phase Bending and Torsion Load Conditions," *Fatigue and Fracture of Engineering Materials and Structures,* Vol. 24, 2001, pp. 153 164.

Journal of ASTM International, September 2004, Vol. 1, No. 8
Paper ID JAI19030
Available online at www.astm.org

J. Petermann,[1] *S. Hinz,*[1] *and K. Schulte*[1]

Degradation Parameters and Two-Stress Block Fatigue of Angle-Ply Carbon Fiber Reinforced Epoxy

ABSTRACT: Experimental studies on carbon/epoxy angle-ply laminates were conducted to prove different variables for their suitability as degradation parameters and to investigate frequency and load sequence effects. Within the investigated limits, the material did not behave in a frequency dependent manner. Although different damage mechanisms dominate at $R = 0.1$ and $R = -1$, the same degradation of fatigue strength per life decade was found. The variation of longitudinal stiffness and Poisson's ratio during fatigue life (the latter being considered superior to detect delaminations) exhibited load dependent characteristics. Under two-stress block fatigue, a significant effect of the load sequence on the fatigue life was found and different mechanisms were discussed.

KEYWORDS: CFRP, fatigue degradation, stiffness, Poisson's ratio

List of Notations

Indices		Latin Symbols	
f	Fiber	D	Damage
m	Matrix	E	Longitudinal
x	Load direction	G	modulus/stiffness
y	Transverse direction	R	Shear modulus
i	Index of load blocks	n	Stress ratio = $\sigma_{min}/\sigma_{max}$
m	Number of load blocks	N	Cycle number
			Fatigue life
Abbreviations		**Greek Symbols**	
CFRP	Carbon fiber reinforced	σ	Stress
COD	polymer	ε	Strain
H	Crack opening displacement	τ	Shear stress
L	High stress load block	γ	Shear strain
ut	Low stress load block	ν	Poisson's ratio
	Ultimate tension		

Introduction

In contrast to metals, where fracture is known to result from the nucleation or initiation and subsequent growth of a single dominant crack, the fracture of fiber reinforced composite

Manuscript received 14 June 2002; accepted for publication 4 March 2003; published September 2004. Presented at ASTM Symposium on Fatigue Testing and Analysis Under Variable Amplitude Loading Conditions on 29 31 May 2004 in Tour, France; P. C. McKeighan and N. Ranganathan, Guest Editors.

[1] Graduate Research Assistants and Professor, respectively, Technical University Hamburg-Harburg, Polymers & Composites, 21071 Hamburg, Germany.

laminates is characterized by the initiation and progression of multiple failures of different modes, such as matrix cracks, interfacial debonding, fiber breaks, and delamination between adjacent plies of a laminate. The types of failure occurring, their distribution, their onset of initiation as a result of the actual load level, and their possible interactions are dependent on many parameters, such as the properties of the fiber/matrix system, the curing process, the stacking sequence of the laminate, and the influence of the environment and temperature. Consequently, there are many more potential failure modes for composite laminates than for metallic materials.

The present work investigates the applicability of different macroscopic parameters to acquire the material degradation of angle-ply CFRP under various test frequencies and load situations. Especially, the effects of block loads on the resulting fatigue lives are addressed. Environmental effects as media corrosion, humidity, temperature, or aging are not within the scope of this work.

Damage Evolution

While the fibers may serve as the primary load carrying constituent, composite properties are closely related to the matrix behavior as well. Indeed, the matrix controls the interlaminar shear and the extension perpendicular to the fiber direction. Interlaminar and intralaminar strains associated with free edges are also controlled by the matrix response [1]. As a result, general laminates subjected to service load conditions may show a substantial time dependent response.

Frequently, the monitoring of different stiffness components is waived in favor of only monitoring the longitudinal stiffness *E*, due to reduced instrumentation effort and experimental simplifications. Because the fibers (index f) are typically much stiffer than the matrix (index m), here $E_f/E_m = 66$, damage modes other than fiber fracture are hardly detectable by variations of the longitudinal stiffness in 0°-dominated or unidirectional laminates. The result is often an uncontrolled rupture of the composite, the so-called "sudden death" behavior [2]. In-plane properties like Poisson's ratio or shear stiffness may be more sensitive in detecting transverse cracks and delaminations than the longitudinal stiffness, as they are calculated from two perpendicular components.

The damage development observed in ± 45°-laminates is firstly the formation of matrix cracks parallel to the fibers and secondly the development of delaminations. The interlaminar shear stresses encourage the matrix cracks in the plies to propagate into the matrix-rich regions between the plies to form delaminations. Finally, failure occurs without fiber fractures. This brief description of damage evolution in ± 45°-laminates indicates that the static and fatigue tensile failure can be called a matrix mode because the types of damage (i.e., matrix cracking and delaminations) are not only governed by the matrix properties but are also located in the matrix [3].

Due to the absence of 0°-layers, angle-ply laminates may not exhibit fiber fracture. The longitudinal stiffness is expected to change distinctively during fatigue life and is thus a suitable degradation parameter. Since angle-ply laminates are also subject to cyclic creep [4], the hysteresis loops may be used to monitor stiffness variations and mean strain evolution.

Material

All experiments were performed on carbon fiber reinforced epoxy HTA(12K)/6376 laminates manufactured from prepreg material with a nominal thickness of 0.125 mm and cured according to the supplier's recommendations. All specimens had a symmetric $[\pm 45]_{2S}$ lay-up and a fiber volume fraction of 60 %. Specimen dimensions (Fig. 1) were 180 mm × 16 mm × 1 mm, with a gauge length of 100 mm. The specimen edges were polished with silicon carbide papers in steps from 160 1200 grit. End tabs of woven glass/epoxy of 1 mm thickness aligned at ± 45° to the load direction were used to ensure that failure occurred in the gauge section away from the grips.

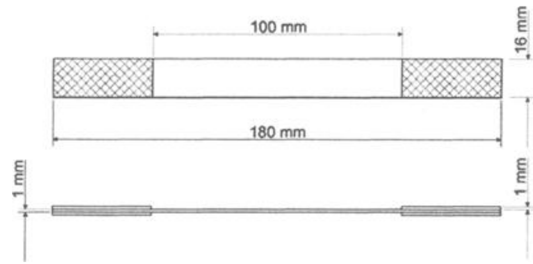

FIG. 1 *Specimen geometry.*

With x as the load direction and y as the in-plane transverse direction, shear stress τ, shear strain γ, shear modulus G, and Poisson's ratio ν are given by Eqs 1 4.

$$\tau_{xy} = \frac{\sigma_{xx}}{2} \tag{1}$$

$$\gamma_{xy} = \varepsilon_{xx} - \varepsilon_{yy} \tag{2}$$

$$\tau_{xy} = G_{xy}\gamma_{xy} \tag{3}$$

$$\nu_{xy} = -\frac{\varepsilon_{yy}}{\varepsilon_{xx}} \tag{4}$$

Table 1 summarizes some mechanical properties of fibers [5], matrix [6], and the laminate (mean value ± standard deviation) determined from tensile tests according to "Plastics – Determination of tensile properties, Part 4: Test conditions for isotropic and orthotropic fiber reinforced plastic composites" (ISO 527-4).

TABLE 1 *Material properties.*

Property	Carbon Fiber HTA (12K)	Epoxy Matrix 6376	Laminate $[\pm 45]_{2S}$
Tensile modulus [GPa]	238	3.6	20.4 ± 1.34
Shear modulus [GPa]			5.2 ± 0.24
Tensile strength [MPa]	3400	105	168 ± 3.4
Tensile strain [%]	1.4	3.1	5.4 ± 0.57
Density [g cm^{-3}]	1.78	1.31	

Figure 2*a* shows that the investigated laminate exhibits large plastic strains and a reduction of modulus prior to ultimate failure. The maximum stress is observed between 2.5 % and 3.5 % longitudinal strain. At further elongation the stress slightly decreases but remains above 95 % of the maximum stress value. The variations of longitudinal and shear stiffness as well as the

Poisson's ratio versus the shear strain are shown in Fig. 2*b*. Contrary to Fig. 2*a*, the curves are not plotted up to failure but up to the strain at maximum stress. The degradation of longitudinal and shear stiffness to ≈ 25 % of the initial values is similar. In contrast, the Poisson's ratio increases up to ≈ 145 % of its initial value. Thus, under quasi-static tensile loading, the biaxial shear stiffness and Poisson's ratio both do not exhibit superior sensitivity to loading when compared to the simple uniaxial longitudinal stiffness.

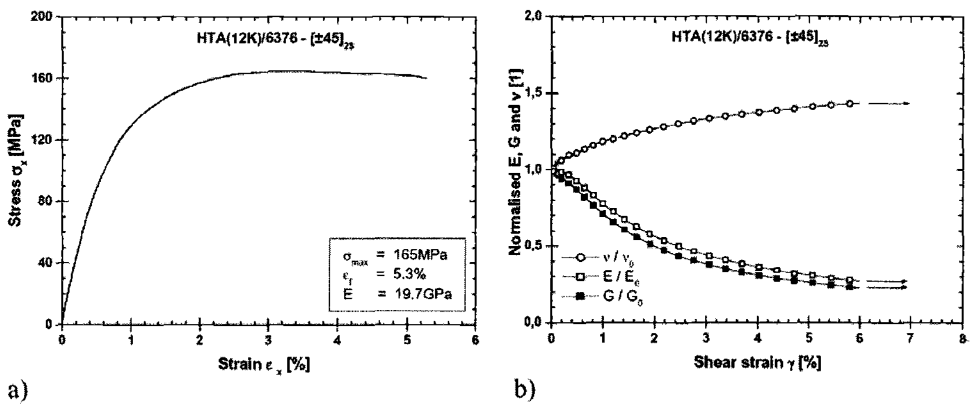

FIG. 2 *Tensile behavior:* a) *stress-strain behavior;* b) *degradation of different properties versus shear strain.*

Frequency Effects

To evaluate fatigue data from variable amplitude loading conditions or loading with varying frequencies, or to compare fatigue data obtained for different test frequencies, the dependency of the fatigue strength on the test frequency must be known. Figure 3*a* compares the fatigue mean life of several [± 45]$_{2S}$ laminates depending on the load frequency, all results being obtained from center hole specimens. Figure 3*b* and Table 2 summarize the specimen geometries.

Investigations of Sun and Chan [7] on T300/5208 and Saff [8] on AS/3501-6, each on [±45]$_{2S}$ carbon/epoxy laminates with a stress ratio of $R = \sigma_{min}/\sigma_{max} = 1/15$, did not show a consistent trend. At a frequency of 1 Hz, the AS/3501-6 material appeared to follow the data from T300/5208. At 10 Hz however, the fatigue life for AS/3501-6 was an order of magnitude shorter than for T300/5208. Sun and Chan noted no obvious differences in the failure mode for different frequencies nor stiffness degradation during fatigue life.

Dan-Jumbo et al. [9] compared the frequency dependencies of [± 45]$_{2S}$ carbon/bismaleimide IM7/5250-2 and carbon/PEEK IM6/APC-2 at R = 1/15. It was evident that the IM7/5250-2 followed the trend of carbon/epoxy systems, such as in [7] and [8]. The fatigue behavior of the thermoplastic IM6/APC-2 system was far better than that of IM7/5250-2 at low frequencies. However, at higher frequencies, the fatigue life of the thermoplastic system was drastically reduced.

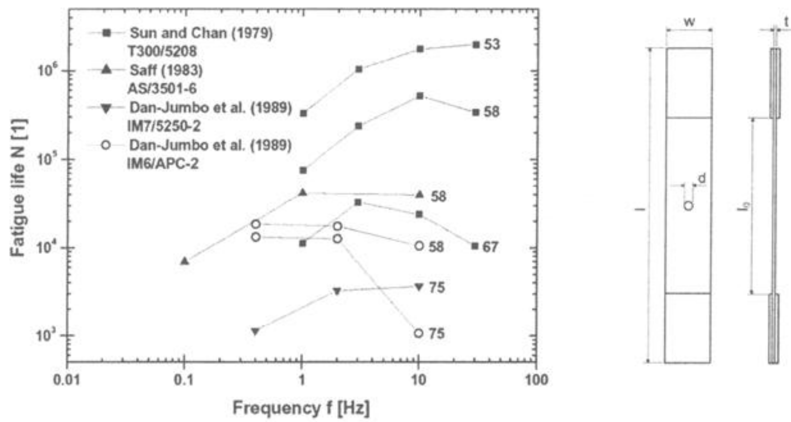

a) b)

FIG. 3 *Effect of load frequency on the fatigue life of different* $[\pm 45]_{2S}$ *laminates with a center hole:* a) *numbers shown with each line indicate loading level as percentage of composite UT-strength (R = 1/15 for all References),* b) *specimen geometry.*

TABLE 2 *Geometry of center hole specimens.*

Reference	l [mm]	l_0 [mm]	w [mm]	t [mm]	d [mm]
Sun and Chan (1979) [7]	254	178	38	1.19	6.35
Saff (1983) [8]	178	51	38	1.27	6.35
Dan-Jumbo et al. (1989) [9]	254	178	38	1.10	6.35

As a consequence of the reported results in [7 9], all of which investigated specimens with a center hole, a frequency range from 1 10 Hz was chosen to determine the variation of fatigue life of unnotched HTA/6376 $[\pm 45]_{2S}$ coupons depending on the load frequency. To amplify possible frequency effects and to exclude the influence of creep [4] reverse fatigue loading ($R = -1$) was applied. Compared to the tension-tension fatigue with $R = 1/15$ from Fig. 3, reverse fatigue describes the more severe load case that additionally includes micro-kinking of the fibers as well as global buckling, due to a reduction of bending stiffness as a result of delamination propagation.

Figure 4, summarizing data from [10] and [11], shows no obvious dependency of the S-N data on the test frequency. The S-N data obtained for different frequencies are well within the range of the fatigue-related scatter for a single test frequency. The half-filled symbols represent samples surviving the indicated number of more than 106 cycles. Therefore, the following conclusions can be drawn:

1. Since unnotched $[\pm 45]_{2S}$ HTA/6376 samples do not behave in a frequency dependent manner between 1 10 Hz, experimental data obtained for any of these frequencies can be used as a data evaluation base.
2. Frequency variations within these limits need not to be accounted for.

3. Because reverse fatigue loading ($R = -1$) is the most severe load case, conclusions 1 and 2 are applicable to other fatigue loads as long as the mean stress does not exceed the threshold value for creep [11].

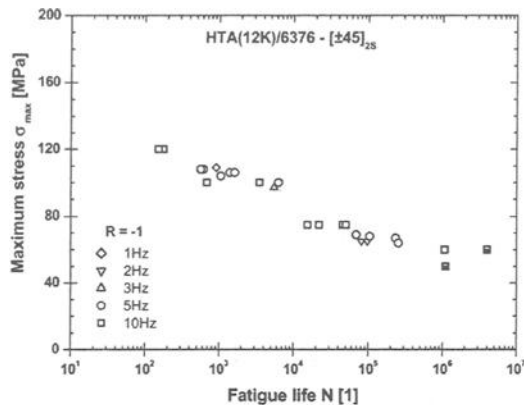

FIG. 4 *S-N data of unnotched HTA/6376 [± 45]$_{2S}$ specimens for reverse ($R = -1$) fatigue loading [10,11].*

Constant Amplitude Fatigue

Constant amplitude fatigue tests of the angle ply laminates were performed in a load controlled Instron-Schenck servo-hydraulic machine. For selected samples the fatigue tests were interrupted at selected cycle numbers to perform a quasi-static hysteresis loop to record contemporaneously longitudinal and lateral strain using extensometers with gauge lengths of 25 and 10 mm, respectively. The stress ratios were $R = 0.1$ and $R = -1$ with a sinusoidal load waveform with a frequency of 10 Hz for $R = 0.1$, and for $R = -1$, the frequency range discussed above. Figure 5 depicts the S-N data of virgin HTA(12K)/6376 [± 45]$_{2S}$ specimens.

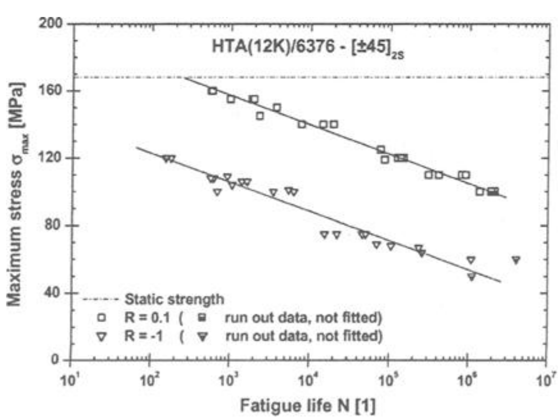

FIG. 5 *S-N data for $R = 0.1$ and $R = -1$.*

The half-filled symbols represent specimens surviving the respective number of cycles. In semi-log presentation, the fatigue data are well-approximated by a straight line. The S-N plot includes the best fit lines determined by the least square method. The numerical expressions are given by Eqs 5 and 6, where N is the fatigue life. It is noticeable that both lines exhibit essentially identical slopes.

$$R = 0.1: \quad \sigma_{max}(N) = 210MPa - 17.5MPa \cdot \lg(N), \quad R^2 = 0.975 \quad (5)$$
$$R = -1: \quad \sigma_{max}(N) = 157MPa - 17.2MPa \cdot \lg(N), \quad R^2 = 0.936 \quad (6)$$

Amplitude Dependent Fatigue Degradation

For T300/934 $[\pm 45]_{4S}$ specimens Rotem [12] reported that under reverse fatigue the shear modulus degradation is very similar to the degradation of longitudinal stiffness. As already discussed, the same trend was observed for static loading in this investigation. The subsequent investigation focuses therefore on the suitability of longitudinal stiffness and Poisson's ratio as degradation parameters.

Figure 6 compares the degradation of longitudinal stiffness and Poisson's ratio at maximum stresses of 66 % σ_{ut} (*a*) and 83 % σ_{ut} (*b*) at a stress ratio of $R = 0.1$. At both stress levels, E and ν tend to decrease with increasing cycle number. At the lower stress level, stiffness and Poisson's ratio remain almost constant for $n < 10^4$. A significant and coinciding decline of both properties is observed at $10^4 < n < 10^5$, which is less than 11 % of fatigue life.

At the higher stress level fatigue damage develops from the very first cycles. After the initial property drop, being much larger for the Poisson's ratio than for the longitudinal stiffness, the second fatigue stage is reached, characterized by $dE = dn \rightarrow 0$. The formation of delaminations is seen at $10^3 < n < 3\ 10^3$. The related clear increase in Poisson's ratio is due to less constraint and thus higher lateral strains. Fiber rotations are less retarded in delaminated areas, promoting an increase in stiffness, as seen in Fig. 6*b*. Such an increase is not expected in the presence of 0 ± –layers [13]. Thus, the variation of the Poisson's ratio as a measure to detect delamination may be preferably applied to:

- detect delaminations, because it accounts for changes of constraint in the lateral direction and
- 0° dominated laminates, which show almost no variation of longitudinal stiffness during static or fatigue loading.

In contrast, the longitudinal stiffness or the related stress and strain values require less experimental effort to record and may be used to monitor matrix dominated laminates such as those investigated here. The longitudinal strain further allows the amount of creep during fatigue loading to be assessed [4,11].

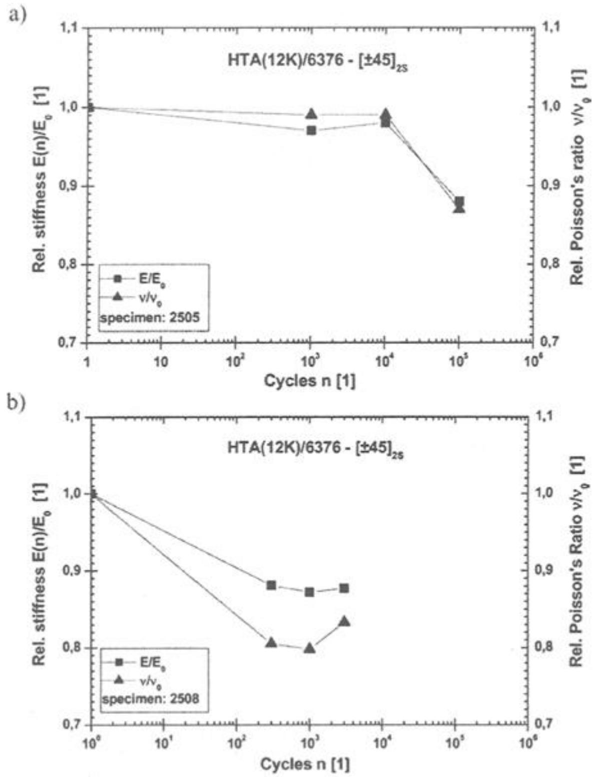

FIG. 6 *Variation of relative longitudinal stiffness and relative Poisson's ratio as a function of cycle number: a) $R = 0.1$, $\sigma_{max} = 110MPa$, $N = 900800$, b) $R = 0.1$, $\sigma_{max} = 140MPa$, $N = 7750$.*

Two-Stress Block Fatigue

Results

To investigate the effect of different load sequences on the fatigue behavior, two-stress block fatigue tests were performed with $R = 0.1$. Maximum stresses of 110 MPa and 140 MPa were chosen for the two stages, referred to here as L (low) and H(high). For both load sequences, the load stages were changed between 25 75 % of the expected fractional fatigue lives determined from Eq 5. At the second stress level, cycling was continued until failure. The linear cumulative damage law given in Eq 7 was used to convert the respective cycle number into the fractional life of the second block. In Eq 7, m is the number of load blocks, and N_i is the expected fatigue life for the i-th block.

$$D = \sum_{i=1}^{m} D_i = \sum_{i=1}^{m} \frac{n_i}{N_i} \tag{7}$$

Figure 7 compares fractional lives of the investigated load sequences. The abscissa shows the fractional fatigue life of the first load block; the ordinate shows the fractional life of the second load block. Based on the actual applied stress, the data points were calculated from Eqs 5 and 7. The diagonal line (D = 1) predicts failure according to the Palmgren-Miner rule [14,15]. The damage accumulation behavior was found to be nonlinear regarding the load sequence. The Palmgren-Miner damage law gives a conservative fatigue life estimation for the H-L loading sequence (D_{mean} = 1.29) but highly overestimates the fatigue life for the L-H sequence (D_{mean} = 0.69).

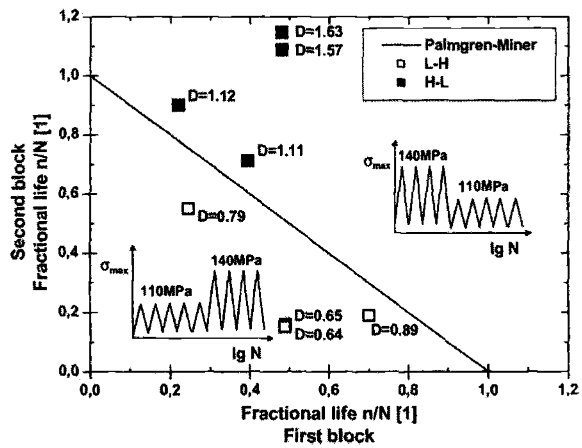

FIG. 7 *Fatigue lives depending on load sequence.*

Discussion

The experimental fatigue lives for the L-H and H-L sequence do not coincide with the linear damage accumulation curve. While for H-L sequence the sum of fractional lives exceeds unity, it is the opposite for the L-H sequence, implying a more damaging character of the L-H load sequence if compared to independent constant amplitude fatigue tests. In contrast, an extension of fatigue life is achieved for the H-L sequence. Similar results for ± 45°-laminates were achieved by Yang and Jones [16] for carbon/epoxy and by Lee and Jen [17] for carbon/PEEK.

An explanation of the different damage accumulation behavior according to load sequence and lay-up is the varying occurrence and dominance of different damage mechanisms, namely cracks inclined with the fiber direction and delaminations, both interacting with each other. The number of crack intersections between the layer interfaces quadratically depends on the crack quantity. Therefore, a lower number of cracks conditions a reduced number of crack intersections and thus, less locations for delamination initiation.

L-H Sequence—Micro-cracks inclined with the fiber direction develop in all layers during the sustained L-block. The corresponding crack opening displacements (CODs) are small as a result of the lower applied stress. Although the maximum stresses exceed the limit of linear elastic behavior (Fig. 2*a*), the amount of permanent deformation due to the applied fatigue load remains low. Due to the high number of cycles, the crack saturation occurs at a low stage [18]. Visible expression (Fig. 8) is the constant strain amplitude during the first load block which determines the longitudinal stiffness. The slight increase of the mean strain is due to plastic deformation in the matrix and at the matrix crack tips. Delaminations may initiate at the crack intersections between the adjacent layers, however, their propagation is retarded because of small CODs.

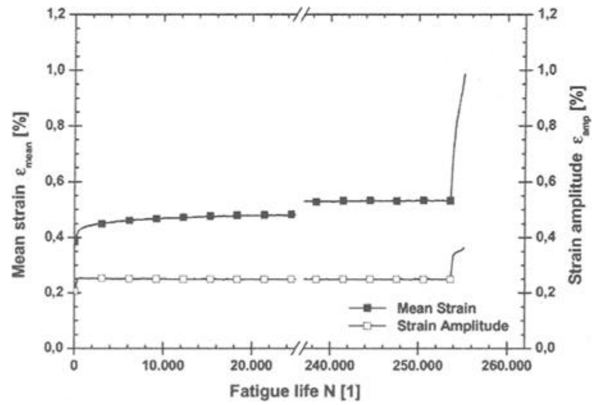

FIG. 8 *Mean strain and strain amplitude evolution for the L-H sequence.*

The change to the higher load causes higher strain levels. The higher load level also shifts the characteristic damage state to higher crack densities [18]. Thus, further cracking occurs, and the increased CODs lead to fast propagation and coalescence of the already initiated and additional delaminations until failure occurs. The last stage is accompanied by a loss of longitudinal stiffness, noticeable at the strain amplitude increase after the higher load level is reached. The resulting fatigue life is reduced.

H-L Sequence—Due to the higher applied load during the first block, the matrix undergoes plastic deformation (Fig. 2*a*) visible at the continuously increasing mean strain in Fig. 9. The initiated matrix cracks exhibit large CODs with reduced stress intensities at the crack tips because of plastic zones related to compressive residual stresses. Thus, the crack propagation is retarded. Due to the low number of cycles at that stress level, the crack distance remains high, and a crack saturation does not occur. From the constant strain amplitude data, it can be concluded that no extensive delamination takes place.

As the L-stage begins, the stress level is reduced, and the formation of further matrix cracks continues with diminished velocity or even stops. The latter depends on the preceding plastic deformation at the crack tips. The compressive residual stresses cause crack closure at reduced stress levels. Further initiation and propagation of cracks as well as the growth and coalescence of delaminations is delayed to higher cycle numbers. Therefore, the resulting fatigue life is extended. The mean strain and strain amplitude remain almost constant (Fig. 9) until failure occurs suddenly.

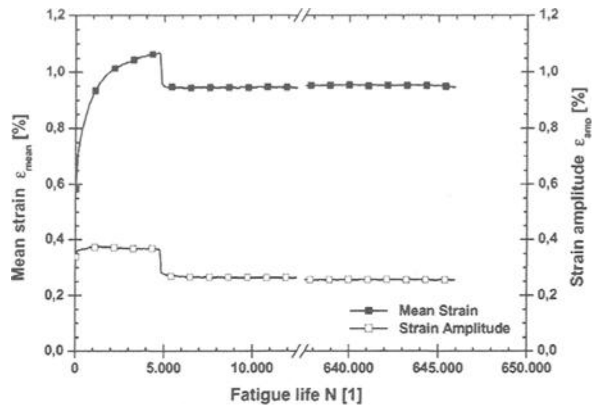

FIG. 9 *Mean strain and strain amplitude for H-L sequence*

Summary

After clarification of the damage evolution behavior in angle-ply laminates, an experimental program aiming to describe the material degradation under static and fatigue loads by a macroscopic parameter was conducted under laboratory conditions, i.e., at room temperature and 60 % humidity. Limited to these conditions, the following results can be summarized:

1. Under static load conditions, biaxial parameters, such as shear stiffness or Poisson's ratio, are not more sensitive degradation parameters than the uniaxial longitudinal stiffness.
2. Constant amplitude S-N data for reverse fatigue loading of unnotched coupons are not frequency-dependent between 1 10 Hz.
3. Although different damage mechanisms dominate at $R = 0.1$ (tension-tension) and $R = -1$ (tension-compression), the same degradation of fatigue strength per life decade is found.
4. The variations of the longitudinal stiffness and the Poisson's ratio during fatigue life exhibit load dependent characteristics. The latter appears superior to detect delamination.
5. Under two-stress block fatigue, a highly nonlinear damage accumulation behavior was observed. The load sequence significantly affects the fatigue life. Different dominating damage mechanisms were assessed and discussed.

With regard to technical applications, the conclusions 2, 3, and 5 must not be transferred to aging effects as a result of UV-radiation, with the consequence that the chemical structure of the constituents and thus the deformation and fracture behavior might have changed. However, the authors believe that conclusions 1 and 4 can be generalized for environmental conditions.

Acknowledgments

The authors gratefully acknowledge support of this work from the collaborative *CFRP Fuselage* programme of the Federal Ministry of Economics (BMWi) and Airbus Germany, and valuable discussions with Prof. A. Plumtree from the University of Waterloo, Canada. The assistance of J. Dahl in carrying out parts of the test program is also acknowledged.

References

[1] Dillard, D. A. and Brinson, H. F., "A Numerical Procedure for Predicting Creep and Delayed Failures in Laminated Composites," *Long Term Behaviour of Composites, ASTM STP 813*, T. K. O'Brien, Ed., ASTM International, West Conshohocken, PA, 1983, pp. 23 37.
[2] Chou, P. C. and Croman, R., "Degradation and Sudden-Death Models of Fatigue of Graphite/Epoxy Composites," *Composite Materials: Testing and Design, ASTM STP 674*, S.W. Tsai, Ed., ASTM International, West Conshohocken, PA, 1979, pp. 431 454.
[3] Wevers, M., *"Identification of Fatigue Failure Modes in Carbon Fibre Reinforced Composites,"* Ph.D. thesis, Katholieke Universiteit Leuven, Belgium, 1987.
[4] Petermann, J. and Schulte, K., "Strain Based Service Time Estimation for Angle-Ply Laminates," *Composites Science and Technology*, 62 (7 8), 2002, pp. 1043 1050.
[5] Enka AG. *Tenax - Industrial Fibres*, May 1986.
[6] Hexcel Composites. *6376 Product Data Sheet*, February 1997. Publication FTA051.
[7] Sun, C. T. and Chan, W. S., "Frequency Effect on the Fatigue Life of a Laminated Composite," *Composite Materials: Testing and Design (Fifth Conference), ASTM STP 674*, S. W. Tsai, Ed., ASTM International, West Conshohocken, PA, 1979, pp. 418 430.
[8] Saff, C. R., "Effect of Load Frequency and Lay-Up on Fatigue Life of Composites," *Long-Term Behaviour of Composites, ASTM STP 813*, T.K. O'Brien, Ed., ASTM International, West Conshohocken, PA, 1983, pp. 78 91.
[9] Dan-Jumbo, E., Zhou, S. G., and Sun, C. T., "Load-Frequency Effect on Fatigue Life of IM6/APC-2 Thermoplastic Composite Laminates," *Advances in Thermoplastic Matrix Composite Materials, ASTM STP 1044*, G. M. Newaz, Ed., ASTM International, West Conshohocken, PA, 1989, pp. 113 132.
[10] Dahl, J., Term thesis, Technical University Hamburg-Harburg, Germany, 2002.
[11] Petermann, J. and Schulte, K., "The Effects of Creep and Fatigue Stress Ratio on the Long Term Behaviour of Angle-Ply CFRP," *Composite Structures*, 57 (1 4), 2002, pp. 205 210.
[12] Rotem, A., "Stiffness Change of a Graphite Epoxy Laminate under Reverse Fatigue Loading," *J Composites Technology & Research*, 11 (2), 1989, pp. 59 64.
[13] Van Dreumel, W. H. M. and Kamp, J. L. M., "Non Hookean Behaviour in the Fibre Direction of Carbon-Fibre Composites and the Influence of Fibre Waviness on the Tensile Properties," *J Composite Materials*, 11, October 1977, pp. 461 469.
[14] Palmgren, A., Die Lebensdauer von Kugellagern. *Zeitschrift des Vereins Deutscher Ingenieure*, 68, 1924, pp. 339 341.
[15] Miner, M. A., "Cumulative Damage in Fatigue," *J Applied Mechanics*, 12 September 1945, pp. A159 A164.
[16] Yang, J. N. and Jones, D. L., "Effect of Load Sequence on the Statistical Fatigue of Composites," *American Institute of Aeronautics and Astronautics (AIAA) Journal*, 18 (12), 1980, pp. 1525 1531.
[17] Lee, C.-H. and Jen, M.-H. R., "Fatigue Response and Modelling of Variable Stress Amplitude and Frequency in AS-4/PEEK Composite Laminates, part 2: Analysis and formulation," *J Composite Materials*, 34 (11), 2000, pp. 930 953.
[18] Lee, J.-W., Daniel, I. M., and Yaniv, G., "Fatigue life prediction of cross-ply composite laminates," *Composite Materials: Fatigue and Fracture, Second Volume, ASTM STP 1012*, Paul A. Lagace, Ed., ASTM International, West Conshohocken, PA, 1989, pp. 19 28.

Journal of ASTM International, October 2004, Vol. 1, No. 9
Paper ID JAI19046
Available online at www.astm.org

Yasumitsu Tomita,[1] *Kiyoshi Hashimoto,*[1] *Naoki Osawa,*[1] *Koji Terai,*[1] *and Yehong Wang*[1]

Study on Fatigue Design Loads for Ships Based on Crack Growth Analysis

ABSTRACT: Although ship structural members are designed to survive 20 years, fatigue crack damage still occurs, often starting very early in the ship's life, with some cracks growing quickly to considerable size. The primary factor causing variability is the sequence of the variable amplitude load cycle, and the others are welding irregularities on the weld toe and variations in mechanical properties in the material. In this paper, the load sequence effect on fatigue life variability is examined by the use of a fatigue design procedure proposed by the authors. It is found that the fatigue lives of ship structural members vary from several months to 20 years, strongly dependent on the sequence of sea state which ships encounter during ocean-going service. The worst possible loading sequence is elucidated for the fatigue life of the ship's hull. Sensitivity study of fatigue life is discussed.

KEYWORDS: fatigue design, crack growth analysis, storm model

Introduction

To ensure that ship structural members survive 20 years or 10^8 stress cycles, engineers have been obliged to apply the Classification Society rules [1 4] to ship design. However, fatigue crack damage still occurs, often starting very early in a ship's life, with some cracks growing quickly to considerable size. Moreover, when two ships sail the same route, fatigue crack damage can occur in one and not in the other. Current fatigue design methods cannot adequately predict or analyze this type of damage and differences in crack growth behavior, which are known as the variability of fatigue life of welded structures.

Under variable amplitude loading conditions, the primary factor causing variability is the sequence of load cycles, but even under constant amplitude loading conditions, this variability exists. The other factors are welding irregularities on the weld toe and variations in the mechanical properties of the material; two factors beyond human control are today's level of welding and steel-making technology.

To develop better fatigue life evaluation, we need to analyze the sources of the variability of fatigue life and understand the extent of the variability. The authors have proposed a new fatigue design procedure for the ship's hull, with the key idea being the adoption of fatigue crack growth analysis, instead of Miner's rule [5,6]. This enables evaluation of the effect of both load sequence and welding irregularities on fatigue life variability.

In this paper, we focus on the load sequence effect on fatigue life variability. Using the proposed procedure, we examine the extent of the variability of fatigue life caused by the sequence of wave-induced loads during ocean-going service and find that fatigue life varies from several

Manuscript received 19 April 2002; accepted for publication 17 July 2003; published October 2004. Presented at ASTM Symposium on Fatigue Testing and Analysis Under Variable Amplitude Loading Conditions on 29 31 May 2002 in Tours, France; P. C. McKeighan and N. Ranganathan, Guest Editors.

[1] Professor, Research Assistant, Associate Professor, and Graduate Students, respectively, Department of Naval Architecture and Ocean Engineering, Graduate School of Engineering, Osaka University, 2-1 Yamada-oka, Suita, Osaka, 565-0871, Japan.

months to 20 years, depending on the load sequence. We also determine the worst possible load sequence for the fatigue design of the ship's hull and discuss the sensitivity study of fatigue life.

New Fatigue Design Procedure

To derive a fatigue design procedure, we first need to determine how to evaluate fatigue strength and how to calculate the working stress and the wave load sequence induced by wave load acting on structural members.

Fatigue Strength Evaluation

Fatigue strength evaluation methods can be grouped into two categories: one is the approach based on linear cumulative damage analysis, Miner's rule; and the other is fatigue crack growth analysis, the Paris equation. Fatigue damage accumulates non-linearly during stress cycles, yet neither method can precisely take into consideration non-linear damage accumulation. Fatigue damage also depends on the sequence of working stress, and any fatigue strength evaluation method should consider the effect of the load sequence.

Conventional fatigue design procedures like the Classification Society rules have adopted linear cumulative damage analysis, which is insufficient for evaluating the effect of the load sequence on fatigue life. The Paris equation (fatigue crack growth analysis), on the other hand, at least calculates the amount at any given moment of crack growth using working stress and crack length, and it can take into consideration the effect of load sequence on fatigue crack growth life. Thus, the proposed new method adopts crack growth analysis.

Working Stress on Structural Members

In order to calculate working stresses on ship structural members, we need a wave scatter diagram (wave height, period, and direction) and the ship's course within a given sailing area. This is because working stresses on structural members vary not only by wave height and period, but also by the angle at which a ship encounters a wave, called the relative angle (Fig. 1). During ocean-going service, a ship meets each new wave at a particular relative angle. As a result, there is a series of relative angle events in any voyage, and a model that incorporates such a series is termed a "sailing model." In order to make a proper sailing model that expresses the true series of relative angles during a voyage, a great deal of data regarding wave direction and ship course is needed. However, at present there are few such data.

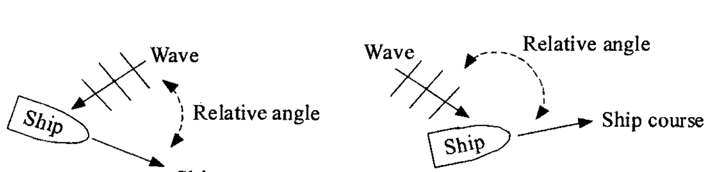

FIG. 1—*Relative angle.*

The conventional fatigue design procedure adopts the all headings model, one of the possible sailing models. This all headings model assumes that every relative angle occurs with equal probability, and the probability of exceedance of stress level σ_x is calculated as the average of the probability of exceedance of every relative angle that produces stress level σ_x (Fig. 2).

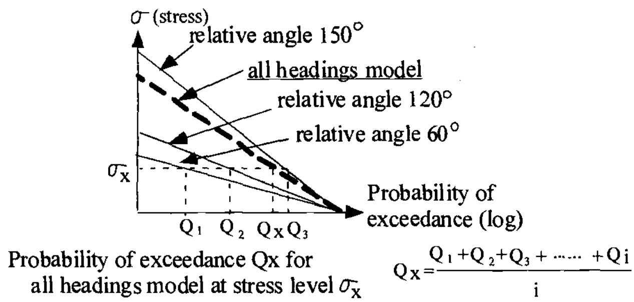

FIG. 2—*Long-term distribution of stress for all headings model.*

It is clear that this model cannot accurately express the actual sequence of relative angles, that is, true working stress during service, which is important in designing a proper model that can simulate sailing conditions. The authors have studied new sailing models, as follows [5,6]:

1. Random sailing model [5]. Relative angle θ_i is limited to increments of 30° of pitch, as follows; θ_i is equal to 0°, 30°, 60°, ---, 300°, 330°. Then, in the random sailing model, θ_i is chosen at random (θ_i = 30°, 150°, 60°, ---) and is kept constant for periods of 1000 and 48 000 stress cycles. The 48 000 cycle period corresponds to the length of any given sea condition, which is assumed to be 3.5 days in the North Pacific (see Sequence of Working Stress and Sailing Model). However, this model occasionally produces unrealistic relative angles; for example, relative angle 180° may occur immediately after relative angle 0°, which is impossible in reality.
2. Random walk model [6]: Relative angle θ_i is determined by the random walk model. The subsequent relative angle (θ_{i+1}) is restricted only to three directions, (θ_{i+1} -30°), (θ_{i+1}), and (θ_{i+1} + 30°) and is kept constant for periods of 1000 and 48 000 stress cycles. The transition probability of each relative angle, which moves one angle to the next, is 1/3. In this paper, the random sailing model is adopted (see Results and Discussion).

Long-term distribution of working stress is the sum of the working stress induced by each wave during ocean-going service. It can be expressed as a Weibull distribution and is usually approximated to be exponential.

Sequence of Working Stress

The conventional fatigue design procedure has employed the time independent random process to describe the sequence of wave load (Fig. 3). The authors have investigated the concept of sequence of wave occurrence during sailing in the North Pacific and have decided that it is not a time independent random process, but a time dependent one. We have also come to the conclusion that wave conditions encountered by ocean-going ships can be grouped into two classes: storm condition and calm sea condition [7]. In storm condition, with higher wave height, the occurrence order of wave height is a time dependent process. Wave height increases linearly over time, reaches a maximum value at one point only, and then begins to decrease gradually. In calm sea conditions with relatively low wave height, on the other hand, it is reasonable to look upon the occurrence order of wave height as a time independent random process. We have composed a storm model as a sequence of working stress, in which these two conditions alternate randomly (Fig. 4).

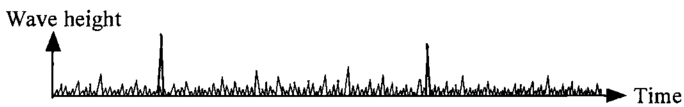

FIG. 3—*Time independent random process model.*

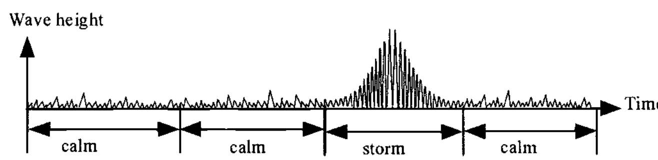

FIG. 4—*Storm model.*

Fatigue Crack Growth Analysis

We employ a modified Paris-Elber's equation to estimate the fatigue crack growth rate, which is based on the linear elastic fracture mechanics theory, as follows

$$\begin{aligned} \frac{da}{dN} &= C\{(\Delta K_{eff})^m - (\Delta K_{eff,th})^m\} \\ \Delta K_{eff} &= K_{\max} - K_{op} \end{aligned} \quad (1)$$

where

C, m = material parameters,
ΔK_{eff} = effective stress intensity factor range,
$\Delta K_{eff,th}$ = effective threshold stress intensity factor range,
K_{max} = maximum stress intensity factor, and
K_{op} = crack opening stress intensity factor.

For the present, engineers cannot derive the material parameters, C and m, the effective threshold stress intensity factor range, $\Delta K_{eff,th}$, and the crack opening point stress intensity factor, K_{op}, from theoretical analysis, and they must obtain them experimentally. $\Delta K_{eff,th}$ and K_{op} vary depending on the loading pattern and mean stress, so it is desirable to use the values obtained from tests performed for loading conditions similar to those encountered during sailing. As for $K_{th,r}$, which is threshold stress intensity factor obtained from fatigue tests under random amplitude load conditions with an exponential distribution, its value is higher than that of $K_{th,c}$, which is threshold stress intensity factor obtained from fatigue tests under constant amplitude load conditions [8]. In this paper, it is conservatively assumed that $K_{th,r}$ is equal to $K_{th,c}$. There are not enough fatigue test data under variable amplitude load conditions similar to actual working stresses on ship structural members to decide material parameters, C and m. For the material parameters, C, m, and $\Delta K_{eff,th}$, we use the value obtained from constant amplitude fatigue test results [9], in which the steels used in fatigue tests are similar to ASTM A515, A573, and A633.

$$C = 1.45\times10^{-11};\quad m = 2.75 \text{ (SI unit)};\quad \Delta K_{eff,th} = 2.45 \text{ MPa}\cdot\text{m}^{1/2}$$

K_{op} of the surface crack also cannot be derived from either analysis or experiment, so by necessity engineers use K_{op} of through-thickness crack. K_{op} is given as Eq 2, derived from the results of storm model fatigue tests [10]. Under variable random loading conditions, in general, a load interaction (retardation/acceleration) occurs every cycle, resulting in quite a different situation in the overall loading cycles. Therefore, in this paper, a load interaction effect is not directly taken into consideration, but it is done partially by using K_{op} obtained from storm model random loading fatigue tests.

$$K_{op} = \begin{cases} -30.6 & (K_{max} \le -31.5\,MPa\cdot\text{m}^{1/2}) \\ 0.75\times K_{max} - 7.0 & (-31.5\,MPa\cdot\text{m}^{1/2} < K_{max} < 38.5\,MPa\cdot\text{m}^{1/2}) \\ 21.9 & (K_{max} \ge 38.5\,MPa\cdot\text{m}^{1/2}) \end{cases} \tag{2}$$

Raju and Newman have proposed an approximated equation to calculate the stress intensity factor for a semi-elliptical surface crack in a finite plate subjected to tension fatigue load, which is as follows [11]:

$$K = \sigma\times\sqrt{\frac{\pi b}{Q}}\times F(\frac{b}{a},\frac{b}{t},\varphi) \tag{3}$$

where

K = stress intensity factor,
σ = nominal stress,
b = depth of surface crack,
a = half length of surface crack,
t = plate thickness,
Q = shape factor for an ellipse,
F = boundary correction factor, and
φ = parametric angle of the ellipse.

Surface fatigue cracks in ships typically initiate along weld toes of wrap-around and fillet welds, where stress concentration due to structural discontinuity and weld geometry are superimposed. When the stress concentration factor of member K_S and the correction factor M_k for weld bead are superimposed on the calculation of the SIF for the surface crack at weld toe, Eq 3 can be transformed as follows. The stress concentration factor K_s is obtained from FEM analysis. M_k is calculated using equations in [12,13]. These factors, at the position of length and depth, change as the surface crack grows.

$$K = \sigma \times \sqrt{\frac{\pi b}{Q}} \times F(\frac{b}{a}, \frac{b}{t}, \varphi) \times K_s \times M_k \tag{4}$$

In general, welding irregularities exist on the weld toe, and as a result, multiple surface cracks initiate there. These cracks are different in terms of size, shape, place, and number, and then grow to become long, shallow, elliptical surface cracks, joining with each other. An example of multiple surface cracks in structural members is shown in Fig. 5, based on tests by Kada et al. [14].

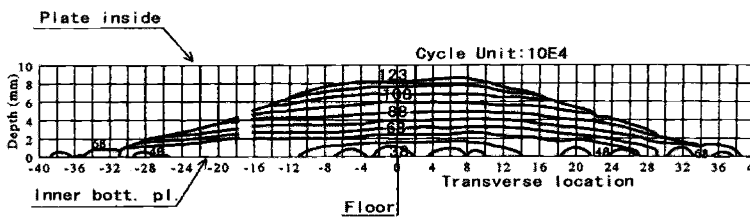

FIG. 5 *Multiple surface crack.*

For engineers to apply fatigue crack growth analysis, they need to determine the initial surface crack occurrence in terms of size, shape, place, and number of surface cracks. However, there are few data on this subject, and no method has been devised for arriving at such determinations. Thus, single crack occurrence is assumed instead, which leads to an overestimation of structural fatigue life and fails to explain long, shallow surface cracks [15].

The aim of our research is to do a comparative study of the effect of load sequence on fatigue life variability. Therefore, we assume that a single surface crack with a semi-circular shape initiating at weld toe grows to become a through-thickness crack. The initial crack size is set to be 0.4 mm in length (= $2a_0$) and 0.2 mm in depth (= b_0). As the surface crack grows, the stress concentration factor of the structural member at the place of the surface crack varies, and this effect is taken into consideration.

Sequence of Working Stress and Sailing Model

The North Pacific route is chosen as the sailing route, and the sequence of wave load (storm model) is composed as follows [7].

1. The total number of waves over 20 years is 10^8, so the mean wave period is about 6.3 s.
2. Calm sea and storm conditions, with assumed durations of 3.5 days (48 000 waves or 48 000 stress cycles), are classified according to the maximum significant wave height. Storm conditions are divided into six kinds, Storms A–F (Table 1).

3. The long-term distribution of wave height is approximated to be an exponential distribution. The wave height condition in a storm is considered to be a stationary short-term random process, so the probability distribution of wave height can be described by the Rayleigh distribution.
4. The frequency of each wave height/wave period combination, which appears in both sea conditions, can be determined by using the frequency of wave height (see 3 above) and the wave scatter diagram for the North Pacific [16].
5. In calm sea conditions, the wave period varies depending on the change of relative angle, but in storm conditions it varies according to wave height.
6. The occurrence probability of each sea condition is decided based on Table 1; for example, the probability of storm F is 1/2084, and the calm sea condition is 1991/2084.
7. A sequence of sea conditions is generated by a sampling with replacement. Therefore, the long-term distribution of generated wave height does not necessarily follow an exponential distribution.
8. In the present simulation, the worst case corresponds to the series of Storm F and the best case to the series of calm sea conditions.
9. The relative angles for storm and calm sea conditions are chosen at random and remain constant for 48 000 stress cycles.

TABLE 1 *Calm sea and storm conditions in the North Pacific.*

Short-Term Sea Condition	Maximum Wave Height, m	Occurrence Probability
Calm Sea Condition	5.0	1991/2084
Storm A	6.0	42/2084
Storm B	7.0	25/2084
Storm C	8.0	12/2084
Storm D	9.0	7/2084
Storm E	11.0	6/2084
Storm F	15.0	1/2084

The loading patterns used are summarized in Fig. 6. Full and ballast loading conditions are chosen and appear by turns every two weeks. Mean stresses at both loading conditions are 80 MPa and –80 MPa, respectively (Fig. 6).

For each sea condition, wave height is approximated to vary by 1 m. Loading Pattern 1 reflects a decreasing storm model; that is, the order of each sea condition is from larger storm to calm sea. Loading Pattern 2 is the opposite of Loading Pattern 1, an increasing storm model, and Loading Pattern 3 reflects a normal storm model; that is, each sea condition appears at random and naturally involves Loading Patterns 1 and 2. Loading Pattern 4 reflects a time independent random loading with mean stress. Twelve different types of load sequences are produced for each Loading Pattern 1 4.

Results and Discussion

We chose the inner bottom plate at lower stool of a bulk carrier as a typical ship structural member and assessed the influence of the load sequence on fatigue crack growth life by numerical simulation (Fig. 7).

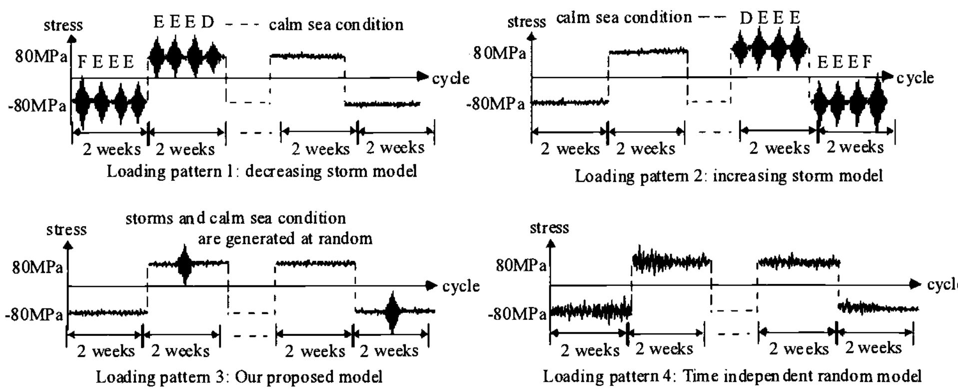

FIG. 6—*Loading patterns.*

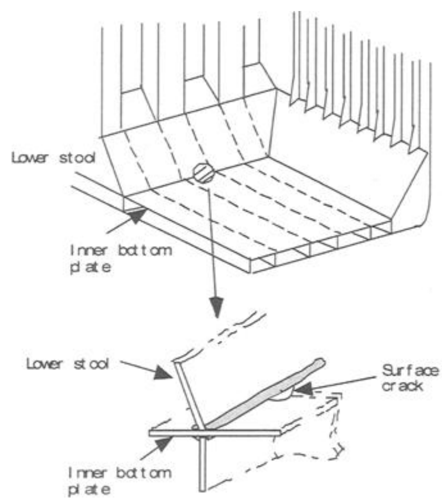

FIG. 7—*Ship structural member for crack growth analysis.*

To calculate wave-induced stress, we used the stress response function of the structural members derived from Ship Research Panel 228, Japan [17]. Wave induced stress is decided by wave height, wave period, and relative angle. The function F', which calculates working stress on structural members, is called stress response function

$$\sigma = F'(h,T,\theta) \tag{5}$$

where

F' = stress response function,
h = wave height,
T = wave period, and
θ = relative angle.

We computed crack growth lives under Loading Pattern 3 for each of 12 different types of load sequence with random and random walk sailing models [5,6]. The relative angle was kept constant for periods of 1000 and 48 000 cycles. Extreme crack growth curves, which indicate the maximum and minimum fatigue lives, are shown in Fig. 8. Average fatigue life and variance are listed in Table 2.

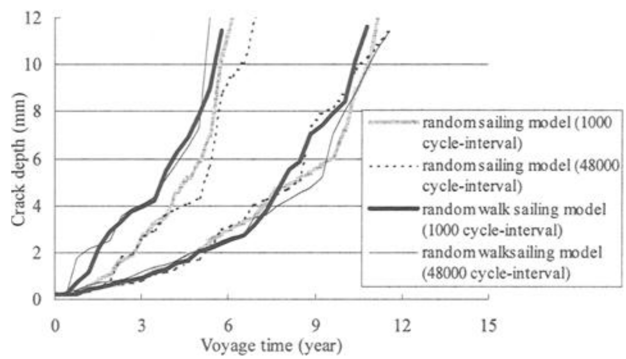

FIG. 8 *Crack growth curves under different sailing models.*

TABLE 2 *Average life and sample variance.*

Sailing Model	Interval Cycle	Average Life, years	Sample Variance
Random sailing model	48 000	9.3	1.8
Random sailing model	1000	9.0	1.2
Random walk sailing model	48 000	8.6	2.3
Random walk sailing model	1000	8.8	1.4

For all cases, the average fatigue life is almost the same, but the variance for the random sailing model with a 1000 cycle-interval is smaller than for the other cases. As stated above, the random sailing model does not always produce a true sailing state. However, when we evaluate the fatigue life of structural members by the use of surface crack growth analysis, it can be said from simulation results that the random sailing model is applicable. Consequently, this paper focuses on crack growth life using the random sailing model with a 48 000 cycle-interval.

In Fig. 9, we show crack growth curves computed for 12 different types of load sequence for both Loading Patterns 3 and 4. The black thin lines represent crack growth curves of the storm model incorporating the all headings model, the broken lines incorporating our random sailing model, and the black thick lines incorporating the time independent random model. Extreme crack growth curves are shown in Fig. 9. Compared to our storm model, it is very important to note that there is little scatter in the patterns of fatigue crack growth life when the load sequence follows the time independent random process model. In other words, when the load sequence follows the time dependent random model, there is a relatively large scatter of fatigue life.

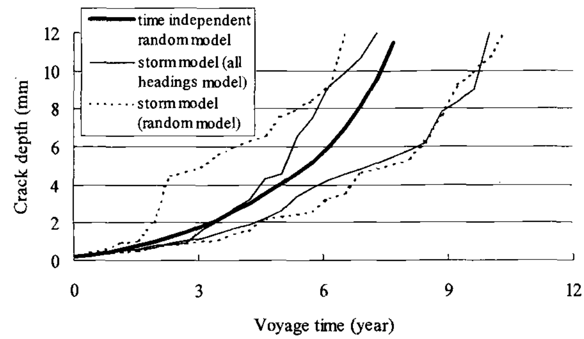

FIG. 9—*Comparison of crack growth curves under storm model and time independent random process model.*

We also compared fatigue life in the all headings model versus the random sailing model under one fixed occurrence order of sea state. Crack growth curves are computed for 12 different types of relative angle sequence (load sequence) for both the all headings model and the random sailing model. Extreme crack growth curves are shown in Fig. 10. In our random sailing model, if the relative angle differs, the amount of crack growth differs. On the other hand, since relative angle is not considered in the all headings model, only a single result emerges, as shown in Fig. 10.

In order to discuss more fully the extent of the variability of fatigue crack growth life, we computed crack growth curves for 12 different types of load sequence under Loading Patterns 1–3, and extreme crack growth curves are shown in Fig. 11 (maximum stress range 260 MPa in Storm F) and Fig. 12 (maximum stress range 182 MPa in Storm F).

From Figs. 9–12, it is obvious that fatigue life is extremely scattered, from several months to 20 years, and it largely depends on the number, the order, and the size of sea conditions, as well as the relative angle sequence (sailing model). However, it turns out that fatigue life evaluated by Miner's rule for all these loading patterns is more than 20 years [6].

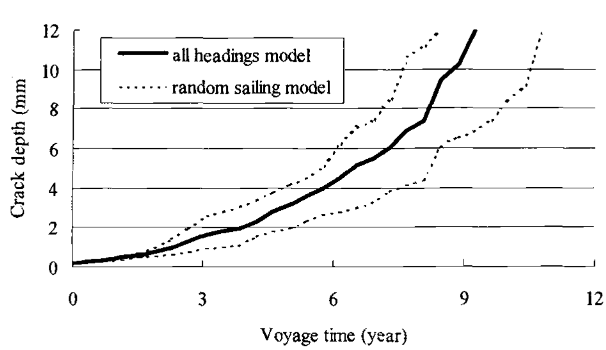

FIG. 10—*Comparison of crack growth curves in the all headings model versus in the random sailing model.*

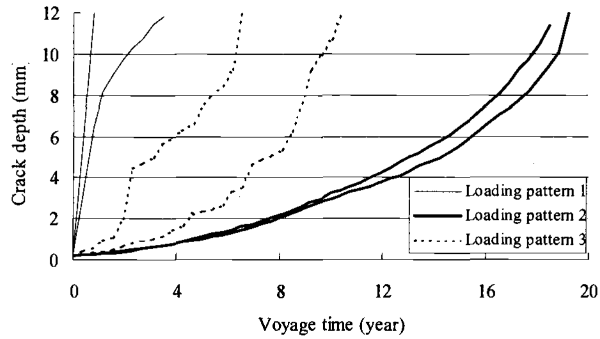

FIG. 11 *Comparison of crack growth curves under different loading patterns (maximum stress range 260 MPa in Storm F).*

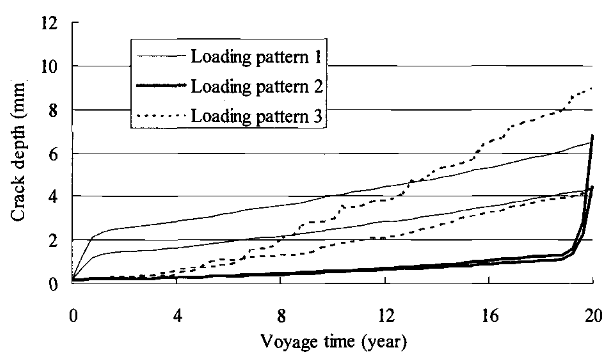

FIG. 12 *Comparison of crack growth curves under different loading patterns (maximum stress range 182 MPa in Storm F).*

Fatigue damage occurs when ships encounter several storms in a row, and it may not occur when they sail only in calm sea conditions. With a compressive mean stress, even if ships encounter storms, little or no crack growth appears. Moreover, it can be assumed that there exists a load sequence that makes cracks grow much faster. The worst possible load sequence would be the decreasing storm model, in which all storms happen in tensile mean stress conditions.

Next, we computed the growth of a surface crack of a depth of 2 6 mm in the case of sailing only in calm sea condition. As shown in Fig. 13, if the surface crack reaches to 4 6 mm in depth for any reason, even if a ship sails only in calm sea conditions, the surface crack grows easily to through-thickness crack. This means that the existence of a surface crack of 4 6 mm in depth is dangerous for residual fatigue life.

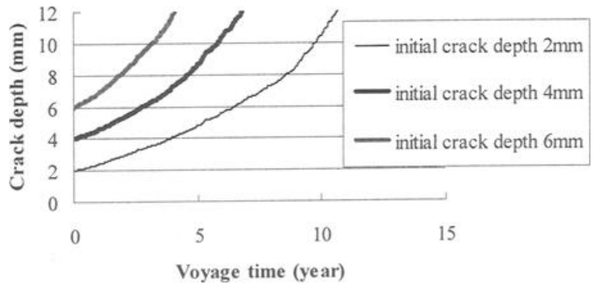

FIG. 13 *Crack growth curves with different initial crack size under calm sea condition.*

In summary, the loading sequence is one reason for the variability of fatigue life, and it also can lead to fatigue crack damage starting very early in a ship's life. Other facts explained by load sequence include why cracks grow to considerable size, and why even when two ships sail the same route, fatigue crack damage may occur in one and not in the other. Therefore, it is very important to choose an appropriate loading pattern for ship design.

We computed crack growth curves for the condition of mean stress 80 MPa and –80 MPa and 40 MPa and –40 MPa under Loading Pattern 3. The K_{op} used is obtained from constant amplitude and storm model fatigue test results [10,18]. Crack growth analyses are performed under 12 different types of load sequences, and extreme crack growth curves are shown in Figs. 14 and 15.

It is apparent that there is a difference in fatigue life with mean stress 40 MPa and –40 MPa and 80 MPa and –80 MPa, and moreover, the amount of crack growth calculated by the use of K_{op} obtained from the constant amplitude loading fatigue test is lower over time than the one obtained from storm model test results. This means that we should carefully calculate mean stress alternation during ocean-going service, and we must use K_{op} obtained from proper fatigue tests using the storm model.

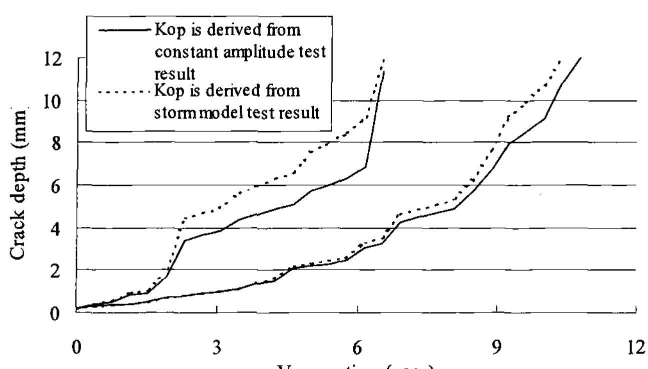

FIG. 14—*Comparison of crack growth curves calculated by using K_{op} obtained from storm model and constant amplitude test result (mean stress alternation: from 40 MPa to –40 MPa).*

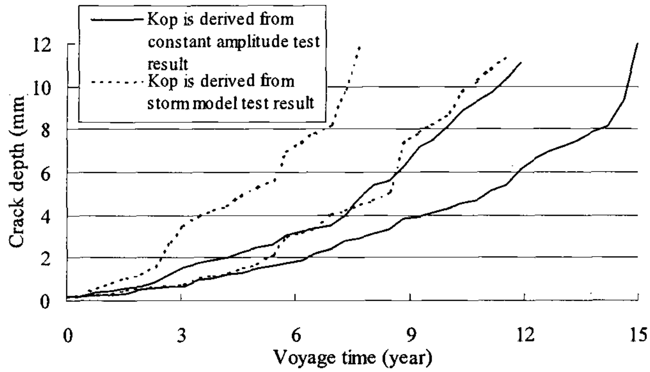

FIG. 15 *Comparison of crack growth curves calculated by using K_{op} obtained from storm model and constant amplitude test result (mean stress alternation: from 80 MPa to –80 MPa).*

Finally, we did a sensitivity study. We reduced the stress intensity factor K by 10 40 % and computed fatigue lives based on various initial crack sizes with the single case of Loading Pattern 3, as shown in Fig. 16. Fatigue life doubled when the stress intensity factor was reduced by 20 %, and it tripled when reduced by 30 %. We can realize a reduction of the stress intensity factor by decreasing nominal stress and also by decreasing the stress concentration factor of the structural members and weld bead. From the design point of view, we first have to try to improve structural details and make a smoother weld bead.

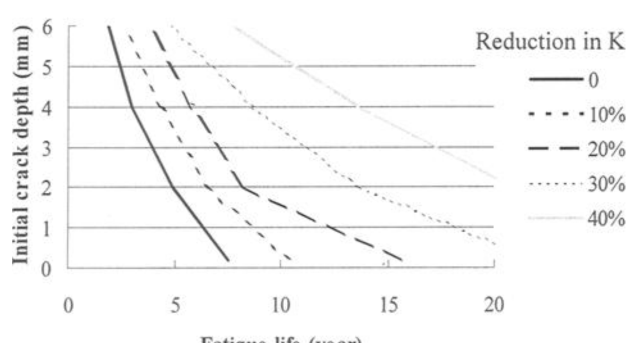

FIG. 16—*Fatigue strength diagram with different initial crack depth (reduction 0 = maximum stress range 260 MPa in Storm F).*

Conclusion

This paper shows that the fatigue life of a ship's hull is strongly affected by the load sequence (the alternating pattern of calm sea and storm conditions). Therefore, it is very important to choose the appropriate loading pattern in ship design. Moreover, reducing the stress intensity factor of structural members with surface cracks is a very effective way to improve the fatigue life of a ship's hull.

In this paper, it is assumed that only a single surface crack initiates at the weld toe. However, in reality, multiple cracks occur there. Ultimately, we need to know the effect of multiple surface crack initiation on the variability of crack growth life. This is a subject we have now started to study.

Reference

[1] "ABS Steel Vessel Rule 2002 Part 5, Chapter 3, Appendix 1, Guide for Fatigue Strength Assessment of Bulk Carriers," *American Bureau of Shiping*, 2002.

[2] "Classification Note 30.7, Fatigue Assessment of Ship Structures," *Det Norske Veritas*, 2002.

[3] "Ship Right, Fatigue Design Assessment procedure," *Lloyd's Register of Shipping*, 1996.

[4] "Guidance for Fatigue Strength Assessment of Bulk Carrier," *Nippon Kaiji Kyoukai*, 2002.

[5] Tomita, Y., Hashimoto, K., Osawa, N., and Terai, K., "Fatigue Strength Evaluation of Ship Structural Members Based on Fatigue Crack Growth Analysis," *Conference Proceedings of International Conference on Ship and Shipping Research, NAV*, Vol. 2, 2000, pp. 10.4.1 10.4.11.

[6] Terai, K., Tomita, Y., Hashimoto, K., and Osawa, N., "Fatigue Design Method of Ship Structural Members Based on Fatigue Crack Growth Analysis," *The Eleventh International Offshore and Polar Engineering Conference, ISOPE*, Vol. 4, 2001, pp. 589 594.

[7] Tomita, Y., Kawabe, H., and Fukuoka, T., "Statistical Characteristics of Long-Term Wave-Induced Load for Fatigue Strength Analysis for Ships," *Practical Design of Ships and Mobile Units, PRADS*, Vol. 2, 1992, pp. 2792 2805.

[8] Tomita, Y. and Hashimoto, K., "Fatigue Crack Growth Rate Diagrams under Random Loading with an Exponential Distribution," *International Institute of Welding*, XIII-1238-87, 1987.

[9] Ship Research Panel 219, "Study on Practical Use for Fatigue Crack Growth Analysis," *Shipping Research Association of Japan*, 1996 (in Japanese).

[10] Tomita, Y., Hashimoto, K., Osawa, N., Terai, K., and Wang, Y., "Experimental Study of Mean Stress Effect on Fatigue Crack Growth Under Variable Amplitude Loading," *Fatigue Testing and Analysis under Variable Amplitude Loading Conditions, ASTM STP 1439*, P. C. McKeighan and N. Ranganathan, Eds., ASTM International, West Conshohocken, PA, 2004.

[11] Newman, J. C. and Raju, I. S., "An Empirical Stress Intensity Factor Equation for the Surface Cracks," *Engineering Fracture Mechanics*, Vol. 15, Nos. 1 2, 1981, pp. 185 192.

[12] Maddox, S. J. and Andrews, R. M., "Stress Intensity Factors for Welded Toe Cracks," *Localized Damage* 90, 1990.

[13] Pang, H. J., "A Review of Stress Intensity Factors for Semi-Elliptical Surface Crack in a Plate and Fillet Weld Joint," *Weld. Inst. Rpt.* 426, 1990.

[14] Kada, K., Matsuoka, K., and Tomita, Y., "Fatigue Strength of Large Structural Model of Double Hull VLCC Bilge Knuckle Part under Variable Amplitude Loading Conditions," *Fatigue Testing and Analysis Under Variable Amplitude Loading Conditions, ASTM STP*

1439, P. C. McKeighan and N. Ranganathan, Eds., ASTM International, West Conshohocken, PA, 2004.

[15] Wang, Y., Terai, K., Tomita, Y., Hashimoto, K., and Osawa, N., "A New Approach to Fatigue Strength Evaluation of Ship Hull," *International Offshore and Polar Engineering Conference, ISOPE*, 2002.

[16] Shinkai, A. and Wan, S., "The Statistical Characteristics of Wave Data in the North Pacific and Long-Term Predictions," *Transactions of the West-Japan Society of Naval Architects*, No. 90, 1995, pp. 115 120 (in Japanese).

[17] Ship Research Panel 228, "Study on Loads and Stress Long-Term Response of Hull Structures in Waves," *Shipping Research Association of Japan*, 1999 (in Japanese).

[18] Kato, A., Kurihara, M., and Kawahara, M., "An Expression of Fatigue Crack Propagation Rates under Wide Ranged Stress Ration," *Journal of the Society of Naval Architects of Japan*, Vol. 153, 1983, pp. 336 343 (in Japanese).

Journal of ASTM International, Nov./Dec. 2004, Vol. 1, No. 10
Paper ID JAI19048
Available online at www.astm.org

Joachim Hünecke[1] *and Dieter Schöne*[1]

Life Prediction by Observation and Simulation of Short Crack Behavior in a Low Carbon Steel

ABSTRACT: Short fatigue cracks were investigated in a 0.14 wt % carbon steel (SAE 1017) in fine grained condition by optical observation of the surface of smooth specimens under fatigue loading. Axial fatigue experiments were carried out under constant and step amplitude conditions. The lifetime to crack initiation was calculated for each ferrite grain with regard to grain size and orientation. For the calculation of crack propagation, the slip band length (grain size) and the distance between crack tip and next barrier (grain boundary) are taken into consideration. Furthermore, the simulation program includes some geometrical aspects for the description of crack coalescence.

KEYWORDS: fatigue, short cracks, crack simulation, optical microscopy, low carbon steel

Introduction

Loading sequence is shown to affect the fatigue damage state. Step tests starting with the high amplitude show a resulting Miner sum smaller than 1 for failure crack formation. Reversed step tests exhibit Miner sums greater than 1. This behavior is a result of load dependent crack initiation rates combined with crack retardation effects at microstructural barriers. The combination of these different effects cannot be calculated properly by a linear accumulation of damage. Instead of the Miner rule, a model should be used, which can describe the origin of material fatigue more accurately. This paper presents a method for optical monitoring of short cracks during fatigue loading. It is well established that short cracks are the major mechanism for failure crack formation in the class of low carbon steels and that the measurement of short cracks can be used to characterize the inherent damage induced by fatigue. Life prediction should be improved by use of a computer based simulation procedure, which took the three stages of short crack behavior into account, and this is in good correlation with the experimental observed short cracks.

Experimental Method

A cold rolled steel SAE 1017 with a sheet thickness of 8 mm has been investigated. The chemical composition of the investigated steel shows low contents of carbon and alloying elements (Table 1).

After a heat treatment (20 min. at 910°C and air cooling), an average grain size of 10 μm resulted (fine grained condition). The microstructure consists of 88 % ferrite and 12 % pearlite

Manuscript received 19 April 2002; accepted for publication 3 October 2002; published November 2004. Presented at ASTM Symposium on Fatigue Testing and Analysis Under Variable Amplitude Loading Conditions on 29 31 May 2002 in Tours, France; P. C. McKeighan and N. Ranganathan, Guest Editors.

[1] Research Scientists, Federal Institute for Materials Research and Testing, Unter den Eichen 87, 12205 Berlin, Germany.

(Fig. 1). Some characteristic mechanical properties of the fine grained steel Cm15 are shown in Table 2.

Experimental investigations were performed on smooth specimens with R = –1 (Fig. 2). The contour of the specimens was prepared in a multi-stage process by milling, grinding, mechanical polishing, and electropolishing.

TABLE 1 *Chemical composition of steel SAE 1017.*

Element	C	Si	Mn	P	S	Cr
Wt %	0.14	0.18	0.56	0.004	0.024	0.13

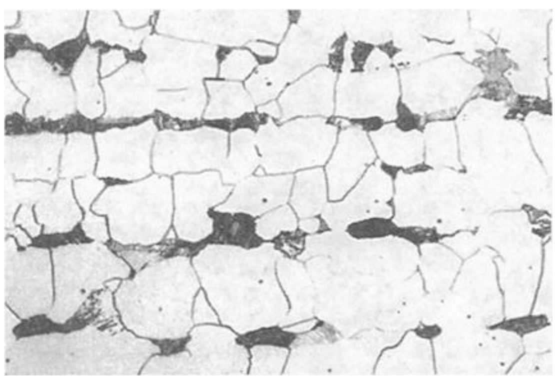

FIG. 1 *Microstructure of the fine grained steel SAE 1017 with banded pearlite grains, image width = 0.11 mm; loading axis was parallel to the pearlite bands, resulting direction of crack propagation perpendicular to the pearlite bands.*

TABLE 2 *Tensile test data of steel SAE 1017 in fine grained condition.*

Lower Yield Stress, MPa	Tensile stress, MPa	True failure stress, MPa	Elongation, %	Reduction of area, %
290	444	853	37.8	58.5

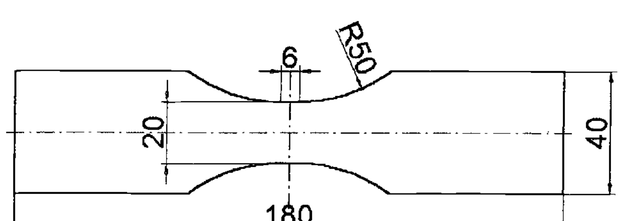

FIG. 2 *Geometry of the tested smooth specimen (notch factor ~ 1.0).*

Strain controlled fatigue experiments were carried out under constant and step amplitude conditions. Step tests were performed on two load levels. The length of the first load block was in all cases defined by a partial Miner sum of 0.5. Two different loading sequences were examined. In the case of the low-high (LH) step tests, 84 500 cycles were applied at the first lower load block ($\varepsilon_a = 0.00130$). For the high-low (HL) step tests, only 17 750 were applied at the initial higher load block ($\varepsilon_a = 0.00216$). After changing to the second load level, the tests were continued until the failure crack length was detected, even if the Miner sum reached values above 1 (for the LH-loading tests). The stress ratio was in all fatigue tests set to $R = -1$ (fully reversed). The strain rate was set to 0.02/s. A test matrix is shown in Table 3.

TABLE 3 *Survey of fatigue tests.*

	Constant Amplitude Loading	Step Amplitude Loading, Sequence High-Low (HL)	Step Amplitude Loading, Sequence Low-High (LH)
No. of experiments with optical crack detection	4	1	1
Total no. of experiments	5	3	3

For measurement of the elongation of the fatigue specimen, an extensometer with a gauge length of 5 mm was used (Fig. 3). The system for optical monitoring consisted of a long-distance microscope (Makroskop M420, manufactured by Leica) with an attached CCD-camera with a resolution of 1520 × 1144 pixels. The complete optical system was mounted with a special tripod to the servo-hydraulic testing machine. The used tripod allowed any selectable area of the specimen surface to be scanned by shifting the complete optical equipment.

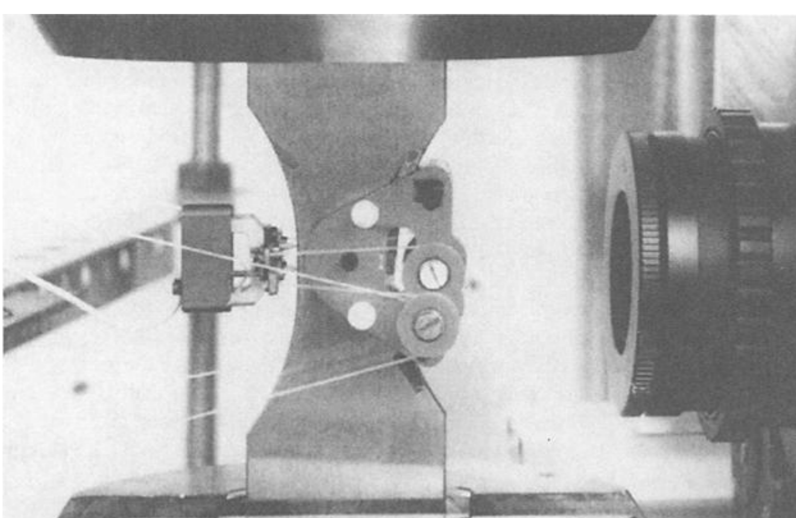

FIG. 3 *Optical examination of smooth specimen surface with attached extensometer.*

CCD images were taken after each block of 5000 10 000 fatigue cycles with a stopped testing machine. The CCD images were stored on a PC system and mounted with high accuracy to panorama pictures consisting of 12 single pictures. The panorama pictures were oriented perpendicular to the loading direction and showed specimen areas of 6 mm^2. An image processing program was used for marking the visible cracks by manual operation in layer technique. Therefore, the panorama pictures containing the original specimen surfaces were used as background layers, whereas the marking of the detected short cracks took place on the transparent foreground layers. For the final calculation of crack lengths, the layers containing the marked images were separated from the original pictures and transferred into a vector graphics format.

Analytical Procedure

For a more realistic analysis, important components of the mechanism-based model were integrated in the crack simulation program. The real microstructure was modelled with regard to grain size, grain orientation and phase boundaries (pearlite phase). These properties of the microstructure influenced the crack initiation as well as the crack propagation.

The two-dimensional simulation procedure started with the generation of a mesh containing 7490 grains for a specimen area of about 0.48 mm^2. Figure 4 shows a part of the simulated specimen surface. Equilateral hexagons were used, which, for a more realistic microstructure, were deformed by moving the six nodes by a random operation. Grain orientations were generated due to a random distribution function. Therefore, the three angles in space were generated by a random operation for each grain. The maximum shear stress was calculated for each ferrite grain by using the Schmid factor equation with regard to each in the bcc-lattice active slipsystem. Additionally, the angle between the direction of the active slip band on the specimen surface and the loading direction was calculated for each grain.

Due to the limited capacity of the used computer system, the simulation was restricted to a small specimen area. So it was possible that one of the propagating tips of a crack was located outside of the generated area of the synthetic microstructure. The propagation rates of these crack tips were set equal to those of the corresponding second crack tip of the same crack.

Calculations of fatigue life to crack initiation were performed for each ferrite grain by using the dislocation pile-up model of Tanaka et al. [1] in analogy to the equation given by Hoshide et al. [2], assuming that crack initiation took place along the predicted slip-bands. Based on a work of de los Rios et al. [3], calculations of crack propagation were performed with regard to slip band length (given by grain size) and the distance between crack tip and next barrier (given by location of grain boundaries and pearlite grains). In accordance with measurements of the short crack propagation behavior [4], the reduced crack growth in the pearlite phase was taken into consideration. Furthermore, the interaction between neighboring cracks was considered. Crack shielding effects between neighboring cracks (resulting in a decreased local crack initiation behavior and a reduced local crack propagation rate) were modelled by the simple assumption that the stress gradient around the crack follows a linear function. Additionally, the interaction of adjacent cracks (resulting in coalescence of the involved cracks) was taken into account. Corresponding to the Dugdale-Barenblatt model, the critical interaction zones of crack tips were calculated for each crack [5].

The simulated short crack behavior was calibrated to the experimental data of the constant amplitude tests with only one consistent parameter set, which was also used for the latter, following short crack simulation under step amplitude loading.

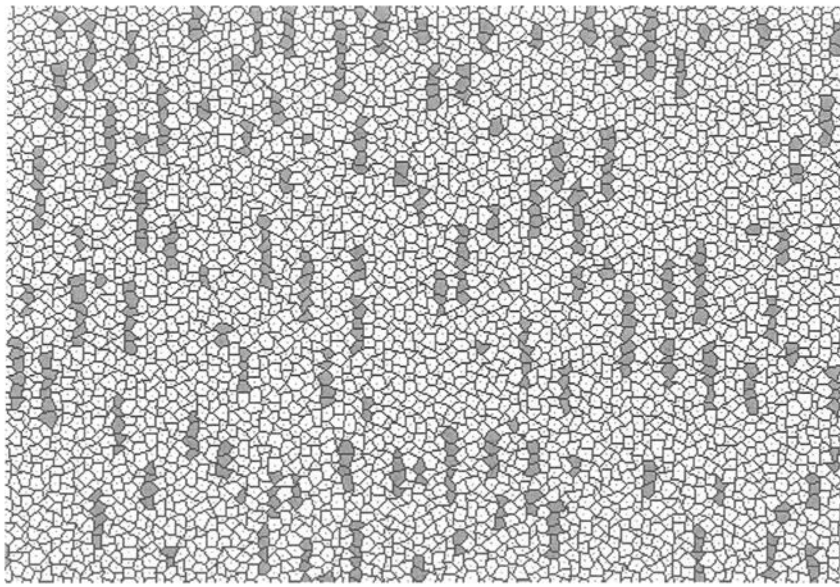

FIG. 4 *Partial view of the simulated smooth specimen surface with banded pearlite grains, image width = 0.6 mm, loading axis parallel to the pearlite bands, resulting in direction of crack propagation perpendicular to the pearlite bands.*

Experimental Results and Verification of the Simulation

The behavior of the total crack density under constant amplitude loading is shown in Fig. 5. Experiments running at high strain levels ($\varepsilon_a = 0.00216$) exhibited extreme values for the total crack density with a peak value before end of specimen life is reached. Contrary to this, the situation in experiments under low strain amplitudes ($\varepsilon_a = 0.00130$) was characterized by a steady increase of the crack density. The critical crack length used to define end of test or specimen failure was 0.5 mm.

The initiation rate of short cracks increased dramatically with increasing strain amplitude (Fig. 6). Near the endurance limit (≤ 0.0007), only a few cracks formed until the end of specimen life was reached. Contrary to this situation, low cycle fatigue was characterized by an enhanced initiation of short cracks. The short crack behavior depended not only on the crack propagation rate but also on the crack initiation rate. The crack initiation rate is defined as the additional amount of cracks per unit area, which are initiated new during a certain number of fatigue cycles. At low strain amplitudes, the cracks were isolated from each other, and specimen life depended mainly on the propagation behavior of the short cracks. Special interest was focussed on the crack, identified later as leading to failure. With increasing strain amplitude, the number of initiated short cracks became more important than the crack propagation rate itself. The higher number of initiated cracks caused an enhanced coalescence behavior of neighboring cracks, which was responsible for the failure crack formation. The possibility for coalescence free crack propagation decreased as the number of cracks increased. Each crack coalescence process reduced the total number of counted cracks, because two cracks were replaced by only one new crack.

The experimental specimen lifetimes for the constant amplitude tests are given in Table 4. In addition to the experimental investigations, a computer based simulation procedure was performed for the constant amplitude tests. The displayed experiments are anchor tests for the step loading tests, because the crack simulation procedure was calibrated to these results. The calibration process includes a realistic short crack behavior, which can be described by the crack density function and the crack length density distribution function. Both must be comparable to the experimental and calculated data with regard to the experimental scatter. Table 4 provides a comparison between the measured lifetimes and lifetimes calculated by the simulation program.

Table 5 provides a comparison of the experimental and calculated results. The top of the table displays the test mode. Letters H and L indicate the reference constant amplitude tests with only high or low block loading. The last two columns (named HL and LH) show the results for the step amplitude fatigue test.

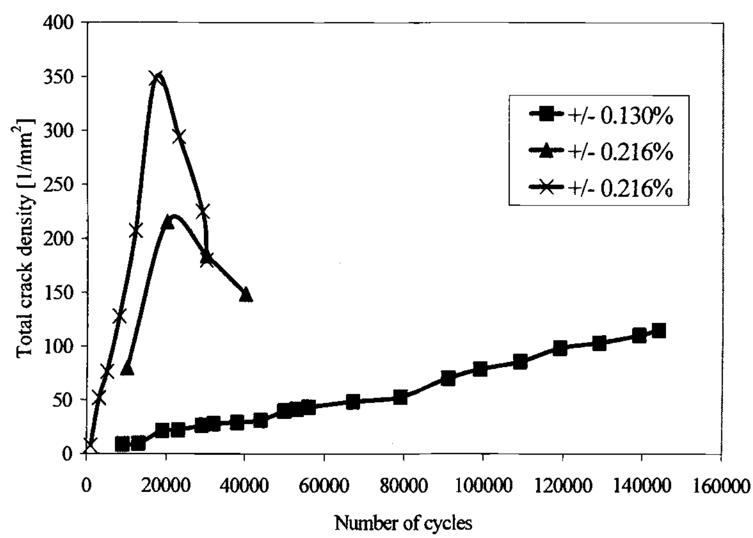

FIG. 5 *Comparison of the total density of measured short cracks for constant amplitude fatigue tests.*

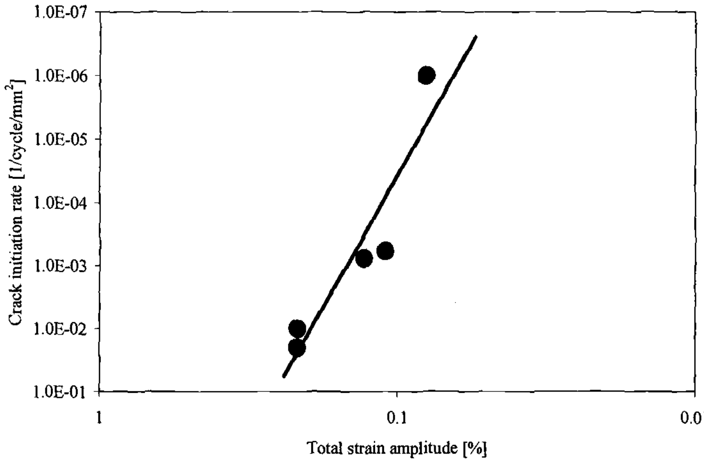

FIG. 6 *Comparison of the short crack initiation rates for the constant amplitude fatigue tests.*

TABLE 4 *Measured and calculated lifetimes in cycles for failure crack formation for the constant amplitude fatigue tests.*

Specimen Loading ε_a R = −1	Experimental Lifetime	Calculated Lifetime
0.00080	725 000	N/A
0.00110	162 380	190 500
0.00130	179 300	169 000
0.00216	40 000	35 500
0.00216	29 948	35 500

TABLE 5 *Measured and calculated lifetimes in cycles for failure crack formation for the step amplitude fatigue tests.*

Loading	H	L	HL	LH
ε_a	0.00216	0.00130	0.00216 → 0.00130	0.00130 → 0.00216
N_H	failure crack	N/A	17 750	failure crack
N_L	N/A	failure crack	failure crack	84 500
N_B Exp.	34 974*	179 300	70 055*	109 491*
N_B Calc.	35 500	169 000	72 000	107 000

*Mean value.

The behavior of the total crack density for the step tests is displayed in Fig. 7. The initial increase of crack density in the case of HL-loading was similar to the constant amplitude loading tests with ε_a = 0.00216. After switching to the lower block, the number of counted cracks decreased. This is a result of the reduced crack initiation rate and the coalescence process of short cracks. Additionally, the lower load amplitude reduced the crack propagation rate. Compared to the reference constant amplitude test with ε_a = 0.00216, an increased specimen lifetime results. Similar observations were made for the LH-loading step tests. The behavior of the total crack density for the first lower load block was comparable to the tests under constant amplitude loading with ε_a = 0.00130. After changing to the higher load block, an increased crack initiation rate was observed. The comparison to the HL-loading test showed a decreased crack density during the first part of the specimen lifetime. After the first loading block was finished, the number of cracks for further propagation was smaller than for the reversed loading sequence. As a result, the possibilities for coalescence of neighboring cracks were reduced, and a higher lifetime and, in consequence, an increased Miner sum resulted.

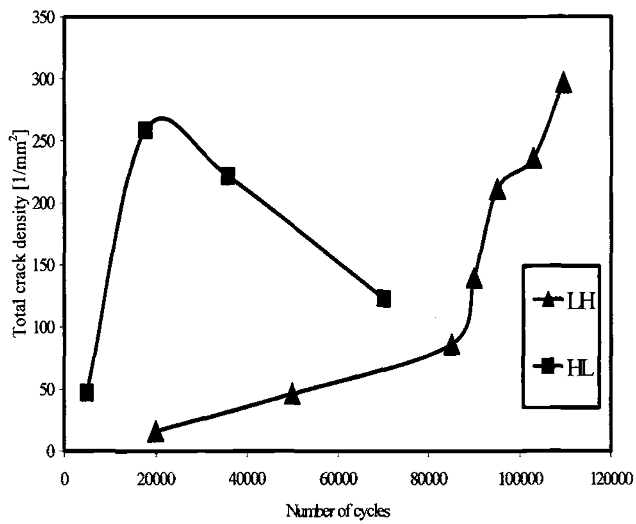

FIG. 7 *Comparison of the total density of measured short cracks for the loading sequences HL (left curve) and LH (right curve).*

The behavior of the accumulated crack length is shown in Fig. 8. The accumulated crack length can be defined as the sum of all measured single crack lengths per unit area. In case of the HL-loading sequence, the high initial crack initiation rate caused a fast increase of the accumulated crack length during the first loading block. In the second block, with reduced initiation and propagation behavior of short cracks, this increase was more moderate. Opposite observations were made for the LH-loading sequence. Please note that for both loading sequences the values of the final accumulated crack length are comparable. Values of similar magnitude can be found for the constant amplitude tests. Therefore, accumulated crack length seems to be a rather good failure criterion [6].

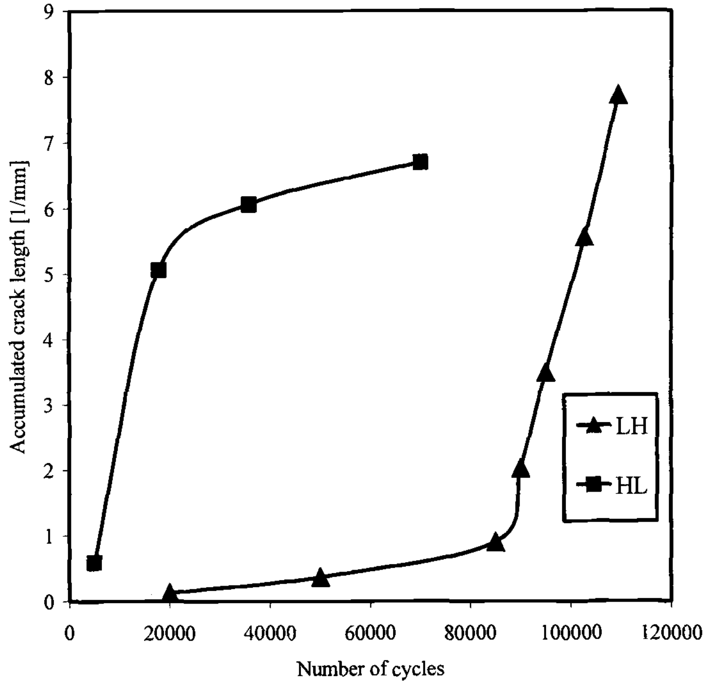

FIG. 8 *Comparison of the accumulated crack length per unit area for the loading sequences HL (left curve) and LH (right curve).*

The measured distribution of crack lengths is displayed for both loading sequences in Fig. 9 after the first block (Miner sum = 0.5) and in Fig. 10 at the end of specimen lifetime. HL-loading produced a large amount of short cracks in the first block. Please note that longer cracks (> 0.1 mm) are not displayed in the diagrams. Only under LH-loading did some cracks reach lengths above 0.1 mm during the first loading block. The mean difference between both loading sequences at the end of the first load block was the increased shape of the distribution of the crack lengths for the HL-loading tests. At the end of specimen lifetime it was observed that the LH-loaded specimen exhibited the greater number of short cracks, whereas the former shape of the distribution of the crack lengths for the HL-loaded specimen was lowered. In this case, crack propagation and coalescence processed during the final load block were such that the cracks that initiated during the first block became larger than 0.1 mm. Due to the reduced crack initiation rate, the number of cracks < 0.1 mm was small.

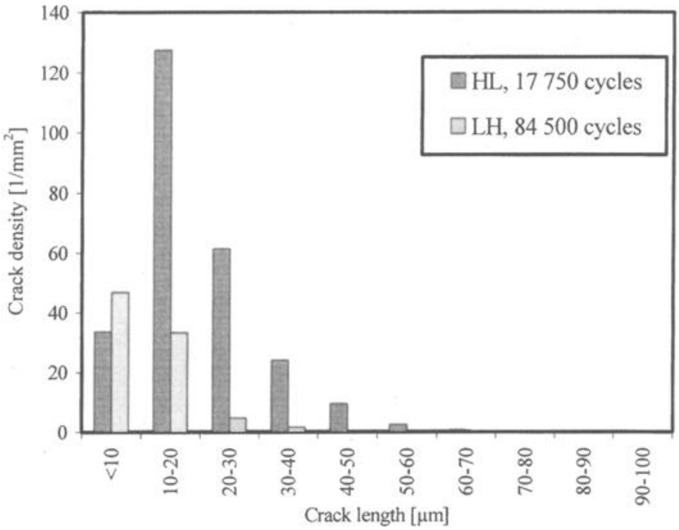

FIG. 9 *Example of the measured short crack length distributions for the loading sequences HL and LH.*

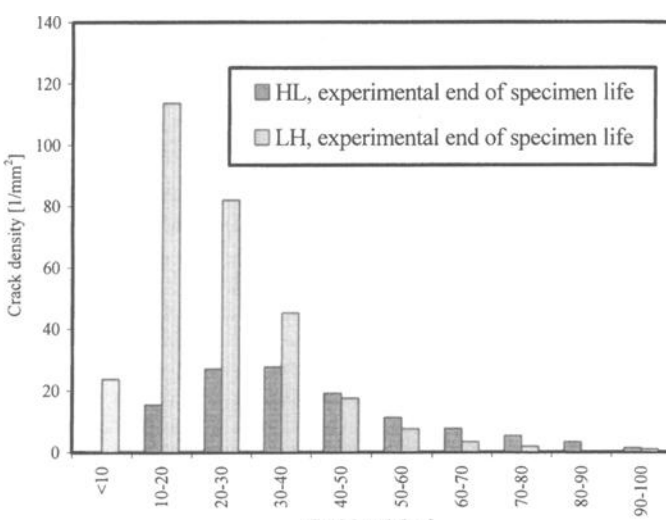

FIG. 10 *Example of the measured short crack length distributions for the loading sequences HL and LH at the end of specimen lifetime.*

Figure 11 shows the simulated specimen surface of a step test starting with the high amplitude loading. The image displays the simulation at the end of the first load block (17 750 cycles, partial Miner sum = 0.5). The arrangement of short cracks for a step test starting with the low amplitude loading (84 500 cycles, Miner sum = 0.5) is shown in Fig. 13. Although the number of fatigue cycles was smaller, the increased crack initiation rate for HL-loading (Fig. 11) caused a higher number of cracks. The increase of crack initiation rate can be explained by the higher resolved shear stresses. Due to the equations given by Hoshide et al. [2] for crack initiation and de los Rios et al. [3] for crack propagation, crack initiation is influenced more by the stress level than crack propagation. An increase of strain load increased the crack initiation rate moreso than the crack propagation rate. Therefore, total damage depended not only on the crack propagation, but also on the number of cracks. Each initiated crack can be a candidate for becoming the failure crack. Even cracks, which are arrested by microstructural barriers, can take part in the failure through the process of coalescence.

Figure 12 displays the specimen surface for the HL-loading sequence at the end of specimen life. It shows the typical cracking morphology that is characteristic for the HL-loading test.

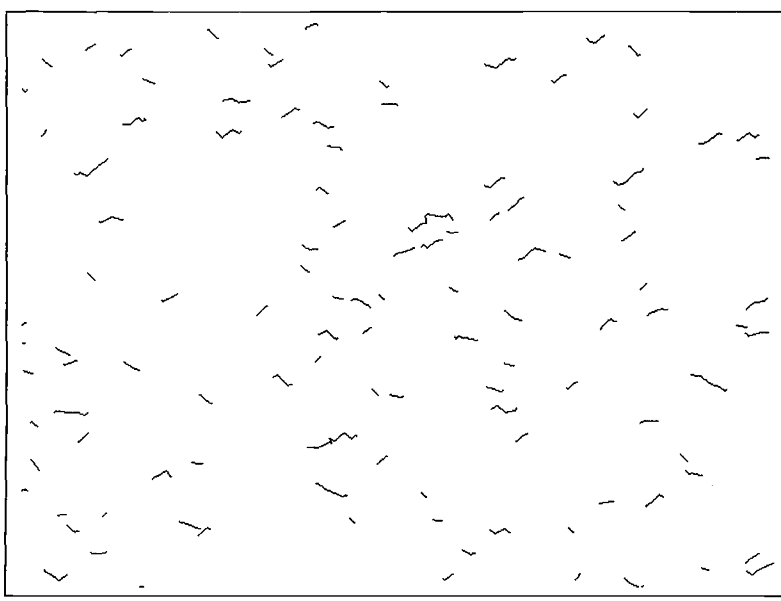

FIG. 11 *Simulated surface, image width = 0.8 mm, HL-load, N = 17 750 cycles.*

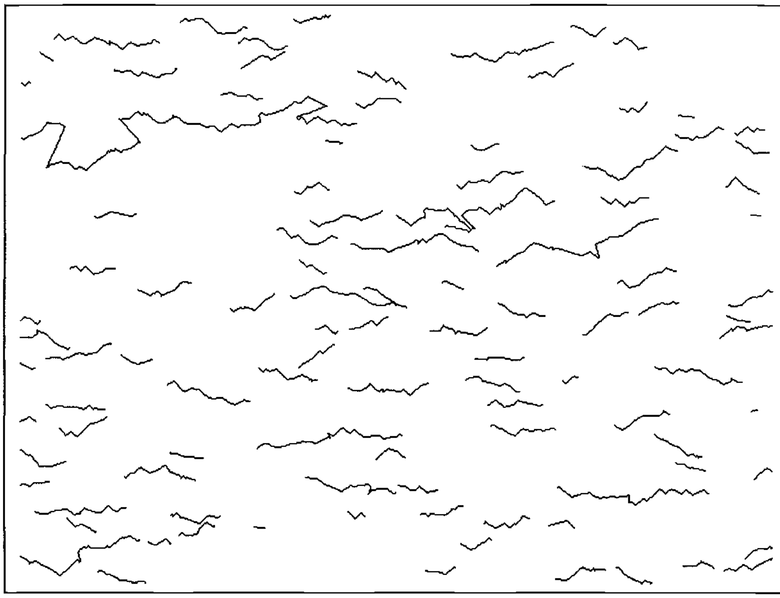

FIG. 12 *Simulated surface, image width=0.8 mm, HL-load, N=72 000 cycles.*

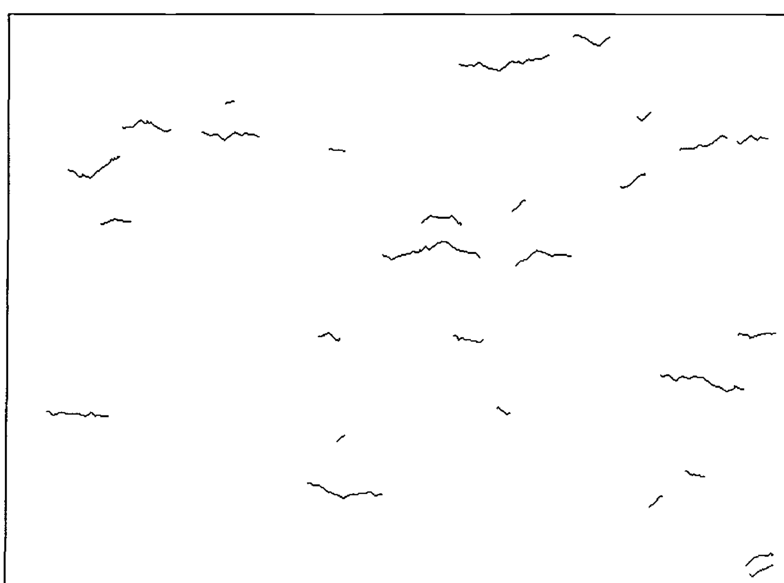

FIG. 13 *Simulated surface, image width = 0.8 mm, LH-load, N = 84 500 cycles.*

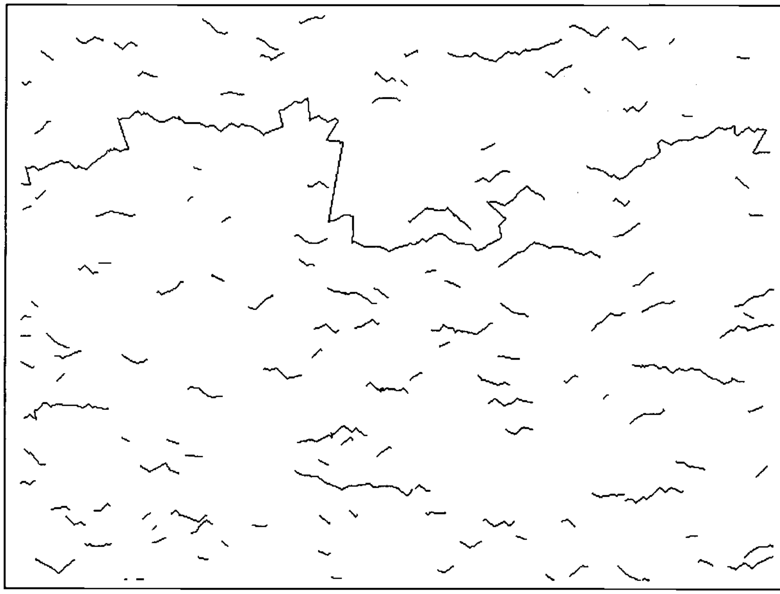

FIG. 14 *Simulated surface, image width = 0.8 mm, LH-load, N = 107 000 cycles.*

As seen in Fig. 14, at the end of specimen life, the LH-loading sequence is characterized by only a few longer cracks, which are surrounded by a large number of short cracks. These short cracks initiated during the second load block. As noted above, the increased stress level enhances the crack initiation. Consequently, the formation of the failure crack depended only on the cracks which initiated in the first loading block. Later initiated cracks only participated in the failure crack formation by coalescence if they were located in the propagating path of one of the longer cracks. The resulting crack length distributions for the LH-loading sequence also can be seen in Figs. 15 and 16. A comparison with Figs. 9 and 10 shows a good agreement to the experimental results. Differences were noted for the cracks shorter than 10 μm. The experimental detection of cracks that short is very difficult to make, especially in the presence of longer cracks.

The resulting crack length distributions of the short crack simulation are displayed in Figs. 15 (situation after the end of the first loading block was reached) and 16 (situation after the end of the specimen life was reached) and can be compared favorably with the experimental data in Figs. 9 and 10. As Table 5 shows, there is a good accordance between the experimental and simulated specimen lives. This is mainly a result of the similar appearance of the short cracks on the real and on the simulated specimen surfaces, resulting in the good accordance between the measured and calculated crack length distributions.

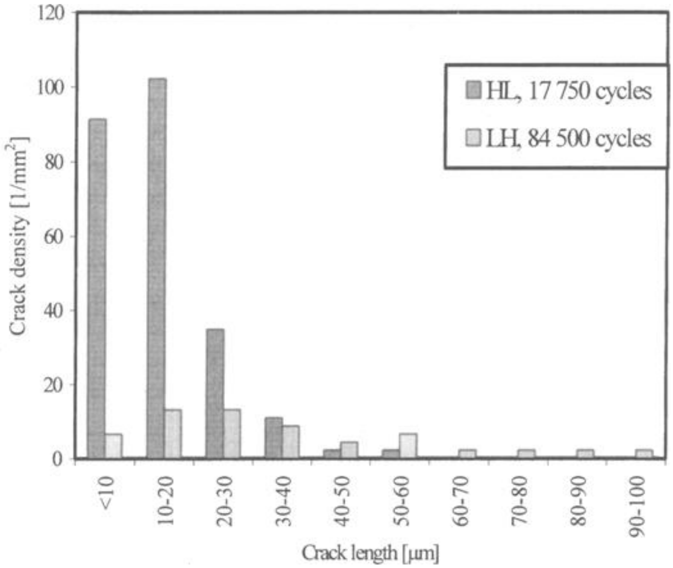

FIG. 15 *Distributions of the crack lengths of calculated short cracks for the loading sequences HL and LH.*

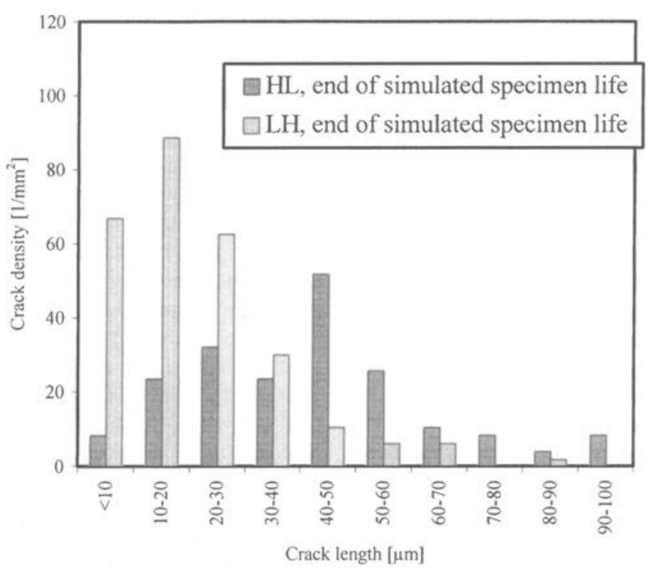

FIG. 16 *Distributions of the crack lengths of calculated short cracks for the loading sequences HL and LH, resulting Miner sum at the end of simulated specimen lifetime.*

Conclusions

The observation of the short crack behavior can be used as a visible indicator (fingerprint) of the fatigue induced damage of the material. The mechanism-based model combines the effects of material microstructure and specimen loading history. If the short crack behavior is measured in constant amplitude tests, lifetime predictions are possible for more complex loading sequences. The experimentally observed crack behavior is in good accordance with the simulation. The appearance of the short cracks on the real and on the simulated specimen surfaces was quite similar, resulting in a good prediction of the specimen lifetimes under different loading sequences. With increasing strain amplitude, the number of initiated short cracks becomes more important than the crack propagation rate itself, resulting in a crack coalescence behavior having increasing rate in failure crack formation. Contrary to the Miner rule, the number of cycles to failure in step amplitude tests depends on the sequence of loading. The influence of the loading conditions on specimen lifetime can be calculated by using the crack simulation program. Step tests starting with the high amplitude (HL) show an increased crack initiation rate. The increased number of the later growing cracks resulted in a decreased lifetime and a resulting Miner sum < 1. Starting the fatigue test with reversed step sequence (LH) reduces the crack initiation rate at the beginning. The decreased number of growing cracks increased the specimen lifetime with a resulting Miner sum > 1.

References

[1] Tanaka, K. and Mura, T., "A Dislocation Model for Fatigue Crack Initiation," *J. Appl. Mech.*, Vol. 48, 1981, pp. 97 103.

[2] Hoshide, T. and Kusuura, K., "Life Prediction by Simulation of Crack Growth in Notched Components with Different Microstructures and under Multiaxial Fatigue," *Fatigue and Fracture of Engineering Materials and Structures*, Vol. 21, 1985, pp. 201 213.

[3] de los Rios, E. R., Mohamed, H. J., and Miller, K. J., "A Micro-Mechanics Analysis for Short Fatigue Crack Growth," *Fatigue and Fracture of Engineering Materials and Structures*, Vol. 8, No.1, 1985, pp. 49 63.

[4] Bomas, H., Hünecke, J., Laue, S., and Schöne, D., "Prediction of Lifetime to Fatigue Crack Initiation under Consideration of Notches in a Low Carbon Steel SAE 1017," *DVM-Report No. 683*, Bremen, 2000, pp.65 80.

[5] Weiss, J. and Pineau, A., "Microstructurally-Based Simulation of Multiaxial Low Cycle Fatigue Damage," *Proceedings of the 3rd International Conference on Low Cycle Fatigue and Elasto-Plastic Behavior of Materials*, K.-T. Rie, Ed., Elsevier Applied Science, London-New York, 1992, pp. 82 87.

[6] Iida, K., "Microcrack Density as an Indication of Accumulated Fatigue Damage," *Proceedings of the 3rd International Conference on Low Cycle Fatigue and Elasto-Plastic Behavior of Materials*, K.-T. Rie, Ed., Elsevier Applied Science, London-New York, 1992, pp. 490 495.

LOAD INTERACTION

Journal of ASTM International, October 2004, Vol. 1, No. 9
Paper ID JAI19054
Available online at www.astm.org

F. Romeiro,[1] *M. de Freitas,*[2] *and S. Pommier*[3]

Effect of Overloads and Underloads on Fatigue Crack Growth and Interaction Effects

ABSTRACT: Under constant amplitude loading, a single variable (ΔK) is required in crack growth relationships. The transferability of fatigue laws, determined under constant amplitude loading, to variable amplitude fatigue requires at least an additional variable, whose evolution with crack length accounts for the interaction effects between cycles of different types. The crack opening level (K_{op}) is usually employed for this purpose because it can be determined from the experiments and compared with predictions from models or FEM analyses. This paper presents an analysis of fatigue crack growth on M(T) specimens of medium carbon steel specimens and using FEM analyses. The specimens are subjected to repeated blocks of cycles made up of one or several overloads separated by a variable number of baseline cycles. The experiments are simulated by FEM analyses, taking into account the cyclic plastic behavior of the low carbon steel. The main objective of this study is to better understand the mechanisms at the origin of interactions effects due to the presence of overloads (or underloads) at different locations of the block loading. It is concluded that the interaction effects are closely related to the cyclic plastic behavior of the material and namely to the Bauschinger effect.

KEYWORDS: variable amplitude loading, plasticity-induced crack closure, overloads, underloads

Introduction

The generalization of damage tolerance to variable amplitude fatigue is of prime importance in order to maintain the reliability of structures and mechanical components subjected to severe loading conditions. Engineering spectra usually contain overloads and underloads whose distribution may not be random. However, for predicting the life of a structure, a simplified spectrum is usually determined from the real one, in order to reduce testing periods on prototypes. It is thus important to know which cycles can contribute to crack growth and which can be neglected. There are various methods for counting cycles, which usually do not take into account the order of application of cycles within the spectrum. However, it is well known that there is a strong interaction between cycles displaying different amplitudes in fatigue crack growth. This effect is known as the overload effect. Skorupa [1] recently published a review on this subject.

Damage tolerance is based on fracture mechanics. With that concept, under constant amplitude loading, a single variable (ΔK) is required in crack growth relationships. The transferability of fatigue laws, determined under constant amplitude loading, to variable amplitude fatigue requires at least an additional variable, whose evolution with crack length

Manuscript received 11 July 2002; accepted for publication 8 April 2003; published October 2004. Presented at ASTM Symposium on Fatigue Testing and Analysis Under Variable Amplitude Loading Conditions on 29 31 May 2002 in Tours, France; P. C. McKeighan and N. Ranganathan, Guest Editors.

[1] Research Assistant, Mechanical Engineering Department, ESTG, Polythenic Institut of Leiria, 2401-951 Leiria, Portugal.
[2] Professor, Mechanical Engineering Department, Instituto Superior Técnico, Av. Rovisco Pais, 1049-001 Lisboa, Portugal.
[3] Assistant Professor, MSS Mat, CNRS UMR 8579, Ecole Centrale Paris, 92295 Chatenay-Malabry, France.

accounts for the interaction effects between cycles of different types. The crack opening level (K_{op}) is usually employed for this purpose, because it can be determined from the experiments and compared with predictions from models [2] or FEM analyses [3,4].

The common practice is to determine the effective stress intensity factor ($\Delta K_{eff} = K_{max} - K_{op}$) during experiments conducted at constant amplitude loading and to transfer the results to variable amplitude fatigue, cycle by cycle, without taking into account the interaction effects between the different cycles of a fatigue spectrum [5]. However, interactions between cycles (overloads for example) are well known to modify significantly the fatigue life of a sample, and attempts have been made to take into account such interactions [6,7]. However, they remain of limited use because of the strong dependence of these effects on the material and loading conditions. Recent studies [8,9] using FEM analyses have shown that two features of the cyclic behavior of a material are of key importance for this kind of problem, namely the Bauschinger effect and the cyclic hardening or softening capabilities of the material. The results presented in [10] show that the presence of consecutive overloads significantly increases the retardation effects in crack growth and that this retardation effect is smaller if the number of baseline cycles between the overloads is reduced. Simulations of crack growth by FEM have shown that the crack opening level increases within the overload plastic zone if the number of consecutive overloads is increased. While these results were consistent with experiments, a need for the experimental evidence was necessary, leading to the present study.

This paper presents an analysis of fatigue crack growth on M(T) specimens of medium carbon steel specimens, using FEM analyses. The specimens are subjected to repeated blocks of cycles made up of one or several overloads separated by a variable number of baseline cycles, and crack opening load levels are measured. The experiments are simulated by FEM analyses taking into account the cyclic plastic behavior of the low carbon steel through a Chaboche law. The main objective is to understand better the mechanisms at the origin of interactions effects due to the presence of overloads (or underloads) at different locations of the block loading.

Material and Experimental Procedure

A DIN CK45 carbon, mild steel was chosen for this study for its high Bauschinger effect. The monotonic tensile properties of the alloy are the following: E = 210 GPa, $\nu = 0.3$, $\sigma_{YS} = 360$ MPa, $\sigma_{UTS} = 600$ MPa. The microstructure is ferritic-pearlitic with an average grain size of 50 μm. The alloy is in a normalized state (850°C for 1 h, followed by air cooling). The chemical composition (% wt) is as follows: C = 0.41, Mn = 0.76, Cr = 0.09, Ni = 0.08, Cu = 0.19, Si = 0.23, P = 0.01, S = 0.02. The cyclic constitutive behavior was determined on the basis of push-pull tests performed on a servo-hydraulic machine. The Chaboche [8] constitutive equations were used to describe the cyclic stress-strain behavior of this alloy. The best fit was obtained by using the parameters given in [8]. The parameters were chosen in order to obtain a realistic balance between the size of the elastic domain and the amplitude of kinematic hardening.

Fatigue crack growth in this alloy was tested using ASTM center cracked specimens – M(T)- with 10 mm thickness, either with 60 mm width and a pre-crack of 15 mm for the tests where overloads were present or with 45 mm width and 8 mm pre-crack when underloads were present. Fatigue tests were carried out on M(T) specimens according to the ASTM Standard Test Method for Measurement of Fatigue Crack Growth Rates (E 647-99). The specimens were subjected to repeated blocks of cycles constituted with baseline cycles with stress ratio R = 0.1 ($P_{max} = 60$ kN, and $P_{min} = 6$ kN) and overloads of $K_{pic} = 1.5\ K_{max}$ or with baseline cycles at R = 0.1 ($P_{max} = 45$ kN and P_{min} = 4.5 kN) with underloads at R = –0.5 or R = –2. The number of baseline cycles between overloads or underloads is set to be 10, 10 000, or 50 000. The number of overloads and underloads applied consecutively was 1, 2, or 6.

For each testing condition, crack length was measured on both sides of the specimen using an optical device, and load/COD cycles were recorded continuously when overloads or underloads were applied and with regular intervals when baseline cycles are applied. COD was measured at the centerline of the specimen in order to determine the crack opening level with the compliance offset method described in ASTM E 647-99. Additionally, crack opening loads were also calculated through a modified reduced differential compliance technique in order to establish clearly the crack opening levels.

Experimental Results

Load/COD data were acquired using 500 data pair of points (250 for loading and 250 for unloading) for all loading cases. Several methods have been proposed for the determination of the opening load, and a procedure is recommended in ASTM E 647-99. This procedure uses the compliance offset method, and an example is shown in Fig. 1 for a crack length of 13.5 mm and the following loading cycles: the last cycle before six overloads, the first cycle after six overloads, 10 000 and 30 000 cycles after the six overloads. Due to the presence of a high variability on the data presented in Fig. 1, alternative methods have been used to determine the opening load. The reduced displacement method is presented in Fig. 2 for the same loading cycles presented in the previous Fig. 1 (six consecutive overloads). Both methods present similar trends of the data. The compliance offset is drastically reduced after the application of the overloads. For the first cycle after the application of six overloads, the compliance offset is close to zero at almost the load range as shown in Figs. 1 and 2, and only 10 000 cycles after the application of the overloads, the crack opening load is of the same level as before the application of the overloads.

Additionally, and in order to compare the experimental data with the numerical results obtained by FEM in the next section, another analysis of these experimental results was performed for the case of one overload, Fig. 3, and for the case of six consecutive overloads, Fig. 4.

The effect of overloads on crack opening level is lower if a single overload is applied than after the application of six overloads. Moreover, the crack opening level decreases earlier, within the first 6000 baseline cycles after one overload, while no evolution was observed after 5000 cycles for six overloads. The load displacement curve is approximated by a quadratic function instead of a linear one, as shown in Fig. 5.

This function allows the comparison of crack mouth opening displacement (CMOD) for the same given load before and after the application of the overloads. The difference between the CMOD after and before the application of one or six overloads versus the applied load is plotted in Fig. 6.

These experiments allowed the display of a second effect of the overloads. During the application of overloads, crack tip blunting occurs and increases significantly during the applications of subsequent overloads. The load/cmod curve for a baseline cycle just before or just after the application of six overloads is plotted in Fig. 5.

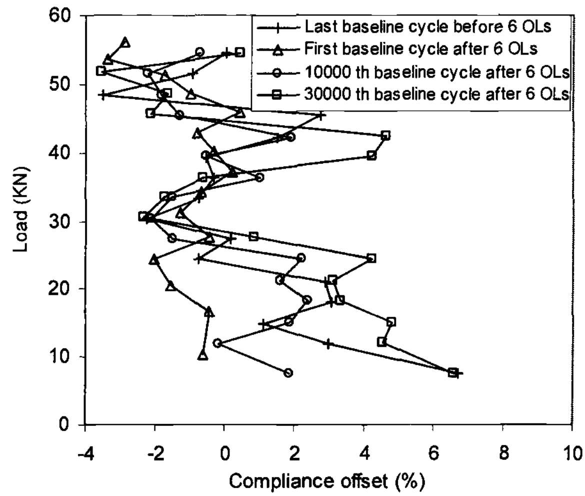

FIG. 1 *Experiment: Compliance offset procedure for crack opening determination for baseline cycles before and after the application of six overloads at* $K_{pic} = 1.5\ K_{max}$.

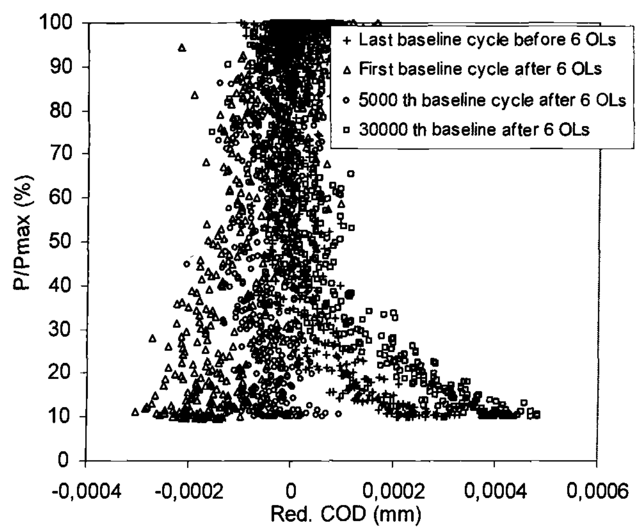

FIG. 2 *Experiment: Reduced displacement method for crack opening evaluation for baseline cycles before and after the application of six overloads at* $K_{pic} = 1.5\ K_{max}$.

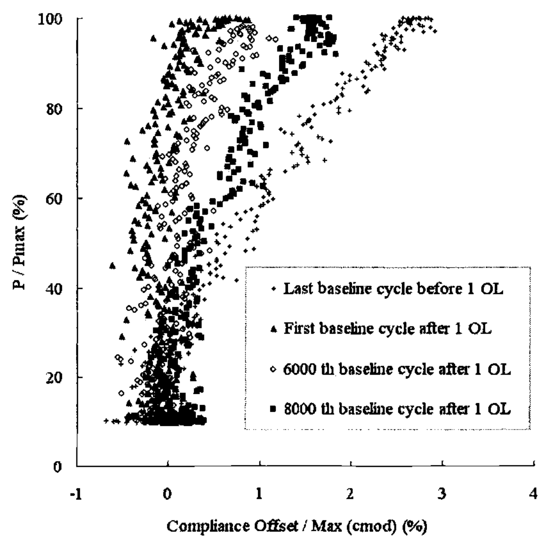

FIG. 3 *Experiment: Compliance offset versus applied load (P) for baseline cycles before and after the application of a single overload at* $K_{pic} = 1.5\ K_{max}$.

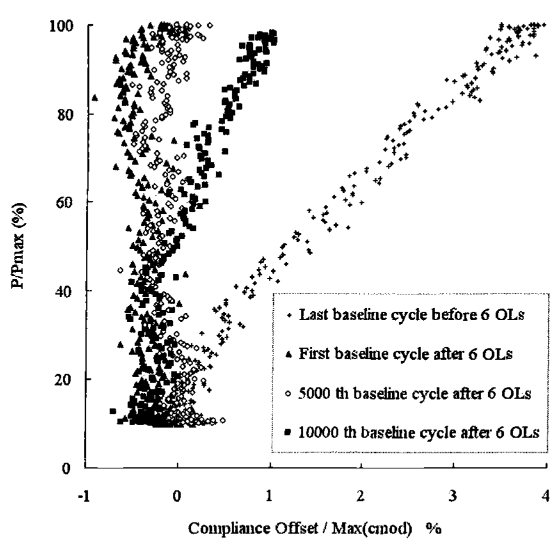

FIG. 4 *Experiment: Compliance offset versus applied load (P) for baseline cycles before and after the application of six overloads at* $K_{pic} = 1.5\ K_{max}$.

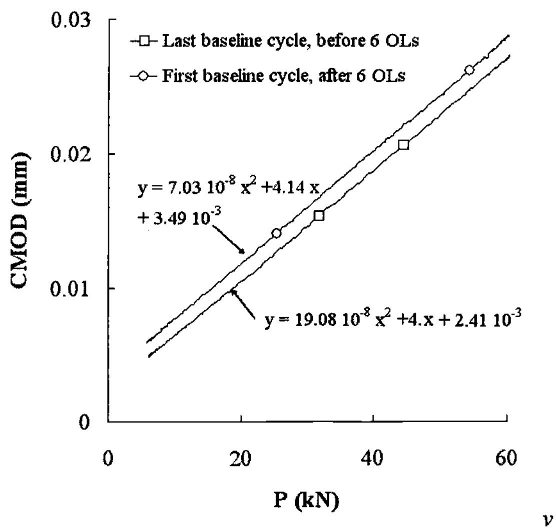

FIG. 5 *Experiment: Load/CMOD curve for baseline cycles just before and after the application of six overloads.*

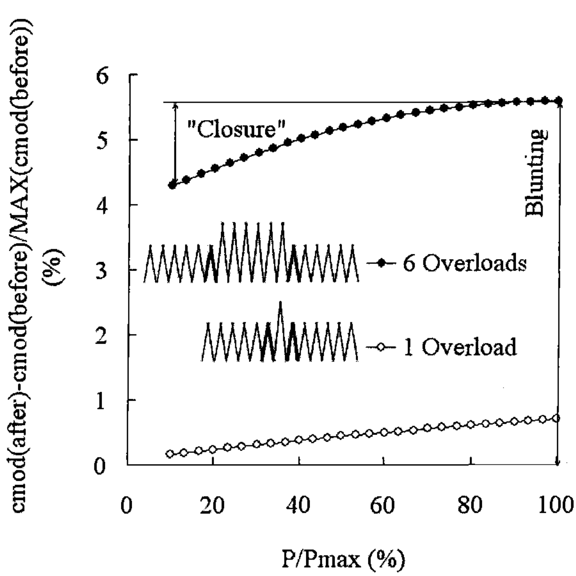

FIG. 6 *Experiment: Analyses of the difference between these curves for single or for six overloads.*

A permanent blunting of the crack faces remains after six overloads. This permanent blunting is much smaller after only one overload (Fig. 6). Out of the permanent blunting at the crack mouth, a "closure effect" is revealed because the movement of the crack faces during the loading part of the baseline cycle occurs is delayed if overloads are applied as compared with the case when no overload has been applied yet (Fig. 6).

The effect is also observed after a single overload but with a lower magnitude. In the experiments, the crack growth rate is significantly lower if six consecutive overloads are applied instead of only one. This retarding effect of consecutive overloads associated with the deflection in the compliance offset/load curves and an increase of crack tip blunting seems is related to cyclic plasticity at crack tip.

Concerning underloads, the following experiment also was performed (see Fig. 7): a crack was grown under baseline cycles with a constant stress intensity factor K_{max} = 20 MPa($m^{1/2}$) and R = 0.1, then either one underload or five underloads at σ_{min} = −140 MPa were applied. The crack growth rate was measured using the potential drop technique. In both cases, the crack growth rate is observed to increase significantly after the application of the underloads, and the increase of the crack growth rate is higher after five underloads than after a single one. CMOD measurements after underloads also have been performed, but the effect of underloads is too faint on the displacement at the crack mouth to allow any discussion on the evolution of K_{op} after underloads.

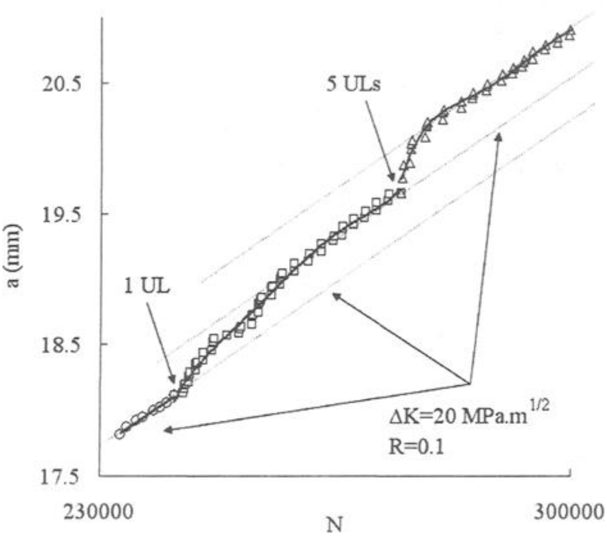

FIG. 7 *Experiment: Evolution of the crack length under baseline cycles at constant K_{max} (K_{max}=20 MPa ($m^{1/2}$) and R = 0.1), after one or five underloads at σ_{min} = −140 Mpa.*

FEM Analysis

The M(T) specimen used on the experiments was modelled by a 2-D finite element model. The calculations were conducted under plane strain conditions. The elements are quadrangular with a reduced quadratic integration scheme. The mesh size in the crack tip plastic zone is of 10 × 10 μm. The mesh size is chosen in order to be lower than one tenth of the size of the cyclic plastic zone at crack tip along the crack plane. Fatigue crack growth was simulated for crack lengths between 13 mm and 15 mm; the mesh size was refined between 12 and 16 mm along the crack plane. The Chaboche constitutive equations [11] were employed to describe the cyclic stress-strain behavior of the material employed in the experiments [10]. These constitutive equations provide non-linear kinematics and isotropic hardenings. Fatigue crack growth was simulated by modifying the boundary conditions along the crack plane. The release rate employed in the calculations is of one element every two cycles. The boundary condition along the crack plane is provided by spring elements with a bi-linear behavior. Their rigidity in compression is always extremely high in order to simulate the contact condition between the crack faces. Then, when a node belongs to the crack face, the rigidity of the spring element attached to this node is set to be null in tension in order to simulate a unilateral contact condition between the crack faces. On the contrary, when a node still belongs to the ligament, the rigidity in tension of the spring element attached to that node is extremely high, in order to impose a non-displacement condition in the direction normal to the crack plane. The crack extent is obtained by modifying the spring element behavior. Since quadratic elements are employed, two nodes are released at each crack extension. And two fatigue cycles are applied before proceeding to each crack extension. A detailed explanation of FEM calculations can be found in [8].

Overloads

The first hypothesis to explain the cumulative effect of consecutive overloads on fatigue crack growth rate was that, due to cyclic plasticity, the material might be hardened by fatigue cycling, which would lead to an increase of the residual stress level at crack tip. However, this hypothesis does not explain the increase of crack tip blunting displayed in Fig. 6. This increase of crack tip blunting corresponds to ratcheting in the crack tip plastic zone. This effect is inherited from the Bauschinger effect of the material.

When the Bauschinger effect of the material is taken into account through the constitutive behavior, both the increase of crack tip blunting with the number of overloads (Fig. 6) and the "closure" effect is reproduced by the FEM (Fig. 8).

In Fig. 8, the displacement of the crack faces is plotted either at the maximum or at the minimum stress of a baseline fatigue cycle. Before this cycle, the crack was grown under baseline cycles only, until a stationary state was reached. There, either one or six overloads were applied. Then, the crack was grown again until a crack extent of 300 μm was reached. In Fig. 8, the increase of permanent blunting of the crack faces with the number of overloads is clear at the minimum applied stress. At the maximum applied stress, the displacement of the crack faces at crack tip is lower if the number of overloads is higher (closure effect), but the order of the curves is reversed at crack mouth. This reversal results from the superposition of a permanent blunting, which increases with the number of overloads, and of a cyclic displacement, which is reduced if the number of overloads is increased.

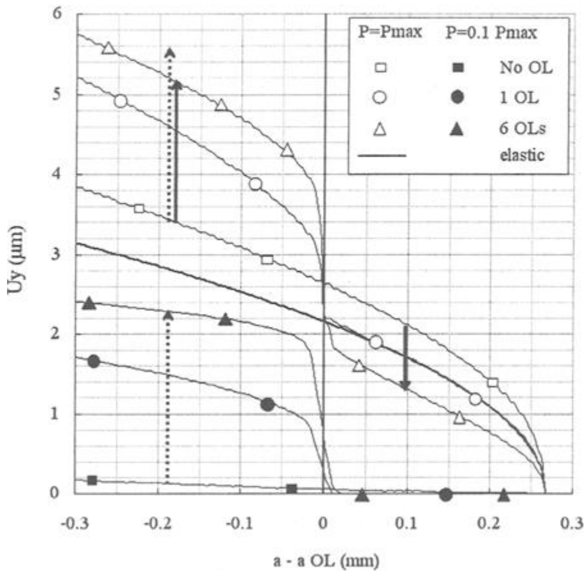

FIG. 8 *FE Analysis: Displacement of the crack faces after 300 μm of crack growth from the application of one, six, or no overloads.*

In addition, the crack opening level was determined at the crack tip in the FEM analyses, and a strong increase of K_{op} is found if the number of overloads is increased (Fig. 9), which is in agreement with the experiments (Figs. 3 and 4).

The explanation of these effects is in the development of residual stresses ahead of the crack tip during the application of overloads. During the first overload, plastic strain occurs at crack tip, and, according to the Bauschinger effect of the material, the yield stress is increased in tension and reduced in compression.

The center of the elastic domain (α) is therefore displaced toward positive stresses (Fig. 10). Consequently, reverse plasticity is easy at unloading, and compressive residual stresses at the crack tip are moderate. However, reverse plasticity also causes a displacement of the center of the elastic domain, toward negative stresses in this case. Consequently, according to the Bauschinger effect of the material, reverse plasticity leads to a reduction of the yield stress in tension, which ensures that forward plasticity can occur during subsequent overloads (Fig. 11). After a while, if the crack tip plastic zone is fully constrained, the fatigue cycle is adapted at the crack tip, and no further development of the stress state at the crack tip is observed during subsequent overloads. During this transient phase of adaptation of the stress state at the crack tip, the center of the elastic domain progresses back to lower values of the stresses. This effect allows residual stresses to be lower and lower at the crack tip, which is at the origin of the increase of the crack opening level K_{op}. Simultaneously, this transient phase of adaptation is accompanied by crack tip blunting and an increase in size of the plastic zone at the crack tip (Fig. 11). When the fatigue cycle at the crack tip is adapted to overload cycles, no further beneficial effect is expected from subsequent overloads. On the contrary, since the crack also grows during overload cycles, subsequent overloads are expected to increase the mean crack growth rate.

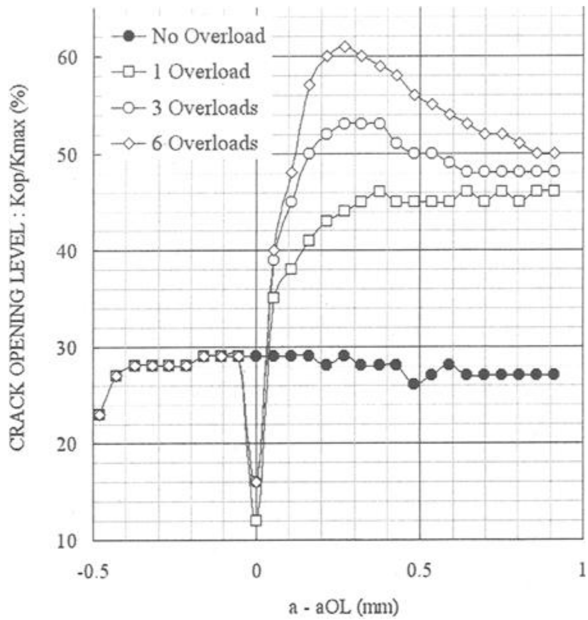

FIG. 9 *FE Analysis: Crack opening level for one, three, six, or no overloads.*

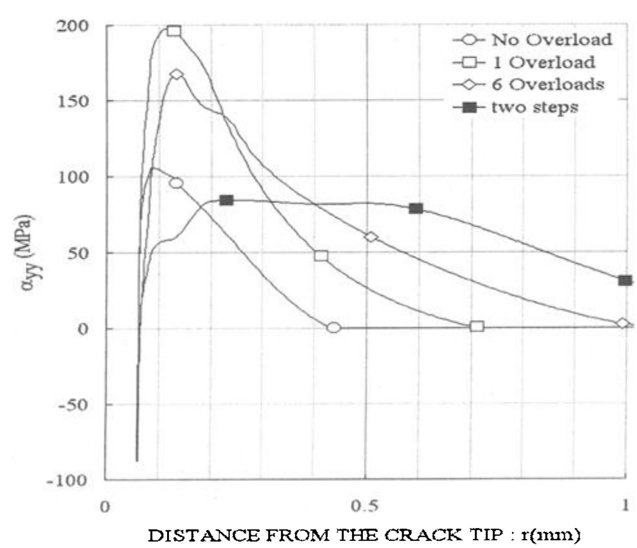

FIG. 10 *FE Analysis: Evolution of the component α_{yy} of the center of the yield surface with the distance to the crack tip after a crack extension of 43 μm, for one overload, six overloads, or a continuous cycling with overload cycles was applied.*

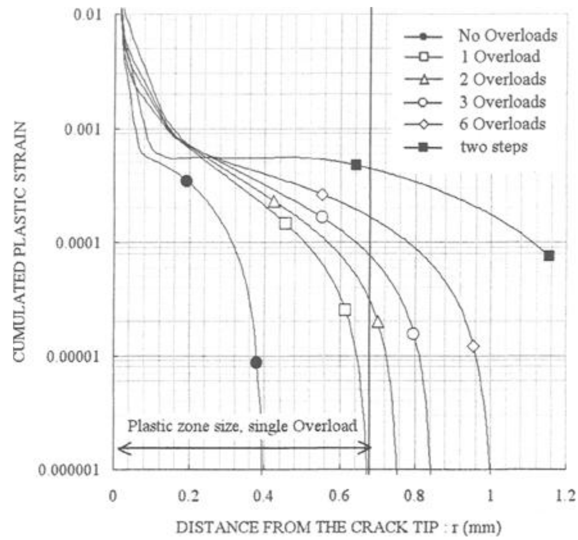

FIG. 11 *FE Analysis: Variation of the cumulated plastic strain for one, two, three, or six overloads.*

Therefore, it was found that the retarding effect is maximum for a given number of overloads, which depends on the cyclic plastic behavior of the material and in particular on its Bauschinger effect. This confirms that interaction between different cycles within a spectrum is of key importance for the prediction of fatigue lives.

Underloads

The same calculations have been performed in the case of underloads. It is worth noting that in both cases (underloads and overloads), crack tip blunting occurs after the application of the overload or the underload (see black symbols), as shown in Fig. 12. An underload does not cause crack tip re-sharpening as expected but an increase of crack tip blunting, just like an overload.

However, (see open symbols) at maximum applied load, the crack tip displacement is lower than that obtained under continuous cycling if an overload was applied, but it is greater than that obtained under continuous cycling, if an underload was applied. This is in agreement with the results obtained for the crack opening level (Fig. 13) and with the evolution of crack growth rates after overloads or underloads.

Evidence of crack tip blunting was found from the load-displacement curves as measured in the experiments and represented in the previous section (Figs. 5 and 6) in the case of single or multiple overloads. However, the effect is too faint in the case of an underload and was not possible to show from the experiments on M(T) specimens.

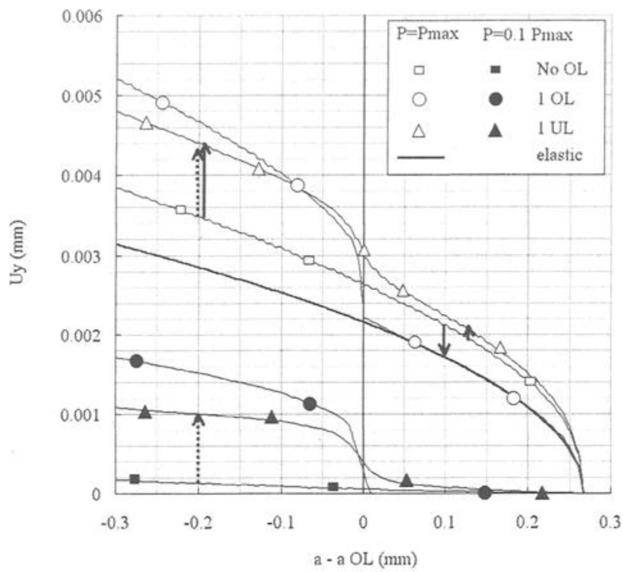

FIG. 12 *FE Analysis: Crack tip displacement after a single overload or a single underload.*

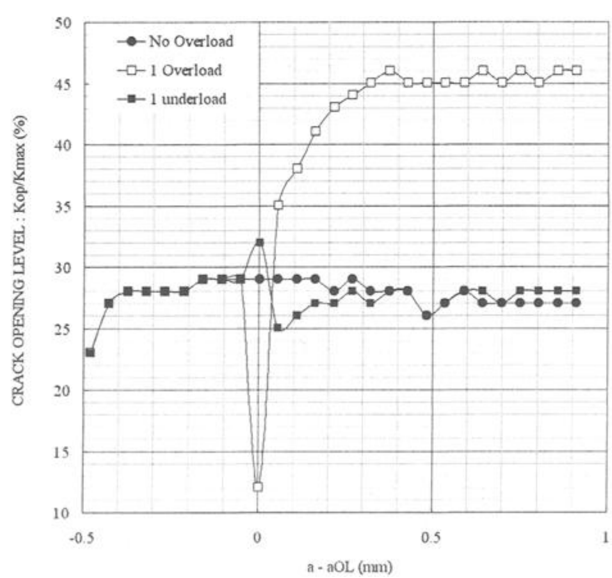

FIG. 13 *FE Analysis: Evolution of the crack opening level after the application of a single overload or single underload.*

Crack tip blunting occurs at the crack tip when an overload or an underload is applied, and this effect corresponds to a significant extension of the crack tip plastic zone size, as shown in Fig. 14. The reason for an extension of the plastic zone due to an underload or to multiple overloads is similar and corresponds to a transient phase of adaptation of the fatigue cycle at the crack tip after underloads or overloads. Before the application of an overload or an underload, the stress state and the hardening state are stationary at the crack tip and adapted to baseline cycles. In this stationary state, if the material displays the Bauschinger effect, the center of the elastic domain is displaced toward positive stresses within the crack tip plastic zone. Therefore, if an underload is applied, the yield stress in compression being small, a large amount of reverse plasticity occurs. Consequently, and according to the Bauschinger effect of the material, the elastic domain of the material is displaced toward negative stresses, which allow crack tip blunting during subsequent baseline cycles and the displacement of the center of the elastic domain toward positive stresses (Fig. 15). The effect is reinforced if a higher number of underloads is applied. This displacement of the center of the elastic domain toward positive stresses results in a reduction of compressive residual stresses at crack tip and consequently to the reduction of K_{op}.

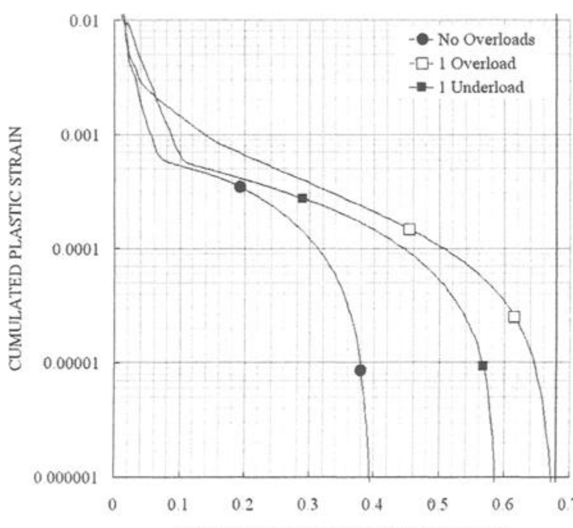

FIG. 14 *FE Analysis: Variation of the cumulated plastic strain for one overload or underload.*

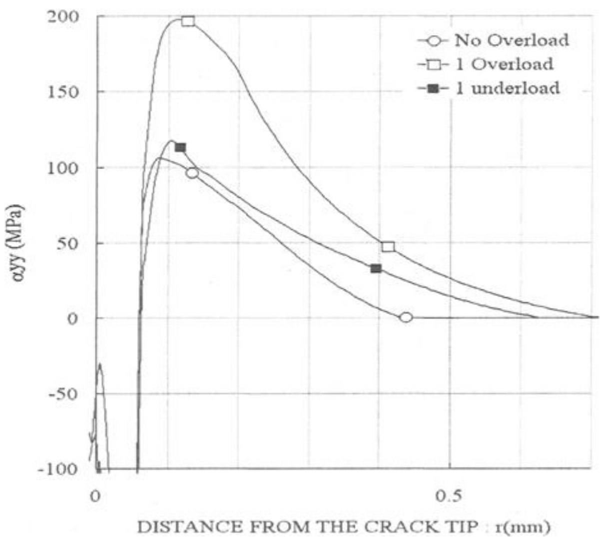

FIG. 15 *FE Analysis: Evolution of the component α_{yy} of the center of the yield surface with the distance to the crack tip after a crack extent of 43 μm, since an overload or an underload was applied.*

Conclusions

Fatigue crack growth testing under loading blocks composed of single overloads or underloads and single underloads, and finite element analysis of the experiments, showed the following:

1. The evolutions of the crack growth rate under variable amplitude fatigue are closely related to the material cyclic plastic behavior.
2. The Bauschinger effect of the material in particular is of key importance in predicting load-load interactions.
3. Though the parameter "K_{op}/K_{max}" is suitable for predicting crack growth rates variation, the term "closure" may be inappropriate. A crack may remain permanently opened after the application of an overload, while internal stresses at the crack tip limit the efficiency of the fatigue cycle.

References

[1] Skorupa, M., "Empirical Trends and Prediction Models for Fatigue Crack Growth under Variable Amplitude Loading," Netherlands Energy Research Foundation ECN, Petten, Netherlands, Report, ECN-R-96-007, June 1996.

[2] Newman, J. C., Jr., "A Crack Closure Model for Predicting Fatigue Crack Growth under Aircraft Spectrum Loading," *Methods and Models for Predicting Crack Growth under*

Random Loading, ASTM STP 748, J. B. Chang and C. M. Hudson, Eds., ASTM International, West Conshohocken, PA, 1981, pp. 53 84.

[3] McClung, R. C. and Sehitoglu, H., "On the Finite Element Analysis of Fatigue Crack Closure – 1. Basic Issue," *Engineering Fracture Mechanics*, Vol. 33, No. 2, 1989, pp. 237 252.

[4] McClung, R. C. and Sehitoglu, H., "On the Finite Element Analysis of Fatigue Crack Closure – 2. Numerical Results," *Engineering Fracture Mechanics*, Vol. 33, No. 2, 1989, pp. 253 272.

[5] Fatigue Crack Growth Computer Program, ESACRACK-NASA/FLAGRO User's Manual, Theory and Operation, ESA Publications Division, ESTEC, The Netherlands, 1995.

[6] de Jonge, J. B., "The Crack Severity Index of Monitored Load Spectra," *AGARD-AG-797, 77th Meeting AGARD Structures and Materials Panel*, 1993, pp. 5-1 to 5-5.

[7] Romeiro, F. and de Freitas, M., "The Effects of Overloads and Underloads on Fatigue Crack Growth," *Anales de la Mecânica de la Fractura*, XVIII Encuentro del Grupo Español de Fractura, 2001, No. 18, pp. 79 85

[8] Pommier, S., Bompard, P., "Bauschinger Effect of Alloys and Plasticity-Induced Crack Closure: A Finite Element Analysis," *Fatigue & Fracture of Engineering Materials & Structures*, Vol. 23, No. 1, 2000, pp. 129 139.

[9] Pommier, S., "A Study on the Relationships Between Variable Amplitude Fatigue Crack Growth and the Cyclic Constitutive Behavior of an Alloy," *International Journal of Fatigue*, Vol. 23, 2001, pp. S111 S118.

[10] Pommier, S. and de Freitas, M., "Effect on Fatigue Crack Growth of Interactions Between Overloads," *Fatigue & Fracture of Engineering Materials & Structures*, Vol. 25, 2002, pp. 709 722.

[11] Chaboche, J. L., "Viscoplastic Constitutive Equations for the Description of Cyclic and Anisotropic Behavior of Metals," *Bulletin de l'Academie Polonaise des Sciences. Série des sciences et techniques*, Vol. 25-1, 1977, pp. 33 39.

Journal of ASTM International, Nov./Dec. 2004, Vol. 1, No. 10
Paper ID JAI19064
Available online at www.astm.org

Narayanaswami Ranganathan,[1] *Abdellah Tougui,*[1] *Florian Lacroix,*[1] *and Jean Petit*[2]

Overload Effects in Aluminum Alloys: Influence of Plasticity and Environment

ABSTRACT: This paper presents the behavior of selected aluminum alloys when subjected to a single overload, with an aim to highlight the effects of plasticity and environment. The delaying effect of a single overload is given in terms of number of delay cycles. The delay behavior is systematically compared with the constant amplitude crack growth resistance. It is shown that for most of the studied alloys, a strong parallel can be drawn between the constant amplitude crack growth behavior and the overload induced delay. Delay induced by an overload in vacuum is higher than that in air for the 7075 and the 2024 alloys, compatible with stronger constant amplitude crack growth resistance in vacuum. The influence of the elastic-plastic behavior is stronger in vacuum than in air. In the case of the Aluminum Lithium alloy, delay in air is higher than that in vacuum, which is opposite to the behavior under constant amplitude loading. The basic mechanisms governing crack growth in aluminum alloys and their influence on the delay induced by an overload are revealed. The experimental results are compared with a phenomenological model, taking into account the cyclic plastic behavior of materials.

KEYWORDS: overload, delay, plasticity, environment, mechanisms, modeling

Introduction

The effect of a single overload has been studied extensively ever since it was shown that a single overload can lead to significant retardation of crack growth [1]. This delaying effect must be taken into account while predicting the crack growth lives of structures subjected to variable amplitude loading conditions, as simple models not including this phenomenon can sometimes lead to over conservative prediction of the observed lives. To study this effect in the laboratory (in the long crack configuration), a crack is grown under a constant amplitude loading condition in a specimen, and at selected crack lengths (thus at selected base line ΔK levels, ΔK_b), a single overload is applied, and the pre-overload test conditions are resumed. The evolution of crack length versus the number of cycles is then studied, which can show the typical delayed retardation effect. The same effect also can be studied with respect to the crack growth rate evolution, which can highlight the transient crack growth. These effects are schematized in Figs. 1*a* and 1*b*.

Manuscript received 14 June 2002; accepted for publication 10 November 2003; published November 2004.
Presented at ASTM Symposium on Fatigue Testing and Analysis Under Variable Amplitude Loading Conditions on 29 31 May 2002 in Tours, France; P. C. McKeighan and N. Ranganathan, Guest Editors.

[1] Professor, Associate Professor, and Graduate Student, respectively, Laboratoire de Mécanique et Rhéologie, University François Rabelais de Tours, 7 avénue Marcel Dassault, 37200 Tours, France.
[2] Director of Research, Laboratoire de Mécanique et de Physique des Matériaux (LMPM), Ecole Nationale de Mécanique et d'aérotechnique (ENSMA), BP 109, 86960 Futuroscope Cedex, France.

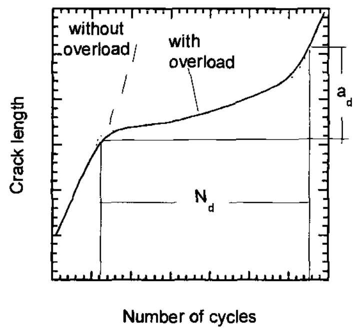

FIG. 1*a*—*Crack length evolution for tests with and without overload.*

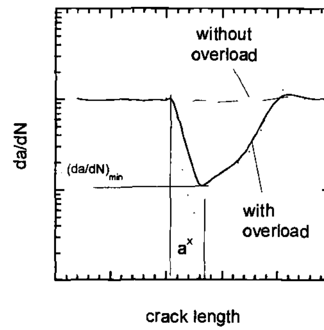

FIG. 1*b*—*Evolution of crack growth for tests with and without overload.*

The following parameters can be used to characterize the delaying effect:

a. The number of delay cycles, N_d, or the number of cycles after the overload, necessary for the crack growth to attain the pre-overload growth rate
b. The crack length, a_d, corresponding to N_d
c. The crack length, a^x, corresponding to the minimum growth rate attained after the overload
d. $(da/dN)_{min}$, representing the minimum growth rate reached after the overload application

Previous studies have shown that many factors influence the delaying effect of a single overload, such as the value of ΔK_b, the base line load ratio at which the tests are conducted, the overload ratio, τ, (defined here as the ratio of the overload to baseline loading amplitude), the thickness of the specimen (determining the existence of plane stress or plane strain conditions), and the environment [2]. Various mechanisms have been proposed to explain this load interaction effect, such as crack tip blunting and resharpening, cyclic hardening in the plastic zone, crack closure effects, or residual stresses in the plastic zone [2 7].

The objective of this paper is to highlight the possible influences of cyclic material properties and the effect of environment in the material behavior under single overload tests as compared to their constant amplitude (CA) fatigue crack growth resistances. The effects of plasticity and environment on the delaying effect are discussed based on experimental results obtained from tests conducted in air and in vacuum in selected high strength aluminum alloys.

Materials and Brief Experimental Details

The aluminum alloys studied here are the 2024 T351; the alloy 7075 in three heat treatments, T351, T651, and T7351; and the 8090 alloy in the T651 condition. The nominal compositions and mechanical properties of the studied alloys are given in Tables 1*a* and 1*b*. The average grain sizes, in μm, for the studied materials are given in Table 2, in the long (L), transverse (T), and short (S) directions [6]. The 2024 alloy and the 8090 alloys also have non-recrystallized grains of about 40 μm diameter.

TABLE 1*a—Composition (in %wt.) of the studied alloys (Al not indicated).*

Alloy	Zn	Mg	Cu	Cr	Fe	Si	Mn	Ti	Li
2024	0.04	1.5	4.46	0.01	0.22	0.1	0.66	0.02	
7075	5.7	2.43	1.5	0.2	0.21	0.16	0.04	0.04	
8090		0.55	1.14		0.05	0.03	0.1	0.03	2.34

TABLE 1*b—Nominal mechanical properties.*

Alloy	Young's Modulus (GPa)	Yield Strength (MPa)	Ultimate Tensile Strength (MPa)	Elongation (%)
2024 T351	73	300	500	16
7075 T351	70	458	583	10.6
7075 T651	71.1	527	590	11
7075 T7351	70.9	470	539	11.7
8090 T651	81.2	430	480	13

TABLE 2 *Average grain sizes.*

Alloy	L	T	S
2024 T351	190	80	70
7075 T351	700	200	50
7075 T651	600	200	40
7075 T7351	600	190	40
8090 T651	300	60	30

The tests described here were carried out using compact tension (C(T)) specimens, 75 mm wide and 10 mm thick for the 2024 alloy and 12 mm thick for the 7075 alloys. For the 8090 alloy, C(T) specimens 40 mm long and 10 mm thick were used. The specimens were tested along the TL orientation for the 2024 alloy and along the LT orientation for the 7075 alloys. More details can be found in [2,6,8]. Single overload tests presented here were carried out in ambient air and in vacuum ($<10^{-3}$ Pa). For the 2024 alloy, a series of tests was conducted in a N_2 environment containing traces of water vapor. Two baseline load ratios of 0.1 and 0.5 were studied. The overload ratio, τ, for all the studied tests was equal to 2.

The crack length was followed optically on the polished face of the specimen using a traveling microscope (×25). In each specimen, up to five overloads were applied covering a wide range of ΔK_b from near threshold to moderate ΔK levels. Care was taken to separate the overloads sufficiently to avoid cumulative effects. The nominal test frequency was 20 Hz in air and 35 Hz in vacuum. The overloads were applied at a frequency of 0.2 Hz.

Experimental Results and Preliminary Analysis

Effect of Plastic Behavior

The effect of elastic-plastic behavior is illustrated on the basis of the studies on the 7075 alloys. In this alloy, the three heat treatment conditions correspond to significantly different elastic-plastic behavior [6]. This alloy in the under-aged, T351 condition shows pronounced cyclic hardening. In the peak aged, T651 condition, a less pronounced cyclic hardening is observed, while in the over-aged T7351 condition, a cyclically stable behavior is observed [6].

Results of overload tests in vacuum at a baseline load ratio of 0.1 are given in Fig. 2*a*. In all three conditions, delay decreases as ΔK_b increases. Delay in the T351 condition is the highest throughout the studied ΔK_b range, while the lowest delays are observed in the over-aged, T7351 condition. For example, for a ΔK_b value of 10 MPa$\sqrt{m}$, delay in the T351 condition is about 1 million cycles, while in the T7351 condition it is about 50 times lower at about 20 000 cycles. In the peak aged condition, high delays are observed at low ΔK_b values, while at moderate ΔK_b levels, much lower delays are observed at levels comparable to those obtained in the T7351 condition. Thus in the T651 condition, a transitional behavior is obtained, i.e., for $\Delta K_b < 10$ MPa$\sqrt{m}$, high delays are observed, while for higher ΔK_b values, low delays are observed.

This behavior is now analyzed in comparison with the CA crack growth resistance of this alloy, shown in Fig. 2*b*. It can be seen here that the under-aged condition has the highest crack growth resistance, characterized by the highest threshold level, ΔK_{th}, and the over aged condition has the lowest ΔK_{th}. The T651 condition exhibits a transitional behavior: while the near threshold behavior is comparable to the T351 condition, at moderate ΔK values, the crack growth resistance is comparable to the T7351 condition. This transition takes place for ΔK values < 7 MPa$\sqrt{m}$. This indicates that the transitional behavior observed under CA conditions is also observed after an overload, even though the associated ΔK values are not the same. Comparing Figs. 2*a* and 2*b*, there is a good correspondence between CA fatigue crack growth resistance (FCG) and delay after an overload (higher FCG – lower delays).

The results of overload tests in air are next given in Fig. 3*a*, and the constant amplitude behavior in Fig. 3*b*.

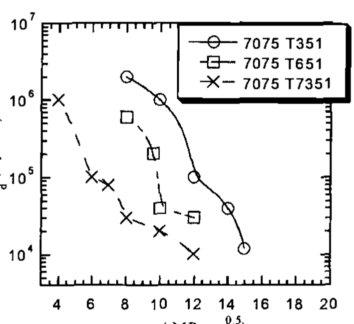

FIG. 2*a*—*Delay behavior in vacuum at a load ratio of 0.1.*

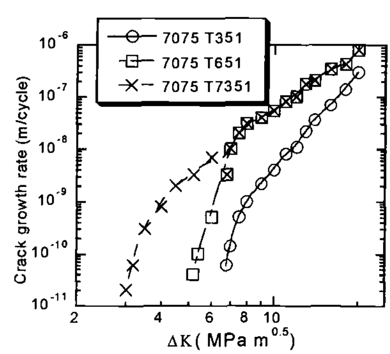

FIG. 2*b*—*Constant amplitude behavior at a load ratio of 0.1, in vacuum.*

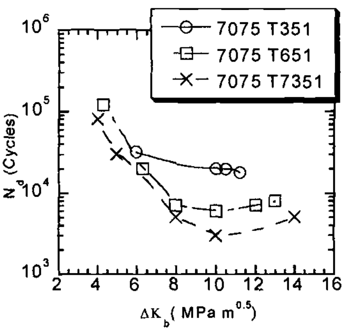

FIG. 3*a*—*Delay behavior in air at a load ratio of 0.1.*

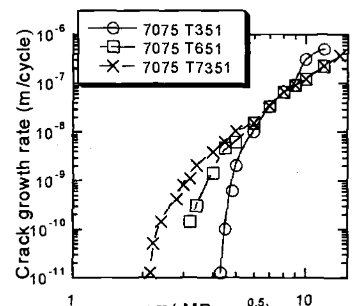

FIG. 3*b*—*Constant amplitude behavior in air at a load ratio of 0.1.*

The number of delay cycles is much lower in air than in vacuum, as can be seen by comparing Figs. 2*a* and 3*a*. When comparing with constant amplitude behavior, given in Fig. 3*b*, it can be seen here that, while the constant amplitude crack growth resistances are very similar for the three conditions at moderate ΔK values, near the threshold, similar differences in air are observed as in vacuum. It appears that, for tests in air, the arguments offered above, drawing a parallel between CA and post overload behavior in vacuum, do not hold. Differences in delay behavior are more pronounced for ΔK_b values greater than about 8 Mpa$\sqrt{m}$, while in this range the CA behaviors are similar in the three heat treatments. Comparing Figs. 2*a* and 3*a*, it is clear that the effects of differences in the elastic-plastic behavior are more evident in vacuum than in air.

Effect of Environment

The results given above indicate that delay in an aggressive environment (air) is much lower than in vacuum. It should be remarked that similar results with respect to the effect of environment on delay have been previously reported [9]. This effect is now studied in detail based on results obtained in the 2024 T351 ally and the 8090 T651 alloy.

2024 T351 Alloy—Figure 4*a* compares delay in vacuum and in air for tests at a baseline load ratio of 0.1. In the range $7<\Delta K_b<16$ Mpa$\sqrt{m}$, delay in vacuum is about 10 times as high as in air. For lowest ΔK_b studied, crack arrest is observed after the overload in air (the crack considered to be arrested after 3 million cycles) while a delay of 2 million cycles is observed in vacuum. It should be noted that for this alloy, delay decreases with ΔK_b, from near threshold to moderate ΔK_b values, while it shows an increase with ΔK_b at high values of the baseline ΔK. The cause of this behavior is discussed later. Comparing with the CA behavior, given in Fig. 4*b*, it is again seen that there is a strong parallel between the CA behavior and the overload induced delay. The constant amplitude crack growth rates are systematically lower in vacuum at a given ΔK compatible with higher delays in this environment (but for the lowest ΔK_b studied).

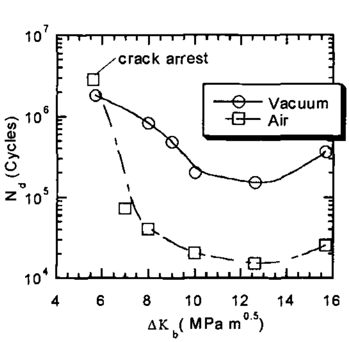

FIG. 4*a*—*Delay behaviors in vacuum and in air, R = 0.1 – 2024 T351.*

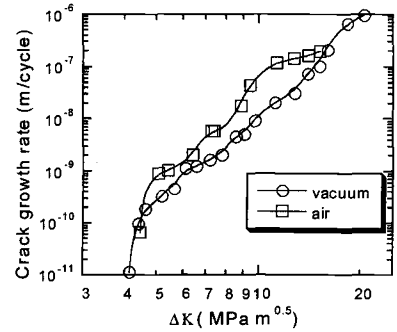

FIG. 4*b*—*Constant amplitude behaviors at R = 0.1 in the same alloy.*

Figure 5*a* gives the results obtained at a baseline load ratio of 0.5 in vacuum, air, and a nitrogen environment containing traces of water vapor. In this case, delay is systematically higher in vacuum than in the other two environments. No significant differences in delay behavior can be noticed between air and N_2. Comparing Figs. 4*a* and 5*a*, it can be seen that, for a given environment, delay at R = 0.5 is less pronounced than at the lower load ratio. Some specific examples are given in Table 3.

Figure 5*b* gives the CA behavior at the same load ratio. From this figure, it can be observed that CA crack growth resistance is systematically higher in vacuum than in air, with much higher values of ΔK_{th} and lower growth rates in the studied ΔK range. In the N_2 environment, crack growth rates are comparable to the ones observed in vacuum at high ΔK values, while near threshold, the crack growth behavior becomes similar to that observed in air. Between these two ranges a near constant crack growth rate, independent of ΔK is observed in a transitional range. Thus, from Figs. 5*a* and 5*b*, it is not possible to establish a similarity between CA behavior and delay for the N_2 environment, while for air and in vacuum there is a concordance between the delay behavior and the CA crack growth resistance, as delay in vacuum is about 10 times as high as in air, and the crack growth resistance is stronger in vacuum.

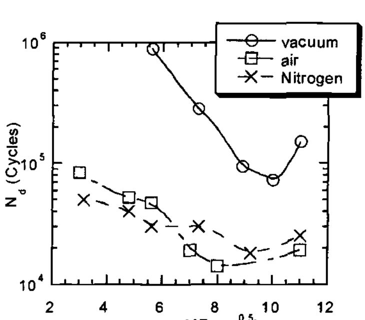

FIG. 5*a*—*Delay behaviors in vacuum, air, and Nitrogen, R = 0.5 – 2024 T351.*

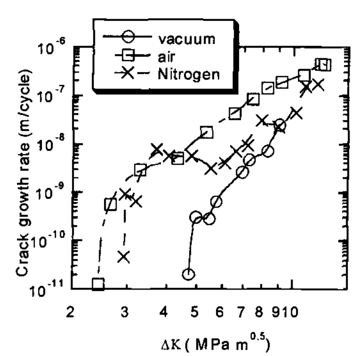

FIG. 5*b*—*Constant amplitude behaviors at R = 0.5 in the same alloy.*

TABLE 3 *Comparison of delay at R = 0.1 and 0.5 in vacuum.*

ΔK_b (MPa√m)	Delay at R = 0.1 (cycles)	Delay at R = 0.5 (cycles)
5.7	1.8 10^6	8.8 10^5
9	4.8 10^5	2.8 10^5
10	2 10^5	7.3 10^4

Effect of Environment in the Al-Li Alloy—The results of overload tests in vacuum and in air are given in Fig. 6*a* for the 8090 T651 alloy at a base line load ratio of 0.1. For this material, a surprising result is obtained – delay in air is systematically higher in air than in vacuum.

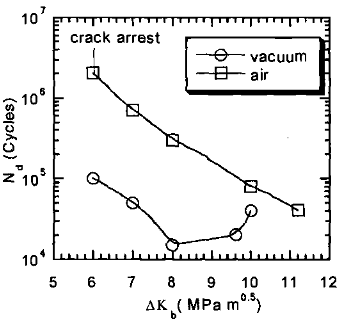

FIG. 6*a*—*Delay behaviors in vacuum and in air, R = 0.1 8090 T651.*

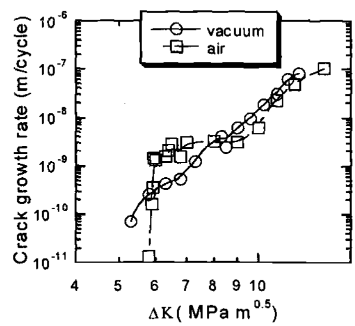

FIG. 6*b*—*Constant amplitude behaviors at R = 0.1 in the same alloy.*

As for the 2024 alloy, crack arrest after the overload is observed in air at the lowest ΔK_b studied. It should be remarked that, for all the other materials studied, delay in vacuum was much higher than in air for almost all the test conditions studied. The CA behaviors in air and in vacuum for the 8090 alloy are given in Fig. 6*b*. There is no significant difference in the threshold values in the two environments. At slightly higher values of ΔK, the crack growth evolution in air shows a transitional behavior at a near constant growth rate of 2×10^{-9} m/ cycle. For ΔK values higher than about 10 Mpa√m, crack growth rates in air are slightly lower than in vacuum.

Discussion

Crack Growth Mechanisms and their Influence on the Delay Behavior

The CA behavior of Aluminum alloys depends upon the precipitate coherency that governs the slip behavior [6,10,11]. For the 7075 alloy in the under-aged condition, Gunier-Preston (GP) zones form the basic precipitate structure. GP zones constitute coherent precipitates, and in this aging condition, planar slip is observed in vacuum throughout the test conditions studied, leading to maximal FCG under CA conditions, as slip reversibility is maximal for a planar slip behavior [10,12]. For the 2024 alloy, the precipitate structure contains GP zones and semi coherent θ' precipitates, and for this material a mixed planar slip-multiple slip behavior is observed in vacuum, and the CA crack growth resistance is slightly lower than that of the 7075 T351 alloy. The 7075 alloy in the over-aged conditions contains large noncoherent M' and T precipitates, and it is characterized by a multiple slip behavior. Such a behavior leads to the least crack growth resistance under CA conditions in vacuum, as slip reversibility is minimal in this case [10,12]. In the T651 condition, precipitate coherency is lower than that in the T351 condition and is characterized by planar slip at low ΔK values, while multiple slip is observed for moderate to high ΔK values [10].

The fracture surface for a planar slip behavior is characterized by large, blocky, out of plane facets which are typically along a (111) plane, while for a multiple slip behavior, the fracture surface is very flat and in general normal to the loading axis [6,13,14].

After an overload, the basic slip mechanism remains the same as can be seen from the fractographs in Figs. *7a* and *7b*, which illustrate a planar slip case and a multiple slip one.

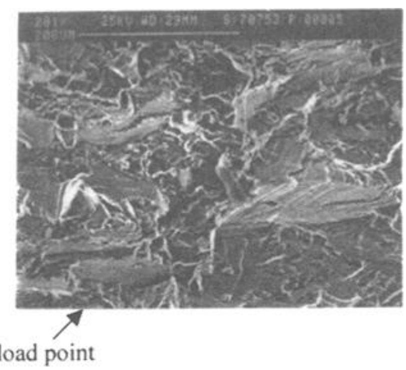

FIG. 7*a*—*Fracture surface appearance for a planar slip behavior 7075 T351 in vacuum.*

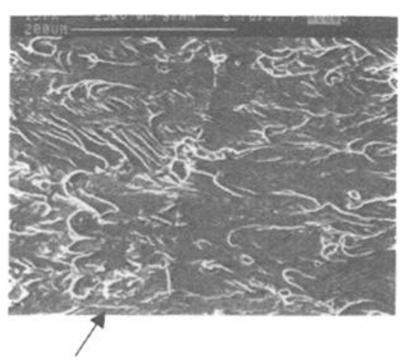

FIG. 7*b*—*Fracture surface appearance for multiple slip behavior 7075 T7351 in air.*

The effect of ambient air has been attributed to physical adsorption of water vapor molecules resulting in a decrease of the surface energy at moderate ΔK values and embrittlement due to nascent H_2 due to water vapor dissociation at low ΔK values near threshold. Under such conditions for most Al alloys, a multiple slip behavior is observed, and slip reversibility is reduced [10,11,13]. The fracture surface is marked by the presence of quasi cleavage facets at low ΔK levels and striations at moderate ΔK values [13,14]. As a result, the crack growth resistance is significantly lower in air than in vacuum.

Figure 8*a* shows a fractograph indicating the overload application point for the 8090 alloy. It should be noticed that before the overload, the fracture surface exhibits a mixed crack growth mode characteristic of planar slip (faceted crack growth) and multiple slip (pseudo cleavage facets). After the overload, one notices a large slip step, probably associated with a large slip band. The fracture surface indicates the presence of oxide in the overload affected region, indicating that the crack was stationary in this region, leading to oxide formation due to rubbing. The fracture surface after the overload affected region is quite comparable with the pre-overload region indicating that the micro mechanisms are the same. It is suggested here that the large slip step at the overload corresponds to slip along a (111) plane, but the post overload loading is not sufficient to maintain a fully planar slip crack growth. It has been shown previously that fully planar slip is activated in such materials in air at large ΔK values [13,14]. The high delay can then be associated with the time required to activate the mixed crack growth process compatible with the loading condition studied. This micromechanical effect should be added to the causes leading to delay following an overload.

For tests in vacuum, as illustrated in Fig. 8*b*, the overload is hardly distinguishable, and the crack growth mechanisms are the same before and after the overload. This can partially explain the low delays observed in this alloy in vacuum.

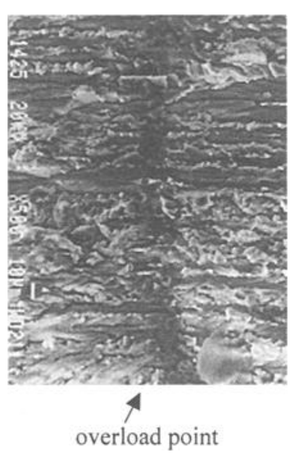

FIG. 8*a*—*Fracture surface observed in the 8090 T651 alloy in air.*

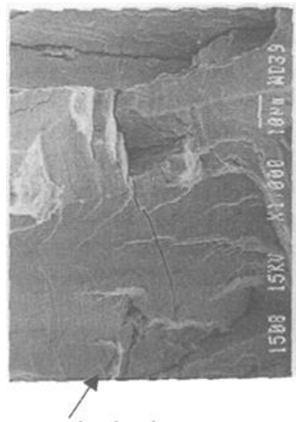

overload point

FIG. 8*b*—*Fracture surface in vacuum for the 8090 T651 alloy.*

Critical Analysis of Overload Effects

Regarding the quantitative effects following an overload, the following questions can be asked:

1. What is the effect of the base line ΔK level and the R ratio? Why in some cases is an increase in delay observed at moderate to high ΔK_b values, resulting in a "U" shaped curve?
2. What is the effect of the cyclic plastic behavior?
3. Why should delay be lower in air than in vacuum?

Answers to some of these questions are now offered based on the model developed by Matsuoka et al. [7]. This analytical model explicitly brings out the effects of the constant amplitude crack growth resistance, the load ratio, and the cyclic behavior of the studied material, which are the parameters studied here. According to this model, the delay is associated with the development of a compressive residual stress field in the cyclic plastic zone created by the overload. The number of delay cycles, N_d, is given by:

$$N_d / N_c = [\{(1\text{-}r/2)+(r/2)\,(a^x/a_d)\}^{1/m} - 1] / [(m-1)(r/2)(1-(a^x/a_d))] \quad (1)$$

where

N_c is the number of cycles necessary for the crack to propagate through the overload affected zone under CA conditions,

m is the exponent of the Elber's crack growth law (corrected for crack closure effects) [5],

r is the ratio between the overload peak stress to the base line peak stress (which is slightly different from τ, defined above),

a^x is the crack length necessary to reach the minimum growth rate after the overload, and

a_d is the crack length affected by the overload.

In the original model, the expression developed by Dugdale [15] for the plastic zones at the crack tip were used to determine the distances a* and ad a^x as related to the cyclic plastic zone at the baseline loading, and a_d is given by

$$a_d = 2.5^* \omega_{rp} - \omega_{m1,} \quad (2)$$

where

ω_{rp} is the cyclic plastic zone size created by the overload, and

ω_{m1} is the monotonic plastic zone at the base line loading.

These plastic zone sizes are estimated according to the Dugdale model, i.e.:

$$\omega_{rp} = (\pi/8)\,(\Delta K_{ol}/\sigma_{yc})^2 \text{ and} \quad (3a)$$

$$\omega_{m1} = (\pi/8)\,(K_{max}/\sigma_{ym})^2 \quad (3b)$$

where

ΔK_{ol} is the overload stress intensity factor amplitude,

K_{max} is the maximum baseline stress intensity factor, and

σ_{yc} and σ_{ym} represent, respectively, the cyclic and monotonic yield strength of the material. The cyclic yield strengths can be found in [6].

Analysis of the crack growth resistances of Al alloys in vacuum after correction for the effect of crack closure shows that the Elber's exponent is 4 for Al alloys in vacuum, and it remains the same in the crack growth range governed by the adsorption effect in air. In the range affected by hydrogen embrittlement, the Elber's slope is lower, with a value of about 2 [10].

The expressions developed in Eqs 1 3 were applied directly to determine the evolution of the number of delay cycles in vacuum and in air for a ΔK_b value of 8 Mpa$\sqrt{m}$, and the results are given in Table 4 and Fig. 9. It was assumed that the plastic zone sizes were the same in air and in vacuum [16,17].

Comparing with the experimental measurements, it can be seen that even though the model predictions are generally much higher than the experimental values, general trends are comparable between the two as enumerated below:

1. The model predicts a decrease in delay for a given material as R ratio increases, as can be seen from the experimental results, and it correctly predicts lowest delay at R = 0.5 in air.
2. Material cyclic properties are translated through the evolution of the plastic zone sizes, and the model correctly predicts lower delays for the 7075 alloy in the T7351 condition than for the T351 condition at R = 0.1. The comparisons between the 2024 and the 7075 alloys are also in agreement with the experimental trends, especially at R = 0.1.
3. The effect of environment in the delay behavior also is predicted correctly (lower delays in air than in vacuum).

TABLE 4 *Estimation of number of delay cycles using Matsuoka's model.*

Material	Vac. R = 0.1	Vac. R = 0.5	Air R = 0.1	Air R = 0.5
2024 T351	2.9e7	4.3e6	7.4e6	1.72e5
7075 T351	7.11e7	1.04e7	7.11e5	1.04e5
7075 T7351	5.05e6	1.07e6	1.52e6	1.86e5

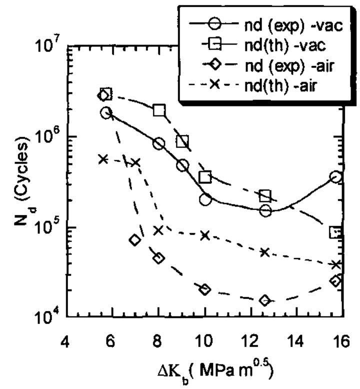

FIG. 9 *Comparison between model predictions and experimental data for tests at $R = 0.1$ in the 2024 alloy.*

It was proposed that differences from model predictions to observed behaviors could arise from the fact that plastic zones at the crack tip for a particular material do not obey the Dugdale model, and using the measured values of a* and a_d for a given material was suggested [7].

The values of these distances for the 2024 alloy for the overload tests described here can be found in [8]. The experimental data are compared with theoretical prediction in Fig. 10. It can be seen here that the theoretical value, which is constant for a given overload ratio, overestimates the measured ones at low ΔK_b values, while theoretical results are comparable with the experimental ones at moderate ΔK_b values, especially in air. It has been shown, for example, that at low ΔK values, the overload affected zone is on the order of the recrystallized grain size, and the parameter a* is on the order of the non recrystallized grain size for the 2024 alloy [2,8]. These microstructural effects must be modeled correctly for accurate predictions of delay.

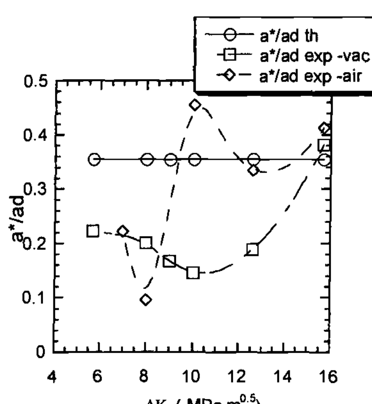

FIG. 10 *Comparison of theoretical and measured values of a^*/a_d.*

The increase in delay high ΔK values is attributed to a changeover from a globally plane strain behavior at low ΔK values to a globally plane stress behavior at high ΔK values. It has been suggested that this changeover occurs when the maximum stress intensity factor due to the overload, called K_t, creates a plastic zone about half the specimen thickness [18] as follows:

$$K_t = \sigma_{YS} \sqrt{b/2} \tag{4}$$

where
K_t is the transition overload stress intensity factor,
σ_{YS} is the yield strength, and
b is the specimen thickness.

The estimated values of this transitional value using this criterion for the studied materials are given in Table 5.

TABLE 5 *Comparison of theoretical and experimental values of transition stress intensity factor.*

Material	K_t (Eq 3)	K_t (when observed)
2024 T351	18.9	27.3
7075 T351	31.7	
7075 T651	36.5	21
7075 T7351	32.6	21
8090 T651	27.2	16.8

It can be seen here that the estimated values are always higher than the experimental ones (except for the 2024 T351 alloy). Moreover, such a transition is not observed in all the test conditions studied. In the 7075 alloy, for example, such a transition is observed only in air, while in the 8090 alloy, it is observed only in vacuum.

It has been suggested that shear lip formation near the specimen surface, indicative of the development of plane stress conditions at the crack tip, takes place at lower ΔK values in vacuum than in air [19]. This would lead to lower K_t values in vacuum than in air, which is contrary to most of the observed results. This aspect needs more rigorous treatment.

Conclusions

1. The delay following an overload depends upon the material cyclic behavior, the loading conditions, the test environment, and the associated micromechanisms of cracking.
2. In general, planar slip behavior leads to a higher crack growth resistance and higher delays after an overload.
3. In most of the studied test conditions, delay in vacuum is higher than that observed in air, except for the 8090 T651 alloy.
4. The observed effects can be explained qualitatively using a plastic zone model.
5. Transition from plane strain to plane stress conditions occurs at different K values for most of the studied alloys, depending upon the environment.

References

[1] Schijve, J., NRL Report MP 195, National Aeronautical and Astronautical Research Institute, Amsterdam, Holland, 1960.

[2] Ranganathan, N., Petit, J., and de Fouquet, J., *Advances in Fracture Research*, Pergamon Press, 1984, 3, pp. 1767 1773.

[3] Willenborg, J., Engle, R. M., and Wood, H. A., Technical Report TFR 71-701, Los Angles Division, North American Rockwell, 1971.

[4] Christensen, R. H., *Metal Fatigue*, McGraw-Hill, 1959.

[5] Elber, W., *Damage Tolerance in Aircraft structures, ASTM STP 486*, ASTM International, West Conshohocken, PA, 1971, pp. 230 242.

[6] Petit, J., Tintillier, R., Ranganathan, N., Ait-Abdedaim, M., and Chalant, G., *Fatigue Crack Growth under Variable Amplitude Loading*, Elsevier Applied Sciences Pubs., 1988, pp.162 179.

[7] Matsuoka, S. and Tanaka, K., "Delayed Retardation Phenomenon of Fatigue Crack Growth Resulting from a Single Application of Overload," *Engineering Fracture Mechanics*, Vol. 10, No. 3, 1978, pp. 515 525.

[8] Ranganathan, N., Quintard, A., Petit, J., and de Fouquet, J., *Environmentally Assisted Cracking, ASTM STP 1043*, ASTM International, West Conshohocken, PA, 1989, pp. 374 390

[9] Wei, R. P. and Shih, T. T., *International Journal of* Fatigue, 10, 1974, pp. 77 82.

[10] Petit, J., *Fatigue Crack Growth Threshold Concepts*, D. L. Davidson and S. Suresh, Eds., AIME, Warrendale, PA, 1984, pp. 1 24.

[11] Hornbogen, H. and Zum Gahr, K. H., "Microstructure and Fatigue Crack Growth in a γ-Fe-Ni-Al Alloy," *Acta Metallurgica*, Vol. 24, No. 6, 1976, pp. 581 592.

[12] Ranganathan, N., Bouchet, B., and Petit, J. *Fractography of Modern Engineering Materials: Composites and Metals, ASTM STP 948*, ASTM International, West Conshohocken, PA, 1987, pp. 424 446.

[13] Kemp, R. M. J., Wilson, R. N., and Gregson, P. J., *Fatigue and Fracture of Engineering Materials and Structures*, 15, 1992, pp. 291 299.

[14] Ranganathan, N., Adiwijayanto, F., Petit, J., and Bailon, J. P., "Fatigue Crack Propagation Mechanisms in an Aluminum Lithium Alloy," *Acta Metallurgica and Materialia*, Vol. 43, No. 3, 1995, pp. 1029 1035.

[15] Dugdale, D. S., "Yielding of Steel Sheets Containing Slits," *Journal of Mechanics and Physics of Solids*, Vol. 8, No. 2, 1960, pp. 100 104.

[16] Ranganathan, N., Petit, J., and Bouchet, B., "A Contribution to the Study of Fatigue Crack Retardation in Vacuum," *Engineering Fracture Mechanics*, Vol. 11, No. 4, 1979, pp. 775 789.

[17] Ranganathan, N. and Petit, J., *Fatigue Mechanisms: Advances in Physical Measurement of Fatigue Damage, ASTM STP 911*, ASTM International, West Conshohocken, PA, 1983, pp. 464 484.

[18] Vecchio, R. S., Hertzberg, R. W., and Jaccard, R., "Overload Induced Crack Growth Rate Attenuation Behavior in Aluminum Alloys," *Scripta Metallurgica*, Vol. 17, No. 3, 1983, pp. 343 346.

[19] Wanhill, R. J. H. and Schijve, J., *Fatigue Crack Growth under Variable Amplitude Loading*, Elsevier Applied Sciences, 1988, pp. 326 339.

Journal of ASTM International, Nov./Dec. 2004, Vol. 1, No. 10
Paper ID JAI19061
Available online at www.astm.org

Bernhard Tabernig,[1] *Reinhard Pippan,*[2] *Jérôme Foulquier,*[3] *Alain Rapaport,*[3] *and Sandrine Sereni*[4]

Periodic Overloads in the Near Threshold Regime

ABSTRACT: The effect of periodic overloads on the crack propagation behavior in the near threshold regime of long cracks and physically (extrinsically) short cracks is investigated. A 20 Vol. % SiC particle reinforced 359 cast aluminum alloy and a 17 Vol. % SiC particle reinforced 2129 aluminum alloy are examined. In the Paris regime the two alloys exhibit a different behavior. In the 2124 reinforced alloy a reduction of the mean crack propagation rate, which is typical for ductile metals, is observed. On the other hand the mean crack propagation rate accelerates in the 359 reinforced cast alloy, which is caused by generation of micro-cracks during the overload.

In the near threshold regime and at smaller stress intensity ranges in the physical short crack regime the behavior of both alloys is very similar. The effective threshold is not affected by the overload, i.e., if the constant amplitudes are smaller than the effective threshold they do not contribute to crack propagation. If both, the constant amplitudes and the overload amplitudes contribute to crack propagation, the build up of crack closure is affected by the load history.

KEYWORDS: periodic overloads, threshold of stress intensity range, short crack, crack closure

Introduction

The effect of variable amplitudes on fatigue crack propagation has been extensively investigated in the Paris regime [1 5]. However, in the threshold regime as well as in the short crack regime, the number of studies is rather limited [6 10]. Nevertheless, the majority of engineering components is designed for finite lives and are subjected to variable amplitude loading with a significant amount of load cycles in the near threshold regime, or they are designed for "infinite" life, where the load amplitudes should be below a certain "threshold" value. The damage-tolerant design tools in this field are extremely underdeveloped.

The main reasons for this situation are:

- Many applications fall into the short-crack regime, where cracks can propagate below the standard measured long crack threshold determined under constant amplitude loading.
- There exists no standard procedure to determine the threshold in the transition regime from short to long cracks.

Manuscript received 14 June 2002; accepted for publication 14 November 2003; published November 2004. Presented at ASTM Symposium on Fatigue Testing and Analysis Under Variable Amplitude Loading Conditions on 29 31 May 2002 in Tours, France; P. C. McKeighan and N. Ranganathan, Guest Editors.

[1] Research Scientist, Erich Schmid Institute of Material Science, now Plansee AG, 6600 Reutte, Austria.
[2] Vice Director and Senior Scientist, Erich Schmid Institute of Materials Science, Austrian Academy of Science, and Christian Doppler Laboratory for local analysis of deformation and fracture, Jahnstrasse 12, 8700 Leoben, Austria, pippan@unileoben.ac.at.
[3] Manager and Research Scientist, respectively, EADS France, GIE EADS CCR, 12 rue Pasteur, Suresnes Cedex, France.
[4] Research Scientist, CENTRO RICERCHE FIAT, Strada Torino 50, 10043 Orbassano, Italy.

- There is a lack of non-destructive techniques to detect sufficiently small flaws with high accuracy.
- The knowledge of load interaction effects in the near threshold regime and the short crack regime is unsatisfactory.

To improve this situation, this paper answers the following questions:

- How do extrinsically (physically) short cracks behave under periodic overloads?
- Is the effective threshold influenced by periodic overloads?
- How do periodic overloads affect the near threshold crack propagation behavior in particle reinforced aluminum alloys?

In order to answer these questions, fatigue crack growth experiments were performed with periodic overloads in the near threshold regime. Standard fracture mechanics specimens were used, and the experiments were started on pre-cracks without crack closure (i.e., with a minimum of crack tip shielding). In other words, the tests were performed on extrinsically short pre-cracks [11,12].

Material and Experimental Procedure

The materials examined in this study are a 20 Vol. % SiC particle reinforced 359 cast aluminum alloy (heat treatment T6) and a 17 Vol. % SiC particle reinforced 2124 aluminum alloy (heat treatment T4). The mean size of the particles in the 359 alloy is about 7 μm; the fracture toughness, K_{IC}, is relatively low at 14 MPa√m; and Young's modulus and tensile strength are 97 GPa and 247 MPa, respectively. A detailed description of the microstructure, the fatigue, and fatigue crack propagation behavior is given in [7,13,14]. In the 2124T4 reinforced alloy, the mean size of the particles is about 1.4 μm; the fracture toughness is 23 MPa√m; and the Young's modulus, the yield stress, and the ultimate tensile strength are about 100 GPa, 400 MPa, and 590 MPa, respectively.

The experiments are performed on standard SENT (width W = 20 mm) and CT-specimens (width W = 40 mm). The notches were machined by spark erosion. Furthermore, a special razor blade cutting technique was applied in order to get extremely sharp notches, with notch radii between 10 and 20 μm. The sharper the notch, the smaller the loads for pre-fatigue, and the smaller are the effects of the residual stress field of the crack tip in front of the pre crack [13]. To initiate a crack of about 40 μm length measured from the notch root, the specimens were pre-fatigued in cyclic compression (load ratio R = 20) at a ΔK = 8 MPa√m and 10 MPa√m in the 359 and the 2124 alloys, respectively.

All periodic overload tests were performed at the same overload ratio, and the number of constant amplitude cycles between two overload cycles was always 1000. The overload ratio – the ratio of the maximum stress intensity factor at the overload to the maximum stress intensity factor of the constant amplitudes (which are called base amplitudes) – was 1.8, and the stress ratio of the base load amplitudes was R = 0.1. The experiments were performed at four loading cases (see Fig. 1):

- At the smallest load amplitude, the constant amplitude and the overload correspond to a ΔK below the effective threshold and between the effective threshold ΔK_{effth} and the long crack threshold ΔK_{th}, respectively.
- In the second case, the base and the overload ΔK lay between ΔK_{effth} and ΔK_{th}.
- In the third case, the base load amplitude corresponds to a ΔK that is between ΔK_{effth} and ΔK_{th}, and the overload ΔK is larger than ΔK_{th}.
- In the fourth case, the base load amplitude corresponds at the beginning of the fatigue test to ΔK equal to ΔK_{th}.

The experiments were performed on a servo hydraulic test machine. The test frequency during base loading was 70 Hz. The experiments were conducted in air at room temperature. The crack length was monitored by a direct current potential drop technique. The accuracy of measuring a change in crack length was about ± 5 μm.

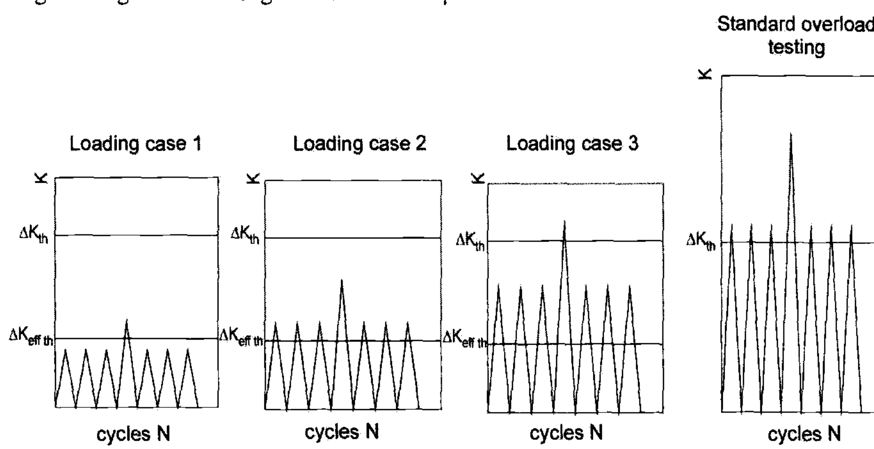

FIG. 1 *Schematic representation of the performed overload experiment. In Experiments 1 3, the initial crack growth behavior of extrinsically short cracks was investigated; in the fourth experiment, the effect of periodic overloads on the standard fatigue crack propagation behavior was examined.*

Results and Discussion

The Long Crack Behavior

In Figs. 2 and 3 the standard fatigue crack propagation rate versus ΔK was determined in a constant amplitude test, and the periodic overload test is depicted for both alloys. In the case of periodic overload results, the mean crack propagation rate is plotted as a function of ΔK determined from the base load amplitudes. The overloads are not taken into account for the determination of the crack driving force, ΔK. In the reinforced 2124 alloy in the Paris regime, the mean crack propagation rate in the periodic overload experiment is significantly smaller than in the constant amplitude test. This is the expected behavior. An overload causes a retardation because the crack extension during the overload is very small compared to the increase of the crack length during base loading between two overloads; the mean crack propagation rate is dominated by the retardation effect. Near the threshold, the behavior is different, the crack propagation rate in the constant amplitude experiment and the periodic overload test is about equal, and it seems that the threshold might be somewhat smaller than in the periodic overload experiment. One reason for this behavior is that near the threshold and somewhat below, the crack propagation during the overload becomes more and more important in relation to the crack propagation caused by the base amplitudes. A further reason for this near threshold behavior may be the change of the different contributions to crack closure [5,12,8,13]. At larger ΔK plasticity, induced crack closure is the dominant closure effect. The retardation in this regime is mainly induced by the increase of this contribution. In the near threshold regime, the roughness induced crack closure and perhaps the oxide induced crack closure are more important. The overloads should increase the contribution of plasticity induced closure for the base amplitudes even in the near threshold regime. However, the overloads may reduce the contribution of roughness induced crack closure, which may induce an increase of the growth rate during base amplitudes.

Near the threshold in the reinforced 359 alloy and the reinforced 2124 alloy, the behavior is very similar. However, at larger ΔK values, the reinforced 359 alloy shows an opposite behavior; the mean crack propagation rate in the overload experiment is larger than in the constant amplitude test. The Paris exponent of the overload curve is significantly larger than that of the constant amplitude experiments. The reason for this unusual behavior is the low fracture toughness of this material. Somewhat above the threshold, the maximum stress intensity factor of the overloads is very near the fracture toughness. On one hand, this induces a relatively large crack extension during the overload, while on the other hand at the overload a certain amount of particle cracking occurred. During the following base amplitude loading, the main crack and the micro cracks coalesce, which induces an increase of the mean crack propagation rate. The reinforced 2124 alloy has significant larger fracture toughness, and in addition the probability of particle cracking is very low, therefore this particle reinforced alloy behaves like a typical ductile material.

The Behavior of Extrinsically Short Cracks

Figures 4 8 show the crack propagation behavior obtained in the periodic overload experiments of the loading cases 1 3, where the base amplitude is always smaller than the long crack threshold. The short pre-crack was generated in cyclic compression at relatively small load amplitudes in deep notched specimens. At the beginning of the fatigue experiment in tension, crack closure should not occur. The increase of crack length during this type of test is very small in relation to the notch depth and the ligament length (W–a, where W is the width, and a is the total crack length); hence the change of ΔK is not significant. Therefore the experiments can be considered as a constant ΔK test on extrinsically short cracks with periodic overloads.

In addition, constant amplitude tests at about the same ΔK as the base amplitude and overload were performed in a type of pre-cracked specimen. These results, i.e., crack extension versus number of load cycles are plotted also in Figs. 4 8. In order to normalize the crack propagation data of the constant amplitude test, which corresponds to the overload ΔK, the number of loading cycles was multiplied by 1000. In the loading case 1 only the constant amplitude data obtained at a ΔK, which is about equal to ΔK of the overloads, are indicated, because in the constant amplitude test at a ΔK equal to base amplitude, such extrinsically short cracks do not grow ($\Delta K < \Delta K_{effth}$).

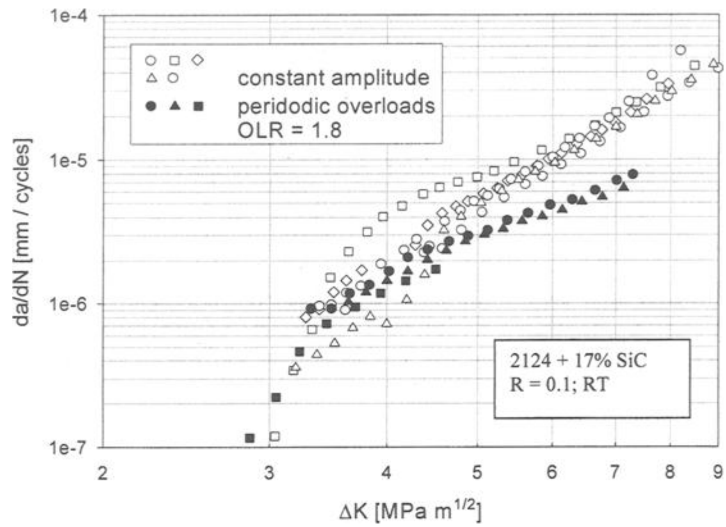

FIG. 2 *Fatigue crack propagation rate versus the stress intensity range determined in constant amplitude experiment at a stress ratio of 0.1 and mean fatigue crack propagation rate versus the stress intensity range of the base load amplitudes in the periodic overload experiment in a particle reinforced 2124 aluminum alloy.*

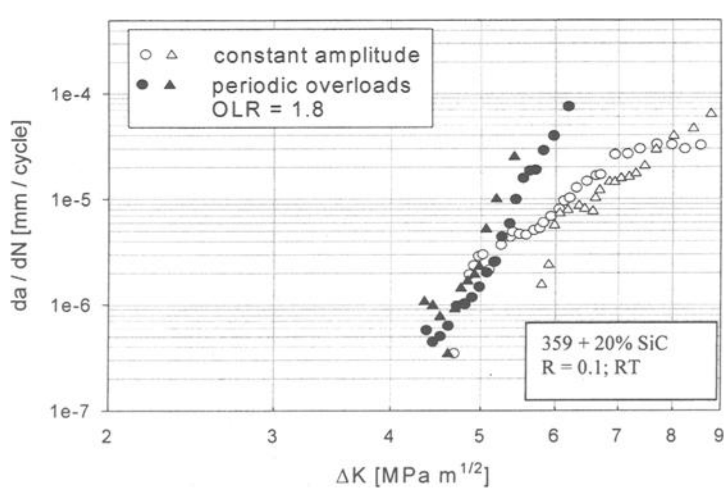

FIG. 3 *Fatigue crack propagation rate versus the stress intensity range determined in constant amplitude experiment at a stress ratio of 0.1 and mean fatigue crack propagation rate versus the stress intensity range of the base load amplitudes in the periodic overload experiment in a particle reinforced 359 cast aluminum alloy.*

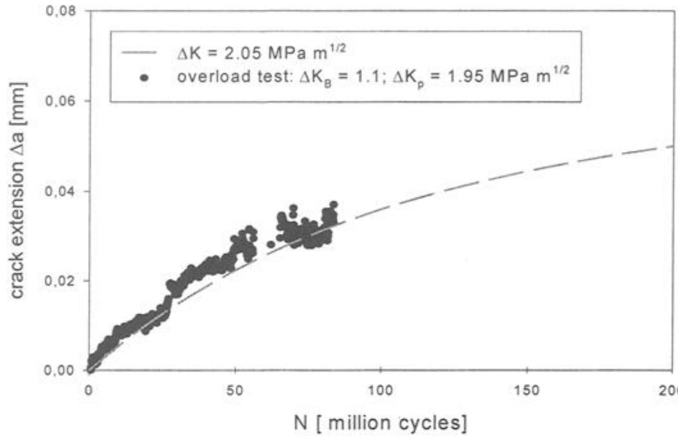

FIG. 4 *Crack extension versus number of base amplitudes for the loading case 1, where the base ΔK is smaller than the effective threshold determined in a constant amplitude test in the particle reinforced 359 alloy, and the crack extension versus number of cycles * 1000 (normalized plot) in a constant amplitude experiment at ΔK = 2.05 MPa$\sqrt{m}$, which is about equal to the overload ΔK.*

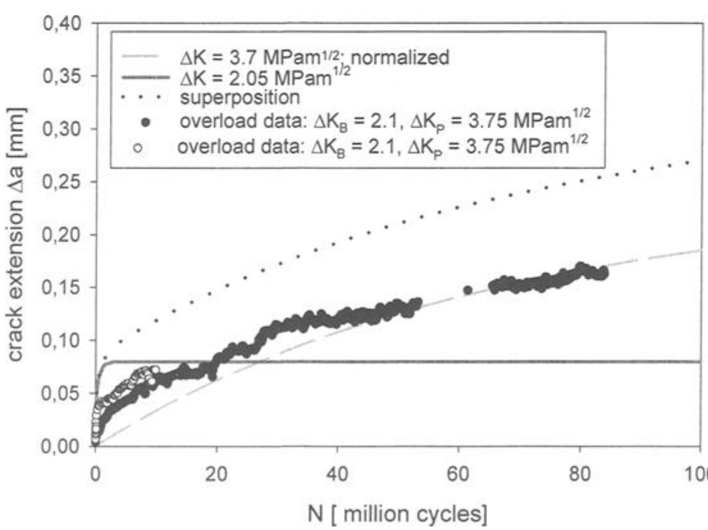

FIG. 5 *Crack extension versus number of load cycles at the base amplitude for the loading case 2 in the reinforced 359 alloy. In addition, the crack extension versus normalized number of load cycles in the corresponding constant amplitude experiments and the linear superposition of normalized constant amplitude tests are indicated.*

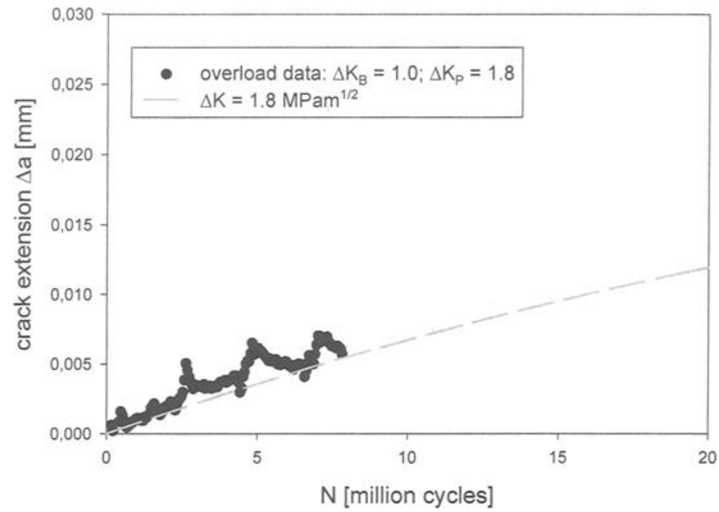

FIG. 6 *Crack extension versus number of base amplitudes for the loading case 1, where the base ΔK is smaller than the effective threshold determined in a constant amplitude test in the particle reinforced 2124 alloy, and the crack extension versus number of cycles * 1000 (normalized plot) in a constant amplitude experiment at ΔK = 1.8 MPa$\sqrt{m}$, which is about equal to the overload ΔK.*

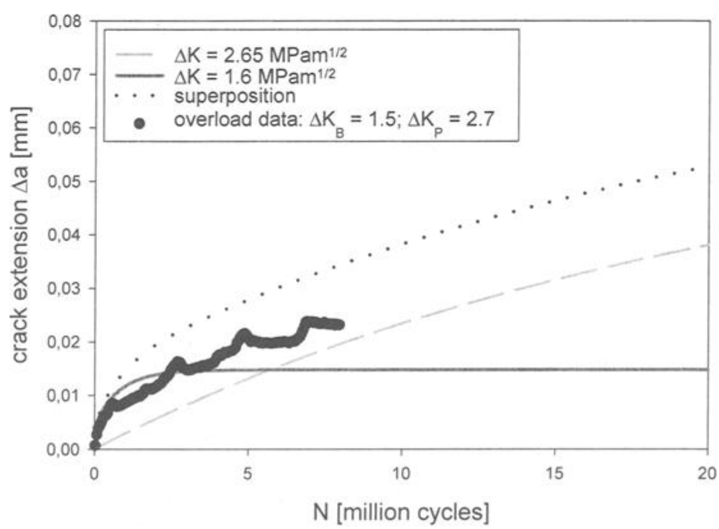

FIG. 7 *Crack extension versus number of load cycles at the base amplitude for the loading case 2 in the reinforced 2124 alloy. In addition, the crack extension versus normalized number of load cycles in the corresponding constant amplitude experiments and the linear superposition of normalized constant amplitude tests are indicated.*

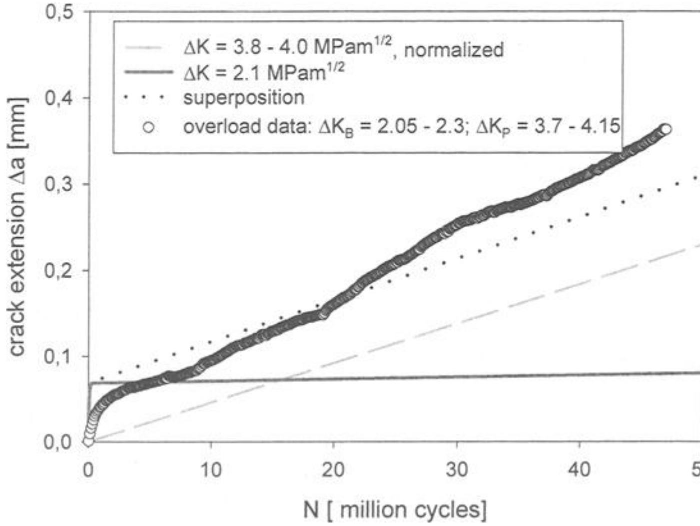

FIG. 8 *Crack extension versus number of load cycles at the base amplitude for the loading case 3 in the reinforced 2124 alloy. In addition, the crack extension versus normalized number of load cycles in the corresponding constant amplitude experiments and the linear superposition of normalized constant amplitude tests are indicated.*

Figures 4 and 6 show that the normalized crack propagation behavior of the constant amplitude test at the ΔK equal to the overload ΔK is identical with the crack propagation behavior in overload experiment. This indicates very clearly that only the overload contributes to the crack propagation, and the base amplitudes, which are only somewhat smaller than ΔK_{effth}, do not affect the crack propagation behavior. In other words, the threshold of stress intensity range is not influenced by variable amplitude loading.

In the loading case 2 (Figs. 5 and 7) the crack propagation behavior is dominated in the beginning by the base load amplitudes. The overloads do not affect the propagation rate in this early stage. This is evident in the good agreement of crack propagation behavior of constant amplitude experiment at ΔK equal to the base amplitude and overload experiment. This indicates that the crack closure behavior of such extrinsically short cracks is not influenced by overloads.

However, after a short extension of the crack, the propagation rate at the base amplitudes is influenced by the overload (it is somewhat smaller than in the corresponding constant amplitude experiment), which indicates that the closure load increases somewhat faster in the periodic overload experiment than during the constant amplitude loading. Therefore, the non-propagation condition is reached at smaller crack extension in the periodic overload experiments than in the case of constant amplitude loading. The R-curve for the threshold of stress intensity range for the base amplitudes should increase somewhat faster than in the case of constant amplitude loading, as schematically depicted in Fig. 9. At "larger" crack extensions only the overloads contribute to crack propagation. This is indicated by the fact that the normalized crack propagation rate in the constant load experiment at a ΔK equal to the overload ΔK agrees with the crack growth rate in the periodic overload experiment.

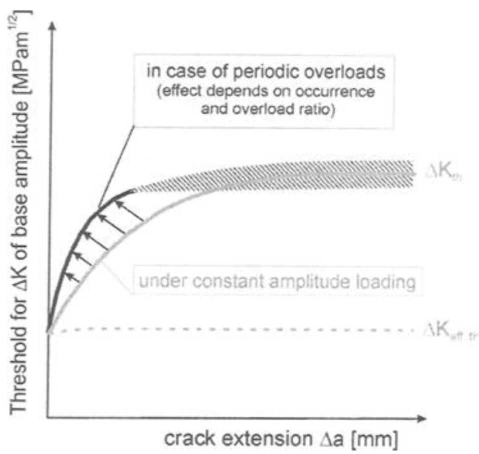

FIG. 9 *Schematic illustration of the influence of periodic overloads on the shape of the R-curve for the threshold of stress intensity range for the base amplitude.*

Figure 8 shows the crack propagation behavior in the loading case 3 in the 2124 particle reinforced alloy. At the beginning the behavior in loading cases 2 and 3 is very similar. A difference between loading case 2 and 3 occurs at larger crack extension; in case 2 the crack will stop after a certain crack extension because the overload ΔK is smaller than the long crack threshold, whereas in loading case 3 it will reach the typical long crack behavior of Figs. 2 and 3, when, due to the increase in crack length, the ΔK value of the base amplitudes reaches the long crack threshold. However, this would need an extremely large number of load cycles in our experiment.

Conclusions

The comparison of periodic overload tests with constant amplitude experiments on extrinsically (physically) short cracks and long cracks in two particle reinforced alloy leads to the following conclusions.

- The effective threshold of stress intensity range is not influenced by periodic overloads, or in other words, amplitudes below the effective threshold of stress intensity range do not affect the crack growth behavior during variable amplitude loading.
- The early stage of crack propagation of extrinsically short cracks is not affected by the overloads in the near threshold regime.
- "The threshold value for the base amplitudes" in a periodic overload case increases faster with crack extension than under constant amplitude loading, which is schematically depicted in Fig. 9.
- Considering the mean crack propagation behavior in relation to the base amplitudes, the crack propagation somewhat below and at the long crack threshold for constant amplitude loading is dominated by the crack propagation during the periodic overloads.

- In the "Paris" regime, the periodic overloads in the reinforced 2124, which is relatively ductile, cause a retardation of the mean crack growth rate, whereas in the relatively brittle particle reinforced 359, the periodic overloads induce an acceleration of the mean crack propagation rate.

Acknowledgments

The authors thank all partners of the BRITE EURAM project MISPOM, Aerospatiale, Teksid, Defence Evaluation and Research Agency, University Politehnica de Catalunga, University di Ancona, National University Galway for collaboration and the European Community for financial support.

References

[1] Socie, D. F., "Prediction of Fatigue Crack Growth in Notched Members under Variable Amplitude Loading History," *Engineering Fracture Mechanics*, Vol. 9, 1977, pp. 849 865.
[2] Schijve, J., "Prediction Methods for Fatigue Crack Growth in Aircraft Materials," *Fracture Mechanics: Twelfth Conference, ASTM STP 700*, ASTM International, West Conshohocken, PA, 1980, pp. 3 34.
[3] Newman, J. C., Jr., "A Crack Closure Model for Predicting Fatigue Crack Growth under Aircraft Spectrum Loading," *ASTM STP 748*, ASTM International, West Conshohocken, PA, 1981, pp. 53 84.
[4] de Koning, A.U., "A Simple Crack Closure Model for Predicting Fatigue Crack Growth under Aircraft Spectrum Loading," *ASTM STP 734*, ASTM International, West Conshohocken, PA, 1980, pp. 63 85.
[5] Suresh, S., "Fatigue of Materials," *Cambridge University Press*, 1998.
[6] Stanzl, S. E., Tschegg, E. K., and Mayer, H. R., "Show Fatigue Crack Growth under Step and Random Loading," *Zeitschrift Metallkunde*, Vol. 77, 1986, pp. 588 594.
[7] Pippan, R., "Threshold Values for Engineering Application," *Proc. Fatigue 96*, G. Lütjering and H. Nowak, Eds., Pergamon, 1996, pp. 419 430.
[8] Tabernig, B., "Das Ermüdungsverhalten Teilchenverstärkter Aluminiumlegierungen," *Universität Leoben*, Austria, 2000.
[9] Bruzzi, M., "Development Models to Predict the Mechanical Response of Aluminum and Aluminium Matrix Composites in Static and Fatigue Loading," Thesis, *National Universität of Ireland*, Galway, 2000.
[10] Topper, T. H. and Yu, M. T., "The Effect of Overloads on Threshold and Crack Growth," *International Journal of Fatigue*, Vol. 7, 1985, pp. 159 164.
[11] Pippan, R., "Fatigue Threshold for Engineering Application," In: *Encyclopedia of Materials: Science and Technology*, 2001, pp. 3001 3006.
[12] Ritchie, R. O., "Mechanisms of Fatigue Crack Propagation in Metal, Ceramics and Composites: Role of Crack Tip Shielding," *Materials Science Engineering*, Vol. 103, 1988, pp. 15 28.
[13] Tabernig, B. and Pippan, R., "Determination of the Length Dependence of the Threshold for Fatigue Crack Propagation," *Engineering Fracture Mechanics*, 2002, pp. 899 907.
[14] Tabernig, B. and Pippan, R., "Effect of Periodic Overloads in Particle Reinforced Aluminum Alloys: The Near Threshold Behavior," *International Journal of Fatigue*, submitted.

Journal of ASTM International, Nov./Dec. 2004, Vol. 1, No. 10
Paper ID JAI19051
Available online at www.astm.org

Philippe Darcis,[1] *and Naman Recho*[1]

Fatigue Reliability Analysis of an Overload Effect in Welded Joints Including Crack Initiation and Plastic Zone as Random Variables

ABSTRACT: This paper deals with the reliability analysis of the influence of an overload on the fatigue design of welded joints. The modeling of the fatigue life is presented as the sum of four parts: the first one concerns the fatigue life initiation, the second one involves the fatigue life between the initiation period and the overload application, the third one deals with the fatigue life behavior from the overload to the total restoration of the crack growth rate, and the fourth is related to the fatigue life between the end of the retardation zone until the failure. Concerning the modeling of the retardation effect, particular attention is given to the calculation of the effective stress intensity factor. Finally, the developed methodology is applied to the case of welded joints in order to evaluate the importance of considering the overload effect in the reliability analysis.

KEYWORDS: reliability analysis, fatigue crack growth, overload, welded joints

Introduction

Several reliability analyses deal with the evaluation of the fatigue life of welded joints. They are based on two deterministic approaches: the S-N curves approach associated to a cumulation model, such as the Miner rule, and the linear fracture mechanics approach using a crack propagation law, such as the Paris law [1]. In the last case, almost all existing applications are founded on the Madsen damage indicator method [2]. Although these analyses are developed by taking into account the variable loading by the use of the stress equivalent concept, they do not take into account the influence of the overload.

When an overload occurs, one observes reduced crack growth rate following the overload. In order to model this phenomenon, the present paper deals with reliability analysis on the basis of the linear elastic fracture mechanics approach in which the limit state function is written as a function of the following random variables: the initial crack length, the fatigue life initiation, the material parameters of the used propagation law, and the size of the plastic zone due to overload.

Proposed Deterministic Approach to Fatigue Crack Growth Following an Overload

This approach considers that the total fatigue life duration N_{Total} is determined as being the sum of four parts: the number of cycles to crack initiation N_i corresponding to an initial crack length a_0, the number of cycles N_1 from a_0 until a_{pic} corresponding to the overload, the number of cycles N_2 from a_{pic} to a_D, which is the crack length corresponding to the total restoration of the

Manuscript received 23 April 2002; accepted for publication 17 July 2003; published November 2004. Presented at ASTM Symposium on Fatigue Testing and Analysis Under Variable Amplitude Loading Conditions on 29 31 May 2002 in Tours, France; P. C. McKeighan and N. Ranganathan, Guest Editors.

[1] Ph.D. and Professor, respectively, LERMES, Laboratoire d'Etudes et de Recherche en MEcanique de Structures, Université Blaise Pascal - Clermont II, IUT de Montluçon, Av. Aristide Briand, 03100 Montluçon - France.

crack growth rate and N_3, the number of cycles from a_D to the critical crack size until failure. This model considers only one overload application during the crack propagation phase.

Fatigue Life Initiation: N_i

The number of cycles to crack initiation N_i may be estimated on the basis of a local strain-life approach by the following equation [3]:

$$\varepsilon_a = \frac{(\sigma'_f - \sigma_m)}{E}.(2.N_i)^b \tag{1}$$

where σ_f' is the fatigue strength coefficient, σ_m is the mean stress, b is the fatigue strength exponent, and ε_a is the strain amplitude. The analysis is performed using cyclic stress-strain relationship for the material in combination with Neuber's rule [4], which allows one to connect the nominal stresses and strains to those close to the notch by the use of K_f, the notch parameter, as follows:

$$K_f^2.\varepsilon_\infty.\sigma_\infty = \varepsilon_a.\sigma_a \tag{2}$$

where ε_∞ and σ_∞ are the nominal strain and stress amplitudes, respectively, and ε_a and σ_a are those at the notch root (local stress and strain).

The steps in the Neuber analysis are shown in Fig. 1. Consider a cyclically stable material (with the Ramberg-Osgood material parameters K', n'). At the initial applied load, the local stress and strain amplitudes at the notch are obtained as corresponding to the intersection point between the Neuber Hyperbola (3.1) and the material stress-strain relationship (3.2). This is given by

$$\begin{cases} \sigma_a.\varepsilon_a = \dfrac{K_f^2.\sigma_\infty^2}{E} & (3.1) \\ \varepsilon_a = \dfrac{\sigma_a}{E} + \left(\dfrac{\sigma_a}{K'}\right)^{\frac{1}{n'}} & (3.2) \end{cases} \tag{3}$$

For the successive load reversals, at the stress concentration zone the variation of the nominal stress $\Delta\sigma_\infty$ will imply variations of stress $\Delta\sigma$ and strain $\Delta\varepsilon$, which are obtained as the solution of the following system

$$\begin{cases} \Delta\sigma.\Delta\varepsilon = \dfrac{K_f^2.(\Delta\sigma_\infty)^2}{E} \\ \Delta\varepsilon = \dfrac{\Delta\sigma}{E} + 2.\left(\dfrac{\Delta\sigma}{2.K'}\right)^{\frac{1}{n'}} \end{cases} \tag{4}$$

Finally, one obtains the mean stress applied to the notch and σ_m and ε_a, which allow one to determine the fatigue life initiation N_i.

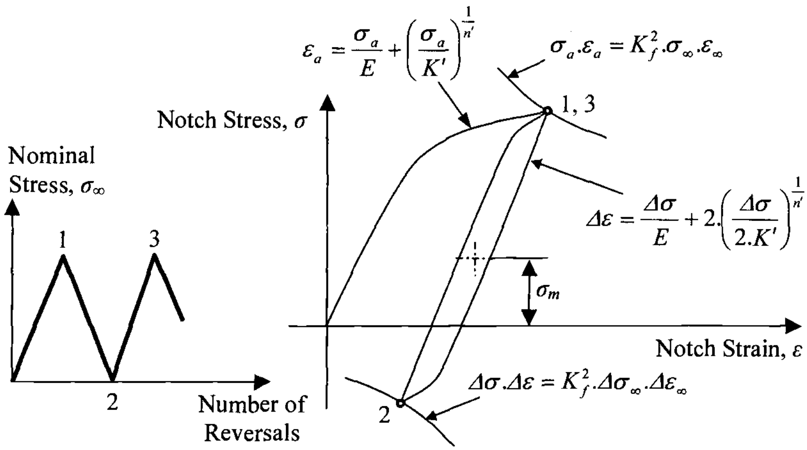

FIG. 1—*Definition of parameters governing crack initiation.*

The First Period: N_1

From the fatigue life initiation until the overload, a crack propagation law such as the Paris law is used

$$\frac{da}{dN} = C\,(\Delta K)^m \tag{5}$$

where C and m are two material constants (C will be considered as function of m in our study).

Note: This relationship uses a classical stress intensity factor variation, ΔK, in order to avoid a highly complicated formulation in the reliability analysis.

The variation of the stress intensity factor is given by

$$\Delta K = \Delta S_\infty.\sqrt{\pi\, a}.f(a) \tag{6}$$

in which $f(a)$ is a function of the geometry and the crack length, and ΔS_∞ is the stress variation induced by the cyclic loading.

Thus, the first period, N_1, is given by integration as follows:

$$N_1 = \frac{1}{C}\int_{a_0}^{a_{pic}} \frac{da}{(\Delta K)^m} \tag{7}$$

where a_0 is the initial crack length, and a_{pic} is the crack where the overload is applied.

The Second Period: N_2

The second period is the most important part to be determined when the overload occurs.

Before analyzing our modeling choices concerning N_2 in more detail, we will discuss the retardation effect, which can be divided into two parts (Fig. 2).

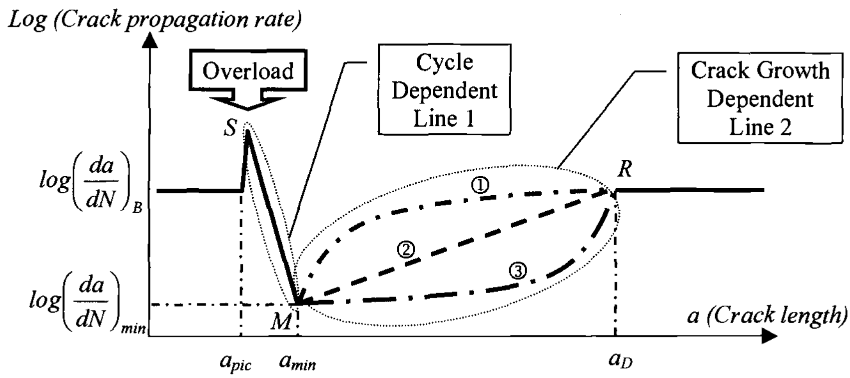

FIG. 2—*Two distinct transition zones due to the retardation effect (for a loading at ΔP constant).*

These two parts are as follows:

- The first part takes into account the effect of the Cycle Dependence at the time of overload peak application. This part concerns the calculation of the lowest crack growth rate and the calculation of the minimum crack length at this lowest point a_{min}.
- The second part takes into account the Crack Growth Dependence; it consists of determining the crack length a_D. This crack length between a_{pic} and a_D is influenced by the retardation effect and reaches the initial crack growth rate (before overload) at a_D.

Cycle Dependence—The two characteristic aspects to determine are the minimum crack growth rate $(da/dN)_{min}$ and the crack length a_{min} at this minimum.

Several authors [5,6] have confirmed that the value of a_{min} is equal to one quarter of the plastic zone given by Irwin representation [7] at the overload. This result agrees with testing analyses for constant ΔK and for constant ΔP.

On the other hand, the calculation of the lowest crack growth rate remains more difficult. Indeed, this calculation consists of the comprehension of the retardation effect. The concept of ΔK_{eff}, established by Elber [8] in the 1970s, is generally admitted, however the calculation of ΔK_{eff} is still discussed because various physical phenomena can explain it.

If we start on the basis of the Elber concept, we can rewrite the Paris law [1] as follows:

$$\frac{da}{dN} = C.(\Delta K_{eff})^m \tag{8}$$

with $$\Delta K_{eff} = K_{max}\text{-}K_R \tag{9}$$

where K_R (R for Retardation) corresponds to the stress intensity factor level from which ΔK induces a crack propagation.

Two aspects are related to Elber's concept:

- The first concerns the total restoration of the initial crack growth rate (before overload).
- The second concerns the physical description of the retardation effect.

Most authors agree with the first aspect because ΔK_{eff} is associated with a classical crack propagation law such as Paris' law. Nevertheless, the second aspect is still controversial. Despite the great use of the Elber's concept, the principle of the crack closure was not admitted by Schijve [9] and Marci [10]. In fact, they explain the retardation effect by studying the residual stress field near the crack tip consequently to the overload. Many experimental observations [11,12] confirmed Marci's studies.

We developed a numerical method in order to take into account the residual compressive stress field ahead of the crack tip when overload occurs [13]. This method was established on the basis of experimental observations of Lang and Marci [10,14], who introduced the term K_{PR} (PR for propagation). This new term results from an experimental methodology called CLPM (Crack Propagation Load Measurement), which makes it possible to determine precisely the effective part of the fatigue crack propagation. Lang and Marci explain, in a broad outline, why K_{PR} is not a parameter of crack closure but is related to the K_{max} required for the propagation of the crack. This new parameter is identified clearly as being the expression of the residual compressive stresses ahead of the crack tip [14].

According to [13], we obtain $(da/dN)_{min}$ for welded joints. The equation of Line 1 is given by the following (see Fig. 2):

$$\frac{da}{dN} = \left(\frac{da}{dN}\right)_0 + \xi . a \tag{10}$$

where ξ is the slope calculated with the points S and M as follows:

$$\xi = \frac{y_M - y_S}{x_M - x_S} = \frac{(da/dN)_{\min} - (da/dN)_0}{a_{\min} - 0} \tag{11}$$

where $(da/dN)_0$ is the crack growth rate before the overload.

Crack Growth Dependence—In this part, we have to determine the crack length a_D and the physical behavior representing the total restoration of the crack growth rate (before overload).

Many studies [6,15,16] recommend taking a_D equal to the monotonic plastic zone due to the overload, although the size of the plastic zone can vary according to authors. For instance, some propose taking the Irwin meaning of the plastic zone size [6,15] and the Rice meaning [16]. Nevertheless, recent papers [6,17] recommend a crack length equal to twice the overload monotonic plastic zone. This recommendation is considered in our work and checked for tests with constant ΔP [18] and with constant ΔK [5].

Concerning the modeling of the total restoration of the crack growth rate, between a_{min} and a_D, the technical literature distinguishes three manners (Fig. 2): convex manner ① [14,19], straight manner ② [5], and concave manner ③ [20,21].

According to a former study [22], we found that the convex manner corresponds to the tests of [5,18] as confirmed also by Ranganathan [19].

Thus, Line 2, which describes the increase of da/dN, can be given by (see Fig. 2):

$$\frac{da}{dN} = \alpha + \beta\, a + \gamma.\sqrt{a} + \left(\frac{da}{dN}\right)_{S'} .\left[\exp\left\{\eta.\left(a - a_{pic}\right)\right\} - 1\right] \tag{12}$$

where α, β, and γ are obtained from the points M and R, and η is the slope between the points S and S' for the test at ΔP constant as we can see in Fig. 3.

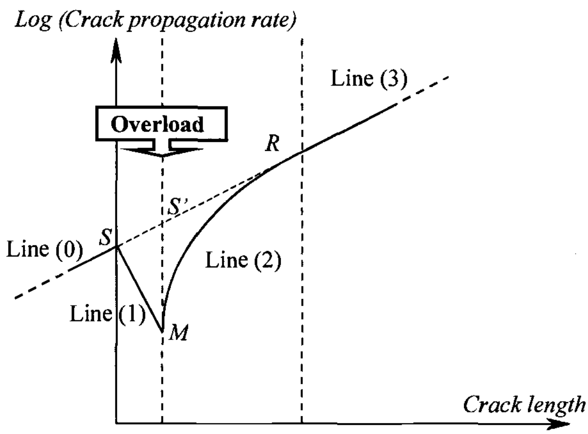

FIG. 3—*Model of fatigue crack growth following an overload at ΔP constant.*

Finally, the crack growth dependence is described by the reduction of the effective stress intensity factor variation $\Delta K_{eff,D}$ from the point M to the point R deduced from the Line 2. We then have:

$$N_2 = \frac{1}{C'} \int_{a_{pic}}^{a_{pic}+a_{min}} \frac{da}{\left(\Delta K_{eff}\right)^{m'}} + \frac{1}{C'} \int_{a_{pic}+a_{min}}^{a_{pic}+a_D} \frac{da}{\left(\Delta K_{eff,D}\right)^{m'}} \tag{13}$$

where C' and m' are the two material parameters that could be different from C and m. Generally, m' is given as equal to m.

The Third period: N_3

This period is not influenced by the overload. It can be determined as follows:

$$N_3 = \frac{1}{C} \int_{a_{pic}+a_D}^{a_c} \frac{da}{(\Delta K)^m} \tag{14}$$

where a_c is the critical crack size to failure.

The total fatigue life duration is then given by

$$N_{Total} = N_i + N_1 + N_2 + N_3 \tag{15}$$

This equation is at the base of the limit state function in the reliability analyses.

Proposed Reliability Approach to Fatigue Crack Growth Following an Overload

This analysis is based on a deterministic model of the retardation effect following overloads. Others material parameters due to the plastic zone, determined in this case, are considered random variables.

In this paper we introduce two new aspects:

- The first takes into account the fatigue life initiation as a random variable.
- The second develops a new reliability analysis associated with fatigue overloads.

From Eqs 1, 7, 13, 14, and 15, the total fatigue life is written as follows:

$$\begin{aligned} N_{Total} = N_i + \frac{1}{C} \int_{a_0}^{a_{pic}} \frac{da}{(\Delta K)^m} + \frac{1}{C'} \int_{a_{pic}}^{a_{pic}+a_{min}} \frac{da}{(\Delta K_{eff})^m} + \\ \frac{1}{C'} \int_{a_{pic}+a_{min}}^{a_{pic}+a_D} \frac{da}{(\Delta K_{eff,D})^m} + \frac{1}{C} \int_{a_{pic}+a_D}^{a_c} \frac{da}{(\Delta K)^m} \end{aligned} \tag{16}$$

The probability to failure of a given crack length at a certain number of cycles N can be modeled by the following safety margin $M(N)$:

$$M(N) = N_{Total} - N \tag{17}$$

Using the definitions presented in Eqs 16 and 17, the failure criterion is written as a limit state function $g(X)$ for reliability analysis

$$g(X) = \begin{pmatrix} N_i + \frac{1}{C} \int_{a_0}^{a_{pic}} \frac{da}{(\Delta K)^m} + \frac{1}{C'} \int_{a_{pic}}^{a_{pic}+a_{min}} \frac{da}{(\Delta K_{eff})^m} + \\ \frac{1}{C'} \int_{a_{pic}+a_{min}}^{a_{pic}+a_D} \frac{da}{(\Delta K_{eff,D})^m} + \frac{1}{C} \int_{a_{pic}+a_D}^{a_c} \frac{da}{(\Delta K)^m} \end{pmatrix} - N \tag{18}$$

The failure occurs when $g(X) < 0$.
The random variables (X) in this equation are:

- a_0, the initial crack length,
- m, the Paris Law exponent,
- r, the radius of the weld toe (used in the calculation of N_i), and
- a_D, the crack length who takes into account the plastic zone as random variable (for this case we multiply this quantity by a bias factor γ_{a_D}, which takes into account the variable random characteristic).

The use of the First Order Reliability Method (FORM) associated with a former limit state function (Eq 18) allows us to determine the reliability index β for a given structural detail. This β index can be compared with a target reliability index in order to consider the structure safe.

Application to a Welded Detail

In order to apply our approach let us consider the cruciform welded joint tested by Lassen [23] and studied by Grous et al. [24] (these joints were tested under constant amplitude loading conditions, but the overload effect corresponds only to a model without experimental verification). Lassen had performed a series of tests at the Agder College of Engineering in order to establish fatigue properties of cruciform welded joints. The test specimens were fabricated from CLC steel plate 25 mm thick. Mechanical and chemical properties are given in Table 1.

TABLE 1 *Mechanical and chemical properties of CLC steel [23].*

Mechanical Properties									
Yield Strength (in MPa)					416				
Tensile Strength (in MPa)					501				
Elongation					26				
Chemical Composition %									
C	Si	Mn	P	S	Cu	Ni	Cr	Mo	Nb
0.08	0.15	1.40	0.006	0.002	0.01	0.02	0.02	0.01	0.008

The welding procedure used is the SMAW procedure (Shielded Metal-Arc welding). The weld geometry is presented in Fig. 4.

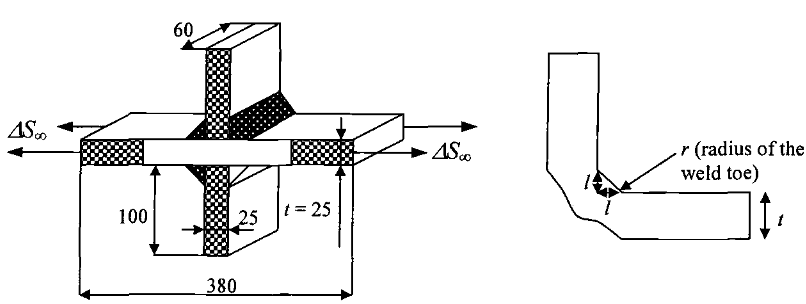

FIG. 4—*Considered welded joint specimen (Lassen [23]).*

In order to evaluate N_i, we used the "Joint of the G4 type" that is referred by Yung and Lawrence [25]. It consists of a cruciform welded joint with full penetration subjected to an axial loading. The law controlling the evolution of the elastic stress concentration factor K_t is described by the following equation:

$$K_t = \beta.\left[1+\alpha.\left(\frac{t}{r}\right)^{\lambda}\right] \tag{19}$$

where α, β, and λ are obtained as follows [25]:

$$\begin{aligned} \alpha &= 0.2\left(2-\frac{l}{t}\right)^{0,5} \\ \beta &= 1 \\ \lambda &= 0.5 \end{aligned} \tag{20}$$

r, l, and t, used in calculations (Eqs 19 and 20) are defined in Table 2.

TABLE 2 *Geometrical parameters of welded joint.*

Toe Length l	Plate Thickness of the Welded Joint t	Notch-Root Radius of the Welded Joint r
8 mm	25 mm	1.75 mm

The determination of K_t enables us to define the fatigue notch factor K_f, knowing the fatigue notch sensitivity factor q defined in [25].

From the tests, we can define the deterministic and random parameters used in our reliability model as follows.

The deterministic parameters are:

- the geometrical parameters (l, t) (excepted the radius of the weld toe),
- the nominal stress variation (ΔS_∞), and
- the mechanical properties of the material (Young's Modulus, yield strength, tensile strength, the Ramberg-Osgood material, etc.).

The random parameters are:

- Parameter m (exponent of the Paris law): we used a gaussian rule with an average of 3 and a standard deviation of 0.03. From considered tests, Grous et al. [24] found a relationship between the parameters C and m of the Paris law

$$C = \frac{6.069.10^{-8}}{24.64^{m}} \text{ ; } units : daN, mm \tag{21}$$

This relationship means that C is also considered a random variable.

- Parameter a_0: Grous et al. take a statistical representation of the initial crack length a_0 as a weibull law with two parameters with an average of $7.267.10^{-3}$ mm and a standard deviation of $3.112.10^{-3}$.
- Parameter r: a statistical representation of the radius [23] of the weld toe r as a Log-Normal with an average of 1.75 mm and a standard deviation of 0.75.
- Parameter γ_{a_D} : in order to take the plastic zone as a random variable, we use a statistical representation of the bias γ_{a_D} as a gaussian rule with an average of 1 and a standard deviation of 0.2.

In the case of a high strength level applied to the cruciform joint, Fig. 5 shows the distribution of the probability of failure P_f and particularly the influence of the overload, which is significant in this case.

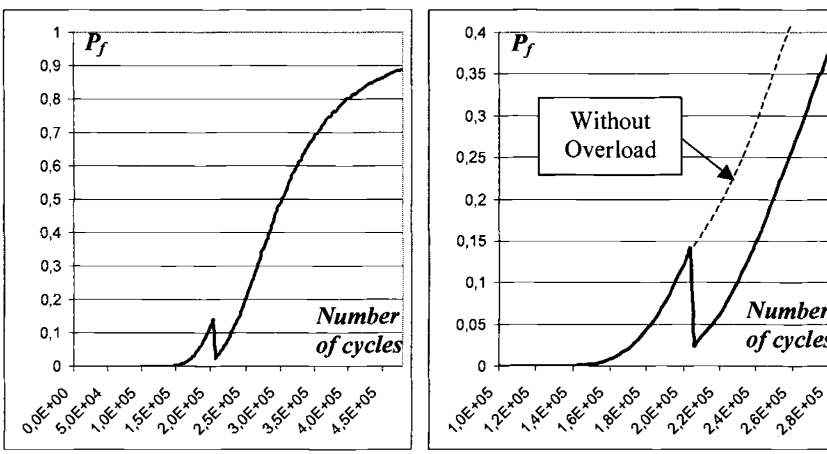

FIG. 5—*Results of the reliability analysis of the fatigue crack growth after an overload.*

This reliability analysis is performed with the FORM method. The following deterministic variables are considered:

- stress ratio: $R = 0$,
- overload ratio: $R_{pic} = 3$,
- crack length where the overload occurs: $a_{pic} = 1.2$ mm,
- critical crack length: $a_c = 0.8 \times t = 20$ mm, and
- nominal stress: $\Delta S_\infty = 150$ MPa.

We note that taking into account the retardation effect in reliability analysis reduced the probability of failure.

In addition, we can compute sensitivity measures of the probability of failure and the reliability index by the omission sensitivity factor γ_i.

The omission sensitivity factor γ_i for a basic variable Z_i is defined as the inverse ratio between the value of the first order reliability index β and the first order reliability index β $(Z_i = m_i)$ with Z_i replaced by a deterministic value, generally its median m_i. This factor is given by [2]

$$\gamma_i(m_i) = \frac{\beta(Z_i = m_i)}{\beta} \approx \frac{1}{\sqrt{1-\alpha_i^2}} \tag{22}$$

where the α_i values are the direction cosines at the design point.

The omission sensitivity factor indicates the parameters that have to be modified in order to reduce uncertainty and increase reliability.

The evolution of the omission sensitivity factor versus the number of cycles for the four random variables a_0, m, r and γ_{a_D} is shown in Fig. 6.

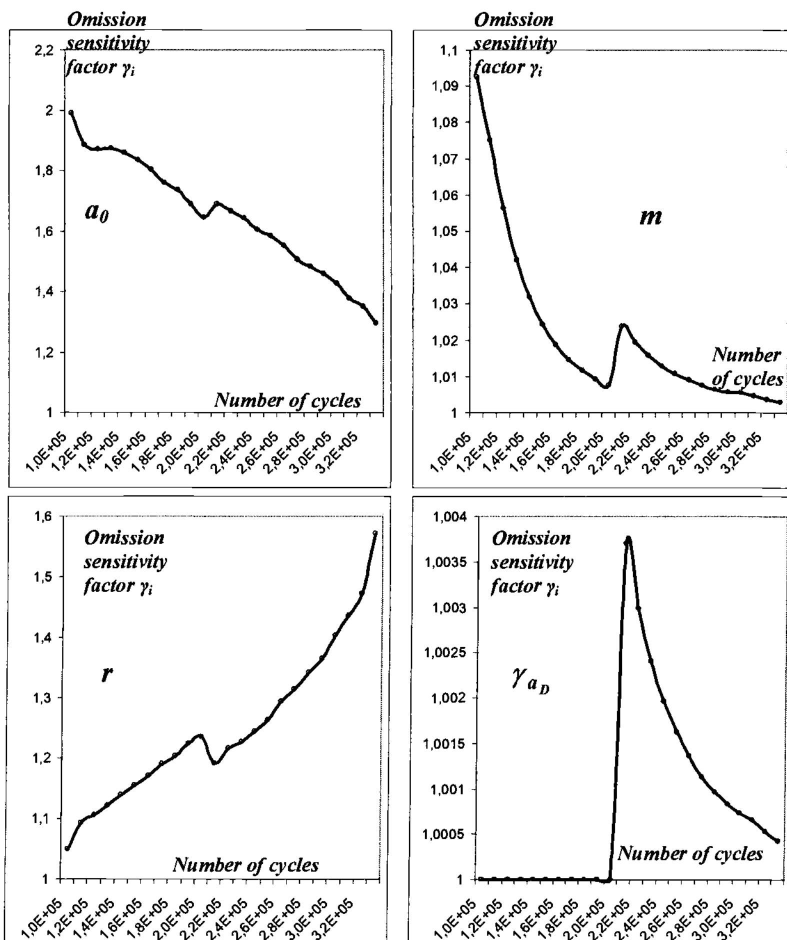

FIG. 6— *Evolution of the omission sensitivity factor for the random variables a_0, m, r, and γ_{a_D}*

We can note that the initial crack length is an important parameter in the probability analyses of failure. The application of the overload increases the importance of the random variable m and, of course, implies the use of the random variable γ_{a_D}. Thus, this reliability analysis shows the importance of:

- the first period, N_1 (thought the parameter a_0),
- the fatigue life initiation, N_I (thought the parameter r),
- and, finally, the influence of the overload period (N_2, N_3).

Conclusion

This paper develops an approach to considering the overload effect in the reliability analysis. This depends on four random variables (initial crack length, material parameter of the crack propagation law, the radius of the weld toe, and the size of the plastic zone). Four parts of the crack propagation mechanism are studied. The first one concerns the crack initiation, the second deals with crack propagation period from the initial crack until the application of the overload, the third takes into account the retardation effect, and the last one corresponds to the restoration of the initial crack growth rate.

The results of the reliability analysis show that a gain of probability of failure is obtained when overload occurs. A sensitivity analysis allows us to study the influence of each random variable on the random fatigue life.

Further work will deal with the case of several overloads.

References

[1] Paris, P. and Erdogan, F., "A Critical Analysis of Crack Propagation Laws," *Journal of Basic Engineering*, Trans. ASME, Vol. 85, 1963, pp. 528 534.

[2] Masden, H. O., Krenk, S., and Lind, N. C., "Methods of Structural Safety," W. J. Hall, Ed., Prentice-Hall, Inc., Enlewood Cliffs, NJ, 1986.

[3] Morrow, J. D., "Cyclic Plastic Strain Energy and Fatigue of Metals," *Internal Friction, Damping and Cyclic Plasticity, ASTM STP 378*, ASTM International, West Conshohocken, PA, 1965, pp. 45 87.

[4] Neuber, H, "Theory of Stress Concentration for Shear Strained Prismatic Bodies with Arbitrary Non-Linear Stress-Strain Law," *Journal of Applied Mechanics*, Vol. 26, No. 4, 1961, pp. 544 550.

[5] Decoopman, X., "Influence des conditions de chargement sur le retard à la propagation d'une fissure de fatigue après l'application d'une surcharge," Ph.D. Thesis, University of Sciences and Technologies of Lille (France), (In French), 1999.

[6] Lang, M., "A Model for Fatigue Crack Growth, Part I: Phenomenology," *Fatigue and Fracture of Engineering Materials and Structures*, Vol. 23, 2000, pp. 587 601.

[7] Irwin, G. R., "Plastic Zone near a Crack and Fatigue Toughness," Mechanical and Metallurgical Behavior of Sheet Material, Proceedings of the 7th Sagamore Ordinance, Materials Research Conference, Section IV, Syracuse Univ. Res. Inst., 1960, pp. 63 71.

[8] Elber, W., "The Significance of Fatigue Crack Closure," *Damage Tolerance in Aircraft Structures, ASTM STP 486*, ASTM International, West Conshohocken, PA, 1971, pp. 230 242.

[9] Schijve, J., "Fatigue Crack Propagation in Alloy Sheet Material and Structure," Advances in Aeronautical Sciences, Vol. 3, 1962, Pergamon Press, Oxford, UK, pp. 387 408.

[10] Marci, G., "Effect of the Active Plastic Zone on Fatigue Crack Growth Rates," *Fracture Mechanics, ASTM STP 667*, C. W. Smith, Ed., ASTM International, West Conshohocken, PA, 1979, pp. 168 186.
[11] Bowles, C. Q., "The Role of Environment, Frequency and Shape During Fatigue Crack Growth in Aluminum Alloys," Doctoral Dissertation, Delft University, 1978.
[12] Paris, P. C., "Paper Presented at the International Congress of Applied Mechanics," Delft University, 1976.
[13] Darcis, P., "Analyse de la fatigue des joints soudés soumis à l'effet d'une surcharge," Ph.D. Thesis, University Blaise Pascal – Clermont II (France), (In French), 2002.
[14] Lang, M. and Marci, G., "The Influence of Single and Multiple Overloads on Fatigue Crack Propagation," *Fatigue and Fracture of Engineering Materials and Structures*, Vol. 22, 1999, pp. 257 271.
[15] Lu, Y. and Li, K., "A New Model for Fatigue Crack Growth after a Single Overload," *Engineering Fracture Mechanics*, Vol. 46, No. 5, 1993, pp. 849 856.
[16] Cotterill, P. J. and Knott, J. F., "Overload Retardation of Fatigue Crack Growth in a 9% Cr 1% Mo Steel at Elevated Temperatures," *Fatigue and Fracture of Engineering Materials and Structures*, Vol. 19, Nos. 2 and 3, 1996, pp. 207 216.
[17] Pommier, S., "Plane Strain Crack Closure and Cyclic Hardening," *Engineering Fracture Mechanics*, Vol. 69, 2002, pp. 25 44.
[18] Kumar, R., Kumar, A., and Kumar, S., "Delay Effects in Fatigue Crack Propagation," *International Journal of Pressure Vessels and Piping*, Vol. 67, 1996, pp. 1 5.
[19] Ranganathan, N., Lafarie-Frenot, M. C., and Petit, J., "Effect of Overloads on the Evolution of Plastic Zones and Its Significance," 8th Congress on Material Testing, Scientific Society of Mechanical Engineers, Omikk-Technoinform, Budapest, 1982, pp. 309 313.
[20] Wheeler, O. E., *Journal of Basic Engineering*, Trans ASME, Vol. 4, 1972, pp. 181 186.
[21] Willenborg, J. D., Engle, R. M., and Wood, H. A., "A Crack Growth Retardation Model Using an Effective Stress Concept," AFFDL-TM-FBR-71-1, USAF Flight Dynamics Lab, 1971.
[22] Filippi, M., Darcis, P., and Recho, N., "Modeling of Crack Growth Retardation Due to Plastic Zone Following an Overload," Symposium on Fatigue Testing and Analysis under Variable Amplitude Loading, Tours, France 29 31 May 2002.
[23] Lassen, T., "The Effect of the Welding Process on the Fatigue Crack Growth," Agder College of Engineering, Grimstad, Norway, Weld, Research Supplement 76-s, 1990.
[24] Grous, A., Recho, N., Lassen, T., and Lieurade, H.P., "Caractéristiques mécaniques de fissuration et de défaut initial dans les soudures d'angles, en fonction du procédé de soudage," Journées d'études sur la fatigue des composants et des structures soudés, CETIM, SIS, GAMI et l'IS, 1992, Senlis, France (In French).
[25] Yang, J. Y. and Lawrence, F. V., "Analytical and Graphical Aids for the Fatigue Design of Weldments," *Fatigue and Fracture of Engineering Materials and Structures*, Vol. 8, 1985, pp. 223 241.

Journal of ASTM International, Nov./Dec. 2004, Vol. 1, No. 10
Paper ID JAI19066
Available online at www.astm.org

Véronique Aubin,[1] *Philippe Quaegebeur,*[1] *and Suzanne Degallaix*[1]

Load History in Fatigue: Effect of Strain Amplitude and Loading Path

ABSTRACT: The low-cycle fatigue behavior of a duplex stainless steel, 60 % α – 40 % γ, is studied under tension-compression/torsion loading at room temperature and under strain control. It is shown that the duplex stainless steel has an isotropic behavior under cyclic proportional loading. The loading path induces an extra-hardening on cyclic hardening of duplex stainless steel but lower than that on austenitic stainless steels. The effect of loading history is studied in terms of strain amplitude, mean strain, and loading path. It is shown that only histories in strain amplitude and loading path have an effect on the stabilized stress.

KEYWORDS: duplex stainless steel, cyclic plasticity, biaxial loading, extra-hardening, experimental study, low-cycle fatigue

Introduction

The use of austenitic-ferritic stainless steels (duplex steels) in branches of industry with severe conditions in terms of corrosion and mechanical resistance has been developed widely over about 30 years. Duplex stainless steels are notably used for applications in power, offshore, petrochemical, and paper industries. The combination of their austenitic and ferritic phases gives them an excellent resistance to corrosion, particularly to intergranular and chloride corrosion and very high mechanical properties, in terms of Yield Stress and Ultimate Tension Strength, as well as in terms of ductility. These high properties result from their "composite" nature and from their very small grain size (10 µm). A nitrogen addition, essentially concentrated in the austenitic phase, is a common practice nowadays. It enables the improvement of corrosion resistance and an increase of Yield Stress [1 3].

The properties of duplex stainless steels are closely linked to the two-phase nature of these materials, in terms of crystallographic structure (FCC and BCC), volume fraction, morphology of each phase, and interactions between phases. These various parameters influence the cyclic mechanical behavior of that composite material and modify its stress response to variable loading, with variations of amplitude and direction in time and in space. Especially, the austenitic phase (FCC) of duplex stainless steels has a low stacking fault energy that favors planar slip. This phase is consequently very sensitive to non-proportional cyclic loadings: the obtained extra-hardening can be observed clearly in austenitic stainless steels such as AISI 304L or 316L [4 12]. Moreover, this phase is sensitive to loading history in terms of loading amplitude and loading path [13,14]. On the other hand, the individual ferritic phase (BCC) shows a low sensitivity to non-proportional loadings and to loading history [15,16].

Manuscript received 30 April 2002; accepted for publication 4 March 2003; published November 2004. Presented at ASTM Symposium on Fatigue Testing and Analysis Under Variable Amplitude Loading Conditions on 29 31 May 2002 in Tours, France; P. C. McKeighan and N. Ranganathan, Guest Editors.

[1] Assistant Professors, and Professor, respectively, Ecole Centrale de Lille, Laboratoire de Mécanique de Lille UMR CNRS 8107, BP 48, 59651 Villeneuve d'Ascq Cedex, France.

Some work has already been performed on the stress response of duplex stainless steels under cyclic loading in push-pull test conditions at room temperature [1 3,16 18] and at high temperature [19,20]. However, few studies analyze the influence of variable cyclic loadings on stress response in low-cycle fatigue of these materials, and, to our knowledge, no work has been carried out on their mechanical behavior under non-proportional cyclic loading.

The present work aims at analyzing the dependence of the cyclic mechanical behavior on non-proportional loadings and identifying the influence of loading history in terms of variations in time and in space.

Material

The material studied is an EN X2CrNiMoN25-07 duplex stainless steel. The material contains approximately 60 % ferrite and 40 % austenite. The composition is given in Table 1. It was supplied in rolled bars 70 mm in diameter, solution treated for one hour at 1060°C, and then water-quenched before machining the specimens. The resulting microstructure consists of long austenitic rods (Ø 10 μm × 1 mm) in a ferritic matrix (Fig. 1). The microstructure is transverse isotropic.

TABLE 1 *Composition of the duplex stainless steel studied (in wt %).*

C	Cr	Ni	Mo	Mn	Si	N	Cu	P	S	Fe
0.024	24.68	6.54	2.84	0.79	0.62	0.17	0.07	0.021	<0.003	Bal.

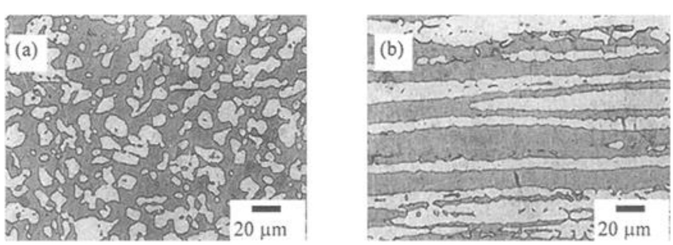

FIG. 1 *Microstructure in planes perpendicular (a) and parallel (b) to the bar axis. The austenite is in white, the ferrite in grey.*

Experimental Procedure

In order to characterize the behavior of the steel studied under complex cyclic loading, tension-compression tests and tension-compression/torsion tests were carried out on servohydraulic machines under strain control. Specimens and grips were designed to avoid any play between the grips and the specimen when the load reverses [21]. A drawing of the specimens is given in Fig. 2. Earlier investigations with both geometries have shown the specimens to be well suited for axial and torsional deformation studies [21].

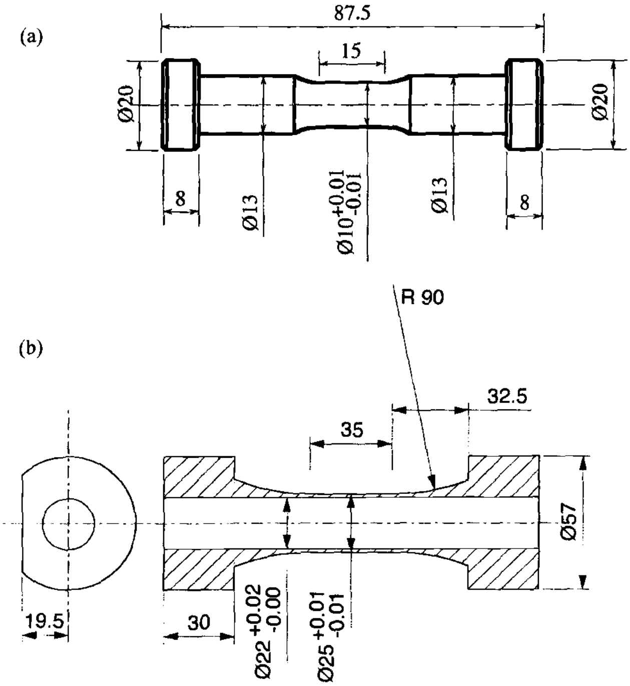

FIG. 2 *Specimen geometries: (a) for tension-compression tests, (b) for biaxial tests; all dimensions are in mm.*

A biaxial extensometer clipped on the biaxial specimens measured axial strain ε and shear strain γ. Axial stress σ and shear stress τ were calculated from load and torque measured by a load cell, using the assumption of thin-walled tubes. Shear stress and shear strain are assumed uniform in the thickness of tubular specimens. Equivalent stress σ_{eq} and equivalent plastic strain ε_{eq}^{p} were defined by von Mises equivalence for tension/torsion loading as:

$$\sigma_{eq} = \sqrt{\sigma^2 + 3\,\tau^2} \tag{1}$$

$$\varepsilon_{eq}^{p} = \sqrt{\varepsilon^{p^2} + \frac{\gamma^{p^2}}{3}} \tag{2}$$

Exponent p designates the plastic part of the total strain ε or of the total shear strain γ. Equivalent strain ε_{eq} was defined by analogy as:

$$\varepsilon_{eq} = \sqrt{\varepsilon^2 + \frac{\gamma^2}{3}} \tag{3}$$

All of the tests were performed under total strain control and at room temperature. A preliminary tension test with progressive stepped strain rates in [6.6 10^{-6} s^{-1}; 6.6 10^{-3} s^{-1}] showed that strain rate sensitivity at room temperature is significant [21]. On this ground, all further tests were carried out with a constant equivalent strain rate equal to 6.6 10^{-4} s^{-1}. A specific program was developed in order to control the biaxial machine with a constant equivalent strain rate. About 500 points were recorded per cycle during the tests.

A given loading is completely defined by its path, its amplitude, and its mean strain in the plane $\left(\varepsilon,\ \gamma/\sqrt{3}\right)$. The loading path amplitude is defined as the radius of the smallest circle circumscribed around the path, and the mean strain is the position vector of the center of this circle. The influence of the history of each of these three parameters on the cyclic stress response was studied separately. The seven selected loading path shapes are shown in Fig. 3. A proportional loading path is a path whose control parameters remain proportional to each other during the test.

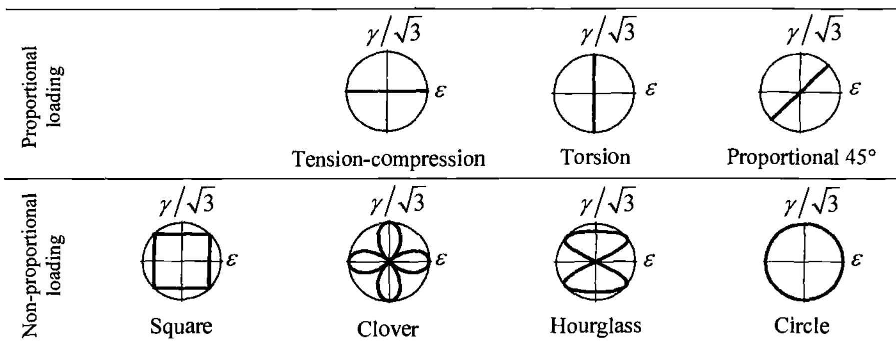

FIG. 3 *Loading paths in* $\left(\varepsilon,\ \gamma/\sqrt{3}\right)$ *plane.*

This work aims at studying the influence of the loading type on the cyclic stress response; therefore the cyclic tests were carried out up to stress stabilization, not until fracture. To study the influence of loading history, cyclic multi-step tests were carried out. The number of cycles at each step was chosen to guarantee the best stabilization with minimal damage. That explains why the material may not be exactly in its steady state at the end of each step.

Experimental Results and Discussion

Cyclic Hardening-Softening Behavior under Proportional Loading

Proportional cyclic tests were conducted in three directions in the plane $\left(\sigma,\ \sqrt{3}\ \tau\right)$: at 0°, 45°, and 90° (see Fig. 3). The cyclic stress-strain responses are shown in Fig. 4 with the monotonic stress-strain curve. It is observed that the duplex stainless steel softens cyclically until stabilization, whatever the loading path. Moreover, stabilized stress levels are similar for the three directions tested; the duplex stainless steel shows an isotropic behavior under cyclic loading. This then validates the use of von Mises equivalents in the following non-proportional tests.

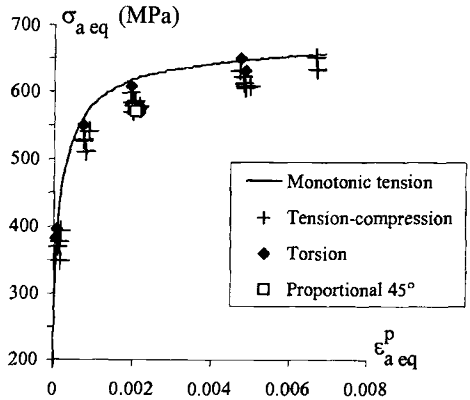

FIG. 4 *Cyclic stress-strain responses at the stabilized cycles for proportional loading paths.*

Cyclic Hardening-Softening Behavior under Non-Proportional Loading

A series of tests using four non-proportional loading paths was performed (see Fig. 3). At each cycle, the radius and the center position of the smallest circles circumscribed around the responses in the plane $\left(\sigma,\ \sqrt{3}\ \tau\right)$ and in the plane $\left(\varepsilon^p,\ \gamma^p/\sqrt{3}\right)$ were calculated. These radii are called *equivalent stress amplitude* and *equivalent plastic strain amplitude*, respectively.

Cyclic hardening-softening curves can be seen in Fig. 5 at a strain amplitude of 0.5 % for the seven loading paths tested, proportional and non-proportional. Whatever the loading path, the cycling leads to quasi-stabilization after a phase of hardening followed by a low softening. Figure 6 shows the cyclic stress-strain responses in terms of equivalent stress amplitude versus equivalent plastic strain amplitude at the stabilized or quasi-stabilized cycles. At a same strain amplitude, for non-proportional loading paths, the duplex stainless steel hardens much more than for proportional paths (Figs. 5 and 6). This cyclic hardening, called *extra-hardening*, depends on the strain amplitude and on the loading path. For a circle path, at the strain amplitude of 0.2 %, there is no extra-hardening, because the plastic strain is about zero. On the contrary, at the strain amplitude of 0.5 %, the stabilized stress is 20 % higher (or 120 MPa higher) than the one for the proportional path. In comparison, on an austenitic stainless steel type AISI 316L at the same strain amplitude, the circle path induces an extra-hardening of 70 % (or 225 MPa) [10 14]. The hardening effect due to loading path, in absolute and in relative values, is lower for duplex stainless steel than for austenitic stainless steel. For the duplex stainless steel, three groups can be defined among the tested loading paths according to the increasing degree of hardening: (i) tension-compression, torsion and proportional 45° paths; (ii) clover path; (iii) circle, square, and hourglass paths.

Influence of Loading History on Cyclic Behavior

In order to underline the sensitivity of the duplex stainless steel to loading history, we compared two tests: one consisting of steps with the successive loading paths: square, clover, hourglass, and torsion, and one torsion test (Fig. 7). On the last step of the first test, the torsion path brings about a cyclic softening that leads to a quasi-stabilization at a higher level than it would be on the virgin material. The difference reaches 55 MPa. The cyclic behavior has thus been modified by the steps carried out previously.

The influence of the history effect was then studied in a methodical way on each of the three loading parameters. In order to avoid scattering among specimens, influences of various loading histories were investigated under a common form. One specimen was loaded by five successive steps A, B, C, D, and E, where steps A, C, and E had exactly the same loading mode and level, while steps B and D differed from other steps in only one parameter: mean strain, strain amplitude, or loading path. Owing to the stress level scattering between specimens loaded in the same conditions, a history effect was judged valid only in the case where the difference in equivalent stress amplitude between two steps was higher than 10 MPa.

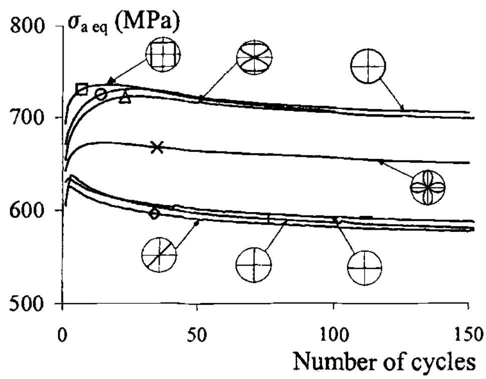

FIG. 5 *Cyclic hardening-softening curves with a strain amplitude of 0.5 %, for seven different loading paths.*

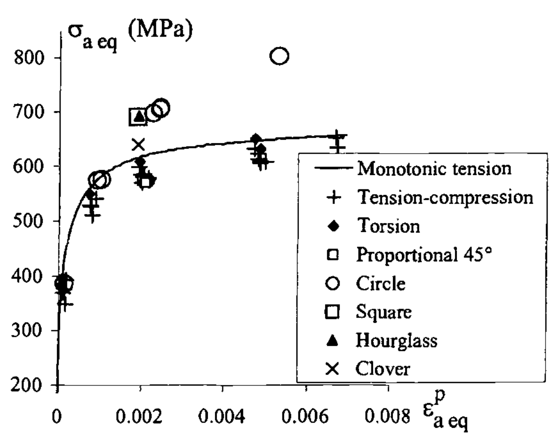

FIG. 6 *Cyclic stress-strain responses at the stabilized or quasi-stabilized cycles for seven different loading paths.*

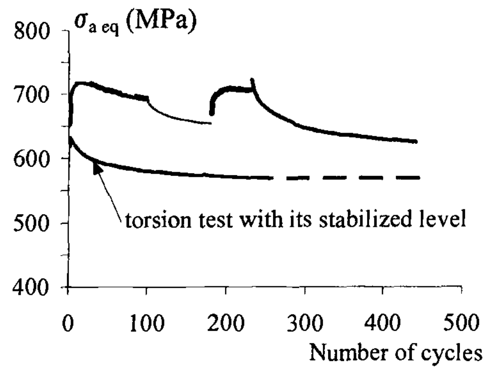

FIG. 7 *Cyclic hardening-softening curves with a strain amplitude of 0.5 % and successive loading paths: square, clover, hourglass, and torsion.*

Influence of Strain Amplitude History—The influence of strain amplitude history was studied using tests with two loading paths: one test with tension-compression path and another with circle path. For both tests, the mean strain was zero, and the strain amplitudes applied were successively 0.35, 0.5, 0.35, 0.8, and 0.35 %. The cyclic hardening-softening curves obtained can be seen in Fig. 8. First, there is no history effect when the strain amplitude increases. The stress level obtained at a strain amplitude of 0.5 or 0.8 % is the same as the one obtained on a virgin specimen at the same strain amplitude. Then, in case the strain amplitude decreases, only step E with a circular path shows a stress amplitude 40 MPa higher than steps A and C do on the last stored cycle (Fig. 8). Thus, a history effect exists only if the difference in stress amplitude between two consecutive steps is higher than 130 MPa. It can be seen that the history effect is connected not only with the difference in strain amplitude between two successive steps, but also with the difference in hardening between two successive steps. This history effect is weak; it does not exceed 25 MPa. It is lower in duplex stainless steels than in austenitic stainless steels [13,14].

Influence of Mean Strain History—The mean strain history was studied by varying the mean strain value and its direction in the plane $\left(\varepsilon,\ \gamma/\sqrt{3}\right)$, and a possible correlation with the strain amplitude was sought. The first test consisted in a series of steps in tension-compression with strain amplitudes of 0.2 %, 0.35 %, and 0.5 % and a mean strain of 0.0 % or 0.1 % in the axial direction (Fig. 9). The second test was carried out with a circle path at a strain amplitude of 0.5 % and with various mean strains at the four corners of a 0.15-length square (Fig. 10). For both tests, at each step, the mean stress is relaxed after a few cycles, except during the step with a strain amplitude of 0.2 % in the first test. At this amplitude, the cycle is actually quasi elastic. No effect on stress amplitude is observed. It can thus be concluded that the mean strain history does not induce a significant history effect.

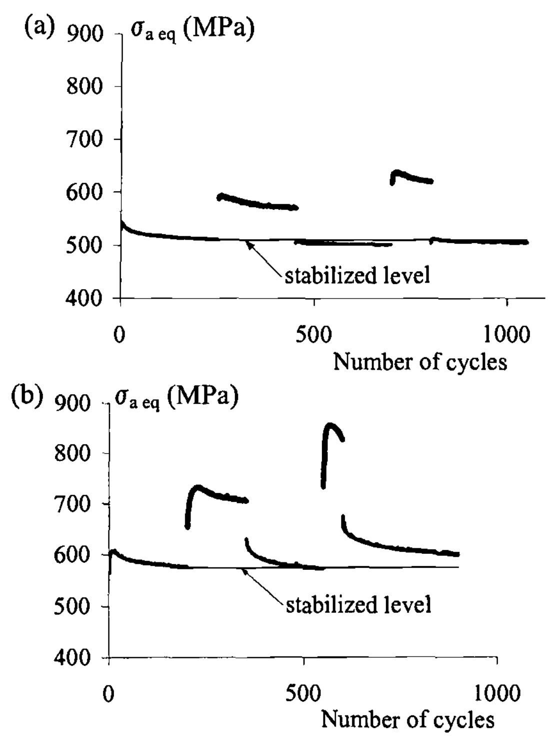

FIG. 8 *Cyclic hardening-softening curves with a tension path (a) and a circle path (b) and successive strain amplitudes of 0.35 %, 0.5 %, 0.35 %, 0.8 %, and 0.35 %.*

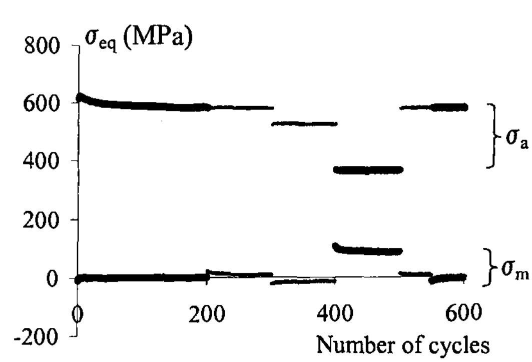

FIG. 9 *Cyclic hardening-softening curves with a tension path, and various strain amplitudes and mean strains of {0.5; (0, 0)}, {0.5; (0.1, 0)}, {0.35; (0, 0)}, {0.2; (0.1, 0)}, {0.5; (0.1, 0)}, and {0.5; (0, 0)}.*

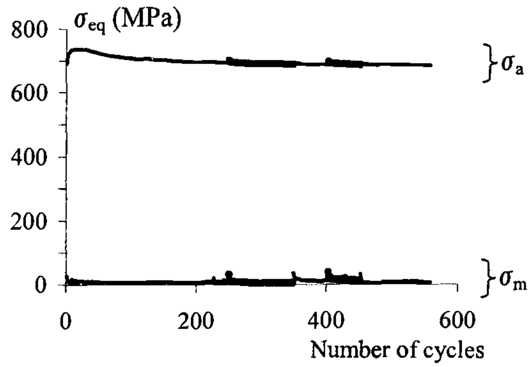

FIG. 10 *Cyclic hardening-softening curves with a circle path, a strain amplitude of 0.5 %, and successive mean strains of (0; 0), (0.15; 0), (0.15; 0.15), (0; 0.15), and (0; 0).*

Influence of Loading Path History—Loading path effect was studied at the strain amplitude of 0.5 % and zero mean strain for proportional, clover, and circle loading paths, which induce various hardening levels. Three tests were carried out. During the first test, the following paths were applied: torsion, clover, torsion, circle, and torsion; during the second test, the sequence clover, circle, and clover was studied; and during the third test, the sequence proportional 45°, circle, proportional 45° was used. Figure 11 shows the cyclic hardening-softening curves obtained. The stress amplitude obtained with a clover or a circle path after a less hardening path is the same as the stress amplitude measured on a virgin specimen. It appears that the stress level at a given step is not significantly affected by the previous less hardening paths. On the contrary, when loading paths are applied in decreasing order of hardening, a history effect can occur, but only if a proportional path follows a circle path. As for strain amplitude history, the loading path history effect is connected with the difference in hardening between steps. A history effect exists if the difference in equivalent stress amplitude between two successive steps is higher than 120 MPa, but it does not exceed 25 MPa. This history effect is weak, compared to the effect of loading path history in austenitic stainless steels, which is up to 100 MPa in the same loading conditions [7].

Carrying out steps with different loading paths which induce the same hardening level may cause a history effect on the stress response. In the case of proportional loading paths, this effect is called *cross hardening*. It was studied using two tests with a strain amplitude of 0.5 % and zero mean strain. The loading paths applied during the first test were tension, torsion, and tension (Fig. 12) and, during the second test, hourglass and square (not shown here). For both tests, at each loading path change, a hardening can be seen, but this hardening is then erased by further cycling. A cross hardening takes place, but it does not lead to a long-range history effect.

The test presented in Fig. 7 shows a history effect of 55 MPa on a torsion path. This level is higher than stress levels obtained in the methodical study of the history effect. During this test, more cycles and more non-proportional loading paths than in other tests were applied before the proportional loading path. It is well-known that for non-proportional loading paths multislip dislocation substructures are observed, i.e., cells and labyrinths [4,5,22]. The high number of cycles may have enhanced the stability of dislocation substructures under proportional loading.

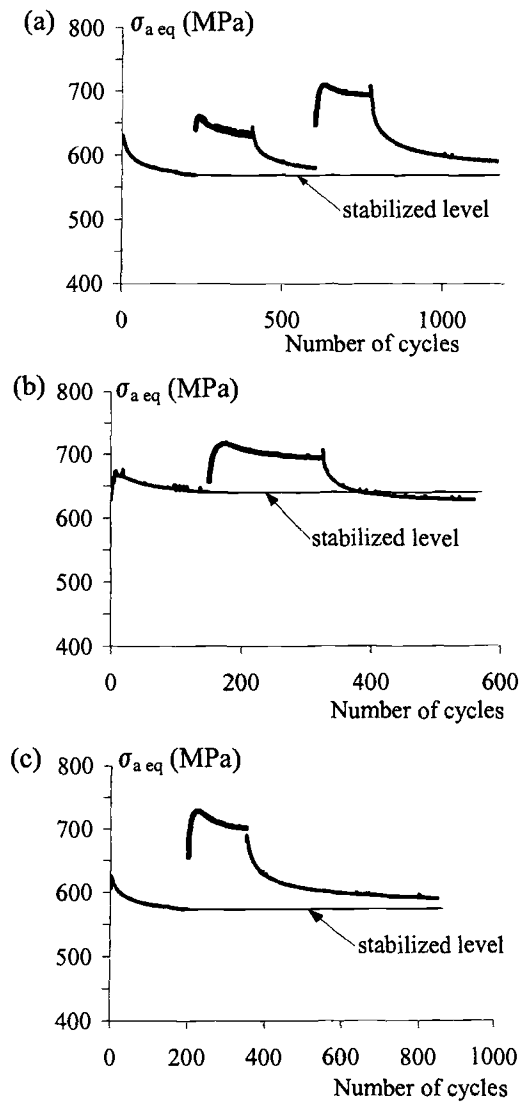

FIG. 11 *Cyclic hardening-softening curves with a strain amplitude of 0.5 % and successive loading paths: (a) torsion, clover, torsion, circle, torsion; (b) clover, circle, clover; (c) proportional 45°, circle, proportional 45°.*

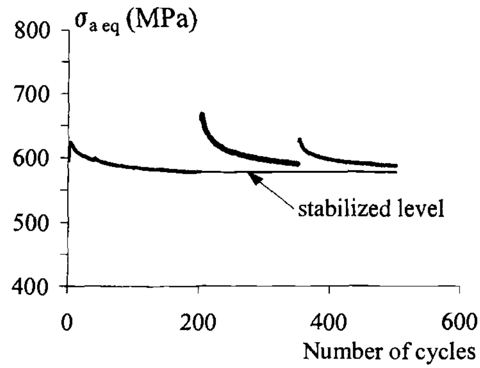

FIG. 12 *Cyclic hardening-softening curves with a strain amplitude of 0.5 % and successive loading paths of tension, torsion, tension.*

History of Plastic Strain Amplitude—The history effect has been studied above as a function of equivalent stress amplitude. Various authors nevertheless model history effect with the use of plastic strain amplitude [23,24]. The evolution of the equivalent plastic strain amplitude for the tests presented in the previous paragraph (Fig. 11) is shown in Fig. 13. At a strain amplitude of 0.5 %, a history effect occurs only if a proportional path follows a circle path. The history effect cannot be linked to the maximal plastic strain amplitude, as the highest plastic strain amplitude is the same for the three tests in Fig. 13, and only two of them show a history effect (Fig. 11). At a strain amplitude of 0.5 %, the equivalent plastic strain amplitude is lower during the cycling with a clover path than during the cycling with proportional paths (Fig. 13). The difference in plastic strain amplitude is then higher during the transition from a circle path to a clover path than during the transition from a circle path to a proportional path. But no history effect exists during the transition from a circle path to a clover path. It can thus be concluded that the history effect is not linked to equivalent plastic strain amplitude.

Conclusion

Cyclic strain controlled tests on a duplex stainless steel were carried out, which allowed a better knowledge of the behavior of this steel under complex biaxial loadings. The influence of loading history was studied in terms of strain amplitude, mean strain, and loading path.

The present work leads to the following conclusions:

- The duplex stainless steel studied has an isotropic cyclic behavior.
- In the range of strain amplitudes studied and whatever the loading path, after a rapid hardening, the steel softens cyclically until stabilization.
- Like austenitic stainless steels, the duplex stainless steel is sensitive to loading path, although the extra-hardening observed is lower for the duplex stainless steel. Three groups of loading paths are distinguished with increasing stress responses at the stabilized cycle: (i) tension-compression, torsion, and proportional 45° paths, (ii) clover path, (iii) square, circle, and hourglass paths.

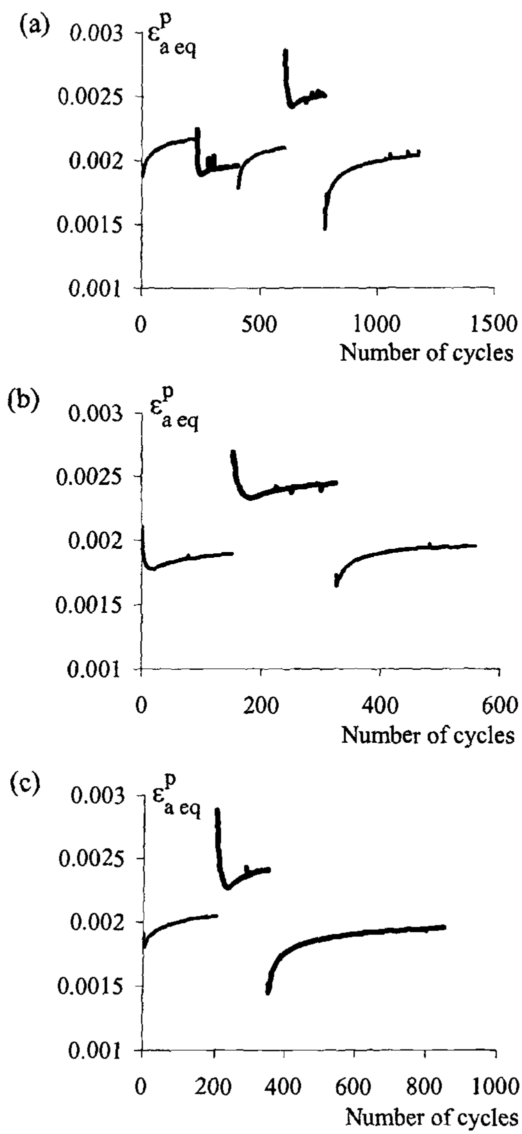

FIG. 13 *Variations of the equivalent plastic strain amplitude with a strain amplitude of 0.5 % and successive loading paths of* (a) *torsion, clover, torsion, circle, torsion;* (b) *clover, circle, clover;* (c) *proportional 45°, circle, proportional 45°.*

- On the contrary, the duplex stainless steel studied is not very sensitive to loading history in terms of strain amplitude, mean strain, and loading path. Sensitivity to history appears only between successive steps that differ greatly from each other in hardening intensity and if the stress amplitude decreases sufficiently when the strain amplitude decreases or when the loading path induces lesser hardening. On duplex stainless steel, no memory of the plastic strain amplitude is observed.

Acknowledgments

The authors are grateful to FEDER and the Nord-Pas-de-Calais Region for their financial support in the purchase of the biaxial equipment.

References

[1] Magnin, T., Lardon, J.-M., and Coudreuse, L., "A New Approach to Low Cycle Fatigue Behavior of a Duplex Stainless Steel Based on the Deformation Mechanisms of the Individual Phases," *Low-Cycle Fatigue, ASTM STP 942*, H. D. Solomon, G. R. Halford, L. R. Kaisand, and B. N. Leis, Eds., ASTM International, West Conshohocken, PA, 1988, pp. 812 823.

[2] Vogt, J.-B., Messai, A., and Foct, J., "Factors Influencing the Low Cycle Fatigue Behaviour of a Duplex Stainless Steel: Effect of Strain Amplitude and Nitrogen Content," *Proceedings of the International Conference on Duplex Stainless Steels*, T. G. Good, Ed., Abington (Cambridge), Woodhead Publishing, 1994, Paper 33.

[3] Degallaix, S., Chtara, H., and Gagnepain, J.-C., "Fatigue Damage in Austenitic-Ferritic Duplex Stainless Steels," *Proceedings of the International Conference on Duplex Stainless Steels*, T. G. Good, Ed., Abington (Cambridge), Woodhead Publishing, 1994, Paper 111.

[4] Doong, S.-H. and Socie, D. F., "Dislocation Substructures and Nonproportional Hardening," *Journal of Engineering Materials and Technology*, Vol. 112, 1990, pp. 23 30.

[5] Clavel, M. and Feaugas, X., "Micromechanisms of Plasticity under Multiaxial Cyclic Loading," *Multiaxial Fatigue and Design, ESIS 21*, A. Pineau, G. Cailletaud, T. C. Lindley, Eds., Mechanical Engineering Publications, London, 1996, pp. 21 41.

[6] Cailletaud, G., Kaczmarek, H., and Policella, H., "Some Elements on Multiaxial Behaviour of 316L Stainless Steel at Room Temperature," *Mechanics of Materials*, Vol. 3, 1984, pp. 333 347.

[7] Tanaka, E., Murakami, S., and Ooka, M., "Effects of Strain Path Shapes on Non-Proportional Cyclic Plasticity," *Journal of Mechanics and Physics of Solids*, Vol. 33, 1985, pp. 559 575.

[8] Delobelle, P., "Synthesis of the Elastoviscoplastic Behavior and Modelization of an Austenitic Stainless Steel over a Large Temperature Range, under Uniaxial and Biaxial Loadings, Part I: Behavior," *International Journal of Plasticity*, Vol. 9, 1993, pp. 65 85.

[9] Itoh, T., Sakane, M., Ohnami, M., and Socie, D. F., "Nonproportional Low Cycle Fatigue Criterion for Type 304 Stainless Steel," *Journal of Engineering Materials and Technology*, Vol. 122, 1995, pp. 1 9.

[10] Calloch, S., "Essais Triaxiaux Non-Proportionnels et Ingénierie des Modèles de Plasticité Cyclique," Thesis, Ecole Normale Supérieure de Cachan, France, 1997.

[11] Bocher, L., Jeune, D., Robinet, P., and Delobelle, P., "On the Utility of Complex Multiaxial Cyclic Loadings in Tension-Torsion-Internal and External Pressures, to

Improve the Formulation of the Constitutive Equations," *Low-Cycle Fatigue and Elasto-Plastic Behaviour of Materials*, K-T Rie and P.D. Portella, Eds., Elsevier, 1998, pp. 223 228.
[12] Calloch, S. and Marquis, D., "Triaxial Tension-Compression Tests for Multiaxial Cyclic Plasticity," *International Journal of Plasticity*, Vol. 15, 1999, pp. 521 547.
[13] Tanaka, E., Murakami, S., and Ooka, M., "Effects of Plastic Strain Amplitudes on Non-Proportional Cyclic Plasticity," *Acta Mechanica*, Vol. 57, 1985, pp. 167 182.
[14] Murakami, S., Kawai, M., and Ohmi, Y. J., "Effects of Amplitude-History and Temperature-History on Multiaxial Cyclic Behavior of Type 316 Stainless Steel," *Journal of Engineering Materials and Technology*, Vol. 111, 1989, pp. 278 285.
[15] Doquet, V. and Pineau, A., "Multiaxial Low-Cycle Fatigue Behaviour of a Mild Steel," *Fatigue under Biaxial and Multiaxial Loading, ESIS 10*, K. Kussmaul, D. McDiarmid, D. F. Socie, Eds., Mechanical Engineering Publications, London, 1991, pp. 81 101.
[16] Moussavi, E., "Ecrouissage Cyclique d'Aciers Inoxydables Austénitique, Ferritique et Austéno-Ferritique: Influence de l'Histoire du Chargement," Thesis, University of Lille I, France, 1997.
[17] Mateo, A., Llanes, L., Iturgoyen, L., and Anglada, M., "Cyclic Stress-Strain Response and Dislocation Substructure Evolution of a Ferrite-Austenite Stainless Steel," *Acta Materiala*, Vol. 44, 1996, pp. 1143 1153.
[18] Kruml, T., Polàk, J., Obrtlìk, K., and Degallaix, S., "Dislocation Structures in the Bands of Localised Cyclic Plastic Strain in Austenitic 316L and Austenitic-Ferritic Duplex Stainless Steels," *Acta Materiala*, Vol. 45, 1997, pp. 5145 5151.
[19] Armas, A. F., Degallaix, G., Alvarez-Armas, I., and Degallaix, S., "Cyclic Internal and Effective Stresses of DIN 1.4460 Duplex Stainless Steels," *Proceedings of the International Conference on Duplex Stainless Steels 2000*, AIM, Venice, 2000, pp. 183 190.
[20] Llanes, L., Mateo, A., Iturgoyen, L., and Anglada, M., "Aging Effect on the Cyclic Deformation Mechanisms of a Duplex Stainless Steel," *Acta Materiala*, Vol. 44, 1996, pp. 3967 3978.
[21] Aubin, V., "Plasticité Cyclique d'un Acier Inoxydable Austéno-Ferritique sous Chargement Biaxial Non-Proportionnel," Thesis, University of Lille 1, France, 2001.
[22] Cailletaud, G, Doquet, V., and Pineau, A., "Cyclic Multiaxial Behaviour of an Austenitic Stainless Steel: Microstructural Observations and Micromechanical Modeling," *Fatigue under Biaxial and Multiaxial Loading, ESIS 10*, K. Kussmaul, D. McDiarmid, D. F. Socie, Eds., Mechanical Engineering Publications, London, 1991, pp. 131 149.
[23] Chaboche, J.-L., Dang Van, K., and Cordier, G., "Modelization of the Strain Memory Effect on the Cyclic Hardening of 316 Stainless Steel," *Proceedings of the Fifth SMIRT Conference*, Berlin, 1979, Paper L 11/3.
[24] Tanaka, E., "A Nonproportionality Parameter and a Viscoplastic Constitutive Model Taking into Account Amplitude Dependences and Memory Effects of Isotropic Hardening," *European Journal of Mechanics A/Solids*, Vol. 13, 1994, pp. 155 173.

PROBABILISTIC AND MULTIAXIAL EFFECTS

Journal of ASTM International, October 2004, Vol. 1, No. 9
Paper ID JAI19053
Available online at www.astm.org

Unyime O. Akpan,[1] *Philip A. Rushton,*[2] *Timothy E. Dunbar,*[2] *and Tamunoiyala S. Koko*[1,3]

Fuzzy Probabilistic Assessment of Aging Aircraft Structures Subjected to Multiple Site Fatigue Damage

ABSTRACT: A strategy is developed for fuzzy probabilistic assessment of the fatigue resistance of aging aircraft structures due to multiple site fatigue damage (MSD). The residual strength of an aircraft structure may be significantly reduced by the existence of fatigue damage at multiple locations. Depending on the level of subjectivity and degree of knowledge, MSD-related parameters may be represented as either purely random variables or fuzzy random variables. The membership functions of probabilistic characteristics of fuzzy random variables, namely mean values and standard deviations, are developed. Mechanistic and probabilistic models used to evaluate multi-site fatigue damage are also presented. A probabilistic solution strategy, employing the first order reliability method (FORM), is combined with the response surface-based fuzzy modeling approach to develop possibility distributions of the probabilistic response quantities (namely reliability indices and failure probabilities) for components subjected to multiple site fatigue damage. Instead of providing the traditional single valued, purely probabilistic measure for reliability, the present formulation proves its merit in its ability to combine experimental data with expert knowledge to provide confidence bounds on the structural integrity of aging aircraft. Moreover, the predicted bounds are dependent on the level of knowledge regarding the fuzzy input parameters, with a higher degree of knowledge resulting in more narrow bounds. An example problem is used to demonstrate the advantages of the proposed methodology.

KEYWORDS: multiple site damage, fuzzy modeling, probabilistic analysis, compounding method, response surface

Introduction

For aircraft structures, in-service aging is an area of major concern. Since both new and aging aircraft must meet or exceed the same structural integrity requirements, aircraft longevity must be diligently considered during both the initial design process and while repair measures are addressed. While the assessment of aircraft structural integrity and reliability is founded upon an accurate prediction of in-service damage accumulation, few in the aviation industry recognize the potentially dire consequences associated with the presence of tiny, virtually undetectable fatigue cracks in aircraft structures, a phenomenon commonly referred to as widespread fatigue damage (WFD). Two categories of WFD include multiple site damage (MSD), which refers to widespread fatigue damage within the same structural element, and multiple element damage (MED), which denotes extensive fatigue-induced damage within adjacent structural components. Widespread fatigue damage may significantly compromise the

Manuscript received 22 April 2002; accepted for publication 20 August 2003; published October 2004. Presented at ASTM Symposium on Fatigue Testing and Analysis Under Variable Amplitude Loading Conditions on 29 31 May 2002 in Tours, France; P. C. McKeighan and N. Ranganathan, Guest Editors.

[1] Senior Research Engineer, Emerging Technologies Group, Martec Limited, 1888 Brunswick St., Ste. 400, Halifax, NS, Canada B3J 3J8.
[2] Research Engineer, Emerging Technologies Group, Martec Limited, 1888 Brunswick St., Ste. 400, Halifax, NS, Canada B3J 3J8.
[3] Group Manager, Martec Limited, 1888 Brunswick St., Ste. 400, Halifax, NS, Canada B3J 3J8.

typically large lead-crack damage tolerance for which aircraft structures are currently designed. Unfortunately, its detection is limited by the capabilities of current inspection technologies. As such, minimizing the effects of WFD requires not only an accurate and reliable estimate as to when WFD-induced reduction in residual strength would become unacceptable but also the repair of the structure prior to such time. Such a formidable task is further complicated by the fact that aircraft structures are continuously aging and often operating beyond their design lives. Enhancing knowledge of multiple site fatigue damage, through both elicitation of Subject Matter Experts (SMEs) and other viable sources, is of utmost importance to both the improvement of aircraft structural designs and also the development of more effective inspection and maintenance management programs for aging aircraft.

The durability and damage tolerance-based strategies employed to evaluate the effects of MSD on aircraft structural integrity are based largely upon the application of fatigue crack growth laws. Such laws constitute the foundation for inspection scheduling and life-extension decisions. However, many of the parameters associated with MSD are largely uncertain. Although much experimental testing has been conducted to evaluate material properties and aircraft structural response, such investigations are usually based on virgin material or artificially aged specimens. As an aircraft structure undergoes in-service aging, its original properties, as well as their inherent uncertainty, tend to degrade somewhat. In some cases, such uncertainties are objective in nature and can be modeled by probabilistic mechanics. In many instances, however, the probabilistic characteristics of the variables involved are not precisely known, rendering their uncertainty subjective. In such cases, the parameters may be suitably modeled using fuzzy logic methods, which combine experimental data with knowledge from subject matter experts (SMEs) to provide confidence bounds on structural reliability. Both parametric uncertainty and in-service aging of aircraft structures may be accounted for through careful fuzzy probabilistic characterization and analysis, in conjunction with expert (SME) elicitation.

The objective of the current study is to develop a fuzzy probabilistic framework with which to model the effects of multiple site fatigue cracking in aircraft structures. The approach synergistically combines the fuzzy modeling strategy developed by Akpan et al. [1] with probabilistic models for MSD, such as those presented in [2], thereby providing a technique for computing the possibility distribution of probabilistic quantities such as reliability index (β) or failure probability (P_f) of aircraft structures under the influence of MSD. Purely probabilistic methods typically yield a single value for β and P_f, which ignores any uncertainty in knowledge of parameters affecting MSD, and whose bounds cannot be defined accurately. The advantage of the approach presented herein is that in lieu of a single probabilistic value for β or P_f, a range of possible values may be specified based on the level of knowledge regarding the relevant input parameters. In general, greater (input) confidence corresponds to a more narrow range of possible output values.

Probabilistic and Mechanistic Modeling

Mechanical Formulation and Probabilistic Reliability Models for MSD Problems

Damage tolerance and reliability of aircraft structures is based upon an accurate prediction of in-service fatigue damage accumulation. Several techniques have been proposed in the literature to account for the detrimental effects of multiple site fatigue damage. With the numerous uncertainties inherent in both the physical process by which MSD progresses and the mathematical models used to evaluate the phenomenon, there is increasing recognition that MSD may be described best by using a probabilistic framework.

Evaluation of fracture characteristics and fatigue crack growth of multiple cracks may be accomplished by a number of means. For example, consider the "link-up" of a lead crack with an MSD crack, which occurs when their corresponding plastic zones meet. Progressive link-up with other MSD cracks would continue until such time as the stress (σ_a) applied to a component exceeds its residual strength (σ_r); that is, $\sigma_r \leq \sigma_a$. The residual strength of a panel of width W may be approximated by [3]

$$\sigma_r = (W - 2a)\left(\sigma_y / W\right) \tag{1}$$

in which a denotes the half-crack length of a given lead or MSD crack, and σ_y is the yield stress. It can be shown that lead crack residual strength may be significantly reduced by MSD, the extent of which is extremely sensitive to structural configuration.

As an alternative to analytical methods such as that mentioned above, finite element (FE) technology may be applied to estimate the stress intensity factor (SIF) for structural components subject to MSD. For cases involving a large number of MSD cracks, the practicality of such an approach is limited by its relatively high computational costs. Other numerical approaches, such as the use of complex stress functions to describe the stress distributions surrounding a given MSD configuration, may also prove computationally expensive.

A fracture mechanics-based technique known as the compounding method has proven to be the most versatile and computationally efficient technique, well suited to the numerous model solutions typically required by a probabilistic analysis. Although approximate, the SIF solutions obtained via the compounding method are, nonetheless, reasonably accurate [2]. As the compounding method will be employed in the current investigation, details regarding its application are discussed in the following paragraphs.

In traditional linear elastic fracture mechanics (LEFM), the mode I stress intensity factor range (ΔK) for a center-cracked panel of finite width W is given by:

$$\Delta K = \Delta\sigma\sqrt{\pi a}Y \tag{2}$$

in which $\Delta\sigma$ represents the applied stress range, a denotes the half-crack length, and Y is a geometric correction factor. The compounding method simply implies the use of an effective or "compounded" geometric correction factor calculated as the product of correction factors from existing solutions for simple geometries. In other words, for a panel subjected to MSD, the effective stress intensity factor range (ΔK_{eff}) is given by

$$\Delta K_{eff} = \Delta\sigma\sqrt{\pi a}Y_{eff} \tag{3}$$

The compounded geometric correction factor (Y_{eff}) is given by

$$Y_{eff} = Y_c Y_h Y_n Y_w Y_m \tag{4}$$

where Y_c accounts for corner cracks, Y_h considers cracks originating at a hole, Y_n accounts for interaction between neighboring holes, Y_w accounts for a plate of finite width, and Y_m accounts for mutual crack interaction effects [2]. For a crack at hole i, Y_n is given by

$$Y_{n_i} = \prod_{i \neq j} Y_{ni,j} \tag{5}$$

where $Y_{ni,j}$ is the hole interaction factor for two neighboring holes i and j. Similarly, the crack interaction factor for crack i is given by

$$Y_{m_i} = \prod_{i \neq j} Y_{mi,j} \tag{6}$$

where $Y_{mi,j}$ is the interaction factor for two cracks i and j. Experimental studies [4,5] have shown the factors of most significance to be Y_w and Y_m, reducing Eq 3 to

$$\Delta K_{eff} = \Delta\sigma\sqrt{\pi a}\left(Y_w Y_m\right) \tag{7}$$

For a panel of finite width (W), Y_w is given by the familiar expression

$$Y_w = \sqrt{\sec\left(\frac{\pi a}{W}\right)} \tag{8}$$

where a denotes the half-crack length. The interaction factors for lead and MSD cracks were developed by Kamei and Yokobori [6].

A number of performance or limit state functions ($g_f(X)$) may be defined for the assessment of structural integrity in the presence of MSD. For cases involving instantaneous fracture and fatigue crack propagation (respectively), two such functions may be formulated in terms of:

a. Exceedance of the corresponding critical crack length (a_{cr}) at any time t, and
b. Exceedance of the critical mode I fracture toughness (K_{IC}) of the material.

The compounding method essentially determines an effective crack configuration (A_{eff}), for which the failure likelihood is given by

$$P_f = P\left(g_{f,A_{eff}} \leq 0\right), \qquad g_{f,A_{eff}} = \varphi\left(A_i\right) \tag{9}$$

where $g_{f,A_{eff}}$ defines the limit state in terms of φ, which is in turn a function of the various crack sizes and geometric configuration. For the fatigue crack growth (FCG) criterion defined in (a) above, the limit state may be specified in terms of damage functions $\xi(a)$ as

$$g_{f,A_{eff}}(t) = \xi\left(a_{cr}\right) - \xi\left(a(t)\right) \tag{10}$$

where a_{cr} denotes the critical crack length, and $a(t)$ represents the crack length at time t. The damage functions $\xi(a)$ are given by

$$\xi(a) = \int_{a_0}^{a}\left[\frac{da}{\left(\sqrt{\pi a}\left(Y_{eff}(a)\right)\right)^m}\right] = \ldots = \int_{N_0}^{N} C\left(\Delta\sigma\right)^m dN \tag{11}$$

where a_0 denotes the initial crack length, N_0 and N are the initial and final number of cycles, respectively, and C and m are the material constants associated with the Paris crack growth law.

One may extend the above approach to cases involving multiple cracks. Consider, for example, the interaction of two cracks i and j, of lengths a_i and a_j, respectively. The corresponding critical damage functions are given by

$$\xi\left(a_{i,cr}\right) = \int_{a_{i0}}^{a_{i,cr}}\left[\frac{da_i}{\left(\sqrt{\pi a_i}\left(Y_{eff}(a_i, a_j)\right)\right)^m}\right] \tag{12}$$

$$\xi\left(a_{j,cr}\right)=\int_{a_{j0}}^{a_{j,cr}}\left[\frac{da_j}{\left(\sqrt{\pi a_j}\left(Y_{eff}(a_i,a_j)\right)\right)^m}\right] \tag{13}$$

while the corresponding damage functions at time t are given by

$$\xi\left(a_i(t)\right)=\int_{a_{i0}}^{a_i(t)}\left[\frac{da_i}{\left(\sqrt{\pi a_i}\left(Y_{eff}(a_i,a_j)\right)\right)^m}\right] \tag{14}$$

$$\xi\left(a_j(t)\right)=\int_{a_{j0}}^{a_j(t)}\left[\frac{da_j}{\left(\sqrt{\pi a_j}\left(Y_{eff}(a_i,a_j)\right)\right)^m}\right] \tag{15}$$

Moreover, an effective FCG-based limit state function for multiple interacting cracks may be defined as

$$g_{f,A_{eff}}(t)=\underset{i=1,2,\ldots,n}{Min}\left\{\xi\left(a_{i,cr}\right)-\xi\left(a_i(t)\right)\right\} \tag{16}$$

For the current investigation, the fracture criterion mentioned in (b) above has been employed, for which the limit state function is defined as

$$g_{f,A_{eff}}=K_{IC}-\left(\psi_{\Delta K}\right)\Delta K_{A_{eff}} \tag{17}$$

in which K_{IC} represents the Mode I fracture toughness, and $\Psi_{\Delta K}$ is a bias correction factor for the estimation of the effective stress intensity factor range for the effective crack configuration ($\Delta K_{A_{eff}}$) [2].

Probabilistic Solution Strategies

Either Eq 16 or Eq 17 may be used to compute the failure probability of an aging aircraft structure subjected to multiple site fatigue damage. However, it should be noted that since some of the model parameters are not only random in nature, but also fuzzy to some extent, there are many possible realizations for the probability of failure and reliability index. A strategy for computing the possibility distribution for these probabilistic response quantities will be developed in the next section. The limit state function ($g(X)$) is typically defined such that

$$\begin{aligned}
g(X)<0 &\Rightarrow \textit{FAILURE}\\
g(X)=0 &\Rightarrow \textit{LIMIT STATE BOUNDARY}\\
g(X)>0 &\Rightarrow \textit{NO FAILURE}
\end{aligned} \tag{18}$$

Discrete values of probability of failure can be computed by using failure probability (P_f), defined in general terms as

$$P_f=P\{g(X)\le 0\} \tag{19}$$

where g(X) = g(X1, X2, ,Xn) represents the limit state or performance function involving n random variables X. Alternatively, the probability of failure can be obtained through integration of the following relation

$$P_f=\int_{\Omega}\ldots\int f_X(x)dx \tag{20}$$

where Ω represents the failure domain $\{g(X) \leq 0\}$, and $f_X(X)$ is the joint probability density function (PDF) for the vector of random variables X. Over the past several years, estimation of failure probability as described by Eq 20 has been the focus of much research. Two procedures have surfaced as practical tools for reliability analysis, namely First Order Reliability Method (FORM) and Second Order Reliability Method (SORM) [7], the former of which will be the focus of the current investigation. The most fundamental components of FORM include the following:

a. A Probability Transformation Scheme with which to transform the random variables and performance (limit state) functions from X-space to the u-space of a standard normal (i.e., Gaussian) distribution, in which all random variables (X) have a mean (μ) of zero, a standard deviation (σ) of one, and are uncorrelated. This transformation is accomplished by means of the following relations

$$X_i \rightarrow u_i = \frac{X_i - \mu_{X_i}}{\sigma_{X_i}} \tag{21}$$

$$g(X) \leq 0 \rightarrow g(u) \leq 0 \tag{22}$$

b. An Optimization Algorithm with which to calculate the reliability index (β), which is given by the minimum distance from the origin to the linearly-approximated surface of the u-transformed performance function (i.e., g(u)). In other words, the objective is to

$$\begin{aligned} &\text{Minimize the distance} \rightarrow \; D = \sqrt{u_i^T u_i} = \beta \\ &\text{Subject to the constraint} \rightarrow \quad g(u_i) = 0 \end{aligned} \tag{23}$$

Using the PDF of the transformed (normal) distribution, denoted by the symbol Φ, the probability of failure can be defined as

$$P_f = \Phi(-\beta) \tag{24}$$

c. A Gradient Computation Algorithm to assess the relative sensitivity or importance of each random variable, which is of major significance to reliability-based research and design.

The proposed methodology has been applied in the solution of several example problems using a fuzzy probabilistic analysis program, which uses COMPASS [7] as its probabilistic computational engine.

Fuzzy Modeling of Probabilistic Response

Many of the parameters included in the models used to describe fatigue crack growth in the presence of MSD are calibrated using a combination of experimental data and expert opinion, including the component width, thickness, applied stress range, material properties, loading, and correction factors. It is well-accepted that no general consensus (even from experts) exists as to the best value for these parameters, especially when components are continuously aging and knowledge regarding the impact of in-service aging is rather limited. Therefore, such parameters cannot be modeled accurately as purely random variables, and they may instead be represented as fuzzy random variables, incorporating a subjective degree of fuzziness in their probabilistic characteristics. Accordingly, a modeling strategy that allows for such parametric subjectivity, namely a fuzzy analysis, may be employed.

Modeling of MSD-Related Fuzzy Random Input Variables

As alluded to previously, some of the parameters used in fatigue crack laws and MSD models may be described as fuzzy random variables. More specifically, the probabilistic characteristics of these random variables (i.e., mean value, standard deviation, etc.) could be fuzzy to some degree, as estimates are typically derived from both experimental data and elicitation of subject matter experts. The process by which fuzzy variables are quantified is known as fuzzification, which is accomplished by constructing a membership function or possibility distribution for the variable. An example of a skewed convex triangular possibility distribution for the mean value of a random variable is illustrated in Fig. 1. The y-axis reflects α, the level of knowledge regarding the mean value of the random variable, with values ranging from 0 1, where $\alpha = 0$ corresponds to "little knowledge" or "highly uncertain," and $\alpha = 1$ (referred to as the normal point) implies "a high degree of knowledge" or being "very confident." The x-axis suggests the upper and lower bounds between which the mean value of the input parameter is thought to lie for a given level of knowledge α. Similar representations can be carried out for the standard deviation of the fuzzy random variables. The fuzzification process involves an aggregation of expert opinion and experimental data.

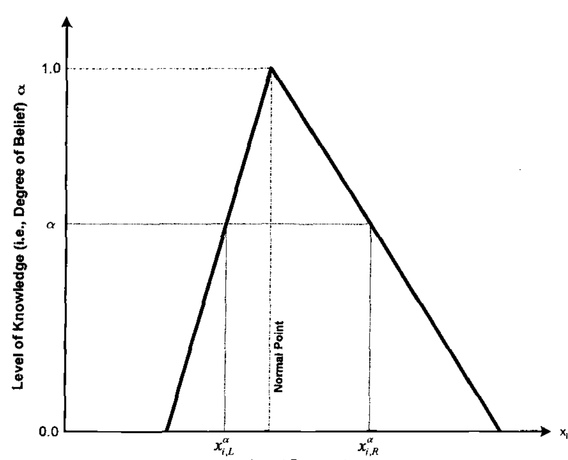

FIG. 1 *Possibility distribution of the mean value of a fuzzy random variable.*

Computation of Fuzzy Probabilistic Response

Upon fuzzification of the characteristic values of random variables, namely mean, standard deviation, correlation, and probability distribution, the fuzzy probabilistic response quantity (i.e., probability of failure or reliability index) must be computed, thereby implying that a possibility distribution also must be constructed for the response quantity. Computation of fuzzy response is based on a fuzzy principle known as the extension principle, which, in some cases, may require an impractical amount of computational resources, depending on the number of fuzzy variables considered. A much-improved solution strategy, which circumvents the limitations of the extension principle, namely the response surface method, was developed by Akpan et al. [8]. The extension principle is briefly discussed in the following section, followed by a presentation of the response surface solution strategy.

Extension Principle—The extension principle associates the possibility distribution for the fuzzy input parameters with that of the fuzzy response function. Given a set of independent fuzzy variables x_i (i = 1,2, ,N, where N = the total number of fuzzy input parameters) upon which a function $y(x_i)$ operates, the extension principle gives the possibility distribution μ_{xi} of the output function $c = y(x_i)$ (probability of failure or reliability index) as

$$\begin{gathered}\mu_{xi}\left(c = y(x_i)\right) = \sup\big|_c\left[\min_i\left(\mu_{xi}\{y(x_i)\}\right)\right] \\ -\infty < y(x_i) < \infty \;\; and \;\; 1 < i < N\end{gathered} \tag{25}$$

where sup represents the supernum operator that gives the least upper bound. Equation 25 essentially states that for a crisp value of the output function $y(x_i)$, there exists either zero, one, or more combinations of the fuzzy variables x_i such that $y(x_i) = c$. In fuzzy set theory, the possibility of a particular outcome is equal to the minimum possibility of its constituent events. When several paths may be used to predict the outcome, each with its own possibility, then the overall possibility of this outcome is given by the maximum of all individual possibilities. Two approximate numerical methodologies, namely the discretization method and the vertex method, are used to compute fuzzy parameters by means of conversion from fuzzy to crisp values. These techniques will be discussed in the following sub-sections.

Discretization Method—The discretization method requires that each fuzzy input variable be discretized into a domain (D_i) of discrete values. The output function y must be evaluated a total of $\Pi_{i=1}^{N}(D_i)$ times. Consider, for example, a problem involving three fuzzy input parameters, each discretized into ten values. In this case, the output function must be solved a total of 1000 times. Unfortunately, this method requires a significant amount of computational resources, thereby making it impractical for computing reliability indices or probabilities of failure.

Vertex Method—In terms of computational expense, the vertex method is much cheaper for numerical implementation of the extension principle. This technique is often referred to as the combinatorial method. The main steps required in the vertex or combinatorial method are to:

1. Discretize the fuzzy input parameters using an α-level representation.
2. Collect all binary combinations of the extreme left (L) and right (R) (i.e., lower and upper, respectively) values of all fuzzy variables at each α-level.
3. Compute the fuzzy response function y for all binary combinations of fuzzy input variables.
4. Select the maximum and minimum values of the response function y at each α-level.

As alluded to earlier, an α-level representation of a fuzzy variable X_i, denoted by the range $\left[X_{i,L}^{\alpha}, X_{i,R}^{\alpha}\right]$, indicates the interval in which the variable is thought to lie with a level of confidence equal to α. Therefore, at any α-level, each fuzzy variable is discretized into a range of crisp values between $X_{i,L}^{\alpha}$ and $X_{i,R}^{\alpha}$. Upon discretization of the fuzzy input parameters, all combinations of their extreme left and right values (at a given α-level) are fed into the output function y. Assuming a total of N fuzzy variables and denoting the combinations by $C_{\alpha,j}$ (j=1,2, ,$N_{c/\alpha}$), where $N_{c/\alpha}$ represents the total number of binary combinations at a given α-level, the fuzzy response can be written as $y(C_{\alpha,j})$. It is easily shown that the total number of binary combinations at a given α-level is equal to 2^N. The fuzzy response at each α-level is given by

$$\left[y_L^{\alpha}, y_R^{\alpha}\right] = \left[\min|_{\lambda,j}\left(y(C_{\lambda,j})\right), \max|_{\lambda,j}\left(y(C_{\lambda,j})\right)\right] \\ \lambda \geq \alpha, \; j = 1,2,\ldots,N_{C/\alpha} \tag{26}$$

For a range of α-levels, the results of Eq 26 are then used to construct a possibility distribution for the response function y. In general, the greater the number of α-cuts, the more accurate the predicted possibility distribution. For a number of α-cuts A, the response function (e.g., β or P_f) must be solved a total of A × 2^N times. It is evident that computational cost grows exponentially with an increasing number of fuzzy input variables. For example, a problem involving three fuzzy variables and five α-cuts requires that the objective function be called 5 × 2^3 = 40 times, whereas one involving five fuzzy parameters and five α-cuts must call the output function a total of 5 x 2^5 = 160 times.

Response Surface Prediction of Fuzzy Response—The response surface method is a classical statistical technique wherein a complicated model is approximated using a simplified relationship between the fuzzy response function and the fuzzy input variables. Instead of collecting the binary combinations of upper and lower fuzzy inputs (mean values, standard deviations of fuzzy random variables), adjustments are made to the normal point of all fuzzy variables, and the resulting impact on response is observed. As most systems are very well behaved, the impact of such adjustments may be used to develop an explicit function (i.e., response surface) relating the input and output variables. For a quadratic response surface, this function is given by the expression

$$\bar{y}(x) = a + \sum_{i=1}^{N} b_i x_i + \sum_{i=1}^{N} \sum_{j=i+1}^{N-1} c_{ij} x_i x_j \tag{27}$$

where N is the number of fuzzy variables x; $\bar{y}(x)$ denotes the response function approximation; and the coefficients a, b, and c are determined through regression of experimental data. Upon calculation of the approximate fuzzy response function, $\bar{y}(x)$, a combinatorial optimization is performed at each α-level to determine the combination of fuzzy variables yielding the extreme values of fuzzy response. More specifically, two combinatorial optimizations are required at each α-level, with the following objectives:

1. To determine the combination of $x_{i,L}^{\alpha}$ and $x_{i,R}^{\alpha}$, denoted by $C_{\alpha/min}$, which minimizes the approximate function $\bar{y}(x)$.

2. To determine the combination of $x_{i,L}^{\alpha}$ and $x_{i,R}^{\alpha}$, denoted by $C_{\alpha/max}$, which maximizes $\bar{y}(x)$.

The true maximum and minimum responses at each α-level are then determined by feeding the values of $C_{\alpha/min}$ and $C_{\alpha/max}$ into a finite element model or other numerical engine. This methodology requires that the response function be solved only twice at each α-level. For a number of α-cuts A, the response surface method requires only $A \times 2$ runs, whereas the vertex method requires $A \times 2^N$ runs. As noted by Akpan et al. [8], the response surface method represents a huge improvement in computational efficiency and permits consideration of a much larger number of fuzzy variables. The response surface approach to fuzzy probabilistic response computation is illustrated schematically in [1].

Example Demonstration

In the following section, an example will be considered to demonstrate the application of fuzzy probabilistic logic to the problem of multiple site fatigue damage. A typical MSD scenario observed in aircraft panels involves a series of cracks emanating from a row of fastener holes, as illustrated in Fig. 2.

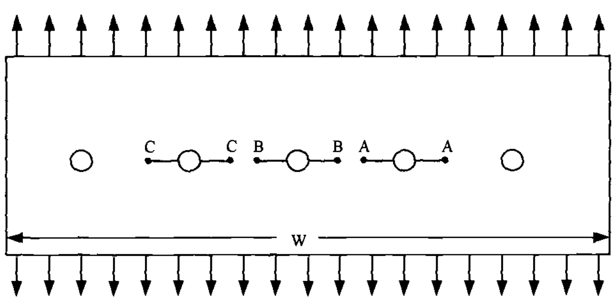

FIG. 2 *Schematic illustration of multi-site fatigue damage in an aging aircraft.*

Consider the fracture-based performance function for MSD, given previously by Eq 17 as $g_{f,A_{eff}} = K_{IC} - (\psi_{\Delta K})\Delta K_{A_{eff}}$, where the Mode I fracture toughness is given by K_{IC}, and $\Psi_{\Delta K}$ is a correction factor for the bias in estimating the effective SIF range for the effective crack configuration (i.e., $\Delta K_{A_{eff}}$). The effective SIF range was given previously by Eq 7 as $\Delta K_{eff} = \Delta\sigma\sqrt{\pi a}\,(Y_w Y_m)$. All model parameters are assumed to be either random variables or fuzzy random variables, with nominal probabilistic characteristics summarized in Table 1. No correlation was assumed between any of the variables. Employing the limit state function defined above, in conjunction with the response surface strategy outlined in Akpan et al. [1,8], a fuzzy probabilistic analysis was performed. Eighteen fuzzy variables were considered, namely the mean and standard deviation of the nine MSD-related parameters summarized in Table 1. Uncertainty or fuzziness in the mean and standard deviation was assumed to lie within (+5 %, –5 %) for all parameters except fracture toughness (K_{IC}) for which the fuzziness in probabilistic characteristics was assumed to lie within the skewed range of (+1 %, –5 %) to approximate the adverse effects of in-service aging.

TABLE 1 *Probabilistic and fuzzy characterization of MSD random variables.*

Description of Random Variable	Distribution	Mean (μ)*	Std. Dev. (σ)*
Applied Stress Range ($\Delta\sigma$)	Gumbel	650.000	100.0000
Crack Size C (a_C)	Normal	0.010	0.0010
Crack Size B (a_B)	Normal	0.010	0.0010
Crack Size A (a_A)	Normal	0.006	0.0006
Tip Separation Between A and B (b_{AB})	Lognormal	0.020	0.0020
Tip Separation Between B and C (b_{BC})	Lognormal	0.020	0.0020
Fracture Toughness† (K_{IC})	Weibull	174.000	17.4000
Panel Width (W)	Normal	0.400	0.0200
Bias Correction Factor (Ψ)	Normal	1.000	0.1000

*Fuzziness in μ and σ assumed to lie within (+5 %, –5 %).
†Fuzziness in K_{IC} assumed to lie within (+1 %, –5 %).

The original probabilistic characteristics of each parameter were then used to obtain a nominal FORM-based estimate of failure probability (P_{f0} = 0.061). The previously outlined response surface technique was then applied to determine a possibility distribution for failure probability. The possibility distribution for failure probability based on the use of fuzzy nominal means is illustrated in Fig. 3, while that based on the use of fuzzy nominal standard deviations is illustrated in Fig. 4. It is seen that the predicted bounds widen significantly as the level of knowledge decreases. It is interesting that although the fuzzy input was linear, the resulting mean-based possibility distribution exhibits a nonlinear variation, while that based on fuzzy standard deviations depicts linear behavior, demonstrating that one cannot predict the nature of fuzzy output simply based on the nature of the fuzzy input from which it was derived.

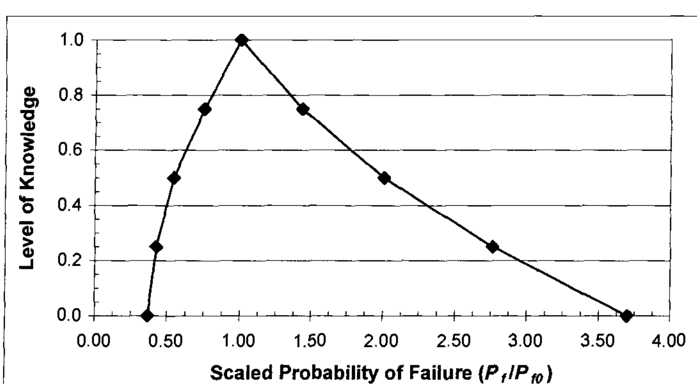

FIG. 3 *Possibility distribution for μ-based probability of failure (P_{f0} = 0.061).*

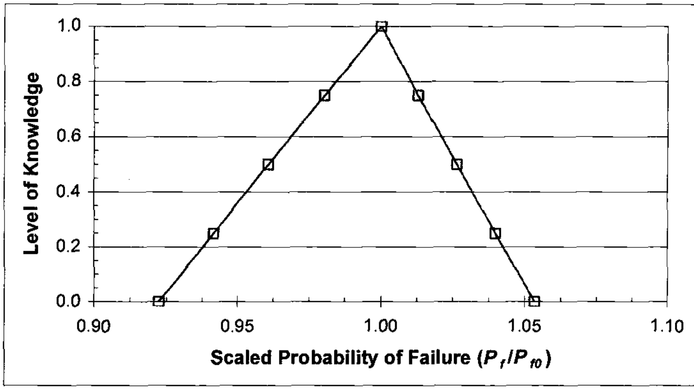

FIG. 4 *Possibility distribution for σ-based probability of failure (P_{f0} = 0.061).*

The corresponding possibility distribution based on combined fuzzy input parameters (i.e., both fuzzy means and fuzzy standard deviations) is shown in Fig. 5. For the current example, it is evident that uncertainty in the mean of the relevant MSD parameters has a much more pronounced effect on the possibility distribution for failure probability than an equal degree of uncertainty in standard deviation does.

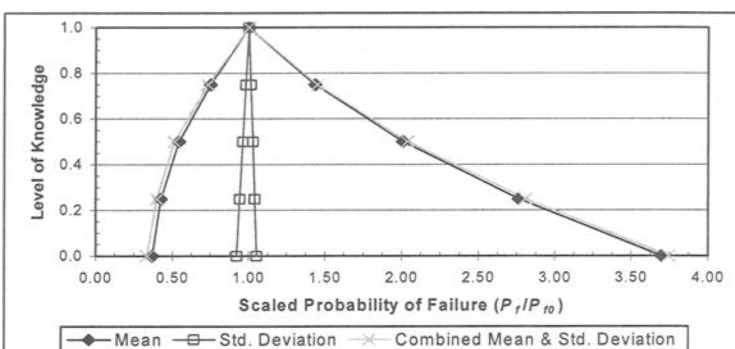

FIG. 5—*Comparison of POF-based possibility distributions for individual & combined fuzzy input parameters.*

As previously mentioned, in lieu of the traditional single-valued probabilistic result for P_f, the x-axis of a fuzzy-based possibility distribution implies an upper and lower bound within which the objective, in this case failure likelihood, is thought to lie for a given level of knowledge. For example, suppose there is 50 % confidence in the fuzziness associated with both the mean and standard deviation of the nominal input parameters (i.e., (+0.5 %, –2.5 %) for K_{IC}, (+2.5 %, –2.5 %) for all other input parameters). As suggested by Fig. 5, the corresponding failure probability would lie between 50 and 200 % of its nominal value, thereby making available to the decision maker both the worst- and best-case scenarios at this particular level of parametric fuzziness.

It is interesting to note that the skewed fuzzy input for fracture toughness (i.e., (+1 %, –5 %)) has resonated through the entire solution to produce a skewed mean-based possibility distribution, thereby indicating the importance of an accurate prediction of K_{IC}. As intuitively expected, the predicted bounds on failure probability based on the use of combined fuzzy random variables (i.e., combined means and standard deviations) are wider than those predicted based on fuzzy nominal means and standard deviations considered individually. For the current example, use of the response surface technique (18 fuzzy variables, 5 α-cuts) in lieu of the vertex method has reduced the number of required solutions from $5 \times 2^{18} = 1\ 310\ 720$ probabilistic runs to only $5 \times 2 = 10$ runs (an improvement in computational efficiency of more than five orders of magnitude).

Conclusions

Multiple site fatigue damage (MSD) is a growing problem for aging aircraft structures, one which is compounded by their continued operation well beyond their original design lives. Moreover, traditional policies for damage tolerance and structural integrity of aircraft structures give little consideration to the potentially catastrophic repercussions associated with the neglect and non-detection of MSD and give even less consideration to the uncertainty inherent in many of the parameters involved.

In the current investigation, emphasis has been placed on assessing the effects of MSD by means of a fracture-based failure criterion. Several mechanistic and probabilistic models for MSD have been presented. The potential for combining probabilistic methods with fuzzy modeling strategies also has been advanced, with focus on use of the response surface method. Depending on the level of knowledge and degree of subjectivity, parameters affecting MSD may be represented either as purely random variables or as fuzzy random variables. A strategy for fuzzy-probabilistic assessment of the impact of multiple site damage on aging aircraft structures has been developed. FORM-based probabilistic solution strategies have been employed to compute discrete values of failure probability for components subjected to MSD. The response surface fuzzy modeling strategy was then used to compute the possibility distributions for P_f. In lieu of providing a crisp value of structural reliability, the merit of the proposed methodology lies in its ability to implement both experimental data and expert opinion in the prediction of confidence bounds on structural integrity of aging aircraft. Such bounds are largely dependent on the knowledge regarding the probabilistic characteristics of the fuzzy input parameters, with a higher degree of knowledge producing much tighter bounds.

An example problem has been presented to demonstrate the merit of the proposed fuzzy probabilistic methodology. For the example presented herein, it was observed that while reliability is greatly affected by uncertainty in parametric mean, variability in standard deviation is of much less significance. A similar investigation need not be limited to the uncertainties specified herein, but it may also include additional parameters, the uncertainty of which could be tailored to match observed variability in experimental data and expert opinion. Moreover, the current methodology is suitable for use with any limit state function deemed appropriate for MSD and should not be limited to those mentioned herein. To the best of the authors' knowledge, no similar investigation has been performed to date.

References

[1] Akpan, U. O., Koko, T. S., Orisamolu, I. R., and Gallant, B. K., "Practical Fuzzy Finite Element Analysis of Structures," *Journal of Finite Element in Analysis and Design*, Vol. 38, 2001, pp. 93 111.

[2] Orisamolu, I. R., "Probabilistic Assessment of the Influence of Multiple Site Cracking on the Damage Tolerance of Aircraft," *Proceedings of ICAF97 Fatigue in New And Aging Aircraft*, Edinburgh, Scotland, 1997, pp. 683 694.

[3] Swift, T., "Widespread Fatigue Damage Monitoring Issues and Concerns," *Proceedings of 5th International Conference on Structural Airworthiness of New and Aging Aircraft*, Hamburg, Germany, June 1993, pp. 133 150.

[4] Nishimura, T., Noguchi, Y., and Vchimoto, T., "Damage Tolerance Analysis of Multiple-Site Cracks Emanating from Hole Array," *Journal of Testing and Evaluation*, Vol. 18, No. 6, 1990, pp. 401 407.

[5] Moukawsher, E. J., Neussl, M. A., and Grandt, A. F., "Fatigue Analysis of Panels with Multiple Site Damage," *Proceedings of the 1992 USAF Aircraft Structural Integrity Program Conference*, San Antonio, TX, 1992, pp. 1263 1305.

[6] Kamei, A. and Yokobori, T., "Two Collinear Asymmetrical Elastic Cracks," Report of the Research Institute for Strength and Fracture of Materials, Tohoku University, Vol. 10, Sections 1 4, 1974, pp. 41 42.

[7] Lui, Q., Orisamolu, I. R., and Chernuka, M. W., "COMPASS Version 1.4 User Manual," Martec Limited, Halifax, NS, 1995.

[8] Akpan, U. O., Koko, T. S., and Orisamolu, I. R., "Response Surface Based Fuzzy Analysis of Structural Systems," *American Institute of Aeronautics and Astronautics Conference*, 2000, AIAA Paper #2000-1634.

[9] Ross, T. J., "Fuzzy Logic with Engineering Applications," McGraw Hill, 1995.

[10] Millwater, H., Wu, J., Burnside, H., and Mear, M., "Application and Extension of Structural Reliability Methods to Multi-Site Damage," *Proceedings of ICAF97 Fatigue in New And Aging Aircraft*, Edinburgh, Scotland, 1997, pp. 671 682.

[11] Mar, J. W., "Preserving Aging Aircraft," *Aerospace America*, January 1996, pp. 38 43.

Michel Huther,[1] Stéphanie Mahérault, Guy Parmentier, Guy Césarine

Probabilistic and Semi-Probabilistic Format in Fatigue Ship Classification Rules

REFERENCE: Huther, M., Mahérault, S., Parmentier, G., and Césarine, G., **"Probabilistic and Semi-probabilistic Format in Fatigue Ship Classification Rules,"** *Fatigue Testing and Analysis Under Variable Amplitude Loading Conditions, ASTM STP 1439,* P.C. McKeigham and N. Ranganathan, Eds., ASTM International, West Conshohocken, PA, 2005.

ABSTRACT: Following a short review of the ship classification principle, of the cyclic fatigue in ship structures, the deterministic format based on S-N curves is reviewed. First, the probabilistic format for fatigue verification using S-N curves is presented with emphasis on the uncertainties and limits of use versus ship structures design. Then the semi-probabilistic format, as used in the new Bureau Veritas BV2000 rules for steel ships is presented. Particular attention is given to the selected partial safety factors versus the other failure modes. The calculation of those partial safety factors is also analysed, based on practical cases. As a conclusion, the interest of the probabilistic approach versus the deterministic one is outlined. Then the limits of practical applications, semi-probabilistic for design and drawing approval, probabilistic for rule developers and RBI are discussed. To end, the research and development needs for future are pointed out.
KEYWORDS: Fatigue, Probabilistic, Semi-probabilistic, Variable loading, Welded joints, Ship design, Classification rules

Introduction

Any merchant ship in operation must be registered to a flag state, and to do so, must comply with the international regulations and be normally classed by a recognised Classification Society. A particularity of the shipping industry is that the rules and regulations that the ship has to fulfil to be classed are edited by the concerned Classification Society itself and not by an official organisation as in other industrial areas.

Classification of ships started early in the 19th century, 1828 for Bureau Veritas for example, one of the two oldest. From that time the Classification Societies develop, edit and maintain rules for the verification of the design and operation quality and safety of the hull structure, of the propulsion plant and equipment and of the ship safety systems, Ref. [1].

Referring to the hull structure, the loads being due to the wave actions, it is clear that they are cyclic and highly variable in time. Therefore the cyclic cumulative fatigue is one of the major origins of structural failure, and the last step of the crack propagation following a crack initiation. The evidence of the fatigue nature of the cracks observed in ship structures appeared in the 60s and fatigue became of first concern for the rules developers in the 70s, when large oil tankers and large containers ships built with high tensile steel were designed and operated.

[1] Deputy Technical Director; Research Engineer, Research Department; Rules Developer, Development Department; respectively, Marine Division, Bureau Veritas, 17 bis Place des Reflets – La Defense 2, 92077 Paris La Defense Cedex (France).

Rules were so edited by the Classification Societies, for Bureau Veritas in 1983, Ref. [2]. Due to the random character of the stresses, they were based on the Miner sum approach and presented in a deterministic format. The worse design loading was defined by a standard long term stress range histogram, the design safe S-N curve was fixed as the S-N curve at two standard deviations below the experimental mean curve and the maximum admissible Miner sum was fixed equal to 1.

This approach was the basis for ship structure design for many years and has allowed the problem raised to be solved by the evolution in shipbuilding with success, as demonstrated by the operation of the half million tons oil tankers in the 1970s.

But the development of the probabilistic approach, mainly in offshore, helped by the fantastic progresses in computers, brought out the limits of the deterministic approach. The deterministic approach does not allow to measure the incidence on the safety level of the various parameters involved in cumulative fatigue, and does not allow to take advantage of the progress in building quality nor of the possibility of optimisation offered by Finite Element Method (FEM).

Probabilistic Format

One of the first probabilistic formulation in marine industries was given for offshore structures by Whirshing, Ref. [3]. This formulation was based on the S-N curve and Miner sum

$$\Delta S^m N = C \tag{1}$$

$$D = \sum \frac{n_i}{N_i} \tag{2}$$

where

ΔS	stress range
N	number of cycles to failure
C, m	S-N curve constants
n_i	number of cycles of the stress range histogram at ΔS_i
N_i	number of cycles of the S-N curve at rupture at ΔS_i
D	Miner sum

in which the parameters C, ΔS and D are considered random, and m deterministic.

Cumulative Fatigue Formulation

Based on this formulation an adaptation has been developed for steel ship structures, Ref. [4,5]. The cumulative fatigue, based on the Miner sum, has been formulated by closed form, (Eq. 3)

$$D = \int_0^\infty \frac{N_t f(\Delta S)\, d\Delta S}{N(\Delta S)} = \frac{N_t}{C} \int_0^\infty \Delta S^m \, f(\Delta S)\, d\Delta S \tag{3}$$

where

$f(\Delta S)$	cumulative probability of long term distribution
N_t	number of cycles for the expected ship's life
$N(\Delta S)$	number of cycles of the S-N curve (Eq. 1) at the stress range level ΔS

The long term cumulative probability $f(\Delta S)$ of the stress range is expressed by a two parameter Weibull law, which are

ξ	shape parameter
ΔS_R	position parameter, reference stress range at the probability level p_R

When the S-N curve is modelled with two slopes, m for $\Delta S > \Delta S_q$ and $(m + \Delta m)$ for $\Delta S < \Delta S_q$, the (Eq. 3) becomes

$$D = \frac{N_t}{C} \frac{\Delta S_R^m}{\left(-\ln(p_R)\right)^{m/\xi}} \mu \Gamma\left(\frac{m}{\xi}+1\right) \qquad (4)$$

where

$\Gamma(x+1)$	Gamma function
μ	coefficient taking into account the change in slope of the S-N curve

$$\mu = 1 - \frac{\left\{\gamma\left(\frac{m}{\xi}+1, \nu\right) - \nu^{-\Delta m/\xi} \gamma\left(\frac{m+\Delta m}{\xi}+1, \nu\right)\right\}}{\Gamma\left(\frac{m}{\xi}+1\right)} \qquad (5)$$

where

$\gamma(a+1, x)$	incomplete Gamma function, Legendre form
ν:	$\nu = -\left(\frac{\Delta S_q}{\Delta S_R}\right)^{\xi} \ln(p_R)$
ΔS_q	stress range at the S-N curve point of change of slope

Fatigue Probabilistic Formulation

The probabilistic formulation implies the definition of a limit state function G so that

$G < 0$	is the domain of failure
$G > 0$	is the safe domain of no failure
$G = 0$	is the limit state surface

and the probability of failure is given by

$$P_f = prob\,(G \le 0) \qquad (6)$$

Different limit state function can be developed. Considering the shipping industry practice, the limit state function is given in terms of time to failure T. Assuming that the parameters C, ΔS_R and D are log-normally distributed, T at failure is a random variable which can be expressed by the following equation

$$T = \frac{(-\ln p_R)^{m/\xi}}{F_w\,\Gamma\left(\frac{m}{\xi}+1\right)}\frac{C\,D}{\mu\,S_R^m} \qquad (7)$$

where

T	time to failure, in seconds
F_w	average wave frequency, in Hz
D	Miner sum at failure

and the probability of failure is given by

$$P_f = prob(T \le T_S) \qquad (8)$$

where

T_S required service time life in seconds

Different safety index formulations are available. The more commonly used is the Hasofer-Lind index, but at the time of its edition, the developers of the guidance note Ref [4] used the Cornell safety index β given by

$$\beta = \frac{\ln(\bar{T}) - \ln(T_S)}{Stdv[\ln(T)]} \qquad (9)$$

The probability of failure can be calculated by

$$P_f = \Phi(-\beta) \qquad (10)$$

where

$\bar{T}$	mean value of T calculated by (Eq. 7)
Stdv	standard deviation of $\ln(T)$
Φ	standard normal cumulative distribution function

Uncertainties

As we have seen, three factors in the equation (7), C - D - S_R , are considered random. The randomness character is represented by uncertainties expressed in terms of coefficient of variation CoV.

The CoV is the standard deviation of the parameter divided by the mean value

$$\mathrm{CoV(x)} = \frac{\mathrm{Stdv(x)}}{\overline{\mathrm{x}}} \qquad (11)$$

The CoV of the S-N curve, constant C, is directly obtained from the statistical analysis of the fatigue test data used to determine the mean S-N curve. The value is in general given or obtained from the S-N curve catalogues data. For example, Ref. [4] provides for butt or fillet welds made by automatic submerged or open arc process and non stop-start positions within their length

$$C_{mean} = 8.855\ 10^{12} \qquad \mathrm{Stdv(logC)} = 0.2041$$

The CoV of the Miner sum D obtained from the analysis of various sources and in Ref. [4] has been taken equal to 0.3.

The more delicate CoV to determine is the stress range S_R CoV as this parameter results from rather complex structural calculations. Following Wirshing Ref. [3], the stress range is expressed as the product of a random variable B by the deterministic calculated stress range S_R

$$S_R(\mathrm{random}) = \mathrm{B}\ S_R(\mathrm{deterministic}) \quad \text{with} \qquad \mathrm{B} = \Pi(\mathrm{B_i})$$

and the uncertainties on B are taken as the combination of the uncertainties of five main factors B_i. Table 1 provides the complete set of values considered by Ref. [4] for calculations.

Table 1 - *Main factors and uncertainties.*

Uncertain factors	**Means**	**CoV**
C	experimental	experimental
D	1	0.30
S_R	calculated	calculated
B_1 - sea states	0.90	0.4 - 0.6
B_2 - ship response on waves	0.85	0.1 - 0.3
B_3 - extreme loads	0.95	0.2 - 0.4
B_4 - FEM modelling	1.10	0.1 - 0.5
B_5 – workmanship	0.90	0.1 - 0.3

The uncertainties are assumed to follow a log normal distribution and so, noting V the CoV, the standard deviation of ln(*T*) is given by

$$Stdv\left[\ln(T)\right] = \sqrt{\ln\left[(1+V_D^2)\,(1+V_C^2)\,(1+V_B^2)\right]} \qquad (12)$$

where

$$V_B = \sqrt{\Pi(1+V_{Bi}^2)-1} \tag{13}$$

Design Context

With respect to a design office the probabilistic formulation presents at least two major difficulties

1. The results are expressed in term of probability of failure and not in stress or geometrical parameters: thickness, modulus, size
2. The format is implicit, there is no formula linking directly a scantling modification to the change in probability of failure.

The first point can be solved by the rules and regulations developed by the Classification Societies, but the second one is inherent in the method.

The second point implies that a first set of scantlings is determined by another explicit method and then adjust by an iterative approach to obtain the required safety level. The experience in R&D shows that such iterative process is rather long and not compatible with the time constraints of a design office, Ref. [6].

Therefore a better adapted approach to design has been developed using the semi-probabilistic format.

Semi-Probabilistic Format

The semi-probabilistic format aims to provide an explicit formulation of the structural element scantling, the safety margins of which being determined from local and global structure probabilities of failure.

Formulation

The semi-probabilistic format for ship design has been derived from civil engineering standards Ref. [7]. The formulation looks like the deterministic one, but every parameter is affected by a partial safety factor while the deterministic formulation has a unique global safety coefficient. For the fatigue verification of ship structure components, the formula becomes

$$\frac{D_f}{\gamma_D} \geq \frac{N_t}{\dfrac{C}{\gamma_C}} \frac{(\gamma_S \Delta S_R)^m}{(-\ln(p_R))^{m/\xi}} \mu \Gamma\left(\frac{m}{\xi}+1\right) \tag{14}$$

with the same parameters than in Eq. 4. The partial safety factors γ_D , γ_C , γ_S , respectively attached to D_f, C , S_R, are defined so that they are greater than 1.

The formulation appears very effective for the designers, easy to apply and allows to take into account the progresses in knowledge about the uncertainties or in building quality.

When the knowledge progresses with respect to the determination of a given parameter, the attached partial safety factor can be reduced. At the opposite, if return experience shows that the range of values of a parameter is underestimated by the design methods, the corresponding partial safety factor can be increased. In both cases the concerned partial safety factor can be adjusted without modification of the others.

Versus building, when the fabrication quality or when the general level of quality of the market is demonstrated better than the quality level considered when developing the rules, the partial safety factors attached to the concerned parameters can be decreased, also without modification of the others.

Therefore, the formulation allows targeted and precise tunings, which represent a great advantage with respect to the deterministic formulation in which a unique global safety coefficient groups all uncertainties, without knowing the weight of each of them.

Partial Safety Factors

The partial safety factors can be expressed versus the characteristics of the probabilistic distribution of the parameters (the standard deviation), the reference values of the parameters being their mean values. Introducing the coefficient of variation V, a partial safety factor can be written as follows

$$\gamma_i = 1 \pm k.V_i \qquad (15)$$

+ or - is selected whether the safe domain corresponds to greater or lower values of the parameter.

k is calculated by fixing the probability level corresponding to an acceptable level of risk, for example, k = 2 for a normal distribution and a probability of 0.975.

The method looks easy, but in reality it is more complex. All partial safety factors being fixed separately for each parameters as said above, the formulation must provide a uniform probability of failure equals the selected target for each structural component and also for the global structure, taking into account redundancies and common failure modes.

Rule Developer Challenge

This condition of a uniform level of safety, local and global, represents for the rule developer a real challenge. The partial safety factors cannot be determined only with respect to the uncertainties attached to each parameter.

The adjustment of the partial safety factors required a calibration procedure based on optimisation methods, according to the following the steps, Ref. [8]:

1. identification of structural classes and calibration points: ship types, ship characteristics, structural components, component position on board, ship loading conditions, environmental conditions;
2. definition of the limit state function format and stochastic modelling of the variables;
3. definition of a penalty function and constraints for optimisation, a function that expresses the difference between the obtained implicit reliability and the target reliability, in terms of safety index;
4. selection of the targeted reliability level: safety indexes, average whole structure target β_T, minimum acceptable individual β_{min},

5. calculation of the structural components scantling with the rule formula and fixed partial safety factors;
6. calculation of the safety indexes of each component and global using the determined scantling in step 5 above)
7. calculation of the penalty function with verification of the constraints; and
8. verification of the optimisation criteria, if not acceptable, determination of a new set of partial safety factors and restart in step 5 above).

This calibration process, for ship structure rules, is in fact very heavy due to the large number of welded details, type of ships, ship operation conditions, number of involved parameters in the formula. A calibration of the partial safety factors of the (Eq. 14) performed for one 292 000 tons tanker, Ref. [9] lead one to consider:

- Three structural welded details on deck in the midship region
- North Atlantic sea state conditions
- Eight wave incidences with equal probability
- Two ship speed versus wave height and incidence
- Two loading conditions, ballast and full load
- Uncertainties as defined in Table 1.

and required calculation of 136 sets of partial safety factors γ_i before obtaining a scatter band of the safety index values less than 5%.

This difficulty is increased by the fact that both factors, uncertainties and safety level, are, unfortunately today not standardised, and many options exists and are discussed in the R&D and engineering communities, Ref. [9].

Conclusions

During the last 30 years Research and Development has allowed development of appropriate probabilistic formulations and data for ship structures design, providing an important progress with respect to the deterministic approach.

In spite of the advantages, the probabilistic formulations present an implicit format of scantling, which is not easy to use and do not allow a direct scantling of the structural components as it is required during the ship project development.

To solve this difficulty, classification rules developers look for a semi-probabilistic format that provides scantling rules identical for their presentation than the classical deterministic format, but with the advantage of a clear identification of the safety margins attached to each variable.

As the partial safety factors are individually attached to each parameter involved in the design formula, it can be considered possible to take advantage of progresses reducing uncertainties or of improvements in building quality by reducing the concerned safety margin, without interfering with the others, which correspond to area without improvements.

Also, if return experience shows that the safety margin attached to a particular parameter has been underestimated, it will be possible to increase the corresponding partial safety factor without interfering with the others.

So the future for standards and design rules will be the semi-probabilistic format. The full probabilistic approach will remain the tool for rules developers, for return experience analysis and for semi-probabilistic rules calibration. The required progress needed concerns,

- the modelling of the different variable probability distributions,
- the determination of the mean and CoV values versus the origin of the data and design/building practices,
- the determination of the safety index of a large set of existing ship components associated with the in-service return experience.

References

[1] *Rules for the Classification of Steel Ships*, Bureau Veritas, June 2000

[2] **"Cyclic Fatigue of Welded Joints on Steel Ships"**, *Bureau Veritas Guidance Note NI 188*, Oct 1983 and *IIW/IIS doc XIII-1169-85*, 1985

[3] Whirshing, PH., **"Fatigue Reliability of Offshore Structures"**, *Journal of Structural Engineering*, Vol 110 (N°10), 1984

[4] **"Fatigue Strength of Welded Ship Structures"**, *Bureau Veritas Guidance Note NI 393 DSM R01 E*, July 1998

[5] Huther, M., Beghin, D., **"A fatigue strength guidance note for welded ship structure assessment"**, *IIW/IIS doc XIII-1724-98 & XV-992-98*, 1998

[6] Beghin, D., Huther, M., Parmentier, G., **"The probabilistic approach, a tool for ship rules improvement"**, *PRADS'92*, Newcastle, May 1992

[7] *International Recommendation for the Design and Building of Concrete Structure*, International Federation for Prestressing, European Concrete Committee, Second edition, 1976

[8] Mahérault, S., Huther, M., Parmentier, G., Recho, N., **"Semi-probabilistic fatigue calibration of partial safety factors"**, *IIW/IIS doc XIII-1794-99*, 1999

[9] Huther, M., Parmentier, G., Mahérault, S., Segrétain, JF., Cervetto, D., Dogliani, M., **"The use of results of R&D in probabilistic approaches"**, *NAV 2000 conferences*, Venice Sept 2000

Journal of ASTM International, September 2004, Vol. 1, No. 8
Paper ID JAI19031
Available online at www.astm.org

Tadeusz Łagoda,[1] *Ewald Macha,*[1] *and Adam Niesłony*[2]

Comparison of the Rain Flow Algorithm and the Spectral Method for Fatigue Life Determination Under Uniaxial and Multiaxial Random Loading

ABSTRACT: This paper presents the strain energy density parameter used for fatigue life calculation under random loading by two methods. The first method is based on schematization of energy parameter histories with the rain flow algorithm. The other one is based on moments of the power spectral density function of the energy parameter. The experimental data of fatigue tests of 10HNAP steel under constant amplitude and random uniaxial loading with non-gaussion probability distribution, zero mean value, and wide-band frequency spectrum used for comparison of the rain flow algorithm and the spectral method gave satisfactory results. Next, histories of the random stress tensor with normal probability distribution, wide-band frequency, and zero mean values corresponding to biaxial tension-compression, combined tension with torsion and triaxial loading with various correlation coefficients were generated, and the lifetime was calculated. It has been observed that both methods of fatigue life determination give almost the same results.

KEYWORDS: life time, biaxial stress, spectral method, strain energy density parameter, non-proportional loading, high cycle fatigue, rain flow algorithm, random loading

Introduction

The known algorithms for fatigue life estimation of machine elements and structures under random loading can be divided into two groups. One of them includes algorithms based on cycle counting. The other group includes algorithms based on spectral analysis of stochastic processes. In the first group, the loading is usually represented by time courses of stress or strain and in the other group by a frequency characteristic of these quantities with the use of the power spectral density function. Lately, the strain energy density parameter has been proposed for estimation of fatigue life under random loading [1 4]. The energy parameter includes information given by strain and stress histories, and it does not neglect the loading frequency characteristic. This parameter seemed to be efficient for fatigue life determination with the cycle counting algorithm [1,2,4]. We may ask if the strain energy density parameter can be applied in the spectral methods, where the power spectral density function plays the most important role.

This paper presents how to adapt the strain energy density parameter to the known spectral models of fatigue life determination under uniaxial stationary and non-Gaussian random loading using tests results of specimens made of 10HNAP steel [5,6].

Manuscript received 12 June 2002; accepted for publication 20 December 2002; published September 2004. Presented at ASTM Symposium on Fatigue Testing and Analysis Under Variable Amplitude Loading Conditions on 29 31 May 2004 in Tour, France; P. C. McKeighan and N. Ranganathan, Guest Editors.

[1] Professor, Technical University of Opole, Department of Mechanics and Machine Design, ul. Mikołajczyka 5, 45-271 Opole, Poland.
[2] Ph.D. Student, Technical University of Opole, Department of Mechanics and Machine Design, ul. Mikołajczyka 5, 45-271 Opole, Poland.

The strain energy density parameter in the critical plane is also used to compare the rain flow algorithm and the spectral method for a fatigue life estimation in high-cycle regime under a simulated random state of stress corresponding to biaxial tension-compression, combined tension with torsion, and general multiaxial non-proportional loading.

The Strain Energy Density Parameter

For the first time the strain energy density parameter for random loading has been defined by Łagoda at al. [1]. Under uniaxial random state of stress, the parameter distinguishes the strain energy density for tension (positive) and the strain energy density for compression (negative) as follows:

$$W(t) = \frac{1}{2}\sigma(t)\varepsilon(t)\frac{\mathrm{sgn}[\varepsilon(t)] + \mathrm{sgn}[\sigma(t)]}{2} \tag{1}$$

where $\sigma(t)$ and $\varepsilon(t)$ are random stress and strain histories, respectively, and functions $\mathrm{sgn}[\sigma(t)]$ and $\mathrm{sgn}[\varepsilon(t)]$ are introduced to respect signs of strain and stress at time t. When cyclic stress and strain reach the maximum values σ_a and ε_a, the amplitude of the energy parameter is

$$W_a = 0.5\sigma_a\varepsilon_a \tag{2}$$

Assuming $W(t)$ according to Eq 1 is the fatigue damage parameter, we can rescale the standard characteristic of cyclic fatigue ($\sigma_a - N_f$) and ($\varepsilon_a - N_f$) and obtain a new one, ($W_a - N_f$). In the case of high-cycle fatigue regime, when the characteristic ($\sigma_a - N_f$) is used, the axis σ_a should be replaced by $W_a = \sigma_a^2/(2E)$, i.e.

$$W_a = \frac{(\sigma'_f)^2}{2E}(2N_f)^{2b} \tag{3}$$

where σ'_f = axial fatigue strength coefficient, E = Young's modulus, N_f = number of cycles to failure, and b = exponent in fatigue relationships.

In [2], the strain energy density parameter in the critical plane has been used for generalization of some known energy criteria of multiaxial cyclic fatigue to the random loading.

The Methods of Fatigue Life Estimation Under Uniaxial Random Loading

From the methods based on schematization of stress histories we choose the rain flow algorithm and the Palmgren-Miner hypothesis of damage accumulation [6]. The lifetime T_{RF} according to the counted cycles at observation time T_o of stress history $\sigma(t)$, is determined from

$$T_{RF} = \frac{T_o}{\sum_{i=1}^{k}\left[n_i/\left(N_0\left(\sigma_{af}/\sigma_{ai}\right)^m\right)\right]} \quad \text{for} \quad \sigma_{ai} \geq a\sigma_{af} \tag{4}$$

where T_o = observation time, n_i = number of cycles with the amplitude of stress σ_{ai}, N_0 = number of cycles corresponding to the fatigue limit σ_{af}, $m = -1/b$ = slope of the Wöhler curve, and a =

0.5 = coefficient allowing to include amplitude below σ_{af} in the damage accumulation process.

From known spectral methods [7 9] we choose:

- Miles model [8] for narrow-band frequency processes

$$T_M = \frac{A}{M^+ (2\mu_\sigma)^{\frac{m}{2}} \Gamma\left(\frac{m+2}{2}\right)} \tag{5}$$

- and Chaudhury-Dover model [9] for wide-band frequency processes

$$T_{Ch\text{-}D} = \frac{A}{M^+(2\mu_\sigma)^{\frac{m}{2}}\left[\frac{\gamma^{m+2}}{2\sqrt{\pi}}\Gamma\left(\frac{m+1}{2}\right)+\frac{3\alpha}{4}\Gamma\left(\frac{m+2}{2}\right)\right]} \tag{6}$$

where T_M = lifetime in seconds, according to Miles model, $T_{Ch\text{-}D}$ = lifetime in seconds, according to Chaudhury-Dover model, $A = \sigma_a^m N_f$ = fatigue curve, $M^+ = \sqrt{\frac{\lambda_4}{\lambda_2}}$ = expected number of peaks in a time unit, $\mu_\sigma = \lambda_0$ = variance of the stress history $\sigma(t)$, $\gamma = \sqrt{1-\alpha^2}$ = coefficient of the spectrum width, $\alpha = \frac{\lambda_2}{\sqrt{\lambda_0 \lambda_4}}$ = coefficient of irregularity, $G_\sigma(f)$ = one-sided power spectral density function of stress history $\sigma(t)$, $\lambda_k = \int_0^\infty f^k G_\sigma(f)df$ = k[th] moment of power spectral density function, and $\Gamma(\,)$ = gamma function.

In the energy notation, Eqs 4 6 can be modified as follows:

$$T_{RF} = \frac{T_o}{\sum_{i=1}^{k}\left[n_i/\left(N_0\left(W_{af}/W_{ai}\right)^{m'}\right)\right]} \quad \text{for } W_{ai} \geq aW_{af}\,,\ a = 0.25 \tag{7}$$

$$T_M = \frac{A_W}{M^+(2\mu_W)^{\frac{m'}{2}}\Gamma\left(\frac{m'+2}{2}\right)} \tag{8}$$

$$T_{Ch\text{-}D} = \frac{A_W}{M^+(2\mu_W)^{\frac{m'}{2}}\left[\frac{\gamma^{m'+2}}{2\sqrt{\pi}}\Gamma\left(\frac{m'+1}{2}\right)+\frac{3\alpha}{4}\Gamma\left(\frac{m'+2}{2}\right)\right]} \tag{9}$$

where $W_{af} = \sigma_{af}^2/2E$ = fatigue limit according to the energy parameter, $A_W = W_a^{m'} N_f$ = energy fatigue curve, $m' = m/2$ = slope of the energy fatigue curve, and $M^+, \mu_W, \gamma, \alpha, \lambda_k$ = like in Eqs 5 and 6 but determined from the power spectral density function $G_W(f)$ of the energy parameter history $W(t)$.

Figure 1 shows the algorithms used for fatigue life estimation with the energy parameter according to two analyzed methods.

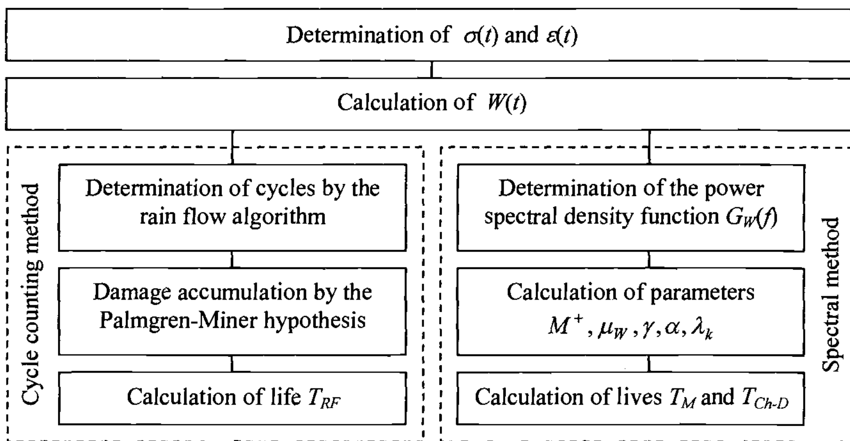

FIG. 1 *Differences and similarities between the algorithms applied for fatigue life calculation.*

Let us note that calculations using the rain flow counting algorithm, according to ASTM E 1049-85 Standard Practices for Cycle Counting in Fatigue Analysis (E 1049-85), are realized in the time domain, and calculations using the spectral method – by estimation of the power spectral density function of the energy parameter – are realized in the frequency domain.

Analysis of Fatigue Test Results

The results of fatigue tests of 10HNAP steel subjected to uniaxial constant amplitude cyclic and random tension-compression loading described in detail in [6] are analyzed. The material tested is a general-purpose structural steel with increased resistance to atmospheric corrosion and has the following composition: C – 0.115 %, Mn – 0.71 %, Si – 0.41 %, P – 0.0082 %, S – 0.028 %, Cr – 0.81 %, Ni – 0.5 %, Cu – 0.3 % and the rest – Fe. The mechanical parameters of 10HNAP steel are as follows: $R_m = 566$ MPa, $R_{0.2} = 389$ MPa, $A_{10} = 31$ %, $Z = 29.1$ %, $E = 215$ GPa, $\nu = 0.29$, $\sigma'_f = 994$ MPa, $b = -0.102$, $\sigma_{af} = 252$ MPa and $W_{af} = 0.147$ MJ/m^3 for $N_0 = 1{,}25 \times 10^6$ cycles. Under random uniaxial tension-compression loading, the tests were conducted for the zero expected value and several loading levels in the range from medium to long-life (see Table 1).

Figure 2 shows the probability density functions $f(\sigma)$ and $f(W)$ and power spectral density functions $G_\sigma(f)$ and $G_W(f)$ of stress $\sigma(t)$ and energy parameter $W(t)$, respectively.

We can see that $f(\sigma)$ is a four-modal non-Gaussian function (excess coefficient < −1, asymmetry coefficient ≈ 0, Fig. 2*a*), while $f(W)$ has values of excess and asymmetry similar to those for the normal probability distribution (excess ≈ 0, asymmetry ≈ 0, Fig. 2*b*). In this case, we can point out that the energy parameter is a more suitable quantity characterizing loading for the spectral methods which assume the normal probability distribution of loading [8,9]. From Figs. 2*c* and 2*d*, it appears that graphs of power spectral density functions of stress $G_\sigma(f)$ and energy parameter $G_W(f)$ have the same shapes. Thus, stress $\sigma(t)$ and energy parameter $W(t)$ are random processes with the same band frequencies.

TABLE 1 *Results of tests and calculations of life time obtained under uniaxial random loading.*

No.	σ_{max} * MPa	$\sigma_{a\,max}$ ** MPa	σ_{RMS} *** MPa	T_{exp} s	T_{RF} s	T_M s	$T_{Ch\text{-}D}$ s
1	292	297	132	111 954, > 327 225 > 327 225, > 327 225	227 460	74 210	183 920
2	312	311	140	72 004, 114 601 > 327 225, > 327 225	144 590	44 450	110 160
3	320	322	146	40 785, 54 150 145 654, 76 037	102 513	30 828	76 791
4	343	348	153	27 933, 76 908 32 918, 74 672	68 235	18 378	46 135
5	351	350	159	24 563, 34 586 53 382, 29 875	51 066	13 878	34 827
6	362	361	165	18 846, 21 013 28 584, 26 323	36 397	9 445	23 828
7	370	377	171	21 764, 9 713 28 116, 17 865	26 327	7 005	17 736
8	386	383	177	17 926, 18 035 24 993, 10 279	24 116	4 889	12 388
9	399	398	186	13 905, 18 379 5 695, 8 770	14 146	3 554	8 978

* σ_{max} = maximum value of stress $\sigma(t)$, **$\sigma_{a\,max}$ = maximum amplitude of $\sigma(t)$ after cycle counting by means of the rain flow algorithm,***σ_{RMS} = root mean square value of $\sigma(t)$.

The results of fatigue tests are compared with the results of calculations according to two analyzed methods using the energy parameter. Figures 3 and 4 include the points corresponding to the calculated life times T_{RF}, T_M, $T_{CH\text{-}D}$ and experimental lifetimes T_{exp}. The observation time T_o = 649 s, and its sampling time $\Delta t = 2.64 \cdot 10^{-3}$ s. The lives T_{RF}, Eq 7, are included in the scatter band coefficient 3 in relation to the experimental lives T_{exp}, such as for the tests with the constant amplitudes and can be accepted [6,8,9]. The lives calculated with the spectral methods are satisfactory for the Chaudhury-Dover model equation $T_{Ch\text{-}D}$, Eq 9, while the lives according to the Miles model T_M, Eq 8, are lower compared to the experimental ones and beyond the scatter band coefficient 3. It means that the Miles model is more sensitive than the Chaudhury-Dover model on type of probability distribution function of energy parameter and gives worse results for non-Gaussian narrow-band frequency process.

Finally, from the experimental data for the steel tested under uniaxial random loading with non-Gaussian probability distribution, zero mean value and wide-band frequency spectrum, we can conclude that the rain flow algorithm and the spectral method (the Chaudhury-Dover model) both gave satisfactory results in lifetime estimation when the strain energy density parameter is used.

The Methods of Fatigue Live Calculation Under Multiaxial Random Loading

Two methods of the fatigue life calculation under multiaxial random loading are compared by computer simulation. Histories of the random stress state components with normal probability distribution, wide-band frequency spectra, and zero expected values corresponding to biaxial tension-compression, combined tension with torsion and more complex loading with various correlation coefficients were generated. In the time domain the random stress state can be expressed by a six-dimensional stationary and ergodic vectorial process

$$\begin{aligned}\mathbf{X}(t) &= \left[X_1(t), \ldots, X_6(t)\right] = \boldsymbol{\sigma}(t) = \\ &= \left[\sigma_{xx}(t),\ \sigma_{yy}(t),\ \sigma_{zz}(t),\ \sigma_{xy}(t),\ \sigma_{xz}(t),\ \sigma_{yz}(t)\right]\end{aligned} \tag{10}$$

where $X_k = \sigma_{ij}(t)$, $(k = 1, \ldots, 6;\ i,j = x, y, z)$.

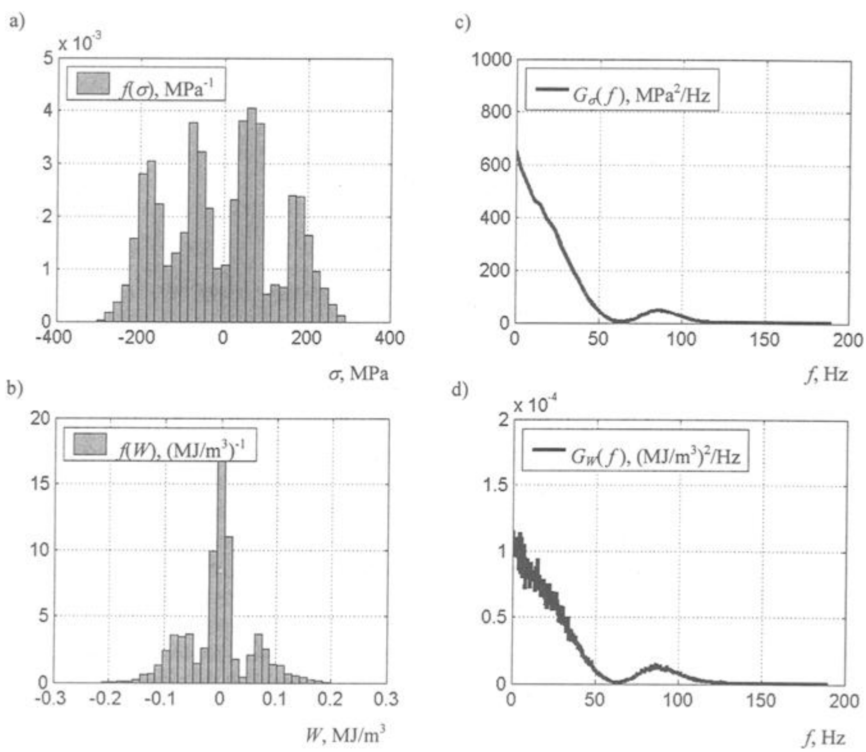

FIG. 2 *Probability density functions for* (a) *stress* $f(\sigma)$ *and* (b) *energy parameter* $f(W)$ *and power spectral density function of* (c) *stress* $G_\sigma(f)$ *and* (d) *energy parameter* $G_W(f)$.

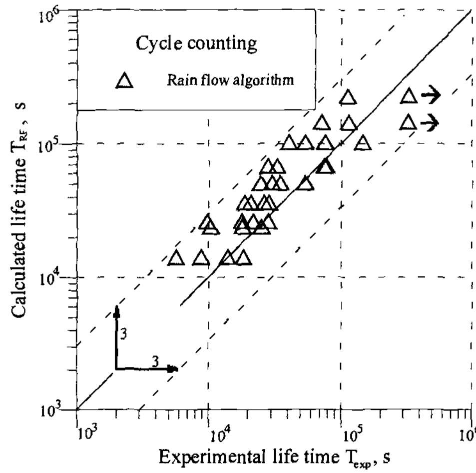

FIG. 3 *Comparison of calculated life T_{RF} according to cycle counting from energy parameter history W(t) with experimental life T_{exp} of 10HNAP steel under uniaxial non-Gaussian random loading.*

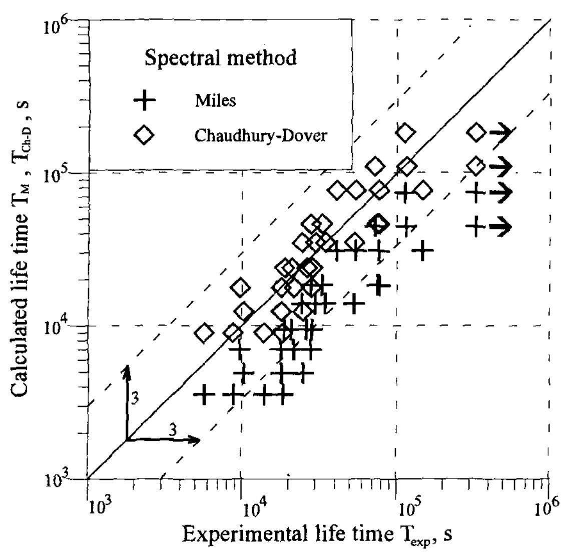

FIG. 4 *Comparison of calculated life T_M and T_{Ch-D} according to spectral methods based on energy parameter W(t) with experimental life T_{exp} of 10HNAP steel under uniaxial non-Gaussian random loading.*

The relations between stress state components are usually described by 6 × 6 dimensional covariance matrix

$$\mu_\sigma = \begin{bmatrix} \mu_{11} \cdots \mu_{16} \\ \vdots \ \ddots \ \vdots \\ \mu_{61} \cdots \mu_{66} \end{bmatrix} \tag{11}$$

In the frequency domain, the random stress state is characterized with the following matrix of power spectral density functions

$$G_\sigma(f) = \begin{bmatrix} G_{11}(f) \cdots G_{16}(f) \\ \vdots \ \ddots \ \vdots \\ G_{61}(f) \cdots G_{66}(f) \end{bmatrix} \tag{12}$$

Similarly, the random strain state can be expressed by a vectorial process

$$\begin{aligned} \mathbf{Y}(t) &= [Y_1(t), \ldots, Y_6(t)] = \boldsymbol{\varepsilon}(t) = \\ &= [\varepsilon_{xx}(t),\ \varepsilon_{yy}(t),\ \varepsilon_{zz}(t),\ \varepsilon_{xy}(t),\ \varepsilon_{xz}(t),\ \varepsilon_{yz}(t)] \end{aligned} \tag{13}$$

where $Y_k = \varepsilon_{ij}(t)$, $(k = 1, \ldots, 6;\ i,j = x, y, z)$.

To reduce the multiaxial stress state to the equivalent uniaxial one, the criterion of maximum normal strain energy density in the critical plane is used. This criterion has been successfully used for fatigue life calculation under biaxial non-proportional random tension-compression of cruciform specimens made of 10HNAP steel [1,2], Thus, for further analysis this criterion has been chosen. According to this criterion, the equivalent strain energy density is

$$W_{eq}(t) = W_\eta(t) = \frac{1}{2}\sigma_\eta(t)\varepsilon_\eta(t)\frac{\operatorname{sgn}[\varepsilon_\eta(t)] + \operatorname{sgn}[\sigma_\eta(t)]}{2} \tag{14}$$

where $\sigma_\eta(t)$ and $\varepsilon_\eta(t)$ are normal stress and strain on the critical plane, respectively, i.e.,

$$\begin{aligned} \sigma_\eta(t) &= l_\eta^2\sigma_{xx}(t) + m_\eta^2\sigma_{yy}(t) + n_\eta^2\sigma_{zz}(t) + 2l_\eta m_\eta\sigma_{xy}(t) + \\ &2l_\eta n_\eta\sigma_{xz}(t) + 2m_\eta n_\eta\sigma_{yz}(t) = \sum_{k=1}^{6} a_k\sigma_k(t) \end{aligned} \tag{15}$$

$$\begin{aligned} \varepsilon_\eta(t) &= l_\eta^2\varepsilon_{xx}(t) + m_\eta^2\varepsilon_{yy}(t) + n_\eta^2\varepsilon_{zz}(t) + 2l_\eta m_\eta\varepsilon_{xy}(t) + \\ &2l_\eta n_\eta\varepsilon_{xz}(t) + 2m_\eta n_\eta\varepsilon_{yz}(t) = \sum_{k=1}^{6} a_k\varepsilon_k(t) \end{aligned} \tag{16}$$

The unit vector $\overline{\eta}(l_\eta, m_\eta, n_\eta)$, normal to the critical plane, is defined by directional cosines l_η, m_η, n_η in relation to the constant system of axes Oxyz.

In the high-cycle fatigue regime where the plastic strain can be neglected, the equivalent strain energy density parameter according to Eq 14 may be simplified as follows:

$$W_{eq}(t)=\frac{\sigma_\eta^2(t)}{2E}\operatorname{sgn}[\sigma_\eta(t)] \tag{17}$$

The power spectral density function of the normal stress in the critical plane after Eq 15 can be calculated from the following formula [10]

$$\begin{aligned} G_{\sigma\eta}(f) &= \sum_{k=1}^{6}\sum_{l=1}^{6} a_k a_l G_{kl}(f) = \\ &= \sum_{k=1}^{6} a_k^2 G_{kk}(f) + 2\sum_{k<l}^{6} a_k a_l \operatorname{Re}[G_{kl}(f)] \end{aligned} \tag{18}$$

where $\operatorname{Re}[G_{kl}(f)]$ is the real part of the complex cross-spectral density function from matrix $G_\sigma(f)$, Eq 12.

It has been confirmed during many simulation calculations that power spectral density function of the equivalent strain energy density after Eq 17 may be determined by means of $G_{\sigma\eta}(f)$ as follows:

$$G_{W_{eq}}(f) \approx \frac{3}{4}\frac{\mu_{\sigma\eta}}{E^2} G_{\sigma\eta}(f) \tag{19}$$

where $\mu_{\sigma\eta}$ is a variance of the normal stress in the critical plane $\sigma_\eta(t)$ (see Eq 15).

Equations 18 and 19 enable one to reduce the multiaxial random stress state to the equivalent uniaxial one in frequency domain by the power spectral density functions of the stress state represented in matrix $G_\sigma(f)$, Eq 12.

For the first method, the simulation in the time domain started from generation of random stress state histories $\sigma_{ij}(t)$ and contained calculations of equivalent strain energy density $W_{eq}(t)$, Eq 17, schematization of $W_{eq}(t)$ history with rain flow algorithm, damage accumulation according to the Palmgren-Miner hypothesis, and life time T_{RF}, Eq 7, determination.

For the second method, the simulation in frequency domain started from a matrix of the power spectral density function of stress state components $G_\sigma(f)$, Eq 12, and ran through the calculations of power spectral density function of the normal stress $G_{\sigma\eta}(f)$, Eq 17, next power spectral density function of the equivalent strain energy density parameter $G_{Weq}(f)$, Eq 18, and life time determination according to the Chaudhury-Dover model, $T_{Ch\text{-}D}$, Eq 9.

In both methods the critical plane position, i.e., the directional cosines l_η, m_η, n_η of the unit vector $\bar{\eta}$, have been determined with use of the damage accumulation method [11]. According to that method, the plane of the maximum fatigue damage or minimum lifetime is the critical plane. To compare life time predicted using rain flow algorithm T_{RF} and spectral method $T_{Ch\text{-}D}$, the matrix of power spectral density functions $G_\sigma(f)$, Eq 12 has been determined from the same generated random stress state histories $\sigma_{ij}(t)$ used in both methods. Figure 5 shows the simulation flow chart of fatigue life calculation with the applied criterion of maximum normal strain energy density in the critical plane according to the rain flow algorithm and the spectral method. Two random states of stress have been generated: 1) with the same variances of stresses (see Table 2) and 2) with different variances of stresses.

Figure 6 shows an exemplary fragment of the generated history of stress $\sigma_{xx}(t)$, and Fig. 7 shows its histogram and one-sided power spectral density function $G_{11}(f)$.

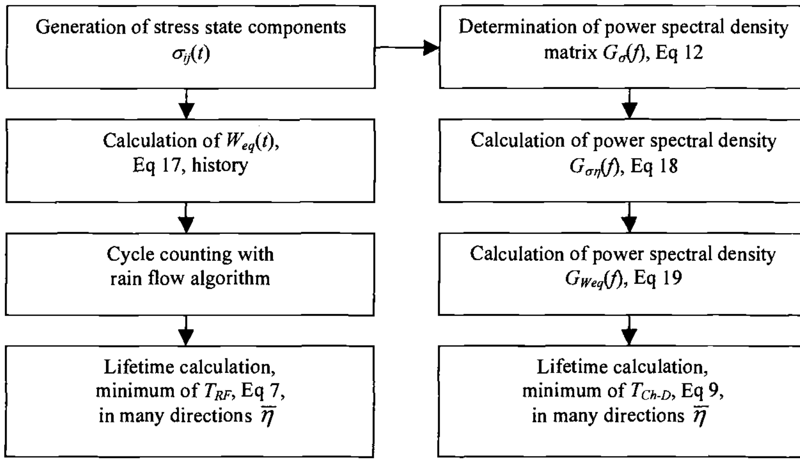

FIG. 5 *Flow chart of fatigue life calculation under multiaxial random loading according to rain flow algorithm and spectral method.*

TABLE 2 *Covariance matrix μ_σ, Eq 11 in MPa^2 of generated random stress state components.*

	xx	yy	zz	xy	xz	yz
xx	9 775.2	7.5	-7.4	-42.2	-77.7	85.7
yy	7.5	9 775.2	-334.2	-145.4	-99.4	-72.7
zz	-7.4	-334.2	9 775.2	358.3	-38.9	12.3
xy	-42.2	-145.4	358.3	9 775.2	31.1	140.5
xz	-77.7	-99.4	-38.9	31.1	9 775.2	175.4
yz	85.7	72.7	12.3	140.5	175.4	9 775.2

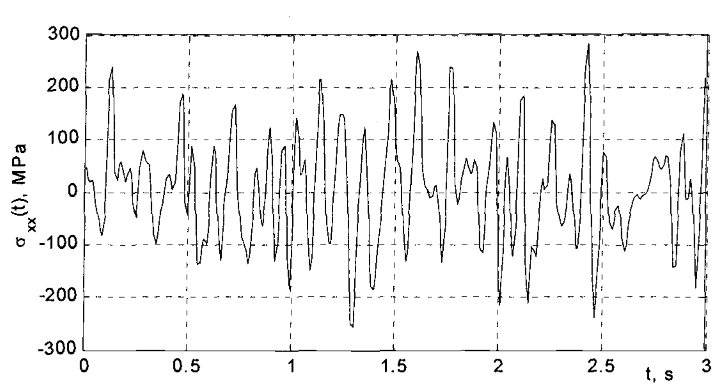

FIG. 6 *Fragment of the generated history of stress $\sigma_{xx}(t)$.*

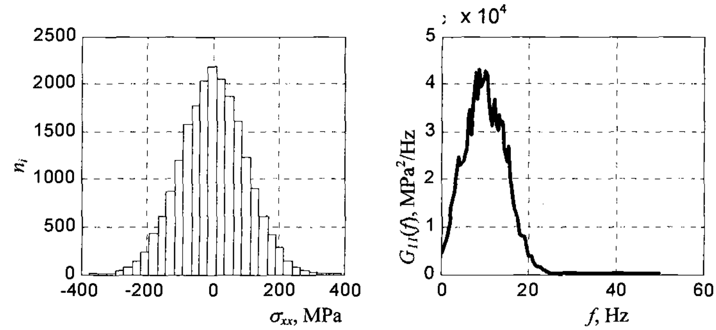

FIG. 7 *Histogram of the generated stress $\sigma_{xx}(t)$ and its power spectral density function $G_{11}(f)$.*

The fatigue life calculations have been done for 10HNAP steel and for three cases of stress state corresponding to biaxial tension-compression BTC [$\sigma_{xx}(t)$, $\sigma_{yy}(t)$], combined tension with torsion CTT [$\sigma_{xx}(t)$, $\sigma_{xy}(t)$], and triaxial tension with torsion TTT [$\sigma_{ij}(t)$]. The results of simulation are presented in Table 3 and Fig. 8.

TABLE 3 *Direction of critical plane $\bar{\eta}(l_\eta, m_\eta, n_\eta)$ and fatigue life in seconds according to the rain flow algorithm T_{RF} and spectral method $T_{Ch\text{-}D}$ for various multiaxial random states of stresses.*

Case of Loading	Rain Flow:	Algorithm:	Spectral:	Method:
	l_η	m_η	l_η	m_η
	n_η	T_{RF}	n_η	$T_{Ch\text{-}D}$
BTC[1] (a)[4]	0.004	0	1	0
	0.999	550 690	0	624 540
BTC (b)[5]	0.004	0	0.004	0
	0.999	215 940	0.999	266 120
CTT[2] (a)	-0.813	0	-0.818	0
	0.582	115 520	0.575	153 050
CTT (b)	-0.906	0	-0.906	0
	0.424	363 300	0.424	487 930
TTT[3] (a)	0.667	-0.707	0.680	-0.707
	0.235	14 864	-0.193	19 169
TTT (b)	0.600	-0.766	0.642	-0.766
	0.231	15 555	-0.022	17 829

[1] Biaxial tension-compression.
[2] Combined tension with torsion.
[3] Triaxial tension with torsion.
[4] Equal variances of stresses.
[5] Different variances of stresses.

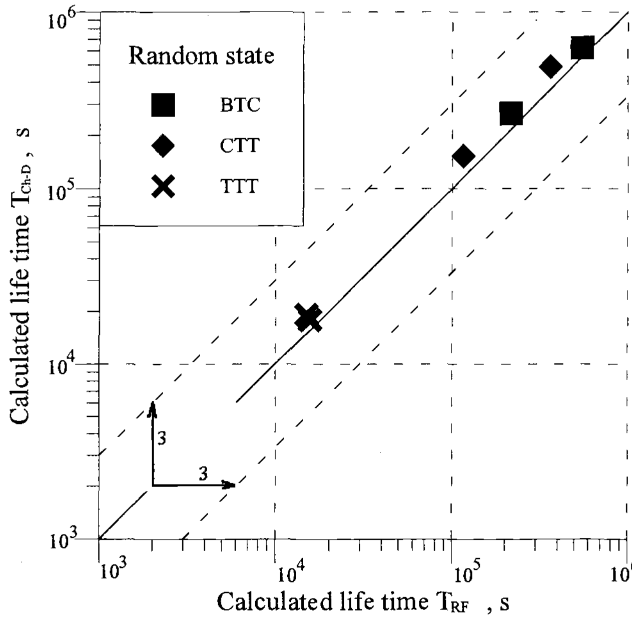

FIG. 8 *Comparison of fatigue lives, T_{RF} from the rain flow algorithm with, $T_{Ch\text{-}D}$ from spectral method for various multiaxial random states of stresses.*

It was observed that for biaxial tension-compression BTC (a) with equal variances of normal stresses $\mu_{11} = \mu_{22}$, two perpendicular critical planes occurred. From Table 3 and Fig. 8, it appears that directions of the critical planes, $\bar{\eta}$ and fatigue lives calculated according to the rain flow algorithm, T_{RF} and the spectral method, $T_{Ch\text{-}D}$ are very close together within acceptable distances. This result allows us to use the rain flow algorithm in time domain or the spectral method in frequency domain equally for life time estimation under multiaxial random loading.

Conclusions

1. The strain energy density parameter defined for random loading may be efficiently applied for lifetime calculation both in the time domain based on the rain flow algorithm and in the frequency domain based on spectral method.
2. The experimental data of fatigue tests of 10HNAP steel under constant amplitude and random uniaxial loading with non-Gaussian probability distribution, zero mean value, and wide-band frequency spectrum used to compare the rain flow algorithm and the spectral method gave satisfactory results.
3. It is observed that the Chaudhury-Dover model for fatigue life calculation is less sensitive than the Miles model to type of probability distribution function of energy parameter and gives better results when some distance from Gaussian narrow-band frequency process appears.
4. From simulation analysis under multiaxial random state of stresses corresponding to biaxial tension-compression, combined tension with torsion and triaxial loading with

various correlation coefficients, it results that the rain flow algorithm and spectral method can be used equally for life time estimation, giving very similar results.

Acknowledgments

This paper was partially realized within the research project PB -1204/T07/2000/19, financed by the State Committee for Scientific Research in 2000-02 and NATO Advanced Fellowships Programme 1|J|2000.

References

[1] Łagoda, T., Macha, E., and Będkowski, W., "A Critical Plane Approach Based on Energy Concepts: Application to Biaxial Tension-Compression High-Cycle Fatigue Regime," *International Journal of Fatigue*, Vol. 21, No. 5, 1999, pp. 431 443.

[2] Łagoda, T., and Macha, E., "Generalization of Energy Multiaxial Cyclic Fatigue Criteria to Random Loadings," *Multiaxial Fatigue and Deformation: Testing and Prediction, ASTM STP 1387*, S. Kalluri and P. J. Bonacuse, Eds., ASTM International, West Conshohocken, PA, 2000, pp. 174 190.

[3] Łagoda, T., "Energy Models for Fatigue Life Estimation Under Random Loading – Part I – The Model Elaboration," *International Journal of Fatigue*, Vol. 23, No. 6, 2001, pp. 467 480.

[4] Łagoda, T., "Energy Models for Fatigue Life Estimation Under Random Loading – Part II – Verification of the Model," *International Journal of Fatigue*, Vol. 23, No. 6, 2001, pp. 481 489.

[5] Lachowicz, C., Łagoda, T., and Macha, E., "Comparision of Analytical and Algorithmical Methods for Fatigue Life Time Estimation of 10HNAP Steel Under Random Loadings," Fatigue '96, Proc. 6IFC Berlin, G. Lutjering and H. Nowack, Eds., Pergamon 1996, Vol. I, pp. 595 600.

[6] Lachowicz, C., Łagoda, T., Macha, E., Dragon, A., and Petit, J., "Selections of Algorithms for Fatigue Life Calculation of Elements Made of 10HNAP Steel Under Uniaxial Random Loadings," *Studia Geotechnika et Mechanica*, Wrocław University of Technology (Poland), Vol. XVIII, Nos. 1 2, 1996, pp. 19 43.

[7] Liu, H. J. and Hu, S. R., "Fatigue Under Non-normal Random Stresses Using Monte-Carlo Method," FATIGUE' 87, R. O. Ritche and E. A. Starke, Jr., Eds., EMAS (U.K.) 1987, Vol. III, pp. 1439 1448.

[8] Miles, J., "On the Structural Fatigue Under Random Loading," JAS, Vol. 21, No. 11, 1954, pp. 753 762.

[9] Chaudhury, G. K. and Dover, W. D., "Fatigue Analysis of Offshore Platforms Subject to Sea Wave Loadings," *International Journal of Fatigue*, Vol. 7, No. 1, 1985, pp. 13 19.

[10] Bendat, J. S. and Piersol, A. G., "Engineering Application of Correlation and Spectral Analysis," John Wiley and Sons, Inc., New York, 1980.

[11] Macha, E., "Simulation Investigation of the Position of Fatigue Fracture Plane in Materials with Biaxial Loads," Mat. –wiss. u. Werkstofftech., WCH Verlagsgesellschaft mbH, D-6940 Weinheim (Germany) 20, 1989, Heft 4/89 pp. 132-136, Heft 5/89 pp. 153 163.

Journal of ASTM International, Nov./Dec. 2004, Vol. 1, No. 10
Paper ID JAI19035
Available online at www.astm.org

Gerhard Fischer[1]

Validation of Complex Wheel/Hub Subassemblies by Multiaxial Laboratory Tests Using Standardized Load Files

ABSTRACT: For the evaluation of safety components like the wheel/hub subassembly, the operational loading, including special event loading as well as the influence of adjacent components and their interaction, must be taken into account. By using the described test procedure in the Biaxial Test Facility, all service-like deformations can be simulated in accelerated program tests. A reliable time, as well cost, saving validation of new designs, materials, and manufacturing technologies can be carried out.

KEYWORDS: wheel/hub subassembly, multiaxial loading, variable amplitude testing, Eurocycle load program

Introduction

The complex design of modern wheel/hub systems for cars and commercial vehicles (Figs. 1 and 2) comprising wheel, hub, brake, bearing, spindle, and hub carrier, including their fasteners and different materials, treatments, and press-fits, requires appropriate testing procedures. The variable loading conditions, caused by operational wheel forces and superimposed brake and torque moments, may result in additional time-varying tolerances and press-fits during operation and, consequently, in different damage mechanisms.

Simplified test principles with constant amplitude loading, such as ISO 3894, SAE J 267a, or others, are no longer meeting lightweight design demands, considering the European product liability legislation for safety components. Besides restriction of the clamping modes and load transfer, the sinusoidal stress amplitudes often create damage mechanisms that are not comparable to real service stresses.

Test Procedure and Results

The validation of the rotating components is carried out in the Biaxial Wheel/Hub Test Facility (Fig. 3, [1 3]) under the standardized, multiaxial load file Eurocycle (Fig. 4, [1 3]). The accelerated test life of 8000 10 000 km for cars and 16 000 20 000 km for commercial vehicles represents the customer usage conditions for a design life of $3 \cdot 10^5$ km to $1 \cdot 10^6$ km, including statistical considerations. By using original components during testing, the influence of different stiffness, wear, bolt pretension, etc. on the fatigue life is also taken into account.

Manuscript received 12 April 2002; accepted for publication 22 October 2003; published November 2004.
Presented at ASTM Symposium on Fatigue Testing and Analysis Under Variable Amplitude Loading Conditions on 29 31 May 2002 in Tours, France; P. C. McKeighan and N. Ranganathan, Guest Editors.

[1] Doctor, Stress Analysis and Strength Evaluation, Fraunhofer Institute for Structural Durability LBF Bartningstrasse 47, D-64289 Darmstadt, Germany, e-mail: fischer@lbf.fhg.de.

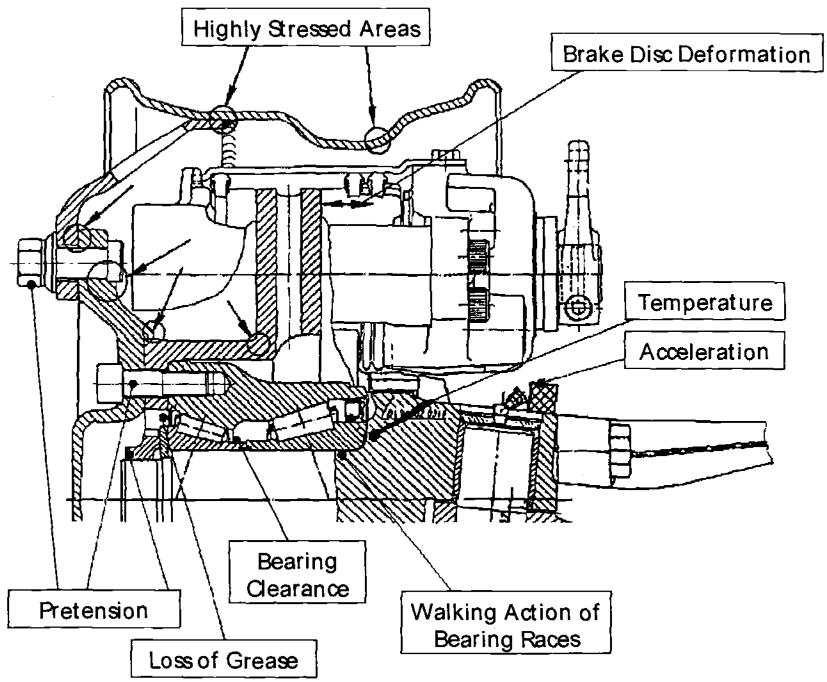

FIG. 1 *Front hub design of commercial vehicles and possible failure modes.*

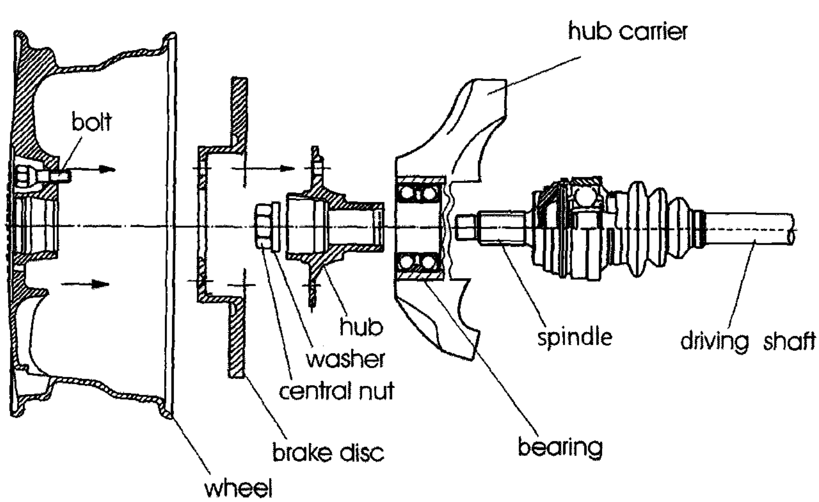

FIG. 2 *Driven wheel/hub components of cars.*

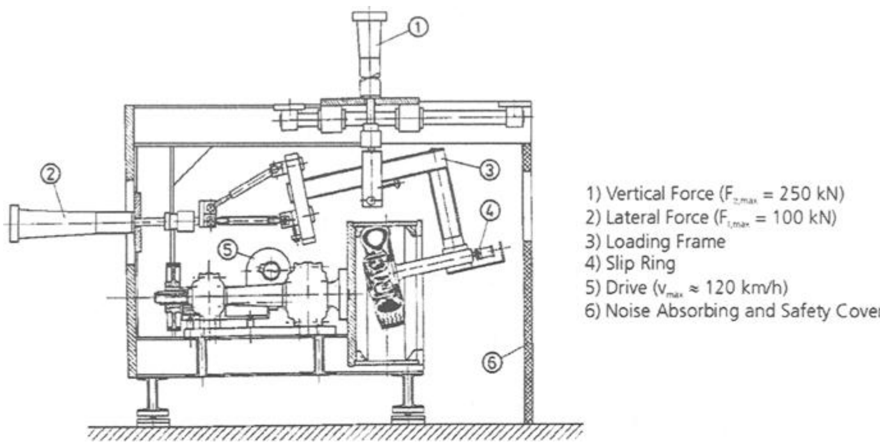

FIG. 3 *Test principle of biaxial wheel/hub test facility for proof of wheel-hub-subassemblies.*

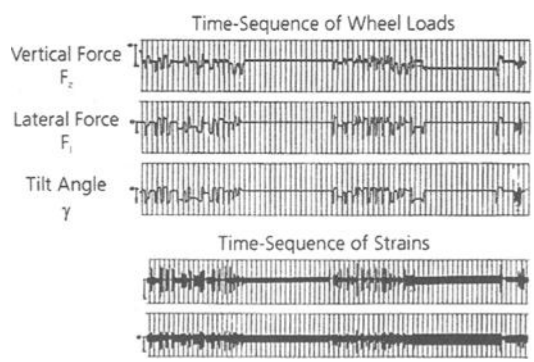

FIG. 4 *Time-sequence of the load proram-Eurocycle in the biaxial wheel/hub test facility, cycles per lap (65 km): H > 10^7, depending on wheel size.*

The computer stored load file may be adapted to different rated wheel loads and vehicle types in advance, before vehicle prototypes become available for load measurements. The design and test spectra, including the Woehler- and Gassner-Curves, are shown in Fig. 5, as examples of commercial vehicle hubs made from cast nodular iron. Both spectra correlate well to service measurements on a round track on public roads and a severe proving ground. After many load program tests, different damaging influences and resulting allowable maximum stress amplitudes were derived (Fig. 6).

These values differ significantly from those derived from constant amplitude tests on specimens. The maximum peak value of the stress spectrum may exceed the component's "endurance limit" by a factor up to 2, depending on the individual spectrum parameters, as well as the stress concentration, pre-stress, stress-state, etc. The allowable stresses also consider the reduction of bolt pretension and fretting fatigue between contacting components at a high number of cycles.

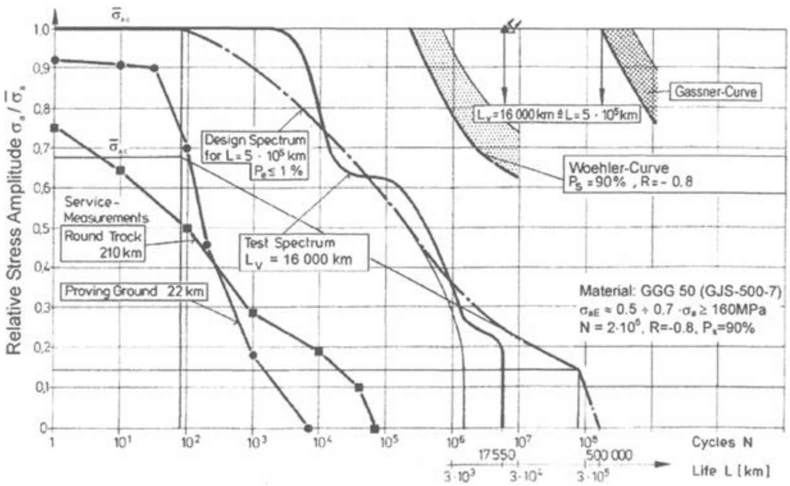

FIG. 5 *Stress spectra for highly stressed hub areas and test results.*

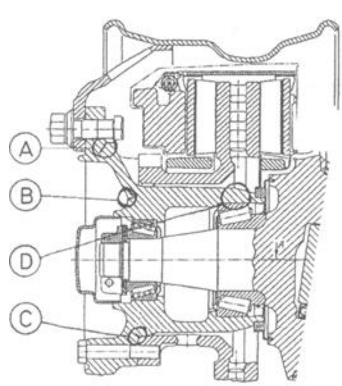

Highly Stressed Areas	Damaging Influence	Allowable Peak Value of the Spectrum
A (machined)	• Pre-stress • Notch effect • Fretting corrosion	$\bar{\sigma}_a \approx \pm 360$ MPa ($\bar{R} \approx 0{,}1$)
B (non machined)	• Notch effect	$\bar{\sigma}_a \approx \pm 320\text{-}350$ MPa ($\bar{R} \approx -1$)
C (machined)	• Pre-stress • Temperature • Notch effect • Fretting corrosion	$\bar{\sigma}a \approx \pm 450\text{-}500$ MPa ($\bar{R} \approx -1{,}5$)
D	• Pre-stress • Fretting corrosion	• required press - fit ΔD = 80-120 μm *)

Material: GGG 50 (EN-GJS-500-7) Design Life: 5 x 10^5 km
Parameters of Spectrum: $\beta \leq 0{,}2$; $\sigma_{a,c} / \sigma_{a,s} \leq 0{,}7$
*)Surface Pore Diameter: $\leq 0{,}5$mm

FIG. 6 *Highly stressed areas of a hub with disc brake and allowable peak stresses.*

Caused by the variety of different, superimposed damage mechanisms, a reliable life estimation is only possible through the described service-like simulation. This is also demonstrated by typical failures on cast nodular iron hubs shown in Fig. 7. The initial cracks start not only from the highly stressed flange radius (A) but also from the lower stressed bearing seat (C), caused by reduced allowable stresses due to surface pores (B) and walking actions of the outer bearing race.

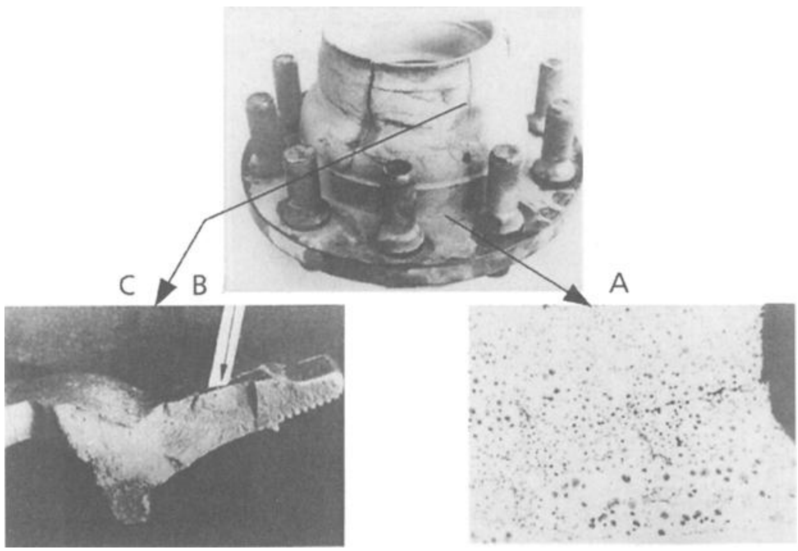

FIG. 7 *Fatigue damage on a cast nodular iron hub for dual wheels.*

The validation testing of modern light alloy car wheels is carried out under the corresponding load file for passenger cars, using the same procedure. The test requirement of 7500 km should be fulfilled without any crack. After 10 000 km, short initial cracks are allowed in specified wheel locations. At 15 000 km, the wheel function should still exist without significant damage in order to guarantee a minimum safety margin. Additional metallurgical investigations allow the study of crack propagation rate in critical areas in order to determine the safety margin of a design to the final rupture (Fig. 8). The fatigue striations of the cracked wheel spoke represent each individual load case of the load file Eurocycle.

Light alloy car wheels with wide rims and low profile tires are also endangered by seldom occurring "special event" loadings while driving over curbstones or through potholes. Such loads may cause local plastic deformations on the rim flange and consequently lead to fatigue cracks due to unbeneficial residual stresses (Fig. 9).

The influence of such special event loading, in conjunction with multiaxial load program testing, on the design of rim flanges for light alloy wheels is described in Fig. 10.

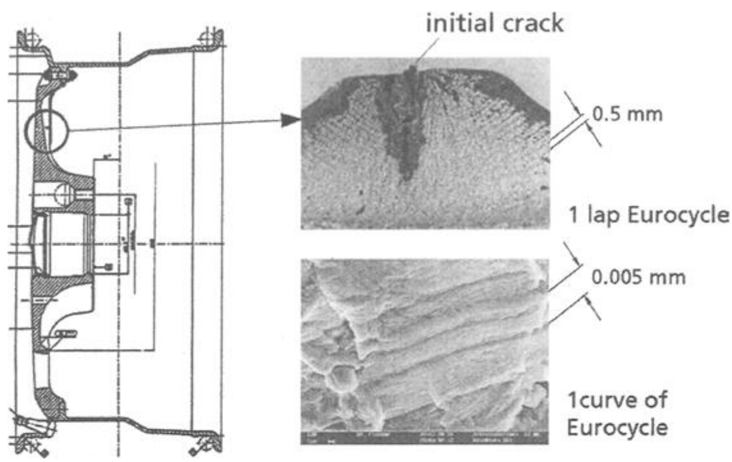

FIG. 8 *Fracture surface after Eurocycle program testing on a forged aluminium wheel disc.*

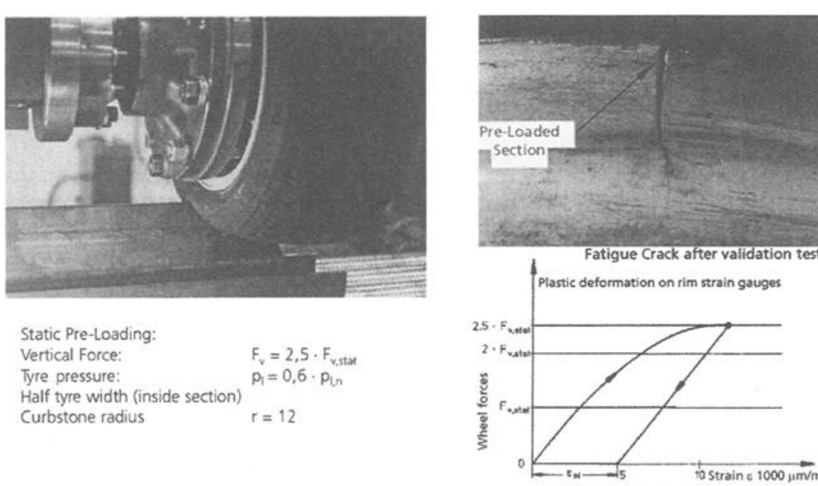

FIG. 9 *Procedure for static pre-loading of wheels.*

Design	Weight [kg]	Plastic Deformation Δ D [mm]	Durability Test Life [km]
A	10.9	- 0.85	cracks at 4 979 ≈ 0.5
B	11	-0.55	cracks at 10 141 ≈ 1.0
C	11.35	-0.35	without cracks 14 920 >1.5

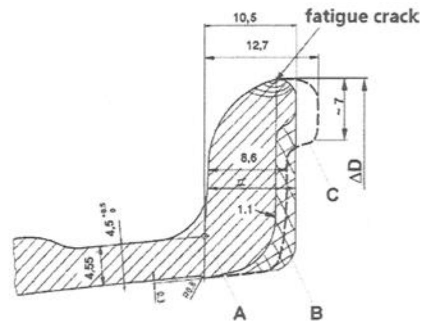

FIG. 10 *Influence of the rim design on plastic deformation and durability life.*

Based on the previous design A, the high plastic deformation and early fatigue cracks on the inner rim flange could be avoided by optimizing the rim design. Wheel design B showed a significant but not sufficient improvement. Design C passed the test requirement without failure and an acceptably low plastic deformation of $\Delta D = -0{,}35$ mm after pre-loading. The slight weight increase of 4 % from design A to C resulted in an increased durability life of more than a factor of 3.

A fatigue life evaluation based only on local stress maxima, disregarding the nominal stress and stress state, can lead to false conclusions and should be validated by a service-like simulation. As an example, the results of a durability approval on a cast aluminium wheel 6 J × 14 (Gk-AlSi12Mg) are presented. Caused by the design, a relatively high maximal local stress of $\sigma_a = \pm$ 135 MPa in the connection between disc and rim on the cooling hole occurs (Spot A_1, Fig. 11), whereas the nominal stress in this section is relatively low, being primarily bending. At area B, the local surface stress on the inner side is about 30 % lower compared to spot A_1, but the nominal stress level is higher because in this section primarily tensile or compressive stresses occur during wheel rolling.

The stress time histories, the analyzed stress spectra, and failure mode development at both areas A_1 and B_1 are plotted in Fig. 12. Initial cracks of approximately 1 mm length were registered in area A, after about 1/3 of the total test life. After 2/3 of the total test life, cracks also occurred in area B. But the crack propagation rate was much higher in area B compared to area A, because of the already mentioned stress state. Finally, the tests were terminated because of the high global wheel deformation due to very deep cracks in area B (see Fig. 11), while the cracks in area A were almost stopped after having achieved a length of 4 mm to maximal 6 mm. The calculated fatigue life up to initial cracks, based on an allowable damage $D \approx 0.5$, coincided well to the experimental results for both areas A and B (Fig. 12). These results allow the conclusion that the improvement and redesign of the wheel in area B is more important than in area A; nevertheless, the local stress in area A is 30 % higher.

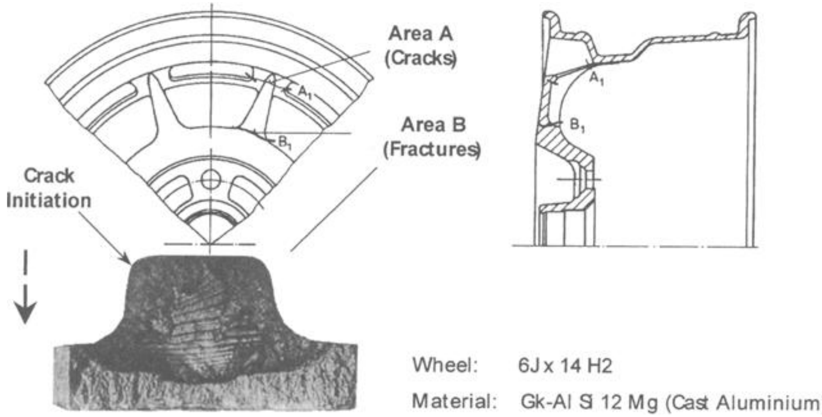

FIG. 11 *Fracture on a passenger car wheel under program tests in the biaxial wheel/hub test facility.*

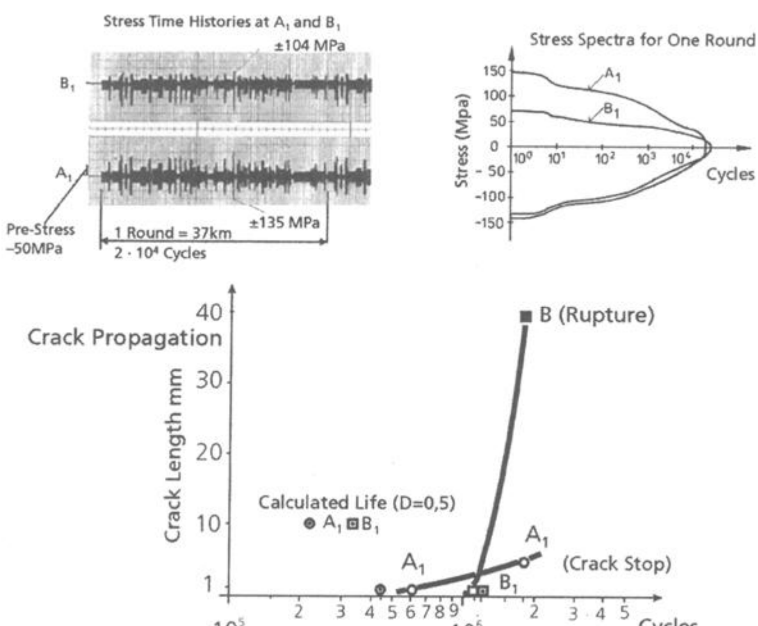

FIG. 12 *Stress-time histories, their spectra, and fatigue life at a cast aluminium wheel (Gk-AlSi12Mg).*

The validation of driven wheel/hub components, as shown in Fig. 2, requires a special test principle and extended load file representing additional brake and torque simulation. The test principle, shown in Fig. 13, allows the use of the original wheel brake and an additional brake disc for simulation of the driving torque. The standardized load file Eurocycle is completed by acceleration and braking operations which are simulated in different driving situations like straight, cornering, and reverse driving (Fig. 14).

With this simulation, influences caused by torque cycles and increased brake temperature on wear, function, and fatigue of bearings, fasteners, and press-fitted joints also are investigated. Consequently, different test requirements are resulting, depending on each damage mechanism. The test program was validated by various car components in relation to proving ground tests and customer usage experience. The adjustment of test parameters is made possible based on vehicle data already in the development phase.

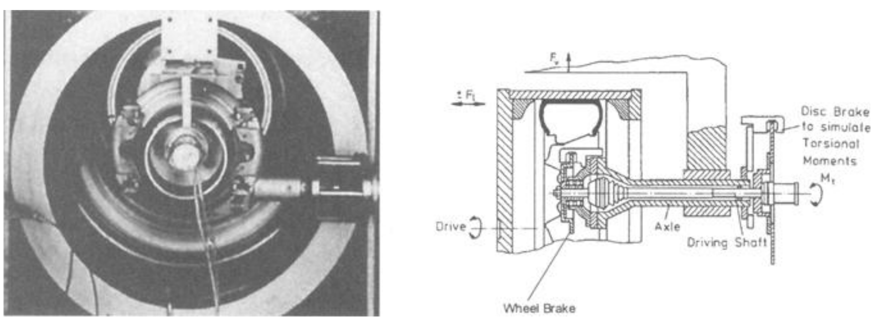

FIG. 13 *Principle of additional brake and torque simulation.*

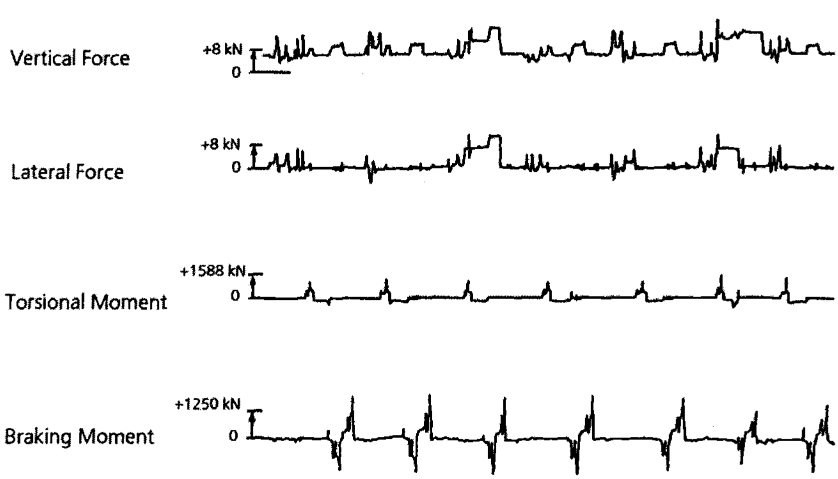

FIG. 14 *Load program Eurocycle for driven wheels and hubs (1 lap = 30 km).*

Conclusion

For the evaluation of safety components like the wheel/hub subassembly, the operational loading, including special event loading as well as the influence of adjacent components, must be taken into account.

By using the described test procedure in the Biaxial Test Facility, all service-like deformations can be simulated in accelerated program tests. A reliable time, as well cost, saving validation of new designs, materials, and manufacturing technologies can be carried out. The results of experimental analysis also serve as input data for the optimization of numerical methods. The procedure presented was introduced by German car producers as test specification and is in preparation as SAE Test Specification (SAE J 2562).

References

[1] Fischer, G. and Grubisic, V., "Design Criteria and Durability Approval of Wheel Hubs," SAE Technical Paper Series 982840.

[2] Grubisic, V. and Fischer, G., "Methodology for Effective Design Evaluation and Durability Approval of Car Suspension Components," SAE Technical Paper Series 970094.

[3] Fischer, G., Hasenmaier, W., and Grubisic, V., "Proof of Wheel Fasteners by Multiaxial Tests in the Biaxial Wheel Test Rig," SAE Technical Paper 1999-01-0781.

Journal of ASTM International, September 2004, Vol. 1, No. 8
Paper ID JAI19040
Available online at www.astm.org

Alexis Banvillet,[1] *Thierry Palin-Luc,*[1] *and Jean-François Vittori*[2]

Fatigue Life of a SG Cast Iron under Real Loading Spectra: Effect of the Correlation Factor Between Bending and Torsion

ABSTRACT: This paper deals with the effect on life of the desynchronism between two variable amplitude load sequences in combined bending and torsion. Experiments were carried out on smooth specimens made of the EN-GJS800-2 cast iron. The comparison between experimental lives and predicted ones with the following fatigue life calculation methods is presented: Smith-Watson-Topper, Fatemi and Socie (method proposed by Bannantine), Wang and Brown, Socie's proposal for high cycle fatigue, and Morel. If the scatter of experiments is considered, these experiments show a low effect of the correlation factor on life. All the simulated fatigue life calculation methods give good results for proportional loads, but their predictions are not good for non-proportional loads. Morel's proposal seems to be the best to predict life of the tested material with our non-proportional fatigue test conditions.

KEYWORDS: variable amplitude, multiaxial fatigue, correlation factor, life prediction, non-proportional loading

Nomenclature

$C_{Mt,Mb}$	Correlation factor between *Mb* and *Mt*
E	Young modulus
G	Shear modulus
Kt	Theoretical stress concentration factor
Mb, Mt	Bending and torsion moment
N_f	Number of cycles to fatigue crack initiation
S_{Mb}, S_{Mt}	Standard deviation of *Mb*, respectively *Mt*
$T_{\sigma,\, RMS}$	Root mean square value of the macroscopic resolved shear stress amplitude
b, b_0	Normal and shear fatigue strength exponent
c, c_0	Normal and shear fatigue ductility exponent
k_1	Material parameter used by Fatemi and Socie
k_2	Material parameter used by Socie
p, q, r	Parameters of the Morel method
s	Material parameter used by Wang and Brown
γ_a	Shear strain amplitude

Manuscript received 23 April 2002; accepted for publication 21 November 2002; published September 2004. Presented at ASTM Symposium on Fatigue Testing and Analysis Under Variable Amplitude Loading Conditions on 29 31 May 2002 in Tours, France; P. C. McKeighan and N. Ranganathan, Guest Editors.

[1] Ph.D. Student (now Dr.) and Senior Lecturer, respectively, ENSAM-Laboratoire Matériaux Endommagement Fiabilité et Ingénierie des Procédés (EA 2727), Esplanade des Arts et Métiers, F-33405 Talence Cedex, France.
[2] Engineer, RENAULT, Technocentre, Dir. Ingénierie des Matériaux, Sce 64130, API: TCR LAB 035, 1 Av. Golf, F-78288 Guyancourt, France.

$\varepsilon_{n,a}$	Strain amplitude normal to the critical plane
ε_f', γ_f'	Normal and shear fatigue ductility coefficient
ν_e, ν_p	Elastic Poisson coefficient, respectively plastic
$\sigma_{n,max}$, $\sigma_{n,mean}$	Maximum and mean normal stress on the critical plane
σ_f', τ_f'	Tensile and shear fatigue strength coefficient
τ_a	Shear stress amplitude experiencing on the critical plane
τ_{lim}	Shear stress treshold of non plastic flow in the Morel model

Introduction

Fatigue life prediction of materials and components under variable amplitude loading, especially under multiaxial stress states, is always an open question. Indeed, many components of a car or a plane, for instance, are loaded by variable amplitude sequences generating multiaxial stress states. There is not a general agreement on the life calculation method able to predict life in such non-proportional load conditions. The aim of this paper is to investigate the effect on life of the desynchronism between two variable amplitude load sequences in combined bending and torsion. The material tested is the EN-GJS800-2 cast iron, and the loading sequences are coming from service records. The comparison between predicted and experimental lives is done for the following fatigue life calculation methods: Smith-Watson-Topper [1], Fatemi and Socie [2] (method proposed by Bannantine [3,4]), Wang and Brown [5,6], Socie's proposal for high cycle fatigue [7], and Morel [8, 9].

In the first section of this paper, test conditions, experiments, and fatigue data are detailed. In the second section, fatigue life calculation methods are described briefly with their simulation conditions. Then, fatigue data and life predictions are compared and discussed.

Experiments

Material and Specimens

All experiments were carried out on smooth specimens (Kt(bending) = 1.07, Kt(torsion) = 1.04) made of the EN GJS 800-2 spheroidal graphite cast iron. These specimens are illustrated in Fig. 1. The microstructure of this material has a bull's eye appearance: the spheroids of graphite are surrounded by ferrite; spheroids and ferrite zone are included in a pearlitic matrix. After the treatment of heating and holding at 920°C for 1 2 h, slow cooling at 870°C for 3 4 h, then air cooling, the main mechanical characteristics of this cast iron are as follows: Young's modulus = 164.9 GPa, Poisson's ratio = 0.275, Proof (0.02 %) stress = 320 MPa, Proof stress (0.2 %) = 462 MPa, maximum tensile strength = 795 MPa, elongation after failure = 9 %, endurance limit in fully reversed plane bending = 294 MPa, endurance limit in fully reversed torsion = 220 MPa. This is the same material as used by Palin-Luc et al. [10] (see this reference for other details).

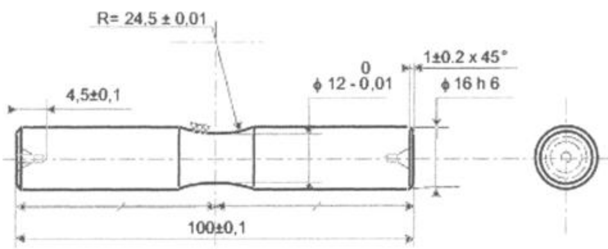

FIG. 1 *Specimen geometry (dimensions in mm).*

Fatigue Testing Machine

Fatigue tests were carried out with a closed-loop servo-hydraulic multiaxial fatigue testing machine designed in our laboratory and able to impose simultaneous bending and torsion moments [11]. The time evolution (i.e., shape) of the loading signal is servo-controlled in real time on each actuator (bending and torsion) together with the synchronism between each loading signal. This means that the evolution of the bending and torsion moments versus time is controlled and equal to the recorded sequence; the servo-control precision is ± 2.5 Nm. Thus, the power spectral density (PSD) of the loading applied on the specimen is very close to the PSD of the recorded sequence [12]. The peaks and valleys of the sequence are also servo-controlled. It must be pointed out that if only the peaks and valleys of the signal were servo-controlled, the PSD of the load signal and its time evolution would not have been like the recorded sequence. The loading sequence was repeated until fatigue macro-crack initiation, which was detected by a 10 % drop of the specimen stiffness. The size of the detected fatigue crack for random sequences is approximately 2 mm in depth on the specimen [12].

Loadings

Experiments were carried out in four point plane bending, in torsion and in combined plane bending and torsion under a random loading sequence (Fig. 2) recorded from strain gauges stuck on a car suspension arm. This sequence, representing a special type of road, is short in time (20 s); nevertheless this is representative of a real severe loading spectrum. A signal analysis of the total recorded sequence (34 s equivalent to a road of 200 m in length) shows that the bandwidth of this signal is 50 Hz (Fig. 3), and its "correlation length" (minimum time window for stationary conditions) is around 1 s, which is very short compared with 20 s. One can conclude that the 20 s of the sequence are long enough to be representative (for a spectral point of view) of the total sequence. The loading applied to the specimens is thus stationary and "pseudo-random." This sequence was applied on the specimens with a null mean value.

The load sequence is Gaussian, as shown in Fig. 4. Its mean value is very close to zero, and the standard deviation of the normalized load is around 0.32.

This short sequence contains around 370 cycles according to the Rainflow cycle counting method (AFNOR standard NF03-406, "Fatigue sous sollicitations d'amplitude variable. Méthode Rainflow de comptage"). The cycles with the highest amplitude are distributed around a zero mean value (Fig. 5). Nevertheless, there are some low amplitude cycles with a great mean value. This kind of loading could discriminate the correction of mean value proposed by the different life calculation methods.

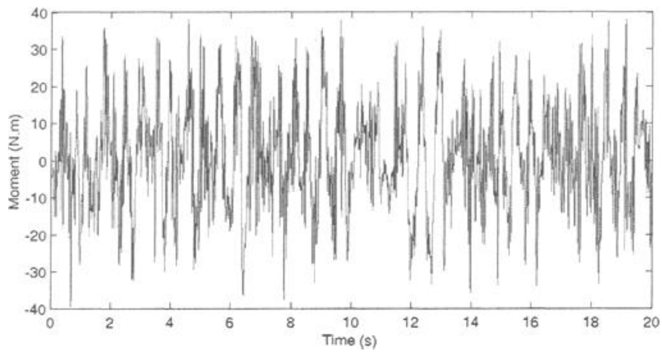

FIG. 2 *Load sequence of the signal applied to the specimens, in plane bending, in torsion, and in combined plane bending and torsion.*

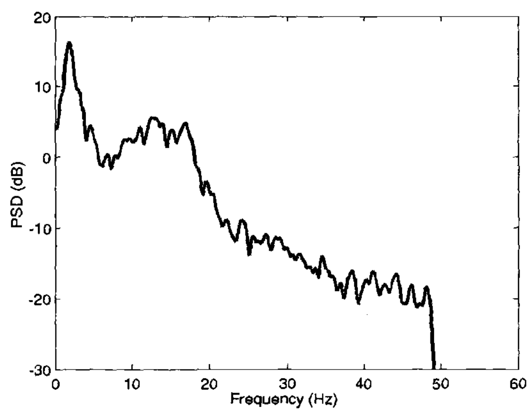

FIG. 3 *Power Spectral Density (PSD) of the signal applied to the specimens, in plane bending, in torsion, and in combined plane bending and torsion.*

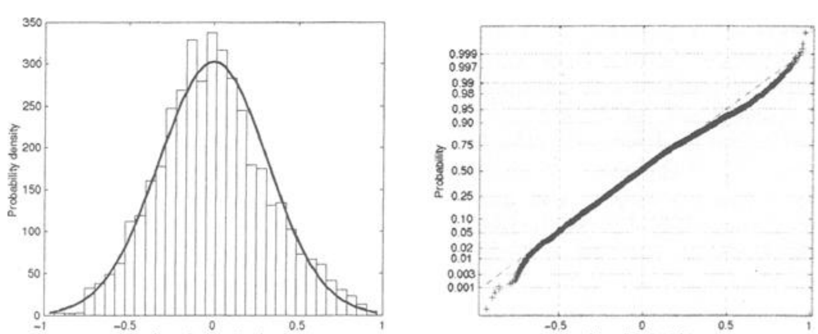

FIG. 4 *Probability density (on the left – dark line is a theoretical gaussian distribution) and probability repartition of the normalized load sequence (on the right).*

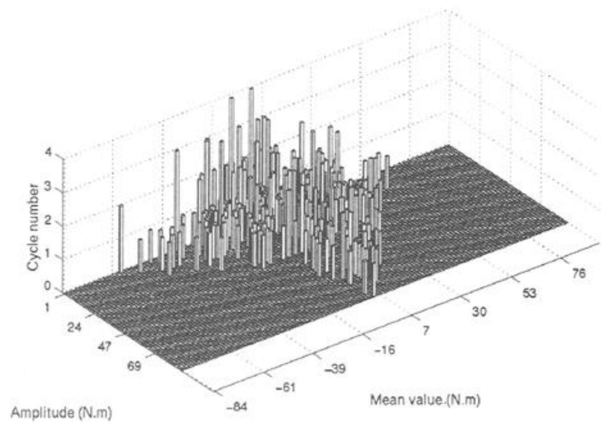

FIG. 5 *Rainflow cycle number versus mean and amplitude moment values (torsion case).*

Two types of fatigue tests under combined loadings were done. First, the same loading sequence (Fig. 2) was applied simultaneously in bending and in torsion with different ranges. The bending and torsion moments were synchronous. Second, the bending and torsion moments follow the same loading sequence but out of synchronism.

Two different de-synchronisms between each loading were tested. For each case the maximum nominal stresses (elastic stresses) are the same because tests were load controlled. The local maximum and minimum stresses on all the sequence are given in Table 1 with the root mean square value of the normal and shear stresses. Maximum and minimum stresses were computed with an elastic-plastic finite element analysis [12].

TABLE 1 *Loading conditions (stresses in MPa).*

Loading	$C_{Mt,Mb}$	σ_{max}	τ_{max}	σ_{min}	τ_{min}	σ_{RMS}	τ_{RMS}
Torsion		0	254	0	-231	0	82
Plane bending		363	0	-313	0	130	0
Pl. bend. + To	0.04	240	186	-248	-172	90	56
Pl. bend + To	0.62	240	186	-248	-172	90	56
Pl. bend + To	0.94	225	167	-233	-147	90	56

To characterize the load desynchronism between *Mt* and *Mb*, the correlation factor, $C_{Mt,Mb}$, was computed for the complete sequence (1).

$$C_{Mt,Mb} = \frac{\operatorname{cov}(Mt,Mb)}{S_{Mt},S_{Mb}} \tag{1}$$

where cov(*Mt,Mf*) is the covariance of the torsion moment *Mt* and the bending moment *Mb*. S_{Mb} and S_{Mt} are, respectively, the standard deviation of *Mb* and *Mt*. When $C_{Mt,Mb}$ is equal to 1, the two loads are synchronous, there is a perfect correlation between them, and the load path is proportional; when $C_{Mt,Mb}$ is equal to 0, there is no correlation between *Mt* and *Mb*. Figure 6 shows the different load paths corresponding to the multiaxial loadings applied to the specimens.

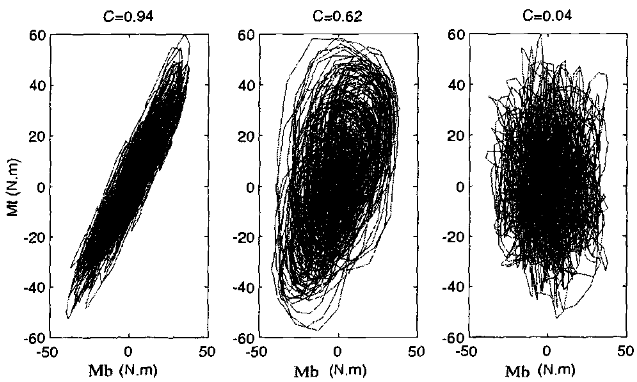

FIG. 6 *Load paths applied on the specimens in combined bending and torsion with different correlation factors $C_{Mt,Mb}$ (noted C).*

Fatigue Test Results

The fatigue test results are given in Table 2. $Nf_{0.5}$ is the median fatigue life, $Nf_{0.16}$ and $Nf_{0.84}$ are, respectively, the fatigue lives for a failure probability of 0.16 and 0.84. The number of specimens is different because test time was very long.

TABLE 2 *Results of the fatigue tests (Nf in number of sequences).*

Loading	$C_{Mt,Mb}$	$Nf_{0.5}$	$Nf_{0.16}$	$Nf_{0.84}$	Nb. specimen
Torsion		19 020	12 688	28 513	10
Plane bending		11 268	5 989	21 270	10
Plane bend. + To	0.04	49 760	21 782	113 677	4
Plane bend + To	0.62	9 587	3 630	25 322	7
Plane bend + To	0.94	16 496	6 269	43 406	8

Life Calculation Method Analysis and Discussion

Brief Literature Review

At present, the main fatigue models presented in literature are based on critical plane approaches. Nevertheless, regarding all the different proposals, the choice of a particular method is not always evident. Models have to be chosen depending on both the material and the observed failure mode. Socie's works on different steels [7] also underlines that the cracking mode may be dependent on the fatigue regime. Nowadays it is usually accepted that for ductile steels, fatigue cracks initiate along the persistent slip bands (local plasticity phenomenon) generated by local shear stress. On the other hand, for brittle materials, crack initiation phase is very short, and the more adapted criteria are based on the maximum tensile stress [13,14]. To take into account all the material behavior, many authors usually propose using a combination of shear and tensile stresses or strains calculated on a critical plane. Different criteria are tested hereafter:

- a strain based one developed for low cycle fatigue (LCF) regime
- stress based approaches proposed for high cycle fatigue (HCF) regime
- a stress-strain one to predict life whatever the regime is

In the following models, except for the Morel's one, the damage parameter used has been proposed originally for cyclic loading, then used by some authors for variable amplitude multiaxial loading [4].

Fatemi and Socie's Model [2 4]—When fatigue crack initiation is dominated by plastic shear strains, these authors recommend the use of the FS model (2). For each material plane oriented by the unit normal vector $\vec{n}$, the cycle counting method is applied on two variables: the shear strains $\varepsilon_{x'n}(t)$ and $\varepsilon_{y'n}(t)$ (see Fig. A.1 in the Appendix: coordinate system definition).

$$\gamma_a\left(1+k_1\,\sigma_{n,\max}/\sigma_y\right)=\frac{\tau_f{}'}{G}\left(2N_f\right)^{b0}+\gamma_f'\left(2N_f\right)^{c0} \tag{2}$$

The right-hand side of Eq 2 is the description of the strain-life Manson-Coffin curve in torsion. The term on the left-hand side represents the damage parameter on the plane experiencing the largest range of the shear strain (critical plane). Finally, life is computed on the critical plane where the total damage is maximum. In this term, k_1 is a material parameter identified by fitting uniaxial against pure torsion fatigue data. This parameter is varying with finite life N_f. When the strain-life Manson-Coffin curve is not known in torsion, FS propose to approximate this curve from the tensile strain-life curve [2].

Smith, Watson, and Topper's Model (SWT) [1]—This model was proposed for the first time in 1974 to take into account the mean stress effect on the tensile fatigue strength. Recently, Socie observed [7] that short fatigue cracks grow on the plane perpendicular to the maximum principal stress and strain (Mode I). He recommends using the SWT damage parameter, $\varepsilon_{n,a}\sigma_{n,max}$ (3) calculated on the maximum normal strain plane. For each material plane, the cycle counting method is applied on the normal strain $\varepsilon_n(t)$ (see Fig. A.1 in the Appendix). The critical plane is the plane where the damage is maximum (total Miner sum is maximum).

$$\varepsilon_{n,a}\sigma_{n,\max}=\frac{\sigma_f{}'^2}{E}\left(2N_f\right)^{2b}+\sigma'_f\,\varepsilon'_f\left(2N_f\right)^{b+c} \tag{3}$$

This criterion, which does not express any influence of the shear stress on life, is more adapted to brittle materials. For a finite life N_f, the ratio between the tensile and torsional fatigue limits is constant whatever the material is and equal to $(1+\nu)^{0.5}$, which corresponds quite well to the GGG40 and GGG60 cast irons [13,14] and the studied one.

Socie's Proposal for HCF Region [7]—According to the previous author for HCF and a ductile material, most of the fatigue life is consumed by crack initiation on planes where the shear stress amplitude is maximum. In this case, Socie proposes the stress based approach (4). The cycle counting algorithm is applied for each material plane on both the shear stresses $\tau_{x'n}(t)$

and $\tau_{y'n}(t)$. For each one of these variables, the critical plane is that experiencing the largest range of the corresponding shear stress. Life is finally computed on the critical plane where the total damage is maximum.

$$\tau_a + k_2 \sigma_{n,\max} = \tau_f'(2N_f)^{b0} \tag{4}$$

The right-hand side of Eq 4 is the elastic part of the strain-life. The terms of the left-hand side represent the damage parameters defined on the plane experiencing the largest range of the cyclic shear stress. k_2 is a material parameter identified by fitting Eq 4 with tension and torsion fatigue data.

Wang and Brown's Model [5,6]—Wang and Brown developed a model restricted first to LCF and MCF according to the hypothesis that fatigue crack growth is controlled by the maximum shear strain with an important additional role of the normal strain excursion over one reversal of the shear strain acting on the plane where the shear strain is maximum. This proposal was extended to HCF (5) by taking into account the mean stress effect on fatigue lifetime by using the Morrow correction. The cycle counting algorithm is applied for each material plane on both the shear stresses $\varepsilon_{x'n}(t)$ and $\varepsilon_{y'n}(t)$. For each one of these variables, the critical plane is this experiencing the largest range of the corresponding shear strain. Life is finally computed on the critical plane where the total damage is maximum.

$$\gamma_a + S.\delta\varepsilon_n = (1+\upsilon_e + S(1-\upsilon_e))\frac{\sigma'_f - 2\sigma_{n,mean}}{E}(2N_f)^b + (1+\upsilon_p + S(1-\upsilon_p))\varepsilon'_f(2N_f)^c \tag{5}$$

$\delta\varepsilon_n$ is the normal strain excursion between two turning points (consecutive extrema) of the shear strain versus time acting on the maximum shear strain plane. S is a material parameter identified by fitting tension against torsion fatigue data.

Morel Approach [8,9]—Morel developed a model for polycrystalline metals in HCF based on the accumulation of mesoscopic plastic strain. He assumes that crack initiation occurs by failure of the most stressed grains along the plane experiencing the maximum value of the parameter $T_{\sigma,RMS}$ defined by (6). This author shows that this quantity is proportional to an upper bound value of the cumulated mesoscopic plastic strain.

$$T_{\sigma,RMS}(\theta,\phi) = \sqrt{\int_0^{2\pi} T^2{}_{RMS}(\theta,\phi,\psi)d\psi} \tag{6}$$

$T_{\sigma,RMS}$ is the root mean square of the macroscopic resolved shear stress amplitude acting on a line determined by the angle ψ from fixed axis in the plane defined by its angles θ and ϕ [7]. According to the author, the number of cycles to crack initiation Nf follows the analytical Eq 7.

$$N_f = p\ln\left(\frac{\tau_a}{\tau_a - \tau_{\lim}}\right) + q\left(\frac{\tau_{\lim}}{\tau_a - \tau_{\lim}}\right) - \frac{r}{\tau_a} \tag{7}$$

In this equation p, q, and r are functions of the hardening and softening material parameters, assuming that the behavior of each grain of the material can be described by a three phases law (hardening, saturation, and softening). They can be identified by fitting an S-N curve or following the procedure described in [9]. τ_a is the amplitude of the macroscopic resolved shear stress on the critical plane. τ_{lim} is the generalized fatigue limit depending on the loading and two endurance limits [9]. Note that for the Morel method, the damage accumulation is done step by step, so calculated life is sensitive to the order of the stress levels.

Life Calculation Procedure Used in This Study [12]

In the present paper, the material parameters k_1 and k_2 are the mean values of these parameters for life varying between 10^5 and 10^6 cycles. Kim and Park [15] observed for different materials that these values are varying with the lifetime and may influence the predictions. Thus, the method to identify them also could have a non-negligible role.

Strain and stress histories are computed from the loading history (bending and torsion moments versus time) by using an elastic-plastic finite element analysis, with the hypothesis that the material (EN GJS 800-2) follows an isotropic hardening rule. Then, on the cycle counting variable of each model, the rainflow cycle counting method was used to extract the cycles from the stress or strain time history. For each extracted cycle i, the elementary damage d_i (according to each author) is calculated and accumulated by using the Palmgren-Miner rule. This damage parameter also is computed on each material plane $P_{\vec{n}}$, oriented by the unit normal vector $\vec{n}$, in order to look for the critical plane $P_{\vec{n}_c}$, which depends on the method. Damage is accumulated by using the same law, with the hypothesis $D = \Sigma_i d_i = 1$ when the fatigue crack initiates. The Morel calculation method was applied using the step by step damage accumulation according to its author.

Comparison Between Predictions and Experiments

As illustrated in Fig. 7, prediction methods (Table 3) seem to be very sensitive to the loading path, especially for the very low correlation factor: $C = 0.04$. The ratios between simulated and experimental life reach the value of 34. Indeed, the predictions are inside the following intervals:

- SWT: Npred $\in$ [Nexp/1.1; 7.7 Nexp],
- WB: Npred $\in$ [Nexp/34.6; 4.3 Nexp],
- So: Npred $\in$ [Nexp/5.3; 16.2 Nexp].
- FS: Npred $\in$ [Nexp/4.5; 7.1 Nexp]
- M: Npred $\in$ [Nexp/1.7; 5.5 Nexp]

For any non-proportional loading tests, the errors are higher than a factor of two, either in the safety area or in the unsafe one. This may be explained by the fact that all the tested methods were mainly developed for ductile materials, while the spheroidal graphite cast iron EN GJS 800-2 is not ductile. Wang-Brown and Fatemi-Socie give correct predictions, but they are much more scattered than Morel's proposal, whose predictions for the tested material with our non-proportional fatigue test conditions are less scattered compared with the experiments. Its predictions are inside the smallest interval [Nexp/1.7; 5.5 Nexp]. For a general point of view, the main predicted lives are longer than experimental lifetimes. This fact is often observed in the literature [13]. To correct this, Sonsino et al. [16] propose to use a damage parameter to crack initiation D (total Miner sum), smaller than 1.

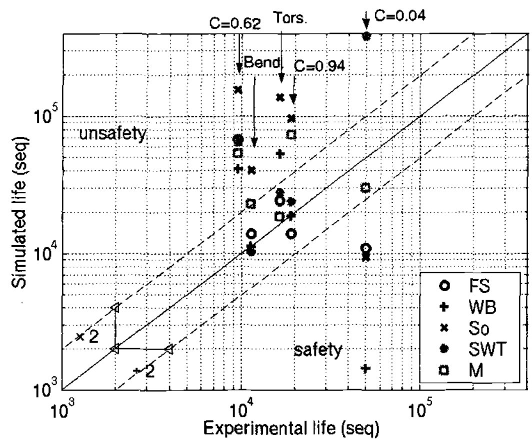

FIG. 7 *Comparison between median experimental lives and simulated lives.*

Table 3 *Simulation results (Nf in number of sequences, SWT = Smith-Watson-Topper, FS = Fatemi-Socie, WB = Wang-Brown, So = Socie HCF, M = Morel).*

Loading	$C_{Mt,Mb}$	SWT	FS	WB	M	So	$Nf_{0.5}$
Torsion		23 965	14 066	18 830	73 408	96 308	19 020
Plane bending		10 297	14 050	11 180	22 797	40 403	11 268
Plane bend. + To	0.04	380 891	11 019	1 438	29 946	9 397	49 760
Plane bend + To	0.62	64 710	67 650	41 016	53 070	155 177	9 587
Plane bend + To	0.94	27 693	24 333	53 309	18 492	137 216	16 496

Effect of the Correlation Factor on Life

Figure 8 shows the experimental lives and the standard deviation of the experimental life (with lognormal distribution hypothesis) for our different fatigue tests under combined loadings. The number of tested specimens is indicated in brackets. According to this figure and due to the scatter of experimental lives (see standard deviation), the influence of the correlation factor on life is low for this material and our tests. Nevertheless, a synchronism shift seems to improve fatigue strength (around a median life factor of five between tests where C = 0.04, and C = 0.94). This observation also has been done on cast iron by Grubrisic [14] and Palin-Luc [10] under sinusoidal loading conditions. For the studied material, under constant amplitude multiaxial fatigue tests (bending and torsion), the phase shift effect on the fatigue limit improves the fatigue strength, but only 7 % at 10^6 cycles [17]. Shift of phase influence is often discussed in literature. For Sonsino, it is dependent on both the type of test (load or strain controlled) [18] and the material [19]: for ductile materials (structural steels), the shift of phase reduces the fatigue strength; semi-ductile materials (forged aluminium, cast steels) are not sensitive to the shift of phase, and the phase shift improves the fatigue strength of brittle materials (cast aluminium, cast iron, sintered steel).

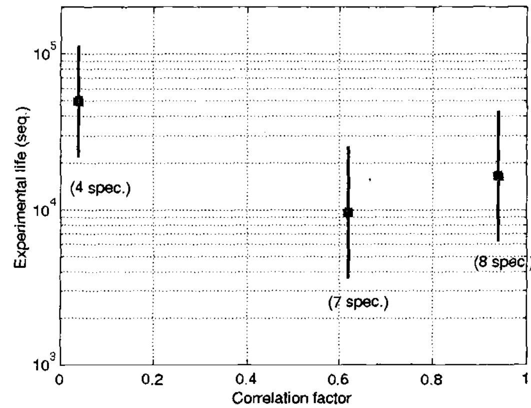

FIG. 8 *Experimental life (in sequences) versus the correlation factor for fatigue tests in combined bending and torsion; 68 % of the possible lives are in the interval illustrated by the vertical straight lines (standard deviation).*

One reason for this low influence is proposed. The material used for machining the specimens is not completely brittle. Furthermore, fatigue tests were carried out under load control: that means that nominal stresses were controlled for each test, but local stresses were different. Elastic-plastic finite element analysis shows that local small plastic strains occurred in the specimens loaded under synchronous loadings. For synchronous combined bending and torsion tests ($C = 0.94$), the maximum Von Mises equivalent stress was equal to 391 MPa. This is higher than the corresponding value for uncorrelated tests ($C = 0.04$), for which the maximum Von Mises equivalent stress was 333 MPa. In this last case, total strains were smaller than under proportional fatigue tests ($C = 0.94$); thus, life may be a little bit longer than under synchronous tests.

Conclusion and Prospects

Random multiaxial fatigue tests (with stress controlled conditions) carried out on smooth specimens made of the EN GJS 800-2 spheroidal graphite cast iron show a low influence on the median life of the correlation factor between the bending and torsion loadings. This effect is not significant in middle high cycle fatigue if the scatter of experiments is considered. Local small plastic strains are pointed out to explain this. Comparison between fatigue data and simulations made with five fatigue life calculation methods shows that their predictions are good for proportional loadings, but there are large errors for non-proportional loadings, probably because most of the methods were proposed for ductile materials. Morel's proposal gives the best predictions for this SG cast iron and these tests. According to the fact that most of the predictions are unsafe, it seems prudent to use a damage parameter lower than 1 to predict crack initiation in design department. This point is in agreement with Sonsino's [16] conclusions.

The knowledge of the material behavior under non-proportional load paths always remains an open question, and research must progress in this way. Future work also must be done to develop a life prediction method adapted to non-proportional loading case.

References

[1] Smith, J., Watson, P., and Topper, T., "A Stress Strain Function for Fatigue of Metals," *Journal of Materials* (JMLSA), 4, No. 5, 1970, pp. 293 298.

[2] Fatemi, A. and Socie, D., "A Critical Plane Approach to Multiaxial Fatigue Damage Including Out-of-Phase Loading," *Fatigue and Fracture of Engineering Materials and Structures*, 11, No. 3, 1988, pp. 149 165.

[3] Bannantine, J., "A Variable Amplitude Life Prediction Method," Ph.D. thesis, University of Illinois, Urbana-Champaign, 1989, p. 270.

[4] Bannantine, J. and Socie, D., "A Variable Amplitude Multiaxial Life Prediction Method," *Fatigue under Biaxial and Multiaxial Loading, ESIS 10*, K. Kussmaul, D. L. McDiarmid, and D.F. Socie, Eds., Mechanical Engineering Publication, London, 1991, pp. 35 51.

[5] Wang, C. and Brown, M., "Multiaxial Random Load Fatigue: Life Predictions Techniques and Experiments," *Multiaxial Fatigue and Design, ESIS 21*, A. Pineau and G. Cailletaud, Eds., Mechanical Engineering Publications, London, 1996, pp. 513 527.

[6] Wang, C. and Brown, M., "Life Prediction Techniques for Variable Amplitude Multiaxial Fatigue. Part I: Theories," *Journal of Engineering Materials and Technology*, 118, 1996, pp. 367 370.

[7] Socie, D., "Critical Plane Approaches for Multiaxial Fatigue Damage Assesment," *Advances in Multiaxial Fatigue, ASTM STP 1191*, D. L. McDowell and R. Ellis, Eds., ASTM International, West Conshohocken, PA, 1993, pp. 7 36.

[8] Morel, F., "A Critical Plane Approach for Life Prediction of High Cycle Fatigue under Multiaxial Variable Amplitude Loading," *International Journal of Fatigue*, 22, 2000, pp. 101 119.

[9] Morel, F., "Fatigue Multiaxiale Sous Chargement d'Amplitude Variable," Ph.D. thesis, ENSMA, Poitiers, France, 1996, p. 210.

[10] Palin-Luc, T., Lasserre, S., and Bérard, J-Y., "Experimental Investigation on the Significance of the Conventional Endurance Limit of a Spheroidal Graphite Cast Iron," *Fatigue and Fracture of Engineering Materials and Structures*, 21, 1998, pp. 191 200.

[11] Palin-Luc, T. and Lasserre, S., "Multiaxial Fatigue Testing Machine Under Variable Amplitude Loading of Bending and Torsion," *Recent Advances in Experimental Mechanics*, J. F. Silva Gomes et al., Eds., A. A. Balkema, Rotterdam, 1994, pp. 965 970.

[12] Banvillet, A., "Prévision de Durée de Vie en Fatigue Multiaxiale Sous Chargements Réels: Vers des Essais Accélérés," Ph.D. Thesis, ENSAM, Bordeaux, France, 2001, p 204.

[13] Lagoda, T., Macha, E., Nieslony, A., and Müller, A., "Fatigue Life of Cast Irons GGG40, GGG60 and GTS45 Under Combined Random Tension with Torsion," *Fracture Mechanics: Application and challenges*, M. E. M. Fuentes and A. Martin-Meizoso, Eds., ECF13, San Sebastian, Spain, 2000, on CD-Rom.

[14] Grubisic, V., "Festigkeitsverhalten von Sphärogub bei Kombinierter Statischer und Dynamischer Mehrachsiger Beanspruchung," Tech. Rep., LBF-Fraunhofer Institute, Darmstadt, Bericht Nr. FB-149, 1979.

[15] Kim, K. S. and Park, J. C., "Shear Strain Based Multiaxial Fatigue Parameters Applied to Variable Amplitude Loading," *International Journal of Fatigue*, 21, 1999, pp. 475 483.

[16] Sonsino, C. M., Kaufman H., and Grubisic, V., "Transferability of Material Data for the Example of a Randomly Loaded Truck Stub Axle," *SAE Tech. paper series*, 970708, 1997, pp. 1 22.

[17] Palin-Luc, T. and Lasserre, S., "An Energy Based Criterion for High Cycle Multiaxial Fatigue," *European Journal of Mechanics, A/Solids*, 17, No. 2, 1998, pp. 237 251.
[18] Sonsino, C. M., "Influence of Load and Deformation-Controlled Multiaxial Tests on Fatigue Life to Crack Initiation," *International Journal of Fatigue*, 23, 2001, pp. 159 167.
[19] Sonsino, C. M. and Kueppers, M., "Fatigue Behavior of Welded Aluminium Under Multiaxial Loading," In: *Proceedings of the 6th International Conference on Biaxial/Multiaxial Fatigue & Fracture*, M. M. de Freitas, Ed., ESIS, Lisboa, Portugal, 2001, pp. 57 64.

Appendix

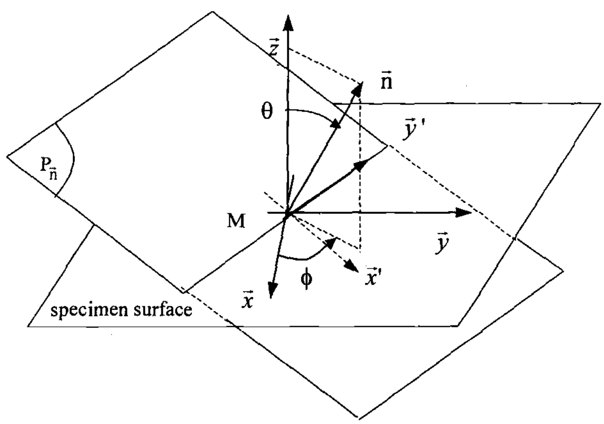

$(\vec{x},\vec{y},\vec{z})$ cartesian coordinates system linked with the specimen surface.
$(\vec{x}',\vec{y}',\vec{n})$ cartesian coordinates system linked with de plane $P_{\vec{n}}$ orientated by $\vec{n}$.

FIG. A.1 *Coordinate systems used to define the unit normal vector* $\vec{n}$ *orientating each material plane* $P_{\vec{n}}$ *at the point M on the surface of the specimen.*

Author Index

Subject Index